Application of diamond nanomaterials in catalysis

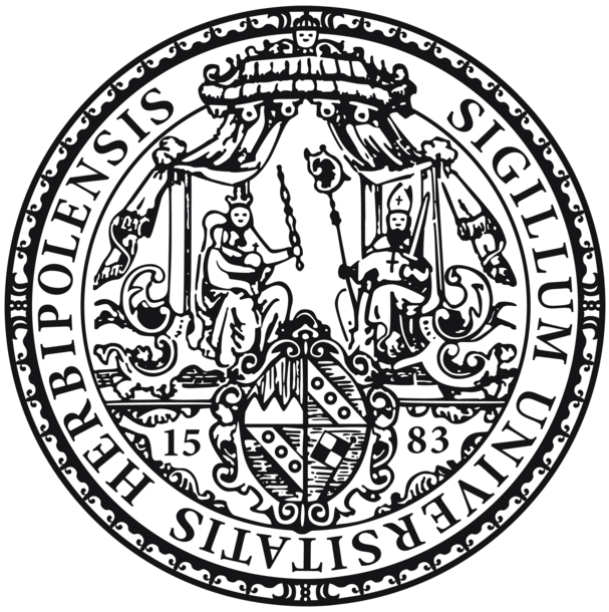

Dissertation zur Erlangung des naturwissenschaftlichen Doktorgrades
der Julius-Maximilians-Universität Würzburg

vorgelegt von

Benjamin Kiendl

aus Feuchtwangen

Würzburg 2019

Eingereicht bei der Fakultät für Chemie und Pharmazie am

14.02.2019

Gutachter der schriftlichen Arbeit

1. Gutachter: Prof. Dr. Anke Krüger

2. Gutachter: Jun.-Prof. Dr. Ann-Christin Pöppler

Prüfer des öffentlichen Promotionskolloquiums

1. Prüfer: Prof. Dr. Anke Krüger

2. Prüfer: Jun.-Prof. Dr. Ann-Christin Pöppler

3. Prüfer: Prof. Dr. Ulrich Schatzschneider

Datum des öffentlichen Promotionskolloquiums:

09.04.2019

Doktorurkunde ausgehändigt am

_____

Once you stop learning, you start dying.

Albert Einstein

Die vorliegende Arbeit wurde im Zeitraum von Dezember 2014 bis Dezember 2018 am Institut für Organische Chemie der Julius-Maximilians-Universität Würzburg angefertigt.

Teile dieser Arbeit wurden bereits veröffentlicht in:

S. Choudhury, B. Kiendl, J. Ren, F. Gao, P. Knittel, C. Nebel, A. Venerosy, H. Girard, J.-C. Arnault, A. Krueger, K. Larsson, T. Petit, ,,Combining Nanostructuration with Boron Doping to Alter Sub-Bandgap Acceptor States in Diamond Materials", *J. Mater. Chem. A* **2018**, *6*, 16645-16654.

Weitere Veröffentlichungen:

M.S. Schuurman, J. Giegerich, K. Pachner, D. Lang, B. Kiendl, R. MacDonell, A. Krueger, I. Fischer, ,,The Photodissociation Dynamics of Cyclopropenylidene, c-C_3H_2", *Chem. Eur. J.* **2015**, *21*, 14486-14495.

F. Holzmeier, I. Fischer, B. Kiendl, A. Krueger, A. Bodi, P. Hemberger, ,,On the Absolute Photoionization Cross Section and Dissociative Photoionization of Cyclopropenylidene", *Phys. Chem. Chem. Phys.* **2016**, *18,* 9240-9247.

Danksagung

An erster Stelle danke ich Frau Prof. Dr. Anke Krüger für die Möglichkeit, diese Arbeit in ihrer Forschungsgruppe im Rahmen des EU-Projekts DIACAT anzufertigen. Die gebotenen Freiheiten, die Projektthematik, sowie der ständige Austausch mit zahlreichen Kooperationspartnern weckten vom ersten Moment an mein Interesse.

Mein Dank geht auch an die Mitarbeiter des Instituts für Organische Chemie und der gesamten Fakultät. Dazu gehören Dr. Michael Büchner aus der Massenspektrometrie, Dr. Vladimir Stepanenko, der ,,Retter in Not“ am SEM, Michael Ramold und Glasbläser Jonathan Landeck, die beide meine Ideen stets erfolgreich in die Tat umsetzen konnten, sowie Anette Krug, Christiana Toussaint und Eleonore Klaus, die den Versand meiner rund 100 Päckchen und Briefe stets zuverlässig in die Wege geleitet haben. Mädels, der Süßigkeitentopf ist ein voller Erfolg!

Bei meinen Kooperationspartnern an der Universität Würzburg, Prof. Dr. Maik Finze, Dr. Michael Drisch, Fabian Keppner, Martin Stübinger, Philipp Scheiderer, Prof. Dr. Jens Pflaum und Jun.-Prof. Dr. Ann-Christin Pöppler möchte ich mich für die hervorragende Zusammenarbeit bedanken und bei Jens und Ann-Christin besonders für die intensive Besprechung/Analyse sämtlicher Ergebnisse. Gleiches gilt für die Kooperationspartner im erweiterten Rahmen des DIACAT-Projekts: Dr. Elke Neu und Michel Challier von der Universität Saarbrücken, Dr. Dmitry Volkov von der Universität Moskau, Prof. Dr. Geraldine Masson und Guillaume Levitre vom ICSN in Gif-Sur-Yvette, Dr. Julien Barjon und Dr. Solange Temgoua vom GEMAC, Universität Versailles, sowie Prof. Dr. Ken Haenen und Dr. Sien Drijkoningen von der Universität Hasselt.

Innerhalb des DIACAT-Projekts danke ich Reka Török und Martin Dietz für die gelungene Organisation sämtlicher Treffen. Dr. Fang Gao und Dr. Peter Knittel vom IAF in Freiburg für zahlreiche Diamantproben sowie interessante Grundsatz-diskussionen mit und ohne Bier. Dr. Jean-Charles Arnault, Dr. Hugues Girard und Amélie Venerosy von CEA List, Gif-Sur-Yvette für sämtliche XPS-Messungen und Probenbehandlungen. Prof. Dr. Karin Larsson von der Universität Uppsala für unzählige theoretische Berechnungen und Diskussion der Ergebnisse. Besonderer Dank geht an die Partner vom HZB, Dr. Tristan Petit, Dr. Franziska Buchner und allen voran Sneha Choudhury, für die Vermessung, Interpretation und Diskussion einer Unmenge an Proben, durch die meine Arbeit ein enormes Maß an Qualität gewinnt. Ganz besonderer Dank geht an Prof. Dr. John Foord und Dr. Emina Hadzifejzovic von der Universität Oxford. Nicht nur für die durchgeführten Experimente, sondern

insbesondere für ihr stetiges Bestreben, ihre Erfahrung jederzeit mit einem jungen Doktoranden zu teilen.

In der Arbeitsgruppe Krüger geht mein Dank an die ehemaligen und aktuellen Mitarbeiter, die mich während meiner Arbeit begleitet haben. Dr. Daniel Lang und Dr. Peter Buschmann für die wissenschaftlichen Diskussionen, Dr. Steffen Heyer, Stefan Wachtler und besonders meinem langjährigen ,,Büropartner“ Andreas Muzha für wertvolle Tipps in der Diamantchemie und die Einweisung in zahlreiche Gerätschaften. Danke Andi für viele anregende Diskussionen! Rachel Buschmann für ihre ruhige, Art und Zuverlässigkeit und Dr. Sarah Schweeberg für den nötigen Schwung in der Gruppe. Der ,,neuen“ Generation um Julia Puck, Sebastian Vettermann und Johannes Ackermann danke ich für die zahlreichen, lustigen Mensabesuche. Die Mensa gibt, die Mensa nimmt! Meinem Abzugspartner Viktor Merz danke ich für das stetige Interesse an meiner Arbeit, seiner Bereitschaft zum ,,Ausprobieren“ und seiner Vorliebe für ,,Schabernack“. Ich bin zudem all denjenigen, die mich im Zuge von Ausbildungen, Abschlussarbeiten oder Praktika unter meiner Betreuung unterstützt haben, zu besonderem Dank verpflichtet. Das sind Christian Saalfrank, Florian Pinzner, Tobias Brückner, Julian Fink, Christian Gentzsch, Johannes Krebs, Christine Heinz, Lukas Englert, Tamara Heinrich, Matthias Maier, Johannes Lang, Martin Stang und Daniel Gillung. Aapo Väänänen danke ich für seine Gastfreundschaft, seine gediegene, finnische Art und seine Trinkfestigkeit. Carsten und Benni für die spaßigen Mensarunden und Heiko für seine extreme Hilfsbereitschaft.

Meinem langjährigen Schulfreund und Weltenbummler Oli danke ich für einige spannende Urlaubsreisen sowie dem intensiven Korrekturlesen meiner Arbeit.

Mein größter Dank gilt meiner Familie, insbesondere meinen Eltern Hermine und Heinrich, ohne deren Unterstützung ich heute nicht da stehen würde, wo ich bin.

Meiner langjährigen Freundin Eileen möchte ich für ihr Verständnis, ihre Unterstützung und Geduld, aber allen voran für ihre wohltuende Liebe danken. Ihre humorvolle Art in Kombination mit unseren zahlreichen Aktivitäten haben mir oft gezeigt, worum es im Leben wirklich geht.

Table of contents

1. Introduction

1.1 The versatile role of carbon dioxide

According to the annual statistical review of world energy from British Petroleum, in 2017, the global carbon dioxide (CO_2) emission from energy has, for the first time since the stagnating years 2014-2016, grown by 1.6%, faster than the 10-year average of 1.3%.[1] Despite CO_2 being a crucial part of life on earth as the main starting material of photosynthesis and the natural greenhouse gas responsible for heating up earth to "working temperature", the increasing production of CO_2 and consumption of fossil fuels by mankind interferes verifiably with the natural carbon cycle.[2] As a result, a significantly improved sustainability can only be achieved if the excessively produced CO_2 can be revalorized and reintroduced in the chemical carbon cycle.[3] In the past, it has been a respectable conception to use exhaust and waste gas for the production of new products, while, nowadays, it turns into a necessity to deal with the ever increasing output of CO_2. So far, there is no viable and scalable technology to deal with this. The challenge starts with carbon capture and storage (CCS).[4] Although, CO_2 is essentially an inexhaustible resource, it has to be captured, cleaned and stored or concentrated as a feedstock for further use.[5] The CO_2 reduction via energy input from homo-/heterogeneous electro- or photocatalysis offers numerous approaches to convert the greenhouse gas into fine chemicals that could either be used directly as fuel (MeOH, EtOH, methane) or be the starting point for more advanced synthetic procedures (CO, formic or acetic acid, MeOH).[6,7] Here, the greatest challenge is to increase the product formation from the nano- or micromolar range by several orders of magnitude. Additionally, the improvement of the cost effectiveness will play an increasingly important role. Several programs established in the last years, such as "CO_2plus" from the German Federal Ministry of Education and Research or the Horizon 2020 framework programme from the European Commission, focus intensively on the investigation to use CO_2 as a reasonable resource.[8] The Horizon 2020 project DIACAT (no. 665085), investigating diamond materials for the photocatalytic conversion of CO_2 to fine chemicals and fuels using visible light, provides the basis for the upcoming experiments, results and discussions in this thesis.

1.2 Synthesis and properties of (un)doped diamond materials

In general, two different kinds of diamond materials are of interest to be applied in the photocatalytic conversion of CO_2 to fine chemicals. The fundamentally different syntheses of nanodiamond (ND) particles and (un)doped diamond films applying the chemical vapor deposition (CVD) method yield materials with specific and characteristic properties.

1.2.1 Nanodiamond particles

Three processes have been established for the synthesis of nanodiamond particles: the high-pressure, high-temperature (HPHT),[9,10] the shock wave[11,12] and the detonation synthesis.[13,14] All methods, including specific properties of the particles, have been intensively described and reviewed.[15-18]

Detonation nanodiamond (DND) contains significant amounts of hydrogen, oxygen and nitrogen, which can be explained by the nitrogen-rich starting materials, trinitrotoluene (TNT) and hexogen, as well as the cooling medium water.[19] Various functional groups on the particle surface, in particular carbonyl, methyl and carboxylic acid groups, but also alcohols, ethers, esters and ketones are the result. These groups can be detected e.g. using infrared (IR) spectroscopy.[20] Roughly 5 wt.% of the carbon present in DND particles are sp^2-hybridized.[19] Beneath the inhomogeneous surface, the ~83 wt.% of sp^3-hybridized carbon atoms can be found in a regular, tetrahedral lattice structure.[21] Apart from applications in optoelectronics,[22-25] the particles are widely used in biomedicine[26-29] and the broad field of catalysis. The latter will be described in chapter 1.5.

1.2.2 CVD diamond materials

The CVD growth of diamond is a well understood process and has already been subject of several detailed reviews,[30,31] focusing on the growth meachnism,[32,33] the growth scaling[34] and the properties and application.[35,36] The CVD process offers valuable qualities, such as the excellent means of control leading to a defined crystal orientation, crystallite size and film thickness, as well as the ability of doping. For example, addition of nitrogen, amines or hydrogen cyanide to the hydrogen/methane mixture leads to nitrogen-doping.[37,38] The conductive properties of insulating, undoped CVD diamond films can be influenced by either p-type doping with boron or n-type doping with phosphorus.[39,40]

Adding a boron-containing precursor during growth, such as diborane[41] or trimethylborane,[42] the trivalent boron atom can be incorporated into the diamond lattice. The resulting shortage of electrons can be compensated by an electron from the valence band (VB) of diamond, which generates holes. Boron induces a shallow acceptor level close to the VB of the diamond. Low boron concentrations (10^{17} - 10^{19} atoms/cm^{-3}) result in an ~0.35 eV activation energy and semi-conducting properties. However, for a concentration > $3 \cdot 10^{20}$ atoms/cm^{-3} the conductivity reaches metallic character at room temperature by decreasing the activation energy of the acceptor level.[43] Most research recently focused on the production of B-doped nanodiamond particles and, so far, three methods, based on the milling of doped CVD material,[44] the high pressure synthesis from organic, boron-containing compounds[45] and the detonation synthesis,[46] have been investigated confirming the expected electronic properties for nanoparticles.

The incorporation of phosphorus into the diamond lattice is more challenging due to the atomic size compared to B, C or N. However, using phosphine[47] or *tert*-butylphosphine[48] as precursor, the growth of n-type doped films with phosphorus in (111),[47,49] (110)[50] or (001)[51-53] orientated films was investigated in detail during the last 20 years. The substitutional phosphorus (up to ~10^{19} atoms/cm^{-3})[54] can be detected by either electron paramagnetic resonance spectroscopy (EPR)[55-57] or phosphorus donor-related cathodoluminescence.[58-60] P-doping introduces several donor-levels at 0.1-0.8 eV below the conduction band (CB) of the diamond.[61] Highly P-doped films ($5 \cdot 10^{20}$ atoms/cm^{-3})[62] are used in Schottky diodes[63,64] and thermionic emission.[62,65] Yet, even though P-doped CVD diamond films are part of present research due to their wide application in electronics, examples for P-containing ND particles are rare. In 2016, Dolmatov *et al.* presented the first approach to fabricate P-doped nanodiamond via shock wave synthesis by adding the ammonium salt of orthophosporic acid either in aqueous solution or as solid to the explosive charge. During activation or decomposition of the related compounds at 3000-4000 K the phosphorus can be incorporated into the diamond crystal lattice.[66] The incorporation of phosphorus was indirectly proven by EPR and X-ray diffraction (XRD) spectroscopy.[67] Despite a measured P-content of 0.1-0.15 wt%, it is still unclear how the P is incooperated.[67] Additional feasible options for the production of P-doped nanoparticles include the growth of doped nanocrystallites via CVD[68] or the implantation of atoms into already existing, undoped nanoparticles.[69]

1.3 Electronic properties of diamond

Pure diamond is usually known as an extraordinarily good insulator[70] with a broad band gap of 5.47 eV.[71,72] As described in chapter 1.2, doping of diamond using boron leads to an electrically conductive material, a semi-conductor.[73,74] Commercially available, boron-doped diamond electrodes are not prone to corrosion and show a high oxygen overpotential in aqueous electrolytes. For H-terminated electrodes, a negative electron affinity (NEA)[75] is observed, which means that the vacuum level – the potential an electron has to reach to exist freely from the original solid body – lies ~1.3 eV below the CB of the diamond (Fig. 1).[71,72,76] For highly P-doped (111) electrodes, a strong electric field is required to extract carrier electrons from CB into vacuum, as the electron affinity is ~-0.1 - +0.2 eV.[77] However, H-termination leads to NEA, as similarly observed for B-doped materials.[78,79] As a consequence of NEA, electrons, which are excited to the CB via irradiation with energy-rich photons (>4.3 eV or <295 nm), diffuse to the diamond surface and can be emitted into the surrounding medium (vacuum, gaseous/liquid phase).[80]

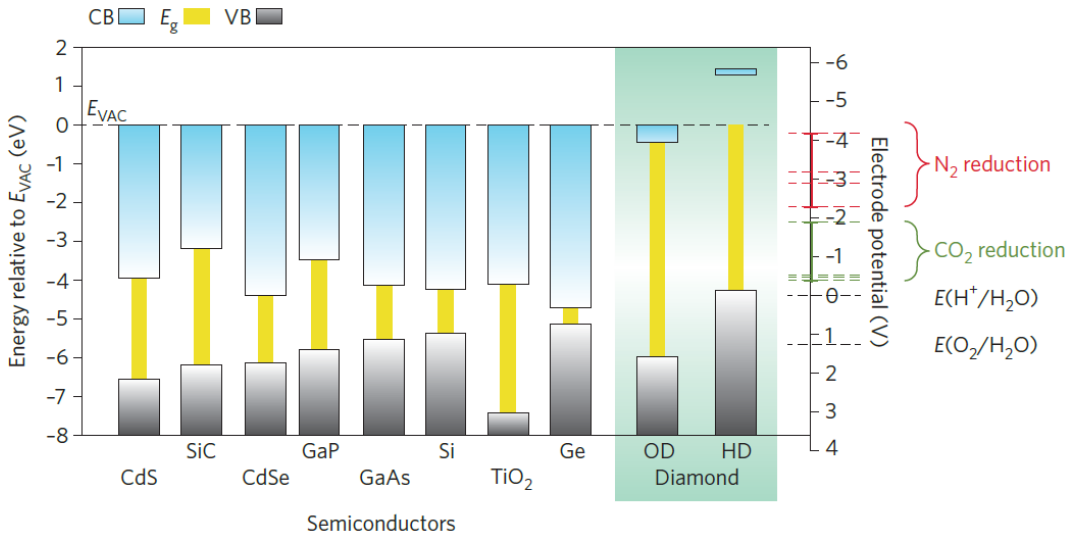

Fig. 1: Energy diagram of valence band (VB), band gap (E_g) und conduction band (CB) in relation to the vacuum level (E_{VAC}) for several metal-based semi-conductors, as well as oxygen (OD) and hydrogen (HD) terminated diamond (adapted with permission from lit.[72], copyright 2013 Macmillan Publishers Limited).

The electron emission into vacuum is associated with an insignificant barrier and has been investigated in detail.[81-83] However, the emission in liquid medium has, until now, been barely analyzed, although solvated electrons are potential reducing agents.[84] The emission is an irreversible process, generating electrons with a lifetime of

~250-300 ns.[85] These electrons enable reduction reactions, which are not practicable for other, semi-conducting photocatalysts due to their low-lying CB (Fig. 1). The shift in the band alignment of diamond as a function of surface termination can be explained by a change in dipole energy from O- to H-terminated diamond.[76] Emitted electrons from H-terminated diamond show a high reduction potential of ~-4.3 eV and are able to reduce nitrogen and CO_2. Nitrogen is reduced in the range of -4.2 V (formation of the nitrogen radical anion) to -2.3 V (ammonia)/SHE (standard hydrogen electrode). Holes in the VB of diamond, which are generated after electron emission, can be characterized using X-ray absorption and emission spectroscopy. Using a similar approach, the electronic structure of B-doped diamond films,[86] the photoemission of films in aqueous medium with the related dynamic of the solvated electrons,[85] as well as the electronic properties of dispersed nanodiamond particles have been characterized.[87]

1.4 Catalytic reduction of CO_2

From a chemical point of view, CO_2 represents a molecule, which cannot be readily converted into more reactive or energy-storage relevant hydrocarbons, in particular due to the electrochemical potential for the reduction of CO_2, which lays between -1.85 - -0.25 V/SHE.

	E^0 vs. SHE (V)
$CO_{2(g)} + e^- \longrightarrow CO_2^{\bullet -}$	-1.85
$CO_{2(g)} + H_2O_{(l)} + 2e^- \longrightarrow HCOO^-_{(aq)} + OH^-_{(aq)}$	-0.665
$CO_{2(g)} + H_2O_{(l)} + 2e^- \longrightarrow CO_{(g)} + 2\ OH^-_{(aq)}$	-0.521
$CO_{2(g)} + 3\ H_2O_{(l)} + 4e^- \longrightarrow HCOH_{(l)} + 4\ OH^-_{(aq)}$	-0.485
$CO_{2(g)} + 5\ H_2O_{(l)} + 6e^- \longrightarrow CH_3OH_{(l)} + 6\ OH^-_{(aq)}$	-0.399
$CO_{2(g)} + 6\ H_2O_{(l)} + 8e^- \longrightarrow CH_{4(g)} + 8\ OH^-_{(aq)}$	-0.246

Fig. 2: Redox potential (E^0) for the reduction of CO_2 and related compounds in aqueous media at neutral pH.

The minimal and maximal values for the redox potential represent, on one side, the one electron reduction forming the $CO_2^{\bullet -}$ radical anion (-1.85 V) and, on the other side,

the eight electron reduction yielding methane (-0.246 V, Fig. 2).[88] Additional reasons for the inertness of CO_2 include the kinetic hindrance of the reduction and the low solubility of the gas in water.[89] To overcome these obstacles, several electro- and photocatalytic methods for the conversion of CO_2 applying various materials have been presented.[90] So far, especially metal oxides have been used for this, for example zirconium oxide (ZrO_2), gallium oxide (Ga_2O_3), tantalum pentoxide (Ta_2O_5) and particularly titanium oxide (TiO_2) or titanium containing salts.[88,91] Both, doping of those metal-based catalysts with added metal-cations (e.g. Fe^{3+}, Zn^{2+}) and non-metal components (e.g. B, C, N, S) and the influence of excitation using visible light on the photocatalytic efficiency, have been intensively studied.[88] Apart from the (doped) oxides, various transition metal (TM) nanoparticles (NP) are applied in the CO_2 reduction reaction (CO_2RR).[92] Photodeposited gold NPs on TiO_x species allow the photocatalytic production of methane.[93] Palladium NPs allow the electro-hydrogenation of CO_2 yielding formate.[94] The electrocatalytic reduction forming CO using the same palladium NPs strongly depends on the size of the used NPs.[95] For transition metal NPs, the number of grain boundaries is also of interest, as it correlates directly with the reducibility. Gold NPs, which are adsorbed on carbon nanotubes, show a linear correlation, for example.[96] TM complexes and clusters also show significant activity regarding CO_2RR. The influence of the metal center on the reduction can be seen for Fe^{2+} and Co^{2+} complexes with pentadentate nitrogen ligands. In electrochemical and photocatalytic experiments, the iron complex yields formate, whereas cobalt leads to the formation of CO as main product.[97] Cu_4-clusters are able to effectively form methanol, outperforming simple Cu NPs.[98] Also, besides TM based catalysts, late main group elements, such as tin or bismuth triflate, enable the selective production of CO in combination with ionic liquids.[99] In summary, applying various (transition) metal based catalysts, the CO_2RR can be controlled to yield diverse reduction products.

An alternative to the costs, toxicity and limited resource availability of required metal compounds regarding CO_2RR is given by biocatalysis. A selective fixation of CO_2 followed by a stepwise reduction using dehydrogenases to form methanol is possible applying enzymes.[100] However, as the production and isolation of enzymes on a large scale is also associated with high costs, a cheap, anthropogenic and safe material for the specific reduction of CO_2 is needed. Here, synthetic diamond materials come into play.

1.5 Use of nanodiamond particles in catalysis

The first examples using ND powder in the field of catalysis date back to around 2000, mainly focusing on synthesis and characterization of ND based materials with minor attention to catalytic applications. However, during the last 5 years, the increase in publications illustrate the emerging interest in diamond-based nanoparticles for catalysis. This trend can in a simple way be explained by the extremely versatile use of ND, as the carbon allotrope can be directly used as catalyst itself or in composites with other carbon materials or metals.

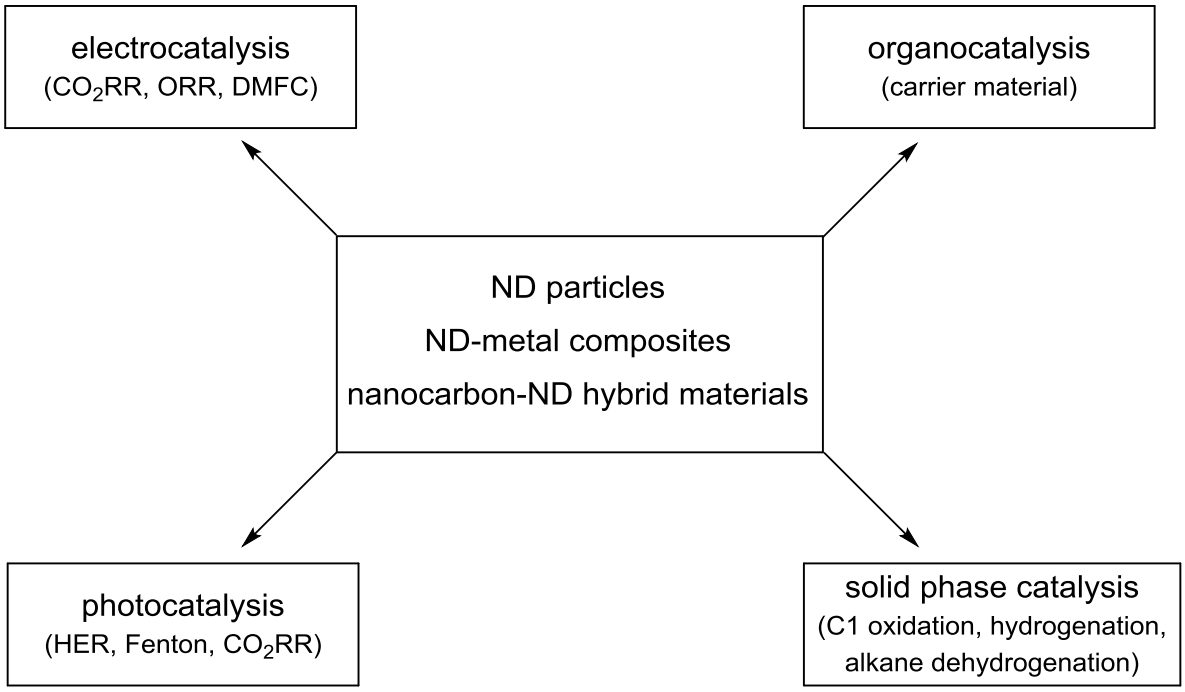

Fig. 3: Fields of catalysis for ND particles, ND-metal composites and metal-free, nanocarbon-ND hybrid materials (abbreviations will be described and discussed in the following chapters).

Numerous applications as a carrier material, e.g. in organocatalysis,[101] substantiate the benefit of the unique properties in catalysis.[101,102] Additionally, ND particles attract more and more attention in fields of electro-, photo- or solid phase catalysis (Fig. 3), where bulk diamond materials have already been utilized. The focus in the past (~2000-2012) was clearly set on ND-metal composites.[103-105] However, it changed considerably towards metal-free, nanocarbon ND-hybrid materials[106,107] or ND particles themselves, targeting a more sustainable and greener chemistry.[108,109] The catalytic properties can be controlled and adjusted by ND doping, surface modifications and functionalizations with selected molecules. ND based, metal-free catalysts help to

find cheaper alternatives for catalytic reactions that have so far only worked with the support of either expensive (e.g. Au, Pd, Pt) or toxic (e.g. Ni, Co) metals.

1.5.1 Organocatalysis

ND particles are insoluble in a great variety of solvents, which allows for a separation from reaction mixtures via centrifugation. In the field of homogeneous catalysis, this is of utmost importance for immobilized catalysts, as the separation leads to a higher efficiency regarding catalyst recycling and purification of catalysis products.[110,111] Organocatalysts, which are known for their non-toxicity, stability under standard conditions and their versatile application in asymmetric catalysis, are suitable candidates for immobilization.[110,112-114] Covalent attachment on carrier materials, like polyhedral oligomeric silsesquioxanes[115] or polymers in general,[116] requires functional groups. The copper(I) catalyzed alkyne-azide cycloaddition (CuAAC) is a commonly used procedure to attach homogeneous catalysts to various NPs.[117-119] The CuAAC reaction complies with the criteria from Sharpless *et al.* regarding a classical "Click reaction" due to its high efficiency and variability.[120] Furthermore, a fast and straightforward reaction at room temperature can be expected, which entails an insignificant formation of side-products and a simple purification of reaction products.[120] The reaction is neither water nor air sensitive, especially when the catalytically active copper(I) species is generated *in situ* by reduction of copper(II) salts.[120] As a result, 1,4-substituted triazoles are synthesized in a highly selective manner, whereas heating of the starting materials without copper catalyst always leads to a mixture of 1,4- and 1,5-regioisomers (Fig. 4).[120,121]

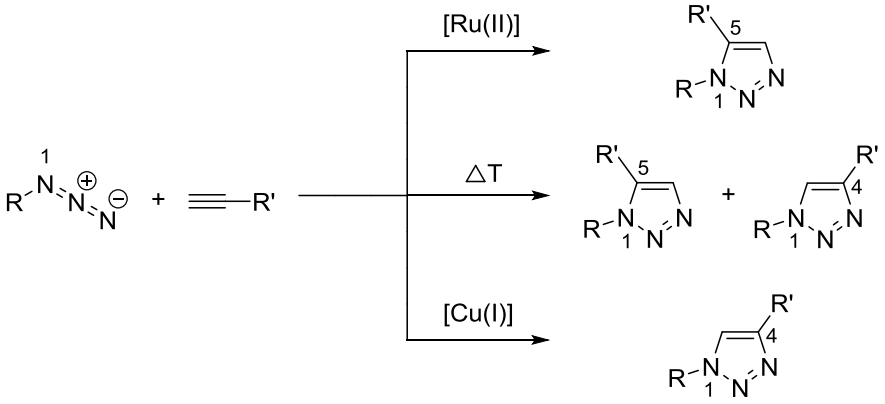

Fig. 4: Correlation of reaction conditions and regiochemistry of CuAAC reactions (R': aryl, alkyl).

Using ruthenium(II) catalysts, a selective synthesis of the 1,5-regioisomer is achievable.[122] Barras *et al.* and Meinhardt *et al.* showed in 2010 that the CuAAC

reaction is possible both with alkyne-functionalized ND particles and organic azides, as well as azide-functionalized ND particles and terminal alkynes.[117,119] However, the success of the cycloaddition depends perceptibly on the reaction conditions and the selected copper catalyst.[117,123]

As mentioned before, the CuAAC reaction is commonly used for the attachment of catalysts, such as L-Proline based organocatalysts, and several carrier materials have already been tested for their suitability.[118] L-Proline (**Pro**) was attached to polystyrene (**PS**)[124] (Fig. 5) and a imidazolidinone-based MacMillan organocatalyst was linked to both magnetic iron NPs and PS.[125] Zeitler *et al*. showed that a diarylprolinol silyl ether organocatalyst, known as Hayashi-Jørgensen catalysts (**Pro1**), could be successfully linked to methoxy polyethyleneglycol (**PEG**).[126]

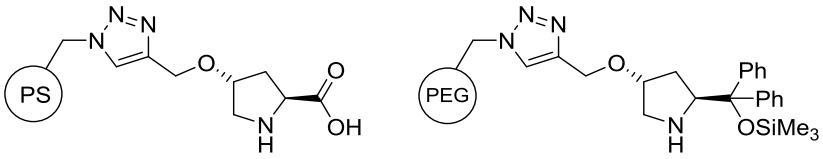

PS-Pro **PEG-Pro1**

Fig. 5: L-Proline (**Pro**) and Hayashi-Jørgensen catalysts (**Pro1**) attached to polystyrene (**PS**) and polyethyleneglycol (**PEG**) via CuAAC reaction.

Both systems yielded promising results in asymmetric enamine catalysis regarding their applicability, conversion rates, enantiomeric excess and their recyclability. Nevertheless, although various NP materials have been used as solid support in the field of organocatalysis, there is only one known example in the literature for the application of ND. In 2009, Zheng *et al.* reported the covalent attachment of the organocatalyst L-Proline on DND using an alkyl linker system.[101] The yields in asymmetric aldol reactions were fairly low and the enantioselectivity was in a moderate range. The reactivity of the attached organocatalyst were significantly decreased and adverse interactions with surface groups of ND are most likely the reason. As the results are still far from those obtained from polymer NP supported catalysts, it is evident that research in this area is required to improve the outcome.

1.5.2 Solid phase catalysis

Focusing on ND particles, ND-metal composites and nanocarbon-ND hybrid materials on the basis of different reactions simplifies the gathering of numerous applications in the field of solid phase catalysis (Fig. 6). In the beginning of this catalysis, especially groups from Japan and Russia contributed enormously to the understanding of catalytic properties of ND.

Nakagawa *et al.* reported in 2002 the decomposition of methanol to hydrogen and CO using nickel NPs on oxidized ND. In comparison to other supporting materials, such as tin oxide (SnO_2), ZrO_2, TiO_2 or aluminium oxide (Al_2O_3), the ND particles showed the best conversion rate and hydrogen selectivity.[127] Tsonecheva *et al.* confirmed the use of Ni for the methanol decomposition and investigated the dependency on ND content and surface functionalities, verifying oxidized ND as the best choice.[128] Ni-loaded catalyst on oxidized ND also showed activity for the methane oxidation to CO and hydrogen, to hydrogen and amorphous carbon, as well as the CO_2 reforming of methane.[129-131] In 2014, Su and co-workers presented the first example of methane decomposition using DND without supporting metals. Mechanistic investigations proved that production of molecular hydrogen was accompanied by the formation of well-graphitized, few-layered graphene from ND itself. The rate of the decomposition was linearly dependent on the number of sp^2 defect sites on the surface.[132] In 2004, it was displayed by Bogatyreva *et al.* that DND particles show catalytic activity in the oxidation of CO to CO_2 at higher temperatures (~230 °C).[133,134] However, ND-metal composites helped to increase conversion rate and to lower temperature.[135] Pd-NPs on a ND-graphene core-shell material show high CO oxidation activity as the result of a strong ND-metal interaction via Pd-C bonds. The sp^3 core in combination with the sp^2 shell induces changes in the Pd electronic structure, thus CO adsorption is significantly lower.[136]

In hydrogenation experiments, mainly composites with group 10 metals can be found in the literature. Metallic nickel deposited on oxidized DND was tested in toluene hydrogenation,[137,138] as well as in the hydrogenation of acetylene.[139,140] For Pd-NPs on ND, the hydrogenation of C=C and C≡C bonds in tolanes, unsaturated acids and enamides was successful.[141] ND as support of Pt- and Pd-NPs in hydrogenating amination outperformed other nanocarbon materials, too, and showed further activity in the hydrogenation of azomethines, unsaturated hydrocarbons and alcohols.[142-146]

The dehydrogenation of alkanes catalyzed by nanocarbon materials and their composites has been an area of great scientific interest over the last 15 years.[147] Different routes, including the oxidative (ODH), direct (DDH) and steam free dehydrogenation, were described using various metal oxides on ND particles, such as chromium(III) oxide (Cr_2O_3) and vanadium(v) oxide (V_2O_5),[148,149] Al_2O_3, zinc oxide (ZnO) and magnesium(II) oxide (MgO)[150] or molybdenum dioxide (MoO_2).[151] Also, Pt-NP embedded in porous diamond spherical particles showed high reactivity in the dehydrogenation of either propane or cyclohexane.[152]

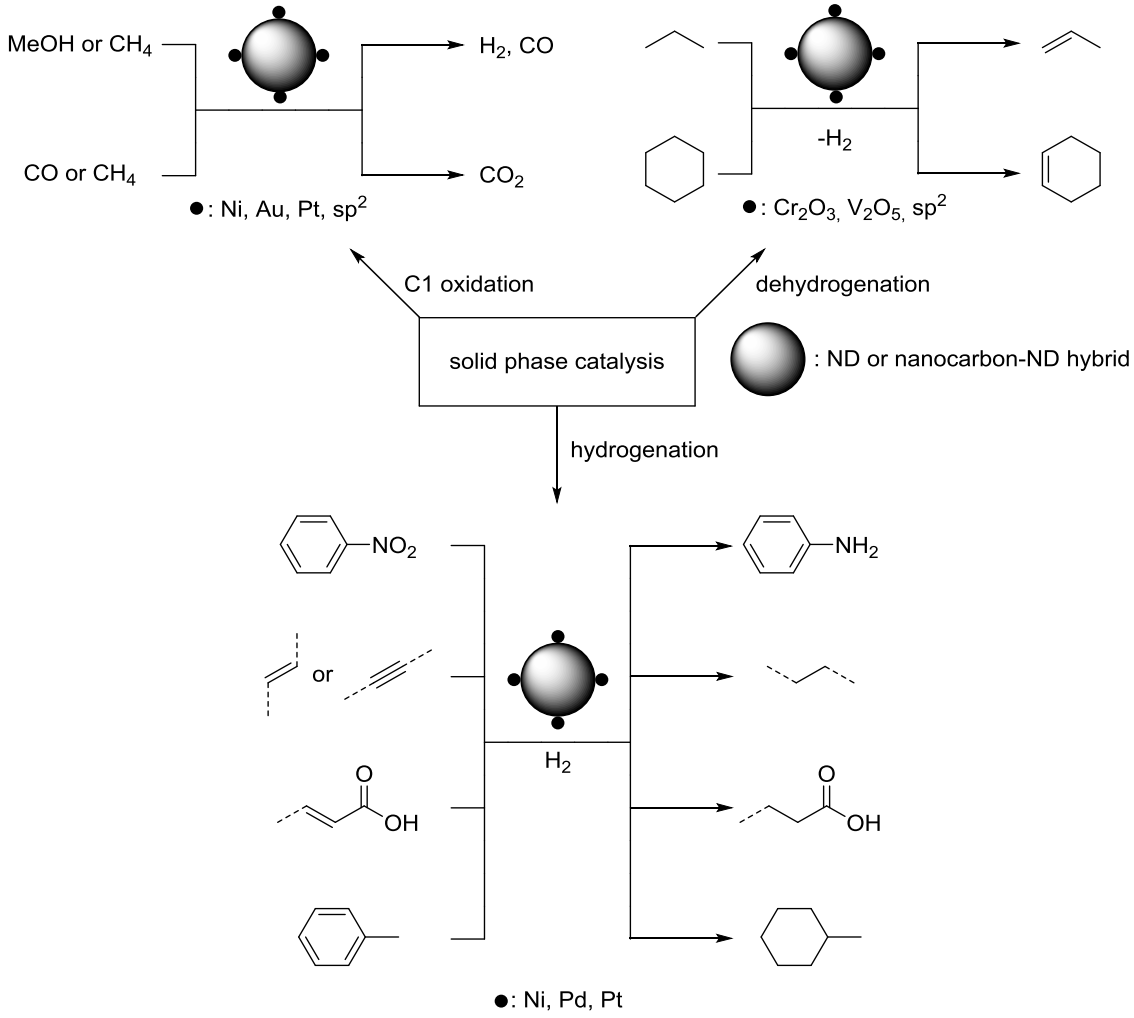

Fig. 6: Generalized overview of ND particles, ND-metal composites and nanocarbon-ND hybrid material application in solid phase catalysis.

Beside the metal-supported alkane dehydrogenation, metal-free ND composites are also widely applied. In 2015, Roldán and co-workers presented a graphene aerogel/ND hybrid material as catalyst in the ODH of propane. ND loading of 2.0 w.t% yielded the best results due to a high sp^3/sp^2 ratio and a huge amount of accessible carbonyl-

quinone groups.[106] In the DDH of ethylbenzene, a carbon nitride layer closed wrapped ND hybrid showed synergistic effects between the two materials, leading to a significantly higher styrene production rate than for pure ND.[153,154] A similar composite material, involving N-doped mesoporous graphene and ND, showed a catalytic performance in the same range.[155] Both were more reactive than the industrially used potassium-iron catalyst. However, hybrids of ND with carbon nanofibers,[156] graphene[156] or few-layer graphene/graphene oxide[157] performed best due to the enhanced number of active sites associated with the 3D-structure. With neither metals nor hybrid composites, modified ND can also be used in dehydrogenation. The reactivity is closely related to sp^2-carbon on the surface. The more sp^2-carbon is formed on the ND particles, the more reactive they become.[158] In the steam-free DDH of ethylbenzene, the unique sp^2-sp^3 hybrid structure of annealed ND results in high activity and stability, as well as the lack of coke formation.[159] Annealed ND particles with onion like carbon shells show the same properties regarding ODH of butane.[160] In the ODH of propane by using annealed ND, the generation of active oxygen species from chemisorbed oxygen was found to be one of the key catalytic steps.[161] In the DDH of propane, the sp^2/sp^3 core-shell is responsible for the C-H bond activation of propane.[162] Diao *et al.* recently tested different amounts of oxygen during the DDH of ethylbenzene using pristine ND, resulting in oxygen-lean conditions to be the most suitable with respect to selectivity and catalyst lifetime.[163] Li *et al.* proposed in 2013 that, based on DFT calculations, N-doping is an effective way of improving the selectivity for ethylene in ODH, as it decreases the adsorption energy of ethylene and lowers the barrier of the first C-H bond breaking of ethane, which represents the rate-limiting step.[164,165] Recent calculations on the DDH of *iso*-butane suggested that the core-shell (sp^2/sp^3) structure is crucial for the ND reactivity, especially for the C-H bond activation involving C=O groups as electron acceptors.[166]

In comparison to the other areas of catalysis, the solid phase catalysis allows for the discussion of several developments in ND catalysis. In some fields, such as hydrogenation, the use of metal oxides on ND particles is indispensable. However, less toxic (no Ni) or cheaper metals in lower amounts (Au, Pd, Pt vs. Fe, Cu) are used more frequently. Regarding C1 oxidation or the dehydrogenation of alkanes, metal-free catalysts are able to substitute their metal-containing analogs. Understanding the involved mechanisms behind the catalytic activities is part of recent investigations.

1.5.3 Electrocatalysis

Electrocatalysis is the most advanced field of catalytic application for diamond materials, as bulk diamond electrodes, in particular, are commonly used and commercially available.[167] The utilized electrode material is generally CVD-grown, bulk boron-doped diamond (BDD), because natural and synthetic diamonds possess insulating properties. The p-type doping leads to semi-conductive, conductive or even super-conductive electrodes, which allow electrochemical experiments at high current densities.[41,168] However, ND powders, in combination with either metal NPs, doping or other nanocarbon materials, are nowadays also used in electrocatalysis. After intensive electrochemical characterization of suitable powders in the early 2000s, ND based electrodes find various applications in electrocatalysis (Fig. 8).

Pressed ND powder electrodes showed low electrocatalytic activity,[169] probably due to missing metallic support. BDD powder coated electrodes,[170-172] as well as DND particles on Si-substrate,[173,174] provided a stable electrocatalyst support material. However, the electrocatalytic activity of undoped ND based electrodes is not self-evident. Holt *et al.* related the activity of a 5 nm layer of oxidized, undoped ND on gold electrodes in redox reactions to available surface states of the ND particles.[175,176] C=O termination and sp^2-surface carbon are supposed to provide those accessible states.[177] These findings were confirmed by Zang *et al*. For thermally annealed ND (750 °C), the activity was lower due to the removal of oxygen-containing surface groups. In turn, reoxidation of the surface resulted in higher activity. Composites with sp^3 core and sp^2 surface, fabricated by annealing at a higher temperature, showed high conductivity and electrochemical activity despite the loss of oxygen, illustrating the influence of sp^2 carbon.[178] Although, surface modifications of ND regarding oxygen and sp^2 content provide several approaches of promoting the electrocatalytic activity, doping ND particles seems to be the most promising metal-free route. For example, B- and N- co-doped ND rod arrays showed superior methanol electrooxidation activity compared to commercial Pt/C electrodes.[179] Solely N-doped ND rod arrays effectively debrominated polybrominated diphenyl ethers, a class of persistent and toxic pollutants, in electroreduction.[180]

In the following section, the application of ND-metal and metal oxide composites in electrocatalysis will be described and discussed, including various metal-free examples for comparison of specific reactions. A TiO_2 layer on undoped DND showed

increased electrochemical activity in comparison to pristine ND regarding the oxidation of nitrite anions.[103] In 2014, Nakata *et al.* showed that CO_2 can be selectively reduced to formaldehyde using BDD electrodes in salt water.[181] The used electrodes were not affected after 20 h of treatment, highlighting the corrosion resistant properties of BDD. N-doped carbon materials in combination with metals are promising catalysts for the electrochemical CO_2RR. The nitrogen moieties act as active site for CO production, whereas metal centers play an important role in the hydrocarbon formation.[182] In 2015, Liu *et al.* prepared N-doped ND on silicon rod arrays, which efficiently reduced CO_2 electrochemically to formate and acetate.[183] First, CO_2 is adsorbed on the electrode surface forming the $CO_2^{\bullet-}$ radical anion (**A**, Fig. 7). Afterwards two routes are possible. If the radical anion is protonated by the carbonate (HCO_3^-) electrolyte (**B**) and electrochemically reduced to still adsorbed HCOO, formate is formed (**C**). If the radical anion attached to the electrodes combines with a free radical, the C2 formation takes place (**D**) and acetate is formed after protonation and reduction (**E**).[183]

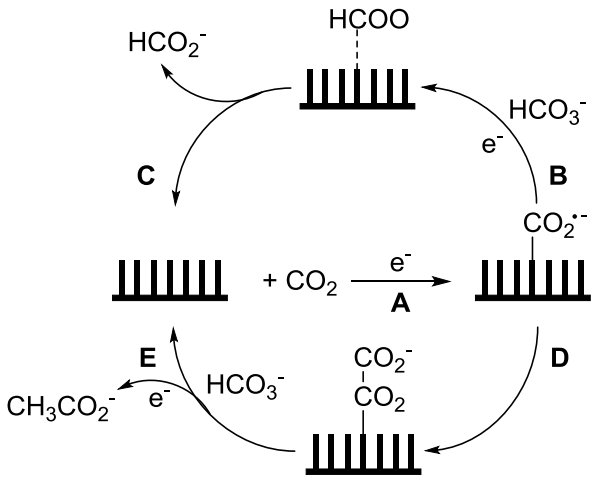

Fig. 7: Schematic pathway for the electrocatalytic conversion of CO_2 into either formate (**A**, **B**, **C**) or acetate (**A**, **D**, **E**) using N-doped ND particles on silicon rod arrays.[183]

Most recently, a B- and N- co-doped ND particle film has been deposited on a silicon substrate and showed electrochemical CO_2 reduction to ethanol with a ND based electrode for the first time.[184]

The electrochemical oxygen reduction reaction (ORR) was also investigated using different ND materials. B- and N- co-doped ND deposited on silicon rod arrays outperformed commercial Pt/C catalyst in current density and stability.[179] Graphitized ND without doping, but attached Pt NPs, showed identical activity in the ORR compared to the doped NDs on silicon rod arrays.[185] The reduction was also tested on

different core-shell structures, using ND as core and N- or B/N- co-doped graphene shells. The synergistic effect among graphitic-N, pyrrolic-N and pyridinic-N, as well as B- and N- co-doping, helped to illustrate high stability and reactivity in aqueous, pH neutral and alkaline reaction media.[186-188] Wu *et al.* recently confirmed that the active nitrogen sites in N-doped ND show a positive charge when active in ORR.[189] A similar material, cobalt-embedded N-doped and annealed ND, showed the same synergistic effects of graphitic nitrogen groups in combination with the metal cobalt.[190] For both, the electrochemical CO_2RR and ORR, it is clear that N- and B-doped ND in composites with other nanocarbons offer a promising alternative for ND-supported metal-catalysts.

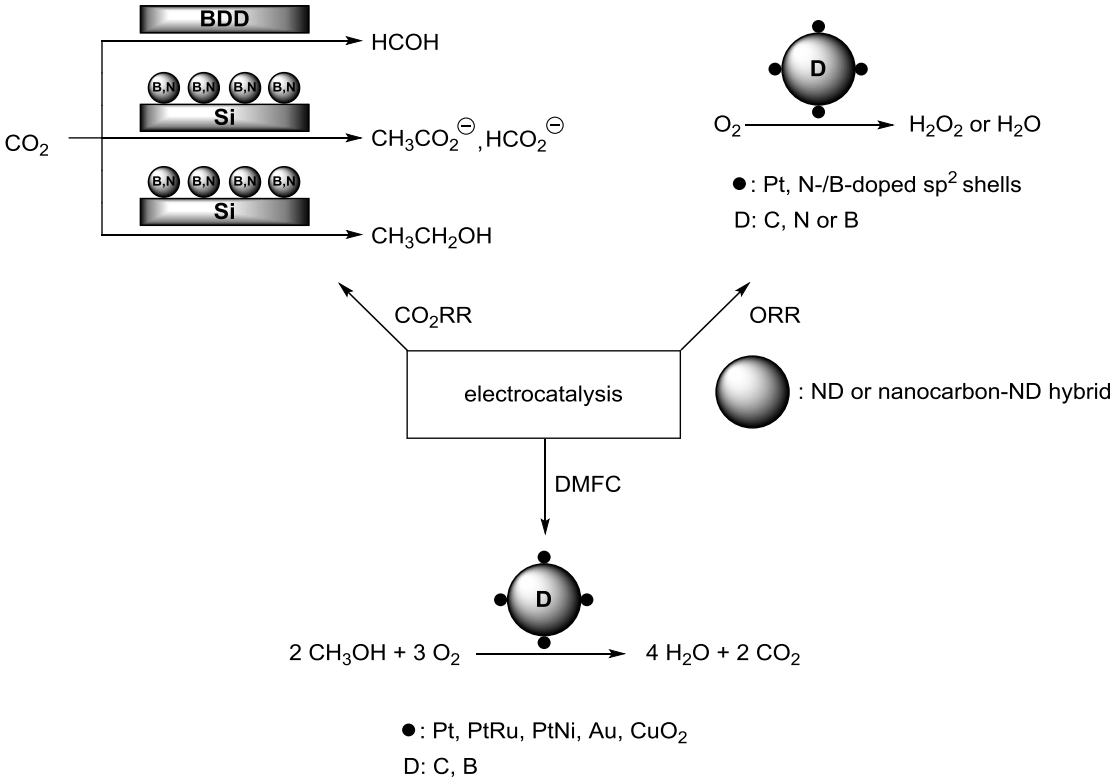

Fig. 8: Generalized overview of ND particles, ND-metal composites and nanocarbon-ND hybrid material application in electrocatalysis.

The major area of ND-metal composite application in electrocatalysis is the field of fuel cells, especially the direct methanol fuel cell (DMFC). BDD powder with deposited metallic oxides (Pt-RuO_x)[191] or in combination with monometallic Pt and bimetallic Pt-Ru were used in DMFCs.[192,105,193] However, undoped ND/Pt composites also showed good catalytic activity,[194] particularly coated 5 nm ND particles.[195] Adding graphene to the carbon support to create a core/shell structure further increased the methanol electrooxidation compared to normal Pt/ND composites.[196] For undoped materials, the surface termination is likely of higher importance, as substantial changes in surface

dipole have greater influence on the relative position of the electronic bands. For doped samples, this effect is effectively compensated by the density of states introduced by the dopant.[197] The most recent publication in the field of DMFCs focused heavily on synergistic effects, using ND particles embedded in a polypyrrole film as support for gold and cuprous oxide (Cu_2O) nanostructures.[104]

In electrocatalysis, metal-free, B-/N-doped ND materials, also in composites with other sp^2 rich nanocarbons, are progressively applied in common reactions, like CO_2RR or ORR. This development presents a first step towards cheaper and more sustainable ND-based electrodes. Regardless, at the moment these materials are not anywhere near to compete with metal NP materials in fuel cells, the main working area in electrocatalysis.

1.5.4 Photocatalysis

Photocatalysis is one of the emerging fields involving ND based materials, as all relevant findings have been published in the 2010s. In general, photocatalysis is related to metal oxides, especially TiO_2, which is a well-known photocatalyst for various applications.[198] It is therefore obvious, that first experiments comprising ND particles have been performed using composites with TiO_2. In such materials, the photocatalytic properties of both materials and the electrochemical characteristics of (un)doped diamond electrodes can be used.[199] Kim *et al.* deposited TiO_2 as atomic layer on ND and investigated the decomposition of toluene gas under UV irradiation (λ = 365 nm). Although bare TiO_2 (type P-25) showed higher reactivity, the thin film created less deactivation by adsorbed reactants, as the ND helped creating strong oxidizing agents, such as OH-radicals, which lead to an overall enhancement of toluene oxidation.[200] Oxidized ND (15 wt%)-TiO_2 composites exhibited higher activity than the respective bare materials regarding degradation of water pollutants, when irradiated in the near-UV/Vis region (λ >350 nm).[201] One of the challenges using this composite material is that due to the wide band gap, no oxidation takes place using visible light (λ >400 nm). However, under simulated solar light irradiation, the material showed efficiencies higher than for neat TiO_2 due to synergistic effects.[202] For the decomposition of volatile organic compounds, ND loaded tungsten(III) oxide (WO_3) composites showed higher efficiency than other well-known co-catalysts (Ag, Pd, Au and Cu_2O) loaded onto WO_3 and similar results to Pt-loaded WO_3. Under sun light irradiation, the ND also induced a higher production of OH-radicals.[203]

A photocatalytic reaction of general interest is the hydrogen evolution reaction (HER). Jang *et al.* displayed the use of DND in the photocatalytic reduction of water. Special emphasis was put on the known influence of surface termination on the electron emission, showing that H-terminated DND was able to produce eight times more hydrogen than O-terminated particles in a multiphoton process induced by a 532 nm laser irradiation.[204] When using graphitized DND under the same conditions, hydrogen and CO evolution was detected, which can be related to the oxidation of graphitic layers. The same reaction proved to be up to two times more effective when composites of ND with noble metal NPs, like Ag or Au, were tested.[205] Lin *et al.* were able to improve the catalytic performance of Cu_2O for HER under simulated solar and visible light irradiation nearly ten times by embedding ND particles in the metal nanocrystals. It was shown that ND particles act as electron-donating component.[206] ND-TiO_2 composites could also be used for HER by photodissociation of water under near-infrared, visible or UV radiation, depending on the used TiO_2-photocatalyst and the band structure in the region between 2-5 eV.[207] Recently, Haleem *et al.* were able to fabricate a photocatalyst consisting of graphitic carbon nitride layers with DND. The material showed a high catalytic activity towards HER, when being irradiated with a 300 W Xe-lamp (cut off: >420 nm).[208] A used platinum co-catalyst was responsible for the actual hydrogen generation and the ND particles act as electron carrier (Fig. 9).

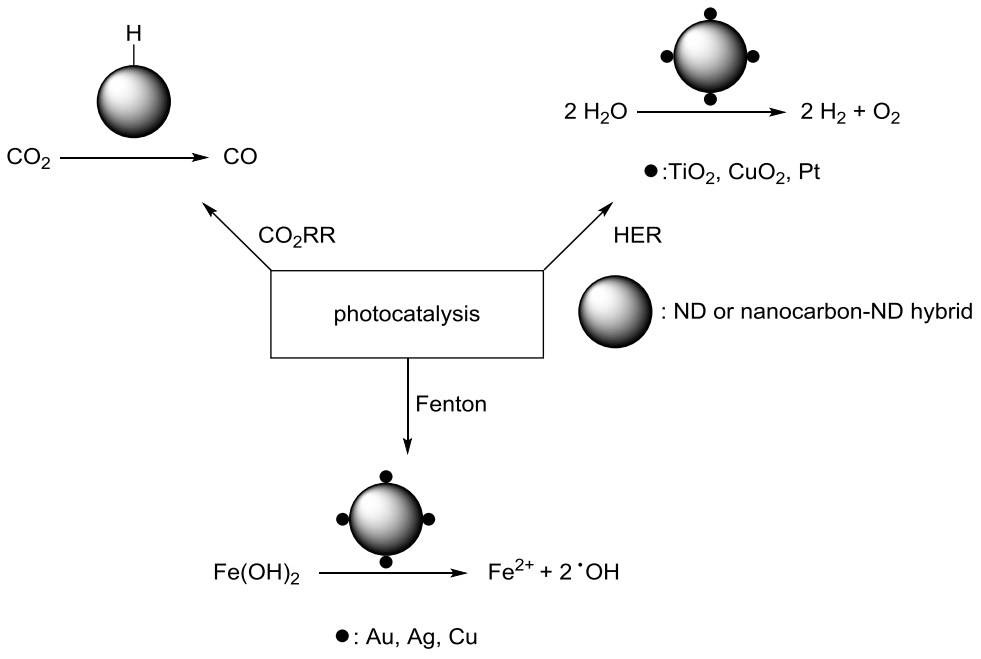

Fig. 9: Generalized overview of ND particles, ND-metal composites and nanocarbon-ND hybrid material application in photocatalysis.

The Garcia group, focusing on Fenton reaction, found out that the catalytic activity of ND-supported gold NPs is enhanced by exciting the NPs at the gold surface plasmon band (532 nm).[209] Solar irradiation enabled milder Fenton conditions, at neutral to basic pH values and lower hydrogen peroxide concentrations, leading to an increase in biodegradability of phenol.[210] Highly hydroxylated ND particles proved to be the best choice for anchoring gold NPs due to the interaction with numerous OH surface groups.[211,212] Changing the metal to silver and therefore also the excitation to the silver surface plasmon band (410 nm), the catalytic activity was further increased. ND outperformed TiO_2 and graphene as support material, as the ND itself was highly active in the decomposition of hydrogen peroxide to free hydroxyl radicals.[213] The Ag/ND composite can be readily used in dye decolorization under visible light irradiation.[214] Using the cheapest group 11 metal, copper, lead to the lowest catalytic activity in comparison to Ag or Au, as the higher sensitivity of Cu towards oxidation was problematic.[215]

In 2012, Dördelmann *et al.* were the first to synthesize TM complex functionalized DND particles. The attached manganese tricarbonyl complex showed CO-releasing properties after photoactivation at 365 nm.[216] Ohtani *et al.* reported that ND can act as electron-acceptor in a donor-acceptor composite with porphyrin under visible light irradiation illustrating that an electron from photoexcited porphyrin can effectively be transferred to the nanodiamonds.[217]

The first report about the photocatalytic activity of pure diamond originating from the production of solvated electrons in aqueous solution was published by Zhu *et al.* in 2013.[80] Hard UV irradiation (<225 nm) of BDD electrodes lead to the formation of solvated electrons and nitrogen was reduced to ammonia.[80] Mechanistic models of the reduction suggested indirect and direct reactions with solvated electrons.[218,219] Zhang *et al.* showed in 2014 that the solvated electrons generated from BDD can also be used for the reduction of CO_2 to CO. Using 210 nm irradiation, the CO_2 radical anion is generated in aqueous solution and photodissociates forming CO.[220] Sahu *et al.* showed that carbon NPs – a mixture of various modifications – reduce CO_2 in aqueous medium under visible light to formate. Surface-coating with a noble metal, like Ag or Au, enhanced the catalytic activity substantially.[221] The ability of DND particles to photocatalytically reduce CO_2 was shown recently by Zhang *et al.* H-terminated DND is able to generate solvated electrons under UV-irradiation (λ <225 nm), which can be

used for CO_2RR. However, oxidation and etching of the ND surface due to intensive irradiation and loss in activity had to be overcome by using high-quality powder.[85,108]

1.6 Functionalization of diamond with TM complexes

As the need for hard UV light is a major limitation of the CO_2RR, the use of visible light is the aim for the photocatalytic reduction to fine chemicals. Energy up-conversion with multi-photon absorption is required to achieve this breakthrough due to the large bandgap of the diamond materials. The necessary, accessible states in the bandgap can be introduced by defects/dopants,[222] virtual states[223] or surface states originating from attached molecules (Fig. 10). The effect of dopants was already discussed in chapter 1.2. For energy up-conversion and multi-photon excitation the generation of virtual states via dressed photons and phonons (DPP)[223] is possible. However, until now, this concept was not applied for a wide band gap material like diamond.

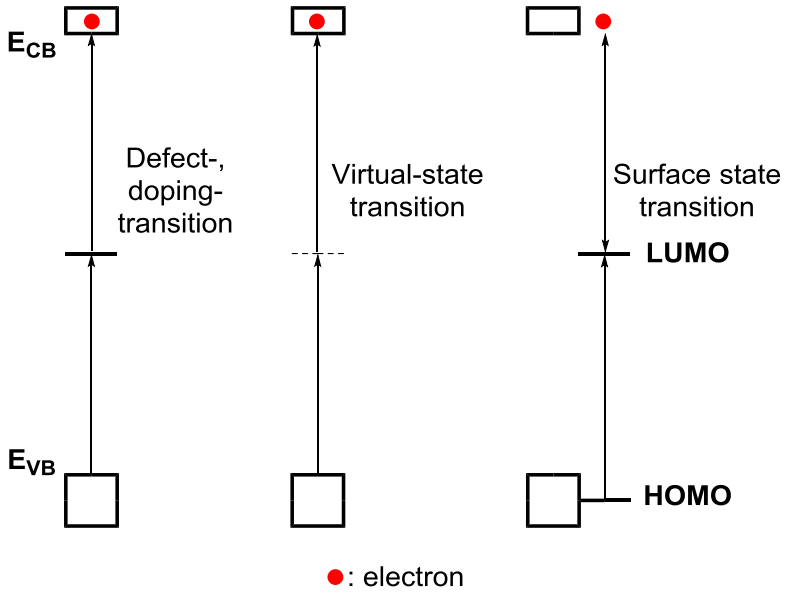

Fig. 10: Possible pathways for energy up-conversion for diamond materials.

The concept of surface modification has already been utilized for established semi-conducting metal oxides, like SnO_2[224] and foremost TiO_2.[225,226] Yet, BDD electrodes have also been employed for anchoring photo- and electrocatalytically active molecules. Diamond based electrodes proved to be suitable carrier materials for numerous reasons, including dopant-dependent conductivity, non-toxicity, low-cost production and especially chemical inertness in photo- and electrochemical processes.[227] In a first dye sensitization, the $Ru(bpy)_3^{2+}$ (bpy = 2,2´-bipyridine) complex was physisorbed to a BDD electrode.[228] Ferrocene was either attached via CuAAC to

an azide-functionalized, conjugated, phenlyene-based linker system on oxygen-terminated BDD[229] or to an azide-functionalized, non-conjugated alkyl chain on hydrogenated BDD.[230] Such alkyl chains can be covalently attached via photoreaction (254 nm) of an terminal alkene group with the diamond surface.[231] The ferrocene unit, attached via an alkyl chain, was freely movable and an electron transfer from the complex to the diamond surface resulted from spatial proximity or tunneling through the aqueous medium.[230] A cobalt porphyrin complex has also been covalently attached using the CuAAC principle.[232] The complex was able to reduce CO_2 electrochemically to CO, however, the acute toxicity of such cobalt compounds is a significant disadvantage. Ruthenium-based complexes offer an alternative, as they provide an established synthesis route, show stable long-lived excited states and possess high redox and photocatalytical stability under ambient conditions.[233-235] Ruthenium(II) complexes can readily act as oxidizing and reducing agent.[236,237] In 2015, Kubiak *et al.* reported on a molecular ruthenium catalyst, which enabled the electrochemical reduction of CO_2 to CO and formate. The efficiency crucially depended on the choice of ligands on the metal center.[238] Thus, more recently both $Ru(tpy)_2^{2+}$ (tpy = 2,2´:6´,2´´-terpyridine)[239] and the N3 dye (*cis*-bis(thiocyanato)bis(2,2´bipyridyl-4,4´-dicarboxylato) ruthenium(II))[240] have been covalently linked to hydrogenated BDD electrodes in order to investigate the suitability of sensitized electrodes as hole transport material in solar cells. In contrast to the $Ru(tpy)_2^{2+}$ sensitized material,[241] the HOMO of the N3 dye and the valence band maximum (VBM) of the BDD electrode match, leading to a hole transfer from dye to BDD.[240] By using ligands with electron-donating substituents or large, conjugated π-systems the complexes can be modified in a way that the frontier orbital match with the band structure of the diamond material. However, the condition that the complexes are stable under the used catalytic conditions, e.g. photocatalytic CO_2RR or electrocatalytic HER, needs to be fulfilled.[242] The use of H-terminated BDD materials in functionalizations with photoactive organic dyes[243] or donor-acceptor systems[244,245] molecules proved that boron-doped materials are a very interesting material class. However, in addition to bulk BDD electrodes the use of (un)doped ND particles of different origin, such as DND[246] or milled CVD films[44], is also of great interest. As the particles illustrate a high surface to volume ratio due to their small size, a higher surface loading with attached photo- and electrocatalytically active molecules can be expected. The nature of the surface, whether specifically functionalized or terminated, is therefore affecting the photo- and electrocatalytical activity to a larger

extent than the bulk structure, providing an example of how surface properties dominate those of the bulk material when looking at nanometer sized particles.[247]

1.7 Surface modifications of diamond nanoparticles

As discussed in chapter 1.2.1, DND particles show various functional groups on the surface due to the applied synthesis procedure. Using several oxidative and reductive methods, a homogenization is possible yielding the surface termination, which is either needed for immobilization of functional molecules or is itself catalytically active.

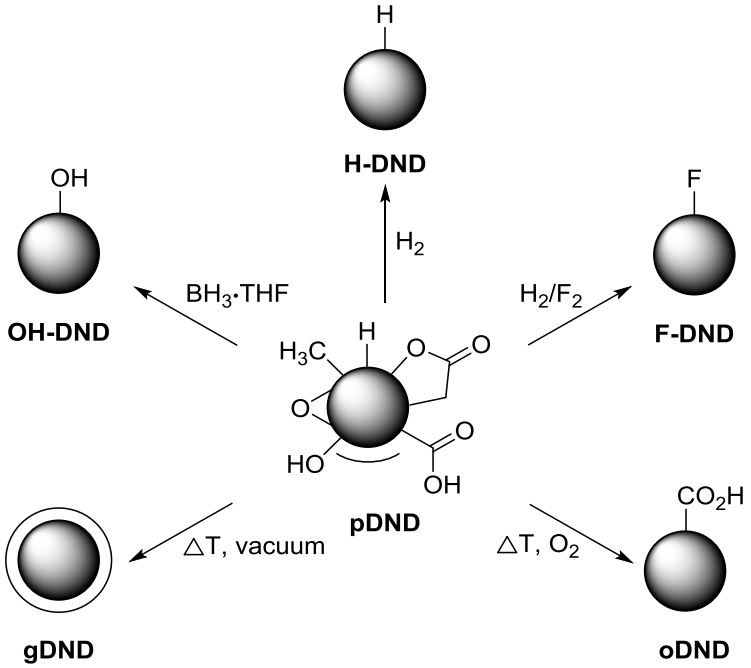

Fig. 11: Methods for the homogenization of the DND particle surface.

The homogenization of pristine DND (**pDND**) via hydrogenation (**H-DND**), hydroxylation (**OH-DND**), oxidation/carboxylation (**oDND**), fluorination (**F-DND**) or thermal annealing (**gDND**), shown in Fig. 11, as well as the nitrogen und sulfur termination, are well-known, intensively described and reviewed procedures.[15,231,248,249] However, as new fluorination techniques are part of this thesis, the state of knowledge will be briefly discussed. In first experiments, larger sized (micrometer scale) particles were used and the reaction of hydrogen- or oxygen-terminated surfaces with fluorine (F_2) gas or tetrafluoromethane (CF_4) plasma was studied under various conditions.[250,251] For H-terminated DND particles, a hydrogen abstraction using F_2 resulting in fluorine chemisorption was observed at a reaction temperature of -10 °C.[252] As alternative fluorine source, chlorine trifluoride (ClF_3) can be used at elevated temperatures (250-400 °C).[253] In 2004, Khabashesku *et al.*

provided the first example of fluorination of DND particles (3.5-6.5 nm) using a F_2/H_2 (3:1) mixture at 150-310 °C for 48 h yielding 8.6 at.% fluorine on the surface of the particles.[254] These harsh reaction conditions are necessary, as the oxygen-containing surface groups of the pristine ND powders are only removed or transformed by fluorination at higher temperatures.[255,256] The obtained particles showed high stability in polar organic solvents.[255] A plasma treatment with CF_4 or sulfur hexafluoride (SF_6) allows ND fluorination within minutes, but with a lower fluorine content of 4.5 at.%.[257] The fluorine surface termination showed high stability, even after 75 days in aqueous media.[258] Huang *et al.* proved that ND particles have been deagglomerated during fluorination with F_2 at 200 °C and the dispersion ability in ethanol was improved.[258] Most recently, a silver-catalyzed radical substitution of surface carboxylic groups of HPHT-ND by fluorine was published using silver nitrate and Selectfluor™, yielding a mixed C-F and C-OH termination.[259] Fluorinated DND particles show slower redox kinetics in comparison to H- or O-terminated materials.[260] For CF_4 treated powders, the major species observed via solid state nuclear magnetic resonance (NMR) spectroscopy is CF,[261] whereas F_2 treated samples show CF, CF_2 and CF_3 groups on the surface.[262-265]

The covalent attachment of functional molecules onto ND particles is required for various areas, in particular bioapplication, where peptides, saccharides, drugs and other biomolecules have already been successfully attached and reviewed.[266]

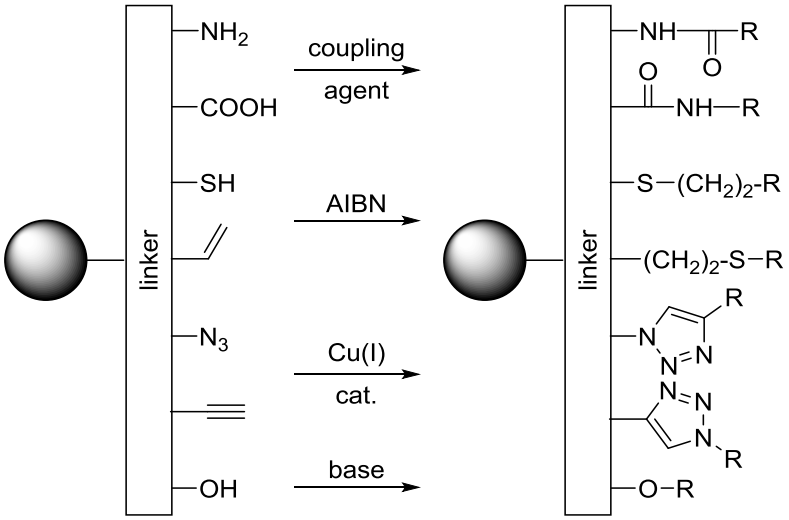

Fig. 12: Attachment methods of functional molecules to linker-functionalized DND particles (R: alkyl, aryl).

The attachment generally takes place via a linker molecule, bearing functional groups for the covalent binding of the active molecule. The most common reactions are carboxamide couplings, thiol-ene reactions, ether formations or CuAAC reactions (see chapter 1.5.1) (Fig. 12).[266,267] The linker molecules themselves can be attached to ND particles using various reactions. Thermally annealed/graphitized DND (**gDND**) with its sp^2 shell on the surface can be functionalized in Diels-Alder,[268] Bingel-Hirsch[269] or Prato reactions.[270] Regarding the Prato-reaction, the dipolarophilic double bonds on the particles surface enable a linker functionalization via a 1,3-dipolar cycloaddition. The reactive 1,3-dipolar molecule is generally formed *in situ* by a decarboxylative condensation of an aldehyde with an α-amino acid (Fig. 13).

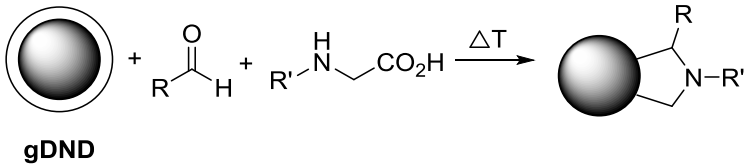

Fig. 13: General procedure of a Prato reaction on **gDND** (R, R': alkyl, aryl).

Another commonly used functionalization of ND materials is the use of aryldiazonium salts, where aryl radical cations are formed, which are able to react with the diamond surface. Generally, the electrons required for radical formation at insulating or semi-conducting materials are provided via reducing agents, such as metal oxides.[117] As the resulting metal oxides are not easily separated from the ND particles, such kind of electron donor is avoided. It was shown that diamond itself can act as an electron donor enabling the formation of reactive aryl radicals either by ultrasonic treatment or under heat. The radicals readily form a covalent C-C single bond with the diamond surface (Fig. 14).[271,272]

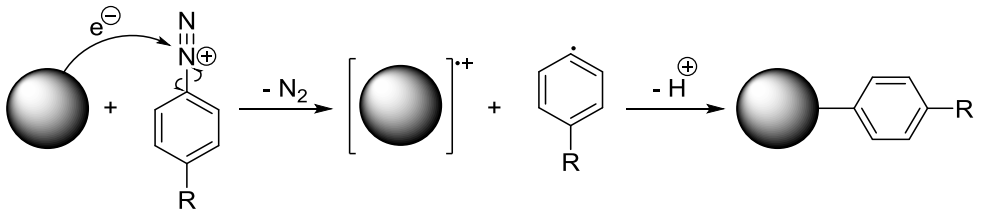

Fig. 14: Possible reaction mechanism for the radical arylation of DND (R: aryl).

A possible explanation for this observation is provided by surface states. These states are generated by overlapping orbitals of functional groups on the surface. As a consequence, delocalized electronic states are generated on the surface, which lie energetically in the band gap of diamond, which explains the oxidative and reductive

properties.[273] An electron can be transferred from the surface states to the diazonium salt, which decomposes under nitrogen cleavage. The generated radical recombines with the diamond surface.

The versatile surface modifications of diamond nanoparticles, either via specific terminations or covalent attachment of functional molecules, provide the basis for several applications in catalysis.

2. Motivation

The aim of this work is to investigate the application of diamond nanomaterials in catalysis. For the investigation of the catalytic activity nanodiamond particles with different dopants and surface terminations, having a significant influence on the electronic structure of the material, are fabricated, characterized and tested for their ability to reduce CO_2 in photo(electro)catalytic experiments. It is analyzed, which type of ND material in combination with different specific terminations yields the highest efficiency for the respective catalytic application.

Furthermore, the fabricated ND particles are used as carrier materials for ruthenium-based photocatalysts. The photocatalysts, attached via flexible, phenylene-based linker systems, are used in both photoredox experiments and the photo(electro)-catalytic reduction of CO_2. In both cases, the stability under irradiation, the recyclability of the functionalized particles and the dispersibility in various media, including ionic liquids, is studied in detail. Synergistic effects between ND material and photocatalyst due to electronic coupling, resulting in an increased reactivity, is discussed by means of advanced spectroscopic techniques.

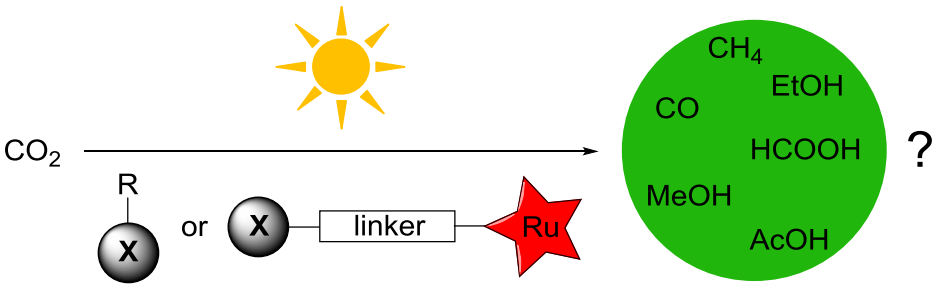

Fig. 15: Photocatalytic reduction of CO_2 to various C1 or C2 products applying specifically terminated (R) ND particles or ND-attached ruthenium (Ru) photocatalysts (X: dopant).

3. Results and Discussion

The photoelectrocatalytic transformation of CO_2 into useful chemicals and fuels utilizing diamond materials in combination with natural sun light illustrates the main objective of this work. As already mentioned in chapter 1.5.4, in particular BDD electrodes[220] and H-terminated DND particles[108] allow for the reduction of CO_2 in photoelectrocatalytic reactions, however, the need for hard UV light is still a major limitation of the process. Thus, the use of visible light is desired. Due to the large bandgap of diamond (5.5 eV, 225 nm) using visible light requires energy-up conversion with multi-photon absorption (chapter 1.6). To achieve this conversion accessible energy states in the band gap need to be introduced, which is possible using different approaches (Fig. 10, chapter 1.6). Either defects or dopants in the nanostructured diamond material in combination with specific surface terminations or the functionalization with photocatalytically active molecules can lead to the required energy states within the band gap and are relevant approaches for this work. Therefore, a variety of nanodiamond particles was fabricated, using known, partially adapted and newly developed methods, to investigate the influences of dopants, nano structuration and different surface terminations on the photoelectrocatalytic activity. Furthermore, the obtained particles were functionalized with transition metal based photocatalysts to assess the energy-up conversion of visible light using surface state transitions. Additionally, the colloidal stability of the fabricated (un)functionalized diamond nanoparticles was analyzed in various solvents in order to evaluate the influence on the photocatalytic activity in CO_2 reduction reactions.

3.1 Diamond nanoparticles with controlled surface and particle properties

As mentioned above, one approach for the energy-up conversion of visible light in nanostructured diamond materials is the introduction of defects/dopants in combination with different surface terminations to enable defect- or dopant-based transitions. Based on the already established methods to produce and specifically terminate (un)doped nanodiamond particles in the literature (chapters 1.2.1, 1.2.2 and 1.7), the fabrication of various diamond nanoparticles and the influence of diverse surface terminations on the material properties is described and discussed.

Furthermore, the focus was also set on the stability of various particle terminations, both as powder and in dispersion, and on how dopants are incorporated into the diamond nanoparticle lattice. The diamond nanoparticles were either fabricated by detonation synthesis or the milling of chemical vapor deposited (CVD) diamond films.

3.1.1 Detonation nanodiamond based materials

In order to provide a set of different detonation nanodiamond (DND) particles, commercially available, pristine DND (**pDND**) powder (Lingyun Granda: ,,Diamond Nano Powder") was used as starting material.

3.1.1.1 Milling of pristine DND (pDND)

Milled DND particles (**mDND**) can be produced by milling **pDND** powders. The grinding of bigger sized diamond agglomerates of **pDND** was achieved by using zirconium oxide beads in a stirred ball mill (Fig. 16).[274,275]

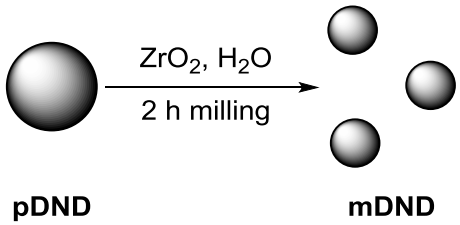

Fig. 16: Deagglomeration of **pDND** into **mDND** particles.

During this procedure the agglomerates were broken due to high shearing forces and aqueous, dark black particle dispersions, with sizes in the sub 10 nm region, were obtained on a gram scale. The shearing forces resulted in the formation of sp^2-hybridized areas on the particle surface.[272,276] The sp^2 content plays an important role in the catalytic activity regarding the solid phase (chapter 1.5.2) and electrocatalysis (chapter 1.5.3) and needs to be taken into account when assessing the activity of **mDND** based catalysts in photoelectrocatalytic CO_2 reduction experiments. Furthermore, the activity of zirconium oxide debris formed during the milling process (up to ~19000 ppm) needs to be considered, as the oxide catalyzes the splitting of water.[277,278]

The characteristic results of **mDND** dispersions are listed in Table 3 (chapter 3.1.1.4) and the spectroscopic characterization is discussed in chapter 3.1.1.5.

3.1.1.2 Purification of pristine DND (pDND)

Although already cleaned after detonation synthesis using acid treatment, **pDND** shows a large amount of impurities (up to 50 elements), mainly alkali and alkaline earth metals and first row transition metals.[279] Inductively coupled atomic emission spectrometry (ICP-AES) and inductively coupled plasma mass spectrometry (ICP-MS) analysis, carried out by Dr. Dmitry S. Volkov from Moscow State University, Russia, using direct slurry nebulization technique,[280] showed that **pDND** has 1088 ±163 ppm impurities, with iron (400 ppm) and aluminum (446 ppm) comprising up to ~80% (Table 2). The entire ICP-MS analysis of **pDND** can be found in the Appendix (Table 53). The **pDND** applied in this work is already relatively free of contaminants in comparison to other analyzed, commercially available samples (see ref.[279] for 18 DND samples, impurities from 2500-55000 ppm, ø ~16800 ppm). Nevertheless, further cleaning of **pDND** to remove the main metal impurities was considered to rule out that an observed photocatalytical activity is the sole result of impurities. As discussed in chapter 1.5, in particular the transition metals present potent solid state, electro- or photocatalysts. In addition to the main impurities observed for **pDND**, **mDND** showed a large amount of zirconia debris, as stated above (19300 ppm, Table 2).

As already described in the literature, a combination of acid cleaning (conc. hydrochloric acid), air oxidation and complexing agents in aqueous solution (potassium thiocyanate, dicyandiamide) was tested for **pDND** and **mDND** to remove the main transition metal impurities iron and titanium.[281-283] However, only hydrochloric acid proved to be suitable to remove iron and slightly minimize the titanium content. This observation suggested that the main iron impurities were iron oxides, which could not be removed by the complexing agents due to their poor solubility in aqueous solution.[283] Using a combination of piranha solution (conc. sulfuric acid/ hydrogen peroxide (30 wt.%) 3:1 v/v) and conc. hydrochloric acid, the iron content was minimized by ~95%. A possible explanation is that piranha solution is able to break agglomerates of **pDND**, which enclose iron impurities. After breaking the agglomerates, the impurities were accessible and could be removed by solvation in hydrochloric acid. In addition, the titanium impurity was also lowered by ~30%. As aluminum impurities cannot be removed applying acidic conditions,[283] test reactions dispersing **mDND** in 40 wt% sodium hydroxide solution were performed. The aluminum content was significantly reduced by ~90% and the zirconium content was

also lowered by ~80% (Table 2). It is possible that the zirconium oxide particles react with sodium hydroxide forming water soluble sodium zirconate.[284] However, as this reaction requires high temperatures (500-1000 °C),[285] a catalyst would be needed to allow for the reaction taking place at 120 °C. Here, the diamond particles themselves might show the required catalytical activity. Combining the obtained impurity cleaning reactions led to the novel stepwise treatment of **pDND** yielding the cleaned particles **cDND** (Table 1).

Table 1: Stepwise cleaning procedure of **pDND** to yield **cDND**

step	conditions	reduced impurities
1	conc. $NaOH_{(aq)}$	Al, Zr
2	conc. H_2SO_4/H_2O_2 (3:1)	Fe, Ti
3	conc. $NaOH_{(aq)}$	Al, Zr
4	conc. H_2SO_4/H_2O_2 (3:1)	Fe, Ti
5	conc. HCl	Fe, Ti

During the treatment flasks made of perfluoroalkoxy alkanes (PFA) were used. Glass materials were generally avoided, as they pose a possible source of contamination due to etching, especially when using highly alkaline solutions, like 40 wt.% sodium hydroxide.[286]

The main impurities of **cDND** were significantly reduced in comparison to **pDND** (Al: ~62%, Fe: ~93%, Ti: ~31%, Table 2). Further elements, e.g. sodium, boron or potassium were detected in concentrations of ca. 32, 31 and 24 ppm. The entire ICP-MS analysis of **cDND** can be found in the Appendix (Table 53). The overall content of impurities was reduced by more than 60% from 1088 ±163 ppm (**pDND**) to 423 ± 63 ppm (**cDND**).

Table 2: ICP-MS analysis results for untreated and treated **pDND** and **mDND**, as well as **cDND**

Element [ppm]	**pDND**	**mDND**	**pDND** (Pir. + HCl)	**mDND** (NaOH)	**cDND** (multistep)
Al	446	1160	596	118	171
Fe	400	500	21	432	26
Ti	35	17	24	39	24
Zr	11	19300	19	3730	4

The majority of commercially available DND powders contains a high amount of chlorine due to the use of acids, like hydrochloric or perchloric acid, during sample purification.[279] The chlorine content cannot be quantified by ICP-MS, as the chlorine detection wavelength (<135 nm) is below the limit of conventional setups (175-800 nm).[279] However, quantification using X-ray fluorescence (XRF),[287] energy dispersive X-ray spectroscopy (EDX) or elemental analysis (EA) is possible.[279,287,288] For **pDND**, a chlorine concentration of 1.17 wt.% (11700 ppm) was determined via EA. The purified **cDND** contained 1.98 wt.% (19800 ppm). The increase by ~70% can be explained using hydrochloric acid during purification. To exclude surface-adsorbed chloride, the obtained particles were dialyzed for several days,[287] resulting in no decrease of the chloride concentration. Therefore, it is more likely that either water insoluble chloride salts were formed with some of the remaining impurities or that chloride was enclosed in particle agglomerates.

Subsequently, the developed cleaning procedure of **pDND** presents a compromise. On one hand, the content of photocatalytically active impurities, such as Al, Fe or Ti, was substantially reduced, however, on the other hand sulfur and in particular chlorine were enriched due to the use of sulfuric and hydrochloric acid. The influence of chloride and sulfate anions on the photocatalytic activity of nanodiamond particles needs to be carefully considered, as it is well-known for photocatalyst TiO_2 that these anions can lead to a surface inactivation and a loss in activitiy.[289]

The **cDND** particles showed smaller particle sizes than **pDND** ($D_V(50)$ 170 nm → 130 nm, Table 3, chapter 3.1.1.4). This observation can be related to the *in situ* breaking of particle agglomerates during the treatment with piranha solution. The spectroscopic characterization of **cDND** is part of chapter 3.1.1.5.

3.1.1.3 Air oxidized DND (oDND)

Milling and cleaning of **pDND** have a significant influence on the particle size and, for both materials, various oxygen containing groups, such alcohols, ethers, ketones, esters or even carboxylic acids, are still present on the particle surface (chapter 1.2.1). Termination of the DND surface with mainly oxygen containing groups showing a high oxidation state, like ketones, carboxylic acids or acid anhydrides, was achieved by oxidizing **pDND** in air.[290] The weight loss during oxidation amounted to 5.5-7.5 %,

mainly due to loss of amorphous carbon. The oxidation was performed in a tube furnace yielding oxidized DND particles (**oDND**) (Fig. 17).

A successful oxidation could be clearly seen by the change of the zeta potential (Table 3, chapter 3.1.1.4) from +43.2 mV (**pDND**) to -42.0 mV (**oDND**) being in good agreement with the literature (-44.1 mV at pH 5.5).[291] The negative zeta potential can be explained by the dissociation of carboxyl and carbonyl groups on the surface.[231]

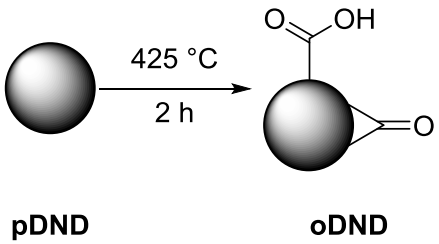

Fig. 17: Air oxidation of **pDND**.

The stable, aqueous dispersion showed an almost identical size distribution in comparison to the **pDND** starting material (D_v(50) 170 nm → 158 nm). Characteristic vibrations of **oDND** in FT-IR and Raman spectra are discussed in comparison to other DND materials in chapter 3.1.1.5.

3.1.1.4 Thermally annealed/graphitized DND (gDND)

Thermal annealing/graphitization is an established method to homogenize the surface of **pDND** (chapter 1.7). **pDND** was pretreated by heating to 170 °C *in vacuo* ($1 \cdot 10^{-3}$ mbar) to remove adsorbed water and minimize traces of acids originating from the commercial powder. As mentioned in chapter 3.1.1.2, **pDND** was treated with hydrochloric and perchloric acid after detonation synthesis. The pretreatment of **pDND** (10.0 g) *in vacuo* yielded small amounts of a highly viscous liquid with a pH <1, presumably remaining acid(s). For the subsequent annealing of the pre-treated powder at 750 °C for 2 h in a argon flushed tube furnace at $1.4 \cdot 10^{-4}$ mbar[268] (Fig. 18), it is mandatory to remove the acid impurities to avoid corrosion of the setup.

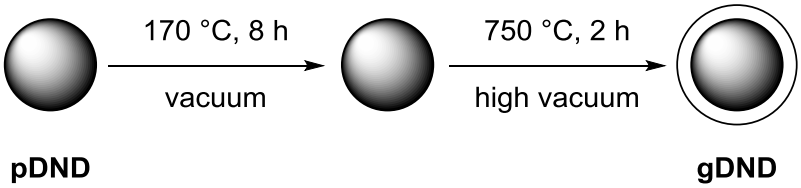

Fig. 18: Thermal annealing of **pDND**.

In comparison to the starting material **pDND**, no significant difference was observed for **gDND** concerning the still highly positive zeta potential (Table 3). The annealed powder **gDND** was more likely to agglomerate in aqueous dispersion, leading to no substantial amount of particles <100 nm when compared to **pDND** (Table 3). The reason for this observation is the quite hydrophobic surface after annealing.[117]

Table 3: Results of zeta potential (ζ) and particle size measurements of **pDND**, **mDND**, **cDND, oDND** and **gDND**

ND material	ζ [mV] (pH)	D_V-(10) [nm]	D_V-(50) [nm]	D_V-(90) [nm]
pDND	+43.2 (6.3)	77.6	170	386
mDND	+30.8 (6.2)	1.36	3.38	5.72
cDND	+50.1 (6.1)	31.9	130	1340
oDND	-42.0 (5.4)	60.4	158	406
gDND	+33.9 (6.3)	132	207	372

Characteristic spectroscopic results of **gDND**, in particular for the formation of a graphitic sp^2-layer at the particle surface, are discussed in comparison to the other DND materials in the following chapter.

3.1.1.5 Spectroscopic characterization of DND materials

The DRIFT spectra of the five DND based particles **pDND**, **cDND**, **mDND**, **oDND** and **gDND** are presented in Fig. 19. All samples present a characteristic peak at 3720 cm^{-1} being related to free OH-vibrations from non-hydrogen bonded water molecules.[292] **pDND**, **cDND** and **mDND** show all the asymmetric (2940-2955 cm^{-1}) and symmetric (2870-2880 cm^{-1}) C-H stretching vibrations, as well as the signals of surface adsorbed water at 1630 cm^{-1} and around 3400 cm^{-1}. This agrees well with the literature.[293] **pDND** and **mDND** exhibit a C=O stretching vibration at 1715 cm^{-1}, representing primarily ketones and aldehydes.[20,294,295] For **cDND**, the vibration is shifted to 1730 cm^{-1}, indicating the additional formation of higher oxidized carbon species, such as esters or lactams.[293] Furthermore, in contrast to **pDND** and **mDND**, **cDND** shows two broader and less intensive signals at 1180 cm^{-1} and 1135 cm^{-1}. Both can be assigned to the asymmetric C-O-C stretching vibration of esters or lactones and the C-O stretching vibration of hydroxyl groups.[296,297] The use of piranha solution during treatment for the production of **cDND** can explain the formation of hydroxyl groups on the surface. Highly reactive hydroxyl radicals, formed in the used mixture of conc. sulfuric acid and

hydrogen peroxide at higher temperature, oxidize amorphous carbon material and recombine with the exposed particle surface to C-OH units.[298,299] **oDND** particles show a very intensive and broad peak at 1807 cm^{-1}, which can be attributed to the C=O stretching vibration of carboxylic acids, anhydrides and keto groups on the surface. At 2270 cm^{-1} and 2165 cm^{-1} two peaks occur. Osswald *et al.* observed the same signals, but did not discuss the origin in detail.[290] In this region of the spectra, (iso)nitrile or alkyne groups are expected. As the oxidation was taking place in air, a nitrogen uptake at the diamond lattice surface was most likely to happen forming graphitic C-N structures.[290,293] The broad signal at around 1410 cm^{-1} can be attributed to the symmetric C=O stretching vibration of deprotonated carboxyl groups.[300,301] The broad shoulder at 1280 cm^{-1} refers to the C-O stretching vibration of carboxylic anhydrides.[293] The obtained results were highly reproducible.

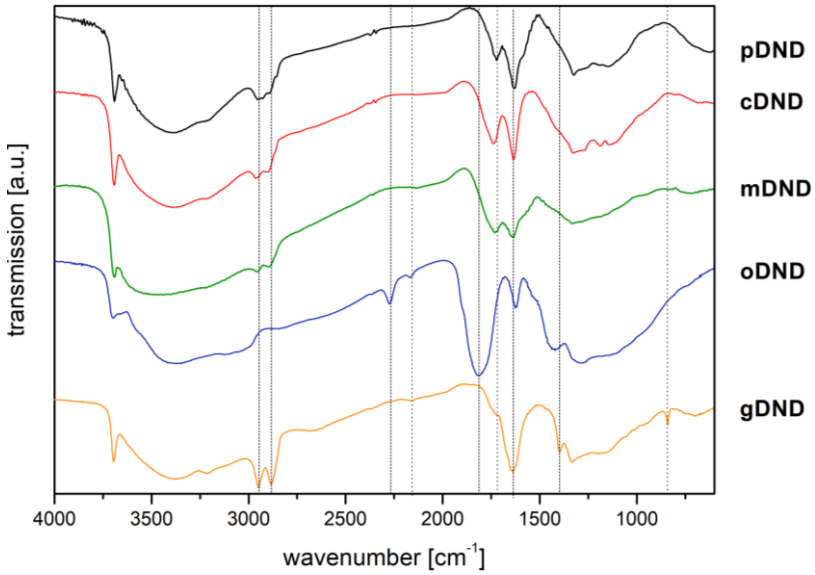

Fig. 19: DRIFT spectra of **pDND**, **cDND**, **mDND**, **oDND** and **gDND**.

For **gDND**, at 2945 cm^{-1} and 2879 cm^{-1}, the asymmetric and symmetric C-H-stretching vibrations are more pronounced than for all other DND particles. The C-H out-of-plane deformation (836 cm^{-1}) and the sym. C-H deformation vibration (1392 cm^{-1}) are clearly visible. The very weak C=O stretching vibration at 1719 cm^{-1} illustrates the altered surface termination. The intense and broadened signal around 1630 cm^{-1} can be explained by a high amount of C=C bonds on the surface in combination with the O-H vibration of adsorbed water. The observed increase of C-H stretching and deformation modes in combination with a drastic reduction of the C=O related vibrations is in good agreement with literature.[268,295]

For all five DND samples, a peak at 1325 cm^{-1} can be observed in the Raman spectra, without a visible shift (Fig. 20). This signal illustrates a superposition of the diamond peak from sp^3 carbon and the D band of graphitic sp^2 carbon.[15] With an increasing sp^3 content, the intensity of the diamond peak increases, while the D band decreases.[15] For **pDND**, **cDND** and **mDND** a broad G band is located around 1600 cm^{-1}. According to Mochalin *et al.* the G band is composed of several vibrations, involving the O-H bending vibration (~1640 cm^{-1}) and mainly the graphitic carbon sp^2 band.[302] For **oDND**, the signal of the G band appears slightly blue-shifted (~1620 cm^{-1}), as the O-H bending vibration of surface adsorbed water molecules is influenced by the highly oxidized surface.[15,293] On the other hand, the band appears redshifted (~1570 cm^{-1}) for **gDND** due to the increased amount of graphitic sp^2 carbon on the particles surface. The contribution of the O-H bending vibration is lower, as water is less adsorbed onto the hydrophobic surface and O-H containing, functional groups were mostly removed during the sample preparation.[302] For **gDND**, the ratio between diamond/D band signal and G band is on the side of the G band due to the high sp^2 content.[302] For **cDND** and **oDND**, the G band decreases in intensity in comparison to the diamond/D band signal due to loss of amorphous/sp^2 carbon during sample treatment/purification.

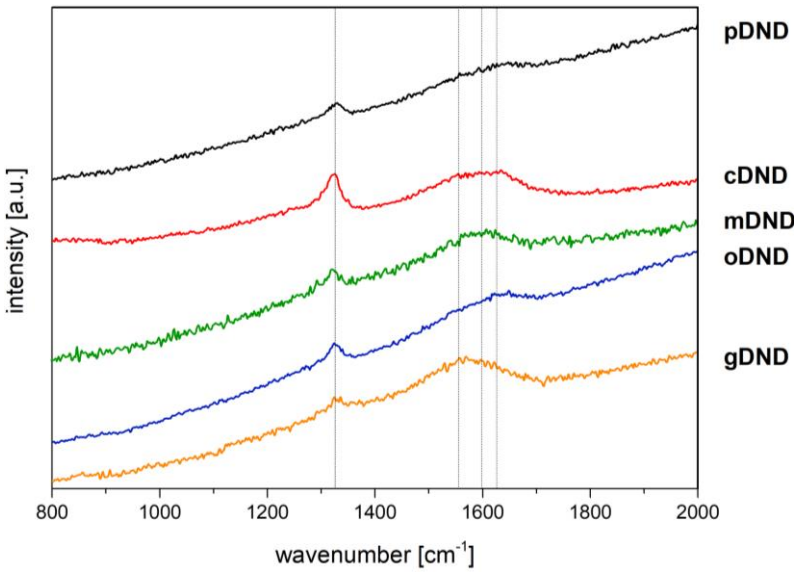

Fig. 20: Raman spectra of **pDND**, **cDND**, **mDND**, **oDND** and **gDND** (excitation at 445 nm).

3.1.1.6 Hydrogenation of DND materials

The hydrogenation of diamond materials presents a method to produce a homogenous surface.[303] Furthermore, the hydrogenation of boron-doped diamond electrodes leads to a negative electron affinity, substantially influencing the electronic properties of

diamond (chapter 1.3).[75] To investigate the influence of a homogenously hydrogenated DND particle surface on the photocatalytic activity, the two main approaches to hydrogenate nanodiamonds, either by exposure to hydrogen plasma or annealing under hydrogen atmosphere,[303] were applied to the five produced DND materials. The hydrogen termination was carried out by cooperation partners within the DIACAT project. Plasma hydrogenation at CEA List, Saclay, France was achieved by Amélie Venerosy under supervision of Dr. Jean-Charles Arnault/Dr. Hugues Girard. Here, a microwave plasma in H_2 atmosphere was used to achieve the hydrogenation of ND powders. The home-made setup allowed the exposure of 20 mg of NDs to a hydrogen plasma. The plasma was applied at 15 mbar and 250 W during 20 min.[303] Particles were placed in a quartz tube, which was inserted into the microwave waveguide cavity. The tube was rotated during the exposure to ensure the homogeneity of the hydrogenation treatment over the whole surface of nanodiamond powder.[304,305] Thermal hydrogenation at Fraunhofer IAF, Freiburg, Germany, was carried out by Dr. Nicola Lang/Dr. Fang Gao. For thermal H-termination, ND samples were loaded in a tube furnace and exposed to 20 mbar hydrogen atmosphere. The annealing was performed at 600 °C for 15 min.[306] To ensure the complete termination, the powdery sample was mixed and annealed again in H_2 atmosphere. This procedure was repeated three times in total. Characteristic results of the DND particles in dispersion before and after hydrogenation are shown in Table 4.

Table 4: Zeta potential (pH range of 5.4-6.4) and particle size in aqueous dispersion before and after hydrogenation using plasma (CEA) or thermal method (IAF)

ND material	ζ_{before} [mV]	ζ_{after} (CEA) [mV]	ζ_{after} (IAF) [mV]	$D_v(50)_{before}$ [nm]	$D_v(50)_{after}$ (CEA) [nm]	$D_v(50)_{after}$ (IAF) [nm]
pDND	+43.2	+45.8	+47.3	170	1060	755
cDND	+50.1	+42.2	+41.2	386	935	965
mDND	+35.2	-[a]	+55.9	3.05	-[a]	18.0
oDND	-20.3	-[a]	+42.8	158	-[a]	864
gDND	33.9	+43.2	+42.8	207	298	310

[a] **mDND** and **oDND** were not hydrogenated by CEA

H-terminated particles showed a highly positive zeta potential, irrespective of the DND starting material. Most significant was the change for **oDND** from -20.3 mV to +42.8 mV. Regarding the particle size, redispersing the powdery samples in water after

H-treatment yielded dispersions of strongly bound agglomerates. Those agglomerates are already formed during the hydrogenation.[303] Two possibilities to remove those agglomerates are conceivable, either by centrifugation or using an ultrasonic horn. As the latter could lead to contamination with metal debris as well as breaking up smaller agglomerates and hence generating non-hydrogenated surface again, centrifugation represented the method of choice.

The successful hydrogen termination can be identified in the DRIFT spectra and is shown, for example, for hydrogenated **H-pDND$_{CEA}$**, **H-pDND$_{IAF}$**, **H-gDND$_{CEA}$** and **H-gDND$_{IAF}$** particles (Fig. 21). The asymmetric and symmetric C-H-stretching vibrations are more pronounced after hydrogenation (2944 cm^{-1}, 2880 cm^{-1}) for **pDND** particles. The C-H out-of-plane deformation vibration at 836 cm^{-1} is clearly visible for each H-terminated sample, but not for the **pDND**. The same is true for the sym. C-H deformation vibration at 1392 cm^{-1}. The non-existent C=O stretching vibration at 1719 cm^{-1} highlights the changed surface termination. **gDND** already shows the characteristic vibrations before the hydrogen annealing, as the thermal annealing at 750 °C needed to produce **gDND** (chapter 3.1.1.4) mainly removes oxygen containing groups and does not affect hydrogen or methyl groups on the surface.[268] Thus, the FT-IR signals of **gDND** and **H-gDND** are almost identical.[293]

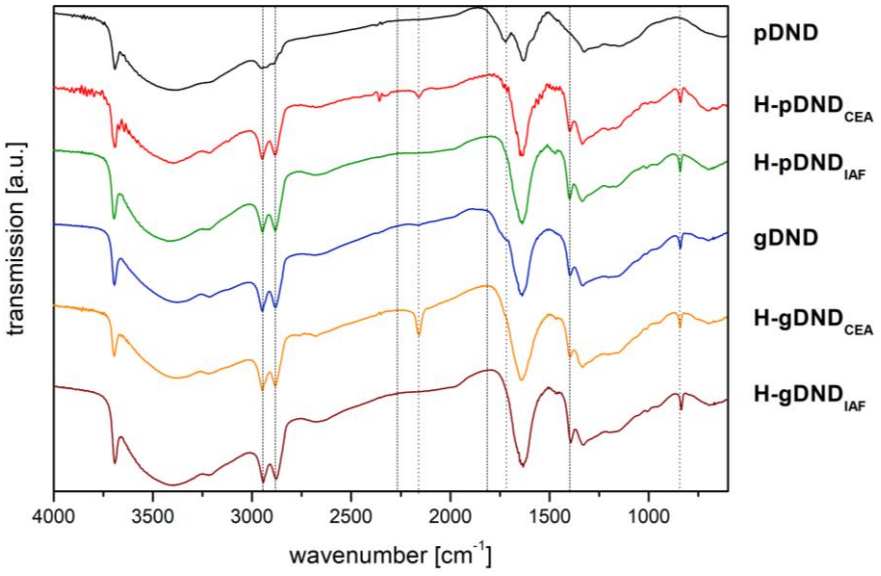

Fig. 21: DRIFT spectra of **pDND**, **gDND** and the hydrogenated samples **H-pDND$_{CEA}$**, **H-pDND$_{IAF}$**, **H-gDND$_{CEA}$** and **H-gDND$_{IAF}$**.

The CEA and IAF treated samples only differ in the vibration at 2153 cm^{-1} for CEA treated samples, which seems to originate from the plasma treatment and may be

related to C-N graphitic structures on the particle surface (cf. chapter 3.1.1.3). Apart from this additional band, the obtained spectra for all hydrogenated particles show the same characteristic bands. The spectra of the hydrogenated particles of **mDND**, **cDND** and **oDND** can be found in the Appendix (Fig. 117) presenting the same results.

3.1.1.7 Fluorination of diamond materials

Alongside annealing and hydrogenation, the fluorination of DND particles provides another method for surface homogenization, as discussed in chapter 1.7. A well-established method to fluorinate ND powders is presented by the treatment at temperatures of <310 °C with a mixture of F_2/H_2 gas.[254] In order to circumvent these challenging conditions, a new fluorination process using liquid HF and elemental F_2 gas at moderate temperatures was developed. The fluorination experiments were carried out in cooperation with the group of Prof. Dr. Maik Finze at the Inorganic Chemistry Institute, University Würzburg, involving the PhD students Michael Drisch and Fabian Keppner. The obtained particles are interesting for catalytic applications, as a surface termination with electronegative fluorine should have substantial effects on the electronic properties, in particular the emission of electrons.

3.1.1.7.1 Fluorination of thermally annealed DND (gDND)

From a general point of view, the sp^2-layer on the particle surface of **gDND** should readily react with fluorine reagents of the HF/F_2 system, as an addition reaction at lower temperatures is conceivable.[307] The electrophilic addition of highly polar, hydrohalic acid HF to the sp^2 hybridized surface should generate a hydrohalogenated surface,[308] whereas the addition of fluorine should lead to a purely halogenated surface.[309] In both these cases, the nucleophilic fluoride anion would react with carbocations on the particle surface.[310] For fluorination, the annealed particles **gDND** were suspended in anhydrous HF and cooled to -78 °C before F_2 was applied gasometrically (Fig. 22).

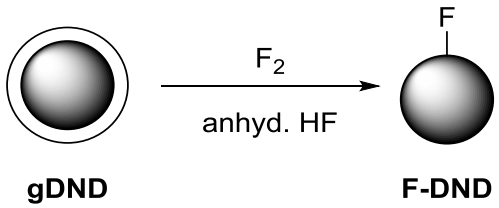

Fig. 22: Fluorination of **gDND**.

For method development, the suspension of **gDND** in 10 mL anhydrous HF was stirred at a defined temperature and for a selected reaction time, applying different amounts of F_2 gas (Table 5). Afterwards, the volatiles, HF and mainly (per)fluorinated hydrocarbons from the non-diamond carbon, were removed *in vacuo* and the recovered powder was dried at $1 \cdot 10^{-3}$ mbar. In total, eight fluorination methods **F-DND1-8** were tested.

Table 5: Amount of **gDND** and fluorine gas, reaction temperature, time and recovered amount of **F-DND1-8**

fluorination method	amount [mg]	F_2 [mol%]	T [°C]	time [h]	recovered amount [mg]
F-DND1	200	-	r.t.	24	182
F-DND2	200	15	r.t.	72	193
F-DND3	200	30	r.t.[a] 35	120 48	198
F-DND4	200	40	50	480	198
F-DND5	100	30	50	120	73
F-DND6	100	45	50	120	81
F-DND7	100	40	50	120	78
F-DND8	50	40	50	120	38

[a] For **F-DND3** the temperature was increased after 120 h from r.t. to 35 °C for further 48 h.

During the reactions yielding **F-DND2-8**, the entire amount of F_2 was consumed. The reaction leading to **F-DND1**, without any F_2 gas applied, served as a control experiment and showed the influence of pure HF on the particle surface. After the first successful fluorination experiments (**F-DND2-4**), for **F-DND5-8** the focus was set on the optimization and reproducibility of the reaction conditions, only varying the amount of added fluorine gas, while the suspension was always stirred at 50 °C for 120 h.

X-ray spectroscopy (XPS) measurements allowed for the quantification of the efficiency of fluorine grafting. The XPS measurements were carried out at CEA List, Saclay, France by Amélie Venerosy under supervision of Dr. Jean-Charles Arnault/Dr. Hugues Girard. Survey spectra of all fluorinated particles are presented in the Appendix (Fig. 118). The detection of a photoemission peak from gold (Au $4f_{7/2}$ at 84 eV) on all samples indicates an incomplete coverage of the gold substrate surface by ND particles. All survey XPS spectra show the presence of oxygen (O1s at 531 eV).

The highest fluorine to carbon ratio was obtained for **F-DND6** and **F-DND7** with 0.13 (Table 6) and the highest atomic concentration at the surface was reached for **F-DND7** with 11.6 at.%, indicating that both an increased amount of fluorine gas and higher temperature are needed for a successful fluorination. As **F-DND1** neither showed any fluorine content nor different atomic percentages than reference **gDND**, two further conclusions can be drawn. First, F_2 is required for a surface fluorination of **gDND** and second, C-F related vibrations in the DRIFT/ATR-FTIR spectra of **F-DND1** must be related to adsorbed/chemisorbed fluorine species, which were removed during XPS sample preparation in ultrahigh vacuum (~$1 \cdot 10^{-10}$ mbar). For example, HF is known to adsorb to H-, O- and F-terminated material.[253]

Table 6: Atomic concentrations of elements detected by XPS (left column) and EA in weight percentages (right column) of **gDND** and **F-DND1-8**

DND material	C1s [at.%]	O1s [at.%]	F1s [at.%]	F/C	C [wt.%]	H [wt.%]	N [wt.%]	F [wt.%]	F/C
gDND	94.2	5.8	-	-	92.44	0.87	0.72	-	-
F-DND1	94.5	5.5	-	-	90.97	1.29	1.89	0.95	0.01
F-DND2	90.1	3.7	6.2	0.07	84.96	1.19	2.26	5.79	0.04
F-DND3	87.1	3.1	9.7	0.11	82.43	0.51	2.41	11.29	0.08
F-DND4	89.8	3.2	7.1	0.08	83.18	1.05	2.02	8.42	0.06
F-DND5	90.7	2.2	7.2	0.08	80.04	1.27	2.26	9.43	0.07
F-DND6	86.2	2.9	10.9	0.13	78.41	1.06	2.48	11.44	0.09
F-DND7	86.3	0.8	11.6	0.13	79.58	0.98	1.99	11.75	0.09
F-DND8	84.5	5.5	10.0	0.12	78.96	1.21	1.37	11.50	0.09

As XPS is a surface sensitive method, probing ~5 nm into the diamond matrix, the absolute values of fluorine for the whole diamond samples were determined via EA. It cannot be excluded that fluorine was also penetrating the diamond core leading to fluorine atoms positioned in diamond lattice interspaces or that strongly agglomerated particles were not fully characterized by XPS due to their size. These atoms cannot be detected by XPS. In accordance with XPS, the sample **F-DND7** showed also the highest fluorine content (11.75 wt.%) and F/C ratio (0.09) in elemental analysis. The F/C-ratio was lower than the value obtained from XPS as all carbon is accounted for. The detected nitrogen originated from the core of the DND particles, as XPS did not detect any surface related nitrogen. The sample **F-DND1**, treated without any fluorine

gas, presented ~0.95 wt% of fluorine, proving that HF or fluorinated hydrocarbons were adsorbed to the DND particles.

For DLS measurements, stable aqueous dispersions were obtained (Fig. 23). For the samples **F-DND1-4**, stronger particle agglomeration was taking place. For the optimized, more homogenous samples **F-DND5-8**, a larger fraction of smaller particles (D_V-(10) ~50 nm) was present. The mean size (D_v-(50) value) was ~25–65 nm smaller than for **gDND**, showing less agglomeration (Table 7). The F_2 gas is able to penetrate the porous ND agglomerates of **gDND** and breaks the covalent interactions while fluorinating the surface and surface groups, thus leading to smaller particles.[258]

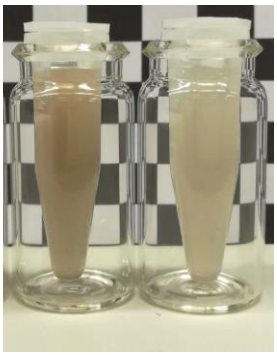

Fig. 23: **gDND** (left) and **F-DND5** (right) in aqueous dispersion (5 mg/ml).

F-terminated particles still showed a positive zeta potential in aqueous dispersion (Table 7). However, Huang *et al*. reported a potential of -30.5 mV for fluorinated DND in ethanol,[258] while Havlik *et al.* measured -46 mV for fluorinated HPHT ND particles.[259]

Table 7: Zeta potential and particle size measurements of **gDND** and fluorinated DND particles **F-DND1-8**

ND material	ζ [mV] (pH)	D_V-(10) [nm]	D_V-(50) [nm]	D_V-(90) [nm]
gDND	+33.9 (6.3)	132	207	372
F-DND1	+34.3 (5.9)	48.8	397	1950
F-DND2	+29.0 (5.7)	214	1200	3470
F-DND3	+35.4 (5.4)	54.3	313	1490
F-DND4	+31.9 (5.6)	38.6	183	1640
F-DND5	+34.8 (5.5)	53.1	142	411
F-DND6	+32.9 (5.3)	50.6	167	432
F-DND7	+34.7 (5.4)	66.6	179	453
F-DND8	+32.4 (5.3)	42.7	158	465

This observation can by explained by the observed XPS and EA results. Related to the amount of fluorine attached to the surface, the samples showed a slightly more acidic pH value (Table 7), which can be related to even small quantities of HF being adsorbed to the surface. The more fluorine groups are covalently attached to the surface, the better HF is adsorbed due to fluorophilic interactions.[253] As a consequence, the pH should get more acidic in aqueous dispersion. The acidity, in combination with remaining graphitic parts of the **gDND** surface after fluorine treatment, can explain the positive surface potential. π electron-rich regions, such as the graphitic ones, located at the basal planes are known to interact with oxonium ions.[311,312] Those oxoniun ions are generated in acidic, aqueous dispersions, generated for example by adsorbed HF molecules, and can adsorb to oxygen-free, π electron-rich carbon sites to provide a particle surface with positive charge.[291] Huang *et al*., reporting -30.5 mV for fluorinated DND, measured the potential in ethanol,[258] which prohibits the formation of an oxonium ion shell. Havlik *et al.* measured -46 mV for fluorinated HPHT ND particles.[259] Here, a remaining amount of carboxylic groups from the starting material, as well as a different pH value, could explain the unchanged potential.

The DRIFT spectrum of **gDND** shows the characteristic C-H vibrations already discussed in chapter 3.1.1.5. For **F-DND1**, these signals are still present, but with lower intensity. **F-DND2-4** show no defined C-H-vibration, however, the broad signal at 2974 cm^{-1} can be related to CH_xF_y groups on the surface (Fig. 24).[254,313]

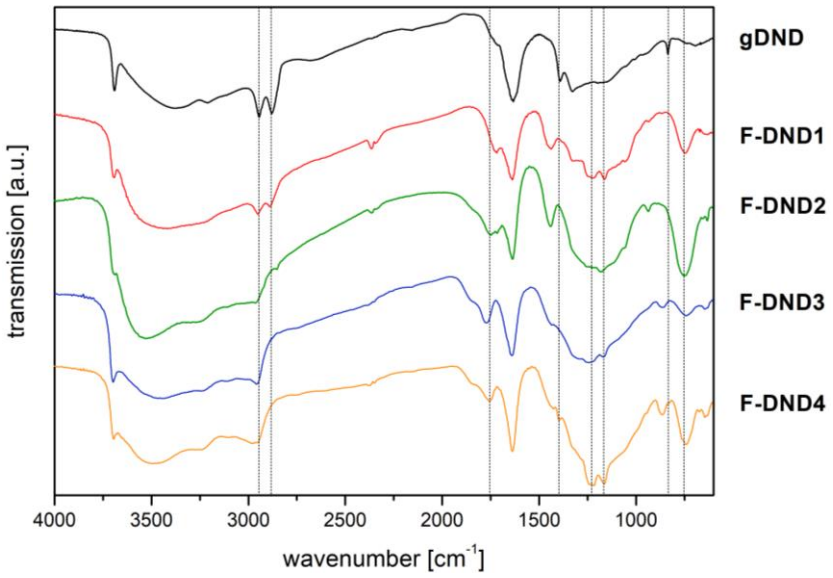

Fig. 24: DRIFT spectra of **gDND** and HF/F_2 treated DNDs **F-DND1-4**.

The stretching vibrations of C-F can normally be found in the region between 1000-1300 cm^{-1}.[251-253] All samples **F-DND1-4** show several superimposed bands between 1050–1260 cm^{-1}, indicating the presence of C-F bonds. The emerging peak at 735 cm^{-1} is attributed to C-F deformation vibrations.[251,252] The new peak after fluorination at around 1750 cm^{-1} is correlated to C=O groups on the surface. This observation can have different reasons. If particle agglomerates of **gDND** are broken during the fluorination process, smaller particles containing oxygen surface groups are generated. The surface of those particles was not accessible during the annealing process fabricating **gDND**. Another possible explanation would be that if the graphitic shell of the diamond particles has reacted with fluorine, the surface beneath the sp^2 layer, still containing C=O groups, is exposed. The observation that the C=O stretching vibration is more prominent at samples with a high fluorine amount (**F-DND3** and **F-DND4**) supports this assumption, as the graphitic shell of these samples increasingly reacted exposing more diamond surface.

DRIFTS measurements present a suitable method to check the alterations regarding the annealed surface, however, the C-F termination is more pronounced and defined in ATR-FTIR spectra.[253] For **F-DND1** and **F-DND2**, almost no C-F stretching vibrations are observable (Fig. 25).

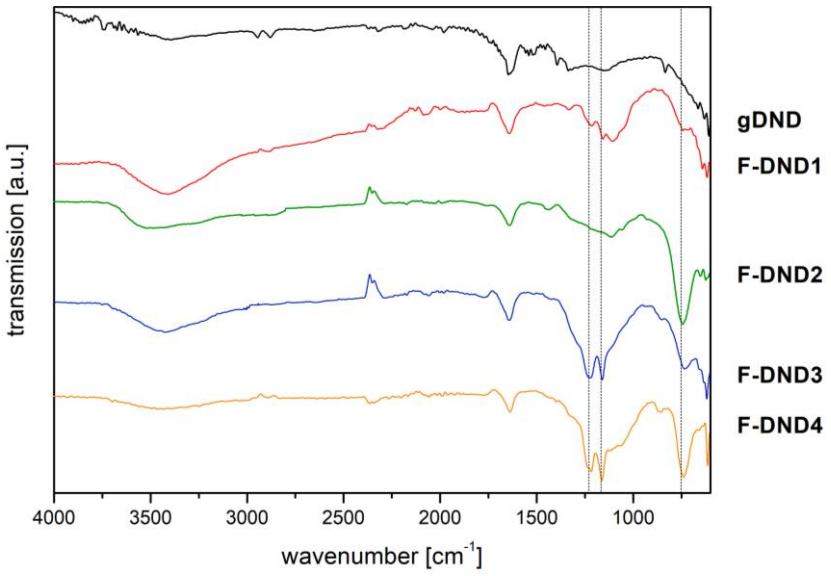

Fig. 25: ATR-FTIR spectra of **gDND** and HF/F_2 treated DNDs **F-DND1–4**.

However, **F-DND3** and **F-DND4**, where higher F_2 amounts and temperatures were used, present substantial signals of asymmetric and symmetric C-F-stretching vibrations at around 1210 cm^{-1} and 1159 cm^{-1} with high intensities. According to the

literature, highly F-terminated diamond samples exhibit a very strong and intensive signal between 1325-1337 cm^{-1} being related to the C-C-vibration of the diamond core influenced by attached F-atoms, which change the dipole moments of the surface C-C bonds.[252] This observation was reported for the cleaning of the diamond surface from non-diamond carbon using the F_2/H_2 mixture and the application of higher temperatures for fluorination.[254] Touhara *et al.* reported that the diamond core C-C vibration is present at fluorination temperatures >100 °C.[256] This indicates that our mild reaction conditions (120 h at 50 °C) for the fluorination of **gDND** and the intentionally established sp^2-surface of **gDND** suppress this vibration, as fluorine atoms are attached only to the surface and not directly to the diamond core. In general, the C-C vibrations of the core are not easily detectable using IR spectroscopy.[253,256] Therefore, complementary Raman spectroscopy was used.[264]

To prove that the observed C-F signals were not originating from fluorinated carbon species other than nanodiamond, the obtained powder **F-DND4**, which showed the most intensive C-F vibrations during the method development, was washed several times using unpolar solvents (cyclohexane, *n*-pentane, *n*-hexane) and re-analyzed again resulting in no detectable differences (Appendix, Fig. 119).

Further results were obtained analyzing **F-DND5-8**, for which the findings from the first four fluorination experiments (**F-DND1-4**) were taken into account. All samples show the already discussed superimposed C-F stretching and C-F deformation vibrations, as well as the vibration of CH_xF_y groups (Fig. 26a).

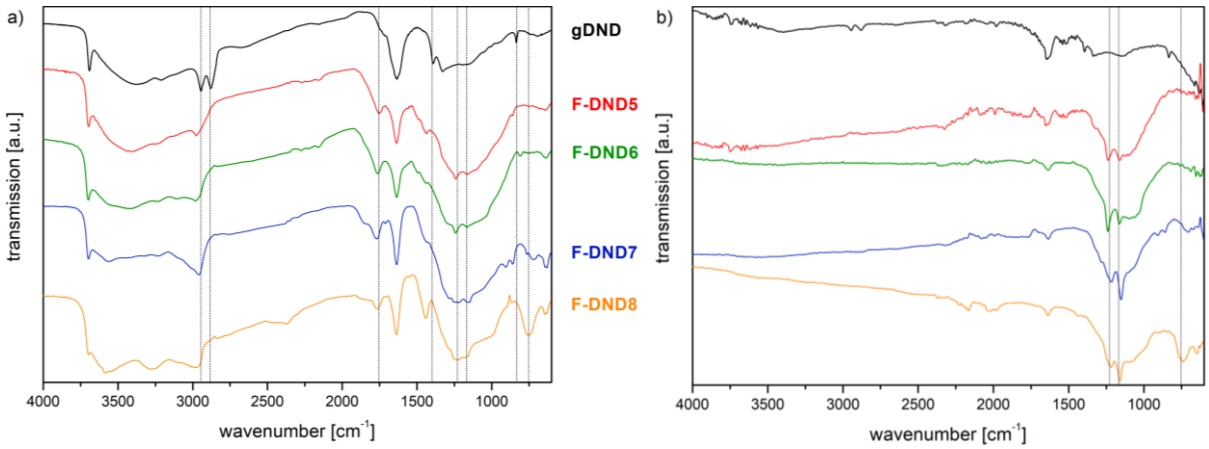

Fig. 26: DRIFT (a) and ATR-FTIR (b) spectra of **gDND** and HF/F_2 treated DNDs **F-DND5-8**.

In the ATR-FTIR spectra (Fig. 26b), the asymmetric and symmetric C-F stretching vibrations can be clearly seen. Additionally, **F-DND5** and **F-DND6** illustrate a very

broad signal at ~1060 cm^{-1}, whose origin will be discussed in the following paragraph(s).

For **F-DND5** and **F-DND6**, the influence of intensive drying in vacuum after fluorination was investigated. Although the used starting material has a very high diamond content, non-diamond, amorphous carbon is still present (chapter 1.2.1). During the treatment this carbon was also fluorinated, leading to highly volatile, perfluorinated molecules.[253] **F-DND5** and **F-DND6** were dried for only five hours *in vacuo* ($1 \cdot 10^{-3}$ mbar) and the removal of adsorbates was confirmed by thermogravimetric measurements. **F-DND6** was heated from 25 °C to 130 °C at 40 °C min^{-1} and kept at 130 °C for 15 min to remove surface-adsorbed water. The sample was further heated (rate of 40 °C min^{-1}) to the chosen final temperatures (Table 8) and kept at this temperature for 2 h. The removal of adsorbates other than water started directly after the additional heating from 130 °C and after 30 min no further mass loss was detected. As the mass loss reached a consistent level at 300 °C and 350 °C, it can be stated that at least 300 °C were required to effectively remove all adsorbates. A temperature above 350 °C was avoided, as, according to the literature, the actual fluorine termination of diamond films starts to decompose.[314]

Table 8: Mass loss of **F-DND6** during thermogravimetric measurements at a specific final temperature

final temperature [°C]	150	200	250	300	350
Mass loss at 15-30 min [Δm-%]	-1.1	-3.2	-5.2	-7.6	-7.7

The pronounced and broad signal at ~1060 cm^{-1}, which is strongly present for **F-DND6** heated at 150 °C, decreases with increasing temperature indicating that it is caused by adsorbates (Fig. 27a), most likely (per)fluorinated hydrocarbons. These molecules generally present broad C-F related signals in this region of the FT-IR spectrum.[315] The C-F vibrations at higher wavenumbers, related to the asymmetric and symmetric stretching vibrations (c.f. Fig. 25), are getting more distinctive again (Fig. 27a).

For **F-DND5**, the influence of treatment duration on the C-F termination at 300 °C was investigated. In Fig. 27b, the ATR-FTIR spectrum prior to thermal treatment (**F-DND5$_0$**) is compared with the samples after 4 h, 8 h and 16 h at 300 °C. After 4 h, the broad signal of the adsorbates at ~1060 cm^{-1} is barely visible, whereas the C-F stretching vibrations at higher wavenumbers are clearly illustrated. After a longer treatment (8 h,

16 h), the C-F termination suffers heavily, leading to a significant loss in signal intensity.

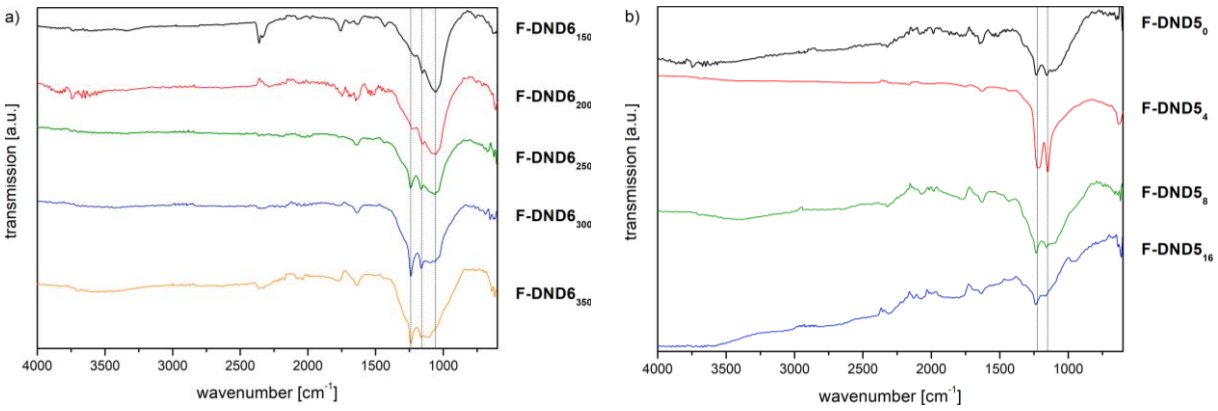

Fig. 27: ATR-FTIR spectra of **F-DND6** after thermal treatment at different temperatures (a) and of **F-DND5** after thermal treatment at 300 °C for different times (b).

Further thermogravimetric analysis proved that the covalent F-termination also started to decompose at temperatures >350 °C for diamond nanoparticles (Fig. 28). For **gDND** and **F-DND1**, no significant difference is visible. **F-DND2-4** illustrate clear steps of the degrading F-termination in the temperature range of 400-700 °C. Depending on the nature of the surface–bound fluorine, the termination is expected to decompose over the entire temperature range.[316] The particles **F-DND5-8** demonstrate an almost identical course in comparison to **F-DND3** (Appendix, Fig. 120).

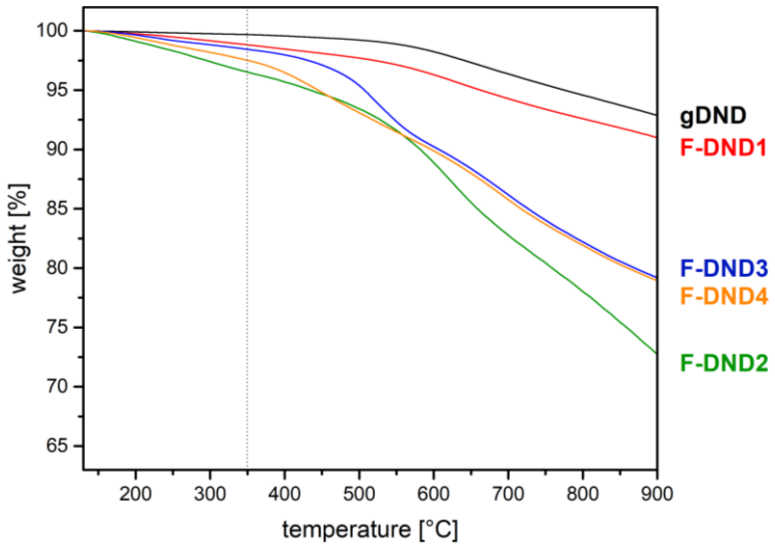

Fig. 28: Thermogravimetric analysis of **gDND** and HF/F_2 treated DNDs **F-DND1-4**.

As previously mentioned, Raman spectroscopy enables to investigate the influence of the fluorination treatment on the diamond core and the sp^2 shell of the particles. For all samples, a diamond peak in combination with the D Band (cf. chapter 3.1.1.5) is

present, as well as a broad G band (λ_{ex} = 445 nm, Fig. 29). The effect of the fluorination on the sp^2 shell can be assessed by the ratio between diamond peak/D band and G band (Table 9).

In comparison to **gDND**, the G band is not shifted for the fluorinated particles. The slight shift of the diamond/D band results from a change in polarizability due to fluorine attachment.[316]

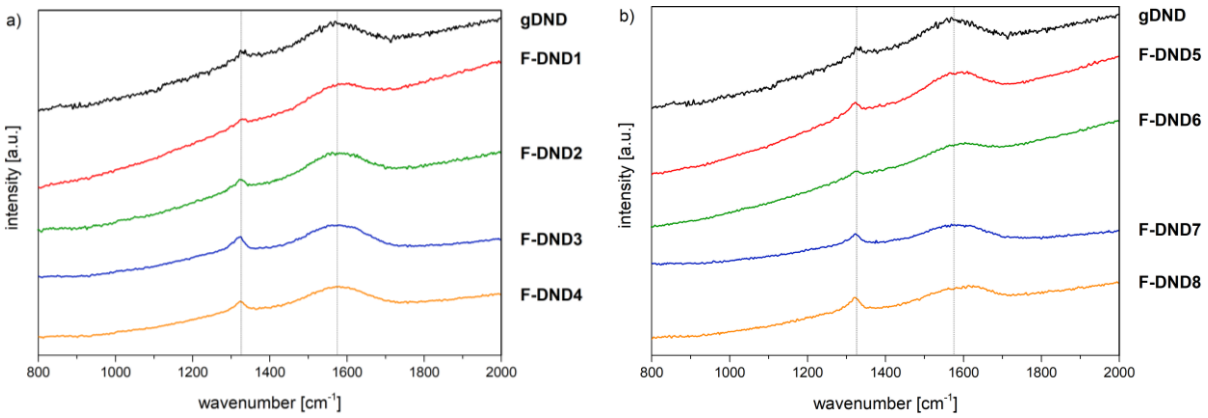

Fig. 29: Raman spectra of **gDND** and **F-DND1-4** (a) and **gDND** and **F-DND5-8** (excitation at 445 nm).

For **F-DND3** and **F-DND6-8**, the ratio is considerably decreased, indicating a loss in sp^2-content due to reaction with fluorine forming sp^3-hybridized carbon atoms. The ratio is getting closer to the one from untreated **pDND**.

Table 9: Comparison of **pDND**, **gDND** and **F-DND1-8** regarding position and intensity of the G band and diamond/D band peak and the ratio between G band and diamond/D band signal

ND material	G band [cm^{-1}]	diamond/D [cm^{-1}]	G band intensity [a.u.]	diamond/D intensity [a.u.]	ratio G band:diamond
pDND	1619	1326	29.1	26.8	1.09
gDND	1565	1326	33.6	17.9	1.88
F-DND1	1570	1331	137	69.4	1.97
F-DND2	1563	1331	72.7	39.0	1.86
F-DND3	1565	1325	145	113	1.28
F-DND4	1578	1328	96.1	66.1	1.45
F-DND5	1569	1325	147	99.4	1.47
F-DND6	1568	1327	88.1	68.2	1.29
F-DND7	1580	1328	86.2	67.9	1.26
F-DND8	1564	1326	83.3	65.1	1.28

The obtained results led to an optimized protocol for the wet-chemical fluorination of thermally annealed DND (**gDND**). Suspending **gDND** (100-200 mg) in anhydrous HF was followed by the addition of 40 mol% F_2 at -78 °C. After stirring at 50 °C for 120 h in a PFA flask, the volatiles were removed *in vacuo* and the obtained powder was dried for at least 24 h at $1 \cdot 10^{-3}$ mbar. The purification was completed by washing with unpolar solvents and thermal annealing (300 °C for 2-4 h). Thus, remaining adsorbates, such as HF or (per)fluorinated hydrocarbons, were removed.

The applied analytical methods provided qualitative and quantitative evidence of the covalent attachment of fluorine to the DND surface. The assessment of the actual nature of the F-containing groups formed on the DND surface proved to be difficult to be performed via XPS. Although the carbon and fluorine XPS core levels were recorded, the broad shape of the C1s, typical for DND particles, prevented to explicitly detect carbon-fluorine bonds, which should be located at higher binding energies with respect to C1s. Hence, the nature of the fluorine bonding cannot be clearly identified via XPS. Therefore, to determine the actual chemical nature of the fluorine surface groups, a series of solid-state NMR experiments was performed by Jun.-Prof. Dr. Ann-Christin Pöppler, Institute for Organic Chemistry, University Würzburg. Two fluorinated samples, **F-DND3** and **F-DND5$_4$**, were investigated. As previously mentioned, the sample **F-DND5$_4$** was post-processed by heating (4 h at 300 °C). In both cases, ^{1}H and ^{13}C NMR experiments, both with direct excitation as well as cross polarization, and ^{19}F experiments were performed. Additionally, ^{1}H-^{13}C and ^{19}F-^{13}C correlation spectra were recorded. For comparison purposes, **gDND** was also investigated. Theoretical calculations (CASTEP) helped complementing the experimental data to obtain possible model structures of fluorinated DND.

A comparison between experimental data and theoretical calculations for ^{19}F NMR spectra identified CF_2 environments (-121 ppm) as the main and well-defined species obtained by this mild fluorination method with only few CF (-70 ppm) and CF_3 groups (-148 ppm) present. The presence of CF_2-groups also agrees with the observation of triplets for the ^{13}C NMR signal at 111.5 ppm. Theoretical modelling resulted in a high electron affinity of these functional groups (~50% surface coverage) in combination with either a Pandey-Chain reconstructed surface or an oxygen-terminated surface. Combined with a hydrogen-terminated surface, a close to zero electron affinity was calculated facilitating the use of the fluorinated powders in photocatalysis, where highly

energetic electrons are required for the reduction of chemically inert molecules, such as CO_2.

Combined with the results from EA, these data allow an estimation of the surface loading with fluorine containing groups. Assuming that ND particles with a size of 5 nm have a specific surface are of 300 m^2g^{-1} (BET),[317] ~15% of the overall carbon is located at the surface. Taking **F-DND3** as an example, with C 82.43 wt.%, H 0.51 wt.%, N 2.41 wt.%, F 11.29 wt%, and O ~3.5 wt.%, almost 12.5 wt.% (~15%) of the carbon is at the surface. With a C/F ratio of ~1:1 and the assumptions that first, all fluorine groups sit on the surface, and second, mainly CF_2 groups are present (ratio of CF_3 and CF groups can be estimated to 1:1, so in average "CF_2"), ~ 50% of the surface is covered with CF_2 groups. The non-fluorinated parts of the surface are likely terminated with hydrogen (cf. EA results) or oxygen (cf. FT-IR results), because the fluorination conditions are not harsh enough for the replacement of both terminations.[254] Additionally, Raman illustrated that parts can still be sp^2-covered.

3.1.1.7.2 Fluorination of other DND materials

The optimized fluorination protocol (chapter 3.1.1.7.1) was also applied to the DND materials **pDND**, **oDND** and **H-DND** (Fig. 30).

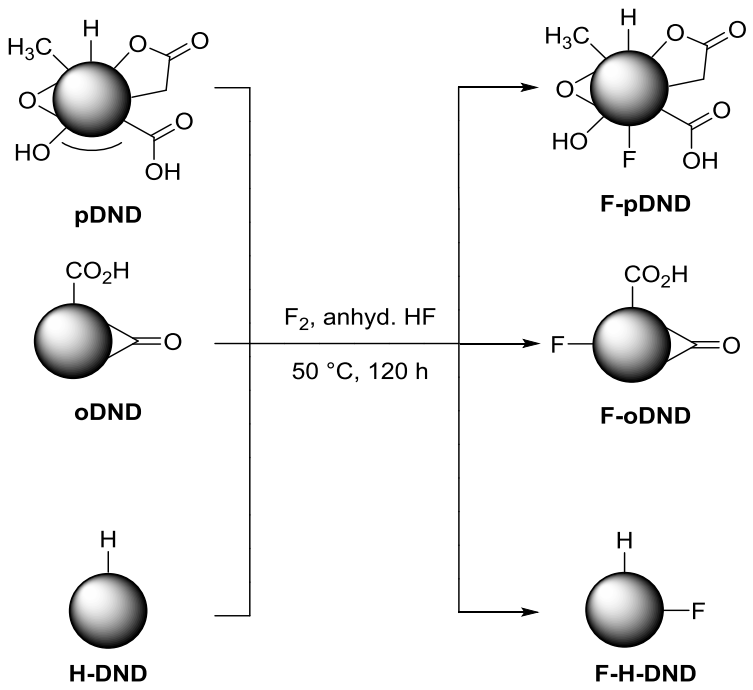

Fig. 30: Fluorination of DND materials **pDND**, **oDND** and **H-DND**.

Using **pDND** particles with their inhomogeneous surface, bearing different hydrogen, oxygen or even nitrogen groups, the importance of a mostly homogeneous surface on the fluorination was investigated. In experiments with **oDND**, the reactivity of the highly oxidized particles surface towards the mild fluorination was studied. For **H-DND**, a complete replacement of hydrogen with fluorine using F_2 gas was observed at r.t.,[252] making **H-DND** an ideal reference material to test the maximum amount of fluorine being attached by the wet-chemical fluorination method. Therefore, the fluorinated particles **F-pDND**, **F-oDND** and **F-H-DND** were analyzed in detail to highlight the impact of the fluorination method on the respective surface of the different staring materials **pDND**, **oDND** and **H-DND**.

In comparison to **pDND**, **F-pDND** showed no substantial changes regarding zeta potential or particle size in aqueous dispersion, yielding particles with a highly positive surface charge and agglomerates in the range of $D_V(50)$ = 162-170 nm (Table 10).

Table 10: Zeta potential and particle size measurements of **pDND**, **oDND**, **H-DND$_{IAF}$** and fluorinated particles **F-pDND**, **F-oDND**, **F-H-DND1** and **F-H-DND2**

DND material	ζ [mV] (pH)	D_V-(10) [nm]	D_V-(50) [nm]	D_V-(90) [nm]
pDND	+43.2 (6.3)	77.6	170	386
F-pDND	+36.2 (5.8)	69.4	162	446
oDND	-41.6 (5.4)	145	1090	2300
F-oDND	-23.1 (5.2)	64.3	237	1280
H-DND$_{IAF}$	+41.2 (6.4)	133	965	1650
F-H-DND1	+31.3 (5.2)	45.7	173	384
F-H-DND2	+32.4 (5.1)	46.4	162	427

The fluorinated particles, **F-oDND**, presented substantially smaller particle agglomerates than the starting material **oDND** ($D_V(50)$ 1090 nm → 237 nm). In addition, the zeta potential of **F-oDND** was also slightly more positive than the potential of **oDND** (-41.6 mV → -23.1 mV). Both observations suggested an effect of the fluorination treatment on the **oDND** particles. The fluorinated **H-DND** particles, **F-H-DND1** and **F-H-DND2**, illustrated significantly smaller particle agglomerates than the starting material **H-DND$_{IAF}$** ($D_V(50)$ 965 nm → 158-173 nm). **H-DND$_{IAF}$** strongly agglomerated in aqueous dispersion due to its hydrophobic character (chapter 3.1.1.6); however, after fluorination treatment, the particles **F-H-DND1** and **F-H-DND2** yielded stable, aqueous dispersions indicating a change in surface termination. The

values for particle size and zeta potential of **F-H-DND1** and **F-H-DND2** represented almost the same results as obtained for the fluorinated particles **F-DND5-8** (Table 7, chapter 3.1.1.7.1). Whether these observations are related to the same fluorine-containing surface groups will be discussed in the following spectroscopic analysis.

The DRIFT spectra of **F-pDND** and **F-oDND** (Fig. 31a) show vibrations of the C-F stretching (1061 cm^{-1} (**F-pDND**) and 1185 cm^{-1} (**F-oDND**)) and deformation vibration (748 cm^{-1} for **F-oDND**) after fluorination treatment. However, the signals appear in broad shape and a clear distinction into asymmetric or symmetric stretching vibration is not possible. For both materials, **F-pDND** and **F-oDND**, several vibrations, such as C-O-(C) stretching and bending, of oxygen containing surface groups (ethers, esters, anhydrides)[293] superpose with C-F vibrations in the region of 1000-1250 cm^{-1}. For **F-oDND**, the intensive signal of the C=O stretching vibration of the starting material **oDND** at 1804 cm^{-1} is significantly shifted to 1844 cm^{-1}. The shift can be attributed to stretching modes of F-substituted carbonyl groups.[254,293] The ATR spectra (Fig. 31b) also illustrate no defined asymmetric or symmetric C-F stretching vibrations for **F-pDND** and **F-oDND**. For **F-pDND**, a very broad and intensive signal at 1043 cm^{-1} is observed, which was already correlated to adsorbed fluorine species (chapter 3.1.1.7.1).

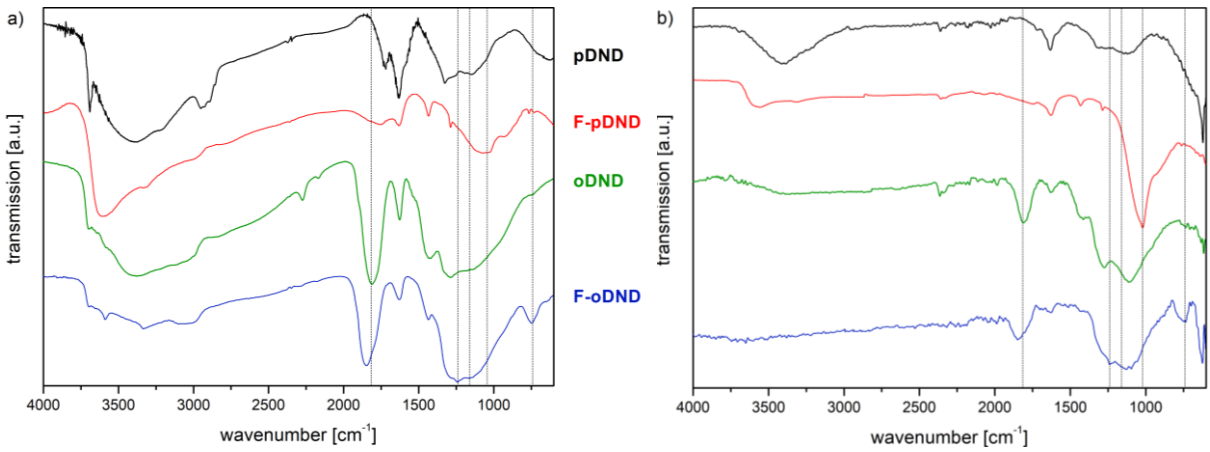

Fig. 31: DRIFT (a) and FTIR-ATR spectra of **pDND**, **oDND** and HF/F_2 treated DNDs **F-pDND** and **F-oDND**.

In accordance to the DRIFT spectra, several superposed C-F and C-O-(C) vibrations can be seen in the region from 1100-1280 cm^{-1} for **oDND**, supplemented by the broad C-F deformation vibration at 747 cm^{-1}. Although there was no defined C-F stretching vibration present in **F-pDND** and **F-oDND**, it can be stated the fluorination treatment

led to different effects on the particle surface. The highly oxidized surface groups of **oDND** are most likely substituted by fluorine groups, forming F-substituted carbonyl groups.[254,318] However, for the pristine particles **pDND**, it is most likely that amorphous, non-diamond carbon, which has been removed from **oDND** during the air oxidative treatment (chapter 3.1.1.3), was primarily fluorinated. The resulting, (per)fluorinated hydrocarbons are strongly adsorbed to the diamond surface, resulting in the intensive signal at 1043 cm^{-1} (Fig. 31b).

The DRIFT spectrum of **H-DND**$_{IAF}$ (Fig. 32a) shows the typical C-H related signals, such as the asymmetric and symmetric stretching (2944 cm^{-1}, 2880 cm^{-1}), the symmetric deformation (1392 cm^{-1}) and the out-of-plane deformation vibration (836 cm^{-1}, cf. chapter 3.1.1.6). The fluorinated DNDs, **F-H-DND1** and **F-H-DND2**, show no defined C-H vibration related to the starting material **H-DND**$_{IAF}$; however, in analogy to the fluorinated samples **F-DND1-8** (chapter 3.1.1.7.1), the broad signal at 2976 cm^{-1} can be related to stretching vibrations of CH_xF_y groups on the surface. The samples illustrate several superimposed bands between 1050-1260 cm^{-1}, indicating the formation of C-F bonds. The emerging peaks around ~820 cm^{-1} and ~735 cm^{-1} can be attributed to C-H and C-F deformation vibrations of CH_xF_y groups on the surface and are more pronounced than for all **F-DNDs** produced from **gDND**. Interestingly, a new, intensive peak at 1433 cm^{-1} is observed, as the fluorination causes a shift in some C-H deformation vibrations. Chemisorbed HF interacting with the hydrogen-termination via hydrogen bonding is most probable.[251-253] In comparison to starting material **H-DND**$_{IAF}$, a new peak at around 1750 cm^{-1} appears after fluorination, which is correlated to carbonyl groups on the surface. ND agglomerates are most likely broken during fluorination and surface areas containing oxygen surface groups are exposed.

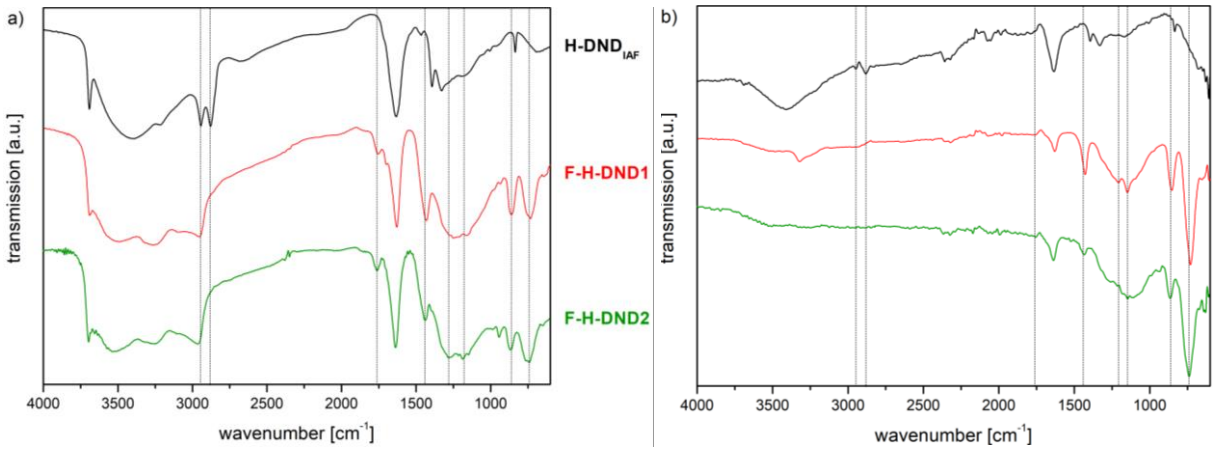

Fig. 32: DRIFT (a) and ATR-FTIR (b) spectra of **H-DND**$_{IAF}$, **F-H-DND1** and **F-H-DND2**.

The ATR-FTIR spectra (Fig. 32b) illustrate the asymmetric and symmetric C-F stretching vibrations (1207 and 1151 cm^{-1}) with higher intensity and the very strong C-H and C-F deformation vibrations (857 and 741 cm^{-1}) are also clearly visible. The results obtained by FTIR spectroscopy suggest that for the fluorine treated particles **F-H-DND1** and **F-H-DND2** a surface with C-F and in particular CH_xF_y groups is present.

Similar to all **F-DNDs**, the particles **F-pDND**, **F-oDND** (Fig. 33a), **F-H-DND1** and **F-H-DND2** (Fig. 33b) show a diamond peak in combination with the D band (cf. chapters 3.1.1.5 and 3.1.1.7.1), as well as a broad G band (Table 11).

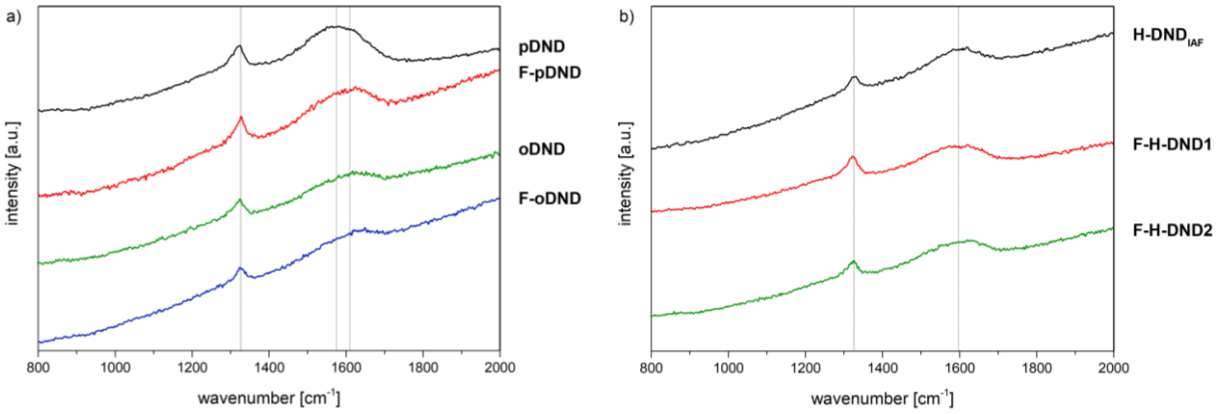

Fig. 33: Raman spectra of **pDND**, **F-pDND**, **oDND**, **F-oDND** (a) and **H-DND$_{IAF}$**, **H-F-DND1**, **H-F-DND2** (b) (excitation at 445 nm).

For **F-pDND**, the G band is significantly redshifted compared to **pDND** due to cleaning of non-diamond carbon during fluorination. For **F-oDND**, **F-H-DND1** and **F-H-DND2** no shift is detectable, as both, **oDND** and **H-DND$_{IAF}$**, are mostly purified from non-diamond carbon during fabrication process.

Table 11: Comparison of **pDND**, **oDND**, **H-DND$_{IAF}$** and **F-pDND**, **F-oDND**, **F-H-DND1**, **F-H-DND2** regarding position, intensity and ratio of the G band and diamond/D band signal

DND material	G band [cm^{-1}]	diamond/D [cm^{-1}]	G band intensity [a.u.]	diamond/D intensity [a.u.]	ratio G band:diamond
pDND	1619	1326	29.1	26.8	1.09
F-pDND	1589	1327	38.4	41.5	0.93
oDND	1615	1326	39.8	39.6	1.00
F-oDND	1611	1326	7.96	9.17	0.87
H-DND$_{IAF}$	1588	1329	80.9	68.9	1.17
F-H-DND1	1578	1228	78.0	94.3	0.83
F-H-DND2	1594	1229	45.9	55.9	0.82

XPS analysis was carried out by Amélie Venerosy to quantify the amount of fluorine attached to the different particles (cf. chapter 3.1.1.7.1). The highly oxidized surface of **oDND** led to an increased amount of oxygen attached to the surface, when compared to **pDND** (5.9 at.% → 19.1 at.%, Table 12). The wet-chemical treatment was able to introduce 5.4 at.% of fluorine at the surface, leading to a mixed O/F-termination. **pDND**, which exhibited a mixed surface termination including C-H and oxidized surface carbons, as well as non-diamond carbon (Fig. 30), was found to be more reactive, leading to 6.5 at.% of fluorine at its surface. However, as already discussed using the ATR-FTIR/DRIFT spectra, the nature of the fluorine groups seemed to be different.

Table 12: Atomic concentrations of elements detected by XPS for **F-pDND**, **F-oDND**, **F-H-DND1**, **F-H-DND1** and references **pDND**, **oDND** and **H-DND$_{IAF}$**

DND material	C1s [at.%]	O1s [at.%]	F1s [at.%]	Cl2p [at.%]	N1s [at.%]	F/C
pDND	94.1	5.9	-	-	-	-
F-pDND	86.2	7.3	6.5	-	-	0.08
oDND	80.9	19.1	-	-	-	-
F-oDND	79.6	15.0	5.4	-	-	0.07
H-DND$_{IAF}$	94.6	1.2	-	3.6	0.6	-
H-F-DND1	88.2	0.4	11.4	-	-	0.13
H-F-DND2	87.0	4.5	8.5	-	-	0.10

The oxygen surface content of H-terminated starting material **H-DND$_{IAF}$** was significantly lower compared to **pDND** and **oDND**. Furthermore, the amount of fluorine on **F-H-DND1** and **F-H-DND2** illustrated the highest values (up to 11.4 at.%). For **F-H-DND2**, the increased amount of oxygen can be related to surface-adsorbed water, which was not completely removed during sample measurement, leading to a smaller amount of fluorine detected (8.5. at%). The O/F ratio for **F-H-DND1** and **F-H-DND2** was significantly lower than for the **F-DND5-8** (cf. chapter 3.1.1.7.1, Table 6), whereas the amount of attached fluorine was on the same level as for **F-DND7** (~11.5 at%). The F/C ratio showed identical values (0.13). Chlorine and nitrogen, present in the starting material **H-DND$_{IAF}$**, were removed during the fluorination treatment, similarly showing the purification potential of the HF/F_2 system.[319]

As the measured at.% of fluorine (~11.5 at.%) and the F/C ratio (~0.13) were almost identical for **F-DND7** and **H-F-DND1**, it was shown that the wet-chemical fluorination

was introducing the maximum amount of fluorine possible. Furthermore, under the used conditions, the oxidized surface of **oDND** was fluorinated, probably mainly by the forming F-substituted carbonyls, leading to a mixed O/F-termination for particles **F-oDND**. The treatment of pristine **pDND** particles essentially led to the fluorination of amorphous, non-diamond carbon. The formed (per)fluorinated hydrocarbons strongly adsorbed to the **pDND** surface. In further experiments to obtain highly fluorinated particles by the wet-chemical fluorination with defined surface groups, such as CF, CF_2(H) or CF_3, **H-DND** particles can also be used in addition to **gDND**.

3.1.1.7.3 Fluorination of bulk diamond materials

The scope of the fluorination method (chapter 3.1.1.7.1) was tested by treating H-terminated, polycrystalline, B-doped CVD diamond (**H-BDD**), which was provided by Dr. Peter Knittel, Fraunhofer IAF, Freiburg (IAF sample: AST815). The **H-BDD** sample was grown on a 500 µm thick silicon [100] substrate, resulting in a 7.5 µm thick diamond film with a boron concentration of $1\text{-}2 \cdot 10^{21}$ atoms cm^{-3}. Two questions are of interest here: i) is the Si-substrate of the diamond affected by the treatment and ii) can the less reactive CVD diamond be fluorinated using the mild conditions?

H-BDD was treated under the established conditions, without addition of F_2 (**F-BDD1**) and once with addition of F_2 (**F-BDD2**). Considering the results of chapter 3.1.1.7.1, a fluorination is expected for the reaction with addition of elemental fluorine, which represents the active species. After removing HF and adsorbates *in vacuo*, the diamond was intensively dried. Subsequently, the fluorine-treated materials **F-BDD1** and **F-BDD 2** were washed with *n*-pentane, acetone and *n*-hexane to remove adsorbed impurities. After the reaction, it was visible to the naked eye that the sample **F-BDD1** (HF) was still undamaged, but sample **F-BDD2** (HF, F_2) showed strong indication of etching the Si-substrate. SEM pictures of **H-BDD, F-BDD1** and **F-BDD 2,** before and after washing, are shown in Fig. 34. For **F-BDD1** and **F-BDD 2**, it can be clearly seen, that some impurities were present on the surface prior to washing with different solvents (**F-BDD1$_{before}$** c), **F-BDD2$_{before}$** e)). After washing, no visible impurities were left ((**F-BDD1$_{after}$** d), **F-BDD2$_{after}$** f)). Compared to the starting material **H-BDD** (a) + b)), the cleaned samples showed no signs of etching regarding the diamond surface and the morphology was unaltered, which is in agreement with the literature.[253] The polycrystalline nature of the **H-BDD** electrode showed crystallites orientated in various

directions, as a result of the CVD growth process. The surface could be described as a combination of [100], [110] and [111] planes. After fluorination treatment, the crystallites were still faceted with defined and detectable crystal planes. It is most likely that the impurities on the surface originate either from etched Si-substrate or fluorinated, non-diamond carbon from the sp^2-containing grain boundaries.

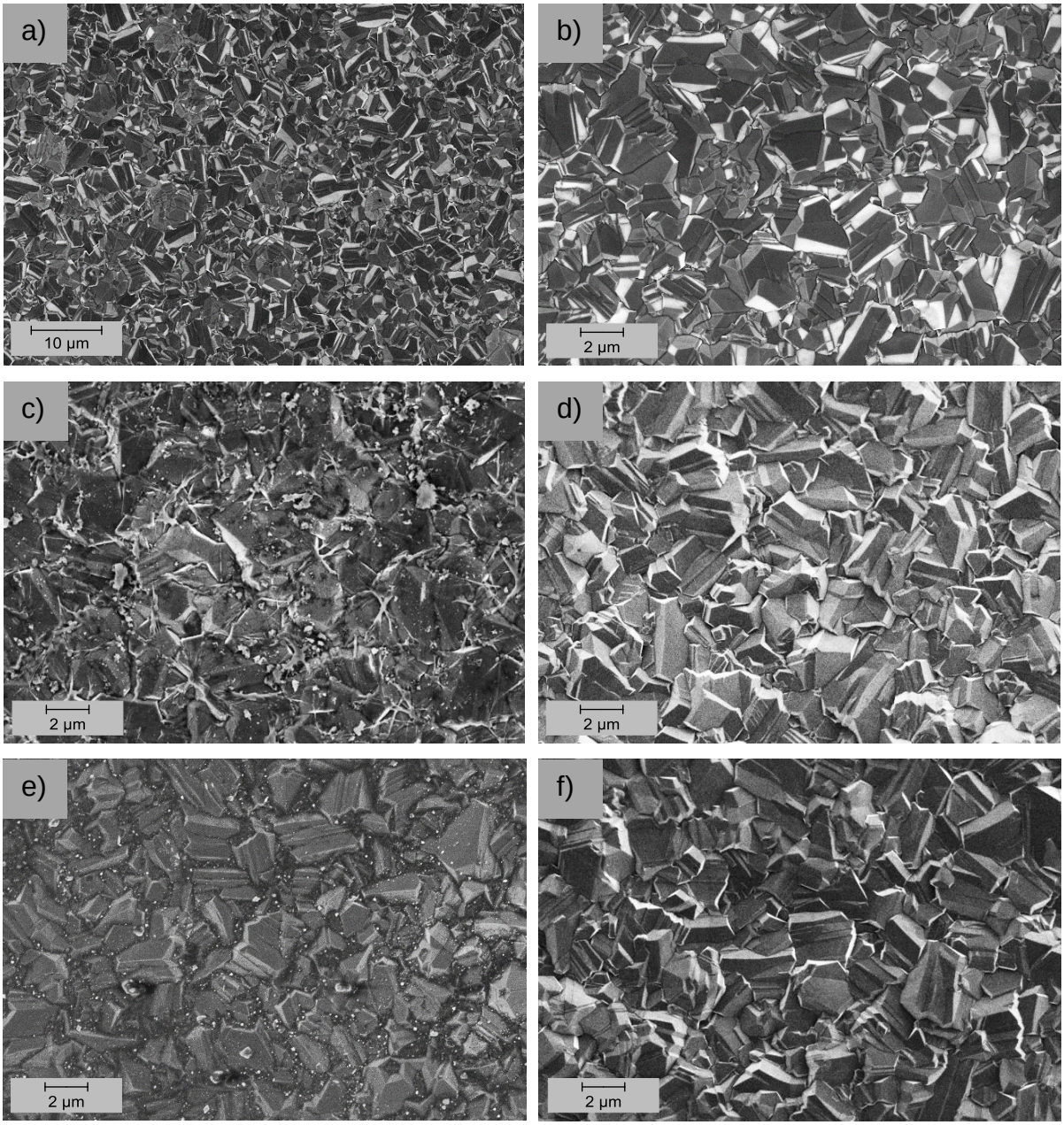

Fig. 34: SEM pictures of starting material **H-BDD** (a) + b)) and treated samples **F-BDD1–2** before (c), e)) and after (d), f)) washing (accelerating voltage: 4.00 kV).

XPS analysis (CEA) showed the presence of fluorine on both treated samples **F-BDD1** and **F-BDD**; however, when treated with HF and F_2 the amount of bound fluorine was

significantly higher (2.6 at.% → 5.7 at.%, Table 13). A chlorine contamination, originating from the starting material **H-BDD**, could not be completely removed.

For experiments with **gDND** (chapter 3.1.1.7.1), the treatment with HF alone did not lead to any fluorine termination according to XPS. Consequently, the doping with boron might play an interesting role. Surface boron atoms, with each boron atom covalently bound to three inner carbons, are electronically stable, therefore leading to a quite stable and virtually chemically unreactive surface.[320] However, due to the small difference in electronegativity between boron and carbon, the boron atoms at the surface possess a slight Lewis acid character. Thus, an adduct formation with fluoride, a Lewis base, is possible and a fluorination on a smaller extent the consequence.

Table 13: Atomic concentrations of elements for fluorine-treated samples **F-BDD1** and **F-BDD2** and reference **H-BDD**

DND material	C1s [at.%]	O1s [at.%]	F1s [at.%]	Cl2p [at.%]	F/C
H-BDD	90.7	5.1	-	4.2	-
F-BDD1	90.0	7.2	2.6	0.2	0.03
F-BDD2	86.0	7.7	5.7	0.6	0.06

For a collaborative project with Dr. Elke Neu, University of Saarbrücken, Germany, a single crystalline, technical grade (Element Six) diamond with different surface terminations (pristine, thermally annealed or oxidized) was fluorinated, involving also nanostructured materials with implanted, shallow negatively charged nitrogen vacancy (NV^-) centers. First experiments showed that the unaltered, pristine termination led to a higher content of fluorine than a fully oxidized termination, similar to DND particles. Also, both nanostructures and NV^--centers were not affected by the treatment. Further experiments regarding charge state measurements, NV^- activation and surface termination stability against biochemical and UV light are currently in progress.

3.1.2 CVD based diamond nanoparticles

As discussed in chapter 3.1, for the energy-up conversion of visible light in nanostructured diamond materials, the introduction of defects/dopants in combination with different surface terminations is required to enable defect- or dopant-based transitions. For the undoped DND materials that were fabricated, characterized and discussed in chapter 3.1.1, different surface terminations, which influence the actual electron emission properties at the surface, were investigated. However, the electronic properties in the bulk part of diamond nanoparticles can be influenced by dopants, such as boron or phosphorus, via the introduction of accessible states within the band gap of diamond (cf. chapters 1.2.2 and 1.2.3). These states allow for multi-photon excitations of electrons from the CB of diamond using visible light. Thus, in addition to the DND based particles, several doped and undoped ND particles were produced by milling of polycrystalline CVD material. The stability of the obtained particles in aqueous dispersion, the particle size and the concentration of the respective dopant, as well as different surface terminations, are of special interest, as these characteristics heavily influence the catalytic activity of doped particles in the photocatalytic CO_2 reduction reaction (cf. chapter 3.4).

The materials used for milling were commercially available polycrystalline, undoped CVD (**PC-D**) and polycrystalline, B-doped CVD (**BDD**) material from Element Six (polycrystalline electronic grade and BDD electrode material). P-doped microcrystalline material (**PDD**) was provided by Prof. Dr. Ken Haenen, Hasselt University, Belgium. Prior to milling of the actual CVD film, each material was treated with conc. potassium hydroxide solution to remove residues of the Si wafer, which it was grown on. After the treatment, neither EDX nor Raman showed any substantial silicon-related signals. The crushing of the material was carried out using a vibration mill and grinding balls made of tempered steel in dry isopropanol (Fig. 35), following a procedure developed by Heyer *et al*.[44]

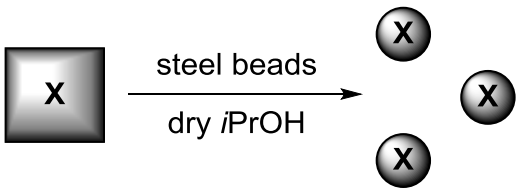

Fig. 35: Milling of polycrystalline CVD diamond material into nanoparticles with or without dopant X (X = C, B, P).

Graphitization of the diamond material was avoided via a multistep milling over 8-12 hours, including 2 h of milling in combination with 15 min cooling. After milling, a mixture of diamond powder and steel debris of the stainless steel (Fe-Cr) grinding bowl was obtained. The steel components, iron and chromium, could be removed using conc. hydrochloric acid. Non-diamond, amorphous carbon was removed during oxidative treatment using a hot mixture of concentrated sulfuric and nitric acid (9:1). EDX measurements proved the complete removal of the abrasion debris.

Dispersing the resulting powder yielded a colloidal solution of diamond particles in water (Fig. 36), with a negative zeta potential caused by acid oxidation.

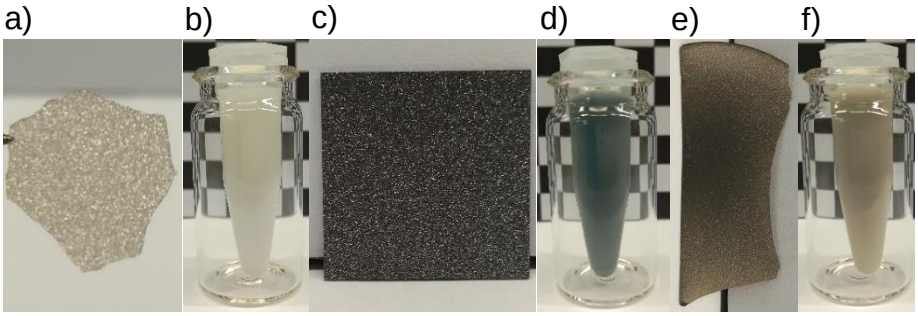

Fig. 36: Undoped starting material **P-CD** (a) and milled nanoparticles **PC-ND** (b), B-doped starting material **BDD** (c) and milled B-doped nanoparticles **BND** (d) and P-doped starting material **PDD** (e) and milled P-doped nanoparticles **PND_1** (f) in aqueous dispersion.

Due to the absorption properties of the CVD based nanoparticles, no meaningful IR spectra (ATR, KBr pellet, DRIFTS) could have been obtained. Nevertheless, the samples were characterized in detail using DLS, zeta potential, Raman, EA, SEM and cathodoluminescence spectroscopy to investigate the effects of size, surface termination and doping on the photocatalytic performance.

3.1.2.1 Undoped ND particles

As reference material for doped CVD based ND particles, undoped polycrystalline material **P-CD** was milled. After milling for 10 h at 50 Hz followed by the described cleaning process, the undoped particles **PC-ND** were obtained as milky-white, aqueous dispersion (Fig. 36b). Characteristic results of the dispersions are shown in Table 14.

The **PC-ND** particles showed the expected negative potential. The bigger particles of the whole sample were separated using a short centrifugation, resulting in a size distribution, which can be confirmed by SEM measurements (Fig. 37a). The whole

sample (**PC-ND**) was also H-terminated, using the plasma technique at CEA, yielding **H-PC-ND** particles. These particles still showed a slightly negative zeta potential, explaining the unstable aqueous dispersions.

Table 14: Zeta potential and particle size of milled undoped ND particles **PC-ND** and hydrogenated particles **H-PC-ND**

ND material	ζ [mV] (pH)	D_V-(10) [nm]	D_V-(50) [nm]	D_V-(90) [nm]
PC-ND (whole sample)	-42.3 (5.4)	550	1190	4340
PC-ND (1 min, 5k rpm)	-41.7 (5.6)	51.3	98.9	325
H-PC-ND	-4.53 (6.4)	669	1070	1600

The agglomeration behavior of **H-PC-ND** in aqueous dispersion can be indirectly proven by SEM. As **H-PC-ND** presented particles in the range of ~80 nm-1600 nm (Fig. 37b), the actual size distribution given by SEM was not reproduced by DLS measurements. This is generally the case if particles agglomerate heavily in the dispersant. The morphology of the **PC-ND** particles was not altered during the hydrogen plasma treatment, and etching was not detected illustrating the diamond quality of starting materials **PC-D** and **PC-ND**.

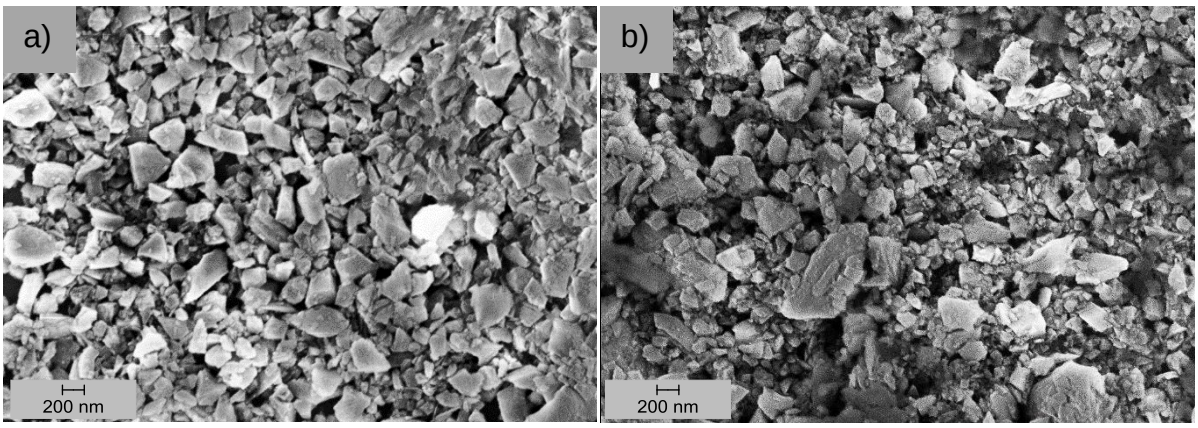

Fig. 37: SEM pictures of **PC-ND** obtained after short centrifugation (a) and **H-PC-ND** (b) (accelerating voltage: 4.00 kV).

The Raman spectra of **PC-DD**, **PC-ND** and **H-PC-ND** show a very sharp and intensive diamond signal at 1335 cm^{-1}, emphasizing the quality of the starting material and the diamond character of the particles (Fig. 38).

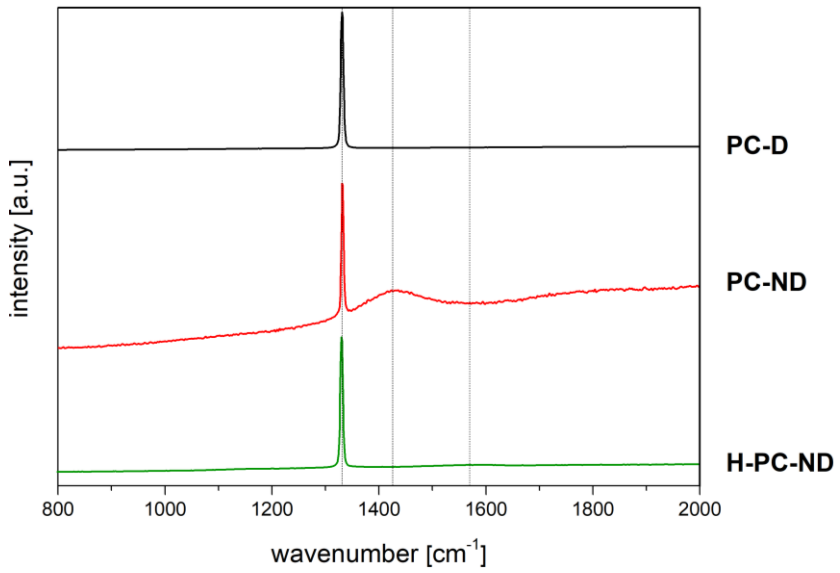

Fig. 38: Raman spectra of **PC-D**, **PC-ND** and **H-PC-ND** (excitation at 445 nm).

After milling, a broad signal at 1428 cm^{-1} is visible resulting from shear force induced changes in the sp^3-lattice of the diamond film during the milling process.[321] After hydrogenation, this signal is not present anymore, indicating that it is a result of lattice-changes at the surface, which are most likely revised by hydrogenation. None of the samples show a visible G band.

3.1.2.2 B-doped ND particles

As previously described in chapter 1.5.3, B-doped diamond electrodes have, so far, been used in electrochemical redox processes, including the reduction of CO_2. Thus, it seems reasonable to produce and characterize B-doped ND (**BND**) particles from commercially available **BDD** electrodes. Boron doping induces a shallow acceptor level close to the valence band of the diamond, allowing for an energy-up conversion and the use of visible light in photocatalytic reactions (cf. chapter 1.2.2). The **BND** particles were obtained as blueish-gray dispersion (Fig. 36d) using the milling method described in chapter 3.1.2 followed by the previously characterized cleaning procedure. Further details regarding the milling of different batches, as well as the characterization of the aqueous particles can be found in Table 15. Several batches were also hydrogenated by either plasma (CEA) or annealing (IAF) approaches (see chapter 1.1.6 for experimental details).

Table 15: Amount of starting material, milling time, zeta potential and particle size measurements of aqueous dispersion of milled B-doped ND **BND1-5** and hydrogenated **H-BND** particles

ND material	amount [mg]	time [h]	ζ [mV] (pH)	D_V-(10) [nm]	D_V-(50) [nm]	D_V-(90) [nm]
BND1	345	8	-37.3 (5.8)	198	732	1400
BND2	650	12	-43.8 (5.7)	307	956	2190
H-BND2$_{CEA}$	-	-	+24.7 (6.2)	330	720	1260
H-BND2$_{IAF}$	-	-	+41.7 (6.5)	384	925	1620
BND3	358	10	-41.0 (5.7)	147	664	942
H-BND3$_{CEA}$	-	-	+25.4 (6.3)	843	1350	4890
BND4	355	8	-39.4 (5.8)	169	606	1230
H-BND4$_{CEA}$	-	-	+27.4 (6.4)	485	781	1200
BND5	334	8	-37.6 (5.8)	146	595	1240

For the milling of **BND2** particles, two **BDD** plates of the starting material were crushed in one run resulting in a higher amount of still micron-sized material. In this case, the grinding bowl volume and the amount of solvent turned out to be the limiting factors, as the obtained mix of diamond particles and steel debris was rather a solid mass than a slurry after milling. Milling one film (~350 mg, **BND1** and **BND3-5**) for 8-10 h was ideal to obtain a ND sample with particles sizes in the submicron range.

All **H-BND** samples showed a positive zeta potential. As the hydrogenated particles were very hydrophobic, stable dispersion could only be obtained for a short time (~10-15 min) in low concentrations (<0.1 wt.%). With varying centrifugation speed, it was possible to isolate several size fractions from the whole sample of **BND3** (Table 16). Further size fractions are shown in the Appendix (Table 54).

Table 16: Particle size measurements of fractions from **BND3**

BND3	D_V-(10) [nm]	D_V-(50) [nm]	D_V-(90) [nm]	fraction name
1.5 min at 3000 rpm	114	197	338	**BND3_200**
5.0 min at 3750 rpm	68.8	106	190	**BND3_105**
5.0 min at 6000 rpm	37.3	60.6	132	**BND3_60**
5.0 min at 9000 rpm	34.9	50.7	80.1	**BND3_50**
5.0 min at 15000 rpm	27.6	41.7	70.8	**BND3_40**
10 min at 15000 rpm	21.7	33.4	59.3	**BND3_30**

The samples with $D_v(50)$ < 60 nm show no blueish color anymore, indicating a very low concentration of particles. The particle sizes measured via DLS are in very good accordance with the crystallite size determined by SEM (exemplary data, Fig. 39).

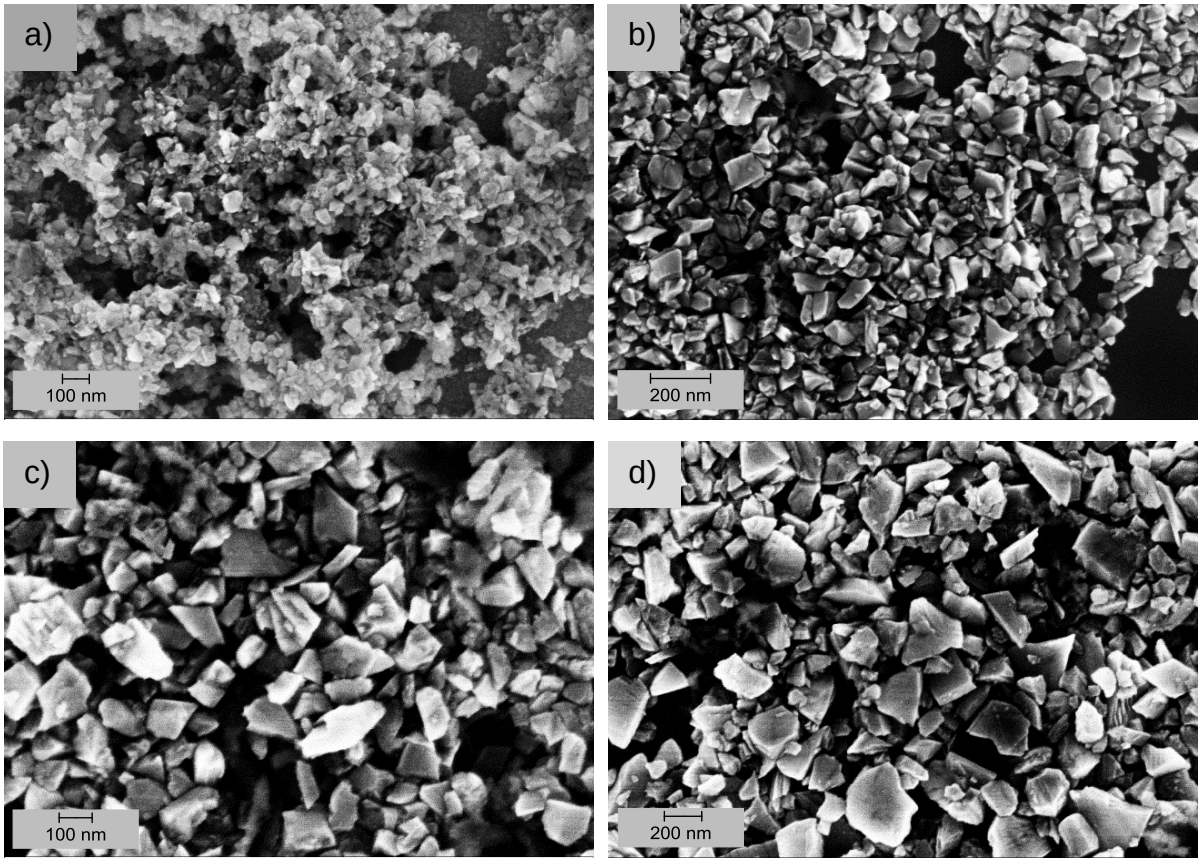

Fig. 39: SEM pictures of particles **BND3_40** (a), **BND3_60** (b), **BND3_105** (c) and **BND3_200** (d) (accelerating voltage: 4.00 kV).

The Raman spectra of **BDD**, **BND3**, **BND3_30** and **H-BND3$_{CEA}$** show some interesting features (Fig. 40). When measuring the front side of the starting material **BDD**, a very sharp peak at 1329 cm^{-1}, related to diamond carbon, is visible. In contrast, the back side shows in addition to the diamond signal the characteristic Fano resonances at ~499 cm^{-1} and ~1228 cm^{-1}, both confirming boron doping above 10^{20} atoms/cm^{-3}.[44,322] The boron concentration at the back side of the **BDD** starting material, where the CVD growth started, is substantially higher than at the front side of the growth end.[31,32,323] After the nucleation process during the CVD growth, the nano-sized crystallites form grain boundaries and resume growing as a continuous film, whereupon the morphology of the growing diamond surface depends on the growth rate of the different diamond planes.[323] The parts of the **BDD** film with smaller grain size are thus richer in grain boundaries, containing disordered sp^3 and sp^2 phases.[324] The incorporation of defects, including boron dopants, is better in grain boundaries,[325] leading to an higher

boron concentration on the back side of the **BDD** plate. The broad signal of **BDD$_{back}$** at 1543 cm^{-1} is a superposition of the Fano resonance and the G band. Due to the higher amount of sp^2-rich grain boundaries, the G band is strongly contributing. The obtained particles **BND3** show no significant boron signals. In addition to the diamond signal at 1329 cm^{-1}, a G band is visible at ~1537 cm^{-1}, which can be explained by the high density of sp^2-containing grain boundaries coming to the surface after milling. The smallest fraction **BND3_30** and the hydrogenated sample **H-BND3$_{CEA}$** also show these characteristic vibrations, however, for **BND3_30**, the G band is slightly amplified in intensity due to the higher amount of sp^2 in the smaller crystallites. This in good accordance with the results obtained by Heyer *et al*.[44]

The lack of any boron-related signal is due to the loss of boron during milling. As discussed, boron is more easily incorporated into grain boundaries; however, the milling of polycrystalline films is also taking place at those boundaries, as they pose the most fragile positions in the diamond lattice.[44] Crushing at the boundaries results in the loss of boron and the dopant concentration is falling below the detection limit for Raman spectroscopy.[44]

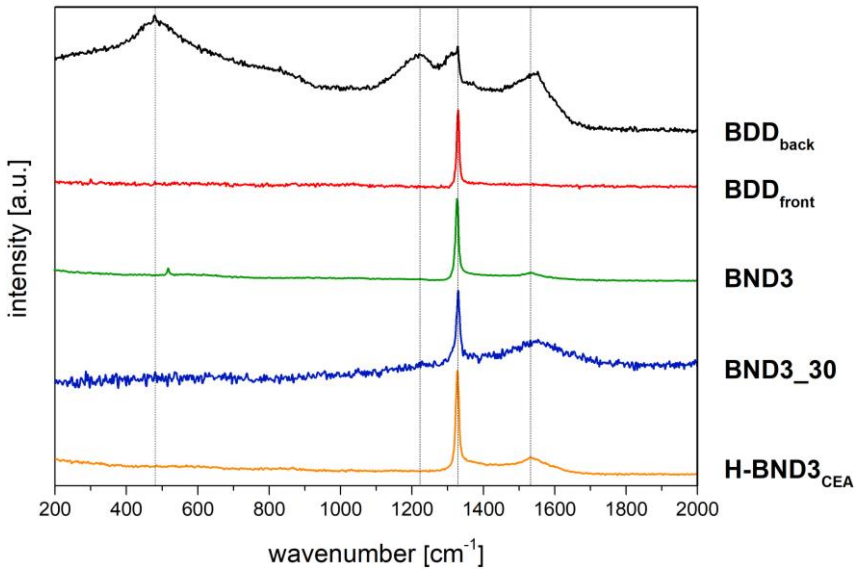

Fig. 40: Raman spectra of **BND3** and **BND3_30**, **BDD** from back (**BDD$_{back}$**) and front (**BDD$_{front}$**) side and hydrogenated particles **H-BND3$_{CEA}$** (excitation at 445 nm).

The amount of boron inside the **BDD** film can be determined either by EA or secondary-ion mass spectrometry (SIMS). For the obtained particles, only EA can be applied, as the samples are not suitable for SIMS due to preparation issues. The results for **BND3** are shown in Table 17.

After milling, ~15% of the initial boron concentration was lost. The slightly increased nitrogen value was within the error range of the EA, but a formation of graphitic C-N structures at the diamond lattice surface during milling and cleaning in air was also conceivable (cf. chapter 3.1.1.5).

Table 17: Boron concentration of **BDD** and **BND3** determined via EA and SIMS

B-doped material	B_{SIMS} [atoms/cm^{-3}]	C_{EA} [wt.%]	H_{EA} [wt.%]	N_{EA} [wt.%]	B_{EA} [wt.%]	B/C	$B_{calc.}$ [ppm]
BDD	~2.2 x 10^{20}	90.33	0.73	0.01	2.72	0.030	~1250
BND3	-	92.24	1.23	0.07	2.36	0.026	~1060

Within the DIACAT project, the **BNDs** were probed by soft X-ray absorption spectroscopy at the carbon K edge. These experiments were conducted at the BESSY II synchrotron by Sneha Choudhury under the supervision of Dr. Tristan Petit, Institute for Methods for Materials Development, Helmholtz Center Berlin. First results have been published recently,[326] involving **BND3**, **BND3_50** and **BND3_30**. **BND3** was measured with an oxidized surface, whereas the last two dispersions were hydrogenated by CEA, yielding **H-BND3_50** and **H-BND3_30**. As boron doping induces acceptor levels within the band gap of diamond (cf. chapter 1.2.2), unoccupied electronic states were analyzed at the BESSY II synchrotron. Surface states close to the valence band maximum, which are strongly present for polycrystalline and single B-doped crystals due to excitonic transitions from C1s core levels to empty surface states, may be saturated upon H-termination of the **BND** particles. This saturation leads to a decrease in signal intensity for **H-BND3_50** and **H-BND3_30**. However, the nanostructuring introduces π^* states close to the conduction band related to C-B bonds at the particle surface. These π^* states are not observed for the poly- or single crystalline B-doped materials. Thus, for **H-BND3_50** and **H-BND3_30** a reduction of the large diamond band gap is determined due to accessible π^* states within the band gap. These findings classify **H-BND** particles as a suitable candidate for photocatalytic CO_2 reduction.

3.1.2.3 P-doped ND particles

Apart from p-type doping of diamond materials with boron, n-type doped diamond films with phosphorus are also of interest. As highlighted in chapter 1.2.2, the production of P-doped ND particles (**PND**) provides a material with a different electronic structure in

comparison to **BND**. P-doping introduces several donor-levels below the conduction band of diamond.[61] Thus, the production of **PND** particles allows for the investigation of an additional material with different electronic properties for photocatalytic reactions. However, P-doped, polycrystalline diamond films are not commercially available. For first experiments, Ken Haenen (Hasselt University) provided a 1" film (**PDD**). The polycrystalline nature of the **PDD** film showed crystallites orientated in various directions, as a result of the CVD growth process. The surface could be described as a combination of mainly [100] and [111] planes. The milling of the diamond film was carried out adapting the protocol for the production of highly B-doped nanodiamond particles.[44] The resulting particles were easily dispersed in ultrapure water, yielding a stable, milky-grayish colored colloidal solution (**PND_1**, Fig. 36f). Overnight, the larger, micron-sized particles settled yielding fraction **PND_2**, whose particles were substantially smaller (Table 18).

Table 18: Particle size distribution of the seven fractions (**PND_1-7**) obtained by fractional centrifugation

P-doped fraction	isolation	ζ [mV] (pH)	D_V-(10) [nm]	D_V-(50) [nm]	D_V-(90) [nm]
PND_1	whole sample	-45.9 (5.7)	340	946	1700
PND_2	supernatant (12 h)	-44.8 (5.6)	125	438	821
PND_3	1 min at 3k rpm	-43.4 (5.9)	96.7	164	286
PND_4	2.5 min at 3k rpm	-44.6 (5.5)	82.9	136	247
PND_5	5 min at 3k rpm	-36.3 (5.6)	66.8	107	208
PND_6	5 min at 5k rpm	-39.8 (5.4)	51.8	77.0	135
PND_7	5 min at 8k rpm	-37.5 (5.8)	33.8	49.1	121

PND_1, containing the entire amount of the crushed diamond sample and therefore all particle sizes, was fractionated by centrifugation resulting in five different size fractions (**PND_3-7**). Particle sizes in aqueous, colloidal suspension are illustrated in Table 18. Fractions **PND_1** and **PND_2** were dominated by particles bigger than 300 nm. The intensified centrifugation process strongly influenced the further fractions, resulting in fraction **PND_7** consisting of particles mostly below 50 nm. Fig. 41 clearly illustrates that the milky-grayish color of the colloidal solutions was substantially reduced from **PND_1-PND_7** due to decreased particle concentration and smaller particle size. As the Rayleigh scattering intensity of smaller particles during DLS measurements depends on the 6^{th} power of the particle size, a colorless particle dispersion is also the

result of substantially decreased scattering intensity.[327] The size distribution by volume correlated with the size assignment by SEM for **PND_1-7** (Fig. 43).

Fig. 41: Colloidal solutions of fractions **PND_1-7** in water.

By varying the used parameters for fractional centrifugation, specific size ranges of the P-doped ND particles can be readily isolated. Due to the oxidative acid treatment the diamond surface was oxidized bearing carboxylic acid groups and other oxygen-containing groups. The DRIFT spectra of all fractions (Fig. 42) show a very intensive peak at ~1800 cm^{-1}, which can be attributed to C=O stretching vibrations of carboxylic acids and anhydrides.

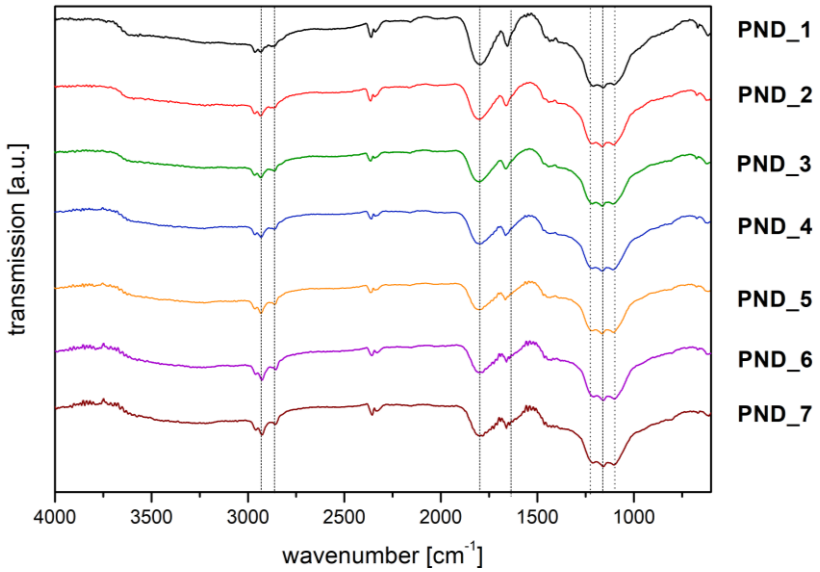

Fig. 42: DRIFT spectra of the fractions **PND_1-7**.

The signals in the range of 1100-1200 cm^{-1} refer to C-O-C stretching vibrations. Moreover, C-H groups on the surface result in additional bands below around 3000 cm^{-1}. Therefore, it is likely that the predominant surface groups are not influenced by the particle size and that even the smaller size fractions show the expected surface termination.

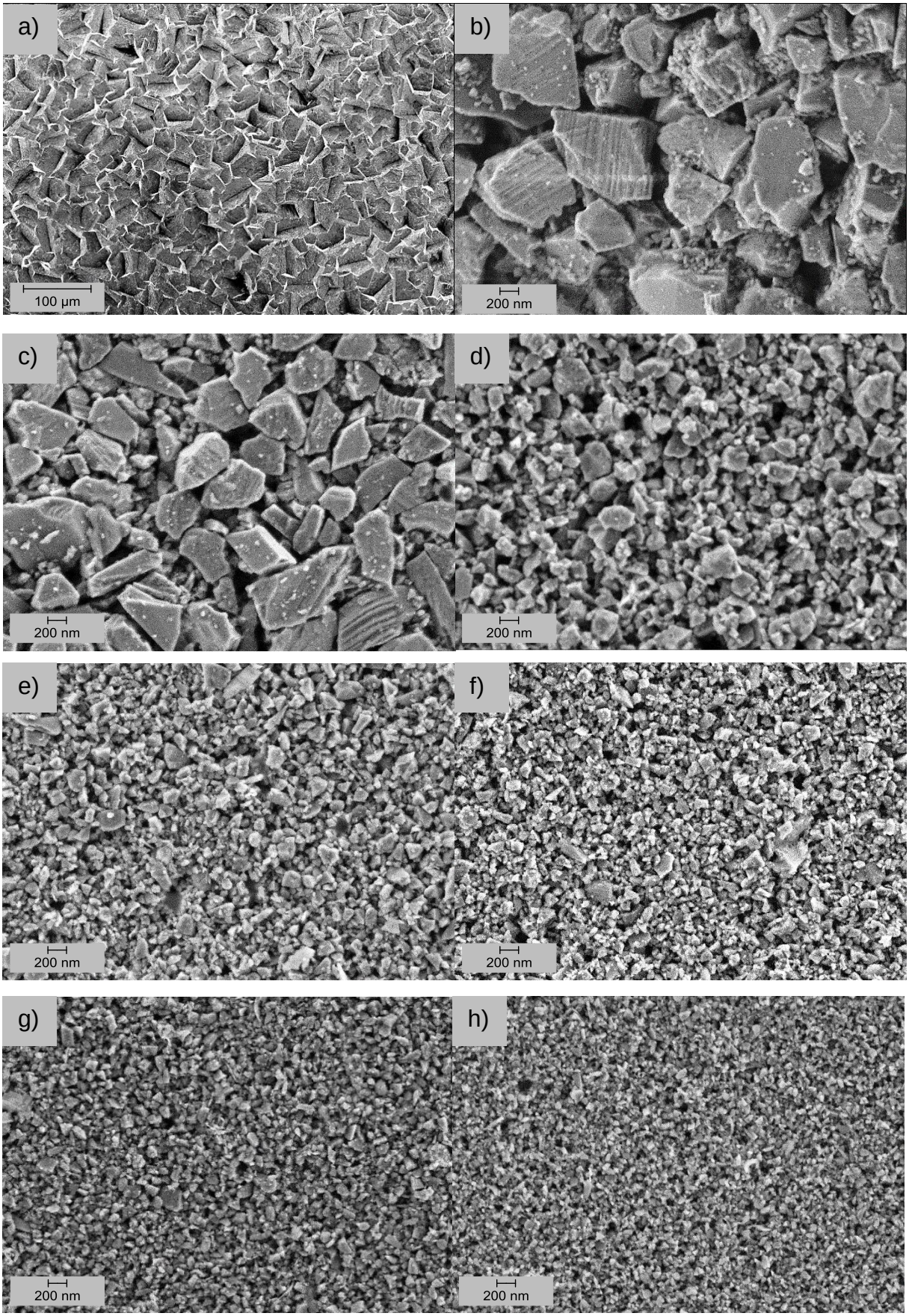

Fig. 43: SEM images of the faceted P-doped film (**PDD**, a) and the ND fractions **PND_1-7** (b-h) proving the particle size getting continuously smaller (accelerating voltage: 4.00 kV).

The surface groups exerted a strong influence on the stability of the colloidal solutions due to Coulomb stabilization of the particles. An additional effect of the oxygenated surface was the highly negative zeta potential for all fractions (Table 18).

The amount of non-diamond was estimated from Raman spectra (Fig. 44). Similar to the starting material **PDD**, all fractions illustrate a distinctive and sharp diamond peak at 1331 cm^{-1}, as well as a broad G-band at 1522 cm^{-1}. For **PDD**, the G band has its origin in the high density of sp^2-containing grain boundaries.[68] The P-doping itself is not visible in the Raman spectrum. For the smaller P-doped particles **PND_7** the G band slightly increases in intensity due to the contribution of non-diamond sp^2-carbon.

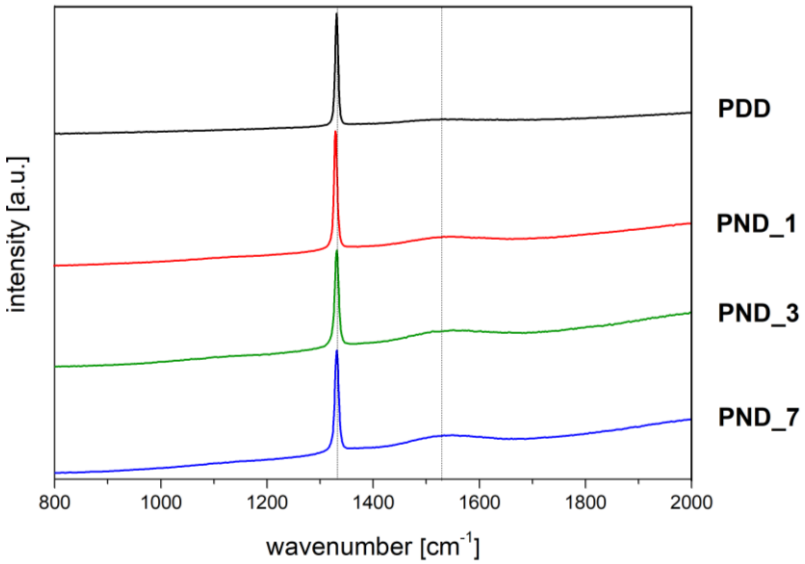

Fig. 44: Raman spectra of the diamond film **PDD** and the fractions **PND_1**, **PND_3** and **PND_7**.

Considering these results, it can be concluded that an efficient method for the production and colloidal dispersion of doped ND particles was successfully modified for P-doped particles. The question of interest is, whether the initial P-concentration of the film can be maintained after milling. For the polycrystalline film, it is well known that cleavage preferentially occurs along low surface energy planes, such as the [111] planes.[328] During subsequent milling, the microcrystallites need to be cleaved. For the B-doped ND particles, the crushing along lattices planes containing defect centers and along highly defective regions is preferred over crushing along defect-free zones.[44] As a result of this process, a decrease in dopant concentration was detected in the final **BND** particles (cf. chapter 3.1.2.2). Similar effects can be expected for other dopants, particularly for those with higher atomic radius and thus a stronger disturbance of the diamond lattice. The concentration of **PDD** was determined by SIMS and EA (Table 19). For **PND_1**, the concentration was measured as powder and in aqueous

dispersions. Fractions **PND_5** and **PND_6** were measured in dispersion due to small sample amount and, for **PND_7**, the amount of sample was too small for analysis. After milling, the whole powdery sample **PND1** showed a loss of ~8% of phosphorus, while ~10% were observed for the aqueous dispersion of **PND1**. It can be assumed that both, carbon and phosphorus, originate from P-doped diamond particles in dispersion. The fractions **PND_5** and **PND_6** showed, as expected for low particle sizes, even smaller P contents, with a maximum loss of ~30%. The nitrogen measured in all samples can be related to the starting material **PDD** showing NV^0 centers. Thus, a certain amount of nitrogen should also be present in the smaller fractions. However, higher amounts than for the **PDD** film were not expected. A nitrogen-contamination in the dispersion is more likely.

Table 19: Phosphorus concentration of **PDD**, **PDD_1** (solid) and **PDD_5**, **PDD_6** determined via EA and SIMS

P-doped material	P_{SIMS} [atoms/cm^{-3}]	C_{EA} [wt.%]	H_{EA} [wt.%]	N_{EA} [wt.%]	P_{EA} [wt.%]	P/C	$P_{calc.}$ [ppm]
PDD	~3.8 x 10^{18}	82.34	0.37	0.02	9.05	0.11	~22
PND_1 (solid)	-	82.39	0.24	0.00	8.39	0.10	~20
PND_1 (liquid)	-	0.41	-	0.03	0.0377	0.09	~19
PND_5	-	0.19	-	0.05	0.0148	0.08	~17
PND_6	-	0.16	-	0.04	0.0146	0.09	~18

In cooperation with Dr. Julien Barjon and Dr. Solange Temgoua from the Group d'Etude de la Matière Condensée (GEMAC), Université de Versailles, France, the dopant concentration was studied investigating the NP cathodoluminescence (CL) properties at 5 K using a field emission SEM at 10 kV. Phosphorus bound excitons were observed in **PND_1** with donor concentrations between 5.0 x 10^{16} and above 10^{18} atoms/cm^3 depending on NPs. Quantitative CL analysis of the **PDD** polycrystalline starting material showed that [111] surfaces of **PDD** incorporate considerably more phosphorus donors than [100].[329] The analysis of **PND_1** revealed that the NP doping almost reflects the **PDD** properties with high doping (>10^{18} atoms/cm^3) in [111] facets and low doping (~10^{16}-10^{17} atoms/cm^3) in [100] facets of the material before milling. P-contribution seemed homogeneous at the core of the **PND** particles and in accordance to the results from EA. For particles with a size of ~100 nm, a concentration of >10^{18} atoms/cm^3 was detected. For particles below 100 nm, the CL signal was too small to obtain a quantitative analysis. The CL results clearly show that the donor character of

the phosphorus, which was observed in the **PDD** starting material, was preserved in the core of **PND** particles after the milling process.

Within the DIACAT project, the particles **PND_1** were probed by soft X-ray absorption spectroscopy at the carbon K edge. These experiments were conducted at the BESSY II synchrotron using the LiXEdrom endstation by Sneha Choudhury under the supervision of Dr. Tristan Petit, Institute of Methods for Materials Development, Helmholtz Center Berlin. The CBM of the particle was estimated to be located at 283.9 eV, the VBM at 289.3 eV, resulting in a band gap of 5.4 eV. The obtained results were in agreement with diamond particles with a good crystalline quality, such as polycrystalline diamond.[326,330] XPS analysis illustrated the contribution of sp^3-carbon and oxygen due to the oxidized particle surface, as no significant indication of sp^2-carbon was observed. Phosphorus was not detected due to the low concentration.

3.2 Transition metal functionalized diamond materials

In chapter 3.1, the influence of dopants and defects in combination with different surface terminations on the electronic properties was discussed for diamond nanoparticles, with a focus on potential application in photocatalysis using visible light. Another approach to enhance the photocatalytic activity of diamond nanomaterials can be achieved by functionalization with transition metal (TM) complexes. As discussed in chapter 1.6, the use of visible light requires energy-up conversion with multi-photon absorption. The necessary and accessible states in the band gap of diamond can be introduced by surface states from covalently attached and photocatalytically active TM complexes. The concept of surface modification has already been utilized for various semi-conductors, such as SnO_2[224] or TiO_2,[225] and diamond based electrodes proved to be suitable carrier material for various ruthenium, iron or cobalt based complexes (cf. chapter 1.6).[228,229,232] The electronic structure of two ruthenium based complexes, $Ru(tpy)^{2+}$ and the N3 dye (Fig. 45), attached to hydrogenated BDD electrodes was investigated in detail using X-ray absorption and photoemission spectroscopy.[240,241]

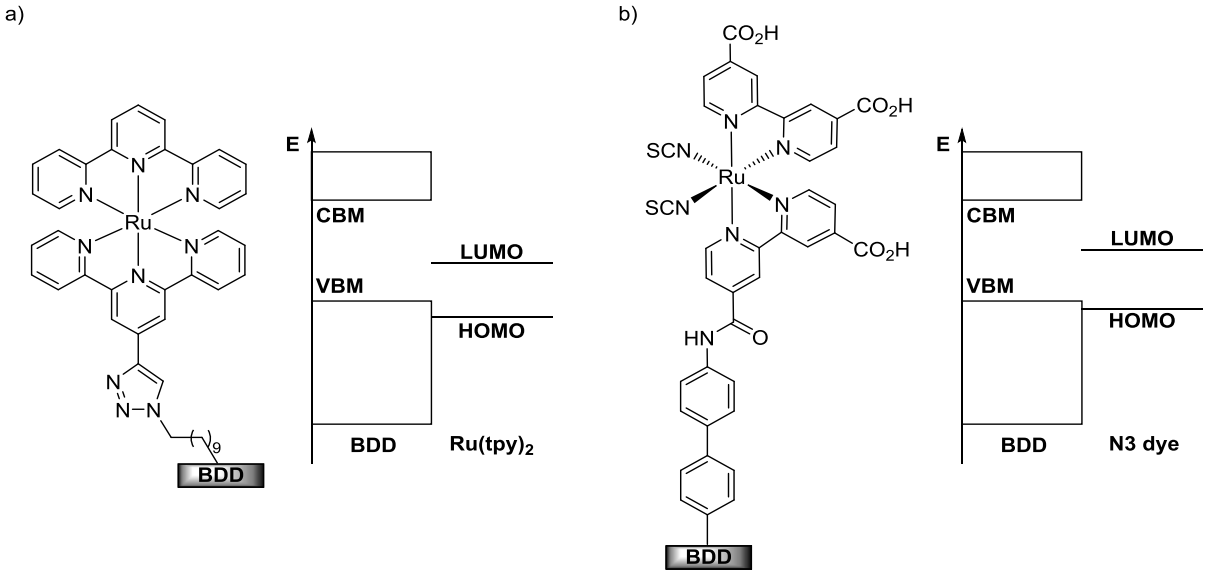

Fig. 45: $Ru(tpy)_2$ (a) and N3 dye functionalized (b) BDD electrodes with schematic illustrations of the frontier orbitals alignment of the attached complexes respective the diamond band gap.

For the $Ru(tpy)_2$ functionalized sample, the VBM of the BDD electrode was determined at 283.8 eV and the CBM at 289.3 eV (band gap of 5.5 eV). The HOMO of the attached Ru complex lies 0.9 eV below the VBM at 282.9 eV and the LUMO at 284.5 eV in the band gap of diamond (schematic illustration, Fig. 45a).[241] Holes generated in the HOMO after photoactivation can be refilled by the diamond; however, the energy

efficiency is quite low with a difference of 0.9 eV to the VBM.[241] The situation is slightly different for attached N3 dye. The HOMO of the Ru complex was measured to be 0.5 eV below the VBM and the LUMO at 284.9 eV. The electron or hole transport between HOMO and VBM is more effective for this system (schematic illustration, Fig. 45b).[240] Considering these results, the functionalization of various nanodiamond particles with Ru complexes is aspired in this work in order to investigate the electronic structure and an application in photocatalysis. Regarding the linkage of those complexes on the particle surface, a functionalization of the deployed ligands is required. The functionalization on diamond can be achieved directly with completely synthesized complexes or indirectly by surface functionalization with a ligand and subsequent metal coordination. Therefore, a standard protocol of functionalizing diamond materials with metal complexes and a set of characterization methods was established. Basic questions, such as suitable ligands for the ruthenium complexes, influences of the diamond starting materials and methods for functionalizing diamond material with complexes, will be addressed within this chapter.

3.2.1 Synthesis of transition metal complexes and linker molecules

3.2.1.1 Alkyne-functionalized ruthenium(II) complexes

As discussed in chapter 3.2, ruthenium complexes are highly suitable due to their electronic properties. The ruthenium(II) complexes shown in Fig. 46 illustrate HOMO-LUMO gaps in the blue light region: 452 nm (2.74 eV, **Ru1**),[235] 483 nm (2.57 eV, **Ru2**)[241] and (2.6 eV, **Ru3**).[240] If the frontier orbitals of these complexes would lead to accessible electronic states inside the band gap of functionalized diamond nanoparticles, the use of visible light in photocatalytic experiments would be possible.

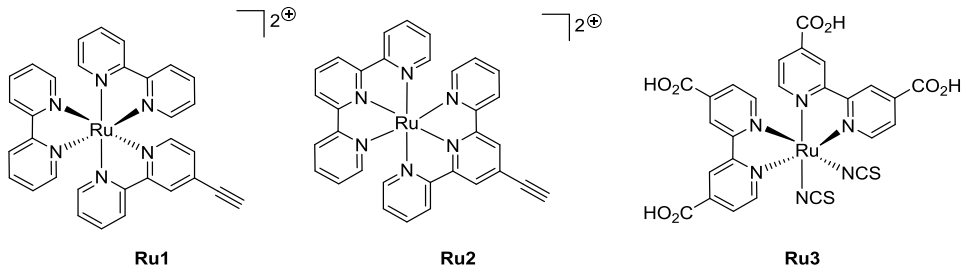

Fig. 46: Photocatalytically active ruthenium(II) complexes **Ru1**, **Ru2** and **Ru3**.

Furthermore, the complexes **Ru1**, **Ru2** and **Ru3** were chosen from literature-known examples of suitable metal-ligand systems, paying special attention to their synthetic availability and photochemical stability.

Polydentate nitrogen containing ligands, such as 2,2':6',2''-terpyridine (tpy) or 2,2'-bipyridine (bpy), are known to strongly influence the absorption properties of their TM complexes.[235] These ligands can be modified with functional groups that allow for a covalent attachment to diamond nanoparticles. A covalent attachment is desired for several reasons, including the reproducibility of the functionalization, the stability of the ND-complex conjugated under intense irradiation and, in particular, the possible electronic coupling between diamond material and complex. An alkyne-functionalization of one attached ligand (**Ru1**, **Ru2**) enables the linkage to azide-functionalized diamond material using the established concept of a CuAAC reaction (cf. chapter 1.5.1). Intensive focus must be set on suitable reaction conditions, in particular the selected copper catalyst.[123,216] Carboxylic acid groups on the ligands (**Ru3**) allow for an attachment via amide bonds on amine-functionalized diamond materials (cf. chapter 1.7).

3.2.1.1.1 Ligand synthesis for ruthenium(II) complexes Ru1-Ru3

Intermediates of the different ligands were successfully synthesized by master students Julian Fink and Christine Heinz during their practical course "Homogeneous catalysis in Organic Chemistry". 2,2':6',2''-terpyridine (**1**) was synthesized in 17% overall yield using the two-step procedure by Jameson *et al.* (Fig. 47).[331]

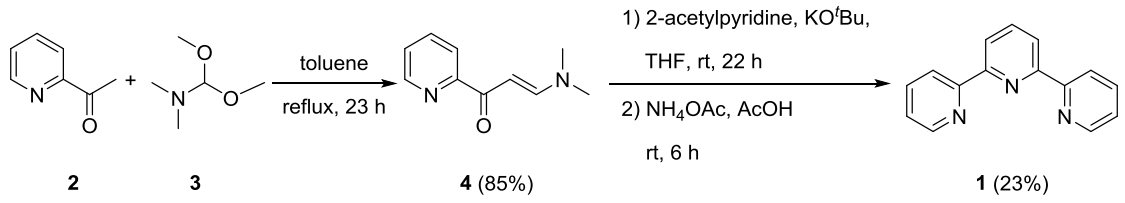

Fig. 47: Synthesis of 2,2':6',2''-terpyridine (**1**).

The alkyne-functionalized analog, 4'-ethinyl-2,2':6',2''-terpyridine (**5**), was obtained after five steps in 18% overall yield using methods reported by Zalas *et al.* and Grosshenny *et al.* (Fig. 48).[332,333]

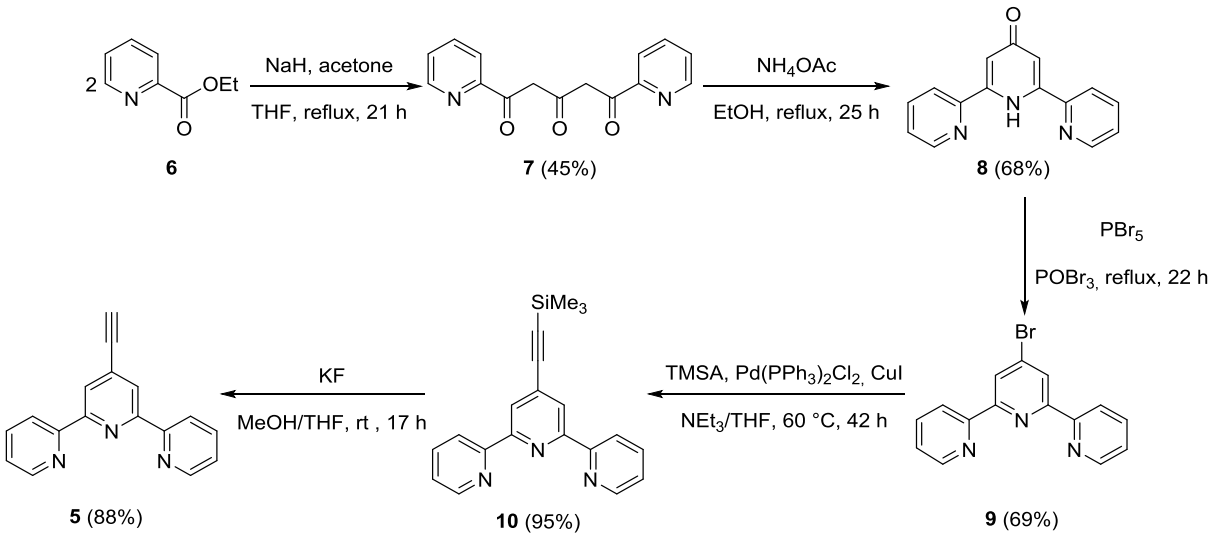

Fig. 48: Synthesis of 4'-ethinyl-2,2':6',2''-terpyridine (**5**).

On the way to the alkyne-functionalized ligand 4'-ethinyl-2,2'-bipyridine (**11**), the first four reaction steps (**13**-**16**), starting with commercially available 2,2'-bipyridine (**12**), were executed according to literature (Fig. 49).[332,334]

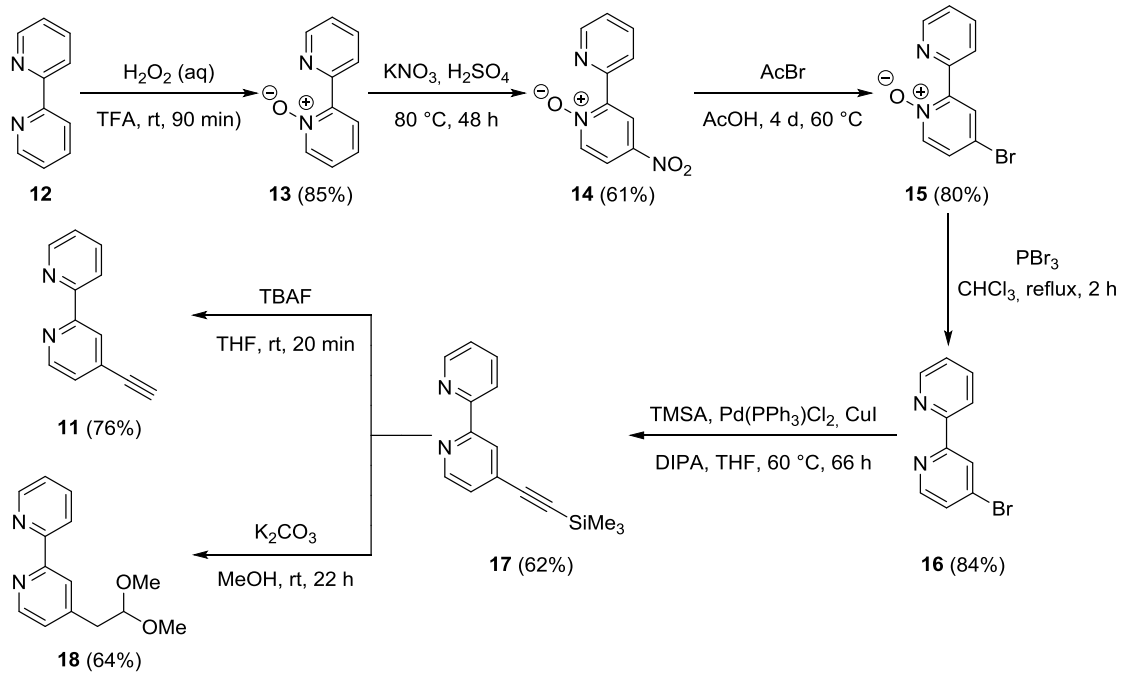

Fig. 49: Synthesis of 4´-ethinyl-2,2´´-bipyridine (**48**).

The brominated species **16**, required for introducing the alkyne group via Sonogashira cross coupling, was the only species where *cis* and *trans* bipyridine isomers could be distinguished in the room temperature ^{1}H-NMR spectra (Appendix, Fig. 121). After cross-coupling,[335] the literature-known protocol for the deprotection of alkyne **17**, using

potassium carbonate in methanol, did not yield the free alkyne species **11**, but **18**, which is the twofold addition product of methanol and the free alkyne, in 64% yield. Yet, the deprotection of **17** was achieved using tetra-*n*-butyl ammonium fluoride.

The functionalized ligand 2,2'-bipyridine-4,4'-dicarboxylic acid (**19**) was synthesized by the oxidation of 4,4'-dimethyl-2,2'-bipyridine (**20**) using potassium permanganate (Fig. 50).[336]

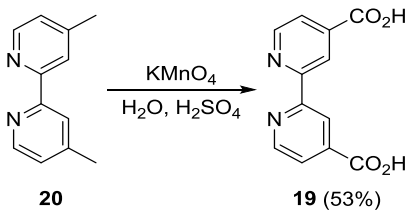

Fig. 50: Synthesis of 2,2'-bipyridine-4,4'-dicarboxylic acid (**19**).

3.2.1.1.2 Synthesis of ruthenium complexes Ru1-Ru4

Commercially available ruthenium(III) chloride hydrate was used to synthesize the stoichiometrically defined precursor complex dichlorotetrakis (dimethylsulfoxide)-ruthenium (II) (**21**) (Fig. 51).[337] The first step towards the alkyne-functionalized complex **Ru1** consisted of the reaction between the *cis*-configured precursor **21** and the bpy-ligand **12** to obtain the charge-neutral *cis*-bis(2,2'-bipyridine)dichloro ruthenium(II) complex (**22**).[338] After coordination of alkyne-functionalized bpy-ligand **11**, complex **Ru1** was precipitated as the hexafluorophosphate salt.[335]

The coordination of the tpy-ligand **1** to precursor **31** led to a mixture of *cis/trans* isomers (~8:2) of Ru(tpy)(DMSO)Cl_2 (**23**).[339] The ratio was determined using the ^{1}H-NMR signals of the protons 1-H/15-H, which differed for each isomer (Appendix, Fig. 122). For the *trans*-isomer of **23**, the signal is located at 9.36 ppm, whereas the protons 1-H/15-H of the *cis*-isomer resonate at 9.02 ppm. The ratio of the two isomers is of great interest, as a coordination of alkyne-functionalized tpy-ligand **5** is only taking place with the *cis*-isomer.[339] After column chromatography, the *trans*-isomer could be isolated; however, the *cis-c*omplex remained on the silica. A conversion from *trans* to *cis* was not possible, as both isomers are thermodynamically stable.[339] After the reaction of *cis*-**23** with ligand **5**, column chromatography enabled the removal of the unreacted *trans*-isomer of **23**, as well as the isolation of the alkyne-functionalized complex **Ru2**. Complex **Ru3** was obtained in a one-step reaction of precursor **21** and

two equivalents of the acid-functionalized ligand **19**.[340] As a reference, complex **Ru4** was synthesized by coordination of tpy (**1**) to ruthenium(III) chloride hydrate.[341]

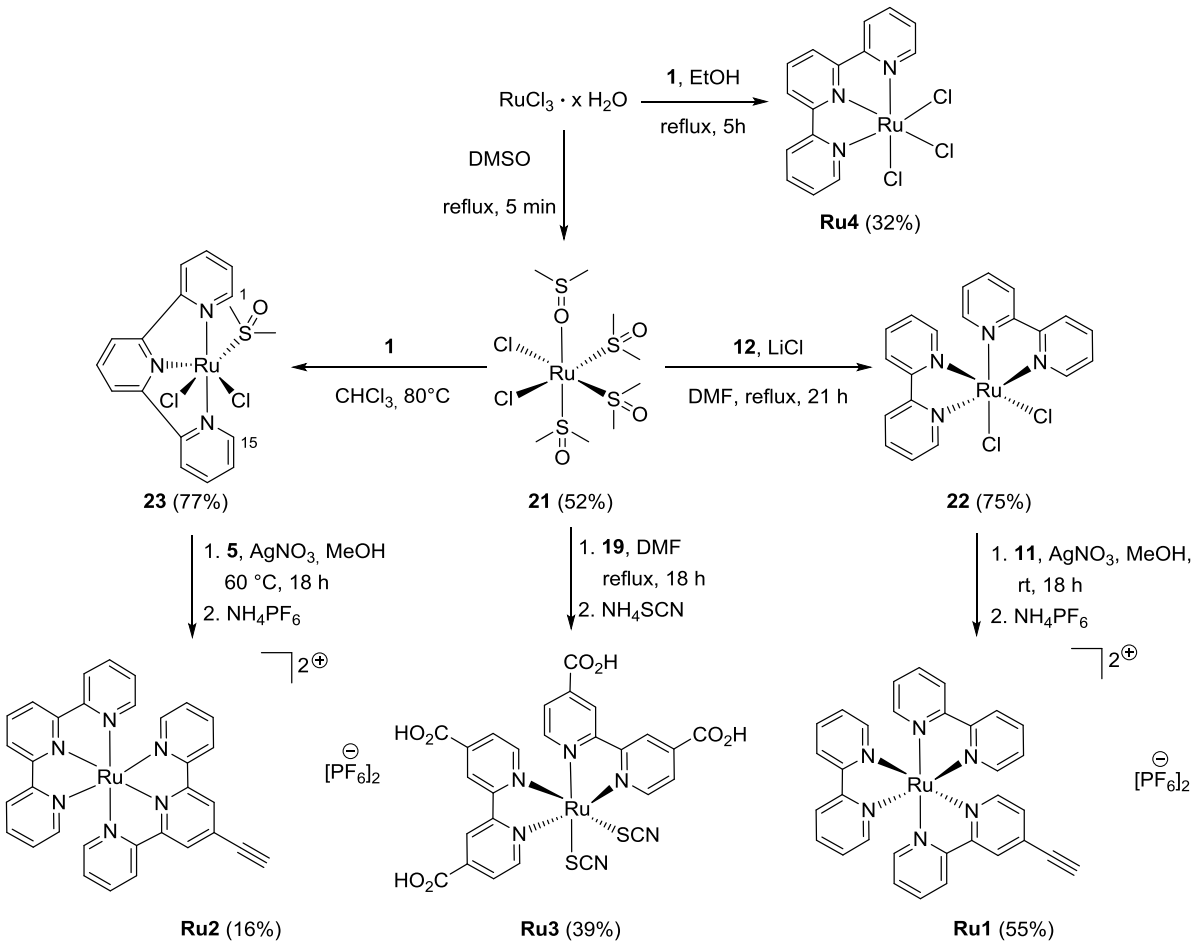

Fig. 51: Synthesis of **Ru1-Ru4** starting from ruthenium(III) chloride hydrate.

3.2.1.2 Synthesis of linker molecules

As the complexes **Ru1** and **Ru2** were planned to be linked to diamond materials using the concept of a CuAAC reaction (cf. chapters 1.5.1 and 3.2.1.1), the DND particles, which provide a variety of different surface groups, but no azides, needed to be functionalized with azide bearing molecules. The two linker systems 4-(2-azidoethyl)aniline (**L1**)[117] and 4-azidoaniline (**L2**)[342] were chosen and synthesized by master students Christian Gentzsch and Christine Heinz during their practical course “Homogeneous catalysis in Organic Chemistry” using literature-known procedures described in the following (Fig. 52).

The main difference between **L1** and **L2** is the non-conjugated/conjugated attachment of the azide group to the phenyl unit. Model systems including the linker molecules and

complexes without diamond were synthesized to obtain photochemical reference systems. Thus, the linker systems (2-phenylethyl)azide (**L3**)[343] and phenylazide (**L4**)[344] without amine functional groups were synthesized (Fig. 52).

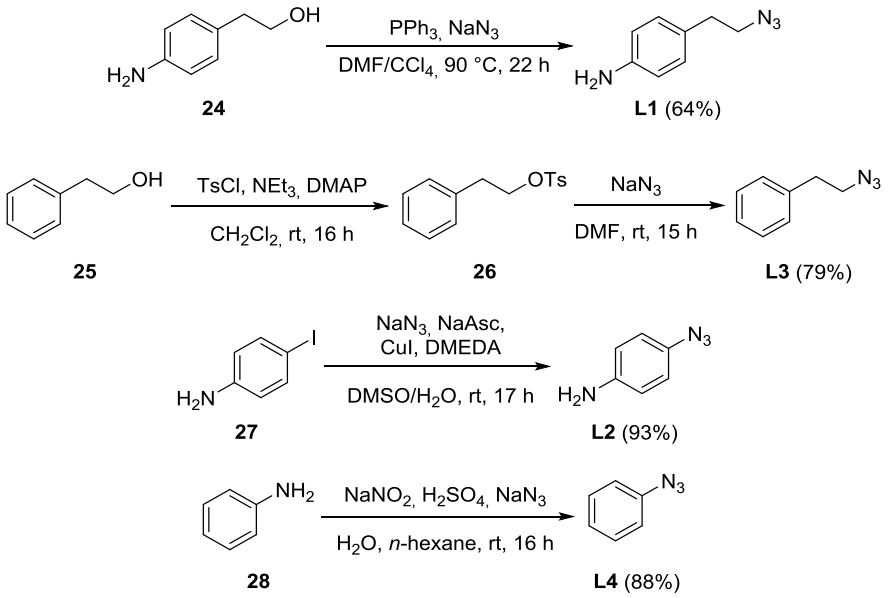

Fig. 52: Synthesis of azide bearing linker systems **L1-L4**.

In addition to the phenylene-based, azide-functionalized linker systems **L1**-**L4**, the extended tolane-based derivates **L5** and **L6** (Fig. 53) were synthesized. The interaction of ruthenium photocatalysts and ND particles in terms of non-specific adsorption might play a crucial role regarding the immobilization of the complexes. The adsorption should be reduced to a minimum by rigid linker systems between NDs and catalyst, such as **L5**.

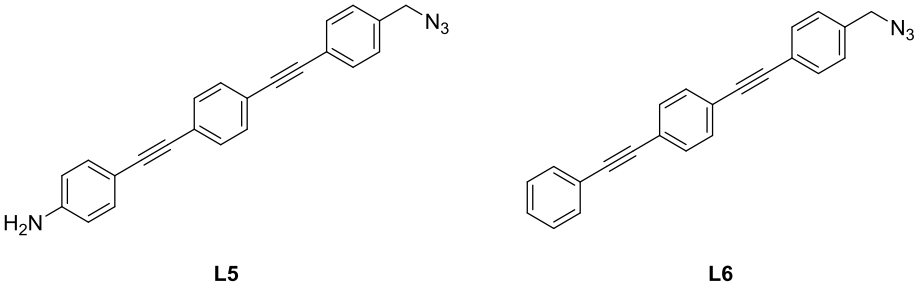

Fig. 53: Tolane-based linker system **L5** and **L6**.

The synthesis of the novel molecule **L5** was part of the master thesis. The synthesis route can be found in the Appendix (Fig. 123). **L5** was synthesized over ten steps with an overall yield of 64%. The amine function of **L5** allows for a ND functionalization via radical arylation.[117] The model system **L6** was synthesized using **L5**. First, the amine

function of **L5** was diazotized, forming the diazonium salt **L7** (Fig. 54). According to Kiesman *et al.*, a diazonium salt can be substituted by a proton via iron(II) sulfate in DMF involving intermediate, free radicals.[345] However, **L5** showed no activity regarding this reaction. Instead, **L7** was suspended in water and hypophosphorous acid was able to substitute the diazo group in presence of catalytically active amounts of copper(II)sulfate pentahydrate (Fig. 54).[346]

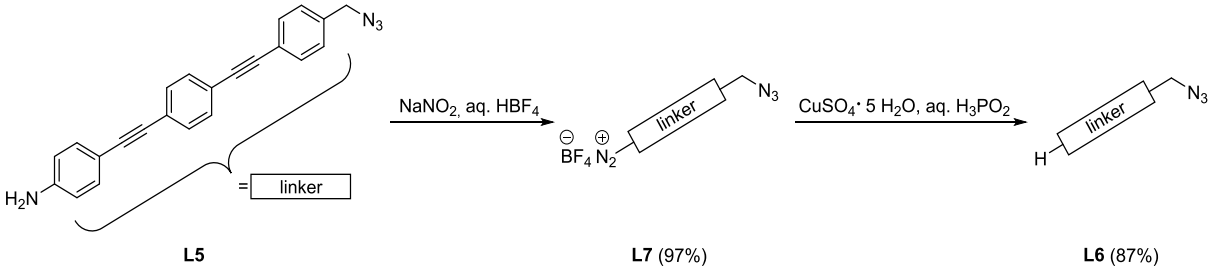

Fig. 54: Diazotation of **L5** and dediazotation of **L7** yielding **L6**.

L6 was obtained as colorless, powdery solid. The azide functionality proved to be stable using the applied acidic reaction conditions. The removal of the amine group led to a loss of color.

The carboxylic acid functionalized complex **Ru3** was intended to be linked to diamond materials using a well-known carboxamide coupling between an acid and an amine. The linker systems 4-(2-aminoethyl)aniline (**L8**)[347] and 4-aminoaniline (**L9**)[348] were chosen as suitable amine bearing linker systems (Fig. 55).

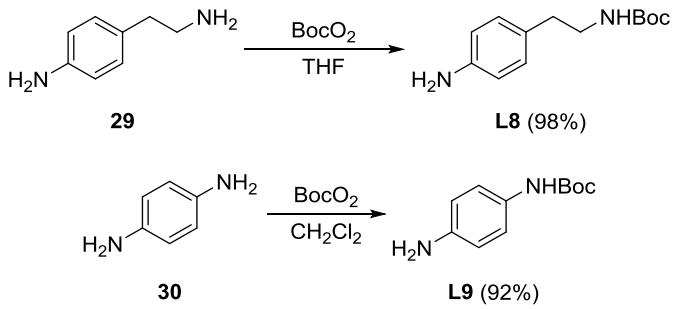

Fig. 55: Synthesis of the amine bearing linker systems **L8** and **L9**.

In a first step, an aliphatic (**L8**) or aromatic (**L9**) amino group was protected. This was selectively done using Boc-anhydride. The protection was necessary to avoid the creation of two diazonium salts when using amyl nitrite *in situ*. The reference linker systems used here, 2-aminoethylbenzene and aniline, are commercially available.

3.2.2 Attachment of transition metal complexes to nanodiamond

3.2.2.1 Functionalization of mDND with phenylene-based linker systems

For the functionalization of ND particles with **Ru1-Ru3**, **mDND** particles have been used due to their smaller size and higher reactivity. The covalent attachment of **L1**/**L2** and **L8**/**L9** onto the **mDND** surface was achieved by means of radical arylation (Fig. 56).[117] The Boc-protected particles **mDND-L8$_{Boc}$**/**mDND-L9$_{Boc}$** were stirred in 6 N hydrochloric acid for several hours to remove the protection group and generate a free amine on the surface.[349] After washing using different organic solvents, the particles were obtained as light gray (**mDND-L1/L8/L9**) and dark brown (**mDND-L2**) dispersion in MQ-water. Characteristic results are shown in Table 20.

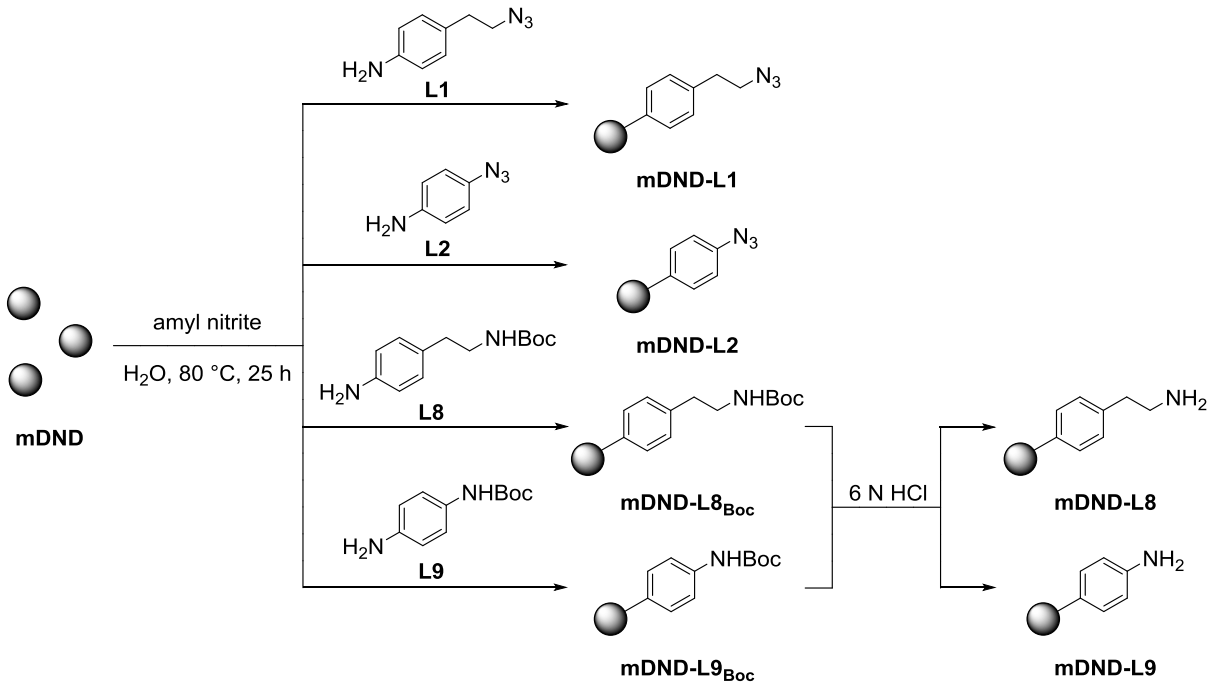

Fig. 56: Functionalization of **mDND** with linker systems **L1**/**L2** and **L8**/**L9**.

mDND-L1/**L2** functionalizations were carried out on different scales: 70 mg, 225 mg and 1000 mg. For **mDND-L1**, upscaling led to lower coverage of the particle surface with linker molecules (0.36 mmol g^{-1} → 0.22 mmol g^{-1}). For **mDND-L2**, no significant difference in surface loading was observed; however, in contrast to **mDND-L1** the functionalized particles generally showed stronger agglomeration in aqueous dispersion. As the conditions were identical for each reaction (25 h at 80 °C), the reactivity of the respective diazonium salts in a radical arylation was most likely the

reason for the different surface loadings. For the linker system **L1**, the reaction time needed to be significantly extended to yield the same loading as for smaller scales.

The hydrophobic character of **L2** in combination with the high surface loading of **mDND-L2** explained the low stability in aqueous dispersions.

Table 20: TGA, zeta potential and particle size measurements of **mDND-L1/L2**, **mDND-L8/L9** and starting material **mDND**

ND material	amount **mDND** [mg]	load. [mmol g^{-1}]	ζ [mV] (pH)	D_V-(10) [nm]	D_V-(50) [nm]	D_V-(90) [nm]
mDND	-	-	+35.2 (6.2)	1.36	3.38	5.72
mDND-L1a	70	0.36	+25.7 (6.1)	51.7	77.1	134
mDND-L1b	225	0.32	+52.5 (6.2)	52.5	81.9	158
mDND-L1c	1000	0.22	+40.8 (6.3)	31.7	54.2	107
mDND-L2a	70	0.42	+41.0 (6.2)	70.8	212	1020
mDND-L2b	225	0.34	+50.5 (6.0)	41.8	211	845
mDND-L2c	1000	0.33	+41.0 (6.1)	49.5	740	1490
mDND-L8$_{Boc}$	300	0.29	+36.0 (6.2)	46.9	77.4	246
mDND-L8	300	0.24	+43.1 (6.2)	25.8	44.7	97.0
mDND-L9$_{Boc}$	200	0.31	+39.7 (6.8)	44.6	68.2	127
mDND-L9	200	0.26	+48.4 (6.9)	56.1	91.5	180

For **mDND-L8/L9**, the slightly more positive zeta potential, as well as the smaller size after deprotection indicated the generation of a free amine on the surface. Free amino groups at the diamond surface lead to highly positive potentials and a good colloidal stability in water due to hydrogen bonding.[291]

The DRIFT spectrum of all **mDND-L1** particles show the significant peaks of **L1** (Fig. 57a). The typical vibrations of the aromatic scaffold at around 1516 cm^{-1} (ν(C=C)) and 822 cm^{-1} (δ(C-H_{arom})) are clearly visible. However, the most prominent indication for a successful functionalization is given by the azide stretch vibration at 2101 cm^{-1}. The same vibrations can also be detected for the shorter system **mDND-L2**. Apart from the asymmetric azide stretch vibration at around 2100 cm^{-1}, which is a doublet for the reactant **L2** due to Fermi resonance,[350] the symmetric azide stretch vibration at around 1265 cm^{-1} is also clearly visible (Fig. 57b). The vibrations around 2256 cm^{-1} and 2413 cm^{-1}, present for **L2** and **mDND-L2**, represent azide overtone vibrations as a

result of the Fermi resonance and are known for aromatic azides.[350,351] The attached azides of both systems, **mDND-L1** and **mDND-L2**, showed high thermal stability and no decomposition was detectable up to 80 °C over 14 d. Nevertheless, at temperatures >100 °C, the characteristic azide peak vanished after several hours, indicating decomposition.

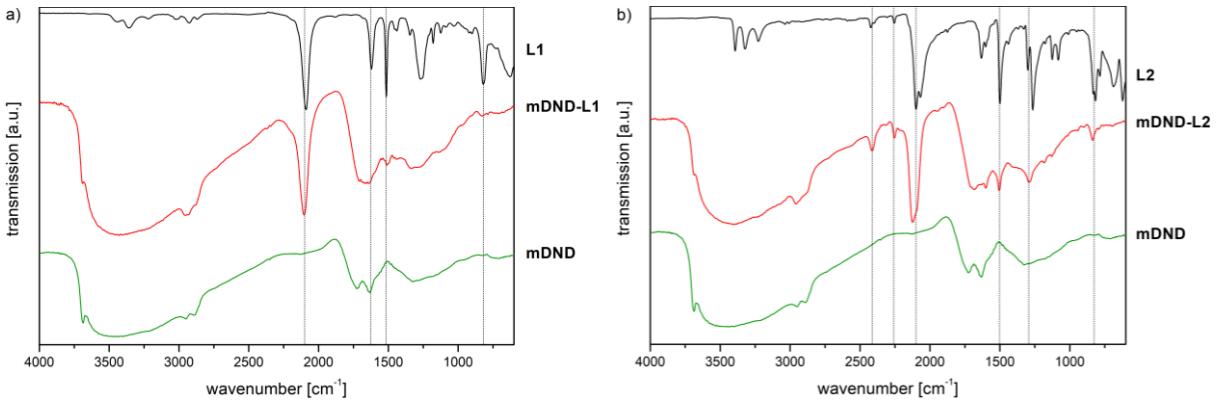

Fig. 57: IR spectra (a) of **mDND-L1**, **mDND** (DRIFT) and **L1** (ATR-FTIR) and IR spectra (b) of **mDND-L2**, **mDND** (DRIFT) and **L2** (ATR-FTIR).

The deprotection of **mDND-L8$_{Boc}$** was verified using the examination of the IR spectra (Fig. 58a). The typical vibrations of the Boc group at around 1682 cm^{-1} (ν(C=O)) and 1165 cm^{-1} (ν(C-O-C)) are clearly visible for **mDND-L8$_{Boc}$**, as well as the signals of the aromatic system at around 1514 cm^{-1} (ν(C=C)) and 822 cm^{-1} (δ(C-H$_{arom}$)).

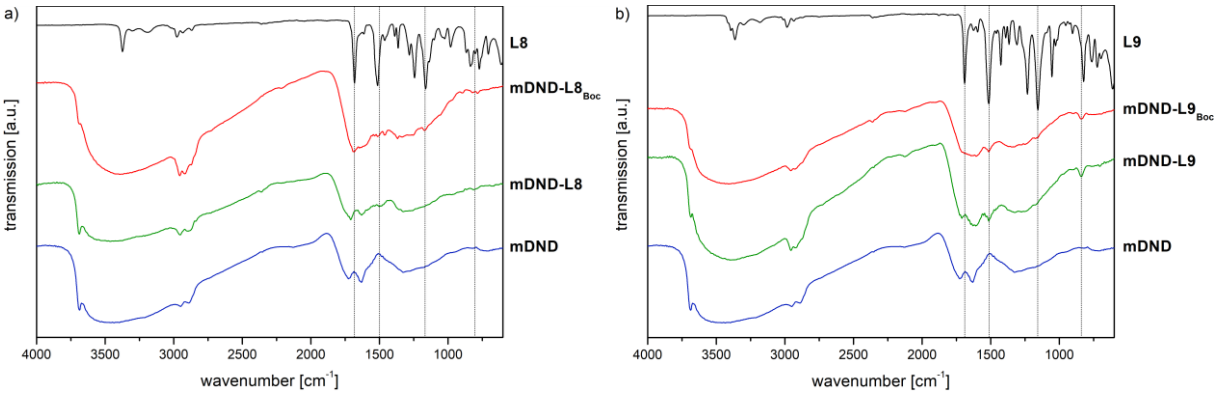

Fig. 58: IR spectra (a) of **mDND-L8$_{Boc}$**, **mDND-L8**, **mDND** (DRIFT) and **L8** (ATR-FTIR) and IR spectra (b) of **mDND-L9$_{Boc}$**, **mDND-L9**, **mDND** (DRIFT) and **L9** (ATR-FTIR).

For **mDND-L8**, the signals of the Boc-group vanished after deprotection, while the vibrations of the aromatic signals are still present. No amine related vibrations can be detected. The DRIFT spectra of **mDND-L9$_{Boc}$** and **mDND-L9** show the same characteristic signals as for **mDND-L8$_{Boc}$** and **mDND-L8** (Fig. 58a). However, in

comparison to the **L8** based samples, the **L9** functionalized samples illustrate a higher intensity of the aromatic scaffold vibrations, as **L8** possesses a higher molecular symmetry due to the amino group directly attached in *para*-position leading to increased vibrations.[352]

3.2.2.2 Functionalization of mDND with tolane-based linker system L5

The amino group of **L5** was used to functionalize **mDND** by means of diazonium salt chemistry. As the nanodiamond itself is able to act as an electron donor (cf. chapter 1.7), aryl radicals are either formed from the isolated diazonium salt **L7** during ultrasonic treatment or thermally from the *in situ* generated salt of **L5** (Fig. 59).

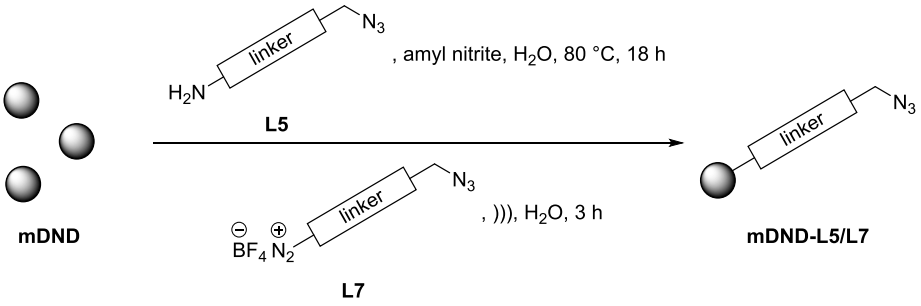

Fig. 59: Functionalization of **mDND** with either **L5** or **L7**.

The generated radicals recombine with the diamond surface forming C-C bonds.[271] After an initial experiment, it was found that the diazonium salt **L7** decomposed within hours during ultrasound treatment. Therefore, the method of choice was the *in situ* generation of the diazonium salt. The tested solvents and amounts of **mDND** and **L5**, as well as reaction times, are shown in Table 21.

Table 21: Reaction conditions for the grafting of **L5**/**L7** onto **mDND**

ND material	**mDND** [mg]	**L5/L7** [mmol]	solvent	reaction time [h]
mDND-L5a	50	0.50	0.5 N HCl	18
mDND-L5b	120	0.30	0.5 N HCl	18
mDND-L5c	200	0.50	0.5 N HCl	23
mDND-L5d	70	0.25	H_2O	22
mDND-L5e	120	0.30	H_2O	18
mDND-L5f	120	0.30	H_2O	72
mDND-L5g	150	1.50	H_2O	19
mDND-L5h	200	0.50	H_2O	72
mDND-L5i	250	0.75	H_2O	67
mDND-L5j	300	1.00	H_2O	24
mDND-L7	100	0.50	H_2O	3

After washing using different organic solvents, the particles were obtained as orange-yellowish (**mDND-L5**, solvent water) or grey-yellowish (**mDND-L7** and **mDND-L5**, solvent hydrochloric acid) aqueous dispersions (Fig. 60), indicating the formation of strongly colored azobenzenes as a side reaction.

Fig. 60: Aqueous dispersions of linker-functionalized particles **mDND-L5e** (left) and **mDND-L7** (right).

Here, the influence of the solvent on the reaction of **mDND** with **L5** was of main interest. In pH-neutral water, an azo-coupling of *in situ* generated diazonium salts with the electron rich amino-bearing phenyl group of **L5**, forming azobenzenes, is possible (Fig. 61).[271] The azobenzenes can then be attached to already linker-functionalized **mDND** with their free amino group, leading to branched structures on the surface with free azide functionalities. However, the undesired side reaction can be avoided by using

0.5 N hydrochloric acid as a solvent. Under acidic conditions, the amino functionality is protonated and loses its electron-donating effect, resulting in a deactivation of the aromatic scaffold and less reactivity regarding azo-coupling.[117]

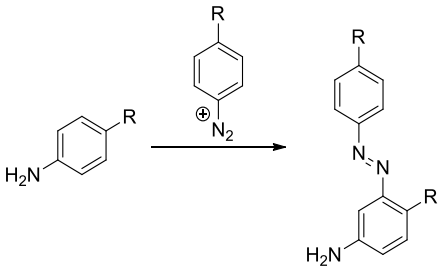

Fig. 61: Schematic representation of an azo-coupling.

The characteristic results in Table 22 clearly indicate that the surface loading with **L5** using hydrochloric acid (~0.10 mmol g^{-1}) was generally 50% lower than for water (~0.20 mmol g^{-1}). The zeta potential was in both cases highly positive (+30-40 mV) and the particle size for samples produced in water was slightly bigger. For **mDND-L7**, the results were almost identical.

Table 22: Results of TGA, zeta potential and particle size measurements of all **L5**/**L7** functionalized DND particles in aqueous dispersion

ND material	surface loading [mmol g^{-1}]	ζ [mV] (pH)	D_V-(10) [nm]	D_V-(50) [nm]	D_V-(90) [nm]
mDND	-	+30.8 (6.2)	1.36	3.38	5.72
mDND-L5a	0.24	+36.6 (6.1)	103	169	279
mDND-L5b	0.11	+30.1 (6.0)	50.5	83.9	205
mDND-L5c	0.10	+35.3 (6.1)	75.1	131	259
mDND-L5d	0.27	+32.2 (6.1)	74.2	285	411
mDND-L5e	0.22	+41.1 (6.2)	97.7	178	332
mDND-L5f	0.45	+36.5 (6.3)	66.8	106	199
mDND-L5g	0.17	+32.7 (6.5)	73.5	121	230
mDND-L5h	0.21	+38.8 (6,4)	61.6	122	321
mDND-L5i	0.22	+32.9 (6.2)	84.6	140	251
mDND-L5j	0.20	+39.7 (6.0)	77.1	164	337
mDND-L7	0.15	+33.5 (6.1)	135	170	212

Besides the higher surface loading, the significant orange-yellowish color of **mDND-L5e** in comparison to **mDND-L5b** provided evidence for the formation of *in situ*

generated azobenzenes, which are known to be intensively colored compounds (Fig. 62), even though identical reaction parameters and washing steps were used. For **mDND-L5f**, an elongated reaction time was tested (72 h). The sample was deeply colored and the increase in surface loading (ca. +120%) was mainly related to azobenzenes.

Fig. 62: Aqueous dispersion of **mDND-L5b** (left) and **mDND-L5e** (right).

Furthermore, the adsorption of **L5** to the **mDND** surface was investigated focusing on the role of the different functional groups of the tolane-based linker system. Therefore, “functionalizations” of **mDND** with **L5** and model system **L6** using identical conditions, but without the amyl nitrite coupling reagent, were executed, followed by identical washing steps. As a result, in water **L5** adsorbed to the **mDND** surface yielding 0.05-0.07 mmol g^{-1} of physisorbed linker. However, when using either 0.5 N hydrochloric acid as solvent or **L6**, the adsorption (~0.02 mmol g^{-1}) was diminished. Thus, the reason for the adsorption of **L5** in water could be the free amino group. For functionalization experiments adding isoamyl nitrite, an adsorption of **L5** to the surface could even be beneficial, as the amino group is converted into diazonium species over time and, hence, the reactive site is close to the surface, favoring a fast C-C bond formation.

The DRIFT spectra of both exemplary particles, **mDND-L5b** and **mDND-L5e**, present almost identical results (Fig. 63). The characteristic C-C-vibrations of the aromatic scaffold are detected at around 1595 cm^{-1} and 1520 cm^{-1}, as well as the C-H deformation vibration of 1,4-disubstituted systems around 838 cm^{-1}. Those vibrations are present for **L5**, **mDND-L5b** and **mDND-L5e**, but not for the starting material **mDND**. Additionally, the functionalized particles show an alkyne stretch vibration at 2209 cm^{-1} and an azide vibration at 2101 cm^{-1}. **mDND-L5b** and **mDND-L5e** illustrate

a vibration at 1921 cm^{-1}. In this region of the IR spectrum in particular, cumulenes and conjugated dienes are expected.[353] However, these structures are not found in **L5**. Further studies are required to investigate the origin of this vibration.

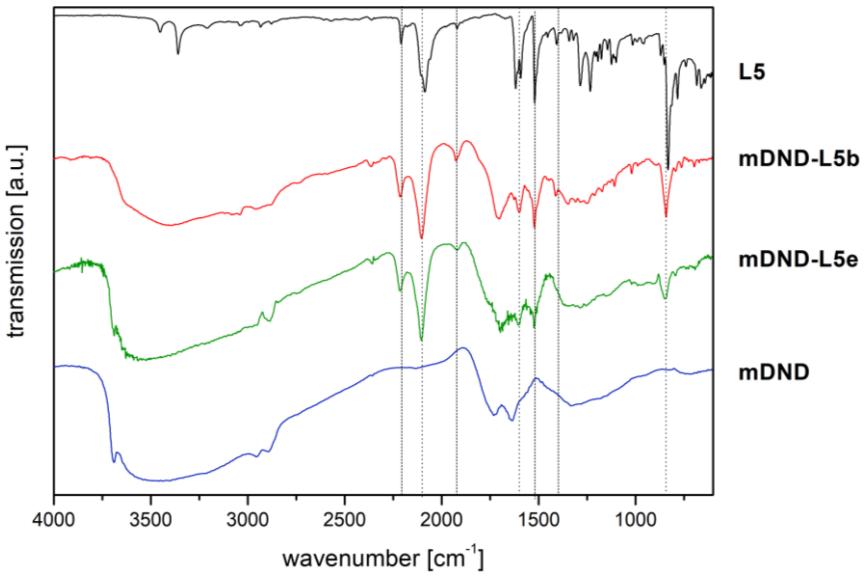

Fig. 63: IR spectra of **mDND-L5b** and **mDNDL5e**, **mDND** (DRIFT) and **L5** (ATR-FTIR).

Additional proof of a successful termination is given by the non-present N-H deformation vibration of **L5** at 1618 cm^{-1} after functionalization. The characteristic vibration of an azo functionality cannot be detected, as the signal would be superimposed by the strong alkyne and azide vibrations. For **mDND-L7**, the same IR vibrations as for **mDND-L5** are present (Fig. 64). Additionally, the successful functionalization can be proven by the missing signal of both the diazonium group (2289 cm^{-1}) and the signal of tetrafluoroborate (1046 cm^{-1}).

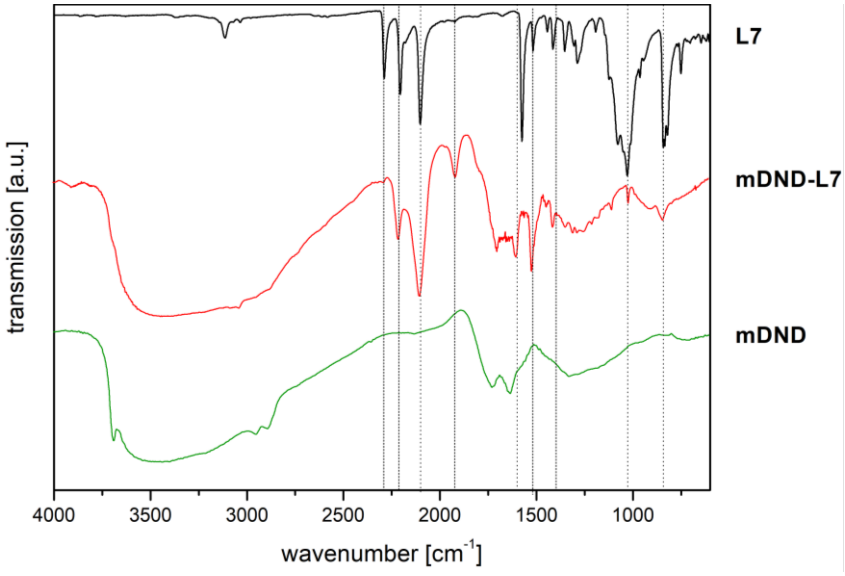

Fig. 64: IR spectra of **mDND-L7**, **mDND** (DRIFT) and linker **L7** (ATR-FTIR).

Similar to the phenylene-based linker systems **mDND-L1** and **mDND-L2**, the attached azides showed high thermally stability and no decomposition was detectable up to 80°C over 14 d, neither as powder nor in dispersion.

In summary, the following optimized conditions were found for a functionalization of **mDND** with linker **L5** (Table 23).

Table 23: Optimized reaction conditions for the functionalization of **mDND** with linker **L5** using amyl nitrite

solvent [ml]	**mDND** [mg]	**L5** [mmol]	time [h]	surface loading [mmol g^{-1}]	generation of azobenzenes?
10 (H_2O)	100	0.25	18-20	~0.20	expected
10 (0.5 N HCl)	100	0.25	18-20	~0.10	not expected

When using 0.5 N hydrochloric acid as solvent, the formation of azobenzenes can be reduced. The azide proved to be stable under acidic conditions. In water, reactivity and surface loading were substantially higher, but the generation of azobenzenes was more likely to happen. A branched and thus extended structure of attached **L5** strongly influenced the interaction of attached molecules with the **mDND** surface by sterical hindrance.

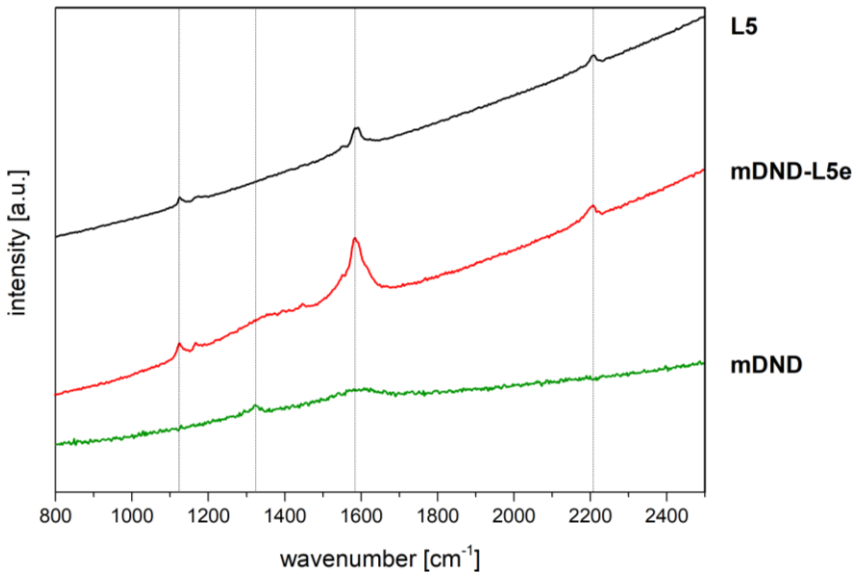

Fig. 65: Raman spectra of **mDND**, **mDND-L5e** (exemplary) and **L5** (measurements with 445 nm laser).

mDND-L5e also shows some interesting signals in the Raman spectrum. At 2209 cm^{-1}, the vibration of the two internal alkynes and, at 1587 cm^{-1}/1150 cm^{-1}, the very intensive

vibration for the C=C-aromatic scaffold can be seen (Fig. 65). No distinctive diamond peak is visible, as the surface of the particles is covered with linker molecules shielding the diamond core.

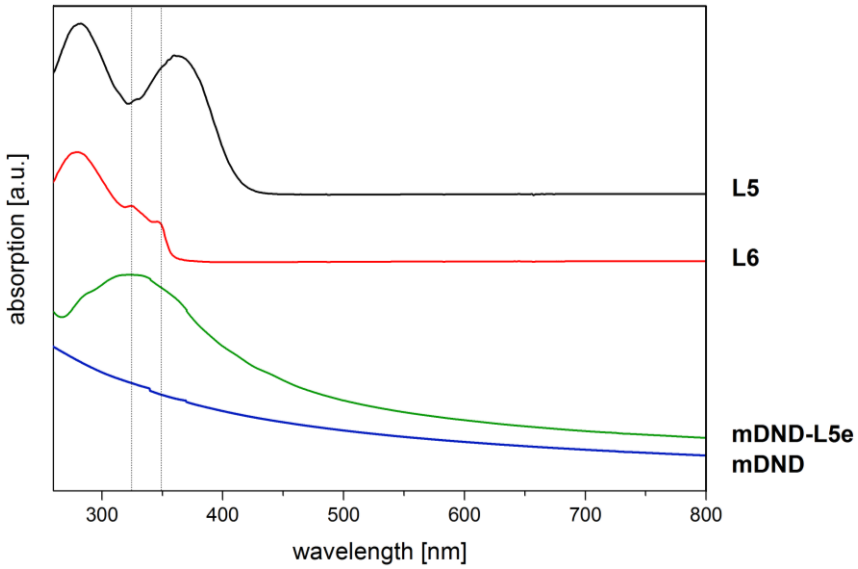

Fig. 66: UV/Vis spectra of **mDND**, **mDND-L5e** and linker systems **L5** and **L6** (measurements in DMSO).

The UV/Vis spectrum of **mDND-L5e** in DMSO shows a broad maximum at 337 nm. This signal can be related to the two smaller maxima of **L6** at 349 nm and 324 nm. The absorption maximum of **L5** at 364 nm is not present for **L6** and **mDND-L5e**. Thus, it is most likely related to the amino group of **L5**, which is missing for **L6** and **mDND-L5e**. The intensive maximum of both linkers **L5** and **L6** at 282 nm is not visible for **mDND-L5e**. When measuring **mDND-L5e** in acetonitrile, a broad shoulder at ~235-260 nm is present, which is typical for the π-π^* transition of benzene rings.[271] The linker systems **L5** and **L6** are not soluble in acetonitrile.

3.2.2.3 Synthesis of mDND TM-complex conjugates via CuAAC reaction

3.2.2.3.1 Attachment of Ru1/Ru2 on mDND

In order to synthesize reference systems for photochemical reactions using linker systems **L3**/**L4** and complexes **Ru1**/**Ru2**, the master students Christine Heinz and Daniel Gillung carried out test reactions during their practical course “Homogeneous catalysis in Organic Chemistry”. For reactions with **Ru1**, copper(II) sulfate in combination with the reducing agent sodium ascorbate was used in a two-phase

system.[335] For reactions with the less reactive **Ru2** complex, the copper complex $(PPh)_3CuI$[354,355] (**31**) proved to be the better choice (Fig. 67).

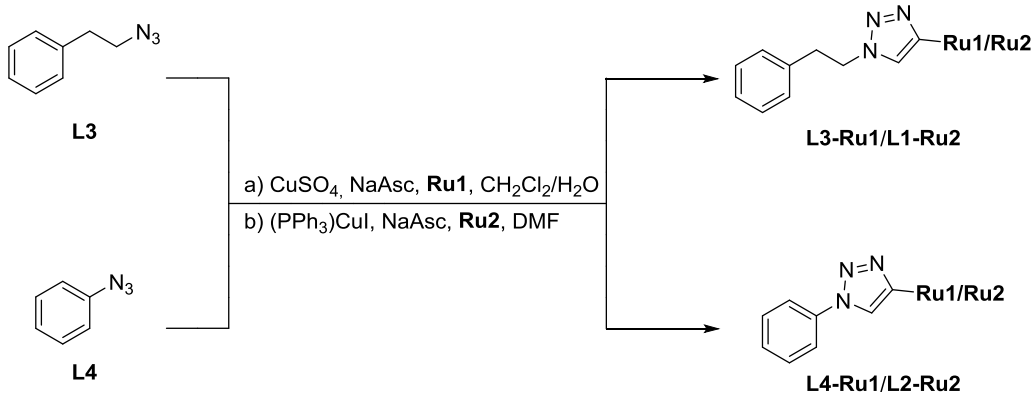

Fig. 67: General CuAAC reaction between azide linker systems **L3**/**L4** and **Ru1**/**Ru2**.

The successful CuAAC reaction between the linker systems **L3**/**L4** and the complexes **Ru1**/**Ru2** can be proven by ATR-FTIR. The systems **L3-Ru1** and **L4-Ru1** lack the asymmetric (2100 cm^{-1}) and symmetric (1265 cm^{-1}) azide stretching vibration (Fig. 68). The characteristic vibrations of the ruthenium complexes, the aromatic C=N and C=C stretching vibrations (1466 and 1442 cm^{-1}), as well as the P-F stretching vibration of the anion (825 cm^{-1}) are clearly visible. The same applies for **L3-Ru2** and **L4-Ru2** (Appendix, Fig. 124).

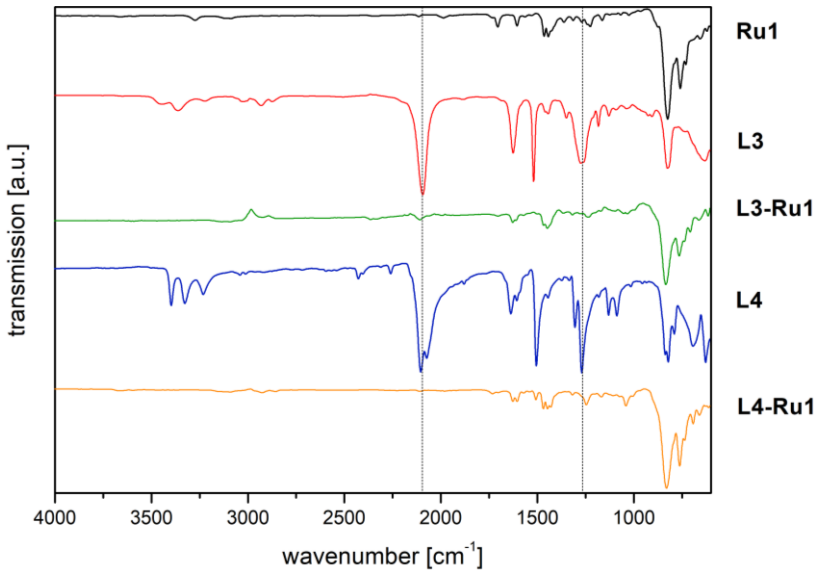

Fig. 68: ATR-FTIR spectra of **Ru1**, azide linkers **L3** and **L4** and the reference systems **L3-Ru1** and **L4-Ru1**.

In the ^{1}H-NMR spectrum of all reference systems, the characteristic singulet signal of the triazole proton is observed at 9.39 ppm (**L3-Ru1**), 8.71 ppm (**L4-Ru1**), 9.01 ppm

(**L3-Ru2**) and 9.63 ppm (**L4-Ru2**). After purification via column chromatography, the reference systems **L3-Ru1**/**L4-Ru1** were obtained as intensively orange colored, crystalline solids and the reference systems **L3-Ru2**/**L4-Ru2** as intensively red colored crystalline solids. Subsequently, **Ru1**/**Ru2** were linked to the azide-functionalized particles **mDND-L1** and **mDND-L2** using the protocols developed for the synthesis of the reference compounds (Fig. 69).

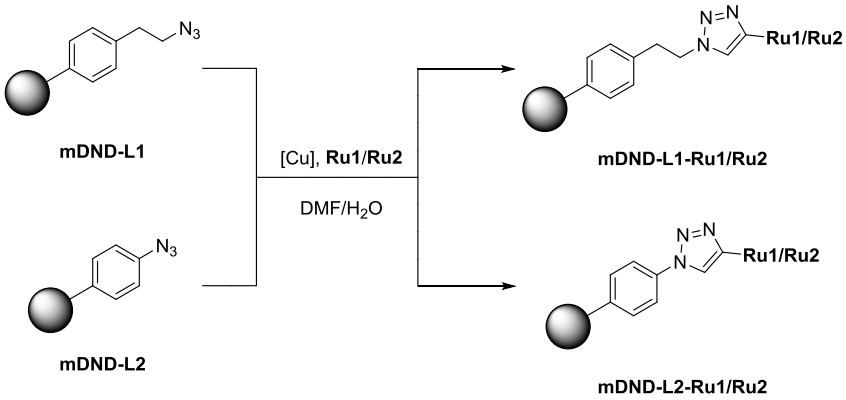

Fig. 69: Functionalization of azide-functionalized DNDs **mDND-L1**/**L2** with ruthenium complexes **Ru1** and **Ru2**.

Different reaction conditions are listed in Table 24. In comparison to the particle-free CuAAC reactions, the duration for the functionalization has to be extended due to involvement of nanodiamond and the related loss in reactivity. At room temperature, no significant decrease of the azide peak was detected, even after several days. Consequently, temperatures between 60-80 °C were used in combination with ultrasonic treatment for 30 min every 24 h. After the azide peak was either minimized to a consistent intensity level or completely vanished in the DRIFT spectrum, the reaction was stopped. For **mDND-L1**, all chosen catalytic copper systems gave satisfactory results. For the reaction of **mDND-L2** with **Ru1**/**Ru2**, the reactivity proved to be different. When applying the protocol successful for **mDND-L1** to the reaction of **mDND-L2** with **Ru1** using the $CuSO_4$/NaAsc system, the azide was still detectable even after several weeks at high temperatures. Additionally, changing the copper(II) to a copper(I) catalyst, e.g. CuI or PPh_3CuI (**31**), proved to be successful (Table 24). In general, the reaction time is essentially extended, as the azide directly attached to the phenyl ring of **L2** is less reactive and sterically more hindered than for **L1**. From a mechanistical point of view, the N1 nitrogen of the azide, which is directly linked to the phenyl group, behaves as an L-type σ-donor, coordinating the *in situ* formed copper(I)

acetylide.[356] As the σ-character of the conjugated azide **mDND-L1** was less pronounced compared to the non-conjugated **mDND-L1**, lower reactivity was observed.

Table 24: Reaction conditions for the CuAAC reactions of **mDND-L1**/**mDND-L2** with complexes **Ru1**/**Ru2**

ND material	starting material (amount [mg])	reaction conditions	T [°C]	time [h]
mDND-L1-Ru1a	**mDND-L1b** (40)	$CuSO_4$, NaAsc, DMSO/H_2O (3:1)	r.t. 60	27 216
mDND-L1-Ru1b	**mDND-L1b** (40)	$CuSO_4$, NaAsc, DMF/H_2O (4:1)	r.t. 60	190 96
mDND-L1-Ru1c	**mDND-L1c** (240)	$CuSO_4$, NaAsc, DMF/H_2O (4:1)	r.t. 70	144 192
mDND-L1-Ru2a	**mDND-L1b** (40)	$CuSO_4$, NaAsc, DMF/H_2O (4:1)	60 80	168 72
mDND-L1-Ru2b	**mDND-L1c** (240)	PPh_3CuI, ,NaAsc, DMF/H_2O (4:1)	r.t. 70	192 120
mDND-L2-Ru1a	**mDND-L2b** (40)	$CuSO_4$, NaAsc, DMF/H_2O (4:1)	60 80 95	96 192 216
mDND-L2-Ru1b	**mDND-L2b** (40)	CuI, DIPEA, NaAsc, DMF/H_2O (4:1)	r.t. 70	96 336
mDND-L2-Ru1c	**mDND-L2b** (40)	PPh_3CuI, ,NaAsc, DMF/H_2O (4:1)	r.t. 70	96 192
mDND-L2-Ru1d	**mDND-L2c** (220)	PPh_3CuI, ,NaAsc, DMF/H_2O (4:1)	70	312
mDND-L2-Ru2a	**mDND-L2b** (40)	PPh_3CuI, ,NaAsc, DMF/H_2O (4:1)	70	216
mDND-L2-Ru2b	**mDND-L2c** (220)	PPh_3CuI, ,NaAsc, DMF/H_2O (4:1)	70	312

In general, all Ru-functionalized particles showed high colloidal stability, small particle sizes (D_V(50) ~70-90 nm) and positive zeta potentials in aqueous dispersion (Table 25). For **Ru1**/**Ru2** on **mDND-L2**, grafting of the complex clearly helped to de-agglomerate the particles. After upscaling the reactions (**mDND-L1-Ru1c** and **mDND-L1-Ru2b**), the surface loading was reduced. For these reactions, an azide shoulder is still visible in the DRIFT spectra (Fig. 71a/b) as a result of inclusions of azide groups

within particle agglomerates. Those agglomerates are more likely to form when higher amounts of DND are used and they are not accessible for CuAAC reactions. Calculating surface loading via thermogravimetric analysis with the assumption that every azide attached to the particles was undergoing a coupling reaction with an alkyne-functionalized complex led, in the case of inaccessible azide groups on the surface, to a lower surface loading. The molecular weight of the leaving surface groups during TGA measurement is strongly overestimated leading to the lower loading values.

Table 25: Results of TGA, zeta potential and particle size measurements in aqueous dispersion for **Ru1**/**Ru2**-functionalized particles

ND material	surface loading [mmol g^{-1}]	ζ [mV] (pH)	D_V-(10) [nm]	D_V-(50) [nm]	D_V-(90) [nm]
mDND-L1-Ru1a	0.17	+49.6 (6.1)	61.3	99.0	195
mDND-L1-Ru1b	0.28	+49.4 (6.0)	56.6	89.5	170
mDND-L1-Ru1c	0.11	+21.9 (6.2)	44.9	70.0	137
mDND-L1-Ru2a	0.27	+48.5 (6.2)	44.7	69.8	137
mDND-L1-Ru2b	0.16	+23.8 (6.3)	42.2	72.0	282
mDND-L2-Ru1a	0.27	+26.9 (6.2)	46.0	72.2	140
mDND-L2-Ru1b	0.33	+23.3 (6.1)	38.9	76.4	139
mDND-L2-Ru1c	0.34	+21.1 (6.2)	38.4	69.4	374
mDND-L2-Ru1d	0.21	+19.1 (6.0)	31.4	74.6	374
mDND-L2-Ru2a	0.22	+24.6 (6.1)	44.8	101	932
mDND-L2-Ru2b	0.16	+24.1 (6.1)	59.2	113	487

The Ru-functionalized particles were obtained as orange brown or red brown aqueous dispersions (Fig. 70).

Fig. 70: Diamond conjugates **mDND-L1-Ru1c**/**Ru2b** and **mDND-L2-Ru1d/Ru2b** (from left to right) in aqueous dispersion.

The attachment of **Ru1**/**Ru2** on **mDND-L1c**/**mDND-L2c** was proven using different spectroscopic techniques. In the following paragraph, the characteristic DRIFT, Raman and UV/Vis spectra are shown for the products of the upscaled reactions, as those particles were used in X-ray absorption and photoemission measurements, as well as photoelectrocatalytic CO_2 reduction. The products of the low scaled reaction were analyzed using the same methods, except for photoemission and –electrocatalytic measurements, and are not shown here. The DRIFT spectra of the ethylene-bridged systems **L1** (Fig. 71a/b) show the characteristic vibrations of the complex ligands, namely the heteroaromatic C=N stretching vibration at 1600 cm^{-1}, the C=N in-plane vibration of the aromatic scaffold in the range of 1470-1380 cm^{-1}, as well as the out-of-plane deformation vibration of C-H_{arom} groups between 730-790 cm^{-1}.

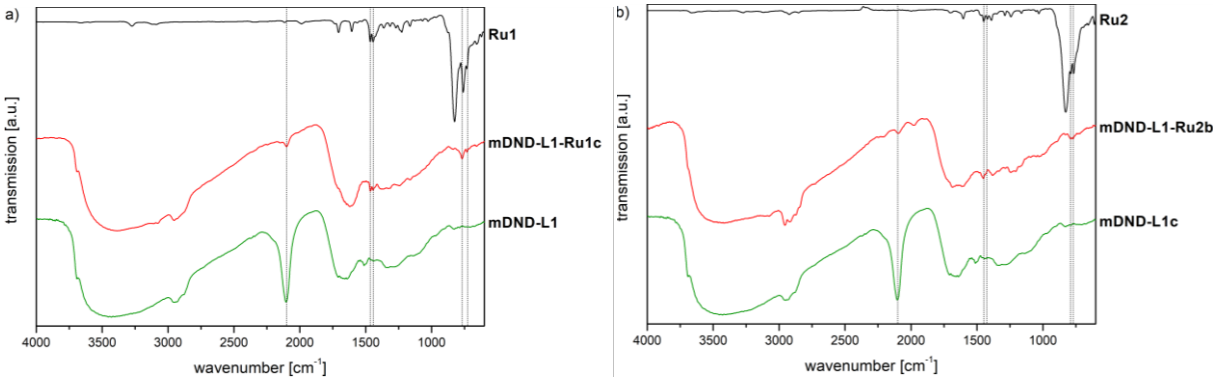

Fig. 71: IR spectra of (a) **mDND-L1c**, **mDND-L1-Ru1c** (DRIFT) and **Ru1** (ATR-FTIR) and of (b) **mDND-L1c**, **mDND-L1-Ru2b** (DRIFT) and **Ru2** (ATR-FTIR).

The deformation vibrations cannot be detected for the pure complexes **Ru1**/**Ru2**, as the much stronger P-F stretching vibration of the hexafluorophosphate counter ion obscures this region. This observation indicates that after CuAAC reaction the positive charge of the complexes is not compensated by PF_6 anions anymore. Either the anion was exchanged with a non-IR active ion, like chloride, or the charge is compensated by the particles themselves. As for the applied **mDND** chloride was detected due to the purification methods of **pDND** (cf. chapter 3.1.1.2), the ND particles themselves can serve as source for chloride anions. Furthermore, theoretical calculations from Prof. Dr. Karin Larsson, University of Uppsala (DIACAT), showed that the electronic charge of the ruthenium complexes in those ND-conjugates was decreased to +0.9-1.1. Thus, the oxidation state of ruthenium complex was lowered to +1 requiring only one counter anion.

The very intensive azide peak at around ~2100 cm^{-1} is minimized to a shoulder for **mDND-L1-Ru1c** and **mDND-L1-Ru2b**, leading to the assumption that almost every linker-azide was connected with a complex-alkyne.

As a complement to IR spectroscopy, both complexes can be investigated with Raman spectroscopy using 445 nm laser excitation. The characteristic signals of **Ru1** are clearly visible for **mDND-L1-Ru1c**, overlapping with the broad G-band at around 1580 cm^{-1} and the diamond/D band signal at ~1330 cm^{-1} (Fig. 72a).

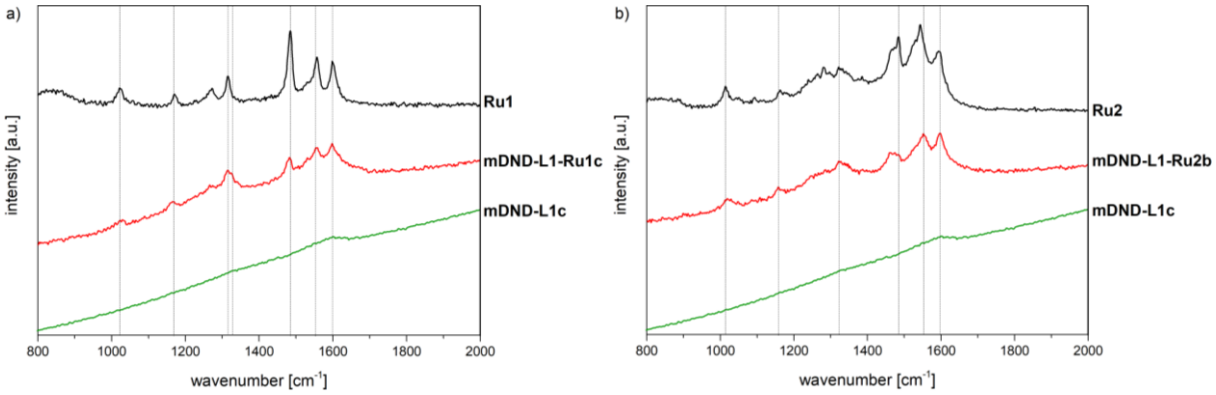

Fig. 72: Raman spectra of (a) **mDND-L1c**, **mDND-L1-Ru1c** and complex **Ru1** and of (b) **mDND-L1c**, **mDND-L1-Ru2b** and **Ru2** (measurements with 445 nm laser).

Both signals, the G band and the diamond/D band, are weak in intensity for **mDND-L1c**, as the surface is highly covered with Raman inactive linker molecules **L1**, shielding the diamond surface. No significant shifts in wavenumbers are visible and the change of intensity for the C=C- and C=N-stretching vibrations in the range of 1450-1600 cm^{-1} originates from the overlap with the G-band. Raman spectroscopic characterization of **mDND-L1-Ru2b** with the complex **Ru2** attached provided the same observations and results (Fig. 72b).

The orange brown color of the aqueous dispersion of **mDND-L1-Ru1c** can be explained by means of UV/Vis absorption (Fig. 73a). The complex **Ru1** and the reference system **L3-Ru1** show four significant absorption maxima. The three maxima in the UV-region below 300 nm can be related to HOMO-LUMO(+X) transitions, whereas the broad signal at 437 nm is related to a charge transfer between ruthenium center and the ligands.[233] This characteristic absorption pattern of **L3-Ru1** illustrates the still intact $Ru(bpy)_3$ coordination sphere after CuAAC reaction. Those four maxima are also present for **mDND-L1-Ru1c**, while being slightly red shifted due to attachment to particles. The maximum at 242 nm is reduced to a broad shoulder, as in this region

the attached phenyl group of **mDND-L1c** obscures the signal by showing absorption itself. For conjugate **mDND-L1-Ru2b**, the color change to red brown can be explained in the same way by the four maxima of **Ru2** (Fig. 73b).

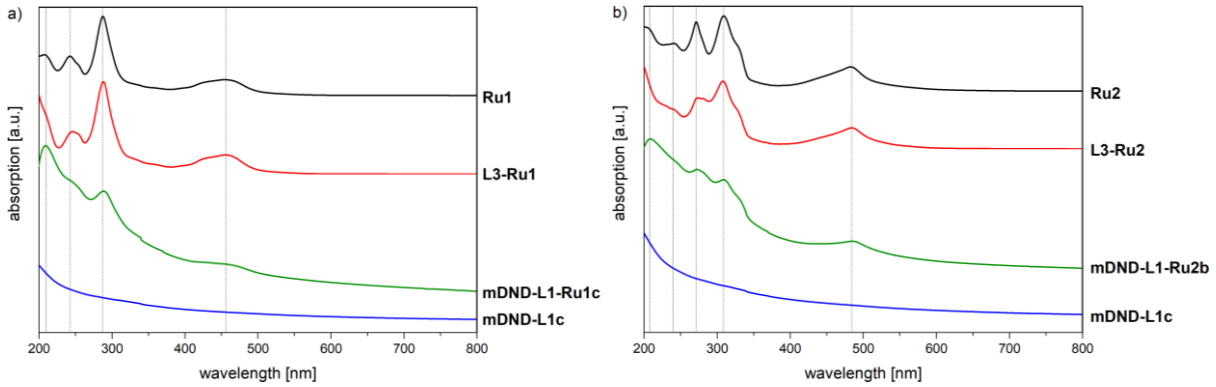

Fig. 73: UV/Vis spectra of (a) **mDND-L1c**, **mDND-L1-Ru1c**, complex **Ru1** and reference **L3-Ru1** and of (b) **mDND-L1c**, **mDND-L1-Ru2b**, complex **Ru2** and reference **L3-Ru2** (measurements in MeCN).

The DRIFT spectra of **mDND-L2-Ru1d** and **mDND-L2-Ru2b** do not show asymmetric and symmetric azide stretch or overtone vibrations anymore (Appendix, Fig. 125a/b). The characteristic vibrations of the linker system (ν(C=C$_{arom}$), δ(C-H$_{arom}$)) and the ligands (ν(C=N$_{arom}$), δ(C=N$_{arom}$), δ(C-H$_{arom}$)) are clearly visible. Likewise, no P-F stretching vibration is visible.

The Raman spectra for **mDND-L2-Ru1d** and **mDND-L2-Ru2b** (Appendix, Fig. 126a/b) show the characteristic signals of the attached complex with changes in intensity for the C=C- and C=N-stretching vibrations in the range of 1450-1600 cm^{-1} due to overlap with the G-band. The UV/Vis spectra of **mDND-L2-Ru1d** and **mDND-L2-Ru2b** (Appendix, Fig. 127a/b) illustrate the characteristic four maxima of the attached complex **Ru2**. The red shift of each maximum is slightly more pronounced than for **mDND-L1-Ru1c** and **mDND-L1-Ru2b**.

IR and Raman spectroscopy clearly proved the successful covalent attachment of the ruthenium complexes **Ru1**/**Ru2** onto the azide-linker functionalized particles **mDND-L1**/**L2**. The observed red shift of the HOMO-LUMO(+X) and MLCT transitions in the UV/Vis spectra of all four obtained ND-complex conjugates is a first indication of electronic coupling between the particles and the complex, as the shifts were not observed for the reference systems **L3**/**L4**-**Ru1**/**Ru2** without nanodiamond. The electronic coupling of the successfully synthesized and spectroscopically characterized samples will be discussed indetail in chapter 3.2.2.3.5

3.2.2.3.2 Coordination of ruthenium(III) on mDND particles

In addition to the attachment of synthesized complexes, such as **Ru1** or **Ru2**, on DND particles, linkage by first attaching a ligand and then forming a complex directly on the particle surface was also investigated (Fig. 74).

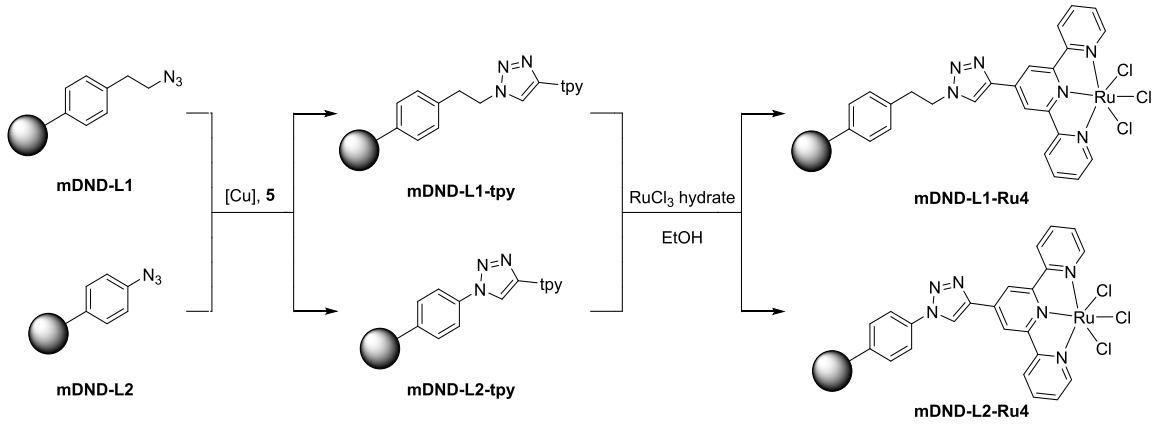

Fig. 74: General CuAAC reaction between **mDND-L1**/**L2** and ligand **5** with subsequent complexation to Ru(III)-conjugates **mDND-L1**/**L2-Ru4**.

This procedure was already applied to other materials, e.g. MOFs.[357] Using an analogous approach, 4'-ethinyl-2,2':6',2''-terpyridine (**5**) was grafted on **mDND-L1**/**L2**. Using **mDND-L1**, the CuI/DIPEA/NaAsc system at r.t. proved successful. With $CuSO_4$ as catalyst, only incomplete conversion was achieved. For **mDND-L2**, the lower reactivity was again overcome using PPh_3CuI/NaAsc at 70 °C (Table 26).

Table 26: Reaction conditions for the CuAAC reaction of **mDND-L1**/**L2** with ligand **5**

ND material	starting material (amount [mg])	reaction conditions	T [°C]	time [h]]
mDND-L1-tpy$_a$	**mDND-L1b** (80)	$CuSO_4$, NaAsc, DMF/H_2O (4:1)	r.t.	168
mDND-L1-tpy$_b$	**mDND-L1b** (40)	CuI, DIPEA, NaAsc, DMF/H_2O (4:1)	r.t.	98
mDND-L1-tpy$_c$	**mDND-L1c** (250)	CuI, DIPEA, NaAsc, DMF/H_2O (4:1)	r.t. 60	216 120
mDND-L2-tpy$_a$	**mDND-L2b** (40)	PPh_3CuI, NaAsc, DMF/H_2O (4:1)	r.t. 70	96 336
mDND-L2-tpy$_b$	**mDND-L2c** (220)	PPh_3CuI, ,NaAsc, DMF/H_2O (4:1)	70	312

The ruthenium complex itself was formed on the diamond surface by adding ruthenium(III) chloride hydrate to the tpy-functionalized particles **mDND-L1-tpy** and

mDND-L2-tpy. For both systems, the grafting of the tpy ligand led to water stable particles with a positive zeta potential (Table 27). The surface loading was almost identical to the starting material in each case (cf. chapter 3.2.2.1, Table 20), indicating a quantitative reaction.

Table 27: Results of TGA, zeta potential and particle size measurements of tpy-functionalized DND particles in aqueous dispersion

ND material	surface loading [mmol g^{-1}]	ζ [mV] (pH)	D_V-(10) [nm]	D_V-(50) [nm]	D_V-(90) [nm]
mDND-L1-tpy$_a$	0.13	+13.2 (6.1)	57.4	88.5	161
mDND-L1-tpy$_b$	0.25	+31.7 (6.2)	64.9	105	207
mDND-L1-tpy$_c$	0.22	+20.7 (5.9)	64.0	101	191
mDND-L2-tpy$_a$	0.34	+19.2 (6.0)	60.9	190	270
mDND-L2-tpy$_b$	0.30	+23.3 (6.2)	93.9	129	182

Characteristic results produced by the complexation reaction of tpy-functionalized particles **mDND-L1-tpy**/**mDND-L2-tpy** with ruthenium(III) chloride hydrate are listed in Table 28. The zeta potential was highly positive at a slightly acidic pH-value. The $Ru(tpy)Cl_3$ complex (**Ru4**), which is known to be acidic as a consequence of the three chloride ligands, leads to acidic pH values in aqueous solutions.[341] The surface loading for the upscaled reactions **mDND-L1-tpy$_c$** and **mDND-L2-tpy$_b$** was almost the same after two functionalizations, thus a quantitative complexation can be considered.

Table 28: Results of TGA, zeta potential and particle size measurements of **Ru4**-functionalized particles in aqueous dispersion

ND material (starting material)	surface loading [mmol g^{-1}]	ζ [mV] (pH)	D_V-(10) [nm]	D_V-(50) [nm]	D_V-(90) [nm]
mDND-L1-Ru4a (**mDND-L1-tpy$_b$**)	0.27	+38.0 (5.2)	56.1	91.7	191
mDND-L1-Ru4b (**mDND-L1-tpy$_c$**)	0.23	+39.9 (5.1)	51.2	81.5	184
mDND-L2-Ru4a (**mDND-L2-tpy$_a$**)	0.26	+40.8 (5.2)	48.6	154	280
mDND-L2-Ru4b (**mDND-L2-tpy$_b$**)	0.31	+38.6 (5.4)	170	249	378

The DRIFT spectra of DND-Ru-conjugates **mDND-L1-Ru4b** and **mDND-L2-Ru4b** show linker and ligand related vibrations (cf. chapters 3.2.2.1 and 3.2.2.3.2). The asymmetric azide stretch vibration is reduced to a shoulder after ligand attachment (Fig. 75a/b), due to the inclusion of functionalized particles in agglomerates (cf. chapter 3.2.2.3.2). For the ruthenium(III) functionalized particles **mDND-L1-Ru4b** and **mDND-L2-Ru4b**, the same vibrations are still present, but slightly shifted towards higher wavenumbers, which is an indication for metal coordination.[358] After the complexation reaction, the azide shoulder vanished. The reaction conditions (72 h at 120 °C) led to a decomposition of the remaining, unreacted azide groups (cf. chapter 3.2.2.1). The reference complex **Ru4**, a dark black, crystalline solid, shows strong IR absorption, therefore no meaningful spectra were obtained for comparison purpose.

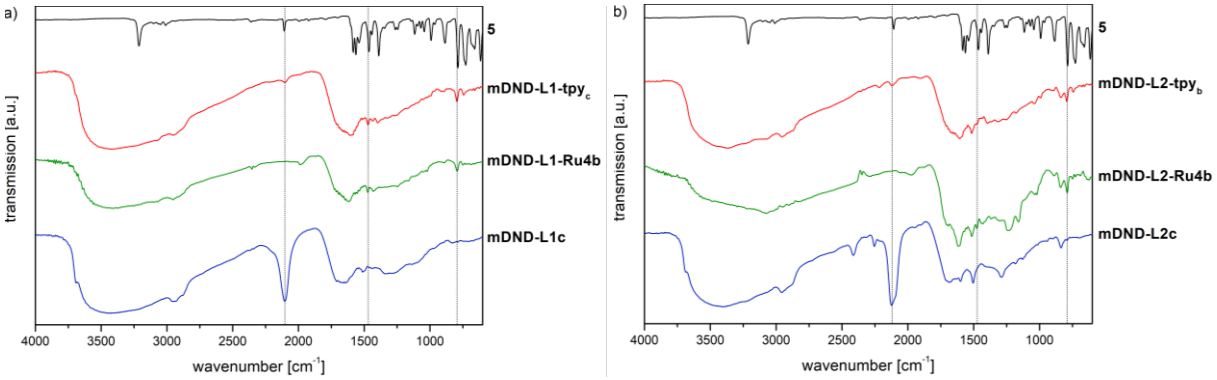

Fig. 75: IR spectra of (a) **mDND-L1c**, **mDND-L1-tpy$_c$**, **mDND-L1-Ru4b** (DRIFT) and **5** (ATR-FTIR) and of (b) **mDND-L2c**, **mDND-L2-tpy$_b$**, **mDND-L2-Ru4** (DRIFT) and **5** (ATR-FTIR).

The resulting particles **mDND-L1-Ru4b**/**mDND-L2-Ru4b** form stable, dark black dispersions in water (Fig. 76).

Fig. 76: ND-ruthenium conjugates **mDND-L1-Ru4b** (left) and **mDND-L2-Ru4b** (right) in aqueous dispersion.

The color change of the dispersions to dark black after complexation cannot be explained by UV/Vis spectroscopy. **mDND-L1-tpy$_c$**/**mDND-L2-tpy$_b$** show a shoulder at

327 nm and a small maximum at 286 nm (Appendix, Fig. 128a/b). Both features originate from the attached tpy-ligand and can also be seen for **mDND-L1-Ru4b**/**mDND-L2-Ru4b**. However, the characteristic MLCT maxima of **Ru4** at 421 and 609 nm are not present after complexation on ND particles.[359] The attached complex is not Raman active. Therefore, the Ru complexation has not been unambiguously proven and will be further discussed in the following chapter.

3.2.2.3.3 Quantification of ruthenium on mDND particles

So far, the successful grafting of ruthenium complexes on the ND surface was proven by spectroscopic characterization. However, different methods are required for quantification. XPS measurements executed by the DIACAT cooperation partner CEA enabled to quantify the amount of ruthenium on the nanodiamond surface. Results are shown and discussed in the Appendix (Table 55). For none of the measured conjugates, the expected ratio of ruthenium and nitrogen, either 1:9 (**Ru1**/**Ru2** samples) or 1:6 (**Ru4** samples), was found. Three explanations are possible: i) values at the XPS detection limit render a comparison unreasonable due to a larger fitting error, ii) the attached complexes change their structure after attachment iii) surface adsorbed water complicates the determination of the exact ratios of elements.

In addition to the XPS measurements, XRF spectra were measured in cooperation with Prof. Dr. Jens Pflaum, Experimental Physics, University of Würzburg, to obtain complementary data for Ru-functionalized samples, where XPS analysis reached its detection limit. Results are shown and discussed in the Appendix (Fig. 129, Fig. 130). XRF proved to be suitable to confirm the results obtained by XPS. The method can provide a qualitative analysis of the samples. However, measuring ligand signals (nitrogen) and quantification of the Ru content were not possible due to either instrumental limitations or the agglomeration behavior of the DND samples.

Considering the limitations of XPS and XRF analysis, elemental analysis proved to be the method of choice for the quantification of ruthenium on functionalized nanodiamond particles. The results of the elemental analysis of all relevant elements for the ruthenium functionalized DND-conjugates and important references can be found in Table 29. In general, residual percentage was related to oxygen content on the diamond surface in terms of functional groups or water adlayer. As for **mDND** no nitrogen was detected via XPS and the 2.68 wt% of nitrogen detected via elemental

analysis resulted from nitrogen inside the diamond core, which was related to nitrogen containing precursors for the detonation synthesis. Nitrogen mostly forms agglomerates in the diamond lattice during detonation synthesis.[360] For the non-conjugated linker system **mDND-L1c** an increase in nitrogen due to attachment of azide bearing linker molecules was detected. For the Ru-functionalized particles **mDND-L1-Ru1c**, the lowest Ru value was obtained (0.52 wt%), which corresponded with the lowest surface loading measured via TGA (0.11 mmol g^{-1}) and the low value/intensity in XPS/XRF measurements. The Ru:N ratio calculated from the wt.%-values amounted to 1:8.3, which is in good accordance with the expected ratio of 1:9. For **mDND-L1-Ru2b**, quite similar results were observed, with a Ru:N ratio of 1:8.1 (expected 1:9). For **mDND-L1-Ru4b**, the expected ratio of Ru:Cl (1:3) was detected; however, the Ru:N ratio of 1:1.2 did not correspond to the expected ratio of 1:6. Here, it is most likely that the added ruthenium(III) chloride salt was not only coordinated to the covalently attached tpy ligand, but also strongly adsorbed to the **mDND** surface due to the oxophilic ruthenium.

Table 29: Elemental analysis of relevant ruthenium-functionalized **mDND**-conjugates and references

ND material	C [wt.%]	H [wt.%]	N [wt.%]	Ru [wt.%]	Cl [wt.%]	∑ [wt.%]
mDND	89.14	1.16	2.68	-	-	92.98
mDND-L1c	84.25	1.87	3.07	-	-	89.19
mDND-L1-Ru1c	82.50	1.47	3.28	0.52	-	87.77
mDND-L1-Ru2b	80.77	1.77	4.00	1.18	-	87.72
mDND-L1-Ru4b	75.80	1.52	3.28	3.77	4.01	88.38
mDND-L2c	74.61	2.60	13.17	-	-	90.38
mDND-L2-Ru1d	78.76	2.21	4.64	1.00	-	86.61
mDND-L2-Ru2b	79.57	2.02	4.15	1.01	-	86.75
mDND-L2-Ru4b	55.85	1.69	4.25	7.44	11.17	80.40

For the conjugated systems, the situation was slightly different. The particles **mDND-L2c** showed a highly increased nitrogen value (13.17 wt.%), though about 3.00 wt% were expected. Therefore, the linker system **L2** was strongly adsorbed to the ND surface. To determine the extent of adsorption, both linker systems **L1** and **L2** were dispersed with **mDND** in control experiments under the same reaction conditions

without adding amyl nitrite coupling reagent. For **L1**, no significant adsorption is detected (Fig. 77a).

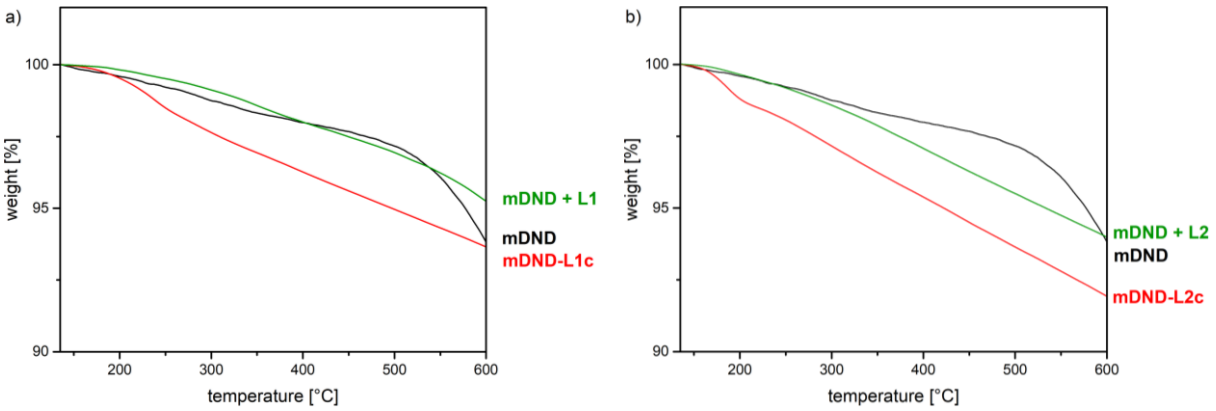

Fig. 77: Thermogravimetric analysis of (a) **mDND**, **mDND-L1c** and adsorption experiment **mDND+L1** and of (b) **mDND**, **mDND-L2c** and adsorption experiment **mDND+L2**.

For **mDND-L1c**, the covalently attached linker molecule **L1** is stepwise cleaved in the temperature range of 150-360 °C. First, the azide is decomposing, then the aromatic system is desorbed. For **mDND-L2c**, the covalently attached linker molecule **L2** is also stepwise cleaved in the temperature range of 150-460 °C (Fig. 77b).

However, the non-covalently grafted material **mDND+L2** also shows some significant mass loss in this area (-1.3 %), which can be related to adsorbed **L2** molecules. From this finding, the non-covalent surface-loading with **L2** can be calculated as 0.10 mmol g^{-1}. In comparison to the reaction with amyl nitrite coupling reagent (-4.1 % mass loss, 0.33 mmol g^{-1}), about one third of the surface loading was related to adsorbed **L2**, bearing amine and azide group. This explained the unexpectedly high amount of nitrogen in the sample **mDND-L2c**. **L2** apparently formed very stable interactions with the diamond surface, as numerous washings with different solvents, in which **L2** was highly soluble, should have normally ensured that all non-covalently linked material was completely removed. However, in this case, this assumption was found to be wrong. Furthermore, the adsorption was indirectly proven by the next reaction step. After attaching the ruthenium complexes **Ru1**/**Ru2**, the amount of nitrogen was significantly lower (4.15 and 4.64 wt.%), corresponding to the expected values. For **mDND-L2-Ru1d**, the Ru:N ratio was determined to be 1:14 and for **mDND-L2-Ru2b**, the Ru:N ratio was calculated as 1:10.5 (both expected 1:9). Therefore, adsorbed linker molecules **L2** of **mDND-L2c** were removed from the surface during the CuAAC reaction course and particle washing. Two reasons are conceivable for the

desorption: either the molecules desorbed over the long CuAAC reaction time or the adsorbed molecules that were bearing an accessible azide-group reacted with the ruthenium complex making an adsorption of the resulting linker-complex molecule more difficult due to the sterically demanding metal complex. The desorbed linker molecules could then be removed by washing. The remaining, slightly higher nitrogen values were also related to azide groups that have not reacted due to sterical blocking (cf. chapter 3.2.2.3.1).

For **mDND-L2-Ru4b**, the ratio of Ru:Cl (1:4.2) was observed to be higher than expected (1:3) and, similarly, the Ru:N ratio of 1:1.5 did not correspond to the expected ratio of 1:6. As discussed before, the added ruthenium(III) chloride salt was not only coordinated to the covalently attached tpy ligand, but also strongly adsorbed to the DND surface due to the oxophilic ruthenium. As the carbon value was very low (~55 wt%) and the oxygen value correspondingly quite high (~20 wt%), an oxidation of the ruthenium either coordinated to the tpy ligand or adsorbed to oxygen surface groups is conceivable. The chloride ligands were most likely exchanged by water.

To conclude, by means of elemental analysis, it could be shown that attached complexes **Ru1**/**Ru2** show the expected Ru:N ratios. The coordination of ruthenium (III) chloride on the pre-functionalized diamond was found to illustrate an inappropriate method for the TM-complex functionalization, due to adsorption, oxidation and presumably ligand exchange.

3.2.2.3.4 CuAAC reaction of mDND-L5 with photocatalyst Ru1

In addition to the linker-functionalized particles **mDND-L1**/**L2**, involving phenylene-based molecules, the azide functionality of tolane-based, linker-functionalized particles **mDND-L5**, was also used to link the photocatalyst **Ru1** via a CuAAC reaction (Fig. 78).

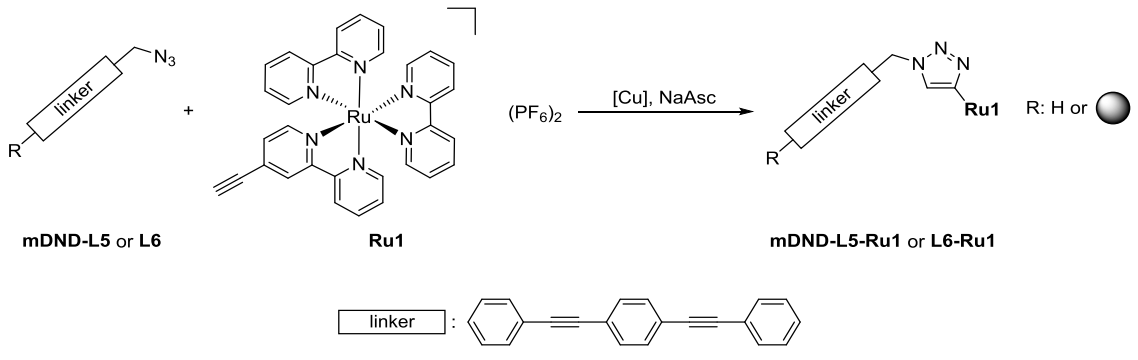

Fig. 78: Synthesis of DND-photocatalyst conjugates **mDND-L5-Ru1** and reference system **L6-Ru1**.

For the CuAAC reaction between **Ru1** and azide linker **L6** to form the photocatalytic reference system **L6-Ru1**, the $CuSO_4$/NaAsc system was applied. The ^{1}H-NMR spectrum clearly showed the singlet signal of the triazole proton at 8.87 ppm for **L6-Ru1**. The ATR-FTIR spectrum of **L6-Ru1** (Appendix, Fig. 131) lacks the azide vibration and a mixture of signals related to both linker and complex is present. For the reaction involving diamond particles, the PPh_3CuI/NaAsc system was used. In comparison to the particle-free reaction, the duration was extended due to involvement of the nanodiamond (Table 30).

Table 30: Amount of the starting material (cf. chapter 3.2.2.2), temperature and reaction time of the CuAAC reactions

ND material	starting material (amount [mg])	T [°C]	time [h]
mDND-L5-Ru1a	**mDND-L1e** (50)	r.t. 70	96 336
mDND-L5-Ru1b	**mDND-L1j** (250)	70 80	120 336

Increased reaction temperature was needed for reaction progress. The Ru-functionalized particles were obtained as orange brown aqueous dispersion. Similar to the systems with short, phenylene-based linkers, the extended linker Ru-functionalized particles also showed high colloidal stability and a positive zeta potential in aqueous dispersion (Table 31). The surface loading will be discussed during the following spectroscopic analysis.

Table 31: Results of TGA, zeta potential and particle size measurements of **mDND-L5-Ru1a**/**Ru1b**

ND material	surface loading [mmol g^{-1}]	ζ [mV] (pH)	D_V-(10) [nm]	D_V-(50) [nm]	D_V-(90) [nm]
mDND-L5-Ru1a	0.11	+33.0 (6.0)	31.3	55.9	123
mDND-L5-Ru1b	0.18	+31.6 (6.1)	58.2	169	303

The following results will be discussed by means of the large batch **mDND-L5-Ru1b**, as only this batch was used in X-ray absorption spectroscopy and photocatalytic test reactions. In addition to the vibrations of the linker molecule, the characteristic C=N stretching and C-H deformation signals of the bpy ligands are clearly visible in the DRIFT spectra (Appendix, Fig. 132) The very intensive azide peak at around ~2100 cm^{-1} is minimized, but still clearly visible. Inclusions in agglomerates and

sterically inaccessible azide groups due to shielding by already attached linker moieties can explain this observation. Calculating surface loading with the assumption that every azide reacted in a CuAAC reaction with the alkyne-functionalized complex led, in this case of inaccessible azides, to a lower surface loading, as the molecular weight of the leaving surface groups during TGA measurement was strongly overestimated. Therefore, the loading was lower than for the starting material **mDND-L5j**. Considering the Raman spectra (Fig. 79), some characteristic signals of **Ru1** are visible for **mDND-L5-Ru1b**; however, the signals of the C=C and C=N of the ligand vibrations overlap with the very intensive C=C signals of the aromatic systems of **L5** at around 1590 cm^{-1}. Basu *et al.* reported that in polarization studies of **Ru1** only totally symmetric modes were observed in the region below 1700 cm^{-1}.[361] Consequently, a possible explanation for the observations made in the Raman spectra is a substantial influence on the symmetry due to the tolane-based linker functionalized particles **mDND-L5j** leading to changes in polarization of **Ru1** and less active modes. This observation was not made for the phenylene-based conjugates (cf. chapter 3.2.2.3.1)

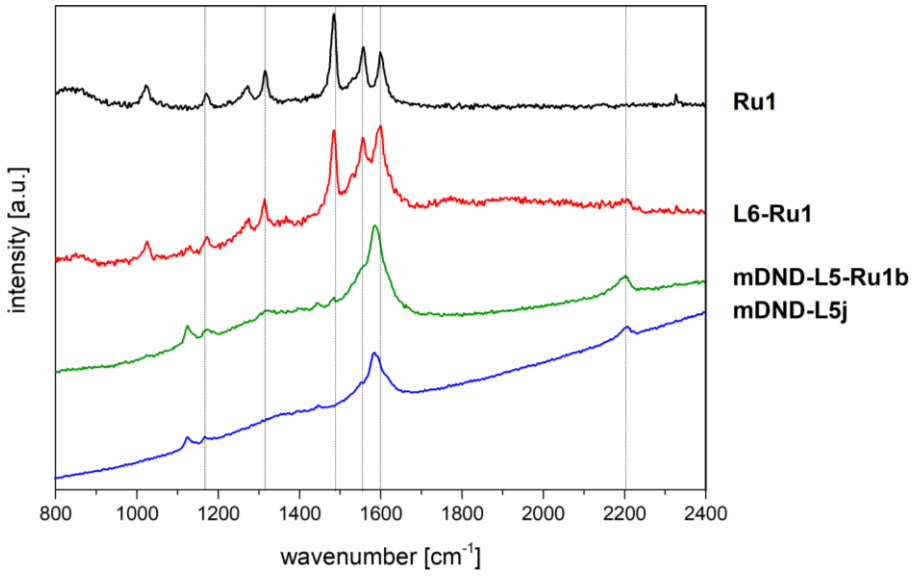

Fig. 79: Raman spectra of **mDND-L5j**, **mDND-L5-Ru1b**, reference **L6-Ru1** and complex **Ru1** (measurements with 445 nm laser).

In contrast to XPS, XRF measurements indicated the presence of ruthenium (Appendix, Fig. 133). Elemental analysis of **mDND-L5-Ru1b** yielded a surface coverage with 0.80 wt.% ruthenium; however, the Ru:N ration was determined to be 1:16 (expected 1:9). This higher percentage of nitrogen can be explained on one hand by the still quite intensive azide signal in the DRIFT spectra, representing unreactive

surface groups, and on the other hand by nitrogen containing azobenzenes, which have been formed during the synthesis of **mDND-L5j** (cf. chapter 3.2.2.2).

Table 32: Elemental analysis of **mDND-L5-Ru1b** and references **mDND** and **mDND-L5j**

ND material	C [wt.%]	H [wt.%]	N [wt.%]	Ru [wt.%]	∑ [wt.%]
mDND	89.14	1.16	2.68	-	92.98
mDND-L5j	81.55	3.60	6.00	-	91.15
mDND-L5-Ru1b	79.79	2.78	4.54	0.80	87.91

The color of the aqueous dispersion can be explained by means of UV/Vis absorption (Fig. 80). The maximum at 207 nm is superimposed by the DND particle absorption, the transition at 242 nm is reduced to a broad shoulder and the redshifted maximum at 287 nm forms a broad signal in combination with the absorption maximum of the linker at 337 nm.

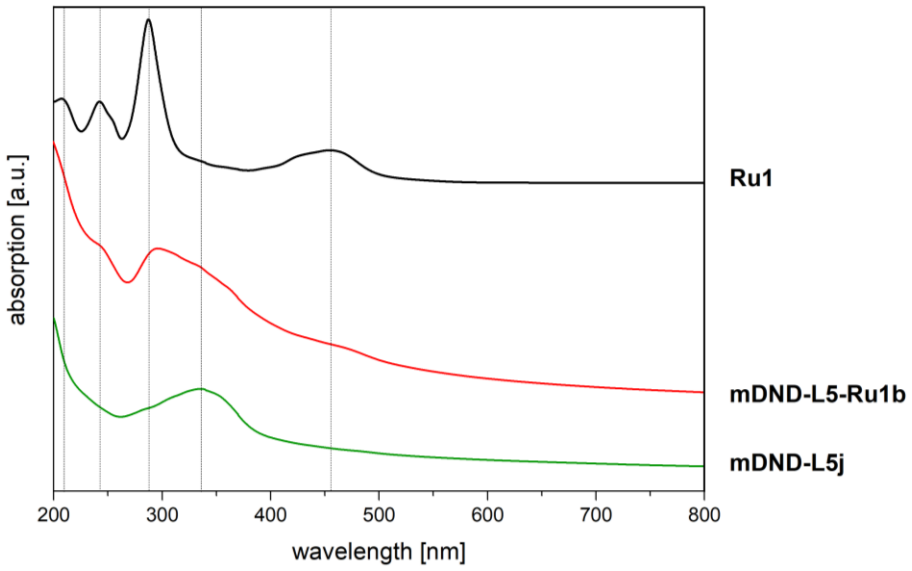

Fig. 80: Comparison of the UV/Vis spectra of **mDND-L5j**, **mDND-L5-Ru1b** and **Ru1** (measurements in MeCN).

The broad MLCT excitation of **Ru1** is clearly red shifted (454 nm → 471 nm), indicating changes in the electronic structure, which will be discussed in the following chapter.

3.2.2.3.5 Advanced spectroscopy and theoretical calculations

mDND particles with the photocatalysts **Ru1, Ru2** and **Ru4** attached via conjugated (**L2**), ethylene-bridged, non-conjugated (**L1**) and extended (**L5)** linker systems were characterized by X-ray absorption spectroscopy (XAS) at the C K edge and N K edge in the total electron yield (TEY) mode. The experiments were carried out by PhD student Sneha Choudhury, Institute of Methods for Materials Development, Helmholtz Center Berlin, under supervision of Dr. Tristan Petit at the BESSY II Synchrotron using the LiXEdrom endstation. The experiments provided insight into the position of unoccupied electronics states from the ligands relative to the conduction band maximum (CBM) of the ND itself, as well as into possible electronic coupling between the ND particles and the attached Ru-photocatalysts. Here, a short summary of the obtained results will be given.

For the three functionalized particles **mDND-L1-Ru1c**, **mDND-L1-Ru2b** and **mDND-L1-Ru4b**, the lowest unoccupied molecular orbital (LUMO) and LUMO+1 levels of the attached dyes were observed in the pre-edge region (285-285.8 eV) of the XA spectra at the C K edge. This indicated a good electronic coupling between the ND particles and the dyes due to orbital overlap between the ligand and ND orbitals. This is in agreement with dye functionalized BDD electrodes reported in the literature (cf. chapter 3.2).[240,241] For all functionalized ND samples, a broad excitonic peak of the diamond itself is observed at 289.3 eV.

The influence of the linker system was tested for **Ru1** functionalized samples **mDND-L1-Ru1c**, **mDND-L2-Ru1d** and **mDND-L5-Ru1b**. A clear difference was observed near the LUMO and LUMO+1 peaks when comparing the three samples. The two samples with linkers **L2** and **L5** showed an additional shoulder close to the LUMO+1 level at 286.3 eV, which is absent for linker **L1**. This additional peak is evidently originating from the sp and sp^2 carbon atoms present in the conjugated linker systems. The state might be of interest as it further reduces the gap between the Ru-related LUMOs and the CBM of diamond. For electron transfer studies a strong electronic coupling between the dye and the diamond molecule is extremely beneficial. Thus, transient absorption experiments with those three samples were performed by Dr. Franziska Buchner, Helmholtz Center Berlin, group of Dr. Tristan Petit. In first experiments, solvated electrons were detected from all samples with UV excitation. It seems that both, the intensity of the transient signal and a bleaching signal at about

580 nm probably due to charge transfer, depend on the linker length and thus the distance between attached **Ru1** complex and **mDND** surface. The longer the linker, the stronger are the transient and bleaching signal. The electron transfer from **Ru1** to the ND particles might be a possible explanation for this observation, as well as the particle surface disturbing the ground- and/or excited-state potentials of **Ru1**. Further analysis is ongoing here.

The band structure of the **Ru1** functionalized sample **mDND-L2-Ru1d** was also investigated using photoemission spectroscopy (PES). The VBM of the NDs lies lower than the HOMO of **Ru1**, whereas the LUMO of the dye lies below the CBM of the ND (Fig. 81). An electron transfer from the LUMO of the dye to the CBM of the NDs is not very likely to happen, as the energy gap is quite large (1.9 eV). However, as the HOMO of the dye is 0.9 eV above the VBM, there is a likelihood of electron transfer from **Ru1** to the VB of ND. Thus, holes in the VB created due to the generation of solvated electrons can be refilled. The measured HOMO-LUMO gap of the attached **Ru1** was 2.69 eV (461 nm), thereby, slightly smaller than for pure **Ru1** (2.74 eV, 452 nm).[235] Consequently, the observed redshift of the MLCT transition (461 nm) in the UV/Vis adsorption spectra of **mDND-L2-Ru1d** can be explained.

In contrast to the ruthenium complex functionalized BDD electrodes described in the beginning of chapter 3.2, the HOMO of the attached ruthenium(II) complex was above the VBM. This observation can be explained by the different diamond starting material, as the relative position of VBM and CBM differ substantially between bulk, boron-doped diamond eletrodes and undoped, milled detonation nanodamond.

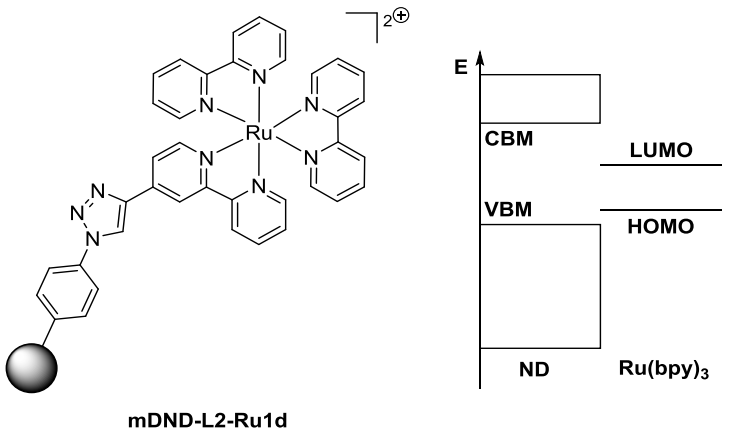

Fig. 81: **mDND-L2-Ru1d** with schematic illustrations of the frontier orbitals alignment of the attached complex **Ru1** respective to the measured ND band gap.

Theoretical calculations, involving spin-polarized Generalized Gradient Approximations (GGA) within Density Functional Theory (DFT), on the two systems **mDND-L1-Ru1** and **mDND-L2-Ru1** were performed by Prof. Karin Larsson, Uppsala University, Sweden. **Ru1** was observed to bind with strong diamond-like covalent C-C bonds to variously terminated diamond [111] and [100]-2x1 surfaces. The partial density of state spectra for **Ru1** showed four levels of electron excitation (from HOMO to LUMO, LUMO+1, LUMO+3, and LUMO+4) at 1.4, 4.2, 4.5 and 5.7 eV, corresponding to the wavelengths 879, 291, 271 and 214 nm, respectively, which was in good accordance with the experimentally obtained data (Fig. 73). The possibility for an electron excitation between the VB of the diamond surface and the LUMO level of **Ru1** was especially focused on for the Ru functionalized diamond surfaces. In addition, the possibility for a second direct excitation to unfilled states at or slightly below the CB of the terminated diamond surface was also investigated. For H- and OH-terminated samples, calculations suggested that an electron transfer from VB to an empty positive surface state via conjugated (**L2**) or non-conjugated (**L1**) linked **Ru1** is possible. The calculations suggested that for these electron transition energy in the visible light region can be used.

3.2.2.3.6 CuAAC of directly azide-functionalized DND particles

As the XAS experiments carried out at the BESSY II synchrotron proved that ruthenium complexes attached in conjugation to **mDND** particles showed an additional absorption shoulder in the band gap region, Johannes Lang investigated the functionalization of directly azide-terminated DND particles (**N_3-DND**) during his bachelor thesis. Kennedy *et al.* recently published a method for the synthesis of **N_3-DND** using light and heat sensitive tosyl azide (**32**) as a source for azide.[362]

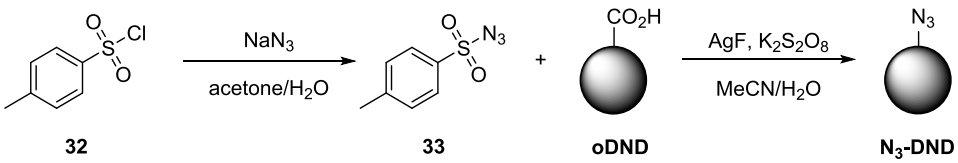

Fig. 82: Synthesis of tosyl azide (**33**) and azide-terminated DND **N_3-DND**.

Under nitrogen atmosphere, silver fluoride, which was required for decarboxylation, potassium persulfate serving as oxidant, and the azide **33** were added to a dispersion of **oDND** (Fig. 82). For the successful azide termination, oxygen-free conditions were mandatory yielding the particles **N_3-DNDa** and **N_3-DNDc**. For subsequent CuAAC

reactions, the bigger batch **N_3-DNDc** was used. A termination attempt under normal atmosphere, yielding the particles **N_3-DNDb**, does not show any azide vibration in the DRIFT spectrum (Fig. 83).

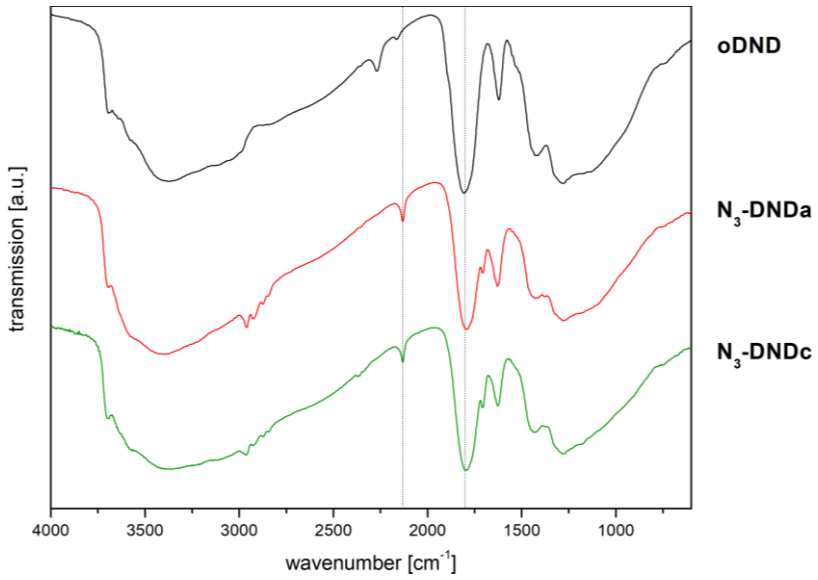

Fig. 83: DRIFT spectra of **oDND** and azide-terminated DNDs **N_3-DNDa** and **N_3-DNDc**.

The particles **N_3-DNDa/c** clearly show the azide vibration at 2132 cm^{-1}. However, no significant decrease in intensity of the C=O stretching vibration at 1796 cm^{-1} is observed. Thus, the reaction is far from quantitative, which could also be seen by the continuously high negative zeta potential (Table 33).

Table 33: Results of TGA, zeta potential and particle size measurements of particles **oDND**, **N_3-DNDa/c**, **N_3-DND-Ru1** and **N_3-DND-Ru2**

ND material	surface loading [mmol g^{-1}]	ζ [mV] (pH)	D_V-(10) [nm]	D_V-(50) [nm]	D_V-(90) [nm]
oDND	-	-42.0 (5.4)	60.4	158	406
N_3-DNDa	-	-40.6 (5.5)	104	221	670
N_3-DNDc	-	-50.6 (5.3)	85.9	156	297
N_3-DND-Ru1	0.08	-33.3 (5.6)	85.3	175	366
N_3-DND-Ru2	0.08	-28.7 (5.6)	77.7	153	365

The CuAAC reaction with **Ru1**/**Ru2** and **N_3-DNDc** was conducted using the conditions as for **mDND-L2-Ru1/Ru2** (cf. chapter 3.2.2.3.1). After one week at rt, applying the PPh_3CuI/NaAsc system, the reactions were finished demonstrating comparatively high reactivity. The particles **oDND** and **N_3-DND-Ru1**/**Ru2** showed a similar particle size. After complex linkage, the zeta potential was less negative (-50.6 mV → -33.3

and -28.7 mV) as a consequence of the attached complex cations. The azide vibration completely vanished and the characteristic vibrations of **Ru1**/**Ru2** were present (Appendix, Fig. 134a/b). No hexafluorophosphate vibration was observed. The low signal intensity was caused by the low amount of attached complex (0.08 mml g^{-1}). This led also to weak absorption in the UV/Vis (Appendix, Fig. 135a/b).

The direct attachment to the DND surface resulted in significant changes in the polarizability of **Ru1** and **Ru2**, as the obtained signals for the complexes were very pronounced after attachment to the particles despite attachment of a low amount (Appendix, Fig. 136a/b). Therefore, the direct attachment to the ND surface is not substantially influencing the symmetry of the attached complexes (cf. chapter 3.2.2.3.4).[361]

The stability of the surface azide groups was tested using the applied CuAAC reaction conditions, but without adding any alkyne. After three days at r.t., no azide peak was visible anymore. The same results were obtained using $CuSO_4$ or CuI. Hence, the CuAAC reaction needs to be really fast, otherwise azide decomposition arises. This is the case for the photocatalysts **Ru1**/**Ru2**, although a surface loading of 0.08 mmol g^{-1} indicates competing decomposition. As an aqueous dispersion of **N_3-DND** still showed an azide peak, even after months, the azide instability during CuAAC reaction is clearly related to a copper mediated decay.

3.2.2.4 Functionalization of other diamond materials with Ru1

3.2.2.4.1 H-terminated DND particles (H-DND)

Regarding the functionalization of further diamond materials, **H-DND** particles were tested in order to investigate the influence of a homogeneous surface termination, on the functionalization without electron-withdrawing oxygen groups and a negative electron affinity (cf. chapter 1.3). In addition, theoretical calculations (cf. chapter 3.2.2.3.5) suggested that **Ru1** on a H-terminated ND surface allows for a two electron excitation from VB to CB via the attached complex. In analogy to **mDND**-conjugates, **H-DND** was functionalized with **L1** and **Ru1** to yield the **H-DND-L1-Ru1** conjugate.

Table 34: TGA, zeta potential and particle size measurements of **H-DND**, **H-DND-L1** and **H-DND-L1-Ru1**

ND material	surface loading [mmol g^{-1}]	ζ [mV] (pH)	D_V-(10) [nm]	D_V-(50) [nm]	D_V-(90) [nm]
H-DND	-	+41.2 (6.4)	133	965	1650
H-DND-L1	0.35	+42.9 (6.2)	68.0	156	706
H-DND-L1-Ru1	0.22	+33.9 (6.1)	37.5	111	279

The stepwise functionalization simultaneously stabilized the particle dispersions and the mean size was decreased by ~90% from **H-DND** to **H-DND-L1-Ru1** (Table 34). One possible explanation for the loss on surface loading after CuAAC reaction is that **L1** was more strongly adsorbed to **H-DND** than to **mDND**. The adsorbed molecules were then removed during the CuAAC reaction and the intensive washing of **H-DND-L1-Ru1**. The DRIFT spectra show the characteristic vibrations of **L1** and **Ru1** (Fig. 84). The very intensive asymmetric and symmetric C-H-stretching vibrations of **H-DND** at 2948 and 2879 cm^{-1} are still visible for **H-DND-L1** and **H-DND-L1-Ru1** indicating that the non-functionalized surface areas are still H-terminated. For **H-DND-L1**, an intensive azide peak is observed, which has completely disappeared after the CuAAC reaction. However, for **H-DND-L1-Ru1** the signals of the attached molecules **L1** and **Ru1** are low in intensity, indicating a low surface functionalization. These findings confirm the assumption that **L1** is heavily adsorbed to the **H-DND** surface. Non-covalently adsorbed **L1** reacts with **Ru1** and the resulting triazole **L1-Ru1** is removed from the particles **H-DND-L1-Ru1** during the washing procedure.

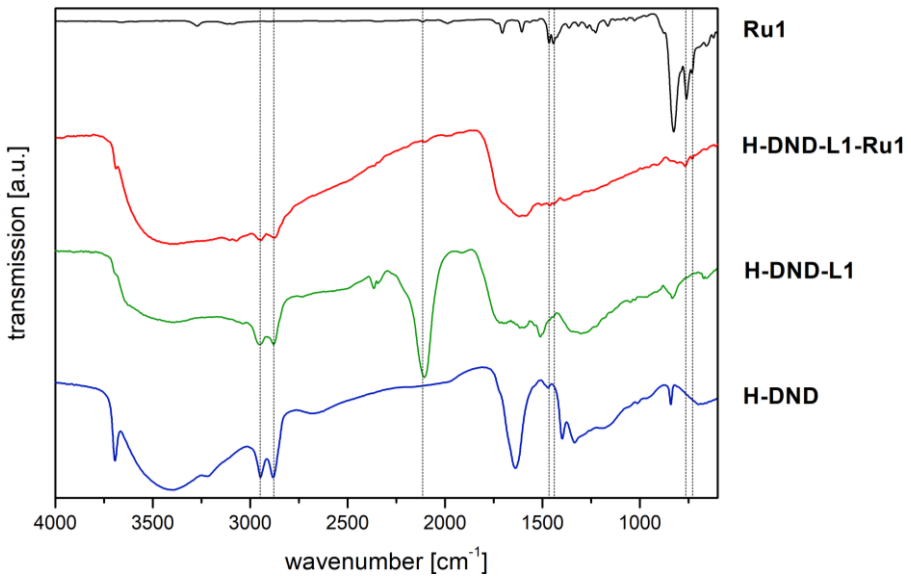

Fig. 84: IR spectra of **H-DND**, **H-DND-L1**, **H-DND-L1-Ru1** (DRIFT) and **Ru1** (ATR-FTIR).

The UV/Vis absorption (Fig. 137a) and Raman (Fig. 137b) spectra show the same characteristic features as for the identically functionalized **mDND** (cf. chapter 3.2.2.3.1). The UV/Vis absorption maxima of **Ru1** are slightly redshifted after grafting to the particle surface and superimposed signals between the bpy ligands with both the G band and the diamond/D band are observed in the Raman spectra. The ruthenium content determined by XPS was 0.8 at.%, which agreed with the results from elemental analysis (0.87 wt.% ruthenium). XRF showed the characteristic emission of ruthenium at ~2.6 keV. For both X-ray measurements no copper was detected, indicating a complete removal of the catalytic system for the CuAAC reaction.

Adsorption and larger particle size in comparison to **mDND** are problematic for the functionalization of **H-DND**. The advantage of having a different electronic structure due to the H-termination, namely a negative electron affinity (cf. chapter 1.3), is influenced during the functionalization. Although **H-DND-L1-Ru1** still shows C-H related vibrations in the DRIFT spectrum, it will be interesting to see whether the remaining H-termination can lead to a substantial difference in comparison to **mDND-L1-Ru1** regarding photocatalytic CO_2 reduction experiments (cf. chapter 3.4).

3.2.2.4.2 B-doped ND particles (B-ND)

B-doped nanodiamond particles are of interest, as they show different electronic properties in comparison to **mDND**. It is well known, that H-terminated BDD electrodes emit electrons under UV irradiation (c.f. chapter 1.3). Hence, it seems to be quite meaningful to investigate the properties of **BND** particles when functionalized with photocatalytically active moieties. The established protocol for the Ru-DND conjugates functionalization was applied for both acid-oxidized (**BND4**) and H-terminated B-doped (**H-BND4$_{CEA}$**) particles (Fig. 85).

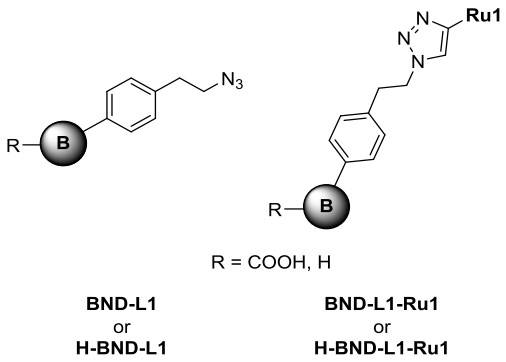

Fig. 85: Functionalization of **BND4** and **H-BND4$_{CEA}$** using first **L1** and then **Ru1**.

For an efficient functionalization, some reaction details needed to be adapted. First of all, different solvents were tested, as **H-BND4$_{CEA}$** particles were not stable in aqueous dispersion and the acid terminated **BND4** particles, though stable in the beginning, agglomerated heavily in water after addition of **L1** and amyl nitrite. Here, only **L1** was used, as the smaller linker **L2** heavily adsorbed the surface of the differently terminated B-doped particles and strong agglomeration during functionalization was observed. The use of either DMF or acetonitrile proved to be appropriate to obtain stable, blueish gray dispersions. The surface loadings that can be achieved were in the same range representing a high reproducibility (Table 35).

Table 35: Results of TGA, zeta potential and particle size measurements of **BND4**, **BND-L1**, **H-BND4$_{CEA}$** and **H-BND-L1**, as well as **Ru1** functionalized samples **BND-L1-Ru1** and **H-BND-L1-Ru1** in aqueous dispersion

ND material	solvent	load. [mmol g^{-1}]	ζ [mV] (pH)	D_V-(10) [nm]	D_V-(50) [nm]	D_V-(90) [nm]
BND4	-	-	-39.4 (5.6)	169	606	1230
H-BND4$_{CEA}$	-	-	+25.4 (6.2)	843	1350	4890
BND-L1a	H_2O	0.11	-41.6 (5.5)	498	777	1180
BND-L1b	MeCN	0.13	-40.7 (5.6)	403	999	1680
BND-L1c	DMF	0.12	-32.9 (5.9)	271	608	1200
H-BND-L1	DMF	0.12	-13.5 (6.1)	209	646	1450
BND-L1-Ru1	DMF/H_2O	0.08	-7.51 (6.2)	209	527	1730
H-BND-L1-Ru1	DMF/H_2O	0.12	+3.79 (6.2)	1000	1350	1750

The loadings themselves were quite low, which could be related to the lower overall surface reactivity of milled CVD nanodiamond material. The surface termination had apparently no influence on the functionalization using *in situ* diazonium salt generation, as no difference was detected between H- and COOH-terminated samples. As expected for the acid terminated particles **BND4**, no significant change in mean size and zeta potential was detected. **BND4** showed no pronounced tendency for agglomeration and the attached **L1** was not affecting the surface charge. **H-BND4$_{CEA}$**, which tended to agglomerate in water even at low concentration (0.1 wt%) after a short time, showed a positive zeta potential indicating the predominant H-termination. For the functionalized particles **H-BND-L1**, a stabilization in aqueous dispersion was taking place demonstrated by reduction of the agglomerate size by 50%. In contrast, the zeta potential changed to a slightly negative value. One explanation could be that the

H-termination is either replaced by the functionalization or damaged during the reaction. Residual acid groups, which are not affected by the functionalization conditions, would then outnumber the H-termination on the surface, leading to a slightly negative potential.

The functionalization with **Ru1**, using the PPh_3CuI/NaAsc system, was stopped after seven days at 70 °C and thorough washing. As a result, **BND-L1-Ru1** and **H-BND-L1-Ru1** were obtained. The gray-blueish **BND4** particles exhibited a slightly yellowish color (**BND-L1-Ru1**), whereas the **H-BND4$_{CEA}$** particles resulted in a stable, dark-gray dispersion for **H-BND-L1-Ru1** (Fig. 86).

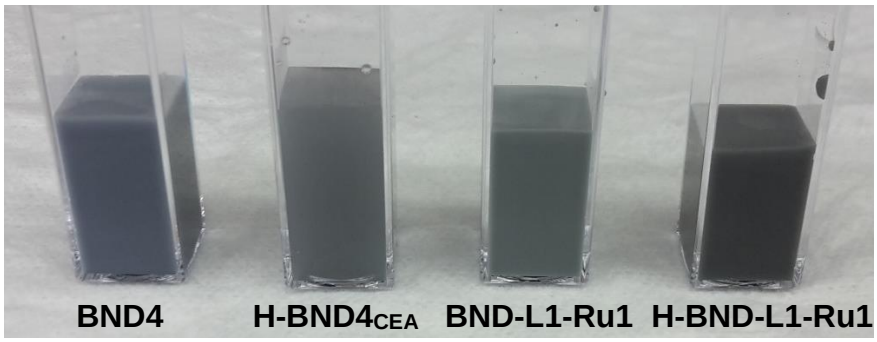

Fig. 86: Non-functionalized (**BND4**, **H-BND4$_{CEA}$**) and Ru-functionalized B-NDs (**BND-L1-Ru1, H-BND-L1-Ru1**) in aqueous dispersion.

The surface loadings of **BND-L1-Ru1** and **H-BND-L1-Ru1** yielded results in the expected range. Both Ru-functionalized samples were easily dispersed in water, whereas **H-BND-L1-Ru1** was slightly more agglomerated. For **BND-L1-Ru1**, the negative charge of the acid termination was almost completely compensated by the two times positively charged **Ru1** complex. An increase in surface loading would probably result in a positive potential. The particles **H-BND-L1-Ru1** showed a positive potential (+3.8 mV) in comparison to **H-BND-L1**. Subsequently, the attached Ru-molecules compensated the residual acid groups in the particles. The absence of an overall surface charge was one reason that the particles tended to agglomerate in aqueous dispersions.

The Raman spectra of both functionalized B-doped ND particles show the characteristic features of **Ru1** (Fig. 87a/b). For **BND-L1-Ru1**, the three dominant vibrations between 1350-1600 cm^{-1} are visible, overlapping with the G-band of **BND4**. Each of the three signals is slightly shifted compared to the isolated complex **Ru1**. At 1330 cm^{-1}, the intensive diamond peak can be seen for **BND4**. For **BND-L1-Ru1**, a

signal of the **Ru1** complex at 1324 cm^{-1} contributes and accounts for broadening of the diamond peak at 1330 cm^{-1} (Fig. 87a).

The Raman spectrum of **H-BND-L1-Ru1** shows largely the same features and shifts. The complex signals are more intensive, which could originate from the higher surface loading of **H-BND-L1-Ru1.**

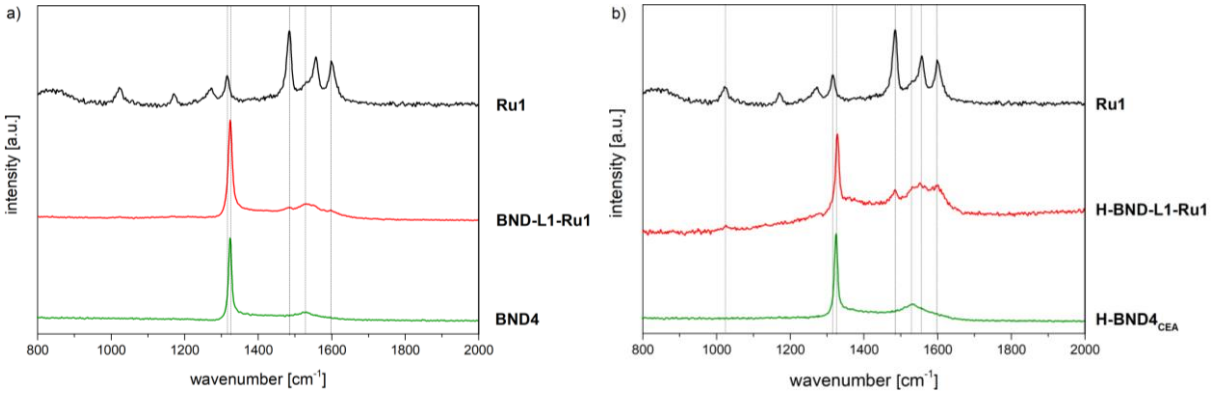

Fig. 87: Raman spectra of (a) **BND4**, **BND-L1-Ru1** and **Ru1** and of (b) **H-BND4$_{CEA}$**, **H-BND-L1-Ru1** and **Ru1** (measurements with 445 nm laser).

Using UV/Vis spectroscopy for **BND-L1-Ru1**, the broad absorption maximum at 454 nm can be detected, as well as the ones at around 287 nm and 209 nm (Fig. 88a). The intensity of the signals is quite low, as the measurements had to be performed in highly diluted solutions. At higher concentrations the particles tended to agglomerate in acetonitrile, which still proved to be the most suitable solvent. The detected maxima are slightly redshifted due to attachment to particles and a strong electronic coupling between the complex and the ND particles, as seen for the Ru-functionalized **mDND** particles (cf. chapter 3.2.2.3.5), can be expected.

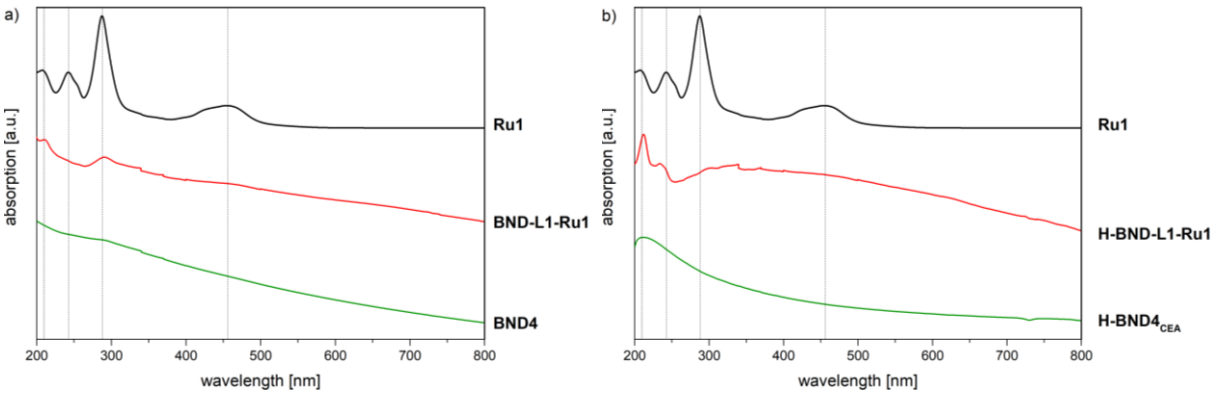

Fig. 88: UV/Vis spectra of (a) **BND**, **BND-L1-Ru1** and **Ru1** and of (b) **BND**, **BND-L1-Ru1** and **Ru1** (measurements in MeCN).

For the particles **H-BND-L1-Ru1**, the situation proved to be considerably different. The broad absorption maximum for the MLCT of **Ru1** at 454 nm is not clearly visible (Fig. 88b) and the intensive HOMO-LUMO+3 transition at 287 nm appears as a small, redshifted shoulder (297 nm). However, the maxima at 242 and 209 nm are present, while the HOMO-LUMO transition occurs at lower energy (212 nm) and the HOMO-LUMO+1 excitation requires more energy (234 nm). This indicates significant changes in absorption behavior of **H-BND-L1-Ru1** due to the electronic coupling of **Ru1** attached to the **H-BND** particles, which showed negative electron affinity (cf. chapter 1.3).

The ruthenium content on the particle surface was determined using elemental analysis (Table 36). For each analysed sample, a boron content in the range of 2.0-2.5 wt.% can be expected (cf. chapter 3.1.2.2). **BND-L1-Ru1** showed a higher ruthenium content in comparison to **H-BND-L1-Ru1** (1.17 wt.% vs. 0.76 wt%) indicating a slightly higher reactivity of the acid-terminated particles **BND4** during the functionalization. Both functionalized samples, **BND-L1-Ru1** and **H-BND-L1-Ru1**, illustrated a Ru:N ratio of 1:8 (expected 1:9). As for both samples, a high content of fluorine was detected and this observation allowed for a determination of the complex counter anions. Noticeably, in contrast to functionalized **mDND** particles (cf. chapter 3.2.2.3.1), for the B-doped particles the charge of the attached **Ru1** complex was still compensated by hexafluorophosphate anions. As **BND4** and **H-BND4$_{CEA}$** showed, in contrast to **mDND**, no chlorine content, an exchange of the anion is unlikely to happen. **H-BND-L1-Ru1** illustrated no substantial higher content of hydrogen in comparison to **BND-L1-Ru1**.

Table 36: Elemental analysis of **BND-L1-Ru1**, **H-BND-L1-Ru1** and references **BND4**

ND material	C [wt.%]	H [wt.%]	N [wt.%]	Ru [wt.%]	F [wt.%]	∑ [wt.%]
BND4	92.25	1.26	0.06	-	-	93.57
BND-L1-Ru1	83.73	1.06	1.23	1.17	6.71	93.90
H-BND-L1-Ru1	81.32	1.00	0.76	0.65	4.63	89.36

The protocol for Ru-functionalization could also be applied on B-doped nanodiamond particles. The combination of Raman, UV/Vis and zeta potential measurements could prove that **Ru1** was attached to the surface. In comparison to DND-based materials, a completeness of the CuAAC reaction cannot be evaluated, as the CVD-based **BND**

particles gave no meaningful IR spectra. However, the obtained Ru:N ratios by elemental analysis suggest a complete reaction. The synthesized particles were investigated regarding the emission of solvated electrons in transient absorption measurements at the DIACAT cooperation partner in Berlin.

3.2.2.4.3 Porous B-doped diamond foam

In addition to the functionalization of diamond nanoparticles of various origin, termination and doping, the chemical reactivity of nanostructured porous diamond materials was also investigated. The protocol of the ND functionalization was slightly adapted and also applied for B-doped diamond foam grown on Si[100]. The foams were provided by Dr. Fang Gao/Dr. Peter Knittel, Fraunhofer, IAF, Freiburg.[243,363] In a first step, the H-terminated foam (**H-Foam**) was functionalized with the azide linker system **L1** prior to attaching **Ru1** using the optimized CuAAC conditions (Fig. 89).

Fig. 89: **H-Foam** before treatment (left) and **H-Foam-L1-Ru1** after complex attachment (right).

The **H-Foam-L1-Ru1** electrode was slightly colored as a result of the attachment of the bright red **Ru1**. For linker functionalization with **L1**, the 15x15 mm foam was immersed in the reactant containing aqueous solution, which was stirred at 80 °C over night. Afterwards, the membranes were cleaned with several organic solvents using either a low power ultrasonic bath (**H-Foam-L1a**) or a shaker (**H-Foam-L1b**) to assess the stability of the material. SEM results can be seen in Fig. 90. Image a) shows the intact ~500 nm diamond foam top layer of **H-Foam**. **H-Foam-L7a** (b), treated with low power ultrasound after functionalization, exhibited some significant alterations. There are areas where the foam layer is still intact, but some of the spheres are broken and the polycrystalline BDD layer is mainly seen. Therefore, cleaning with ultrasound is not recommendable. However, covering the functionalized membrane with solvent and using a shaker for cleaning seemed to be suitable. The foam layers (c), as well as the single spheres (d) stayed intact and no remaining salts crystals were observed.

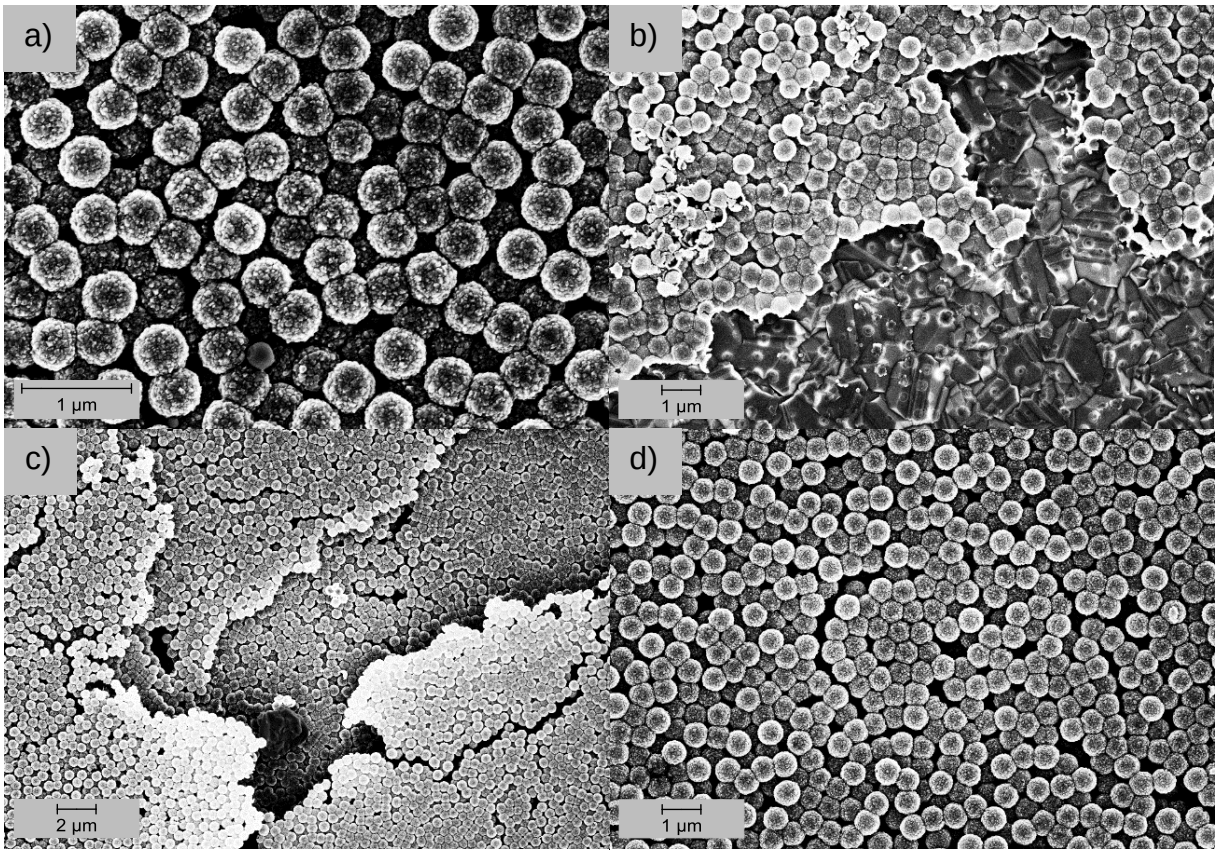

Fig. 90: SEM picture of **H-Foam** (a), the ultrasonic bath cleaned sample **H-Foam-L1a** (b) and the shaker cleaner sample **H-Foam-L1b** (c + d).

As can be seen in Fig. 91, neither the layer structure nor the foam spheres themselves were damaged during the CuAAC reaction (SEM pictures were taken at several spots showing identical results).

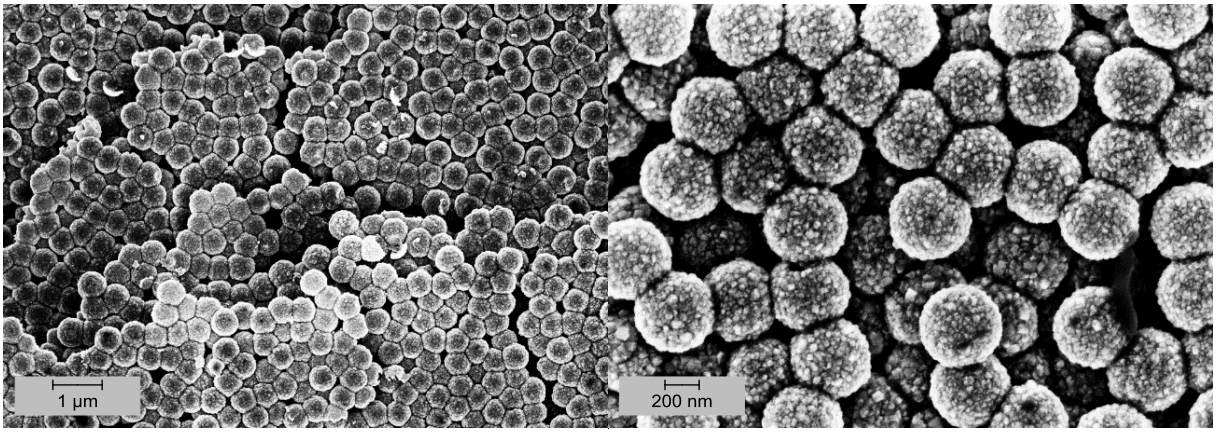

Fig. 91: SEM pictures of **H-Foam-L1-Ru1** at different magnifications.

In the Raman spectra, a mixture of signals from **Ru1** and **H-Foam** can be detected for **H-Foam-L1-Ru1** (Fig. 92). The most intensive signals were present at the slightly darker areas of **H-Foam-L1-Ru1** indicating higher local ruthenium concentration. A clear Raman peak of diamond is detected at 1332 cm^{-1}. The peaks at around

1150 cm^{-1} and a broad, flat signal at 1430 cm^{-1} are still related to *trans*-polyacetylenes in the grain boundaries.[243] The shoulder at round 1350 cm^{-1} and the broad band between 1400 and 1600 cm^{-1} can be attributed to amorphous/graphitic carbon (D and G bands). The characteristic signals of **Ru1** between 1450 and 1630 cm^{-1} are superimposed by the strong G band and are less intensive for **H-Foam-L1-Ru1**.

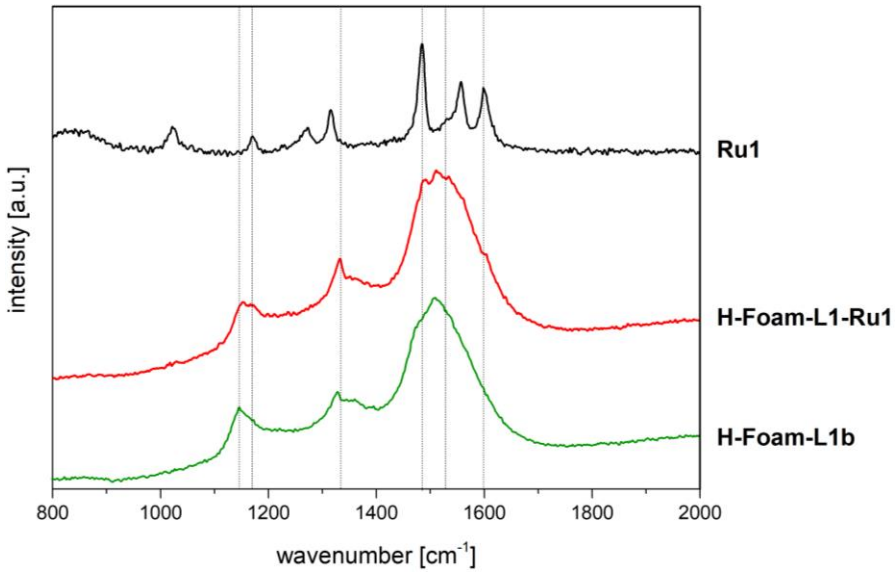

Fig. 92: Raman spectra of **H-Foam-L1b**, **H-Foam-L1-Ru1** and **Ru1** (measurements with 445 nm laser).

The XPS analysis revealed the presence of silicon and chlorine contaminations (Table 37). These impurities characteristic of **H-Foam** were also found for **H-Foam-L1-Ru1** and a small amount of Ru was detected.

Table 37: Atomic concentrations of elements detected from XPS analysis for **H-Foam** and **H-Foam-L1-Ru1**

diamond material	C1s [at.%]	O1s [at.%]	$Si2p_{5/2}$ [at.%]	Cl2p [at.%]	N1s [at.%]	$Ru3d_{5/2}$ [at.%]
H-Foam	93.9	5.9	0.7	0.6	0.1	-
H-Foam-L1-Ru1	85.5	8.7	0.8	3.4	1.4	0.1

From the XRF-data in Fig. 93, the effect of the chlorine impurity is clearly visible. As already stated for the **Ru4** functionalized particles (cf. chapter 3.2.2.3.3), the signal at ~2.6 keV is a combination of the ruthenium, as well as the chlorine emission lines. For the original, unreacted foam (**H-Foam**) no signal is detected, while the chlorine content appears to be below detection limit. After functionalization with increasing amounts of

Ru and chlorine according to XPS analysis, a signal emerges, likely originating from either salt impurities or an exchanged chloride counter anion of the complex.

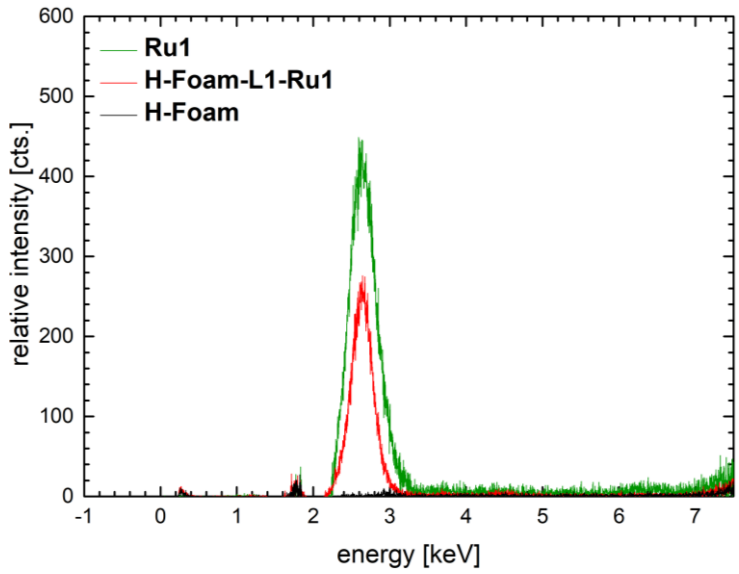

Fig. 93: XRF spectra of **Ru1**, **H-Foam** and **H-Foam-L1-Ru1**.

3.2.2.4.4 Diamond spheres

Cooperation partner CEA provided porous, dispersed diamond material in the form of hollow, open spheres with shell thickness of 20-50 nm.[364] In a first experiment, H-terminated diamond spheres (**H-spheres**) were functionalized with linker molecule **L1**. Similar to the **H-BND** particles, the **H-spheres** did not form a stable dispersion in aqueous media. Therefore, the functionalization was executed in acetonitrile. Subsequently, the spheres were cleaned with several organic solvents using a low power ultrasonic bath and centrifugation at 500 rpm. These conditions were used to avoid the risk of collapsing spheres due to strong centrifugal forces. As the amount of **H-spheres** was quite low (~1.5 mg), the complex **Ru1** was directly attached using the developed CuAAC conditions after washing **H-spheres-L1**. The functionalized spheres (**H-spheres-L1-Ru1**) were more dispersible in water than the starting material; however, almost all spheres settled overnight. The deep-black color of the dispersion did not change after the reaction.

The almost neutral zeta potential explained the low stability of the spheres in dispersion (Table 38). The difference in size can be explained using SEM pictures before and after functionalization.

Table 38: Results of zeta potential and particle size measurements of **H-spheres** and **H-spheres-L1-Ru1** in aqueous dispersion

diamond material	solvent	ζ [mV] (pH)	D_V-(10) [nm]	D_V-(50) [nm]	D_V-(90) [nm]
H-spheres	MeCN	-3.90 (6.0)	340	705	1160
H-spheres-L1-Ru1	H_2O	+12.9 (6.2)	647	844	1090

For **H-spheres**, the sphere structure can be clearly seen and only few individual spheres are damaged. After functionalization, the situation changed. The majority of **H-spheres-L1-Ru1** was damaged or collapsed and the samples show a mixture of different diamond fragments and (un)collapsed spheres, resulting in higher particle sizes due to agglomeration (Fig. 94).

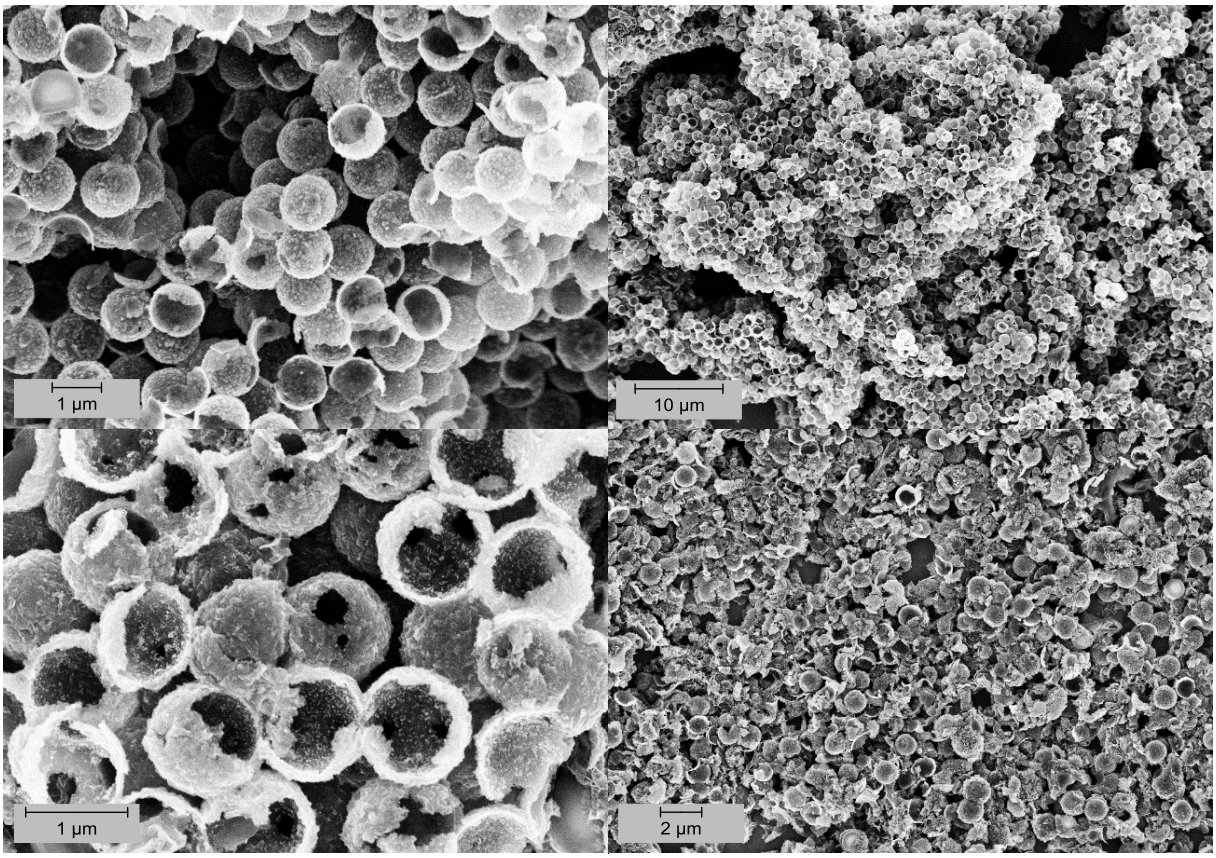

Fig. 94: SEM pictures of **H-spheres** (upper row) and **H-spheres-L1-Ru1** (lower row) at different magnifications.

H-spheres-L1-Ru1 shows a mixture of signals from **Ru1** and **H-spheres** in the Raman spectrum (Fig. 95). Next to the D and G band at 1373 cm^{-1} and 1582 cm^{-1}, which are shifted to higher wavenumbers in comparison to the starting material, the most intensive C=N-vibration at 1484 cm^{-1} is clearly visible. In the same region, the starting material **H-spheres** shows the signal for *trans*-polyacetylene within the grain

boundaries.[364] The other intensive signals of **Ru1** are superimposed by the strong G band, but contribute as signal shoulders.

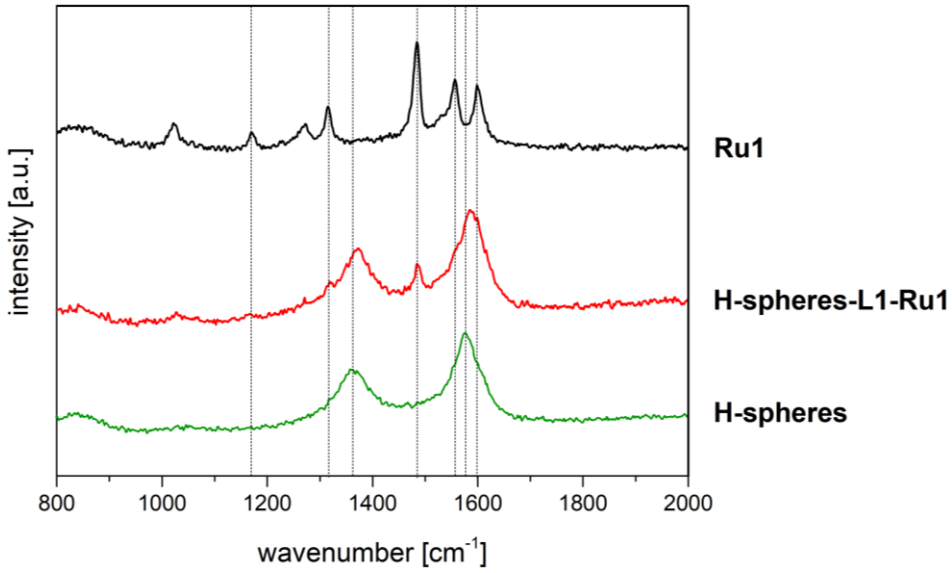

Fig. 95: Raman spectra of **H-spheres**, **H-spheres-L1-Ru1** and **Ru1** (measurements with 445 nm laser).

Although the obtained dispersion is still black, the UV/Vis absorption illustrates some of the characteristic maxima of **Ru1** (Fig. 96). The broad signal at 454 nm of **Ru1**, significantly shifted to 478 nm and the very intensive maximum at 287 nm, reduced to a broad shoulder, and another transition at 214 nm, slightly redshifted compared to pure complex **Ru1**, are also present for **H-spheres-L1-Ru1**.

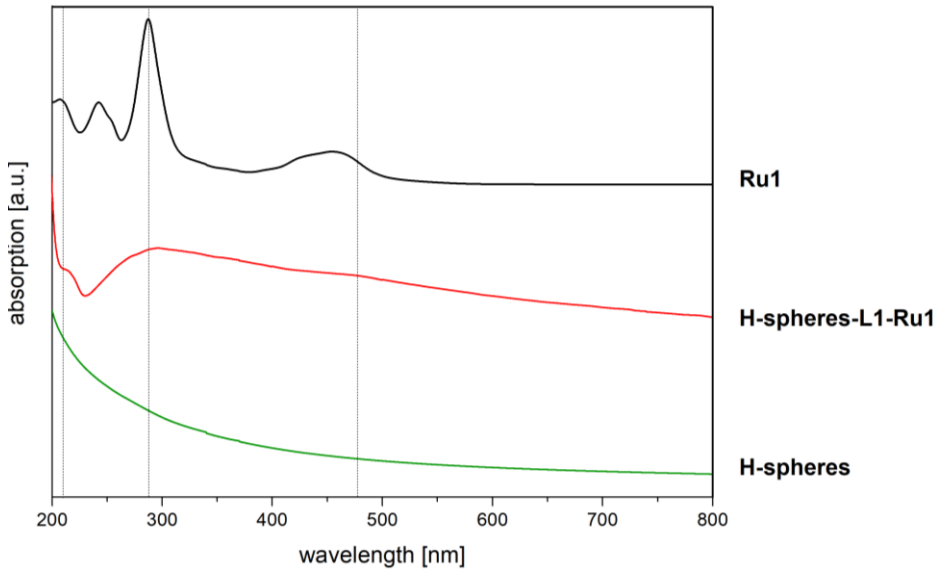

Fig. 96: Comparison of the UV/Vis spectra of **H-spheres**, **H-spheres-L1-Ru1** and **Ru1** (measurements in MeCN).

All in all, the functionalization with **Ru1** was successful, but not necessarily on intact diamond spheres, as the material is heavily affected by the reaction conditions and the cleaning afterwards. In conclusion the mechanical stability of hollow spheres is not sufficient for a wet-chemical, post-production functionalization

3.2.2.5 Attachment of Ru3 on mDND via carboxamide coupling

As already mentioned in chapter 3.2.1.1, the complex **Ru3** was also synthesized due to several reasons. On one hand, the influence of other ligands on the ruthenium center, as well as a different method of grafting should be investigated. On the other hand, the **Ru3** illustrates a slightly different electronic structure in comparison to **Ru1** and **Ru2** (cf. chapter 3.2), which might further help positioning complex-related orbitals within the band gap of diamond allowing for use of visible light in photocatalysis. With the amino-linker functionalized DNDs **mDND-L8**/**L9** at hand, carboxylic acid functionalized complex **Ru3** was attached using a well-known carboxamide coupling involving the peptide coupling reagents 1-Ethyl-3-(3-dimethylaminopropyl)-carbodiimide (EDC) and *N*-hydroxysuccinimide (NHS) to form the conjugates **mDND-L8-Ru3**/**mDND-L9-Ru3** (Fig. 97).[243]

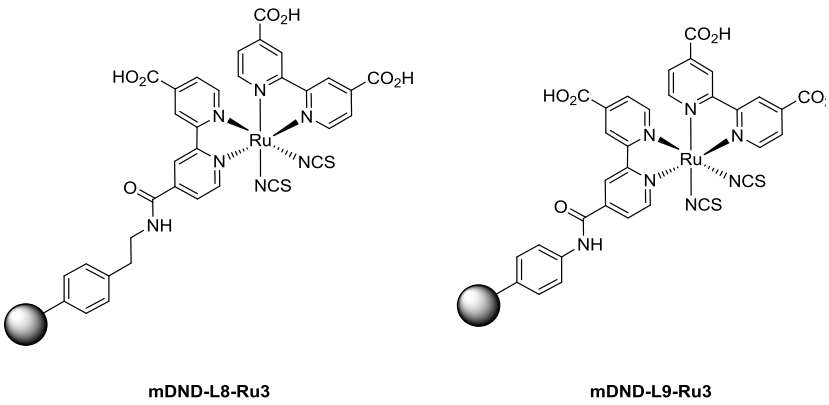

Fig. 97: Carboxamide coupled Ru-DND conjugates **mDND-L8-Ru3** and **mDND-L9-Ru3**.

After two days stirring at r.t., the reactions were stopped and the particles intensively washed with different solvents. The DNDs **mDND-L8-Ru3**/**mDND-L9-Ru3** were obtained as slightly purple aqueous dispersions. The change in zeta potential indicated the successful grafting of **Ru3** (Table 39). The particle size was getting bigger for both samples **mDND-L8-Ru3** and **mDND-L9-Ru3**, no stable dispersions were formed at slightly acidic pH-value (particle sedimentation after ~15 min).

Table 39: Results of TGA, zeta potential and particle size measurements of **mDND-L8**/**mDND-L9** and ruthenium(II) conjugated particles **mDND-L8-Ru3**/**mDND-L9-Ru3** in aqueous dispersion

ND material	surface loading [mmol g^{-1}]	ζ [mV] (pH)	D_V-(10) [nm]	D_V-(50) [nm]	D_V-(90) [nm]
mDND-L9	0.24	+43.1 (6.2)	25.8	44.7	97.0
mDND-L9-Ru3	0.19	-11.0 (5.6)	183	488	1360
mDND-L8	0.26	+48.4 (6.9)	56.1	91.5	180
mDND-L8-Ru3	0.11	-10.4 (5.7)	106	373	1320

The DRIFT spectrum of **mDND-L8-Ru3** shows the characteristic vibrations of the N3 dye (**Ru3**) (Fig. 98). At 2104 and 1989 cm^{-1} the stretching vibration of the two differently coordinated thiocyanate ligands can be seen. At 1544 cm^{-1} (ν(C=C, C=N)) and 787 cm^{-1} (δ(C-H_{arom})) the vibrations of the ligands are observed. At 1612 cm^{-1} the broad amide I vibration is detected and at 1365 cm^{-1} the amide III vibration. Amide II, the N-H bending vibration, is most likely contributing to the signal at 1544 cm^{-1}. The intensive C=O stretching vibration at 1722 cm^{-1} of the carboxylic acids is not distinctive for **mDND-L8-Ru3**, indicating an amide formation and a shift to lower wavenumbers. The DRIFT spectrum of **mDND-L9-Ru3** shows the same characteristic vibrations (Appendix, Fig. 138).

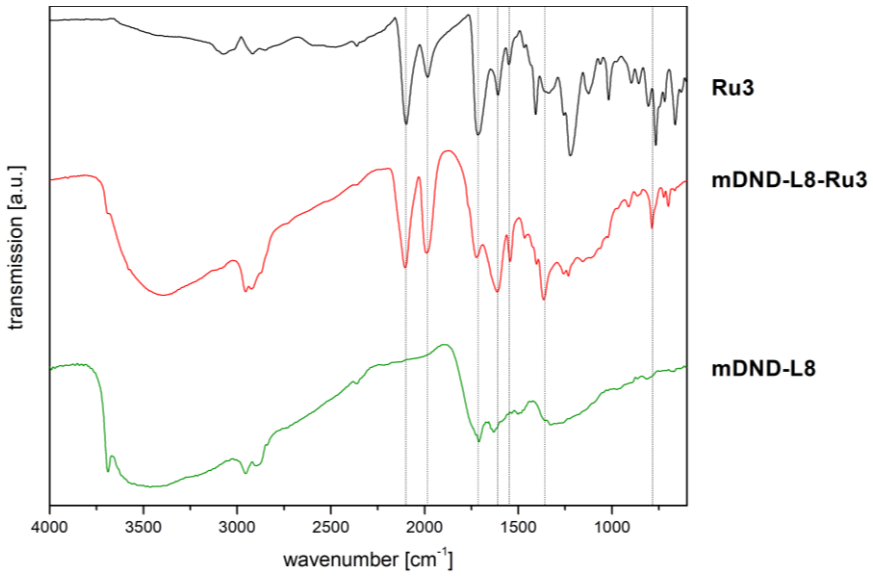

Fig. 98: IR spectra of **mDND-L8**, **mDND-L8-Ru3** (DRIFT) and **Ru3** (ATR-FTIR).

The surface loading of both particles was significantly lower compared to linker-functionalized starting materials **mDND-L8/L9**. The most reasonable explanation is

that the amino-functionalized particles **mDND-L8** coupled with almost every acid group, forming covalent aggregates (Fig. 99). Thus, **Ru3** was attached as expected.

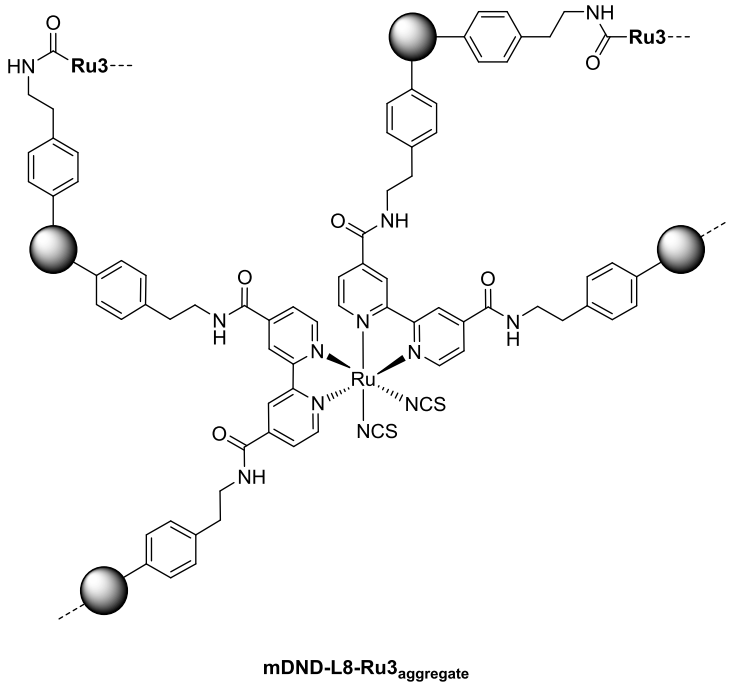

Fig. 99: Aggregate formation of **mDND-L8-Ru3**.

The agglomerate formation explained the larger particles and the instability in aqueous dispersion, as the stabilizing acid groups were not accessible anymore. The lack of free acid groups also explained the missing C=O stretching vibration in the DRIFT spectrum.

In UV/Vis spectroscopy, a very intensive maximum at 315 nm is observed. **Ru3** shows three further absorption maxima at 542, 400 and 251 nm resulting in a deep purple color (Fig. 100). The HOMO-LUMO transition at 251 nm is visible as small shoulder; however, none of the metal-to-ligand charge transfer signals (400 + 542 nm) can be clearly seen when attached to **mDND** particles. This indicates some changes in the complex structure, which will be discussed in detail when investigating the photostability under UV irradiation in chapter 3.4.1. The equivalent spectrum of **mDND-L9-Ru3** can be found in the Appendix, Fig. 139.

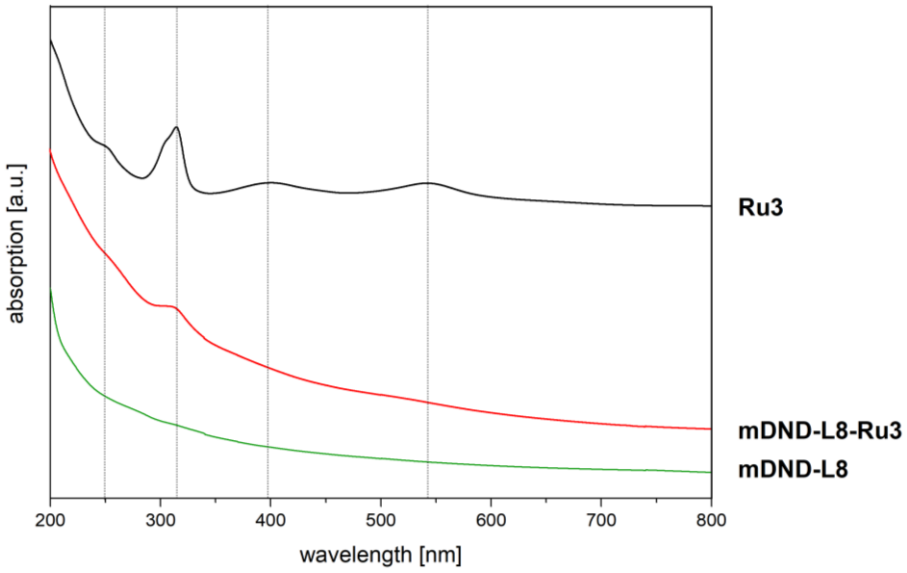

Fig. 100: UV/Vis spectra of **mDND-L8**, **mDND-L8-Ru3** and **Ru3** (measurements in MeCN).

The Raman spectrum of Ru(II)-DND conjugate **mDND-L8-Ru3**, was measured using the 532 nm laser for excitation (Fig. 101). In contrast to the attached complexes **Ru1**/**Ru2**, which were measured using the 445 nm laser (cf. chapter 3.2.2.3.1), the complex **Ru3** is more efficiently excited using the higher wavelength due to the MLCT absorption at 542 nm. However, the spectrum itself is not significantly different in comparison to the other Ru(II) complexes investigated so far. It shows the characteristic features of **Ru3**, which are again overlapping with the broad G-band at around 1592 cm^{-1} and the diamond/D band signal at 1328 cm^{-1} (Fig. 101). The same is observed for **mDND-L9-Ru3** (Appendix, Fig. 140).

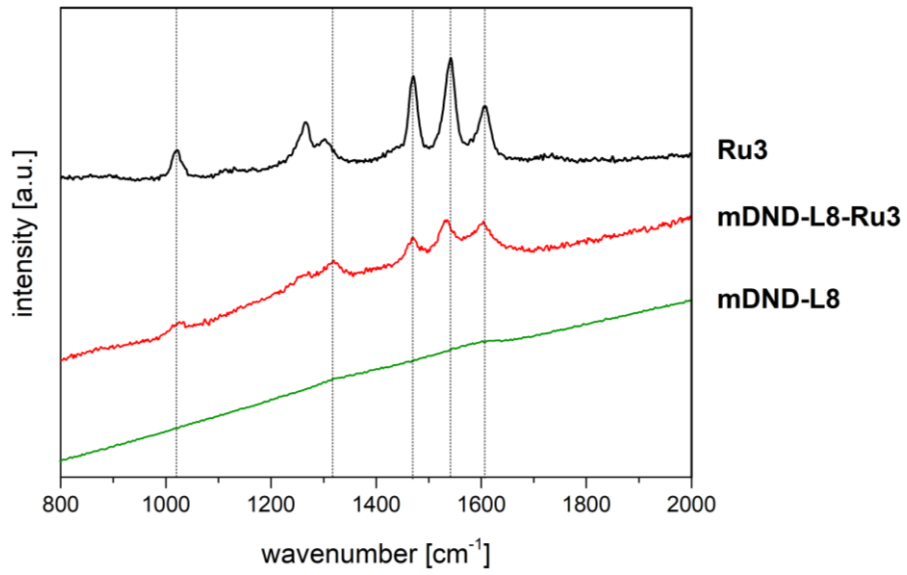

Fig. 101: Raman spectra of **mDND-L8**, **mDND-L8-Ru3** and **Ru3** (measurements with 532 nm laser).

XPS and XRF analysis of the obtained samples **mDND-L8-Ru3**/**mDND-L9-Ru3** confirmed the presence of ruthenium. Quantification was carried out using elemental analysis (Table 40). The Ru:S ratio was calculated to be 1:2.2 for both samples (expected 1:2), confirming the presence of NCS-ligands. The Ru:N ratio (expected 1:7) was determined to by 1:19 (**mDND-L8-Ru3**) and 1:12 (**mDND-L9-Ru3**). The substantial increased nitrogen value can be explained by either the formation of the covalent aggregates mentioned above or the adsorption of coupling reagents. For **mDND-L9-Ru3**, the aggregation, leading to an expected Ru:N ratio of 1:10 due to the reaction of each carboxylic acid with one amino group, can explain the measured values. Additionally, for **mDND-L8-Ru3** the possible adsorption of nitrogen-rich coupling reagents, such as EDC, needs to be considered.

Table 40: Elemental analysis of **mDND-L8**/**mDND-L9** and **mDND-L8-Ru3**/**mDND-L9-Ru3**

ND material	C [wt.%]	H [wt.%]	N [wt.%]	Ru [wt.%]	S [wt.%]	∑ [wt.%]
mDND	89.14	1.16	2.68	-	-	92.98
mDND-L8	83.23	4.39	7.89	-	-	95.51
mDND-L8-Ru3	72.57	3.15	4.29	0.62	0.43	81.06
mDND-L9	86.38	2.09	3.65			92.12
mDND-L9-Ru3	75.82	2.09	4.57	0.67	0.48	83.63

In conclusion, it was possible to link **Ru3** to amine-functionalized **mDND** particles using carboxamide formation. However, the commercially available N3 dye (**Ru3**) needs to be modified, if attached to ND particles. First, only one carboxylic acid group in the ligand periphery is required to avoid covalent agglomeration. Second, the thiocyanate ligands, which are not stable in aqueous dispersion over time, need to be replaced by a strongly coordinating ligand, such as a third functionalized bpy ligand.

3.2.3 Metal-coating of ND particles

In addition to the functionalization of diamond nanomaterials with TM complexes, the coating of nanostructured diamond with TM metals or metal oxides provides another possible approach to introduce surface states on diamond materials, which could allow for the use of visible light in photocatalysis. As already discussed in chapter 1.5, metal or metal oxide coated nanodiamond particles have been applied in various fields of catalysis. In solid phase catalysis, the dehydrogenation of alkanes was intensively

studied using various coatings on ND particles, e.g. ZnO or MoO_2 (cf. chapter 1.5.2). In direct methanol fuel cells, Ru, Pt or Cu_2O particles, deposited on the ND surface, were used showing improved catalytic activity (cf. chapter 1.5.3). Atomic layer coatings of photocatalyst TiO_2 on ND particles were used in the degradation of water pollutants using light with $\lambda > 365$ nm.[200,201] Regarding the photocatalytic reduction of CO_2, the deposition of metal (oxides) on nanostructured materials can improve the CO_2 adsorption and activation.[92] Roy *et al.* recently presented that Ag nanoparticles, deposited on BDD electrodes increased the photoelectrochemical reduction of CO_2 forming CO.[365] Another interesting noble TM metal, copper, is known to reduce CO_2 electrochemically producing formaldehyde, methanol and methane.[89] Considering the established coating of BDD electrodes with cuprous oxide using electrodeposition,[366] copper-modified BDD electrodes were used in the electroreduction of CO_2 yielding formaldehyde, formic and acetic acid.[367] Therefore, the fabrication of copper-coated nanodiamond particles[368] was targeted by providing a composite material with each component, diamond and copper, showing activity in the reduction of CO_2 in (photo)electrochemical reactions.[369]

As starting materials for the coating with copper, milled, air oxidized DND (**oDND**) particles and milled, amine-terminated DND (**NH_2-DND**), both provided by Carbodeon Ltd. Oy, Finland (µdiamond Vox D and µdiamond Amine D), were used, as they are able to precoordinate metal cations in dispersion.[368] For copper coating, copper(II)acetate was used and reduced *in situ* with hydrazine (Fig. 102).[368]

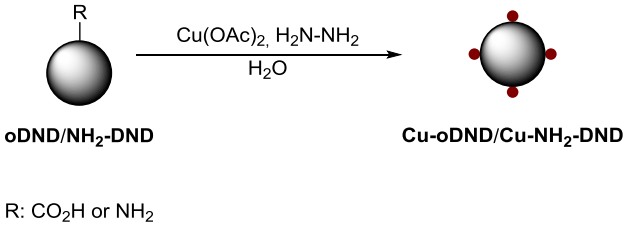

Fig. 102: Coating of **oDND/NH_2-DND** particles by *in situ* reduction of copper(II) salts.

The reduction method was tested on the metal salt in the absence of ND particles. Reduction with hydrazine yielded reddish copper particles (**Cu**). The reddish dispersions of **Cu-oDND/Cu-NH_2-DND** formed after reduction are shown in Fig. 103.

Fig. 103: **Cu-oDND**/**Cu-NH$_2$-DND** in aqueous dispersion.

For the Cu-coated sample **Cu-oDND**, significant changes in the particle properties were observed showing a slightly positive zeta potential and the formation of large particle agglomerates (Table 41). Ultrasound treatment during the reduction reaction to minimize the agglomeration was not possible due to the sensitivity of the pre-coordinated copper cations. For the reduction using **NH$_2$-DND**, the agglomeration after a deposition was less pronounced for **Cu-NH$_2$-DND** than for **Cu-oDND**. The zeta potential slightly decreased (+44.1 → +34.2 mV). The coordination of amine groups to reduced copper on the surface is a possible explanation.[368]

Table 41: Results of zeta potential and particle size measurements of **oDND**, **NH$_2$-DND**, metal reference (**Cu**) and coated NDs (**Cu-oDND**/**Cu-NH$_2$-DND**) in aqueous dispersion

ND material	ζ [mV] (pH)	D_V-(10) [nm]	D_V-(50) [nm]	D_V-(90) [nm]
oDND	-41.7 (5.4)	6.10	18.2	37.6
NH$_2$-DND	+44.1 (6.2)	5.75	11.4	31.2
Cu[a]	+34.2 (6.8)	640	1250	2550
Cu-oDND	+8.56 (6.1)	552	1310	5260
Cu-NH$_2$-DND	+38.6 (6.2)	39.7	377	1090

[a] **Cu** particles were obtained as reference material using reduction with hydrazine

The pure **Cu** particles show characteristic IR vibrations at very low wavenumbers (Fig. 104a). For **Cu-oDND** a copper vibration at 633 cm^{-1} is visible and the characteristic C=O stretching vibration of **oDND** at 1790 cm^{-1} is shifted to 1769 cm^{-1} indicating a copper coordination.[368] The broad shoulder at 1570 cm^{-1} is related to the O-H bending vibration of water molecules, which are interacting with the copper on the surface.[293,294] **Cu-NH$_2$-DND** shows copper related vibrations at 610 cm^{-1} and 523 cm^{-1} and the characteristic C-H stretching vibrations of starting material **NH$_2$-DND** at 2882 cm^{-1} and 2949 cm^{-1} are still present (Fig. 104b) indicating the existence of primary and

secondary amines. Most interestingly, the N-H deformation vibration, which superimposes with the O-H vibration of water at 1630 cm^{-1} for **NH_2-DND**, is shifted to 1561 cm^{-1} indicating that some amino groups are coordinated to copper, causing a shift to lower wavenumber.

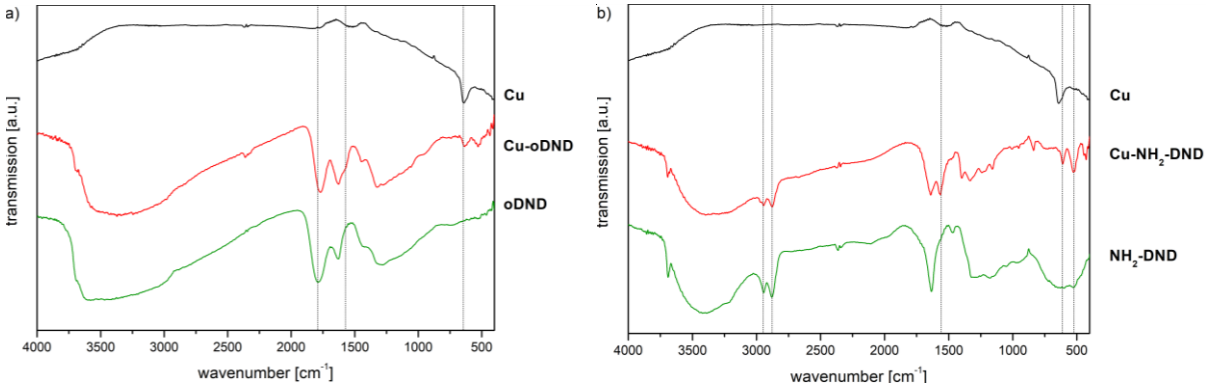

Fig. 104: DRIFT spectra of (a) **Cu-oDND**, **oDND** and **Cu** reference and of (b) **Cu-NH_2-DND**, **NH_2-DND** and **Cu** reference.

The Raman spectra confirm the obtained results. For **Cu-oDND**, copper related signals (633 cm^{-1} and 851 cm^{-1}) can be detected (Fig. 104a), as well as the characteristic diamond/D band signal (1326 cm^{-1}) and the broad G band (1591 cm^{-1}). For **Cu-NH_2-DND**, identical results are obtained (Fig. 104b).

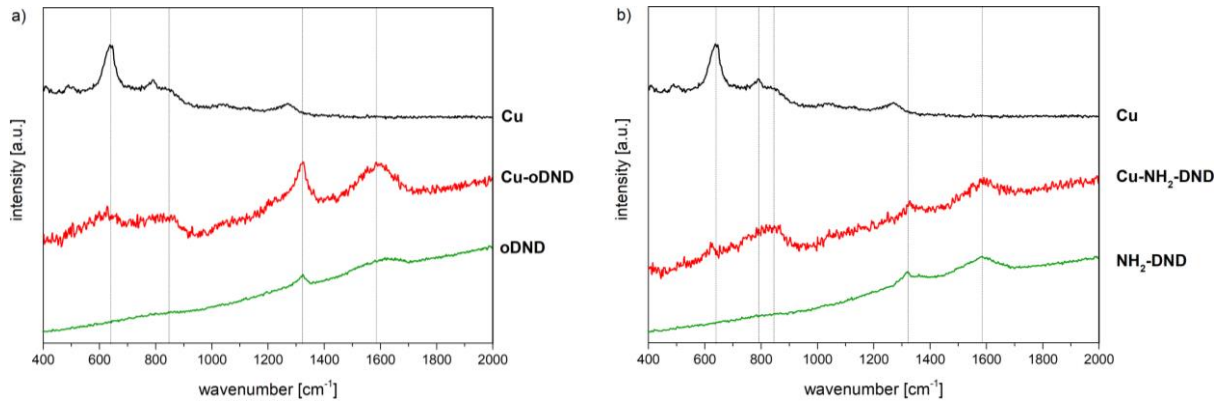

Fig. 105: Raman spectra of (a) **Cu-oDND**, **oDND** and **Cu** reference and of b) **Cu-NH_2-DND**, **NH_2-DND** and **Cu** reference (measurements with 445 nm laser).

Electron microscopy (SEM, TEM) in combination with EDX was used in order to investigate whether the DND particles are coated with metallic copper or whether copper and DND particles are coexisting.

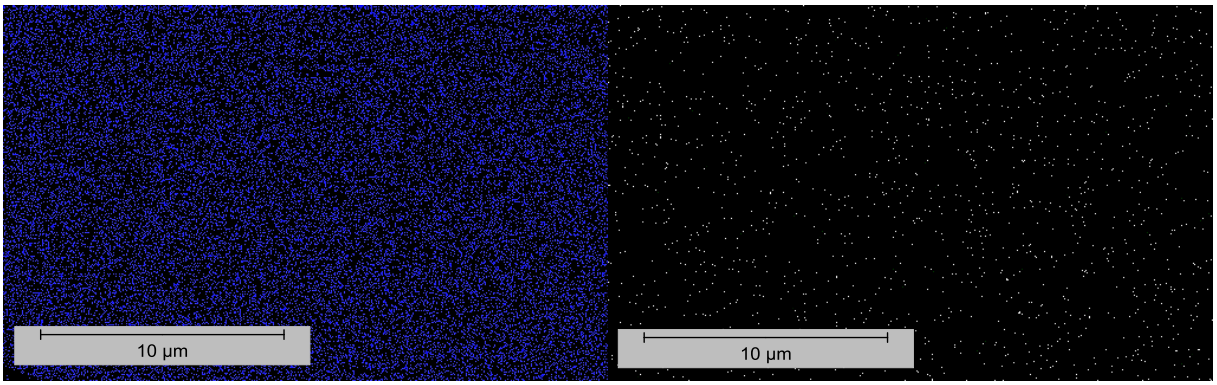

Fig. 106: EDX mapping of **Cu-oDND**. Carbon distribution (left figure, blue spots) and copper distribution (right figure, white spots) from the same sample area.

As can be seen in Fig. 106, scanning a broad area of the samples shows that copper is equally distributed all over the sample and no larger crystal can be detected. TEM measurements of **Cu-oDND** show the diamond nanoparticles and at the same time no metal particles are observed (Fig. 107). This observation in combination with the detected copper by EDX mapping suggests that the metal distribution is very homogenous and occurs most likely in the form of a very thin coating. Consequently, it is difficult to unambiguously visualize the metallic layer of copper around the ND particles in TEM, which was already reported by Turcheniuk *et al*.[368]

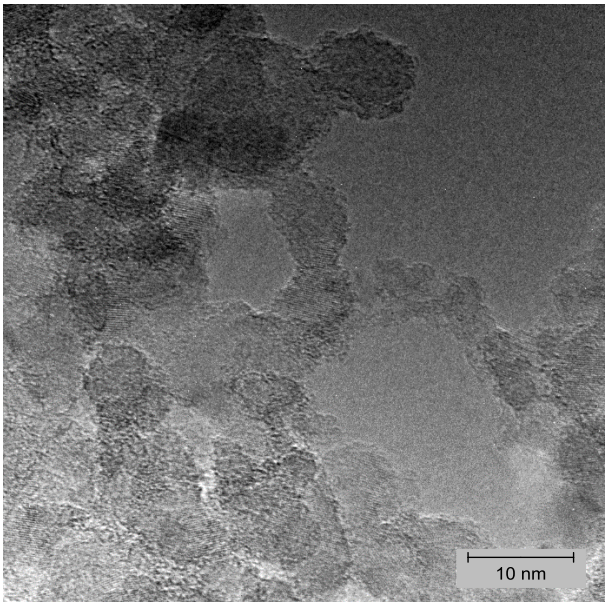

Fig. 107: TEM images of **Cu-oDND**.

The protocol for copper deposition was also used to coat acid-terminated **BND** particles yielding **Cu-BND**. The particle size ($D_v(50)$) did not increase significantly

(595 nm → 625 nm) and the zeta potential was less negative (-37.6 mV → -20.7 mV). Raman spectra illustrated a weak contribution of copper.

The amount of copper attached to the particles **Cu-oDND**, **Cu-NH$_2$-DND** and **Cu-BND** was determined via XPS, which was carried out by DIACAT-partner CEA, and elemental analysis (Table 42).

Table 42: Atomic concentrations of elements detected from XPS and EA for **Cu-oDND**, **Cu-NH$_2$-DND** and **CuBND**

material	C1s [at.%]	O1s [at.%]	N1s [at.%]	Cu2p$_{3/2}$ [at.%]	Cu [wt.%]
Cu-oDND	74.7	19.1	-	6.2	15.29
Cu-NH$_2$-DND	78.2	3.4	13.1	5.3	10.75
Cu-BND	75.1	20.3	-	4.6	-

The results are in accordance with the values obtained by EA. **oDND** coordinated more copper than **NH$_2$-DND**. Clearly, the used **oDND** showed a higher binding strength towards the copper(II) cation than **NH$_2$-DND** leading to higher surface coverage. Additionally, XPS analysis gave further insight into the oxidation state of the attached copper. For **Cu-NH$_2$-DND**, mainly copper(II) was present (96%), either as copper(II) oxide (CuO) or copper(II) hydroxide (Cu(OH)$_2$), which can be formed during storage in water. Only a small amount of 4% could be related to metallic copper or copper(I) oxide (Cu$_2$O). For **Cu-oDND**, the amount of metallic copper or CuO was slightly bigger (~15%), whereas for **Cu-BND** the ratio between Cu/Cu$_2$O and CuO/Cu(OH)$_2$ was almost 50:50. CuO only weakly coordinates to amine functionalities,[368] which could further explain the observed surface loading with copper. On the contrary, the oxidized surface of **DND** or **BND** particles could be incorporated into the oxide layer of the CuO resulting in an increased surface amount of copper. The obtained **Cu-oDND** particles were tested in photocatalytic CO_2 reduction experiments (cf. chapter 3.4.3).

3.3 Preparation of diamond nanoparticle dispersions

As discussed previously in chapter 1.6, in comparison to bulk diamond materials, diamond nanoparticles illustrate a high surface to volume ratio due their small size, affecting the photo- and electrocatalytic activity to a larger extent than in the bulk structure.[247] Also, a higher surface loading with catalytically active molecules can be

expected due to the enlarged surface area and the higher reactivity regarding covalent functionalization.[249] However, to take advantage of the increased surface, the particles need to be dispersed in a solvent. Dispersing nanoparticles is possible, if the interaction of the particle surface with the applied solvent is strong enough to overcome differences in density, which are generally responsible for a material either settling or floating in the liquid solvent.[370] The colloidal dispersions are typically stabilized by electrostatic repulsion and steric hindrance.[249] Considering these results, the solvent has to fulfill several requirements for the application of (functionalized) ND particle dispersions in photocatalysis. Besides sustaining a stable colloidal suspension, the solvent should be able to dissolve significant amounts of CO_2, as well as possible reduction products. It should also enable mass transport of these species within the solvent. When used in photoelectrocatalysis, the solvent should also be able to provide an ion conductive medium, therefore acting as an electrolyte.

So far, all described nanodiamond particles were dispersed in water. Considering usual dispersion procedures,[275] involving ultrasonic bath treatment, pH-adjustment and centrifugation, stable aqueous dispersions covering a broad range of particle sizes and concentrations were prepared. However, for H-terminated particles based on CVD material, the dispersibility in water was limited due to the hydrophobicity of the particles. The preparation of dispersions was possible, but only in low concentrations and with a high tendency of the particles to agglomerate in a short time.

3.3.1 Stability in electrolytes

Initial work focused on exploring aqueous media, especially containing the commonly used electrolyte salts sodium sulfate (Na_2SO_4) and potassium bicarbonate ($KHCO_3$).[371] In general, it was observed that dispersions of **mDND** and **oDND** in $KHCO_3$ solution were more stable than in Na_2SO_4 solution (Table 43).

Table 43: Maximum electrolyte concentrations for stable particle dispersions of **mDND**/**oDND** in Na_2SO_4 and $KHCO_3$

electrolyte	stability of **mDND** (23 mg/ml)	stability of **mDND** (2.3 mg/ml)	stability of **oDND** (6.7 mg/ml)
Na_2SO_4	$<1\cdot10^{-3}$ M	$<1\cdot10^{-5}$ M	$<1\cdot10^{-3}$ M
$KHCO_3$	$<1\cdot10^{-3}$ M	$<1\cdot10^{-3}$ M	$<1\cdot10^{-2}$ M

If stably dispersed, the particle size of the respective DND was comparable to the size observed in pure water. **oDND** particles were less sensitive towards electrolytes than **mDND**. The different zeta potential of **oDND** in comparison to **mDND** (-42.0 mV vs. +35.2 mV) and in particular the presence of particle agglomerates for **oDND** compared to de-agglomerated **mDND** ($D_V(50)$ = 158 nm vs. 3.38 nm) influenced the stability in the electrolyte solutions significantly.[372] Due to the formation of agglomerates for **oDND**, a lower amount of surface was accessible for interactions with electrolyte ions compared to **mDND**. Thus, higher salt concentrations were required to cause strong agglomeration of **oDND**. The larger surface area of de-agglomerated **mDND** particles was more easily interacting with the electrolyte ions, leading to agglomeration at lower salt concentrations. For Na_2SO_4, the particle concentration of **mDND** played an important role. In a concentrated **mDND** sample (23 mg/mL), the increased amount of particles could form stable interactions with the ions at higher electrolyte concentration ($1 \cdot 10^{-3}$ M), whereas the same electrolyte concentration led to agglomeration in the lower concentrated particle dispersion (2.3 mg/mL). These findings are in good agreement with the literature.[373,374] Under slightly basic conditions ($KHCO_3$), stability in a concentration range suitable for photoelectrochemical reactions (~$1 \cdot 10^{-2}$ M) can be achieved using **oDND** (Table 43). These results showed that the particle stability in electrolytes depended on many different factors, including the particle size and concentration. Thus, for each differently functionalized/terminated ND material, the type and concentration of the electrolyte needs to be determined in order to obtain a stable dispersion.

3.3.2 ND particle dispersion in ionic liquids

Apart from dispersing ND particles in commonly used electrolytes, room temperature ionic liquids (RTILs) illustrate a promising alternative due to their interesting properties and specific application fields.[375] The lack of a measureable vapor pressure, which prevents the emission of volatile organic compounds, characterizes the ionic systems i. a. as green solvents.[376] RTILs generally possess a high chemical stability, e.g. regarding hydrolysis or pH changes; however, when ILs are used as solvents or electrolytes in a specific reaction, possible side-reactions of the IL with reactants need to be taken into account.[377] Application in electrochemistry showed that RTIL provided a large electrochemical window up to 6 V, allowing for a broad range of reactions and applications as gas sensors.[378,379] The stability of the RTILs using energy-rich

irradiation (up to gamma rays) depends on the structure of the cation/anion and needs to be evaluated regarding each specific irradiation reactions.[380] Apart from the electrochemical properties and the given irradiation stability for selected ionic liquids, the CO_2 solubility,[381] which is typically up to 20 times higher than in water, particularly opens up the possibility for application in the CO_2 reduction reaction and for higher chemical conversion rates.[382,383] Thus, the dispersion experiments of ND particles were further extended to dispersibility in RTILs. The DIACAT consortium partner IoLiTec, Heilbronn, Germany provided all tested ILs (Table 44).

Table 44: Physicochemical properties of RTILs

ionic liquid	abbreviation	viscosity [mPa s]	refractive index (λ = 589 nm)
1-butyl-3-methylimidazolium hexafluorophosphate	BMIM PF_6	310 (25 °C)	1.40920 (25 °C)
1-ethyl-3-methylimidazolium trifluoromethanesulfonate	EMIM OTf	40.0 (25 °C)	1.43488 (25 °C)
1-ethyl-3-methylimidazolium dicyanamide	EMIM DCA	16.8 (20 °C)	1.39054 (20 °C)
1-propyl-1-methylpyrrolidinium bis(trifluoromethylsulfonyl)imide	PMPyrr BTA	47.0 (20 °C)	1.42640 (20 °C)
1-hexyl-3-methylimidazolium bis(trifluoromethylsulfonyl)imide	HMIM BTA	88.0 (20 °C)	1.43657 (20 °C)
butyltrimethylammonium bis(trifluoromethylsulfonyl)imide	N_{1114} BTA	100 (25° C)	1.41228 (25 °C)
ethyldimethylpropylammonium bis(trifluoromethylsulfonyl)imide	N_{1123} BTA	78.5 (25 °C)	1.41455 (25 °C)
N_{1114} BTA/butyltrimethylammo–nium tricyanomethanide	N_{1114} BTA/N_{1114} TCM (9:1), **Mix1**	88.4 (25 °C)	1.41825 (25 °C)
N_{1123} BTA/butyltrimethylammo–nium tricyanomethanide	N_{1123} BTA/N_{1114} TCM (9:1), **Mix2**	62.0 (25 °C)	1.42019 (25 °C)

For various ND particles the dispersibility (1 mg/ml), the particle size of the whole sample and the supernatant after short centrifugation (5 min at 15k rpm), as well as the long-term colloidal stability in RTILs was investigated. BMIM PF_6, EMIM OTf and EMIM DCA were tested using **pDND**, **mDND**, **gDND**, **oDND** **H-pDND$_{IAF}$** and **H-DND$_{CEA}$**. Here, either the high viscosity (BMIM PF_6) or the structure of the anion (EMIM OTf) led to undispersed, heavily agglomerated samples. For EMIM DCA stable

colloidal dispersion was obtained; however, the RTIL decomposed under irradiation, rendering EMIM DCA unsuitable.

Another set of RTILs, differing in the cation (PMPyrr, HMIM, N_{1114}, N_{1123}), was tested with H-terminated samples **H-pDND$_{IAF}$**, **H-pDND$_{CEA}$**, **H-gDND$_{IAF}$** and **H-gDND$_{CEA}$**. The dispersion ability for all BTA ILs was provided; however, colloidal stability of up to four days was only observed for the N_{1114}/N_{1123} cations. In PMPyrr and HMIM, all particles settled after one hour. Although, settling of the larger agglomerates started after eight hours for the N_{1114}/N_{1123} cations, the remaining particles appeared to be dispersion stable even after four days. The mean particle size (D_v(50)) of the H-DNDs in N_{1114}/N_{1123} BTA were measured to be ~150 nm (whole sample) and ~40 nm (supernatants), which agreed with the results obtained in aqueous dispersion. Particles dispersed in PMPyrr and HMIM BTA already tended to agglomerate during measurements of particle sizes of the whole sample (HMIM) or the supernatant (PMPyrr).

From the dispersion experiments, N_{1114} BTA was found to enable the preparation of concentrated, stable DND dispersions. However, its comparatively high viscosity (100 mPa s (25° C)) could generate technical issues while the ND slurry is handled inside a photochemical reactor. Thus, N_{1123} BTA, while possessing similar properties, but exhibiting lower viscosity (78.5 mPa s (25 °C)), was tested as an alternative. The slightly different alkyl groups at the ammonium cation were found to improve CO_2 solubility due to less efficient packing leading to increased free volume within the ionic liquid.[384,385]

The samples chosen for detailed testing were **pDND**, **H-pDND$_{IAF}$**, **BND3**, **H-BND3$_{CEA}$**, **mDND-L2-Ru1d** (short, conjugated linker) and **mDND-L5-Ru1b** (extended tolane-based linker). The samples, which were available as an aqueous dispersion, were washed three times with a small amount of N_{1123} BTA and subsequently dispersed in 1 ml of IL. The use of a warm ultrasonic bath (bath temperature ~40-45 °C) proved to be suitable for dispersing different types of ND particles. Using this approach, the viscosity of the RTIL was slightly lowered and the particles were more easily dispersed. Treating the dispersed particles for a few minutes in a cooled bath (T ~15 °C) illustrated the colloidal stability. If the particles started to agglomerate again, more IL had to be added, as the particle concentration was too high. The diluted dispersion was again tested for r.t. stability. The colloidal stability of the six test samples was investigated

over time (Appendix, Fig. 141). Stable dispersions with concentrations up to 1.0 wt% were obtained for each sample using the described ultrasound treatment (t = 0). The particles **pDND** and **H-pDND$_{IAF}$** cannot be stably dispersed for >48 h. However, **BND3** and also **H-BND3$_{CEA}$** showed surprisingly high colloidal stability, even over several days. The dispersion stability of **BND3** and **H-BND3$_{CEA}$** in N_{1123} BTA can also be assessed by looking at the size of the homogenous dispersions at t = 0 h and after centrifugation at 15k rpm for 5 min (Table 45). Larger particles of the B-doped dispersions settled, but the supernatants were cloudy, still showing particles with comparable size (D_V(50) 116 nm vs. 150 nm). However, for the Ru-functionalized samples, the mean particle sizes of the supernatants increased substantially, most likely due to agglomeration induced by very low particle concentration. The mean particle size of the whole Ru-functionalized samples showed very small values, indicating that the attached complexes helped to stabilize the particles in the IL.

Table 45: Comparison of the particle sizes (D_V(50)) in N_{1123} BTA before and after centrifugation

ND material	whole sample (t = 0 h) [nm]	supernatant [nm]
pDND	324	202
H-pDND$_{IAF}$	296	238
BND3	262	116
H-BND3$_{CEA}$	247	150
mDND-L2-Ru1d	173	437
mDND-L5-Ru1b	214	515

N_{1123} BTA was found to enable the formation of stable nanoparticle dispersions of various kinds, concentrations and sizes. These findings allow for fine-tuning the liquid properties and the focus was therefore extended to 9:1 (v:v)-mixtures of N_{1123} BTA or N_{1114} BTA with N_{1114} TCM, which showed an increased CO_2 uptake due to the TCM anion (Fig. 108).[386]

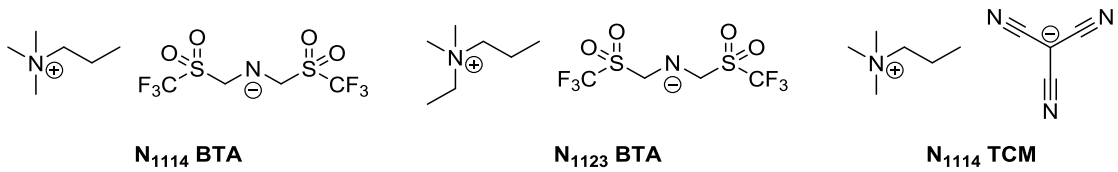

Fig. 108: Ionic liquids N_{1114} BTA, N_{1123} BTA and N_{1114} TCM.

As can be seen in Table 44, the viscosity of both mixtures, **Mix1** and **Mix2**, was lower than for the corresponding pure IL. Thus, it was investigated whether this property is beneficial for the dispersibility. The samples and protocol chosen for testing were identical to pure N_{1123} BTA. Good dispersibility was observed for each mixture and the influence of the viscosity was of minor relevance. For the test samples, concentrations up to 1.0 wt% were stable at t = 0 (Appendix, Fig. 142). After 24 h, more particles settled, but the supernatant still contained visible amounts of nanodiamonds. Initial differences between **Mix1** and **Mix2** appeared. The particles **H-pDND$_{IAF}$** were not stable in **Mix2** anymore after 24 h. After 48 h, the particles **pDND**, **H-pDND$_{IAF}$**, **mDND-L2-Ru1d** and **mDND-L5-Ru1b** precipitated in **Mix2**. For **Mix1**, only the Ru-functionalized samples settled and **H-pDND$_{IAF}$** dispersions started to become unstable. However, **BND3** and also **H-BND3$_{CEA}$** still showed high colloidal stability in both mixtures. In general, regarding the whole sample, **Mix1** was better at stabilizing the particles than **Mix2**, leading to smaller agglomerates (Table 46). However, for both mixtures, the size after centrifugation was not significantly smaller. This observation is most likely related to the TCM anion, which might induced particle agglomeration at lower particle concentrations, e.g. after centrifugation. The same was already observed when testing the structurally related DCA anion in EMIM DCA. In comparison to pure N_{1123} BTA, **Mix1** generally showed smaller or quite similar particle sizes, whereas the particles agglomerated more strongly in **Mix2**.

In summary, N_{1114}/N_{1123} BTA showed the best results regarding dispersibility and long-term stability for a great variety of ND particles. These two ILs are also suited with respect to UV transmission (experiments in Berlin), (electro-)chemical stability (IAF measurements) and CO_2 solubility (IoLiTec). The mixture of N_{1114} BTA with N_{1114} TCM (9:1) (**Mix1**) showed the same properties as pure N_{1123} BTA for concentrated samples (~ 1.0 wt%). However, mixtures of this kind were not suitable for diluted samples (<< 1.0 wt%). The mixture of N_{1123} BTA with N_{1114} TCM (9:1) (**Mix2**) performed poorly compared to **Mix1**.

3.3.3 Comparison of dispersion media

As water is the most common solvent for ND dispersions, a comparison with the obtained results in N_{1123} BTA and **Mix1** was necessary. As can be seen in Table 46,

pDND and funct. **mDND** particles (**mDND-L2-Ru1d** and **mDND-L5-Ru1b**) are much better stabilized in aqueous dispersion.

Table 46: Particle sizes ($D_v(50)$) in **Mix1**, **Mix2**, N_{1123} BTA and water before and after centrifugation

ND particles	N_{1123} BTA whole [nm]	**water** whole [nm]	**Mix1** whole [nm]	**Mix2** whole [nm]	N_{1123} BTA supern. [nm]	**Mix1** supern. [nm]	**Mix2** supern. [nm]
pDND	573	170	457	631	376	586	586
H-pDND$_{IAF}$	557	965	391	764	463	416	507
BND3	502	464	400	471	239	404	412
H-BND3$_{CEA}$	425	/	464	652	284	645	655
mDND-L2-Ru1d	413	76.4	433	479	813	461	482
mDND-L5-Ru1b	337	70.0	512	458	868	402	587

For **BND3**, no substantial difference between dispersion in water or ionic liquid was detected. However, **H-pDND$_{IAF}$** particles were better stabilized in N_{1123} BTA and **Mix1** than in water. As mentioned before, **H-BND3$_{CEA}$** particles did not form any stable, concentrated aqueous dispersion, whereas N_{1123} BTA and **Mix1** both stabilized the particles. The so far obtained results, including dispersibility, long-term stability and stability of concentrated dispersions (~1.0 wt%), are generalized and summarized in Table 47. Regarding **pDND** and functionalized **mDND** particles, all used ILs led to significantly bigger agglomerates when compared to water. However, for **H-DND** particles, the ILs provided better dispersion properties.

Table 47: Suitability of different media for the dispersion of ND materials in high concentration (✔ ✔: highly suitable; ✔: suitable; O: suitable with limitations; X: not suitable)

ND particles	N_{1123} BTA or N_{1114} BTA	N_{1114} BTA/ N_{1114} TCM (9:1)	water
pDND/funct. **mDND**	O	O	✔ ✔
H-DND	✔	✔	O
milled (un)doped ND (CVD based)	✔	✔	✔ ✔
H-term. milled (un)doped ND (CVD based)	✔	✔	X

The slightly different results for diluted dispersions (<<1.0 wt%), i.e. the supernatants, are generalized and summarized in Table 48. Functionalized **mDND** particles strongly

agglomerated using pure N_{1123} or N_{1114} BTA. In the used mixture (N_{1114} BTA/N_{1114} TCM (9:1), **Mix1**) no smaller particles were expectedly detected after centrifugation, eliminating this mixture as suitable solvent for diluted dispersions.

Table 48: Suitability of different media for the dispersion of ND materials in low concentration (✔ ✔: highly suitable; ✔: suitable; O: suitable with limitations; X: not suitable)

ND particles	N_{1123} BTA or N_{1114} BTA	N_{1114} BTA/ N_{1114} TCM (9:1)	water
pDND/funct. **mDND**	X	O	✔ ✔
H-DND	✔	O	✔
milled (un)doped ND (CVD based)	✔	O	✔ ✔
H-term. milled (un)doped ND (CVD based)	✔ ✔	O	O

3.4 Application of ND particles in photocatalysis

As described in chapter 1.5.4, photocatalysis is one of the emerging fields for the application of ND based materials, with all relevant findings being published in the 2010s. Three fields within photocatalysis were highly focused on so far (cf. chapter 1.5.4): first, the photocatalytic Fenton reaction involving ND particles coated with group eleven elements (Cu, Ag, Au),[209,214,215] second, the hydrogen evolution reaction by water splitting applying particles coated with TiO_2,[207] CuO_2[206] or Pt,[208] and, third, the CO_2 reduction reaction utilizing H-terminated ND particles.[108] Considering that these results have already been presented in the literature, in this work, the influence of surface-termination (cf. chapter 3.1.1), functionalization with photoactive molecules (chapter 3.2), as well as doping of the particles on the electronic structure (chapter. 3.1.2) and consequently on the catalytic activity offers parameters to be investigated and optimized. The stability of ND modifications/functionalization under irradiation, as well as in dispersions, present further challenges for the application of diamond materials as photo(electro)catalysts. Thus, this chapter focuses on the photostability of various nanodiamond samples, described in chapter 3.1 and 3.2, and their application in photo-, photoelectro- and photoredox catalysis.

3.4.1 Photostability under UV/Vis irradiation

For the photocatalytic reduction of CO_2 involving non-functionalized ND particles, the generation of solvated electrons, which is achieved under UV-irradiation ($\lambda < 225$ nm),

is required.[108] According to the first results from Zhang *et al.*,[108] a 500 W Hg/Xe lamp system from *Newport Corp.* was installed and used for photostability testing (Fig. 109). The Hg/Xe lamp was installed in an air-cooled lamp housing **A**. The condenser **B** rendered the divergent light beam emitted by the Hg/Xe lamp first into a parallel and then into a converging beam. **B** was separated from a water filter **C**, which filtered infrared irradiation and should therefore reduce sample heating via a shutter. The to be irradiated ND samples (**E**) were placed in a lightproof box **D** and could be saturated with gas according to the reaction requirements.

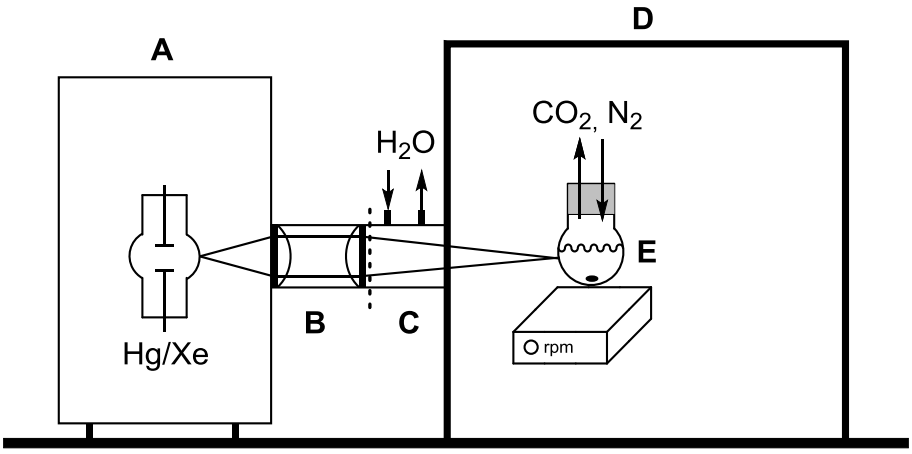

Fig. 109: Schematic illustration of the 500 W Hg/Xe lamp system.

Consequently, in this setup the stability of the dispersed ND samples can be assessed regarding the influence of UV/Vis radiation on the particle termination/functionalization, as well as regarding heat development during irradiation. The emission spectrum of the 500 W Hg/Xe lamp (Appendix, Fig. 143) showed five intensive maxima in the visible light region (579, 577, 546, 436, 405 nm), as well as several emission lines in the UV region (365, 334, 296 nm).

Freshly prepared dispersions of eight ND samples, differing in surface termination, doping and concentration, were irradiated in an intial set of experiments for 5 min in a quartz beaker covered with a lid (Table 49). These experiments were carried out in cooperation within the DIACAT project at Oxford University, United Kingdom, at Prof. Dr. John S. Foords group by senior researcher Dr. Emina Hadzifejzovic.

The particles were re-analyzed in dispersion and as powder. After irradiation, the samples showed a temperatures increase of ΔT = 5.0-7.0 °C. The mean particles size of **H-pDND$_{IAF}$**, **H-gDND$_{IAF}$** and **H-BND2$_{IAF}$** illustrated smaller agglomerates after irradiation and, in particular, the hydrophobic particles **H-BND2$_{IAF}$** showed an

increased dispersion stability (Table 49). Zhang *et al.* reported that, due to UV irradiation in water, a loss of H-termination leading to OH-termination is possible.[108] OH-termination would then lead to less hydrophobic particles and increased dispersion stability. The decrease in zeta potential, specifically for **H-BND2$_{IAF}$** (+40.3 → -8.94 mV), documented the loss in H-termination, as well as an observed decrease in intensity for C-H related vibrations in the ATR-FTIR and DRIFT spectra. All non-hydrogenated particles were slightly more agglomerated after irradiation; however, the zeta potential showed no significant difference. The DRIFT spectra of **oDND** lacked the vibrations at 2168 and 2272 cm^{-1}. If those vibrations were related to graphitic C-N structures on the surface formed during air oxidation (chapter 3.1.1.5), UV irradiation would lead to decomposition of those surface structures.[387] The Raman spectra of all samples did not show any sp^2-formation. Thus, short UV irradiation had no influence on the diamond itself, but on the surface termination. For concentrated **mDND** samples (>2.5 wt%), it was observed that longer irradiation in combination with increased sample heating led to strong agglomeration, as water evaporation leads to an increase in concentration of **mDND**.

Table 49: Zeta potential and particle size measurements of variously terminated, (un)doped ND particles before and after 5 min irradiation in water with a 500 W Hg/Xe lamp

ND particle	ζ_{before} [mV] (pH)	ζ_{after} [mV] (pH)	D_V-(50) $_{before}$ [nm]	D_V-(50) $_{after}$ [nm]
pDND (0.1 wt.%)	+41.1 (6.0)	+30.4 (6.2)	154	433
pDND (1.0 wt%)	+43.2 (5.5)	+34.4 (5.8)	170	982
H-pDND$_{IAF}$ (0.33 wt%)	+47.3 (6.3)	+31.6 (6.7)	755	584
oDND (0.5 wt.%)	-20.3 (5.1)	-35.9 (5.0)	158	434
gDND (0.5 wt.%)	+33.9 (5.9)	+33.2 (6.0)	207	997
H-gDND$_{IAF}$ (0.33 wt%)	+41.8 (6.2)	+37.7 (6.2)	1050	409
mDND (1.5 wt.%)	+30.9 (5.9)	+33.1 (5.8)	4.52	18.3
mDND (2.5 wt.%)	+36.9 (5.6)	+39.3 (5.7)	3.38	9.50
BND2 (0.1 wt.%)	-37.3 (6.0)	-38.3 (6.1)	732	1020
H-BND2$_{IAF}$ (0.2 wt%)	+40.3 (6.4)	-8.94 (6.2)	1120	519

Considering the results obtained for variously terminated (un)doped ND particles, the photostability of functionalized ND particles and the respective reference molecules was also investigated. The first experiments for functionalized ND samples were conducted with the pure ruthenium complexes **Ru1-Ru4**, as well as reference systems

L3/**L4-Ru1**, **L3**/**L4-Ru2** and **L6-Ru1**. The complexes were dissolved/dispersed in water (concentration 2 mM) and irradiated for 60 min in a quartz beaker covered with tinfoil. A temperature increase to 75-80 °C was detected, although the water filter attached to the Hg/Xe lamp filtered the infrared radiation >950 nm, which was mainly responsible for the heating. The nine complexes were dried *in vacuo*, analyzed via Raman, ATR-FTIR, NMR and UV/Vis spectroscopy and compared to the data prior to irradiation. The five reference systems, **L3**/**L4-Ru1**, **L3**/**L4-Ru2** and **L6-Ru1**, presented the same characteristics before and after irradiation. Also, the spectra of **Ru1**/**Ru2** showed no difference. The irradiation was not affecting the terminal alkyne species, which was documented by the still present singulet at 4.43 (**Ru1**) and 4.55 ppm (**Ru2**) with an integral of one in the ^{1}H-NMR spectra. After irradiation, **Ru3** still showed the significant vibrations of the bpy ligands in ATR-FTIR and Raman spectra, however, no thiocyanate related signals can be seen in the ATR-FTIR spectrum and different coordination spheres were detected in the ^{1}H-NMR spectrum. For **Ru4**, the signals of the tpy ligand were clearly shifted in the ^{1}H-NMR spectra. This shift was most probably caused by a ligand exchange from chloride to water proving the lability of the chloride ligands. In addition to the results obtained by XPS analysis, **Ru3**/**Ru4** were not only unstable when stored for a long time in water, but also under intensive UV/Vis irradiation.

Freshly prepared dispersions of all nine ruthenium-functionalized ND particles (3.3 mg/ml) were also irradiated for 60 min (Table 50). After irradiation, the particles were washed with several solvents, in which potentially cleaved complex, linker and ligand fragments would be soluble. The supernatants were dried *in vacuo* and analyzed by NMR spectroscopy. TGA, zeta potential and particles size of **mDND-L1-Ru1c/mDND-L2-Ru1d** and **mDND-L1-Ru2b/mDND-L2-Ru2b** gave comparable results after irradiation and the ^{1}H-NMR spectra of the supernatants did not present any aromatic signal, indicating the stable, covalent attachment of the linker-complex structure. Other spectroscopic methods yielded the same characteristic signals before and after irradiation, e.g. the very characteristic MLCT band was still visible in the UV/Vis spectra. For **mDND-L1-Ru4b/mDND-L2-Ru4b**, a direct spectroscopic proof of chloride exchange with water was not obtained, as the characteristic Ru-Cl vibration (~320 cm^{-1})[388] was not within the measuring range of the ATR-FTIR setup. However, the OH-vibrations at ~3400 and 1610 cm^{-1} were very prominent, even for intensively dried samples (4 h, 135°C), indicating coordination of water. All other measurements

were unobtrusive. Relating to the reference experiments with **Ru4**, an (partial) exchange of chloride can be expected. Both diamonds, **mDND-L8-Ru3** and **mDND-L9-Ru3**, showed only one thiocyanate signal in the ATR-FTIR spectrum and the dispersions were slightly more stable after irradiation. If the SCN ligands were exchanged by water, the two times positive complex charge needed to be compensated, evidently by SCN counter anions. This exchange would also explain the more positive zeta potential.

Table 50: TGA, zeta potential and particle size measurements of all ruthenium-functionalized ND particles before and after irradiation in water with a 500 W Hg/Xe lamp for 60 min

mDND particle	$load_{before}$ [mmol g^{-1}]	$load_{after}$ [mmol g^{-1}]	ζ_{before} [mV] (pH)	ζ_{after} [mV] (pH)	D_V-(50) $_{before}$ [nm]	D_V-(50) $_{after}$ [nm]
L1-Ru1c	0.13	0.12	+34.6 (5.8)	+41.9 (5.9)	82.3	133
L2-Ru1d	0.17	0.16	+41.1 (6.3)	+45.7 (6.2)	95.4	96.2
L5-Ru1b	0.18	0.08	+36.0 (6.2)	+43.8 (6.4)	158	126
L1-Ru2b	0.13	0.11	+31.8 (6.1)	+45.8 (5.9)	80.4	103
L2-Ru2b	0.13	0.13	+40.1 (6.1)	+46.8 (6.3)	90.5	97.0
L8-Ru3	0.08	0.07	-2.01 (5.3)	+19.6 (4.0)	2530	892
L9-Ru3	0.11	0.09	+4.53 (5.3)	+18.6 (4.1)	1990	1440
L1-Ru4b	0.23	0.20	+46.9 (4.4)	+40.8 (4.5)	76.7	76.6
L2-Ru4b	0.33	0.30	+46.7 (3.8)	+43.4 (3.1)	99.0	78.5

The **mDND-L5-Ru1b** particles were not stable under irradiation. The ^{1}H-NMR spectra of the supernatant showed signals in the aromatic region and the surface loading was significantly decreased (0.18 → 0.08 mmol g^{-1}). A UV degradation mechanism could explain this observation. UV light < 365 nm is able to break π-bonds of internal alkynes and photopolymerization reactions forming cyclic structures are possbile.[389] Those structures, formed by adsorbed linker molecules **L5**, desorb from the surface, accelerated by the higher sample temperature, consequently leading to a lower

loading. The four ND-conjugates **mDND-L1-Ru1c**, **mDND-L1-Ru2b**, **mDND-L2-Ru1d** and **mDND-L2-Ru2b** exhibited sufficient stability under prolonged UV/Vis irradiation. These results are to some extent unexpected, as especially the tris(bipyridine)-ruthenium(II) complex is known to photodecompose under short-wavelength UV irradiation.[390-392] However, a few factors could improve the stability of the complex. The use of non-ligating anions, like PF_6, and the weakly coordinating solvent water do not favor the formation of intermediates after bpy cleavage. However, the role of the ND particles is more interesting. It was reported that the encapsulation of the complexes in rigid media, such as cation-exchange polymer-resin or zeolites, reduces the photolability due to destabilization of low-lying, metal-centered d-d states, which are populated during irradiation and initiate decomposition.[393] Apparently, the ND-complex interaction led to a destabilization of those d-d states, resulting in improved photostability.

3.4.2 Photoredox activity of ruthenium functionalized particles

The photocatalytic properties of the UV stable conjugates **mDND-L1-Ru1c/mDND-L2-Ru1d** and **mDND-L2-Ru2b** were studied in cooperation with the group of Prof. Dr. Geraldine Masson, Institut de Chimie des Substances Naturelles (ICSN), Gif-Sur-Yvette, France. The systems were tested and evaluated in the α-functionalization of carbamates[394,395] and the trifluoromethylation of olefins[396] under visible light irradiation (5 W blue LED) by PhD student Guillaume Levitre (Fig. 110). For the α-arylation of **34**, only 1 mol.% of **mDND-L1-Ru1c/mDND-L2-Ru1d**, calculated via TGA surface loading, instead of 2.5 mol.% using the pure photocatalyst **Ru1**, were required. **mDND-L2-Ru2b** also gave satisfactory results. Thus, two conclusions can be drawn. First, the DND carrier particles provide a significant benefit regarding the photocatalytic reaction. Due to the strong electronic coupling of DND particles and the Ru-based photocatalyst (cf. chapter 3.2.2.3.5), an efficient blue light absorption is possible leading to an enhanced interaction of substrates and excited metal complex. Second, neither complex ligand (bpy or tpy) nor linker system (conjugated vs. non-conjugated) influences the catalyst efficiency.

The scope of application was further tested in the trifluoromethylation of various olefins **37**, which readily reacted yielding the α-aryl-β-trifluoromethyl compounds **39**. In all reactions, the immobilized ruthenium-based photocatalysts illustrated comparable

activity as their homogenous analogues. After recycling of the ND-based catalytic system by simple centrifugation and washing, up to thirteen times no loss in activity was detected. In control experiments without any DND supported photocatalysts or with only **mDND**, no desired product was observed. Thus, the Ru-based photocatalyst was essential for the photocatalytic process. Furthermore, no complex leaching from the ND particles was detected, even after 24 h of irradiation using blue LEDs, which was expected after the exhibited stability under irradiation using a 500 W Hg/Xe lamp (cf. chapter 3.4.1).

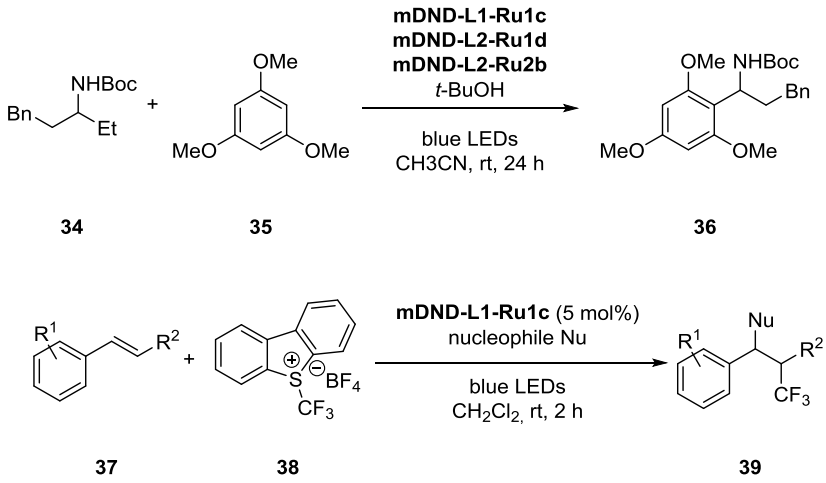

Fig. 110: Photocatalyzed α-arylation of **34** and trifluoromethylation of olefins **37**.

The attached Ru-complexes showed no loss in photocatalytic activity after attachment, but rather an enhancement due to strong electronic coupling. Irradiation stable ruthenium photocatalyst are not prone to deactivation by hydrogen bonding or steric hindrance, as no stronger interactions or sterical hindrance occur due to the lack of functional groups and the stable, octahedral geometry. Additionally, the ND particles influence the excited ruthenium complexes, leading to an extended exciton lifetime and consequently improving electron-hole separation.[397]

During photocatalytic experiments it is most likely that hydroxyl radicals are formed out of surface absorbed water by the Ru-based complexes, leading to an increased OH-termination of the ND particle surface. This side effect would decrease the generation of solvated electrons due to raising the valence band above the vacuum level (cf. chapter 1.3). Thus, the reduction reactions requiring solvated electrons, such as N_2 or CO_2, would be inhibited; however, a termination-exchange of the surface area, which is not covered with linker-complex structures, has no influence on the activity of

attached photocatalysts when being used in the shown photoredox reactions. In summary, the ruthenium-functionalized ND conjugates conclusively illustrate highly efficient photoredox catalysts and additionally convince with their recyclability.

3.4.3 Photocatalytic reduction of CO_2

Regarding the photocatalytic reduction of CO_2, a whole range of diamond materials comprising bare diamond electrodes, nanodiamond thin film coatings and dispersed nanodiamond suspensions were evaluated during this thesis. Different surface terminations of these materials, involving COOH- and H-termination, as well as Ru-complex functionalization were investigated, considering the results obtained by the photostability experiments in chapter 3.4.1. The liquid media used include aqueous $KHCO_3$, ultrapure water and the ionic liquids N_{1114} BTA and N_{1123} BTA.

3.4.3.1 Photoelectrochemical CO_2 reduction

Within the DIACAT project the cooperation partner from Oxford (Dr. Emina Hadzifejzovic and Dr. Mailis Lounasvouri, group of Prof. Dr. John S. Foord) investigated the photoelectrochemical reduction of CO_2, including several ND particles tested in chapter 3.4.1. **BDD** electrodes were coated with ND films by dropcoating 50 µl of 0.75 mg mL^{-1} suspension of various ND particles onto the clean **BDD** surface resulting in nanodiamond loadings of ~38 µg cm^{-2}. Hydrogenation of the (coated) electrodes was executed using H_2 plasma for 45 min at 600 °C. Higher current densities were obtained with hydrogen termination and using nanodiamond film coatings in comparison to uncoated, oxygen terminated **BDD** electrodes. The photoelectrocatalytic performance of the diamond electrodes was tested by chronoamperometry at -1.2 V vs. Ag/AgCl (1 M KCl) in 0.5 M $KHCO_3$ and -1.7 V vs. Ag/AgCl in 3:1 IL:DMSO containing 1 mol l^{-1} water. Sample irradiation was performed with either a commercial LCS-100 solar simulator from *Oriel Corporation* or a 500 W Hg/Xe arc lamp source from *LOT-Quantum Design* with the schematic setup shown in Fig. 109. The solar simulator operated a 100 W Xe lamp with integrated reflector equipped with an AM1.5G standard filter. In all experiments with this source, the samples were positioned at the distance as to enable the constant irradiation with the total output power of 1 Sun (100 mW/cm^2 illumination). After 1 h of reaction, a sample was extracted from the reaction volume and analyzed for the main CO_2 reduction product, formate, by ^{1}H NMR spectroscopy. For almost all samples, minor amounts of

methanol were also detected. The amounts of formate produced in one hour of photoelectrochemical CO_2 reduction reaction in aqueous 0.5 M $KHCO_3$ solution for variously treated diamond electrodes are shown in Table 51. Transitioning from dark conditions (electrochemical) to UV illumination (photochemical) the amount of formate increased, which indicates the involvement of solvated electrons originating from diamond due to UV irradiation.

In accordance with the results from Hamers *et al.*, no formate was detected for **O-BDD** under any irradiation conditions, whereas, for **H-BDD** formate production was observed (solar + UV).[220] ND film coatings (**pDND**, **BND**) improved the formate yield and allowed detection even for **O-BDD** cathodes due to surface enlargement of the nanostructured particles. H-terminated ND films produced the highest amount of formate, illustrating the influence of the termination on the electronic structure. Furthermore, the influence of the **BND** size was investigated (D_v(50) 730 nm vs. 175 nm). No difference in activity was seen illustrating that size did not affect formate production. The cleaned particles **cDND** showed a slight decrease in formate yield compared to **pDND**, indicating that impurities in the **pDND** sample accounted for some of the activity observed.

The three **Ru1**-functionalized samples **mDND-L1-Ru1c**, **mDND-L2-Ru1d** and **mDND-L5-Ru1b** were dropcoated on **O-BDD**, as the **O-BDD** electrode showed no catalytic activity in aqueous electrolyte and lower activity in RTILs compared to **H-BDD** correlating an observed activity of Ru-DND coated **OBDD** electrodes to the ruthenium functionalized ND particles. As the **Ru1**-functionalized samples were specifically investigated in detail using XAS and PES (cf. chapter 3.2.2.3.5), the photoelectrochemical experiments were focused on these samples leaving out **Ru2**-functionalized samples. Ru-functionalization improved the formate yield from 0.04 (**pDND-OBDD**) up to 0.09 µmol cm^{-2} h^{-1} (**mDND-L1-Ru1c-OBDD**). Control experiments in CO_2-saturated solution under UV irradiation in the absence of potential and in the dark did not yield detectable amounts of formate confirming that formate was the product of photoelectrochemical CO_2 reduction. For **mDND-L5-Ru1b**, decomposition of the linker or ligands under UV irradiation was also detected by the Oxford team.

A significant improvement in CO_2 reduction was observed in experiments involving ionic liquids N_{1114} BTA and N_{1123} BTA (Table 51). Due to the increased CO_2 solubility in ILs, a purely electrochemical CO_2 reduction reaction was observed for **H-BDD** in the

dark (0.09 µmol cm^{-2} h^{-1} of formate). Photocurrent induced by solar irradiation improved photoelectrocatalytic activity and formate production significantly. Comparison of the results with those obtained in aqueous electrolyte confirmed that CO_2 reduction was much more efficient in IL, resulting in an up to ~10-fold improvement in formate production rate corresponding to the enhanced solubility of CO_2 in ILs.[381,383]

Table 51: Formate production rates for diamond electrodes using different irradiation conditions in aqueous 0.5 M $KHCO_3$, 3:1 N_{1123} BTA:DMSO with 1 M H_2O and 3:1 N_{1114} BTA:DMSO with 1 M H_2O

Electrode	light source	formate ($KHCO_3$) [µmol cm^{-2} h^{-1}]	formate (N_{1123} BTA) [µmol cm^{-2} h^{-1}]	formate (N_{1114} BTA) [µmol cm^{-2} h^{-1}]
O-BDD	dark	0	-	-
	solar	0	0.10	0.16
	UV	0	-	-
H-BDD	dark	0	0.08	-
	solar	0.02	0.39	0.18
	UV	0.04	-	-
BND-OBDD	dark	-	-	-
	solar	-	0.46	0.74
	UV	0.04	-	-
pDND-OBDD	dark	-	-	-
	solar	-	0.31	0.42
	UV	0.04	-	-
H-BND-HBDD	dark	-	-	-
	solar	-	0.30	1.50
	UV	0.08	-	-
H-pDND-HBDD	dark	-	-	-
	solar	0.01	0.33	0.84
	UV	0.10	-	-
H-cDND-HBDD	UV	0.08	-	-
mDND-L1-Ru1c-OBDD	dark	0	-	-
	solar	0	-	0.74
	UV	0.09	-	-
mDND-L2-Ru1d-OBDD	dark	0	-	-
	solar	0	0.56	0.76
	UV	0.06	-	-
mDND-L5-Ru1b-OBDD	dark	0.16	-	-
	solar	0.08	0.78	1.17
	UV	-	-	-

In addition to a clear correlation between the diamond termination and product yield, it was also observed that N_{1114}BTA performed better than N_{1123}BTA for all tested electrodes. Furthermore, a significantly higher Faradaic efficiency was obtained. This improvement was observed both under dark conditions and with solar irradiation. These results suggested that it is possible to move from UV to solar irradiation, if ionic liquids are used.

The obtained results illustrated that Ru-functionalized DND films performed better than non-functionalized DND and bare **BDD** electrodes when irradiated with solar light. The formate yield in RTILs was similar for both non-conjugated (**L1**) and conjugated (**L2**) linker and substantially higher than in aqueous media under UV irradiation (0.74 µmol cm^{-2} h^{-1} vs. 0.09 µmol cm^{-2} h^{-1}). The system bearing the extended linker **L5** showed further enhanced activity, while exhibiting sufficient stability under solar light irradiation. In general, the formate yield in RTILs was on average two times greater for Ru-functionalized ND films than for non-functionalized ND-films. In summary, hydrogen-termination of the pure diamond electrodes, light irradiation and surface modification via ruthenium functionalization can be identified as factors that increase product yield in the photoelectrochemical CO_2 reduction reaction. For the ruthenium functionalized samples, coated on an **O-BDD** electrode, the observed catalytic activity using solar light could be related to solvated electrons, which were generated by a two-photon absorption via accessible surface states introduced by the ruthenium complex; however, transient absorption experiments by the DIACAT partner in Berlin still need to verify the generation.

Theoretical calculations from Uppsala University, Sweden (Prof. Karin Larsson and Dr. Shuainan Zhao) within the DIACAT project were performed to investigate the electron transfer between a terminated diamond surface and an attached liquid adlayer (water- or ion-based). Results from these calculations helped to understand how the electronic structure of the diamond-electrolyte surface is influenced by solvents and termination. The effects of a water adlayer on the electronic structure of a terminated diamond [111] surface were calculated using DFT. For H-terminated, undoped diamond no electron transfer was observed to a neutral water adlayer, whereas, for OH-termination this transfer was likely to happen. If one CO_2 molecule was added to the neutral water adlayer, the degree of electron transfer for OH-terminated surfaces was also reduced. However, substitutional B-doping was largely affecting and promoting the possibility

for an electron transfer from a terminated diamond [111] surface to a water-based adlayer. The interaction between N_{1123} BTA and differently terminated diamond [111] surfaces was also investigated. The most stable IL adsorption geometry was obtained for the situation with the sulfonyl groups of the BTA anion (cf. Fig. 108) positioned towards the H-terminated diamond surface (adhesion energy -6.5 eV). As the degree of electron transfer from surface to IL was not greater than for the water adlayer, the changed interfacial situation was not contributing to the improved CO_2 reduction. The latter was therefore solely due to the improved solubility of CO_2 in RTILs.

3.4.3.2 Photocatalytic CO_2 reduction by ND particle dispersions

Besides the photoelectrochemical reduction of CO_2 using modified, bulk **BDD** electrodes, the photocatalytic activity of nanodiamond particles in CO_2 reduction was also tested by irradiating nanodiamond dispersions without applying bias. First experiments were performed in Oxford using either solar or UV irradiation. 0.2 wt% of ND particles were dispersed in 15 mL of pure water or 0.1 wt% in 2 mL RTIL:DMSO (3:1) containing 1 mol l^{-1} water. After CO_2 saturation, the samples were irradiated for 1 h. The dispersions were centrifuged for 10 min at 10k rpm and the supernatants analyzed by ^{1}H NMR spectroscopy. Results from Oxford are presented in Table 52 and marked with a superscript. In comparison to the photoelectrochemical reactions, the results from photocatalytic testing with ND dispersions also exhibited formate and methanol production in pure water under UV irradiation. For **BND**, photo-induced etching of diamond, which was reported by Hamers *et al.*,[85] was detected, as formate was also formed in N_2-saturated dispersion. Carbon surface atoms of the milled particles show higher reactivity and are more readily cleaved from the lattice under UV irradiation, thus enabling formate formation.[108] After electron excitation/emission, the valence band holes needed to be refilled. Thus, in the absence of an electrical circuit, the oxidation reactions must either be mediated by a hole scavenger or the nanodiamond particles themselves. Oxidation of the diamond particle surface is most likely to happen, as water oxidation is not favored for diamond materials due to high overpotential.[85] UV irradiation of **H-BND**, dispersed in $N_{1123/1114}$ BTA/DMSO (3:1), was carried out for 10 min as DMSO was not stable under UV irradiation. The formate production rate was comparable to aqueous dispersions. Traces of formate (<1 µM) were detected in experiments with **H-BND** and **mDND-L2-Ru1d** dispersed in N_{1123} BTA under solar irradiation.

Based on the results from Oxford, the setup that was already used for the photostability testing (cf. chapter 3.4.1, Fig. 109) was tested in combination with GC-MS analysis of CO_2 reduction products. Using a polar free fatty acid phased column (type: SH-Stabilwax-DA), the detection of methanol and formic acid was possible. However, reaction solutions need to be acidified using phosphoric acid to generate formic acid from formate (pK_a = 3.75).[398] The tested, aqueous ND samples (0.2 wt.%) were CO_2-saturated and UV irradiated for 60 min. **mDND**, **pDND** and **H-pDND** showed no liquid product formation. The influence of metal impurities, i.e. zirconia debris for **mDND** and iron, aluminium and titanium for **pDND**, was investigated, but showed no effect on CO_2 reduction. Zhang *et al.* reported CO to be the main reduction product and did not detect methanol or formate when irradiating H-terminated, undoped DND particles.[108] Thus, for **BND** and **H-BND**, which showed formation of formate and methanol (Table 52), as well as photo-induced etching (**BND**) shown by Oxford, the production of CO was monitored qualitatively via IR analysis of the gas phase. Reference spectra of CO_2 and CO were measured in a gas cell (Appendix, Fig. 144a/b). For both molecules, the characteristic P- and R-branch were clearly seen and a detection of both species simultaneously was possible as there was no overlap between the key features of the gases.[108] For the CO monitoring experiments, the aqueous particle dispersion (0.2 wt.%) was placed in a quartz flask, which was closed with an gas-tight septum. After saturation with, first, N_2 (30 min) and then CO_2 (60 min), the dispersions were irradiated using the 500 W Hg/Xe lamp for a specific time, followed by injecting the gaseous supernatant directly from the gas-tight flask into the IR gas cell. For **BND** and **H-BND**, no CO was detected after 1 h and 2 h irradiation, although CO_2 was still present. Experiments at 4 h showed CO_2 and CO in the FT-IR spectra (Fig. 111a/b).

Due to saturation of the ATR spectrum with CO_2, the spectral region between 2080-2230 cm^{-1} was magnified to identify the P- and R-branch of CO for both, **BND** and **H-BND** (Fig. 111a/b, green graphs). However, control experiments in N_2-saturated solution also yielded CO after 4 h irradiation, proving that photo-induced etching that was reported for H-terminated ND particles by Zhang *et al.*[108] equally occurred for H- and COOH-terminated, B-doped particles **BND** and **H-BND**. A control experiment of **H-BND** in N_2-saturated dispersion for 4 h in the dark did, as expected, not yield any CO. Consequently, apart from CO produced from CO_2 by photocatalytic reduction, the photo-induced etching yielding CO also needs to be considered. For quantification, isotopic labelling using $^{13}CO_2$ would be required to determine the amount of ^{13}CO in

relation to ^{12}CO that was etched from the diamond nanoparticles. In the liquid phase of all tested dispersions, irradiated for 1 h, 2 h or 4 h, neither formate nor methanol were detected using GC-MS analysis.

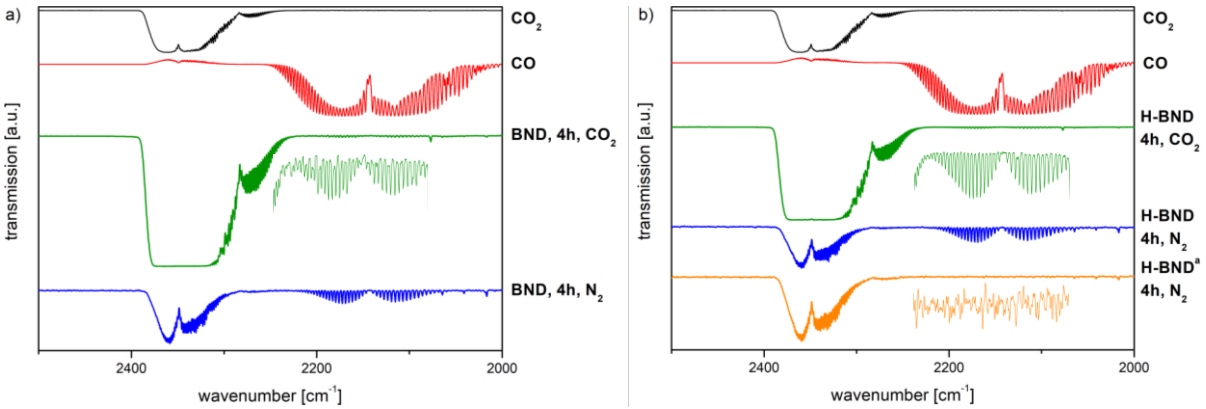

Fig. 111: FT-IR spectra of (a) CO_2, CO and **BND** irradiated for 4 h under CO_2 and N_2 saturated atmosphere and (b) CO_2, CO and **H-BND** irradiated for 4 h under CO_2 and N_2 saturated atmosphere and [a]4 h under N_2 saturated atmosphere without irradiation.

As repeated experiments using **BND** and **H-BND** particles showed no methanol or formic acid products using GC-MS analysis, the reasons for these unexpected results were investigated, which included determing the detection limit of the GC-MS system, the light emission of the 500 W Hg/Xe arc lamp below 225 nm and possible side reactions of the reduction products with the ND particles. In order to determine the retention of reduction products on the ND surface by adsorption, dispersions of **BND** and **H-BND** were prepared in aqueous solutions of methanol (5 and 50 ppm) and formic acid (50 and 100 ppm). After stirring for 60 min at r.t., the samples were centrifuged and the supernatant analyzed by GC-MS. The concentration of the added CO_2 reduction product in the supernatant remained unchanged, excluding product adsorption as the reason for non-detection. A re-oxidation of generated formate under UV irradiation was also ruled out, as no loss in formic acid was detected after 60 min irradiation of **BND**. The arc lamp system emitted light below 225 nm, which is needed to generate solvated electrons, despite being an extremely small amount (Appendix, Fig. 143). The system consisted of three parts containing quartz optics/windows, which could further decrease the amount of emitted short-wavelength UV: the lamp bulb itself, the condenser and the water filter. In Fig. 143, it can be clearly seen that without the water filter, the amount of UV light <230 nm can be increased. When removing water filter and condenser, up to ten times more UV was emitted. However, without the condenser, the light beam cannot be focused on the samples anymore and the beam

path cannot be closed by a shutter inducing a safety issue. As the samples also heat up when using a water filter, removing the latter presents a way to increase the UV output.

Table 52: Formate and methanol production rates for ND particles dispersed in different CO_2-saturated media under irradiation for 60 min

ND material	light source	solvent	formate production [µmol h^{-1}]	methanol production [µmol h^{-1}]
pDND	UV	H_2O	-	-
pDND[a]	UV	H_2O	-	-
H-pDND	UV	H_2O	-	-
BND[a]	UV	H_2O	0.04	0.02
BND	UV	H_2O	traces	-
BND	UV (no water filter)	H_2O	0.04	traces
BND	UV (no water filter) (no condenser)	H_2O	0.03	-
H-BND[a]	UV	H_2O	0.11	0.02
H-BND[a]	UV	H_2O	0.01	traces
H-BND	UV	H_2O	-	-
H-BND	UV (no water filter)	H_2O	-	-
H-BND[a]	UV[b]	N_{1123} BTA	0.15	-
H-BND[a]	UV[b]	N_{1114} BTA	0.04	-
mDND-L1-Ru1c	UV	H_2O	-	-
mDND-L2-Ru1d	UV	H_2O	-	-
Cu-oDND	UV	H_2O	-	-
pDND[a]	solar	N_{1123} BTA	-	-
pDND[a]	solar	N_{1114} BTA	-	-
BND[a]	solar	N_{1123} BTA	-	-
BND[a]	solar	N_{1114} BTA	-	-
H-BND[a]	solar	N_{1123} BTA	traces	-
H-BND[a]	solar	N_{1114} BTA	-	-
mDND-L2-Ru1d[a]	solar	N_{1123} BTA	traces	-

[a]experiments done at Oxford, [b]irradiated for 10 min, formate production calculated as per hour for comparison.

The supernatants obtained from reactions with **BND** and **H-BND** in the setup in Würzburg were additionally analyzed in Oxford using the 700 MHz ^{1}H-NMR setup with a sensitivity down to 0.5 µM (<100 ppb). As can be seen in Table 52, removal of the water filter was required to obtain significant formate production for **BND** dispersions (0.04 µmol h^{-1}). Without the condenser the yield was slightly decreasing due to the unfocused light emitted (0.03 µmol h^{-1}). Formate was the main product again and methanol was detected in traces. For **H-BND**, no formate production was detected in water. As the particles heavily agglomerated and showed extremely hydrophobic behavior, i.e. sticking to the stirring bar and beaker wall, no dispersed particles were available for photocatalysis. Insignificant formate production was observed for those particles of the same batch (0.01 µmol h^{-1}) in the setup in Oxford. Considering these analysis results, the sensitivity of the GC-MS setup detecting the reduction products in the µM range (<<1 ppm) was the limiting factor. Further method and split mode optimization of the GC-MS setup led to detection limits of 0.5 µM for MeOH and 1.0 µM for formic acid, while all formed formate can be effectively protonated by adjusting the pH to 1.5 with conc. phosphoric acid. However, irradiation of **mDND-L1-Ru1c**, **mDND-L2-Ru1d** and **Cu-oDND** using the protocol described in the beginning of chapter 3.4.3.2 in combination with the optimized analysis did neither yield methanol nor formate, indicating that for the analysis using GC-MS a higher conversion of CO_2 is mandatory.

In summary, it was shown that dispersed ND particles also exhibit activity regarding the reduction of CO_2. However, for the irradiation of ND particles, the stability in dispersion, the electronic structure, as well as the photo-induced etching of the NDs need to be considered. B-doped ND particles enabled the reduction of CO_2; however, diamond etching forming CO was observed. The involvement of solvated electrons during the reduction process is currently further investigated in transient absorption experiments carried out at the DIACAT partner in Berlin. The most challenging part of irradiating dispersion is the generation of stable dispersions before and during irradiation. Hydrophobic particles, such as **H-BND**, diminish or impede surface reactivity due to strong agglomeration. Surface oxidation during irradiation can lead to a loss of reactivity; however, addition of hole scavengers, e.g. the sodium sufite/sulfate system,[220] to prevent the oxidation led to strong agglomeration, even for **BND** particles. In RTILs, the colloidal stability was given, but the analysis of reduction products is challenging, as injecting ionic liquids supernatants on a GC column is not possible,

except for utilizing a sacrificial pre-column. A concentration of the CO_2 reduction products by extraction in aqueous phase in the µM range is not feasible, unless the reaction volumes are increased substantially. For ^{1}H-NMR spectroscopy of experiments in RTILs, DMSO needs to be added, which decomposes within minutes under UV irradiation. Moving to solar irradiation prevents this degradation, but also the emission of electrons from the B-doped materials. Thus, in future work the efficiency of the CO_2 reduction needs to be improved to ensure product detection using the GC-MS setup. One possible conception would be to extend the photoelectrocatalytic approach already successfully established for ND-coated diamond electrodes by the partner from Oxford (cf. chapter 3.4.3.1) also for ND dispersions.

4. Summary

In this work the catalytic activity of nanodiamond particles with different dopants and surface terminations and of diamond nanomaterials funtionalized with ruthenium-based photocatalysts was investigated, illustrating materials application in photoredox chemistry and the photo(electro)catalytic reduction of CO_2. Regarding the application of diamond nanomaterials in photocatalysis, methods to fabricate and characterize several (un)doped nanoparticles with different surface termination were successfully developed. Various photocatalysts, attached to nanodiamond particles via linker systems, were tested in photoredox catalysis and the photo(electro)catalytic reduction of CO_2.

In addition to the production and characterization of well-known detonation nanodiamond materials, such as milled (**mDND**),[274,275] air oxidized (**oDND**),[290] thermally annealed/graphitized (**gDND**)[268] and hydrogenated (**H-DND**)[304-306] DND, the focus was set on the purification of pristine DND (**pDND**). The developed multistep cleaning of **pDND**, involving the use of conc. hydrochloric acid, sodium hydroxide and piranha solution, allowed for the reduction of the overall content of impurities by more than 650 ppm (60%). Yet, the developed cleaning procedure presented a compromise. On the on hand, the content of photocatalytically active impurities (Al, Fe, Ti) was substantially reduced. However, on the other hand, sulfur and in particular chlorine were enriched due to the use of sulfuric and hydrochloric acid.

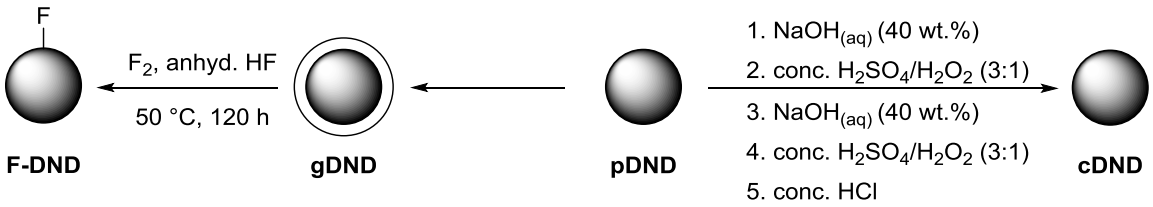

Fig. 112: Newly developed synthesis routes for DND-based materials **cDND** and **F-DND**.

For the production of fluorinated DND (**F-DND**), a mild wet-chemical fluorination technique, using anhydrous hydrogen fluoride and elemental fluorine at moderate temperature (50 °C) and ambient pressure, was developed. This procedure allowed for the fabrication of highly fluorinated ND particles (up to 11.5 wt.% fluorine). Solid-state NMR spectroscopy, assisted by theoretical calculations, proved highly suitable to determine the nature of the surface-bound fluorine to be $CF_2(H)$.

The scope of the reaction was also successfully demonstrated on polycrystalline, B-doped and single-crystalline CVD material. Milling of (un)doped, polycrystalline CVD material, following and adapting a procedure developed by Heyer *et al.*,[44] yielded undoped (**PC-ND**), boron-doped (**BND**) and phosphorus-doped (**PND**) nanodiamond particles. The doped materials enable energy-up conversion to use visible light by introducing dopant related electronic states in the band gap of diamond. For electrochemical grade **BDD**, the initial boron concentration was reduced by 15% after milling, yielding a boron content of ~1060 ppm in the particles. The nanostructuring introduced π^*-states close to the conduction band of diamond, related to C-B bonds at the particle surface. Thus, a reduction of the large diamond band gap made the **BND** particles a suitable candidate for photocatalytic CO_2 reduction.[326] **PND** particles were produced by milling a P-doped, polycrystalline CVD film. A homogenous phosphorus distribution inside the [111] facets and a concentration of ~20 ppm for particle sizes down to ~75 nm was observed (~8% loss during milling). Cathodoluminescence measurements clearly showed that the donor character of the phosphorus was preserved in the **PND** particles.

The surface preparation of diamond materials towards enhanced photocatalytic activity by introducing accessible surface states in the diamond band gap was achieved by functionalization with transition metal complexes. A standard protocol of functionalizing diamond materials with metal complexes and a set of characterization methods was developed and established. The alkyne-functionalized ruthenium(II) complexes **Ru1**[335,339] and **Ru2**[339] were attached via CuAAC reactions to **mDND** particles bearing the azide-functionalized, phenylene-based linker system **L1** and **L2**, as well as the tolane-based system **L5** (Fig. 113).

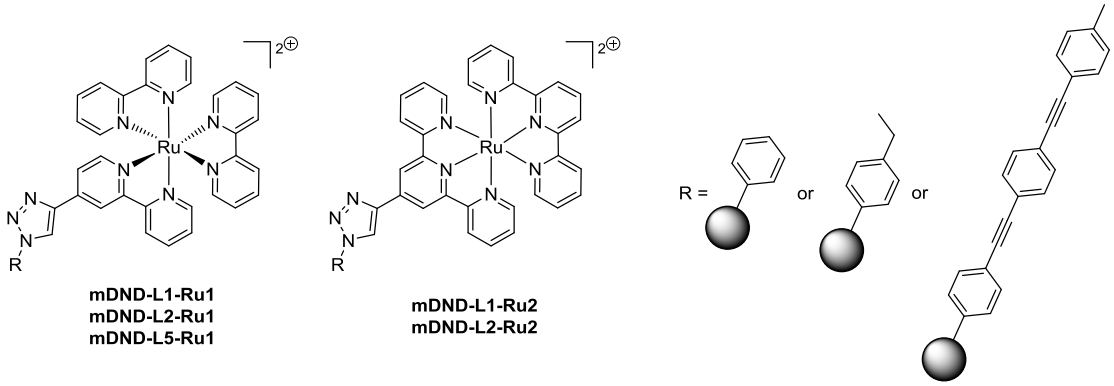

Fig. 113: Synthesized **Ru1**- and **Ru2**-DND-conjugates.

Applying the developed protocol allowed for the attachment of up to ~1.20 wt.% ruthenium on the particle surface. The scope of the protocol was demonstrated by the TM complex functionalization of directly azide-functionalized particles **N_3-DND**,[362] **H-DND**, as well as acid- and hydrogen-terminated, B-doped particles **BND** and **H-BND**.

X-ray absorption spectroscopy indicated an efficient electronic coupling between the ND particles and the ruthenium dyes due to orbital overlap between the ligand and ND orbitals. Photoemission spectroscopy revealed that the HOMO of the dye was 0.9 eV above the VBM and that an electron transfer from **Ru1** to the VB of ND was likely. DFT calculations suggested that an electron transfer from the VB to an empty positive surface state via a conjugatively (**L2**) or non-conjugatively (**L1**) linked **Ru1** was possible using visible light excitation.

Acid-functionalized **Ru3**[340] was successfully attached to amine-functionalized **mDND-L8**/**L9** particles via carboxamide coupling (Fig. 114). However, **Ru3** needs to be modified in two ways, if attached to ND particles. First, only one carboxylic acid group in the ligand periphery is required to avoid covalent aggregation. Second, the thiocyanate ligands, which were not stable in aqueous dispersion over time, need to be replaced. Direct formation of complex **Ru4** on tpy functionalized ND particles proved not suitable as on the one hand the oxophilic ruthenium precursor strongly adsorbed to the ND surface and on the other hand the chloride ligands easily exchanged with water molecules. Copper-coating of oxidized DND (**oDND**) and amine terminated DND (**NH_2-DND**)[368] yielded particles with up to ~15 wt.% of copper on the particle surface, mainly consisting of copper(II) due to oxidation by oxide or hydroxide formation.

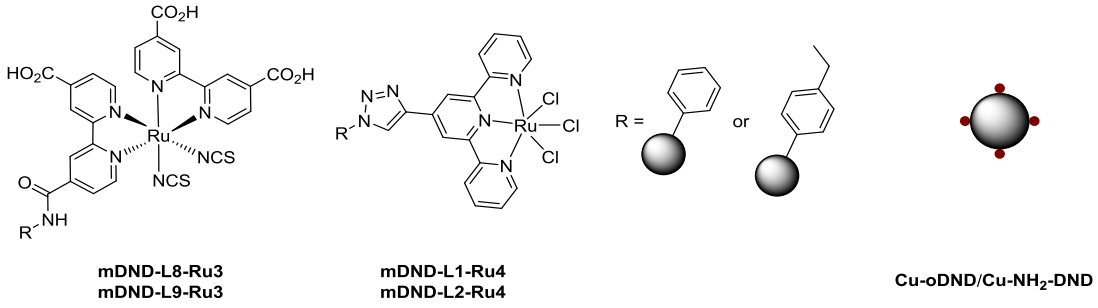

Fig. 114: **Ru3**- and **Ru4**-functionalized Ru-DND-conjugates and copper-coated particles **Cu-oDND** and **Cu-NH_2-DND**.

Photostability experiments of various ND samples demonstrated that UV irradiation had no influence on the diamond itself, but on the surface termination. H-termination of particles was damaged significantly. The functionalized particles **mDND-L1/L2-Ru1** and **mDND-L1/L2-Ru2** were highly stable.

Furthermore, **mDND-L1/L2-Ru1** and **mDND-L2-Ru2** showed a high efficiency as photoredox catalyst in organic reactions under blue light irradiation (365 nm). High recyclability of the conjugates was successfully proven with no decrease in catalytic activity (Fig. 115).

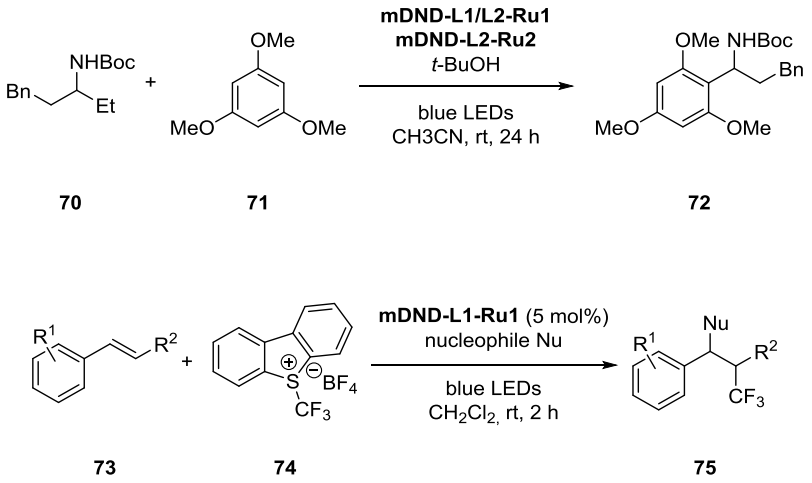

Fig. 115: Photoredox catalyzed reactions of DND-Ru-conjugates.

Photoelectrochemical CO_2 reduction experiments, applying bare diamond electrodes and nanodiamond film coatings in aqueous electrolyte solution, showed that CO_2 can be efficiently reduced. Formate was the main liquid product, with also minor amounts of methanol also being detected by ^{1}H-NMR analysis. ND film coatings (**pDND**, **BND**) on **BDD** electrodes improved the formate yield due to surface enlargement. Ru-functionalization improved the formate yield from 0.04 (**pDND-OBDD**) up to 0.09 µmol cm^{-2} h^{-1} (**mDND-L1-Ru1c-OBDD**). A significant improvement in CO_2 reduction was obtained involving ionic liquids. CO_2 reduction proceeds more efficiently in RTILs, resulting in an up to ~10-fold improvement in formate production rate in comparison to the aqueous electrolyte. It was possible to move from UV to solar irradiation, if ionic liquids were used. The obtained results showed that Ru-functionalized DND films performed better than non-functionalized DND and bare BDD electrodes when irradiated with solar light. The formate yield in IL was similar (0.74 vs. 0.76 µmol cm^{-2} h^{-1}) for both non-conjugated (**L1**) and conjugated linker (**L2**) (Fig. 116).

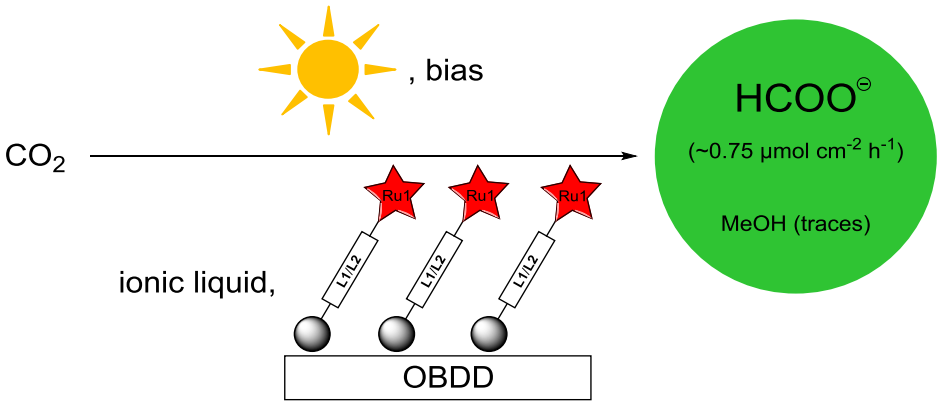

Fig. 116: Photoelectrocatalytic conversion of CO_2 into formate using **mDND-L1/L2-Ru1** coated **OBDD** electrodes in ionic liquid.

The extended, tolane-based linker **L5** exhibited even higher activity (1.17 µmol cm^{-2} h^{-1}) under solar light irradiation. In general, in ILs, the formate yield for functionalized ND-films was on average two times higher than for non-functionalized ND-films. Thus, hydrogen-termination of the diamond, light irradiation, use of ionic liquids and surface functionalization with TM complexes could be identified as factors that increased product yield.

ND particles illustrated activity regarding the reduction of CO_2 as well. For the irradiation of ND particles, the dispersion stability, the electronic structure, as well as the crystalline quality of the NDs were of utmost importance. The most challenging part was the generation of stable dispersions before and during irradiation. Hydrophobic **H-BND** particles exhibited reduced reactivity due to strong agglomeration; however, **BND** particles readily reduced CO_2 to formate (0.04 µmol cm^{-2} h^{-1}) under UV irradiation.

5. Zusammenfassung

In dieser Arbeit wurde die katalytische Aktivität von Nanodiamant-Partikeln mit unterscheidlichen Dotierungen und Oberflächenterminierungen, sowie von Diamant-Nanomaterialien, die mit Photokatalysatoren auf Rutheniumbasis funktionalisiert wurden, untersucht. Die Verwendung der Materialien in Photoredox-Experimenten und in der photo(elektro)katalytischen Reduktion von CO_2 konnte verdeutlicht werden. Für die Verwendung von Diamant-Nanomaterialien in der Photokatalyse wurden erfolgreich Methoden zur Herstellung und Charakterisierung zahlreicher (un)dotierter Nanopartikeln mit unterschiedlicher Oberflächenterminierung entwickelt. Verschiedenartige Photokatalysatoren, die mit Hilfe von Linker-Systemen an Nanodiamant-Partikel angebunden wurden, wurden in der Photoredox-Katalyse und der photoelektrokatalytischen Reduktion von CO_2 untersucht.

Neben der Herstellung und Charakterisierung von bereits bekannten Detonations-Nanodiamant Materalien, wie beispielsweise gemahlenem (**mDND**),[274,275] luft-oxidiertem (**oDND**),[290] thermisch behandeltem/graphitisiertem (**gDND**)[268] und hydriertem (**H-DND**)[304-306] DND, wurde spezielles Augenmerk auf die Aufreinigung von kommerziell erhältlichem DND (**pDND**) gelegt. Das entwickelte, mehrstufige Aufreinigungsverfahren von **pDND** beinhaltete die Verwendung von konz. Salzsäure, Natronlauge und Piranha-Lösung und ermöglichte es, die Gesamtverunreinigungen um mehr als 650 ppm (60%) zu verringern (Abb. 1). Dennoch stellte die Aufreinigungsmethode einen Kompromiss dar. Auf der einen Seite wurde der Anteil an photokatalytisch aktiven Verunreinigungen (Al, Fe, Ti) erheblich verringert, auf der anderen Seite jedoch Schwefel und inbesondere Chlor durch die Verwendung von Schwefel- und Salzsäure angereichert.

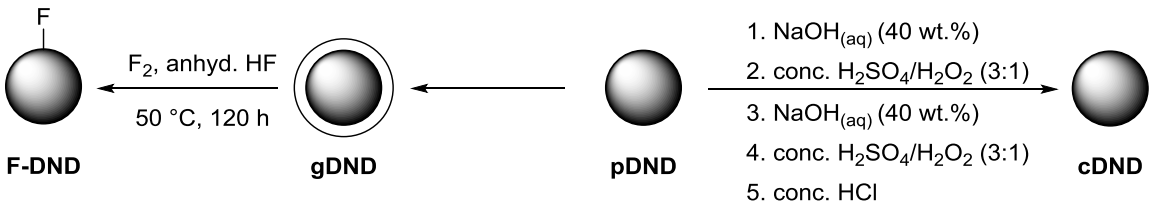

Abb. 1: Neu entwickelte Syntheserouten für die DND-basierten Materialien **cDND** und **F-DND**.

Für die Herstellung von fluorierten DND-Partikeln (**F-DND**) wurde eine nass-chemische Fluorierungsmethode entwickelt, die wasserfreien Fluorwasserstoff und elementares Fluor unter moderaten Temperaturen (50 °C) und Umgebungsdruck verwendete (Abb. 1). Das Vorgehen ermöglichte die Produktion von in hohem Maße fluorierten ND Partikeln mit einem Fluorgehalt von bis zu 11.5 wt.%. Festkörper NMR-Spektroskopie in Kombination mit theoretischen Berechnungen identifizierten die an der Oberfläche angebundenen Fluor-Atome als CF_2(H)-Gruppen. Die Anwendungsbreite der Reaktion konnte mit der Fluorierung von polykristallinem, B-dotiertem und einkristallinem CVD Material nachgewiesen werden.

Das Vermahlen von (un)dotiertem, polykristallinem CVD Material erfolgte unter Verwendung und Anpassung eines von Heyer *et al.*[44] entwickelten Verfahrens und erzielte undotierte (**PC-ND**), Bor-dotierte (**BND**) und Phopshor-dotierte (**PND**) Nanodiamant-Partikel. Die dotierten Materialien ermöglichten eine Verwendung von sichtbarem Licht, indem die Dotierungsstoffe elektronische Niveaus in der Bandlücke des Diamanten einführen. Für **BDD** Elektroden mit elektrochemischem Reinheitsgrad wurde die ursprüngliche Bor Konzentration nach dem Vermahlen um 15% reduziert, was zu einem Borgehalt von ~1060 ppm in den Partikeln führte. Die Nanostrukturierung hatte die Einführung von π^*-Zuständen nahe des Leitungsbandes von Diamant zur Folge, was auf C-B Bindungen an der Paritkeloberfläche zurückzuführen war. Aufgrund dieser Beobachtung stellten **BND** Partikel geeignete Kandidation für die photokatalytische CO_2 Reduktion dar.[326] **PND** Partikel wurden durch die Vermahlung eines P-dotierten, polykristallinen CVD Films hergestellt. Eine homogene Verteilung des Phosphors innerhalb der [111]-Facetten und eine Konzentration von ~20 ppm für Partikel mit einer Größe bis zu ~75 nm konnten nachgewiesen werden (~8% Masseverlust durch Mahlprozess). Kathodolumineszenz-Messungen belegten eindeutig, dass der Donor-Charakter des Phosphors in den **PND** Partikeln erhalten blieb.

Die Oberflächen-Modifikation von Diamant-Materialien hin zu erhöhter photokatalytischer Aktivität aufgrund der Einführung elektronisch zugänglicher Oberflächenzustände innerhalb der Diamant-Bandlücke wurde durch die Funktionalisierung mit Übergangsmetall-Komplexen erzielt. Ein Standardprotokoll zur Funktionalisierung von Diamant-Materialein mit Metall-Komplexen und ein Set an Charakterisierungsmethoden wurden entwickelt und etabliert. Die Alkin-

funktionalisierten Ruthenium(II)-Komplexe **Ru1**[335,339] und **Ru2**[339] wurde mittels einer CuAAC Reaktion an **mDND** Partikel, die die Azide-funktionalisierten, Phenylen-basierten Linker-Systeme **L1** und **L2**, sowie das Tolane-basierte System **L5** tragen, angebunden (Abb. 2). Es konnten so bis zu ~1.20 wt.% Ruthenium auf der Partikel-Oberfläche angebunden werden. Die Anwendungsbreite der Methode konnte durch die Funktionalisierung von direkt Azid-funktionalisierten Partikeln **N_3-DND**,[362] **H-DND**, sowie Säure- und Wasserstoff-terminierten, B-dotierten Partikeln **BND** und **H-BND** mit Übergangsmetall-Komplexen nachgewiesen werden.

Röntgenabsorptionsspektroskopie-Messungen deuteten eine effiziente elektronische Kopplung zwischen den ND Partikeln und den Ruthenium-Farbstoffen an, basierend auf einer Orbitalüberlappung zwischen Ligand- und ND-Orbitalen. Photoelektronen-spektroskopie belegte, dass das HOMO von **Ru1** energetisch gesehen 0.9 eV überhalb des VBM liegt und ein Elektronentransfer von **Ru1** in das Valenzband des ND möglich ist. DFT Berechnungen legten zudem nahe, dass ein Elektronentransfer vom VB in einen leeren, positiven Oberflächenzustand über den konjugiert (**L2**) oder nicht-konjugiert (**L1**) angebundenen **Ru1** Komplex bei Anregung mit sichtbarem Licht möglich ist.

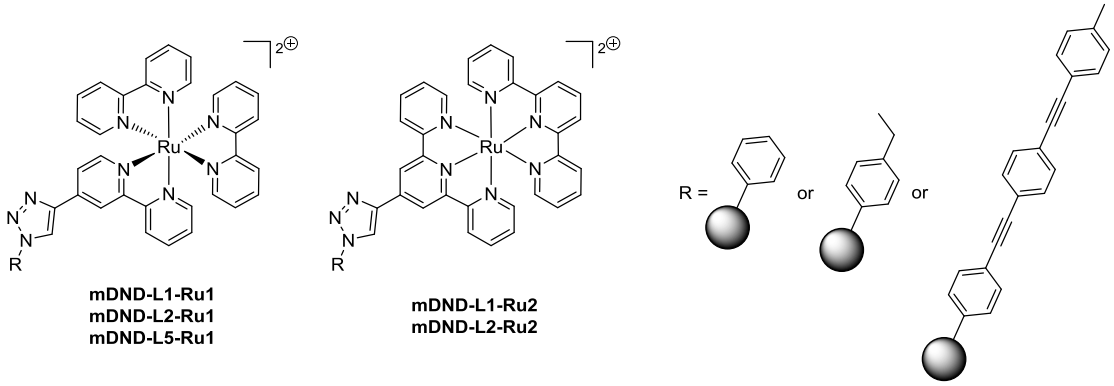

Abb. 2: Synthetisierte **Ru1**- and **Ru2**-DND-Konjugate.

Der Säure-funktionalisierte Komplex **Ru3**[340] wurde erfolgreich an die Amin-funktionalisierten Partikel **mDND-L8/L9** mittels Carbonsäureamid-Kupplung angebunden (Abb. 3). Dennoch muss der Komplex **Ru3** bei der Anbindung an ND-Partikel modifiziert werden. Zum einen ist es zwingend notwendig, dass nur eine Säurefunktion in der Ligandensphere vorhanden ist, um kovalente Aggregation zu verhindern. Zum anderen sollten die Thiocyant-Liangend ausgetauscht werden, da sie über längere Zeit in wässriger Dispersion nicht stabil sind.

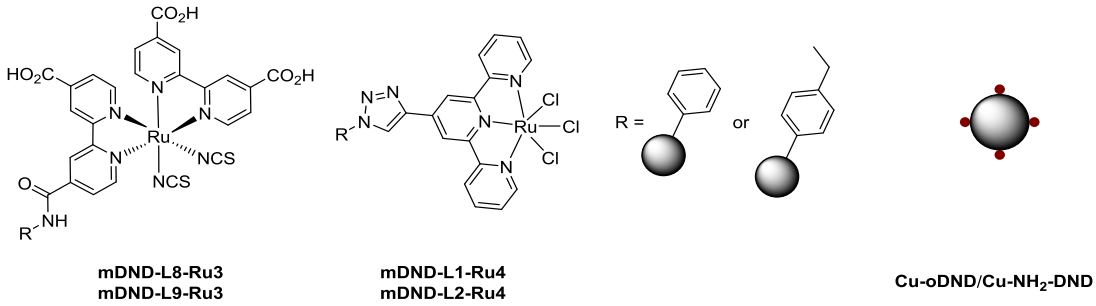

Abb. 3: **Ru3**- und **Ru4**-funktionalisierte Ru-DND-Konjugate und Kupfer beschichtete Partikel **Cu-oDND** und **Cu-NH$_2$-DND**.

Die direkte Komplexierung von **Ru4** auf tpy-funktionaliserten ND Partikeln erwies sich als ungeeignet, da einerseits die oxophile Ruthenium-Vorstufe an die ND-Oberfläche adsorbierte und andererseits die Chlorid-Liganden leicht durch Wassermoleküle ausgetauscht wurden. Die Beschichtung von oxidiertem DND (**oDND**) und Amin-terminierten DND (**NH$_2$-DND**)[368] mit Kupfer erzielte Partikel mit bis zu ~15 wt.% Kupfer auf der Oberfläche, wobei hauptsächelich Kupfer(II), aufgrund von Oxidation durch Oxid- oder Hydroxid-Bildung, vorliegt.

Experimente zur Untersuchtung der Photostabilität verschiedener ND-Proben belegten, dass Bestrahlung mit UV-Licht keinen Einfluss auf den Diamant selbst, aber auf die Oberflächen-Terminierung hat. Die H-Terminierung der Partikel wurde erheblich beschädigt. Die funktionalisierten Partikel **mDND-L1/L2-Ru1** und **mDND-L1/L2-Ru2** wiesen erhöhte Photostabilität auf.

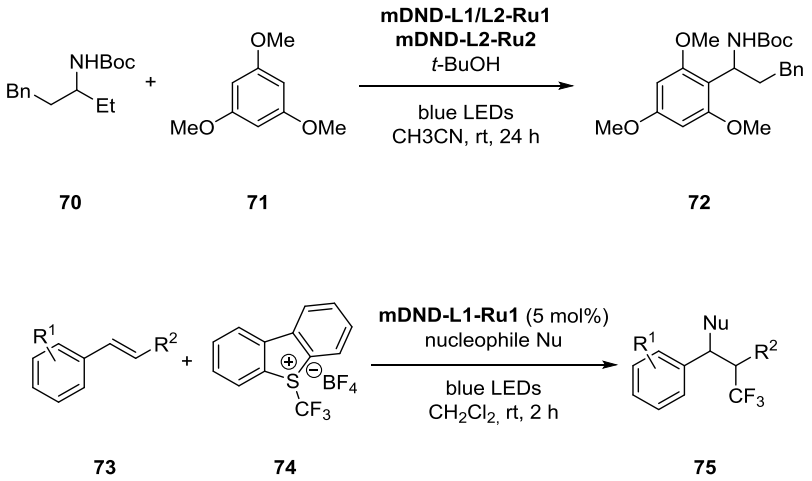

Abb. 4: Photoredox katalysierte Reaktionen von DND-Ru Konjugaten.

Des Weiteren fanden **mDND-L1/L2-Ru1** und **mDND-L2-Ru2** als hoch-effiziente Photoredox-Katalysatoren Anwendung in organischen Reaktionen unter Bestrahlung

mit blauem Licht (365 nm). Die Wiederverwertbarkeit der Konjugate wurde erfolgreich nachgewiesen und dabei kein Verlust der katalytischen Aktivität festgestellt (Abb. 4).

Photoelektrochemische Experimente zur Reduktion von CO_2 unter Verwendung von reinen Diamant-Elektroden und Nanodiamant-Beschichtungen in wässriger Elektrolytlösung zeigten, dass CO_2 wirksam reduziert wurde. Das flüssige Hauptprodukt war Formiat, wobei in der ^{1}H-NMR Analyse auch kleinere Mengen an Methanol detektiert wurden. ND-Beschichtungen (**pDND**, **BND**) auf **BDD** Elektroden verbesserten die Ausbeute an Formiat aufgrund der Oberflächenvergrößerung. Die Ru-Funktionalisierung der Partikel führte zu einer weiteren Verbesserung der Formiat-Ausbeute von 0.04 (**pDND-OBDD**) zu 0.09 µmol cm^{-2} h^{-1} (**mDND-L1-Ru1c-OBDD**). Eine deutliche Optimierung in der CO_2 Reduktion wurde durch die Verwendung von ionischen Flüssgkeiten beobachtet. Die CO_2 Reduktion verlief in RTILs effizienter, was in einer im Vergleich zu wässrigen Elektrolyt-Lösungen bis zu zehnmal höheren Ausbeute an Formiat resultierte. Zudem war es mit der Verwendung von ionischen Flüssigkeiten möglich, Sonnenlicht an Stelle von UV zu nutzen. Die erhaltenen Ergebnisse zeigten, dass Ru-funktionalisierte ND-Beschichtungen eine höhere Aktivität als unfunktionalisierte ND Filme und reine BDD Elektroden unter Bestrahlung mit Sonnenlicht besaßen. Die Formiat-Ausbeute in ILs lieferte nahezu identische Ergebnisse (0.74 vs. 0.76 µmol cm^{-2} h^{-1}) für das nicht-konjugierte (**L1**) und konjugierte (**L2**) Linker-System (Abb. 5).

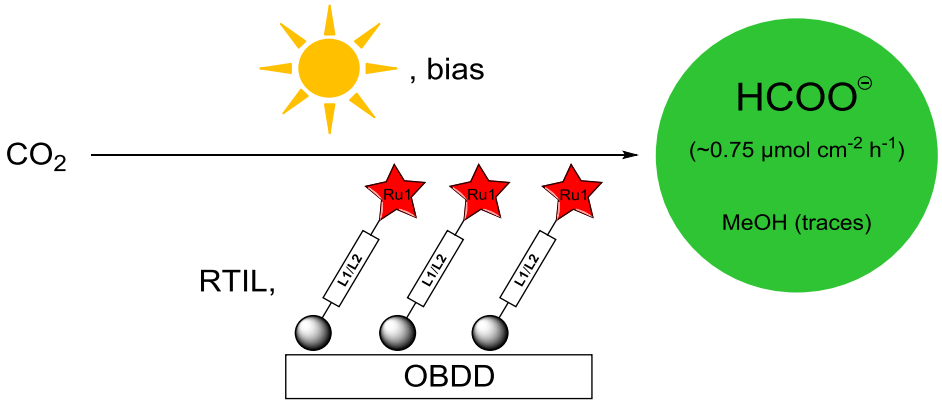

Abb. 5: Photoelektrokatalytische Umwandlung von CO_2 in Formiate unter Verwendung von **mDND-L1/L2-Ru1** beschichteten **OBDD** Elektroden in ionischen Flüssigkeiten (RTIL).

Mit einer Formiat-Produktion von 1.17 µmol cm^{-2} h^{-1} wies der Tolan-basierte Linker **L5** die höchste Aktivität unter Sonnenlichteinstrahlung auf. Im Allgemeinen ist die Ausbeute an Formiat in ILs für funktionalisierte Beschichtungen im Durchschnitt etwa

doppelt so groß wie für unfunktionalisierte ND-Beschichtungen. Folglich konnten die H-Terminierung von Diamant, Sonnenlichteinstrahlung, die Verwendung von ionischen Flüssigkeiten und die Oberflächen-Funktionalisierung mit Übergangsmetall-Komplexen als Einflussfaktoren auf die Formiat-Ausbeute identifiziert werden.

ND Partikel wiesen zudem Aktivität bei der Reduktion von CO_2 auf. Für die Bestrahlung von ND Partikeln waren sowohl die Dispersionsstabilität, als auch die elektronsiche Struktur der Partikel und die Kristallqualität von großer Bedeutung. Die Herstellung und Gewährleistung von stabilen Dispersionen vor und während der Bestrahlung stellte die größte Herausforderung dar. Hydrophobe **H-BND**-Partikel zeigten aufgrund von starker Agglomeration eine verringerte Reaktivität. **BND**-Partikel hingegen reduzierten CO_2 zu Formiat (0.04 µmol cm^{-2} h^{-1}) unter UV Bestrahlung.

6. Experimental section

6.1 Methods and devices

6.1.1 Chemicals and diamond materials

Chemicals, solvents and gases

All chemicals used for synthesis were reagent grade, obtained from either *Acros Organics*, *Alfa Aesar*, *Fluka*, *Merck* or *Sigma Aldrich* and, if not stated otherwise used without further purification.

All used solvents were distilled prior to use and, if required, dried using standard procedures. Purified water was obtained from demineralized water using reverse osmosis in an *Elga LabWater* Purelab Classic DI apparatus, with a resistivity R = 18.2 MΩcm^{-1} and a total amount of carbon (TOC) < 15 ppb (manufacturer`s specification). In this work, “water” is always referring to purified water.

As protective gas either nitrogen 5.0 or argon 5.0 (purity: 99.99990%) and for photocatalytic testing carbon dioxide (purity: >99.5%), all from *Linde*, were used.

Diamond materials

Acid purified detonation diamond (**pDND**, batch number: ND-0062) was purchased from *Gansu Lingyun Corp.* (P. R. China). Air oxidized (**oDND**, µdiamond Vox D) and amine-terminated (**NH_2-DND**, µdiamond Amine D) detonation diamond dispersions were purchased from *Carbodeon Ltd. Oy*., Finland. Polycrystalline, undoped CVD diamond (**PC-D**, polycrystalline electronic grade, 160-409-POLY2) and polycrystalline, B-doped CVD diamond (**BDD**, BDD Electrode Material, 145-500-0469) were purchased from *Element Six*, United Kingdom. P-doped microcrystalline CVD diamond material (**PDD**, 1-170117) was provided by Prof. Dr. Ken Haenen, Hasselt University, Belgium.

6.1.2 Working techniques

Degassing of reaction mixtures

Degassing of reaction mixtures was done using the freeze-pump-thaw method. The reaction mixture, which was frozen using liquid nitrogen, was degassed and unfrozen in vacuo in a sealed flask. In total, the procedure was performed three times.

Thin-layer chromatography

TLC was done on ALUGRAM Xtra SIL G/UV$_{254}$ plates from *Machery-Nagel*. Detection was possible by fluorescence quenching of the indicator at an excitation wavelength of 254 nm, by fluorescence excitation of the to be analyzed reagents at 365 nm or by means of suitable staining reagents.

Column chromatography

Purification using column chromatography was done on Geduran Si 60 silica from *Merck*. Length and diameter of the columns were specifically adjusted to each reaction. The used solvent mixtures are stated in percent by volume (v:v).

Milling and thermal treatment of diamond materials

For milling of CVD diamond films a *Fritsch* Pulverisette 23, equipped with grinding bowl and balls (3 mm) made from tempered steel, was used. Pristine DND (**pDND**) was milled using a *Netzsch* MiniCer stirred ball mill with zirconium oxide beads.

For air oxidation (**oDND**) a *HORST* Rohrofen 36 (1500 W) and for thermal-annealing (**gDND**) a *Carbolite* STF 16/450 oven have been used.

6.1.3 Analytics

NMR spectroscopy

^{1}H, ^{13}C, ^{19}F and ^{31}P NMR spectra were recorded at 27 °C with a *Bruker* AVANCE 400 FT-NMR spectrometer. The chemical shift δ is given in ppm. As internal standard for ^{1}H and ^{13}C spectra, the respective ^{1}H/^{13}C resonance signal of the used solvents was used. Signal assignment in proton-decoupled ^{13}C-spectra was supported by DEPT-135 spectra. For literature-unknown compounds, COSY, HSQC and HMBC spectra assisted signal assignment.

FT-IR spectroscopy

FT-IR spectra were either recorded with a *Jasco* FT/IR-430 equipped with an ATR unit (4000-600 cm^{-1}) or a *Thermo Fisher Scientific* Nicolet iS5 equipped with a DRIFTS unit (4000-400 cm^{-1}). The DRIFTS unit was only used for diamond containing samples.

Raman spectroscopy

Raman spectra were recorded with a *Thermo Scientific* DRX Raman microscope. The to be analyzed powders and (in)organic substances were homogenously and evenly distributed on a glass slide. The measurements were carried out using 30-100 scans with an exposure time of 2-5 sec and a laser power of 1-3 mW. The excitation wavelength was either 445 nm or 532 nm.

UV/Vis spectroscopy

UV/Vis spectroscopy was done with a *Jasco* V-630 spectrometer. If not stated otherwise, the solvent used was HPLC grade acetonitrile. The measurements range was 200-800 nm using a quartz cuvette with a layer thickness of 10 mm. The ND concentration was 25 µg/ml.

Elemental analysis

Elemental analysis (EA) for non-diamond samples was carried out with an *Elementar* Vario Micro Element Analyzer. EA for ND particles was done at Mikrolab Kolbe with an *Elementar* Vario Micro Cube CHNS for carbon, hydrogen and nitrogen. Fluorine and chlorine were determined using a *Metrohm* 883 Plus IC. Ruthenium was measured using a *Perkin Elmer* Analyst 200 AAS. The dopant levels of boron and phosphorus were determined with an *Analytik Jena* UV/Vis Specord 50 Plus.

Mass spectrometry

Mass spectrometry was carried out either with a *Finnigan* MAT Incos 500 or MAT 90 (EI) or a *Bruker Daltonics* mircOTOF Focus II (ESI). MALDI-TOF measurements were performed with a *Bruker Daltonics* autoflex II mass spectrometer, equipped with a 337 nm MidiNitrogen laser MNL. All MALDI-TOF spectra were acquired in the linear positive mode.

Melting points

Melting points were determined using a *Reichert Austria* Kofler heating stage in a range of 20-330 °C.

Thermogravimetry

Thermogravimetry (TGA) was carried out using a Perkin-Elmer STA 6000 under a flow of high purity nitrogen (60 ml min^{-1}). For the analysis, the sample (5-10 mg of fine

powder) was heated from 30-130 °C with a heating rate of 10 K/min. After holding temperature for 60 min at 130 °C, the heating continued with a rate of 5 K/min.

Particle size and zeta potential

Particle size determination and zeta potential measurements were performed in purified water at 25 °C using a *Malvern* Zetasizer Nanoseries Nano-ZS (dynamic light scattering, 173° backscatter mode). The ND dispersion (1 mg/ml) was not centrifuged and the pH value measured using the pH electrode. Zeta potentials were measured as single points. Size distributions were obtained using the Marquardt method and are given as volume distributions.

Electron microscopy

SEM images have been recorded at a *Zeiss* Ultra plus FESEM equipped with an *Oxford Instruments* X-Max EDX-detector. Aqueous ND samples were drop-coated on a silicon substrate and leave to air dry. CVD diamond films were directly glued on an aluminum support with conductive silver lacquer. Images were taken either using the Inlens or the SE2 detector with an acceleration voltage of 4.00 kV at different magnifications. For EDX measurements the voltage was increased to 15.0 kV.

For TEM imaging a *FEI* Titan 80-300 (300 kV) was used. The samples were dropcoated on a lacey carbon support and leave to air dry. Images were recorded by Prof. Dr. Martin Kamp.

X-ray spectroscopy

XRF measurements were performed by Prof. Dr. Jens Pflaum on a *General Electrics* reflectometer using Cu-K-alpha irradiation, whereas the $K\alpha_2$ part was filtered by means of a Ge-crystall/monochromator. For sample preparation, the DND powders were placed on a Si (100) substrate and, for the measurement itself the inclination angle was 15°. All spectra were already Si-background corrected.

XPS was performed by Amélie Venerosy, Dr. Hugues Girard and Dr. Jean-Charles Arnault using a monochromatized Al Kα anode (1486.6 eV) calibrated versus the Au $4f_{7/2}$ peak located at 84.0 eV. The spectrometer was equipped with an EA 125 hemispherical analyzer. The path energy in the analyzer was 20 eV corresponding to an energy resolution of 0.6 eV. The atomic concentrations of ruthenium, nitrogen, chlorine, carbon and oxygen were calculated from XPS spectra after corrections by the

photo-ionization cross-sections. Areas of the corresponding XPS core levels were obtained after a Shirley correction of the background.

6.1.4 Other devices

Sonication

For sonication of ND particles, a *Bandelin* Sonorex Digitec Typ DT52 (max. 80 W, 35 kHz) ultrasonic bath was used.

Centrifugation

For centrifugation either a *Hettich* EBA 21 Typ 1004 benchtop centrifuge with fixed angle rotor (max. 15k rpm) or a *Thermo Scientific* Sorvall MTX 150 ultracentrifuge with swing-out rotor (max. 52k rpm) was used. Containers made of polypropylene with a capacity of 1.5 mL (benchtop) and 4.0 mL (ultra) were used for centrifugation.

Vacuum pumps

Diaphragm and oil pumps of various kinds from *Vacuubrand* were used.

6.2 Production of ND materials

6.2.1 Detonation nanodiamond based materials

6.2.1.1 Pristine DND (pDND) and cleaned, pristine DND (cDND)

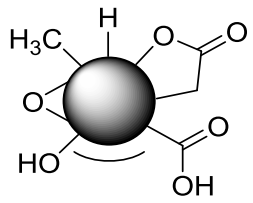

pDND/cDND

Commercially available, pristine DND (**pDND**) powder was analyzed as reference material.

FT-IR (DRIFTS): $\tilde{\nu}$ = 3691 (m), 3385 (br, ν(O-H)), 2951 (w, ν_{as}(C-H)), 2892 (w, ν_s(C-H)), 1719 (m, ν(C=O)), 1630 (s), 1326 (w), 1129 (br) cm^{-1}; **FT-IR** (ATR): $\tilde{\nu}$ = 3386 (br, ν(O-H)), 2948 (w, ν_{as}(C-H)), 2895 (w, ν_s(C-H)), 1722 (w, ν(C=O)), 1631 (s), 1319 (w), 1122 (br) cm^{-1}; **Raman** (λ_{ex} = 445 nm): $\tilde{\nu}$ = 1325 (m, ν(diamond), D band), 1592 (m, G band) cm^{-1}; **EA**: C 93.32, H 0.93, N 3.20 , Cl 1.17 wt.%; **DLS** (H_2O): 10% < 77.6 nm, 50% 170 nm, 90% < 386 nm; ζ (H_2O): +43.3 mV (pH = 6.3).

Each cleaning step of **pDND** was carried out in a 250 mL PFA flask. 1.00 g **pDND** was dispersed in 80 mL conc. sodium hydroxide solution (40 wt.%). After stirring at 120 °C for 24 h, the basic solvent was removed via centrifugation and the particles were washed with water (5x) until neutral pH value. Tubes for centrifugation are made of polypropylene. The particles were dispersed in 80 mL piranha solution (60 mL conc. sulfuric acid, 20 mL hydrogen peroxide (30 wt.%)) and stirred at 70 °C for 20 h. The particles were isolated and washed with water (5x). Afterwards, each of the two steps was repeated using the same conditions. For the last purification step the particles were dispersed in 80 mL conc. hydrochloric acid and stirred at 120 °C for 20 h. After removal of the acid and washing with water (5x), **cDND** was obtained as bright-gray, stable aqueous dispersion.

Recovery: 100 mL (8.5 mg/mL); **FT-IR** (DRIFTS): $\tilde{\nu}$ = 3690 (m), 3391 (br, ν(O-H)), 2958 (w, ν_{as}(C-H)), 2888 (w, ν_s(C-H)), 1734 (m, ν (C=O)), 1630 (s), 1323 (w), 1182 (w), 1138 (br) cm^{-1}; **FT-IR** (ATR): $\tilde{\nu}$ = 3407 (br, ν(O-H)), 2951 (w, ν_{as}(C-H)), 2893 (w, ν_s(C-H)), 1757 (w, ν(C=O)), 1635 (s), 1315 (w), 1157 (br) cm^{-1}; **Raman** (λ_{ex} = 445 nm): $\tilde{\nu}$ = 1325 (m, ν(diamond), D band), 1588 (m, G band) cm^{-1}; **EA**: C 92.39, H 1.02, N 2.87, Cl 1.98 wt.%; **DLS** (H_2O): 10% < 31.9 nm, 50% < 130 nm, 90% < 1340 nm; ζ (H_2O): +50.1 mV (pH = 6.1).

6.2.1.2 Milled DND (mDND)[274,275]

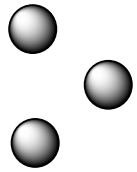

mDND

25.0 g **pDND** were dispersed in 200 mL of water and milled in a stirred ball mill at 4000 rpm using zirconium oxide beads. After 2 h of milling, the dispersion showed a stable particle size and the dark black dispersion was collected yielding three fractions. The first fraction was analyzed in detail and used for all experiments involving **mDND**.

Recovery: 300 mL (47.0 mg/mL), 300 mL (32.0 mg/mL); 250 mL (8.00 mg/mL); **FT-IR** (DRIFTS): $\tilde{\nu}$ = 3687 (w), 3436 (br, ν(O-H)), 2951 (m, ν_{as}(C-H)), 2891 (m, ν_s(C-H)), 1727 (s, ν (C=O)), 1632 (s), 1327 (w) cm^{-1}; **FT-IR** (ATR): $\tilde{\nu}$ = 3400 (br, ν(O-H)), 2947 (m, ν_{as}(C-H)), 2897 (m, ν_s(C-H)), 1724 (m, ν (C=O)), 1633 (s), 1317 (w), 1128 (br) cm^{-1}; **Raman** (λ_{ex} = 445 nm): $\tilde{\nu}$ = 1325 (m, ν(diamond), D band), 1590 (m, G band) cm^{-1}; **EA**: C 89.14, H 1.16, N 2.68 wt.%; **DLS** (H_2O): 10% < 1.36 nm, 50% < 3.38 nm, 90% < 5.72 nm; ζ (H_2O): +30.8 mV (pH = 6.2).

6.2.1.3 Air oxidized DND (oDND)[290]

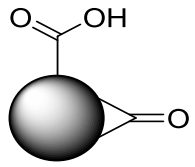

oDND

500 mg **pDND** were placed in a tube furnace and heated to 425 °C (rate 40 K min^{-1}) in air. After maintaining the temperature for 2 h, the oven was let to cool down to r.t. The **oDND** particles were obtained as gray powder.

Recovery: 481 mg; **FT-IR** (DRIFTS): $\tilde{\nu}$ = 3694 (w), 3375 (br, ν(O-H)), 2270 (m), 2164 (w), 1808 (s, ν(C=O)), 1622 (m), 1416 (w), 1280 (m, ν(C-O-C)) cm^{-1}; **FT-IR** (ATR): $\tilde{\nu}$ = 1796 (s, ν(C=O)), 1625 (m), 1421 (w), 1281 (m, ν(C-O-C)), 1099 (w) cm^{-1}; **Raman** (λ_{ex} = 445 nm): $\tilde{\nu}$ = 1325 (m, ν (diamond), D band), 1618 (m, G band) cm^{-1}; **DLS** (H_2O): 10% < 60.4 nm, 50% < 158 nm, 90% < 406 nm; ζ (H_2O): -42.0 mV (pH = 5.4).

6.2.1.4 Thermally annealed/graphitized DND (gDND)[268]

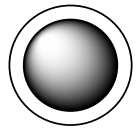

gDND

4.00 g **pDND** were placed in a Schlenk flask and heated to 170 °C under vacuum ($1.0 \cdot 10^{-3}$ mbar) for 8 h. 3.75 g of the pre-dried **pDND** were placed in a ceramic boat and put inside an argon flushed tube furnace. The oven was heated to 750 °C with a rate of 5 K min^{-1}. After maintaining

the temperature for 2 h at $1.4 \cdot 10^{-4}$ mbar, the oven was let to cool down to r.t. (rate 5 K min^{-1}). The **gDND** particles were obtained as dark gray powder.

Recovery: 3.67 g; **FT-IR** (DRIFTS): $\tilde{\nu}$ = 3691 (m), 3369 (br, ν(O-H)), 3211 (w), 2945 (s, ν_{as}(C-H)), 2879 (s, ν_s(C-H)), 1633 (s), 1392 (w, δ(C-H)), 1328 (m, δ(O-H)), 837 (m, γ(C-H)) cm^{-1}; **FT-IR** (ATR): $\tilde{\nu}$ = 3396 (br, ν(O-H)), 2945 (s, ν_{as}(C-H)), 2877 (s, ν_s(C-H)), 1647 (s), 1396 (w, δ(C-H)), 1336 (m, δ(O-H)), 1149 (w), 833 (m, γ(C-H)) cm^{-1}; **Raman** (λ_{ex} = 445 nm): $\tilde{\nu}$ = 1325 (m, ν(diamond), D band), 1584 (m, G band) cm^{-1}; **EA**: C 92.44, H 0.87, N 0.72 wt.%; **DLS** (H_2O): 10% < 132 nm, 50% < 207 nm, 90% < 372 nm; ζ (H_2O): +33.9 mV (pH = 6.3).

6.2.1.5 Hydrogenated DND (H-DND)[304-306]

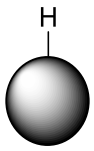

H-DND

As described in chapter 3.1.1.6, various DND materials were hydrogenated using the outlined plasma or annealing techniques from cooperation partners CEA and IAF. In further experiments, only the hydrogenated **pDND** particles (**H-pDND**) were used.

H-pDND$_{CEA}$: **FT-IR** (DRIFTS): $\tilde{\nu}$ = 3692 (s), 3348 (br, ν(O-H)), 3211 (w), 2946 (s, ν_{as}(C-H)), 2879 (s, ν_s(C-H)), 2154 (w), 1633 (s), 1392 (w, δ(C-H)), 1328 (m, δ(O-H)), 836 (m, γ(C-H)) cm^{-1}; **FT-IR** (ATR): $\tilde{\nu}$ = 3386 (br, ν(O-H)), 2947 (s, ν_{as}(C-H)), 2877 (s, ν_s(C-H)), 1635 (s), 1392 (w, δ(C-H)), 1323 (w, δ(O-H)), 1146 (w), 833 (m, γ(C-H)) cm^{-1}; **Raman** (λ_{ex} = 445 nm): $\tilde{\nu}$ = 1330 (m, ν(diamond), D band), 1573 (m, G band) cm^{-1}; **DLS** (H_2O): 10% < 140 nm, 50% < 935 nm, 90% < 4230 nm; ζ (H_2O): +45.8 mV (pH = 6.4).

H-pDND$_{IAF}$: **FT-IR** (DRIFTS): $\tilde{\nu}$ = 3691 (s), 3398 (br, ν(O-H)), 3211 (w), 2944 (s, ν_{as}(C-H)), 2879 (s, ν_s(C-H)), 1633 (s), 1394 (m, δ(C-H)), 1328 (m, δ(O-H)), 835 (m, γ(C-H)) cm^{-1}; **FT-IR** (ATR): $\tilde{\nu}$ = 3410 (br, ν(O-H)), 2947 (s, ν_{as}(C-H)), 2881 (s, ν_s(C-H)), 1635 (s), 1394 (w, δ(C-H)), 1331 (m), 1172 (w), 831 (m, γ(C-H)) cm^{-1}; **Raman** (λ_{ex} = 445 nm): $\tilde{\nu}$ = 1329 (m, ν(diamond), D band), 1584 (m, G band) cm^{-1}; **DLS** (H_2O): 10% < 140 nm, 50% < 935 nm, 90% < 4230 nm; ζ (H_2O): +45.8 mV (pH = 6.4).

6.2.1.6 Fluorination of DND materials

Fluorination of DND materials was carried out by Dr. Michael Drisch and PhD student Fabian Keppner at the laboratory of Prof. Maik Finze according to the following general

procedure: In a 100 mL PFA round bottom flask equipped with a magnetic stirring bar 100 mg (for **F-DND7**) or 50 mg (for **F-pDND**, **F-oDND** and **F-H-DND1**) DND powder was dispersed in 10 mL of anhyd. hydrogen fluoride. The suspension was cooled to -78°C and vacuum was applied for 5 min. 40 mol.% elemental fluorine was carefully added at -78 °C. After the suspension was warmed to r.t., it was stirred for 120 h at 50 °C. After removal of the volatiles *in vacuo* the obtained powder was dried for at least 24 h at $1 \cdot 10^{-3}$ mbar. Further purification is done by washing with unpolar solvents (3x with cyclohexane, *n*-pentane, *n*-hexane) and thermal annealing (300 °C for 2 h), yielding the particles as gray to dark gray powder.

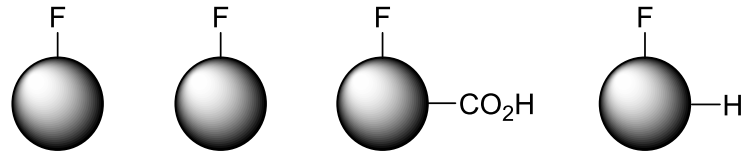

F-DND7 **F-pDND** **F-oDND** **F-H-DND1**

F-DND7 (starting material: **gDND**); **Recovery**: 78 mg; **FT-IR** (DRIFTS): $\tilde{\nu}$ = 3694 (m), 3428 (br, ν(O-H)), 3104 (w), 2976 (w, ν(FC-H)), 1757 (m, ν(C=O)), 1631 (s), 1237 (m, ν_{as}(C-F)), 1161 (m, ν_s(C-F)), 804 (w), 633 (m, δ(C-F)) cm^{-1}; **FT-IR** (ATR): $\tilde{\nu}$ = 1724 (w, ν(C=O)), 1630 (m), 1234 (s, ν_{as}(C-F)), 1155 (s, ν_s(C-F)), 636 (w, δ(C-F)) cm^{-1}; **Raman** (λ_{ex} = 445 nm): $\tilde{\nu}$ = 1328 (m, ν(diamond), D band), 1580 (m, G band) cm^{-1}; **EA**: C 79.58, H 0.98, N 1.99, F 11.75 wt.%; **DLS** (H_2O): 10% < 66.6 nm, 50% < 179 nm, 90% < 453 nm; ζ (H_2O): +32.4 mV (pH = 5.3).

F-pDND (starting material: **pDND**); **Recovery**: 43 mg; **FT-IR** (DRIFTS): $\tilde{\nu}$ = 3585 (m), 3331 (m), 1843 (s, ν(C=O)), 1625 (m), 1430 (m), 1237 (br, ν(C-F)), 743 (m, δ(C-F)) cm^{-1}; **FT-IR** (ATR): $\tilde{\nu}$ = 1849 (s, ν(C=O)), 1635 (m), 1236 (m, ν_{as}(C-F)), 1124 (m, ν_s(C-F)), 739 (m, δ(C-F)) cm^{-1}; **Raman** (λ_{ex} = 445 nm): $\tilde{\nu}$ = 1327 (m, ν(diamond), D band), 1589 (m, G band) cm^{-1}; **DLS** (H_2O): 10% < 69.4 nm, 50% < 162 nm, 90% < 446 nm; ζ (H_2O): +36.2 mV (pH = 5.8).

F-oDND (starting material: **oDND**); **Recovery**: 39 mg; **FT-IR** (DRIFTS): $\tilde{\nu}$ = 3693 (m), 3487 (br, ν(OH)), 3266 (w), 2956 (w, ν(FC-H)), 1755 (m, ν(C=O)), 1632 (s), 1433 (s), 1251 (m, ν(C-F)), 862 (s, δ(C-H)), 734 (s, δ(C-F)) cm^{-1}; **FT-IR** (ATR): $\tilde{\nu}$ = 3323 (w), 1631 (m), 1431 (s), 1207 (m, ν_{as}(C-F)), 1151 (s, ν_s(C-F)), 856 (s, δ(C-H)), 732 (vs, δ(C-F)) cm^{-1}; **Raman** (λ_{ex} = 445 nm): $\tilde{\nu}$ = 1330 (m, ν(diamond), D band), 1611 (m, G

band) cm^{-1}; **DLS** (H_2O): 10% < 64.3 nm, 50% < 237 nm, 90% < 1280 nm; ζ (H_2O): +23.1 mV (pH = 5.2).

F-H-DND1 (starting material: **H-pDND$_{IAF}$**); **Recovery**: 41 mg; **FT-IR** (DRIFTS): $\tilde{\nu}$ = 3694 (m), 3428 (br, ν(OH)), 3104 (w), 2976 (w, ν(FC-H)), 1757 (m, ν(C=O)), 1631 (s), 1237 (m, ν_{as}(C-F)), 1161 (m, ν_s(C-F)), 804 (w), 633 (m, δ(C-F)) cm^{-1}; **FT-IR** (ATR): $\tilde{\nu}$ = 1724 (w, ν(C=O)), 1630 (m), 1234 (s, ν_{as}(C-F)), 1155 (s, ν_s(C-F)), 636 (w, δ(C-F)) cm^{-1}; **Raman** (λ_{ex} = 445 nm): $\tilde{\nu}$ = 1326 (m, ν(diamond), D band), 1578 (m, G band) cm^{-1}; **DLS** (H_2O): 10% < 42.7 nm, 50% < 158 nm, 90% < 384 nm; ζ (H_2O): +32.4 mV (pH = 5.1).

6.2.1.7 Azide terminated DND (N_3-DND)[362]

6.2.1.7.1 Synthesis of tosyl azide (33)

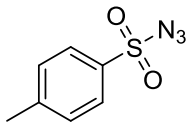

33

4-toluenesulfonyl chloride (**32**) (2.00 g, 10.0 mmol, 1.00 eq.) was dissolved in 40 mL acetone and 12 mL water. After addition of sodium azide (871 mg, 13.4 mmol, 1.28 eq.) the mixture was stirred for 2 h at r.t. Acetone was removed *in vacuo* and the residue was extracted with EtOAc (3x 40 mL). The combined organic phase was washed with water and dried over magnesium sulfate. The solvent was removed *in vacuo* and **33** (2.22 g, 11.2 mmol, 107%) was obtained as colorless oil. Due to the potentially explosive character of **33** further drying was avoided and the product stored in the freezer.

TLC (CyH/EtOAc, 5:1 v/v): R_f = 0.50; **FT-IR** (ATR): $\tilde{\nu}$ = 2927 (w, ν(C-H)), 2357 (w), 2123 (s, ν(N=N=N)), 1676 (s), 1595 (m), 1495 (w), 1450 (w), 1367 (s, ν_{as}(S=O)), 1300 (w), 1255 (w), 1163 (s, ν_s(S=O)), 1120 (w), 1086 (s), 1018 (w), 814 (s, δ(C-H_{arom})), 744 (s, δ(C-H_{arom})), 702 (w), 658 (s) cm^{-1}.

6.2.1.7.2 Azide substitution of oDND

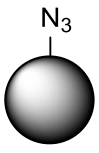

N_3-DND

Under nitrogen atmosphere, **oDND** (150 mg) was dispersed in a mixture of 10 mL MeCN and 10 mL water. After degassing silver fluoride (38.1 mg, 0.30 mmol, 1.00 eq.), potassium peroxodisulfate (162 mg, 0.60 mmol, 2.00 eq.) and **33** (177 mg, 0.90 mmol, 3.00 eq.) were added and the reaction was stirred for 18 h at 50 °C in the dark. The particles were

isolated via centrifugation and washed with MeCN (2x), water (3x), acetone (3x), isopropanol (3x) and water (3x). **N_3-DNDc** was obtained as gray dispersion.

Recovery: 14 mL (9.80 mg/mL); **FT-IR** (DRIFTS): $\tilde{\nu}$ = 3379 (s, ν(O-H)), 2965 (m, ν(C-H), 2132 (m, ν(N=N=N)), 1796 (s, ν(C=O)), 1708 (w), 1626 (s, ν(C=C)), 1433 (w, δ (C-H)), 1280 (s) cm^{-1}; **Raman** (λ_{ex} = 445 nm): $\tilde{\nu}$ = 1328 (m, ν(diamond), D band), 1600 (m, G band) cm^{-1}; **DLS** (H_2O): 10% < 85.9 nm, 50% < 156 nm, 90% < 297 nm; ζ (H_2O): -50.6 mV (pH = 5.3).

6.2.2. CVD based diamond nanoparticles

General procedure[44]: The used CVD diamond film was treated in conc. sodium hydroxide solution (40 wt.%) in a PFA flask at 120 °C for 18 h. After washing with water (5x) and drying at 130 °C the film was placed in a material grinding bowl (10 mL) together with 20 grinding balls made of tempered steel (ø 5 mm) and 5 mL of dry isopropanol. For crushing, a vibration mill was used in a multistep milling at 50 Hz, including four steps of 2 h milling in combination with 15 min cooling after each milling cycle. The obtained diamond powder and iron abrasion mixture was collected, and the isopropanol removed *in vacuo*. 100 mL of conc. hydrochloric acid was added at 0 °C and the dispersion was stirred at 120 °C for 48 h. The yellowish green supernatant was removed via centrifugation (6k rpm, 30 min) and the particles washed with water (5x). The particles were dispersed in 90 mL conc. sulfuric acid and after addition of 10 mL conc. nitric acid the dispersion was oxidized at 160 °C for 48 h. The acid was removed via centrifugation (6k rpm, 45 min) and the particles washed with water (7x) until neutral pH values was obtained.

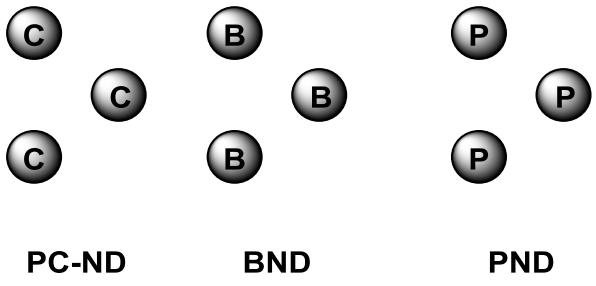

PC-ND (starting material: **PC-D** 638 mg); **Recovery**: 75 mL with 8.2 mg/mL; **Raman** (λ_{ex} = 445 nm): $\tilde{\nu}$ = 1335 (s, ν(diamond), D band), 1428 (w) cm^{-1}; **DLS** (H_2O): 10% < 550 nm, 50% < 1190 nm, 90% < 4340 nm; ζ (H_2O): -42.3 mV (pH = 5.4).

BND3 (starting material: **BDD** 358 mg); **Recovery**: 35 mL with 9.8 mg/mL; **Raman** (λ_{ex} = 445 nm): $\tilde{\nu}$ = 1329 (s, ν(diamond), D band), 1543 (m, sp^2, G band) cm^{-1}; **EA**: C 92.24, H 1.23, N 0.07, B 2.36 wt.%; **DLS** (H_2O): 10% < 147 nm, 50% < 664 nm, 90% < 942 nm; ζ (H_2O): -41.0 mV (pH = 5.7).

PND2 (starting material: **PDD** 136 mg); **Recovery**: 12 mL with 10.1 mg/mL; **FT-IR** (DRIFTS): $\tilde{\nu}$ = 3588 (m), 1807 (vs, ν(C=O)), 1629 (m), 1212 (m, ν(C-O-C)), 1158 (s, ν(C-O-C)), 799 (m) cm^{-1}; **Raman** (λ_{ex} = 445 nm): $\tilde{\nu}$ = 1331 (s, ν(diamond), D band), 1522 (m, sp^2, G band) cm^{-1}; **EA**: C 82.39, H 0.24, N 0.00, P 8.39 wt.%; **DLS** (H_2O): 10% < 340 nm, 50% < 946 nm, 90% < 1700 nm; ζ (H_2O): -45.9 mV (pH = 5.7).

6.3 Synthesis of organic linker molecules

6.3.1 Synthesis of phenylene based linker systems

6.3.1.1 Synthesis of 4-(2-azidoethyl)aniline (L1)[117]

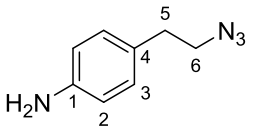

L1

Sodium azide (1.63 g, 25.0 mmol, 1.20 eq.), 4-aminophenylalcohol (**24**) (3.51 g, 21.0 mmol, 1.00 eq.) and triphenylphosphine (5.51 g, 21.0 mmol, 1.00 eq.) were added to a mixture of 15 mL tetrachloromethane and 60 mL DMF. The orange suspension was heated to 90 °C for 22 h. After cooling to r.t., 75 mL water were added and the mixture stirred for 10 min, followed by extraction with diethyl ether (5x 50 ml). The combined organic phases were washed with brine and dried over sodium sulfate. The solvent was removed *in vacuo* and the crude product was purified using column chromatography on silica (CyH/EtOAc = 2.1) yielding **L1** (2.20 g, 13.5 mmol, 64%, Lit.[117]: 58%) as yellow-orange oil.

TLC (CyH/EtOAc 1:2 v/v): R_f = 0.67; **^{1}H-NMR** (400 MHz, $CDCl_3$): δ = 7.01 (m, 2H, 3-H), 6.65 (m, 2H, 2-H), 3.57 (br. s, 2H, NH_2), 3.44 (t, $^3J_{6,5}$ = 7.2 Hz, 2H, 6-H), 2.79 (t, $^3J_{5,6}$ = 7.2 Hz, 2H, 5-H) ppm; **^{13}C-NMR** (101 MHz, $CDCl_3$): δ = 145.2 (C_q, C-1), 129.7 (C_t, C-3), 128.0 (C_q, C-4), 115.5 (C_t, C-2), 52.9 (C_s, C-6), 34.6 (C_s, C-5) ppm; **FT-IR** (ATR): $\tilde{\nu}$ = 3446 (w, ν(N-H)), 3359 (w, ν(N-H)), 3221 (w, ν(N-H)), 3018 (w, ν(C-H)), 2927 (w, ν(C-H)), 2870 (w), 2090 (vs, ν(N=N=N)), 1622 (m), 1516 (s, $\nu(C=C)_{arom}$), 1441 (w), 1346 (w), 1271 (m), 1180 (w), 1124 (w), 1032 (w), 903 (w), 822 (s, $\delta(C\text{-}H_{arom})$), 627 (m) cm^{-1}.

6.3.1.2 Synthesis of (2-phenylethyl)azide (L2)[343]

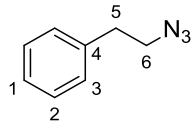

L2

Under nitrogen atmosphere 2-phenylethanol (**25**) (1.22 g, 10.0 mmol, 1.20 mL, 1.00 eq.) was dissolved in 80 mL abs. CH_2Cl_2. Triethylamine (1.26 g, 12.5 mmol, 1.73 mL, 1.25 eq.) and 4-dimethylaminopyridine (147 mg, 1.20 mmol, 0.12 eq.) were added and the reaction cooled to 0 °C. After addition of *p*-tosylchloride (2.19 g, 11.5 mmol, 1.15 eq.), the reaction mixture was stirred for 16 h at r.t. The solution was washed with water (3x 80 mL), the organic phase dried over magnesium sulfate and the solvents removed *in vacuo*. The yellow oil was dissolved in 30 mL DMF and cooled to 0 °C. Sodium azide (975 mg, 15.0 mmol, 1.50 eq.) was added and the mixture was stirred at r.t. for 15 h. 150 mL of water were added, followed by extraction with diethyl ether (5x 80 mL). The combined organic phases were dried over magnesium sulfate and the solvent was removed *in vacuo*. The crude product was purified by column chromatography on silica (CyH) yielding the azide **L2** (1.16 g, 7.88 mmol, 79 %, lit.[343]: 95 %) as colorless liquid.

TLC (CyH): R_f = 0.80; **H-NMR** (400 MHz, $CDCl_3$): δ = 7.34-7.31 (m, 2H, 2-H), 7.28-7.21 (m, 3H, 1-H, 3-H), 3.51 (t, $^3J_{5,6}$ = 7.4 Hz, 2H, 5-H), 2.90 (t, $^3J_{5,6}$ = 7.4 Hz, 2H, 6-H) ppm; **^{13}C-NMR** (101 MHz, $CDCl_3$): δ = 138.1 (C_q, C-4), 128.9 (C_t, C-2). 128.8 (C_t, C-3), 126.9 (C_t, C-1), 52.6 (C_s, C-6), 35.5 (C_s, C-5) ppm; **FT-IR** (ATR): $\tilde{\nu}$ = 3064 (w, ν_{as}(C-H)$_{arom}$), 3030 (w, ν_s(C-H)$_{arom}$), 2929 (w, ν_{as}(C-H)), 2871 (w, ν_s(C-H)), 2090 (s, ν(N=N=N)), 1603 (w), 1496 (w), 1454 (w), 1348 (w), 1259 (m), 1082 (w), 1030 (w), 941 (w), 920 (w), 899 (w), 825 (w), 746 (s, δ(C-H)$_{arom}$), 698 (s, δ(C-H)$_{arom}$) cm^{-1}.

6.3.1.3 Synthesis of 4-azidoaniline (L3)[342]

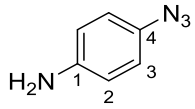

L3

Under nitrogen atmosphere, 4-iodoaniline (**27**) (3.94 g, 18.0 mmol, 1.00 eq.) was dissolved in a mixture of 24 mL DMSO and 6 mL water. After sodium azide (2.34 g, 36 mmol, 2.00 eq.) and sodium ascorbate (180 mg, 0.89 mmol, 0.05 eq.) were added, the solution was degassed. Copper(I) iodide (340 mg, 1.79 mmol, 0.10 eq.) and N,N´-dimethylethylenediamine (160 mg, 1.81 mmol, 195 µL, 0.10 eq.) were added and the dark-green solution was stirred at r.t. for 17 h. Brine was added and the mixture was extracted with ethyl acetate (5x 50 mL). The combined organic phases were dried over magnesium sulfate, after removing the solvent *in vacuo* the crude product was purified using

column chromatography on silica (CyH/EtOAc = 1:2). **L3** (2.24 g, 16.7 mmol, 93%, Lit.[342]: 98%) was obtained as orange-yellow, crystalline solid.

mp: 67-68 °C; **TLC** (CyH/EtOAc 1:2 v/v): R_f = 0.75; **^{1}H-NMR** (400 MHz, $CDCl_3$): δ = 6.84 (m, 2H, 3-H), 6.67 (m, 2-H), 3.64 (br. s, 2H, NH_2) ppm; **^{13}C-NMR** (101 MHz, $CDCl_3$): δ = 143.8 (C_q, C-1), 130.3 (C_q, C-4), 120.1 (C_t, C-3), 116.4 (C_t, C-2) ppm; **FT-IR** (ATR): $\tilde{\nu}$ = 3394 (w, ν(N-H)), 3323 (w, ν(N-H)), 3228 (w, ν(N-H)), 3037 (w, ν(C-H)$_{arom}$), 2592 (w), 2422 (w), 2256 (w), 2100 (vs, ν(N=N=N)), 2069 (s, ν(N=N=N)), 1876 (w), 1633 (w), 1601 (w), 1500 (s, ν(C=C)$_{arom}$), 1440 (w), 1331 (w), 1300 (m), 1265 (vs), 1176 (w), 1126 (w), 1084 (w), 1011 (w), 833 (s, δ(C-H$_{arom}$)), 816 (s), 785 (m), 688 (s), 623 (s) cm^{-1}.

6.3.1.4 Synthesis of phenylazide (L4)[344]

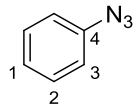

L4

Aniline (**28**) (1.86 g, 20.0 mmol, 1.83 mL,1.00 eq.) was mixed with 15 mL water and cooled to 0 °C. After addition of conc. sulfuric acid (7.95 g, 80.0 mmol, 4.26 mL, 4.00 eq.) a solution of sodium nitrite (1.52 g, 22.0 mmol, 1.10 eq.) in 9 mL water was added dropwise. 30 mL *n*-hexane was added and a solution of sodium azide (1.43 mg, 22.0 mmol, 1.10 eq.) in 8 mL water was added dropwise. The reaction mixture was stirred at 0 °C for 2 h and for 16 h at r.t. After phase separation the aqueous phase was extracted with *n*-hexane (3x 80 mL). The combined organic phases were dried over sodium sulfate and the solvent removed *in vacuo*. **L4** (2.10 g, 17.6 mmol, 88 %, lit.[344]: 96 %) was obtained as yellowish, clear liquid.

TLC (CyH/EtOAc 1:1 v/v): R_f = 0.88; **^{1}H-NMR** (400 MHz, $CDCl_3$): δ = 7.41-7.36 (m, 2H, 2-H), 7.20-7.7.16 (m, 1H, 1-H), 7.08-7.05 (m, 2H, 3-H) ppm; **^{13}C-NMR** (101 MHz, $CDCl_3$): δ = 140.1 (C_q, C-4), 129.8 (C_t, C-2), 124.9 (C_t, C-1), 119.1 (C_t, C-3) ppm; **FT-IR** (ATR): $\tilde{\nu}$ = 3246 (w), 3064 (w, ν(C-H)$_{arom}$), 2416 (w), 2256 (w), 2123 (s, ν(N=N=N)), 2089 (s, ν(N=N=N)), 1940 (w), 1591 (m, ν(C=C)$_{arom}$), 1491 (s, ν(C=C)$_{arom}$), 1338 (w), 1292 (s), 1174 (w), 1128 (w), 1074 (w), 1024 (w), 895 (w), 814 (w), 746 (s, δ(C-H$_{arom}$)), 685 (s, δ(C-H$_{arom}$)), 667 (s, δ(C-H$_{arom}$)), 615 (w) cm^{-1}.

6.3.1.5 Synthesis of *N*-Boc-(4-aminophenyl)ethylamine (L8)[347]

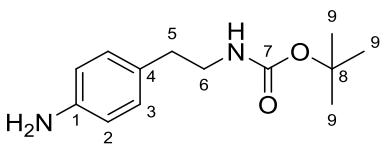

L8

2-(4-aminophenyl)ethylamine (**29**) (1.00 g, 7.34 mmol, 1.00 eq.) was dissolved in 50 mL THF and a solution of of Di-*tert*-butyldicarbonate (1.68 g, 7.71 mmol, 1.65 mL, 1.05 eq.) in 30 mL THF was added dropwise. After stirring for 2 h at r.t., the mixture was diluted with EtOAc (200 mL), washed with 1 N hydrochloric acid (100 ml), 1 M sodium hydroxide solution (150 mL), saturated sodium bicarbonate (150 mL) and brine (150mL) and dried over sodium sulfate. The solvent was removed *in vacuo* and the crude product was purified by column chromatography on silica (CyH/EtOc = 1:4) yielding **L8** (1.70 g, 7.20 mmol, 98 %, lit.[347]: 98%) as colorless, crystalline solid.

mp: 69-71 °C; **TLC** (CyH/EtOAc 1:1 v/v): R_f = 0.45; **^{1}H-NMR** (400 MHz, $CDCl_3$): δ = 6.99-6.97 (m, 2H, 3-H), 6.65-6.63 (m, 2H, 2-H), 4.53 (br. s, 1H, NH), 3.60 (br. s, 2H, NH_2), 3.31 (t, $^3J_{5,6}$ = 6.9 Hz, 2H, 6-H), 2.67 (t, $^3J_{5,6}$ = 6.9 Hz, 2H, 5-H) 1.43 (s, 9H, 9-H) ppm; **^{13}C-NMR** (101 MHz, $CDCl_3$): δ = 156.0 (C_q, C-7), 144.9 (C_q, C-1), 129.8 (C_t, C-2), 129.0 (C_q, C-4), 115.5 (C_t, C-3), 79.2 (C_q, C-8), 42.1 (C_s, C-6), 35.5 (C_s, C-5), 28.5 (C_p, C-9) ppm; **FT-IR** (ATR): $\tilde{\nu}$ = 3375 (s, ν(N-H)), 3301 (br, ν(N-H)), 3194 (w), 2977 (w, ν_{as}(C-H)), 2933 (w), 2870 (w, ν_s(C-H)), 1682 (s, ν(C=O)), 1614 (w), 1514 (vs, $\nu(C=C)_{arom}$), 1461 (w), 1388 (w), 1363 (w), 1282 (w), 1244 (s, δ (C-N)), 1163 (s, δ(C-N)), 1024 (w), 981 (m), 867 (w), 837 (m, $\delta(C\text{-}H_{arom})$), 800 (w), 773 (m), 706 (m), 613 (m) cm^{-1}.

6.3.1.6 Synthesis of *N*-Boc-4-aminoaniline (L9)[348]

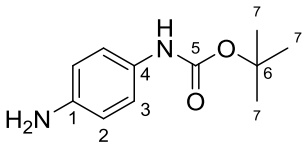

L9

1,4-diaminobenzene (**30**) (5.95 g, 55.0 mmol, 5.00 eq.) was dissolved in 150 mL CH_2Cl_2 and cooled to 0 °C. After dropwise addition of Di-*tert*-butyldicarbonate (2.40 g, 11.0 mmol, 2.35 ml, 1.00 eq.) in 30 mL CH_2Cl_2 the ice bath was removed and the mixture stirred at r.t. for 18 h. The solvent was removed *in vacuo* and the crude product was purified by column chromatography on silica (CyH/EtOc = 2:1 → 1:1) yielding **L9** (2.11 g, 10.1 mmol, 92 %, lit.[348]: 95%) as colorless powder.

mp: 116-118 °C (Lit.[348]: 114-116 °C); **TLC** (CyH/EtOAc 2:1 v/v): R_f = 0.25; **^{1}H-NMR** (400 MHz, $CDCl_3$): δ = 7.14-7.12 (m, 2H, 3-H), 6.65-6.61 (m, 2H, 2-H), 6.28 (br. s, 1H,

NH), 3.53 (br. s, 2H, NH_2), 1.50 (s, 9H, 7-H) ppm; **^{13}C-NMR** (101 MHz, $CDCl_3$): δ = 153.5 (C_q, C-5), 142.5 (C_q, C-1), 129.8 (C_q, C-4), 121.0 (C_t, C-3), 115.7 (C_t, C-2), 80.2 (C_q, C-6), 28.5 (C_p, C-7) ppm; **FT-IR** (ATR): $\tilde{\nu}$ = 3394 (w, ν(N-H)), 3363 (m, ν(N-H)), 3302 (w), 3184 (w), 2985 (w, ν(C-H)), 2935 (w, ν(C-H)), 2360 (w), 1691 (s, ν(C=O)), 1626 (w), 1597 (w), 1514 (s, $\nu(C=C)_{arom}$), 1460 (w), 1427 (m), 1390 (w), 1367 (m), 1309 (m), 1232 (s, δ(C-N)), 1157 (s, δ(C-N)), 1055 (s), 1028 (m), 955 (w), 904 (w), 823 (s, $\delta(C\text{-}H_{arom})$), 764 (m), 725 (m), 696 (m), 611 (s) cm^{-1}.

6.3.2 Synthesis of tolane based linker-molecules

6.3.2.1 Synthesis of 4-((4-((4-(azidomethyl)phenyl)ethynyl)phenyl)ethynyl)-benzenediazonium tetrafluoroborate (L7)

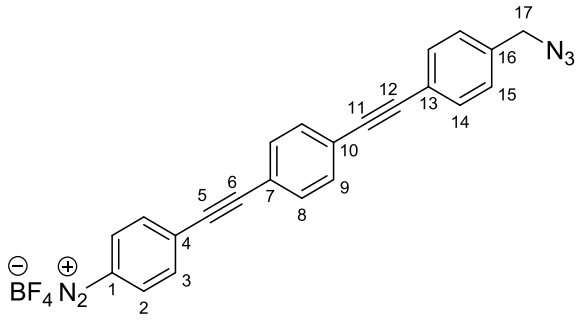

L7

4-((4-((4-(azidomethyl)phenyl)ethinyl)-phenyl)ethinyl)aniline (**L5**) (523 mg, 1.50 mmol, 1.00 eq.) was dispersed in 7.50 mL of a 50% tetrafluoroboric acid and cooled with an ice bath. To that mixture a solution of sodium nitrite (119 mg, 1.73 mmol, 1.15 eq.) in 2.50 ml water was added. After 2 h stirring at r.t. the precipitated solid was isolated by filtration and rinsed with a very small amount of cold 50% tetrafluoroboric acid and diethyl ether (20 mL). The diazonium salt **L7** (651 mg, 1.46 mmol, 97%) was isolated as bright orange powder.

mp: > 330 °C; **TLC** (CyH/EtOAc, 2:1 v/v): R_f = 0; **^{1}H-NMR** (400 MHz, acetone-*d_6*): δ = 8.91-8.88 (m, 2H, 2-H), 8.22-8.19 (m, 2H, 3-H), 7.74-7.72 (m, 2H, 8-H), 7.69-7.67 (m, 2H, 9-H), 7.64-7.62 (m, 2H, 14-H), 7.49-7.47 (m, 2H, 15-H), 4.53 (s, 2H, 17-H) ppm; **^{13}C-NMR** (101 MHz, acetone-*d_6*): δ = 137.8 (C_q, C-16), 137.0 (C_q, C-4), 134.8 (C_t, C-3), 134.1 (C_t, C-2), 133.4 (C_t, C-8), 132.6 (C_t, C-14), 129.5 (C_t, C-15), 126.2 (C_t, C-9), 123.5 (C_q, C-13), 121.9 (C_q, C-7), 114.5 (C_q, C-1), 101.0 (C_q, C-10), 92.8 (C_q, C-12), 91.9 (C_q, C-6), 89.9 (C_q, C-5), 89.8 (C_q, C-11), 54.7 (C_s, C-17) ppm; **^{19}F-NMR** (371 MHz, acetone-*d_6*): δ = -150.9 (s, 4F, B*F_3*) ppm; **FT-IR** (ATR): $\tilde{\nu}$ = 3114 (w), 3035 (w, ν_{as}(C-H)), 2289 (s, ν(N≡N)), 2206 (s, ν(C≡C)), 2103 (s, ν(N=N=N)), 1922 (w), 1576 (s, $\nu(C=C)_{arom}$), 1518 (m), 1443 (w), 1415 (w), 1354 (m), 1289 (m), 1194 (w), 1030 (vs,

ν(B-F)), 836 (vs, δ (C-H$_{arom}$)), 752 (m), 647 (w) cm^{-1}; **UV/Vis** (DMSO): λ_{max} (lg ε) 385 (2.68), 284 (2.90) nm (c = 1.49·10^{-3} mol l^{-1}); **HRMS** (ESI, +): [M]$^+$ calc. for [$C_{23}H_{14}N_5$ - BF_4]: 360.12437; found, 332.11863 [M - BF_4 - N_2]$^+$, 360.12453 [M - BF_4]$^+$; **EA** (calc., found for $C_{23}H_{14}BF_4N_5$): C (61.77, 61.85), H (3.16, 3.20), N (15.66, 14.74).

A satisfying elemental analysis of **L7** could not be obtained. The compound is probably cleaving nitrogen.

6.3.2.2 Synthesis of 1-(azidomethyl)-4-((4-(phenylethinyl)phenyl)ethinyl)-benzene (L6)

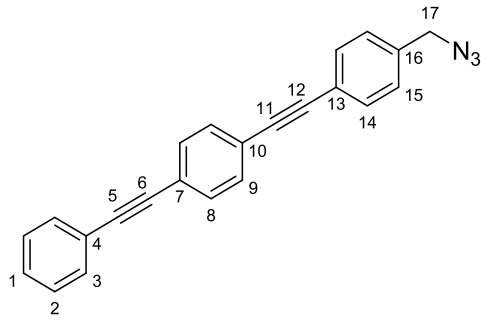

L6

L7 (200 mg, 0.48 mmol, 1.00 eq.) was suspended in 10 mL water und cooled to 10 °C. After addition of hypophosphorous acid (15 mL) the suspension was stirred for 20 min at 10 °C. Copper(II) sulfate pentahydrate (9.00 mg, 36.0 µmol, 0.08 eq.) was added and the mixture stirred for 5 h at r.t. After quenching with water, the resulting precipitate was filtered off, washed several times with purified water and dried *in* vacuo. The crude product was purified by column chromatography on silica (CyH/EtOAc = 3:1) to yield **L6** (139 mg, 0.42 mmol, 87%) as a colorless powder.

mp: 154-156 °C; **TLC** (CyH/EtOAc, 3:1 v/v): R_f = 0.70; **^{1}H-NMR** (400 MHz, CD_2Cl_2): δ = 7.58-7.55 (m, 4H, 3-H/14-H), 7.54 (s, 4H,8-H/9-H), 7.39-7.37 (m, 3H, 1-H/2-H), 7.35-7.34 (m, 2H, 15-H), 4.39 (s, 2H, 17-H) ppm; **^{13}C-NMR** (101 MHz, CD_2Cl_2): δ = 136.5 (C_q, C-16), 132.3 (C_t, C-14 or C-3), 131.9 (C_t, C-8 or C-9), 131.9 (C_t, C-8 or C-9), 129.0 (C_t, C-1), 128.8 (C_t, C-2), 128.6 (C_t, C-15), 123.6 (C_q, C-7 or C-10), 123.3 (C_q, C-4 or C-13), 123.3 (C_q, C-7 or C-10), 91.6 (C_q, C-5), 91.0 (C_q, C-12), 89.8 (C_q, C-6 or C-11), 89.2 (C_q, C-6 or C-11), 54.8 (C_s, C-17) ppm; **FT-IR** (ATR): $\tilde{\nu}$ = 2923 (m, ν_{as}(C-H)), 2853 (m, ν_s(C-H)), 2209 (w, ν(C≡C)), 2088 (s, ν(N=N=N)), 1925 (w), 1595 (m, ν(C=C)), 1518 (s, ν(C=C)), 1442 (w), 1410 (w), 1345 (w), 1308 (w), 1244 (m), 1185 (w), 1157 (w), 1104 (m), 1070 (w), 1018 (w), 919 (w), 877 (w), 837 (vs, δ(C-H$_{arom}$)), 789 (s), 758 (vs), 692 (vs), 669 (w) cm^{-1}; **UV/Vis** (DMSO): λ_{max} (lg ε) = 324 (6.91), 346 (674) nm (c = 3.31·10^{-5} mol l^{-1}); **MS** (EI, 70 eV): m/z (%) = 333.2 ([M$^+$], 87), 305.2 ([M$^+$-(N_2)], 100), 291.2 ([M$^+$-(N_3)], 83), 276.1 ([M$^+$-CH_2N_3], 38), 179.1 (12), 124.1 (16); **HRMS**

(EI): $[M]^+$ calc. for $C_{23}H_{15}N_3$: 333.12605; found, 333.12573; **EA** (calc., found for $C_{23}H_{15}N_3$): C (82.86, 82.60), H (4.54, 4.82), N (12.60, 10.46).

A satisfying elemental analysis was not obtained, even after additional column chromatography, recrystallization and intensive drying.

6.4 Synthesis of transition metal complexes

6.4.1 Synthesis of pyridine based ligands

6.4.1.1 Synthesis of (*E*)-3-dimethylamino-1-(pyridin-2-yl)prop-2-en-1-one (4)[331]

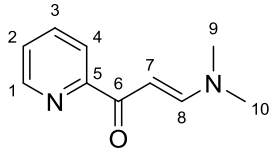

4

2-acetylpyridine (**2**) (3.63 g, 30.0 mmol, 3.36 mL, 1.00 eq.) and *N*,*N*-dimethylformamide dimethyl acetal (**3**) (4.36 g, 36.6 mmol, 4.86 mL, 1.22 eq.) were added to 30 mL toluene and the solution was heated to reflux for 23 h. The reaction was stopped twice to remove MeOH *in vacuo*. The solvent was removed *in vacuo* and the crude product recrystallized using 15 mL CyH. The precipitate was filtered, washed with 30 mL CyH and dried *in vacuo* to afford **41** (4.47 g, 25.4 mmol, 85%, lit.[331]: 86%) as a yellow, crystalline solid.

mp: 128-130 °C (Lit.[331]: 125-127 °C); **TLC** (CH_2Cl_2/MeOH, 10:1 v/v): R_f = 0.48; **^{1}H-NMR** (400 MHz, $CDCl_3$): δ = 8.63 (ddd, $^3J_{1,2}$ = 4.8 Hz, $^4J_{1,3}$ = 1.8 Hz, $^5J_{1,4}$ = 0.9 Hz, 1H, 1-H), 8.14 (ddd, $^3J_{4,3}$ = 7.9 Hz, $^4J_{4,2}$ = 1.3 Hz, $^5J_{4,1}$ = 0.9 Hz, 1H, 4-H), 7.91 (d, $^3J_{8,7}$ = 12.7 Hz, 1H, 8-H), 7.80 (ddd, $^3J_{3,4}$ = 7.9 Hz, $^3J_{3,2}$ = 7.5 Hz, $^4J_{3,1}$ = 1.8 Hz, 1H, 3-H), 7.36 (ddd, $^3J_{2,3}$ = 7.5 Hz, $^3J_{2,1}$ = 4.8 Hz, $^4J_{2,4}$ = 1.3 Hz, 1H, 2-H), 6.45 (d, $^3J_{7,8}$ = 12.7 Hz, 1H, 7-H), 3.17 (s, 3H, 10-H), 2.99 (s, 3H, 9-H) ppm; **^{13}C-NMR** (101 MHz, $CDCl_3$): δ = 186.9 (C_q, C-6), 156.3 (C_q, C-5), 155.0 (C_t, C-8), 148.3 (C_t, C-1), 137.0 (C_t, C-3), 125.6 (C_t, C-2), 122.2 (C_t, C-4), 91.2 (C_t, C-7), 45.3 (C_p, C-10), 37.6 (C_p, C-9) ppm; **FT-IR** (ATR): $\tilde{\nu}$ = 3105 (w), 3016 (w, ν(C-H)), 2922 (w, ν(C-H)), 2821 (w, ν(C-H)), 2360 (w), 2175 (w), 2131 (w), 1633 (m, ν(C=O)), 1583 (w, ν(C=C)$_{olefin.}$), 1562 (m, ν(C=C)$_{arom,}$ ν(C=N)$_{arom}$), 1529 (s, ν(C=C)$_{arom,}$ ν(C=N)$_{arom}$), 1493 (m), 1446 (m), 1427 (s), 1404 (m), 1358 (s), 1284 (m), 1259 (s), 1236 (m), 1128 (m), 1061 (s), 1038 (m), 1012 (m), 989 (m, δ(C-H)$_{olefin}$), 901 (m), 814 (m), 769 (s), 748 (s, δ(C-H)$_{arom}$), 692 (m), 677 (s), 615 (m) cm^{-1}.

6.4.1.2 Synthesis of 2,2':6',2''-terpyridine (1)[331]

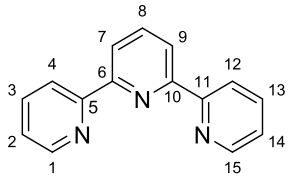

1

Under nitrogen atmosphere potassium *tert*-butoxide (14.1 g, 126 mmol, 2.00 eq.) was dissolved in 350 mL anhydrous THF. After adding 2-acetylpyridine (**2**) (7.63 g, 63.0 mmol, 7.05 mL, 1.00 eq.), the beige suspension was stirred for 2 h at r.t. **4** (11.1 g, 63.0 mmol, 1.00 eq.) was added in a single portion and the dark red mixture was stirred at r.t. for 20 h. Afterwards the solution was treated with ammonium acetate (48.6 g, 631 mmol, 10.0 eq.) and 160 mL acetic acid and was stirred for further 30 min at r.t. THF was removed by distillation over a time period of 5 h, the remaining acetic acid was removed *in vacuo.* The black residue was mixed with 350 mL water and solid sodium carbonate was carefully added until gas development stopped. The mixture was extracted with CH_2Cl_2 (4x 100 mL), the combined organic phases were dried over magnesium sulfate and the solvent removed *in vacuo*. The oily residue was dissolved in 500 mL toluene and filtered through Celite, leaving a black precipitate. The filtrate was concentrated *in vacuo*, the residue was dissolved in 300 mL *n*-hexane, activated carbon powder was added and the suspension heated to reflux for 30 min. After a hot filtration, the solvent was removed *in vacuo* and the slightly brownish crude product was purified by column chromatography on silica (CyH/EtOAc = 6:1) yielding **1** (3.43 g, 14.7 mmol, 23%, lit.[331]: 55%) as off-white powder.

mp: 83.5-85.5 °C (Lit.[331]: 84-86 °C); **TLC** (CyH/EtOAc, 6:1 v/v): R_f = 0.20; **^{1}H-NMR** (400 MHz, $CDCl_3$): δ = 8.71(ddd, $^3J_{1/15,2/14}$ = 4.8 Hz, $^4J_{1/15,3/13}$ = 1.8 Hz, $^5J_{1/15,4/12}$ = 0.9 Hz, 2H, 1-H/15-H), 8.63 (ddd, $^3J_{4/12,3/13}$ = 8.0 Hz, $^5J_{4/12,1/15}$ = 0.9 Hz, $^4J_{4/12,2/14}$ = 1.2 Hz, 2H, 4-H/12-H), 8.47 (d, $^3J_{7/9,8}$ = 7.6 Hz, 2H, 7-H/9-H), 7.97 (dd, $^3J_{8,7/9}$ = 7.84 Hz, 1H, 8-H), 7.85-7.89 (m, 2H, 3-H/13-H), 7.34 (ddd, $^3J_{2/14,3/13}$ = 7.5 Hz, $^3J_{2/14,1/15}$ = 4.8 Hz, $^4J_{2/14,4/12}$ = 1.2 Hz, 2H, 2-H/14-H) ppm; **^{13}C-NMR** (101 MHz, $CDCl_3$): δ = 156.3 (C_q, C-5/C-11), 155.4 (C_q, C-6/C-10), 149.2 (C_t, C-1/C-15), 138.1 (C_t, C-8), 137.2 (C_t, C-3/C-13), 124.0 (C_t, C-2/C-14), 121.4 (C_t, C-4/C-12), 121.1 (C_t, C-7/C-9) ppm; **FT-IR** (ATR): $\tilde{\nu}$ = 3051 (w, ν(C-H)), 3010 (w, ν(C-H)), 2360 (w), 1918 (w), 1666 (w), 1581 (m, $\nu(C=C)_{arom}$, $\nu(C=N)_{arom}$), 1560 (m, $\nu(C=C)_{arom}$, $\nu(C=N)_{arom}$), 1502 (w), 1468 (w), 1454 (w), 1419 (s), 1335 (w), 1263 (w), 1147 (w), 1097 (w), 1078 (m), 1038 (w), 989 (m), 962 (w), 895 (w), 833 (w), 758 (vs, $\delta(C-H)_{arom}$), 685 (w), 654 (m), 623 (m) cm^{-1}.

6.4.1.3 Synthesis of 1,5-bis(2-pyridyl)pentane-1,3,5-trione (7)[332]

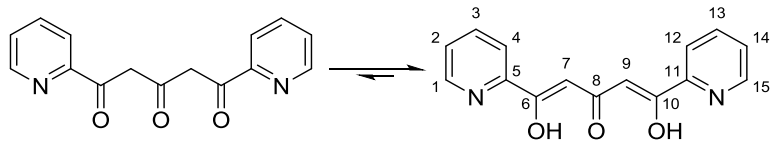

7 **7**

Under nitrogen atmosphere a 60 wt.% suspension of sodium hydride in paraffin oil (3.89 g, 97.3 mmol, 3.68 eq.) was suspended in 55 mL anhydrous THF. After cooling to 0 °C, a mixture of acetone (1.53 g, 26.4 mmol, 1.94 mL, 1.00 eq.) and ethyl-2-picolinate (**6**) (12.1 g, 80.0 mmol, 10.8 mL, 3.03 eq.) in 55 mL anhydrous THF was added dropwise over a period of 5 h. The dark red solution was heated to reflux for 21 h. The solvent was removed *in vacuo*, the solid residue was treated with 450 mL water and insoluble parts were filtered. The aqueous filtrate was set to pH = 9 using acetic acid. The precipitate was filtered off, washed several times with water and dried *in vacuo*. After recrystallization of the crude product in 10 mL ethanol, the product **7** (3.21 g, 12.0 mmol, 45%, lit.[332]: 55%) was obtained as yellow, crystalline solid.

mp: 105-107 °C (lit.[332]: 106-107 °C); **TLC** (CyH/EtOAc, 3:1 v/v): R_f = 0.20; **^{1}H-NMR** (400 MHz, $CDCl_3$): δ = 14.6 (br.s, 2H, OH), 8.65-8.70 (m, 2H, 1-H/15-H), 8.01 (ddd, $^3J_{4/12,3/13}$ = 7.9 Hz, $^4J_{4/12,2/14}$ = 1.2 Hz, $^5J_{4/12,1/15}$ = 1.0 Hz, 2H, 4-H/12-H), 7.81-7.88 (m, 2H, 3-H/13-H), 7.39 (ddd, $^3J_{2/14,3/13}$ = 7.6 Hz, $^3J_{2/14,1/15}$ = 4.7 Hz, $^4J_{2/14,4/12}$ = 1.2 Hz, 2H, 2-H/14-H), 6.80 (s, 2H, 7-H/9-H) ppm; **^{13}C-NMR** (101 MHz, $CDCl_3$): δ = 195.8 (C_q, C-8), 171.3 (C_q, C-6/C-10), 151.3 (C_q, C-5/C-11), 149.6 (C_t, C-1/C-15), 137.1 (C_t, C-3/C-13), 125.8 (C_t, C-2/C-14), 121.7 (C_t, C-4/C-12), 98.9 (C_t, C-7/C-9) ppm; **FT-IR** (ATR): $\tilde{\nu}$ = 3053 (w, ν(C-H)), 3007 (w, ν(C-H)), 2360 (w), 1606 (s, ν(C=O)), 1560 (s, ν(C=C)$_{arom}$, ν(C=N)$_{arom}$), 1473 (w), 1444 (s), 1373 (s, δ(O-H)), 1279 (s), 1146 (s, ν(C-O)), 1080 (m), 984 (s), 864 (m), 837 (s, δ(C-H)$_{olefin}$), 787 (s, δ(C-H)$_{arom}$), 735 (s), 673 (m), 646 (m), 615 (m) cm^{-1}.

6.4.1.4 Synthesis of 2,6-bis(2-pyridyl)-4-(1*H*)-pyridinone (8)[332]

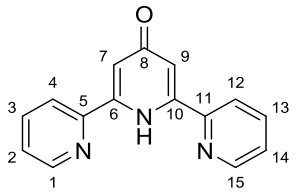

8

A mixture of **7** (3.15 g, 11.7 mmol, 1.00 eq.) and ammonium acetate (7.00 g, 90.8 mmol, 7.76 eq.) in 70 mL ethanol was heated under reflux for 25 h. The solvent was removed *in vacuo* and the brown crude product was recrystallized from ethanol (15 mL). The formed precipitate was filtered off, washed with ethanol (5 mL) and dried *in vacuo*. **8** (2.00 g, 8.02 mmol, 68%, lit.[332] 65%) could be isolated as off-white, crystalline solid.

mp: 112-114.5 °C (lit.[332]: 166-166.5 °C); **TLC** (CH_2Cl_2/MeOH, 10:1 v/v): R_f = 0.29;**^{1}H-NMR** (400 MHz, $CDCl_3$): δ = 12.2 (br.s, 1H, N-H), 8.79 (ddd, $^3J_{1/15,2/14}$ = 4.8 Hz, $^4J_{1/15,3/13}$ = 1.7 Hz, $^5J_{1/15,4/12}$ = 1.0 Hz, 2H, 1-H/15-H), 7.96 (ddd, $^3J_{4/12,3/13}$ = 8.0 Hz, $^4J_{4/12,2/14}$ = 1.2 Hz, $^5J_{4/12,1/15}$ = 1.0 Hz, 2H, 4-H/12-H), 7.90 (ddd, $^3J_{3/13,4/12}$ = 8.0 Hz, $^3J_{3/13,2/14}$ = 7.4 Hz, $^4J_{3/13,1/15}$ = 1.7 Hz, 2H, 3-H/13-H), 7.45 (ddd, $^3J_{2/14,3/13}$ = 7.4 Hz, $^3J_{2/14,1/15}$ = 4.8 Hz, $^4J_{2/14,4/12}$ = 1.2 Hz, 2H, 2-H/14-H), 7.30 (s, 2H, 7-H/9-H) ppm; **^{13}C-NMR** (101 MHz$CDCl_3$): δ = 175.1 (C_q, C-8), 149.6 (C_t, C-1/C-15), 148.5 (C_q, C-5/C-11), 144.8 (C_q, C-6/C-10), 137.9 (C_t, C-3/C-13), 125.4 (C_t, C-2/C-14), 120.7 (C_t, C-4/C-12), 113.6 (C_t, C-7/C-9) ppm; **FT-IR** (ATR): $\tilde{\nu}$ = 3290 (w, ν(N-H)), 3070 (w, ν(C-H)$_{arom}$), 3010 (w, ν(C-H)$_{arom}$), 2360 (w), 1880 (w), 1685 (m, ν(C=O)), 1631 (m, ν(C=C)$_{arom}$, ν(C=N)$_{arom}$, ν(C=C)$_{olefin.}$), 1572 (m, ν(C=C)$_{arom}$, ν(C=N)$_{arom}$), 1510 (m), 1468 (m), 1429 (m), 1362 (m), 1296 (m), 1153 (m), 1080 (m), 1059 (m), 993 (s), 879 (s, δ(C-H)$_{arom}$)), 777 (s, δ(C-H)$_{arom}$), 741 (s, δ(C-H)$_{arom}$), 714 (s), 696 (m), 648 (m), 619 (m) cm^{-1}.

6.4.1.5 Synthesis of 4-bromo-2,6-bis(2-pyridyl)pyridine (9)[332]

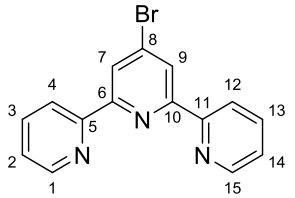

9

Under nitrogen atmosphere a mixture of **8** (1.95 g, 7.82 mmol, 1.00 eq.), phosphorus pentabromide (5.37 g, 12.5 mmol, 1.59 eq.) and phosphorus oxybromide (24.2 g, 84.2 mmol, 10.8 eq.) was heated at 100 °C for 22 h. After adding more phosphorus pentabromide (2.70 g, 6.27 mmol, 0.80 eq.) the dark brown mixture was heated at 100 °C for another 23 h. After cooling to r.t., 200 mL of ice water were carefully added and the solution was neutralized with potassium carbonate. The purple-colored aqueous phase was extracted four times with CH_2Cl_2. The combined organic phases were dried over magnesium sulfate and the solvent was

removed *in vacuo* to give **9** (1.68 g, 5.38 mmol, 69%, lit.[332] 78%) as off-white, crystalline solid.

mp: 135-137.5 °C (lit.[332]: 137-138 °C); **TLC** (CyH/EtOAc, 3:1 v/v): R_f = 0.56;**^{1}H-NMR** (400 MHz, $CDCl_3$): δ = 8.71 (ddd, $^3J_{1/15,2/14}$ = 4.8 Hz, $^4J_{1/15,3/13}$ = 1.8 Hz, $^5J_{1/15,4/12}$ = 0.9 Hz 2H, 1-H/15-H), 8.67 (s, 2H, 7-H/9-H), 8.60 (ddd, $^3J_{4/12,3/13}$ = 8.0 Hz, $^4J_{4/12,2/14}$ = 1.2 Hz, $^5J_{4/12,1/15}$ = 0.9 Hz, 2H, 4-H/12-H), 7.86-7.90 (m, 2H, 3-H/13-H), 7.37 (ddd, $^3J_{2/14,3/13}$ = 7.5 Hz, $^3J_{2/14,1/15}$ = 4.8 Hz, $^4J_{2/14,4/12}$ = 1.2 Hz, 2H, 2-H/14-H) ppm; **^{13}C-NMR** (101 MHz, $CDCl_3$): δ = 156.5 (C_q, C-6/C-10), 154.9 (C_q, C-5/C-11), 149.3 (C_t, C-1/C-15), 137.3 (C_t, C-3/C-13), 135.3 (C_q, C-8), 124.5 (C_t, C-2/C-14), 124.4 (C_t, C-7/C-9), 121.6 (C_t, C-4/C-12) ppm; **FT-IR** (ATR): $\tilde{\nu}$ = 3086 (w, ν(C-H)), 3059 (w, ν(C-H)), 3014 (w, ν(C-H)), 2112 (w), 1950 (w), 1772 (w), 1695 (w), 1631 (w, $\nu(C=C)_{arom}$, $\nu(C=N)_{arom}$), 1545 (s, $\nu(C=C)_{arom}$, $\nu(C=N)_{arom}$), 1464 (m), 1433 (w), 1387 (m), 1319 (w), 1263 (m), 1146 (w), 1109 (w), 1088 (w), 1063 (m, $\nu(C\text{-}Br)_{arom}$), 991 (m), 877 (m, $\delta(C\text{-}H)_{arom}$), 781 (s), 731 (s), 669 (m), 654 (m), 619 (m) cm^{-1}.

6.4.1.6 Synthesis of 4'-(2-(trimethylsilyl)-1-ethinyl)-2,2':6',2''-terpyridine (10)[333]

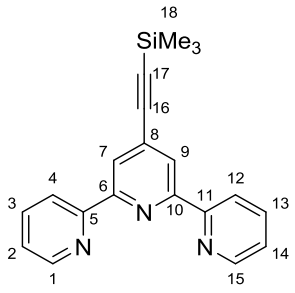

10

Under nitrogen atmosphere **9** (1.60 g, 5.13 mmol, 1.00 eq.) was dissolved in 100 mL triethylamine and 100 mL THF. After addition of bis(triphenylphosphine)palladium(II)-chloride (180 mg, 256 µmol, 0.05 eq.) and copper(I) iodide (24.4 mg, 128 µmol, 0.025 eq.) the solution was degassed. Trimethylsilylacetylene (529 mg, 5.38 mmol, 746 µL, 1.05 eq.) was added and the mixture was stirred for 24 h at 60 °C. The solvents were removed *in vacuo* and the crude product purified by column chromatography on silica (CH_2Cl_2/MeOH = 99:1) yielding **10** (1.61 g, 4.89 mmol, 95%, lit.[333] 87%) as off-white, crystalline solid.

mp: 102-104.5 °C (Lit.[333]: 100-101 °C); **TLC** (CH_2Cl_2/MeOH, 99:1 v/v): R_f = 0.84; **^{1}H-NMR** (400 MHz, $CDCl_3$): δ = 8.72 (ddd, $^3J_{1/15,2/14}$ = 4.8 Hz, $^4J_{1/15,3/13}$ = 1.8 Hz, $^5J_{1/15,4/12}$ = 0.9 Hz, 2H, 1-H/15-H), 8.61 (ddd, $^3J_{4/12,3/13}$ = 8.0 Hz, $^4J_{4/12,2/14}$ = 1.2 Hz, $^5J_{4/12,1/15}$ = 0.9 Hz, 2H, 4-H/12-H), 8.51 (s, 2H, 7-H/9-H), 7.85-7.90 (m, 2H, 3-H/13-H), 7.35 (ddd, $^3J_{2/14,3/13}$ = 7.5 Hz, $^3J_{2/14,1/15}$ = 4.8 Hz, $^5J_{2/14,4/12}$ = 1.2 Hz, 2H, 2-H/14-H), 0.27 (s, 9H, 18-H) ppm; **^{13}C-NMR** (101 MHz, $CDCl_3$): δ = 155.6 (C_q, C-5/C-11), 155.5 (C_q,

C-6/C-10), 149.2 (C_t, C-1/C-15), 137.2 (C_t, C-3/C-13), 133.4 (C_q, C-8), 124.2 (C_t, C-2/C-14), 123.4 (C_t, C-7/C-9), 121.4 (C_t, C-4/C-12), 102.7 (C_q, C-16), 99.9 (C_q, C-17), -0.13 (C_p, C-18) ppm; **FT-IR** (ATR): $\tilde{\nu}$ = 3049 (w, ν(C-H).), 3010 (w, ν(C-H)), 2956 (w, ν_{as}(C-H)), 2897 (w, ν_s(C-H)), 2164 (w, ν(C≡C)), 2102 (w), 1776 (w), 1583 (m, ν(C=C)$_{arom}$, ν(C=N)$_{arom}$), 1564 (m, ν(C=C)$_{arom,}$ ν(C=N)$_{arom}$), 1549 (w), 1466 (w), 1442 (w), 1390 (m), 1296 (w), 1248 (m), 1176 (w), 1117 (w), 1090 (w), 1070 (w), 1041 (w), 991 (w), 926 (m), 891 (w), 841 (vs, δ(C-H)$_{arom}$), 787 (s, δ(C-H)$_{arom}$), 762 (m), 737 (s, δ(C-H)$_{arom}$), 700 (m), 658 (m), 619 (m) cm^{-1}.

6.4.1.7 Synthesis of 4'-ethinyl-2,2':6',2''-terpyridine (5)[333]

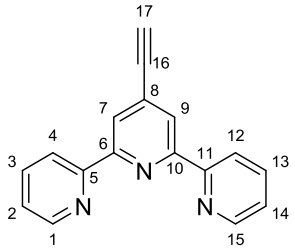

5

10 (1.61 g, 4.89 mmol, 1.00 eq.) was solved in a mixture of 50 ml MeOH and 80 ml THF. After adding potassium fluoride (341 mg, 5.87 mmol, 1.20 eq.) the clear, slightly orange solution was stirred at r.t. for 17 h. The solvents were removed *in vacuo* and the crude product was extracted with $CHCl_3$ (5x 75 mL). The combined organic phases were washed with brine, dried over magnesium sulfate and the solvent removed *in vacuo.* Purification via column chromatography on silica (CH_2Cl_2/MeOH/TEA = 98:1:1) yielded **5** (1.11 g, 4.31 mmol, 88%, lit.[333] 95%) as colorless, crystalline solid.

mp: 175-176 °C (Lit.[333] 173-175 °C); **TLC** (CH_2Cl_2/MeOH/TEA, 99:1:1 v/v/v): R_f = 0.82;**^{1}H-NMR** (400 MHz, $CDCl_3$): δ = 8.71 (ddd, $^3J_{1/15,2/14}$ = 4.8 Hz, $^4J_{1/15,3/13}$ = 1.8 Hz, $^5J_{1/15,4/12}$ = 0.9 Hz, 2H, 1-H/15-H), 8.60 (ddd, $^3J_{4/12,3/13}$ = 8.0 Hz, $^4J_{4/12,2/14}$ = 1.2 Hz, $^5J_{4/12,1/15}$ = 0.9 Hz, 2H, 4-H, 12-H), 8.54 (s, 2H, 7-H/9-H), 7.87 (ddd, $^3J_{3/13,2/14}$ = 8.0 Hz, $^3J_{3/13,4/12}$ = 6.9 Hz, $^4J_{3/13,1/15}$ = 1.8 Hz, 2H, 3-H/13-H), 7.35 (ddd, $^3J_{2/14,3/13}$ = 6.9 Hz, $^3J_{2/14,1/15}$ = 4.8 Hz, $^5J_{2/14,4/12}$ = 1.2 Hz, 2H, 2-H/14-H), 3.33 (s, 1H, 17-H) ppm; **^{13}C-NMR** (101 MHz, $CDCl_3$): δ = 155.6 (C_q, C-5/C-11), 155.5 (C_q, C-6/C-10), 149.3 (C_t, C-1/C-15), 137.2 (C_t, C-3/C-13), 132.5 (C_q, C-8), 124.3 (C_t, C-2/C-14), 123.6 (C_t, C-7/C-9), 121.4 (C_t, C-4/C-12), 81.7 (C_q, C-16), 81.6 (C_q, C-17); **FT-IR** (ATR): $\tilde{\nu}$ = 3213 (m, ν(≡C-H)), 3099 (w, ν(C-H)), 3049 (w, ν(C-H)), 3010 (w, ν(C-H)), 2108 (m, ν (C≡C)), 1583 (m, ν(C=C)$_{arom}$, ν(C=N)$_{arom}$), 1564 (m, ν(C=C)$_{arom}$, ν(C=N)$_{arom}$), 1539 (w), 1464 (m), 1442 (w), 1390 (m), 1263 (w), 1246 (w), 1117 (w), 1093 (w), 1070 (w), 1043 (w), 991 (m), 885 (m), 786 (s, δ(C-H)$_{arom}$), 729 (s, δ(C-H)$_{arom}$), 661 (m), 615 (m) cm^{-1}.

6.4.1.8 Synthesis of 2,2'-bipyridine-1-oxide (13)[332]

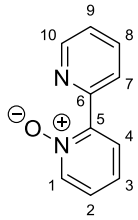

13

2,2´-bipyridine (**12**) (7.81 g, 50.0 mmol, 1.00 eq.) was dissolved in 40 mL 50 wt% trifluoroacetic acid and cooled to 0 °C. Over a period of 30 min a 30 wt% hydrogen peroxide solution (8.67 g, 76.4 mmol, 7.81 mL, 1.53 eq.) was added and the mixture stirred für 90 min at r.t. After addition of 100 mL $CHCl_3$, the two phases were separated. The organic phase was washed with 3 M sodium hydroxide (3x 75 mL). The combined aqueous phases were extracted with $CHCl_3$ (10x 80 mL). The combined organic phases were dried over sodium sulfate and the solvent removed *in vacuo*. The crude product was purified using column chromatography on silica ($CHCl_3$/MeOH = 10:1) yielding **13** (7.28 g, 42.3 mmol, 85%, lit.[332] 100%) as grayish, crystalline solid.

mp: 55-57 °C (Lit.[332]: 56-57 °C); **TLC** (CH_2Cl_2/MeOH 9:1 v/v): R_f = 0.50; **^{1}H-NMR** (400 MHz, $CDCl_3$): δ = 8.89 (dd, $^3J_{7,8}$ = 8.1 Hz, $^4J_{7,9}$ = 1.0 Hz, $^5J_{7,10}$ = 1.0 Hz, 1H, -7-H), 8.73 (ddd, $^3J_{10,9}$ = 4.8 Hz, $^4J_{10,8}$ = 1.8 Hz, $^5J_{10,7}$ = 1.0 Hz, 1H, 10-H), 8.32 (ddd, $^3J_{1,2}$ = 6.5 Hz, $^4J_{1,3}$ = 1.2 Hz, $^5J_{1,4}$ = 0.5 Hz, 1H, 1-H), 8.18 (ddd, $^3J_{4,3}$ = 8.0 Hz, $^4J_{4,2}$ = 2.2 Hz, $^5J_{4,1}$ = 0.5 Hz, 1H, 4-H), 7.84 (ddd, $^3J_{8,7}$ = 8.1 Hz, $^3J_{8,9}$ = 7.6 Hz, $^4J_{8,10}$ = 1.8 Hz, 1H, 8-H), 7.34-7.41 (m, 2H, 3-H/9-H), 7.27-7.30 (m, 1H, 2-H) ppm; **^{13}C-NMR** (101 MHz, $CDCl_3$): δ = 149.7 (C_t, C-10), 149.5 (C_q, C-6), 147.4 (C_q, C-5), 140.8 (C_t, C-1), 136.6 (C_t, C-8), 128.1 (C_t, C-4), 126.1 (C_t, C-3), 125.7 (C_t, C-7), 125.5 (C_t, C-2), 124.5 (C_t, C-9) ppm; **FT-IR** (ATR): $\tilde{\nu}$ = 3377 (w), 3111 (w), 3068 (w, ν(C-H)$_{arom}$), 3043 (w, ν_s(C-H)$_{arom}$), 2468 (w), 2360 (w), 2330 (w), 2079 (w), 1928 (w), 1612 (w, ν(C=C)$_{arom}$, ν(C=N)$_{arom}$), 1579 (m, ν(C=C)$_{arom}$, ν(C=N)$_{arom}$), 1493 (w, ν(C=C)$_{arom}$, ν(C=N)$_{arom}$), 1462 (m), 1441 (m), 1417 (s), 1315 (w), 1250 (s, ν(N-O)$_{arom}$), 1234 (s, ν(N-O)$_{arom}$), 1155 (m), 1119 (w), 1097 (w), 1059 (w), 1032 (m), 991 (w), 953 (w), 876 (w), 847 (s, δ(C-H)$_{arom}$), 793 (m), 760 (vs, δ(C-H)$_{arom}$), 739 (s, δ(C-H)$_{arom}$), 719 (s), 642 (m), 617 (m) cm^{-1}.

6.4.1.9 Synthesis of 4-nitro-2,2'-bipyridine-1-oxide (14)[332,399]

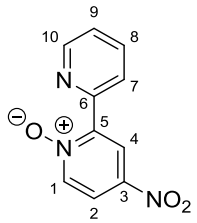

14

13 (7.28 g, 42.3 mmol, 1.00 eq.) and potassium nitrate (23.2 g, 229 mmol, 5.43 eq.) were dissolved in 55 mL conc. sulfuric acid. The reaction mixture was stirred for 48 h at 80 °C. The slightly yellowish solution was poured on 165 g ice and the pH was adjusted to 9 using 25 wt% sodium hydroxide solution. The precipitate was filtered off, washed with ice water und dried *in vacuo*. The crude product was

solved in CH_2Cl_2 and insoluble components filter off. After removing the solvent *in vacuo*, **14** (5.60 g, 25.8 mmol, 61%, lit.[332] 90%) was obtained as yellowish, crystalline solid.

mp: 188-190 °C (Lit.[399]: 184-186 °C); **TLC** (EtOAc) R_f = 0.71; **^{1}H-NMR** (400 MHz, $CDCl_3$): δ = 9.16 (d, $^4J_{4,2}$ = 3.3 Hz, 1H, 4-H), 8.88 (ddd, $^3J_{7,8}$ = 8.1 Hz, $^4J_{7,9}$ = 1.1 Hz, $^5J_{7,10}$ = 1.0 Hz, 1H, 7-H), 8.79 (ddd, $^3J_{10,9}$ = 4.7 Hz, $^4J_{10,8}$ = 1.8 Hz, $^5J_{10,7}$ = 1.0 Hz, 1H, 10-H), 8.36 (dd, $^3J_{1,2}$ = 7.2 Hz, $^5J_{1,4}$ = 0.4 Hz, 1H, 1-H), 8.07 (dd, $^3J_{2,1}$ = 7.2 Hz, $^4J_{2,4}$ = 3.3 Hz, 1H, 2-H), 7.88 (ddd, $^3J_{8,7}$ = 8.1 Hz, $^3J_{8,9}$ = 7.6 Hz, $^4J_{8,10}$ = 1.8 Hz, 1H, 8-H), 7.44 (ddd, $^3J_{9,10}$ = 4.7 Hz, $^3J_{9,8}$ = 7.6 Hz, $^4J_{9,7}$ = 1.1 Hz, 1H, 9-H) ppm; **^{13}C-NMR** (101 MHz, $CDCl_3$): δ = 149.9 (C_t, C-10), 148.3 (C_q, C-5), 147.7 (C_q, C-6), 142.6 (C_q, C-3), 142.6 (C_t, C-1), 136.9 (C_t, C-8), 125.5 (C_t, C-9), 125.3 (C_t, C-7), 122.8 (C_t, C-4), 119.0 (C_t,C-2) ppm; **FT-IR** (ATR): $\tilde{\nu}$ = 3118 (w), 3059 (m, ν(C-H)$_{arom}$), 2854 (w), 2457 (w), 2112 (w), 1928 (w), 1807 (w), 1604 (w, ν(C=C)$_{arom}$, ν(C=N)$_{arom}$), 1581 (m, ν(C=C)$_{arom}$, ν(C=N)$_{arom}$), 1512 (s, ν_{as}(N=O)), 1464 (w), 1442 (m), 1408 (w), 1338 (s, ν_s(N=O)), 1273 (s, ν(N-O)$_{arom}$), 1230 (s, ν(N-O)$_{arom}$), 1201 (m), 1157 (m), 1111 (s), 1051 (m), 1034 (m), 987 (m), 910 (m), 895 (m), 847 (s, δ(C-H)$_{arom}$), 793 (s, δ(C-H)$_{arom}$), 744 (s, δ(C-H)$_{arom}$), 706 (s), 656 (s), 615 (m) cm^{-1}.

6.4.1.10 Synthesis of 4-bromo-2,2'-bipyridine-1-oxide (15)[399]

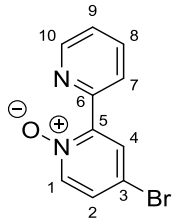

15

Under nitrogen atmosphere **14** (5.51 g, 25.4 mmol, 1.00 eq.) was dissolved in 200 mL abs. AcOH and stirred at 60 °C. Acetyl bromide (31.2 g, 0.25 mol, 18.9 mL, 10.0 eq.) was added and the bright-orange suspension was stirred for 4 d at 60 °C. After cooling to r.t., the mixture was poured onto 150 g ice and was neutralized with sodium carbonate. The suspension was extracted with CH_2Cl_2 (5x 50 mL) and the combined organic phases dried over sodium sulfate. The solvent was removed *in vacuo* and the yellowish crude product was purified using column chromatography on silica (EtOAc/TEA = 99:1) yielding **15** (5.06 g, 20.2 mmol, 80%, lit.[399] 80%) as off-white powder.

mp: 115-117 °C (Lit.[399] 107-108 °C); **TLC** (EtOAc/TEA 99:1 v/v): R_f = 0.38; **^{1}H-NMR** (400 MHz, $CDCl_3$): δ = 8.94 (ddd, $^3J_{7,8}$ = 8.1 Hz, $^4J_{7,9}$ = 1.1 Hz, $^5J_{7,10}$ = 1.0 Hz, 1H, 7-H), 8.73 (ddd, $^3J_{10,9}$ = 4.8 Hz, $^4J_{10,8}$ = 1.8 Hz, $^5J_{10,7}$ = 1.0 Hz, 1H, 10-H), 8.40 (dd, $^4J_{4,2}$ = 2.9 Hz, $^5J_{4,1}$ = 0.4 Hz, 1H, 4-H), 8.16 (dd, $^3J_{1,2}$ = 7.0 Hz, $^5J_{1,4}$ = 0.4 Hz, 1H, 1-H), 7.85

(ddd, $^3J_{8,7}$ = 8.1 Hz, $^3J_{8,9}$ = 7.6 Hz, $^4J_{8,10}$ = 1.8 Hz, 1H, 8-H), 7.40-7.36 (m, 2H, 2-H/9-H) ppm; **^{13}C-NMR** (101 MHz, $CDCl_3$): δ = 149.6 (C_t, C-10), 148.4 (C_q, C-6), 148.0 (C_q, C-5), 141.6 (C_t, C-1), 136.7 (C_t, C-8), 130.9 (C_t, C-4), 128.5 (C_t, C-2), 125.7 (C_t, C-7), 125.0 (C_t, C-9), 119.4 (C_q, C-3) ppm; **FT-IR** (ATR): $\tilde{\nu}$= 3086 (w, ν_{as}(C-H)$_{arom}$), 3064 (w, ν(C-H)$_{arom}$), 3022 (w, ν_s(C-H)$_{arom}$), 2191 (w), 1896 (w), 1583 (w, ν(C=C)$_{arom}$, ν(C=N)$_{arom}$), 1564 (w, ν(C=C)$_{arom}$, ν(C=N)$_{arom}$), 1479 (w), 1460 (m), 1435 (m), 1392 (m), 1281 (w), 1252 (s, ν(N-O)$_{arom}$), 1234 (s, ν(N-O)$_{arom}$), 1144 (w), 1093 (m), 1059 (w, ν(C-Br)$_{arom}$), 1039 (w), 993 (w), 868 (w), 823 (s, δ(C-H)$_{arom}$), 785 (m), 758 (m, δ(C-H)$_{arom}$), 735 (m), 719 (m), 646 (vs) cm^{-1}.

6.4.1.11 Synthesis of 4-bromo-2,2'-bipyridine (16)[334]

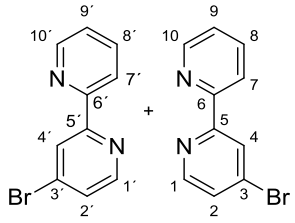

16

15 (5.00 g, 19.9 mmol, 1.00 eq.) was dissolved under nitrogen atmosphere in 100 mL abs. $CHCl_3$ and cooled to 0 °C. After addition of phosphorus tribromide (18.9 g, 69.7 mmol, 6.56 mL, 3.50 eq.), the clear dark brown reaction mixture was heated to reflux for 2 h. After cooling to r.t., ice water was added, the solution was neutralized using 20 wt.% sodium hydroxide and was subsequently extracted with $CHCl_3$ (5x 50 mL). The combined organic phases were dried over sodium sulfate, the solvent was removed *in vacuo* and the crude product purified via column chromatography on silica (CyH/EtOAc = 4:1) yielding **16** (3.91 g, 16.6 mmol, 84%, lit.[334] 83%) as colorless, crystalline solid.

mp:58-59 °C (Lit.[334] 53-55 °C); **TLC** (CyH/EtOAc 4:1 v/v): R_f = 0.48,**^{1}H-NMR** (400 MHz, $CDCl_3$): *cis isomer*: δ = 8.67 (ddd, $^3J_{10,9}$ = 4.9 Hz, $^4J_{10,8}$ = 1.8 Hz, $^5J_{10,7}$ = 1.0 Hz, 1H, 10-H), 8.55 (dd, $^3J_{1,2}$ = 5.3 Hz, $^5J_{1,4}$ = 0.5 Hz, 1H, 1-H), 8.45 (dd, $^4J_{4,2}$ = 2.1 Hz, $^5J_{4,1}$ = 0.5 Hz, 1H, 4-H), 8.38 (ddd, $^3J_{7,8}$ = 7.9 Hz, $^4J_{7,9}$ = 1.1 Hz, $^5J_{7,10}$ = 1.0 Hz, 1H, 7-H), 7.82 (ddd, $^3J_{8,7}$ = 7.9 Hz, $^3J_{8,9}$ = 7.6 Hz, $^4J_{8,10}$ = 1.8 Hz, 1H, 8-H), 7.34-7.29 (m, 2H, 2-H/9-H) ppm; *trans isomer*: δ = 8.67 (ddd, $^3J_{10',9'}$ = 4.9 Hz, $^4J_{10',8'}$ = 1.8 Hz, $^5J_{10',7'}$ = 1.0 Hz, 1H, 10´-H), 8.63 (dd, $^4J_{4',2'}$ = 2.0 Hz, $^5J_{4',1'}$ = 0.6 Hz, 1H, 4´-H), 8.48 (dd, $^3J_{1',2'}$ = 5.2 Hz, $^5J_{1',4'}$ = 0.6 Hz, 1H, 1´-H), 8.38 (ddd, $^3J_{7',8'}$ = 7.9 Hz, $^4J_{7',9'}$ = 1.1 Hz, $^5J_{7',10'}$ = 1.0 Hz, 1H, 7´-H), 7.82 (ddd, $^3J_{8',7'}$ = 7.9 Hz, $^3J_{8',9'}$ = 7.6 Hz, $^4J_{8',10'}$ = 1.8 Hz, 1H, 8´-H), 7.48 (dd, $^3J_{2',1'}$ = 5.2 Hz, $^4J_{2',4'}$ = 2.0 Hz, 1H, 2´-H), 7.36-7.31 (m, 1H, 9´-H) ppm; **^{13}C-NMR** (101 MHz, $CDCl_3$): *cis isomer*: δ = 157.8 (C_q, C-5), 155.0 (C_q, C-6), 150.1 (C_t, C-1), 149.4 (C_t, C-10), 145.4 (C_q, C-3), 137.2 (C_t, C-8), 124.4 (C_t, C-9), 124.0

(C_t, C-2), 121.6 (C_t, C-4), 121.5 (C_t, C-7) ppm; *trans isomer*: δ = 157.3 (C_q, C-5´), 154.7 (C_q, C-6´), 149.9 (C_t, C-1´), 149.3 (C_t, C-10´), 137.4 (C_t, C-8´), 134.3 (C_q, C-3´), 127.1 (C_t, C-2´), 124.8 (C_t, C-4´), 124.5 (C_t, C-9´), 121.6 (C_t, C-7´) ppm; **FT-IR** (ATR): $\tilde{\nu}$ = 3095 (w, ν(C-H)$_{arom}$), 3051 (w, ν(C-H)$_{arom}$), 2921 (w, ν(C-H)$_{arom}$), 1564 (w, ν(C=C)$_{arom}$, ν(C=N)$_{arom}$), 1545 (w, ν(C=C)$_{arom}$, ν(C=N)$_{arom}$), 1450 (m), 1385 (m), 1315 (w), 1279 (w), 1127 (w), 1149 (w), 1117 (w), 1082 (w), 1066 (w, ν(C-Br)$_{arom}$), 993 (m), 885 (w), 833 (w), 785 (s, δ(C-H)$_{arom}$), 741 (w), 7278 (w), 706 (w), 683 (w), 658 (w), 615 (w) cm^{-1}.

6.4.1.12 Synthesis of 4-[2''-(trimethylsilyl)-1''-ethinyl]-2,2'-bipyridine (17)[335]

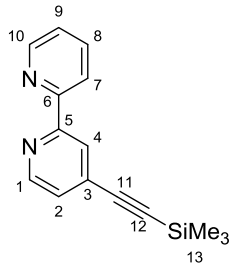

17

Under nitrogen atmosphere **16** (1.90 g, 8.08 mmol, 1.00 eq.) was dissolved in 50 ml diisopropylamine and 50 ml THF. After addition of bis(triphenylphosphine)-palladium(II) chloride (284 mg, 0.40 mmol, 0.05 eq.) and copper(I) iodide (38.5 mg, 0.20 mmol, 0.025 eq.), the reaction was degassed. Trimethylsilylacetylene (873 mg, 8.89 mmol, 1.23 mL, 1.10 eq.) was added dropwise and the solution was stirred for 66 h at 60 °C. The solvents were removed *in vacuo* and the crude product was purified using column chromatography (CyH/EtOAc = 5:1) giving the alkyne **17** (1.26 g, 4.99 mmol, 62%, Lit.[335] 98%) as off-white powder.

mp: 64-65 °C (Lit.[335]: 60-61 °C); **TLC** (CyH/EtOAc 4:1 v/v): R_f = 0.40; **^{1}H-NMR** (400 MHz, $CDCl_3$): δ = 8.68 (ddd, $^3J_{10,9}$ = 4.9 Hz, $^4J_{10,8}$ = 1.8 Hz, $^5J_{10,7}$ = 1.0 Hz, 1H, 10-H), 8.62 (dd, $^3J_{1,2}$ = 5.0 Hz, $^5J_{1,4}$ = 0.9 Hz, 1H, 1-H), 8.46 (dd, $^4J_{4,2}$ = 2.1 Hz, $^5J_{4,1}$ = 0.9 Hz, 1H, 4-H), 8.38 (ddd, $^3J_{7,8}$ = 7.9 Hz, $^4J_{7,9}$ = 1.1 Hz, $^5J_{7,10}$ = 1.0 Hz, 1H, 7-H), 7.82 (ddd, $^3J_{8,7}$ = 7.9 Hz, $^3J_{8,9}$ = 6.9 Hz, $^4J_{8,10}$ = 1.8 Hz, 1H, 8-H), 7.34-7.30 (m, 2H, 2-H/9-H), 0.27 (s, 9H, 13-H) ppm; **^{13}C-NMR** (101 MHz, $CDCl_3$): δ = 156.1 (C_q, C-5), 155.5 (C_q, C-6), 149.3 (C_t, C-10), 149.1 (C_t, C-1), 137.2 (C_t, C-8), 132.5 (C_q, C-3), 125.7 (C_t, C-2), 124.2 (C_t, C-9), 123.7 (C_t, C-4), 121.3 (C_t, C-7), 102.4 (C_q, C-11), 100.2 (C_q, C-12), -0.16 (C_q, C-13) ppm; **FT-IR** (ATR): $\tilde{\nu}$ = 3060 (w, ν(C-H)$_{arom}$), 3020 (w, ν(C-H)$_{arom}$), 2962 (w, ν(C-H)$_{arom}$), 2160 (w, ν(C≡C)), 1596 (w), 1582 (m, ν(C=C)$_{arom}$, ν(C=N)$_{arom}$), 1567 (w, ν(C=C)$_{arom}$, ν(C=N)$_{arom}$), 1535 (w), 1459 (m), 1390 (m), 1297 (w), 1249 (w), 1191 (w), 1149 (w), 1115 (w), 1092 (w), 1069 (w), 1043 (w), 988 (w), 892 (s), 839 (s, δ(C-H$_{arom}$)), 792 (m), 756 (m), 743 (m), 703 (w), 661 (w), 650 (w), 631 (w), 618 (w) cm^{-1}.

6.4.1.13 Synthesis of 4'-ethinyl-2,2'-bipyridine (11)[335]

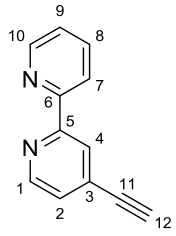

11

17 (1.06 g, 4.20 mmol, 1.00 eq.) was dissolved in 30 ml THF and after dropwise addition of a 1 M TBAF solution in THF (0.42 mL, 0.42 mmol, 0.10 eq.) the reaction mixture was stirred for 20 min at r.t. The solvent was removed *in vacuo* and after column chromatography on silica (CyH/EtOAc = 1:1) the product **11** (578 mg, 3.21 mmol, 76%) was obtained as colorless, crystalline solid.

mp: 78-79 °C (Lit.[335] 75-76 °C); **TLC** (CyH/EtOAc 1:1 v/v): R_f = 0.78; **^{1}H-NMR** (400 MHz, $CDCl_3$): δ = 8.66 (ddd, $^3J_{10,9}$ = 4.9 Hz, $^4J_{10,8}$ = 1.9 Hz, $^5J_{10,7}$ = 1.0 Hz, 1H, 10-H), 8.63 (dd, $^3J_{1,2}$ = 5.0 Hz, $^5J_{1,4}$ = 0.9 Hz, 1H, 1-H), 8.48 (dd, $^4J_{4,2}$ = 2.1 Hz, $^5J_{4,1}$ = 0.9 Hz, 1H, 4-H), 8.36 (ddd, $^3J_{7,8}$ = 7.9 Hz, $^4J_{7,9}$ = 1.1 Hz, $^5J_{7,10}$ = 1.0 Hz, 1H, 7-H), 7.82 (ddd, $^3J_{8,7}$ = 7.9 Hz, $^3J_{8,9}$ = 7.1 Hz, $^4J_{8,10}$ = 1.9 Hz, 1H, 8-H), 7.34 (dd, $^3J_{2,1}$ = 5.0 Hz, $^4J_{2,4}$ = 2.1 Hz, 1H, 2-H), 7.30 (ddd, $^3J_{9,8}$ = 7.9 Hz, $^3J_{9,10}$ = 4.9 Hz, $^4J_{9,7}$ = 1.1 Hz, 1H, 9-H), 3.31 (s, 1H, 12-H) ppm; **^{13}C-NMR** (101 MHz, $CDCl_3$): δ = 156.4 (C_q, C-5), 155.4 (C_q, C-6), 149.3 (C_t, C-10), 149.3 (C_t, C-1), 137.1 (C_t, C-8), 131.4 (C_q, C-3), 126.0 (C_t, C-2), 124.2 (C_t, C-9), 123.8 (C_t, C-4), 121.2 (C_t, C-7), 81.9 (C_q, C-12), 81.3 (C_q, C-11) ppm; **FT-IR** (ATR): $\tilde{\nu}$ = 3223 (m, ν(≡C-H)), 3060 (w, ν(C-H_{arom})), 3030 (w, ν(C-H_{arom})), 3011 (w, ν(C-H_{arom})), 2922 (w, ν(C-H)), 2108 (w, ν(C≡C)), 1599 (w), 1582 (m, ν(C=C)$_{arom}$, ν(C=N)$_{arom}$), 1563 (w), 1539 (m, ν(C=C)$_{arom}$, ν(C=N)$_{arom}$), 1454 (s), 1387 (m), 1289 (w), 1270 (w), 1250 (w), 1226 (w), 1192 (w), 1147 (w), 1094 (w), 1066 (w), 1042 (w), 990 (w), 913 (w), 899 (w), 857 (w), 841 (w), 792 (s, δ(C-H_{arom})), 748 (w), 735 (w), 707 (w), 684 (w), 662 (w), 624 (m) cm^{-1}.

6.4.1.14 Synthesis of 4-(2,2-dimethoxyethyl)-2,2'-bipyridine (18)

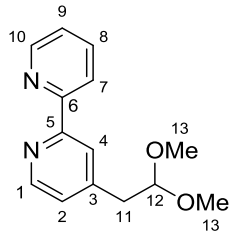

18

17 (955 mg, 3.78 mmol, 1.00 eq.) was dissolved in 80 ml MeOH and after addition of potassium carbonate (1.58 g, 11.4 mmol, 3.00 eq.) the suspension was stirred for 22 h at r.t. The solvent was removed *in vacuo* and the crude product was purified using column chromatography on silica (CH_2Cl_2/MeOH 98:2) yielding the side-product **18** (595 mg, 2.43 mmol, 64%) as a yellow oil.

TLC (CH_2Cl_2/MeOH 98:2v/v): R_f = 0.31; **^{1}H-NMR** (400 MHz, $CDCl_3$): δ = 8.68 (ddd, $^3J_{10,9}$ = 4.9 Hz, $^4J_{10,8}$ = 1.9 Hz, $^5J_{10,7}$ = 1.0 Hz, 1H, 10-H), 8.58 (dd, $^3J_{1,2}$ = 5.0 Hz, $^5J_{1,4}$ = 0.9 Hz, 1H, 1-H), 8.39 (ddd, $^3J_{7,8}$ = 7.9 Hz, $^4J_{7,9}$ = 1.1 Hz, $^5J_{7,10}$ = 1.0 Hz, 1H, 7-H), 8.28 (dd, $^4J_{4,2}$ = 2.1 Hz, $^5J_{4,1}$ = 0.9 Hz, 1H, 4-H), 7.80 (ddd, $^3J_{8,7}$ = 7.9 Hz, $^3J_{8,9}$ = 7.1 Hz,

$^4J_{8,10}$ = 1.9 Hz, 1H, 8-H), 7.29 (dd, $^3J_{2,1}$ = 5.0 Hz, $^4J_{2,4}$ = 2.1 Hz, 1H, 2-H), 7.22 (ddd, $^3J_{9,8}$ = 7.9 Hz, $^3J_{9,10}$ = 4.9 Hz, $^4J_{9,7}$ = 1.1 Hz, 1H, 9-H), 4.64 (t, $^3J_{12,11}$ = 5.7 Hz, 1H, 12-H), 3.36 (s, 6H, 13-H), 3.00 (d, $^3J_{11,12}$ = 5.7 Hz, 2H, H-11) ppm;**^{13}C-NMR** (101 MHz, $CDCl_3$): δ = 156.2 (C_q, C-6), 156.1 (C_q, C-5), 149.2 (C_t, C-1/C-10), 147.1 (C_q, C-3), 137.0 (C_t, C-8), 125.0 (C_t, C-2), 123.7 (C_t, C-9), 122.1 (C_t, C-4), 121.3 (C_t, C-7), 104.3 (C_t, C-12), 53.6 (C_p, C-13), 39.2 (C_s, C-11) ppm; **FT-IR** (ATR): $\tilde{\nu}$ = 3060 (w, ν_{as}(C-H)$_{arom}$), 3020 (w, ν(C-H)$_{arom}$), 2962 (w, ν_s(C-H)$_{arom}$), 1596 (w), 1582 (m, ν(C=C)$_{arom}$, ν(C=N)$_{arom}$), 1567 (w, ν(C=C)$_{arom}$, ν(C=N)$_{arom}$), 1535 (w), 1459 (m), 1390 (m), 1297 (w), 1249 (w), 1191 (w), 1149 (w), 1115 (w), 1092 (w), 1069 (w), 1043 (w), 988 (w), 892 (s), 839 (s, δ(C-H$_{arom}$)), 792 (m), 756 (m), 743 (m), 703 (w), 661 (w), 650 (w), 631 (w), 618 (w) cm^{-1}.

6.4.1.15 Synthesis of [2,2'-bipyridine]-4,4'-dicarboxylic acid (19)[336]

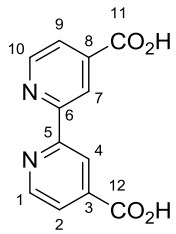

19

4,4'-dimethyl-2,2'-bipyridine (**20**) (1.84 g, 10.0 mmol, 1.00 eq.) was suspended in 30 mL of a conc. sulfuric acid water (1:1) mixture and cooled to 0 °C. Potassium permanganate (3.97 g, 25.0 mmol, 2.50 eq.) was added and after 15 min at 0 °C more potassium permanganate (3.97 g, 25.0 mmol, 2.50 eq.) was added. After further 15 min at 0 °C, the reaction was heated at 150 °C for 18 h. The reaction was quenched with 70 mL purified water and cooled to 0 °C. The precipitate was filtered off, washed with water and dried *in vacuo*. **19** (1.30 g, 5.31 mmol, 53%, lit.[336]: 74%) was obtained as beige powder.

mp: 264-266 °C; **TLC** (CH_2Cl_2/MeOH 9:1 v/v): R_f = 0.0; **^{1}H-NMR** (400 MHz, DMSO-*d*$_6$): δ = 16.0-12.0 (br.s., 2H, COOH), 8.92 (d, *J* = 4.4 Hz, 2H, 1-H/10-H), 8.85 (s, 2H, 4-H/7-H), 7.91 (d, *J* = 4.4 Hz, 2H, 2-H/9-H) ppm; **^{13}C-NMR** (101 MHz, DMSO-*d*$_6$): δ = 166.0 (C_q, C-4/C-7), 155.5 (C_q, C-3/C-8), 150.7 (C_t, C-1/C-10), 139.5 (C_q, C-6), 123.5 (C_t, C-5), 119.5 (C_t, C-2/C-9) ppm; **FT-IR** (ATR): $\tilde{\nu}$ = 3113 (w, ν(C-H)$_{arom}$), 2430 (w), 1878 (w), 1709 (m, ν(C=O)), 1604 (w), 1562 (w), 1456 (w), 1363 (m), 1284 (s), 1265 (s), 1238 (s), 1138 (m), 1066 (s), 1012 (s), 912 (m), 866 (m), 820 (m), 762 (s, δ(C-H$_{arom}$)), 721 (w), 679 (s) cm^{-1}.

6.4.2 Synthesis of ruthenium complexes

6.4.2.1 Synthesis of $[Ru(DMSO)_4Cl_2]$ (21)[337]

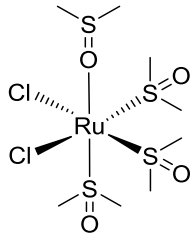

21

Under argon atmosphere dry DMSO (5.0 mL) was degassed for 30 min. Afterwards ruthenium(III) chloride hydrate (1.04 g, 5.00 mmol) was added. The dark black solution was heated to reflux for 10 min until it turned red-brownish. After cooling to r.t., the solvent was removed under nitrogen flow. The remaining, deeply orange viscous liquid was covered with acetone (50 mL) and stored in the fridge overnight. The precipitate was filtered off, washed with cold acetone (3x 5 mL) and diethyl ether (5x 5 mL) und dried intensively *in vacuo* to yield complex **21** (1.25 g, 2.58 mmol, 52%, lit.[337] 72%) as yellowish-orange, crystalline solid.

mp: 209-211 °C (lit.[337] 208 °C); **TLC** (CH_2Cl_2/MeOH 95:5 v/v): R_f = 0.42; **FT-IR** (ATR): $\tilde{\nu}$ = 3020 (w, ν_{as}(C-H)), 2922 (w, ν_s(C-H)), 1402 (w), 1308 (w), 1109 (s), 1088 (s), 1018 (m, ν(S=O$_{S\text{-bond}}$)), 991 (m), 960 (w), 931 (s, ν(S=O$_{O\text{-bond}}$)), 715 (m, ν_{as}(S-CH_3)), 677 (s, ν_s(S-CH_3)) cm^{-1}; **UV/Vis** (MeCN): λ_{max} (lg ε) 352 (5.19), 303 (5.13) nm ($c = 2.56 \cdot 10^{-4}$ mol l^{-1}).

6.4.2.2 Synthesis of $[Ru(bpy)_2Cl_2]$ (22)[338]

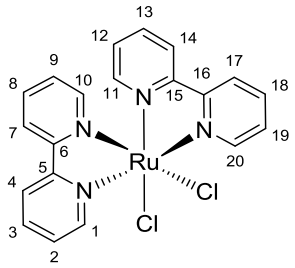

22

Under argon atmosphere 20 mL DMF were degassed for 30 min. After adding **21** (485 mg, 1.00 mmol, 1.00 eq.), 2,2'-bipyridine (**12**) (312 mg, 2.00 mmol, 2.00 eq.) and lithium chloride (2.12 g, 50 mmol, 50.0 eq.) the yellowish reaction mixture was heated to reflux for 21 h. After cooling to r.t., the dark purple solution was added to 250 mL acetone and stored in the fridge overnight. The precipitate was filtered off and washed with cold water (5x 5 mL), until the filtrate was colorless. The dark purple solid was further washed with cold ethanol (1x 5 mL) and diethyl ether (6x 5 mL) and intensively dried *in vacuo*. **22** (365 mg, 0.75 mmol, 75%, lit.[338]: 60%) was obtained as dark purple, crystalline solid.

mp: >330 °C; **TLC** (CH_2Cl_2/MeOH 9:1 v/v): R_f = 0.73;**^{1}H-NMR** (400 MHz, DMSO-d_6): δ = 9.97 (d, $^3J_{1/10,2/9}$ = 5.0 Hz, 2H, 1-H/10-H), 8.64 (d, $^3J_{4/7,3/8}$ = 8.0 Hz, 2H, 4-H/7-H), 8.48 (d, $^3J_{11/20,12/19}$ = 8.0 Hz, 2H, 11-H/20-H), 8.06 (ddd, $^3J_{3/8,4/7}$ = 8.0 Hz, $^4J_{3/8,1/10}$ = 1.4

Hz, 2H, 3-H/8-H), 7.77 (ddd, $^3J_{2/9,1/10}$ = 5.0 Hz, $^4J_{2/9,4/7}$ = 1.2 Hz, 2-H/9-H), 7.67 (ddd, $^3J_{12/19,11/20}$ = 8.0 Hz, $^4J_{12/19,14/17}$ = 1.3 Hz, 2H, 12-H/19-H), 7.51 (d, $^3J_{14/17,13/18}$ = 5.4 Hz, 2H, 14-H/17-H), 7.10 (ddd, $^3J_{13/18,14/17}$ = 5.4 Hz, $^4J_{13/18,11/20}$ = 1.1 Hz, 2H, 13-H/18-H) ppm; **^{13}C-NMR** (101 MHz, $CDCl_3$): δ = 160.2 (C_q, C-15/C-16), 158.2 (C_q, C-5/C-6), 153.2 (C_t, C-1/C-10), 152.0 (C_t, C-14/C-17), 134.6 (C_t, C-3/C-8), 133.3 (C_t, C-12/C-19), 125.4 (C_t, C-2/C-9), 125.3 (C_t, C-13/C-18), 122.9 (C_t, C-11/C-20), 122.5 (C_t, C-4/C-7) ppm; **FT-IR** (ATR): $\tilde{\nu}$ = 3479 (br.), 3099 (w, ν(C-H)$_{arom}$), 3068 (w, ν(C-H)$_{arom}$), 1668 (w), 1601 (m), 1460 (m, ν(C=C)$_{arom}$, ν(C=N)$_{arom}$), 1442 (w, ν(C=C)$_{arom}$, ν(C=N)$_{arom}$), 1417 (m), 1308 (w), 1265 (w), 1155 (w), 1122 (w), 1063 (w), 1016 (m), 976 (w), 903 (w), 798 (w), 764 (s, δ (C-H$_{arom}$)), 727 (m), 656 (w) cm^{-1}.

6.4.2.3 Synthesis of [Ru(bpy)$_2$(bpy-CCH)](PF$_6$)$_2$ (Ru1)[335]

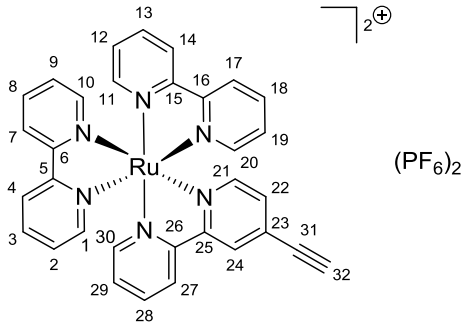

Ru1

Under argon atmosphere 10 mL MeOH were degassed for 30 min. After addition of **22** (95.0 mg, 0.20 mmol, 1.00 eq.) and silver(I) nitrate (66.6 mg, 0.39 mmol, 2.00 eq.) the mixture was stirred at r.t. for 3 h under exclusion of light. The solution was then transferred vie cannula to an argon flushed schlenk flask containing **11** (38.9 mg, 0.22 mmol, 1.10 eq.) and heated to reflux under light exclusion for 18 h. The solvent was removed *in vacuo*, the residue again dissolved in a small amount of MeOH and added dropwise to 20 mL of a saturated ammonium hexafluorophosphate solution. The red precipitate was filtered off, washed with cold water (3x 5 mL), diethyl ether (5x 5 mL) and dried *in vacuo*. The crude product was purified via column chromatography on silica (CH_2Cl_2/MeOH = 95:5 → 92:8) yielding the complex **Ru1** (95.0 mg, 0.11 mmol, 55%, Lit.[335]: 91%) as an intensively red, crystalline solid.

mp: 190-192 °C; **TLC** (CH_2Cl_2/MeOH 95:5 v/v): R_f = 0.20 (red-orange spot); **^{1}H-NMR** (400 MHz, acetone-*d*$_6$): δ = 8.94 (br. d, $^3J_{27,28}$ = 8.0 Hz, 1H, 27-H), 8.87 (br. d, $^4J_{24,22}$ = 1.1 Hz, 1H, 24-H), 8.84-8.81 (m, 4H, 4-H/7-H/14-H/17-H), 8.26-8.19 (m, 5H, 3-H/8-H/13-H/18-H/18-H), 8.17-8.04 (m, 6H, 1-H/10-H/11-H/20-H/21-H/30-H), 7.61-7.54 (m, 6H, 2-H/9-H/12-H/19-H/22-H/29-H), 4.43 (s, 1H, 32-H) ppm; **^{13}C-NMR** (101 MHz, acetone-*d*$_6$): δ = 158.6 (C_q, C-25), 158.0, 157.9, 157.9, 157.9 (4 C_q, C-5/C-6/C-15/C-16), 157.5 (C_q, C-26), 152.8, 152.7, 152.6, 152.5 (6 C_t, C-1/C-10/C-11/C-20/C-21/C-

30), 139.0, 139.0, 138.9, 138.8 (5 C_t, C-3/C-8/C-13/C-18/C-28), 132.3 (C_q, C-23), 130.3 (C_t, C-22), 129.1, 128.8, 128.8 (5 C_t, C-2/C-9/C-12/C-19/C-29), 127.4 (C_t, C-24), 125.7 (C_t, C-27), 125.3, 125.3 (4 C_t, C-4/C-7/C-14/C-17), 88.1 (C_t, C-32), 80.4 (C_q, C-31) ppm; **^{19}F-NMR** (376 MHz, acetone-d_6): δ = -72.3 ppm (d, 12F, PF_6); **^{31}P-NMR** (162 MHz, acetone-d_6): δ = -144.3 ppm (septett, 1P, PF_6); **FT-IR** (ATR): $\tilde{\nu}$ = 3274 (w), 3089 (w, ν(C-H)$_{arom}$), 2921 (w, ν(C-H)$_{arom}$), 2116 (w, ν(C≡C)), 1606 (m), 1466 (m, ν(C=C)$_{arom}$, ν(C=N)$_{arom}$), 1444 (w, ν(C=C)$_{arom}$, ν(C=N)$_{arom}$), 1315 (w), 1271 (w), 1238 (w), 1165 (w), 1028 (w), 825 (vs, ν(P-F)), 756 (vs, ν(P-F)), 731 (w), 658 (w), 621 (w) cm^{-1}; **Raman** (λ_{ex} = 445 nm): $\tilde{\nu}$ = 663 (m), 844 (br), 1023 (m), 1171 (m), 1269 (m), 1314 (m), 1482 (s), 1555 (s), 1599 (s), 2327 (w); **UV/Vis** (MeCN): λ_{max} (lg ε) = 454 (5.43), 287 (6.13) 242 (5.83), 207 (5.84) nm (c = 1.26·10^{-4} mol l^{-1}).

6.4.2.4 Synthesis of [Ru(tpy)(DMSO)Cl$_2$] (23)[339]

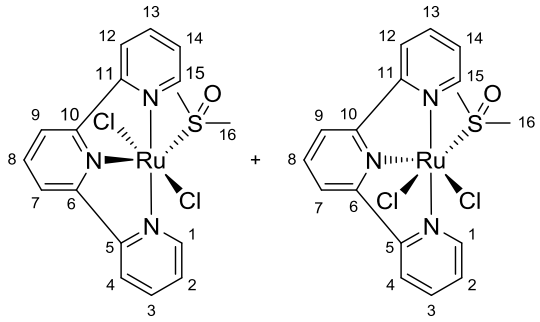

23

Under argon-atmosphere a mixture of 5 mL ethanol and 1.2 ml MeOH was degassed for 30 min. After addition of **21** (242 mg, 0.50 mmol, 1.00 eq.), the yellow solution was heated to reflux for 15 min. **1** (117 mg, 0.50 mmol, 1.00 eq.) was added and the mixture was heated to reflux for further 6.5 h. After cooling to r.t., the precipitate was filtered off, washed with cold water (4x 7 mL), cold ethanol (3x 5 mL) and diethyl ether (5x 5mL) and dried *in vacuo*. The complex **23** (185 mg, 0.38 mmol, 77%, Lit.[339]: 88%) was obtained as a black purple, powdery mixture of isomers.

In a second attempt, 10 mL $CHCl_3$ were degassed for 30 min under argon atmosphere. **21** (242 mg, 0.50 mmol, 1.00 eq.) and **1** (117 mg, 0.50 mmol, 1.00 eq.) were added and the reaction mixture heated to reflux for 17 h. After cooling to r.t., the precipitate was filtered off, washed with cold water (4x 7 mL), cold ethanol (3x 5 mL) and diethyl ether (5x 5mL) and dried *in vacuo*. The complex **23** (120 mg, 0.25 mmol, 50%, Lit.[339] 85%) was obtained as a purple-brownish, powdery mixture of isomers. The pure *trans* isomer of **23** (11.2 mg, 93.3 µmol) could by isolated from this mixture.

mp: >330 °C (pure *trans* isomer) + >330 °C (mixture of isomers); **TLC** (CH_2Cl_2/MeOH 9:1 v/v): R_f = 0.50 (*trans*, brown spot), 0.38 (*cis*, purple spot); **^{1}H-NMR** (400 MHz,

DMSO-d_6): *trans isomer:* δ = 9.36 (d, $^3J_{1,15/2,14}$ = 6.5 Hz, 2H, 1-H/15-H), 8.76 (d, $^3J_{7,9/8}$ = 8.0 Hz, 2H, 7-H/9-H), 8.59 (d, $^3J_{4,12/3,13}$ = 7.5 Hz, 2H, 4-H/12-H), 8.19 (t, $^3J_{8/7,9}$ = 8.0 Hz, 1H, 8-H), 8.01-7.97 ($^3J_{3,13/4,12}$ = 7.7 Hz, $^3J_{3,13/2,14}$ = 7.7 Hz, $^4J_{3,13/1,15}$ = 1.2 Hz, 2H, 3-H/13-H), 7.53 (ddd, $^3J_{2,14/3,13}$ = 7.5 Hz, $^3J_{2,14/1,15}$ = 6.5 Hz, $^4J_{2,14/4,12}$ = 1.2 Hz, 2H, 2-H/14-H), 3.59 (s, 6H, 16-H) ppm; isomeric mixture *(cis isomer):* δ = 9.02 (d, $^3J_{1,15/2,14}$ = 5.5 Hz, 2H, 1-H/15-H), 8.58 (d, $^3J_{4,12/3,13}$ = 7.7 Hz, 2H, 4-H/12-H), 8.53 (d, $^3J_{7,9/8}$ = 8.0 Hz, 2H, 7-H/9-H), 8.15 (dt, $^3J_{3,13/2,14}$ = 8.0 Hz, $^3J_{3,13/4,12}$ = 7.7 Hz, $^4J_{3,13/1,15}$ = 1.3 Hz, 2H, 3-H/13-H), 8.02 (t, $^3J_{8/7,9}$ = 8.0 Hz, 1H, 8-H), 7.79 (ddd, $^3J_{2,14/3,13}$ = 8.0 Hz, $^3J_{2,14/1,15}$ = 5.5 Hz, $^4J_{2,14/4,12}$ = 1.3 Hz, 2H, 2-H/14-H), 3.59 (s, 6H, 16-H) ppm; **^{13}C-NMR** (101 MHz, DMSO-d_6): *trans isomer:* δ = 158.8 (C_t, C-5/C-11), 157.0 (C_p, C-6/C-10), 155.8 (C_t, C-1/C-15), 136.9 (C_t, C-3/C-13), 136.2 (C_t, C-8), 126.4 (C_t, C-2/C-14), 123.1 (C_t, C-4/C-12), 121.5 (C_t, C-7/C-9), 44.6 (C_p, C-16) ppm; isomeric mixture *(cis isomer):* δ = 159.3 (C_t, C-6/C-10), 159.1 (C_p, C-5/C-11), 153.1 (C_t, C-1/C-15), 137.3 (C_t, C-3/C-13), 133.5 (C_t, C-8), 127.4 (C_t, C-2/C-14), 123.1 (C_t, C-4/C-12), 122.2 (C_t, C-7/C-9), 42.0 (C_p, C-16) ppm; **FT-IR** (ATR): $\tilde{\nu}$ = 3479 (br. m), 3099 (w, ν(C-H)$_{arom}$), 3068 (w, ν(C-H)$_{arom}$), 1668 (w), 1601 (m), 1460 (m, ν(C=C)$_{arom}$, ν(C=N)$_{arom}$), 1442 (w, ν(C=C)$_{arom}$, ν(C=N)$_{arom}$), 1417 (m), 1308 (w), 1265 (w), 1155 (w), 1122 (w), 1063 (w), 1016 (m), 976 (w), 903 (w), 798 (w), 764 (s, δ(C-H$_{arom}$)), 727 (m), 656 (w) cm^{-1}.

6.4.2.5 Synthesis of [Ru(tpy)(tpy-CCH)](PF$_6$)$_2$ (Ru2)[339]

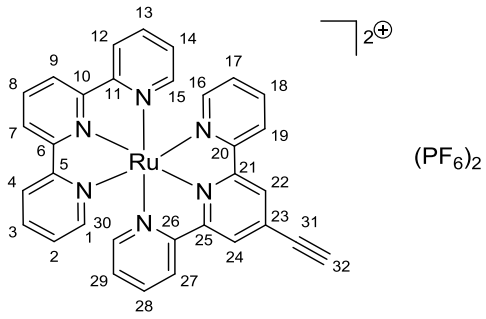

Ru2

Under argon atmosphere 20 mL MeOH were degassed für 30 min. After an isomeric mixture of **23** (169 mg, 0.35 mmol, 1.00 eq.) and silver(I) nitrate (119 mg, 0.70 mmol, 2.00 eq.) were added, the mixture was stirred at 80 °C for 6 h under exclusion of light. The solution was then transferred via cannula to an argon flushed schlenk flask containing **5** (95.2 mg, 0.37 mmol, 1.05 eq.) and stirred at 60 °C under light exclusion for 18 h. After cooling to r.t., a 10 ml saturated ammonium hexafluorophosphate solution was added dropwise and the solvent slowly removed *in vacuo*. The precipitate was filtered of, washed with cold water (3x 10 mL), diethyl ether (5x 10 mL) and dried *in vacuo*. The crude product was purified using column

chromatography on silica (/MeOH = 92.8) yielding the complex **Ru2** (48.0 mg, 54.4 4 µmol, 16%. Lit.[339]: 58%) as dark red, crystalline solid.

mp: 251-253 °C ; **TLC** (CH_2Cl_2/MeOH 98:2 v/v): R_f = 0.13; **^{1}H-NMR** (400 MHz, acetone-*d_6*): δ = 9.10 (s, 2H, H-22/H-24), 9.05 (d, $^3J_{7/9,8}$ = 8.1 Hz, 2H, 7-H/9-H), 8.89 (ddd, $^3J_{19/27,18/28}$ = 8.1 Hz, $^4J_{19/27,17/29}$ = 1.4 Hz, $^5J_{19/27,16/30}$ = 0.8 Hz, 2H, 19-H/27-H), 8.79 (ddd, $^3J_{4/12,3/13}$ = 8.2 Hz, $^4J_{4/12,2/14}$ = 1.3 Hz, $^5J_{4/12,1/15}$ = 0.8 Hz, H4-H/12-H), 8.58 (t, $^3J_{8,7/9}$ = 8.1 Hz, 8-H), 8.10-8.03 (m, 4H, 3-H/13-H/18-H/28-H), 7.75 (ddd, $^3J_{1/15,2/14}$ = 5.7 Hz, $^4J_{1/15,3/13}$ = 1.6 Hz, $^5J_{1/15,4/12}$ = 0.7 Hz, 2H, 1-H/15-H), 7.73 (ddd, $^3J_{16/30,17/29}$ = 5.6 Hz, $^4J_{16/30,18/28}$ = 1.6 Hz, $^5J_{16/30,19/27}$ = 0.7 Hz, 2H, 16-H/30-H), 7.34 (ddd, $^3J_{17/29,18/28}$ = 7.7 Hz, $^3J_{17/29,16/30}$ = 5.6 Hz, , $^4J_{17/29,19/27}$ = 1.4 Hz, 2H 17-H/29-H), 7.30 (ddd, $^3J_{2/14,13/3}$ = 7.7 Hz, $^3J_{2/14,1/15}$ = 5.7 Hz, $^4J_{2/14,4/12}$ = 1.3 Hz 2H, 2-H/14-H), 4.51 (s, 1H, 32-H) ppm; **^{13}C-NMR** (101 MHz, acetone-*d_6*): δ = 159.0 (C_q, C-5/C-11), 158.6 (C_q, C-20/C-26), 156.6 (C_q, C-21/25), 156.1 (C_q, C-6/10), 153.6 (C_t, C-1/C-15), 153.5 (C_t, C-16/C-30), 139.3 (C_t, C-3/C-13), 139.2 (C_t, C-18/C-28), 137.4 (C_t, C-8), 130.2, 128.9 (C_t, C-19/27), 128.6 (C_t, C-4/C-12), 126.9 (C_t, C-22/C-24), 125.7 (C_t, C-17/C-29), 125.5 (C_t, C-2/C-14), 124.9 (C_t, C-7/C-9), 87.1 (C_t, C-32), 81.4 (C_q, C-31) ppm; **^{19}F-NMR** (376 MHz, acetone-*d_6*): δ = -72.7 ppm (d, 12F, P*F*$_6$); **^{31}P-NMR** (162 MHz, acetone-*d_6*): δ = -144.3 ppm (septett, 1P, *P*F_6); **FT-IR** (ATR): $\tilde{\nu}$ = 3269 (w), 2924 (w, ν(C-H)$_{arom}$), 2852 (w, ν(C-H)$_{arom}$), 1604 (m), 1448 (m, ν(C=C)$_{arom}$, ν(C=N)$_{arom}$), 1421 (w, ν(C=C)$_{arom}$, ν(C=N)$_{arom}$), 1390 (w), 1288 (w), 1242 (w), 1163 (w), 1031 (w), 827 (vs, ν(P-F)), 768 (vs, ν(P-F)), 609 (w) cm^{-1}; **Raman** (λ_{ex} = 445 nm): $\tilde{\nu}$ = 663 (m), 844 (br), 1023 (m), 1171 (m), 1269 (m), 1314 (m), 1482 (s), 1555 (s), 1599 (s), 2327 (w); **UV/Vis** (MeCN): λ_{max} = (lg ε) 483 (br, 5.37), 309 (5.86), 271 (5.82) 241 (5.83), 205 (5.67) nm (c = 2.24·10^{-4} mol l^{1}).

6.4.2.6 Synthesis of *cis*-Ru(dcb)$_2$(NCS)$_2$ (Ru3)[340]

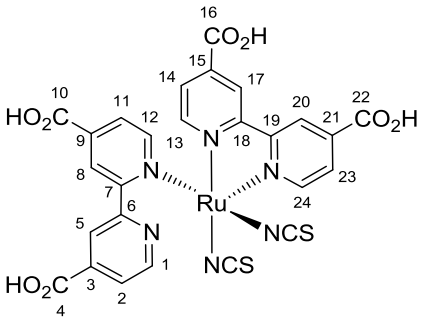

Ru3

Under argon atmosphere 50 mL abs. DMF were degassed für 30 min. After addition of **21** (100 mg, 206 µmol, 1.00 eq.) and **19** (50.5 mg, 206 µmol, 1.00 eq.), the mixture was stirred in the dark at 60 °C for 4 h. After further addition of **19** (50.5 mg, 206 µmol, 1.00 eq), the reaction solution was heated under reflux for 18 h. Ammonium thiocyanate

(236 mg,3.10 mmol, 15.0 eq.) was added and the reaction heated again under reflux for 18 h. After cooling to r.t., DMF was removed *in vacuo* and purified water (35 mL) was added. The suspension was filtered off, washed with cold water (3x 10 mL) and dissolved in MeOH. MeOH was removed *in vacuo* and the crude product was redissolved in a small amount of MeOH and water (40 mL) was added. After one night at 2 °C, the solid was filtered off, washed with old wate r(3x 10 mL) and dried *in vacuo* yielding complex **Ru3** (57.0 mg, 80.8 µmol, 39 %, Lit.[340]: 70%) as a dark-purple, crystalline solid.

mp: >330 °C; **TLC** (CH_2Cl_2/MeOH 9:1 v/v): R_f = 0.00; **^{1}H-NMR** (400 MHz, MeOD): δ = 9.62 (d, *J* = 5.8 Hz, 2H, 1-H, 24-H), 9.09 (s, 2H, 5-H, 20-H), 8.93 (s, 2H, 8-H, 17-H), 8.34 (d, *J* = 5.8 Hz, 2H, 2-H, 23-H), 7.83 (d, *J* = 5.8 Hz, 2H, 12-H, 13-H), 7.67 (d, *J* = 5.8 Hz, 2H, 11-H, 14-H) ppm; **^{13}C-NMR** (101 MHz, MeOD): δ = 123.7 (C_t, C-8, C-17), 124.0 (C_t, C-5, C-20), 126.5 (C_t, C-2, C-23), 127.4 (C_t, C-11, C-14), 139.6 (C_q, C-6, C-19), 140.2 (C_t, C-7, C-18), 153.6 (C_t, C-12, C-13), 155.2 (C_t, C1, C-24), 159.1 (C_q, C-3, C-21), 160.8 (C_q, C-6, C-15), 166.2 (C_q, C-4, C-22), 166.7 (C_q, C-10, C-16) ppm; **FT-IR** (ATR): $\tilde{\nu}$ = 3074 (w), 2918 (w, ν(C-H)$_{arom}$), 2848 (w, ν_s(C-H)$_{arom}$), 2476 (w), 2362 (w), 2098 (s, ν(SCN)), 1984 (m, ν(SCN)), 1714 (s, ν(C=O)), 1608 (m), 1550 (w), 1468 (w), 1408 (s), 1336 (m), 1255 (s), 1223 (s), 1124 (m), 1065 (w), 1018 (m), 978 (w), 897 (m), 858 (m), 806 (s, δ(C-H$_{arom}$)), 768 (s, δ(C-H$_{arom}$)), 719 (m), 663 (s), 631 (m) cm^{-1}; **Raman** (λ_{ex} = 532 nm): $\tilde{\nu}$ = 677 (m), 1021 (m), 1171 (br), 1266 (m), 1302 (m), 1471 (s), 1542 (s), 1608 (s); **UV/Vis** (MeCN): λ_{max} (lg ε) = 544 (br, 5.14), 397 (br, 5.18), 315 (5.68), 303 (sh., 5.51), 251 (5.49) nm (c = 5.86·10^{-4} mol l^{1}).

6.4.2.7 Synthesis of [Ru(tpy)Cl)$_3$] (Ru4)[341]

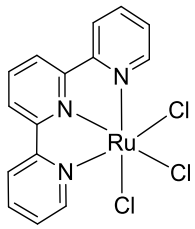

Ru4

Under argon atmosphere ruthenium (III) chloride hydrate (207 mg, 1.00 mmol, 1.00 eq.) was dissolved in 105 mL EtOH. After addition of **1** (233 mg, 1.00 mmol, 1.00 eq.), the mixture was refluxed for 5 h. After cooling to r.t., the precipitate was filtered and washed with cold EtOH (3x 15 ml), diethyl ether (5x 15 ml) and dried *in vacuo* yielding **Ru4** (142 mg, 320 µmol, 32%) as brown-black, powdery solid.

mp: >330 °C; **TLC** (CH_2Cl_2/MeOH 98:2 v/v): R_f = 0.25; **FT-IR** (ATR): $\tilde{\nu}$ = 3065 (m, ν(C-H)$_{arom}$), 1658 (m), 1650 (m), 1596 (m), 1566 (w), 1445 (m, ν(C=C)$_{arom}$, ν(C=N)$_{arom}$),

1385 (w, ν(C=C)$_{arom}$, ν(C=N)$_{arom}$), 1280 (w), 1234 (w), 1156 (w), 1095 (m), 1032 (w), 777 (s, δ(C-H$_{arom}$)), 725 (m) cm^{-1}.

Due to the paramagnetic Ru(III)-center no meaningful NMR-spectra have been measured.

6.4.3 CuAAC reactions with ruthenium complexes

General procedure (R1): Under argon atmosphere **Ru1** (1.00 eq.), the used azide (**L1**, **L2** or **L6**) and sodium ascorbate were dissolved in 4 mL CH_2Cl_2 and 4 mL water. The mixture was degassed, copper(II) sulfate was added and the solution stirred at r.t. for a specific time. The reaction mixture was diluted with water and CH_2Cl_2 and the phases were separated. The aqueous phase was extracted with CH_2Cl_2 (8x 30 mL). The combined organic phases were washed with water, dried over sodium sulfate and the solvent removed *in vacuo*. The residue was solved in MeOH and a solution of ammonium hexafluorophosphate solution (73.4 mg, 453 µmol, 10.0 eq.) in water was added dropwise while stirring. After one night in the fridge, the precipitate was filtered off, washed with cold MeOH (1x 5 mL), cold water (1x 5 mL) and diethylether (5x 5 mL). The crude product was purified using column chromatography on silica (CH_2Cl_2/MeOH = 92:8).

6.4.3.1 CuAAC reaction between L1 and Ru1

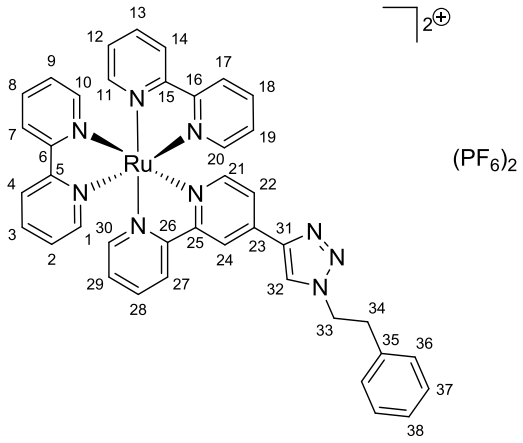

L1-Ru1

Amounts/parameters used in **R1**: **Ru1** (40.0 mg, 45.3 µmol), **L1** (16.2 mg, 99.7 µmol, 2.25 eq.), sodium ascorbate (6.00 mg, 30.3 µmol, 0.66 eq.), copper(II) sulfate (1.61 mg, 10.1 µmol, 0.22 eq.), ammonium hexafluorophosphate (73.4 mg, 453 µmol, 10.0 eq.); time 18 h. **L1-Ru1** (16.0 mg, 15.5 µmol, 35 %) was isolated as orange, crystalline solid.

mp: 155-157 °C; **TLC** (CH_2Cl_2/MeOH 9:1 v/v): R_f = 0.08; **^{1}H-NMR** (400 MHz acetone-*d$_6$*): δ = 9.09 (s, 1H, 24-H), 8.82 (d, *J* = 8.0 Hz, 1H, 27-H), 8.81 (d, *J* = 8.0 Hz, 4H, 4-H/7-H/14-H/17-H), 8.71 (s, 1H, 32-H), 8.23-8.19 (m, 6H, 3-H/8-H/13-H/18-H/28H/30-H), 8.07-8.03 (m, 5H, 1-H/10-H/11-H/20-H/21-H), 7.92 (dd, *J* = 6.0 Hz, *J* = 2.0 Hz, 1H,

22-H), 7.60-7.56 (m, 5H, 2-H/9-H/12-H/19-H/29-H), 7.27-7.23 (m, 5H, 36-H/37-H/38-H), 4.80 (t, $^3J_{6'''',5''''}$ = 7.2 Hz, 2H, 33-H), 3.32 (t, $^3J_{6'''',5''''}$ = 7.2 Hz, 2H, 34-H) ppm; **^{13}C-NMR** (101 MHz, acetone-*d*$_6$): δ = 158.6 (C_q, C-25), 158.1 (C_q, C-5/C-15), 158.1 (C_q, C-6/C-16), 158.1 (C_q, C-26), 152.9 (C_t, C-1/C-11), 152.9 (C_t, C-10/C-20), 152.7 (C_t, C-21), 152.7 (C_t, C-30), 143.7 (C_q, C-31), 141.2 (C_q, C-23), 138.9 (C_t, C-3/C-8/C-13/C-18), 138.3 (C_t, C-28), 137.4 (C_q, C-35), 129.6 (C_t, C-36), 129.4 (C_t, C-38), 128.8 (C_t, C-29), 128.8 (C_t, C-2/C-9/C-12/C-19), 127.6 (C_t, C-37), 125.5 (C_t, C-27), 125.3 (C_t, C-4/C-7/C-14/C-17), 125.1 (C_t, C-32), 123.7 (C_t, C-22), 120.6 (C_t, C-24), 52.3 (C_t, C-33), 36.8 (C_t, C-34) ppm; **^{19}F-NMR** (376 MHz, acetone-*d*$_6$): δ = -72.2 ppm (d, 12F, P*F*$_6$); **^{31}P-NMR** (162 MHz, acetone-*d*$_6$): δ = -144.6 ppm (septett, 1P, *P*F_6); **FT-IR** (ATR): $\tilde{\nu}$ = 2360 (w), 2104 (w), 1701 (w), 1622 (w), 1606 (w), 1564 (w, ν(C=C)$_{arom}$, ν(C=N)$_{arom}$), 1462 (m, ν(C=C)$_{arom}$, ν(C=N)$_{arom}$), 1442 (m), 1360 (w), 1313 (w), 1228 (w), 1167 (w), 1047 (w), 1028 (w), 829 (s, ν(P-F)), 760 (m, ν(P-F)), 702 (m), 656 (w), 609 (w) cm^{-1}; **Raman** (λ_{ex} = 445 nm): $\tilde{\nu}$ = 664 (w), 842 (br), 1023 (m), 1172 (m), 1270 (m), 1314 (m), 1484 (s), 1556 (s), 1599 (s), 2328 (w); **UV/Vis** (MeCN): λ_{max} (lg ε) = 455 (4.91), 288 (5.59), 246 (5.25) nm (c = 3.26·10^{-4} mol l^{-1}); **HRMS** (m/z, ESI,+): [M]$^+$ calc. for $C_{40}H_{33}N_9Ru$: 370.5946; found, 370.5952; **EA** (calc., found for $C_{40}H_{33}N_9RuP_2F_{12}$): C (46.61, 46.25), H (3.23, 3.15), N (12.23, 12.33).

6.4.3.2 CuAAC reaction between L2 and Ru1[335]

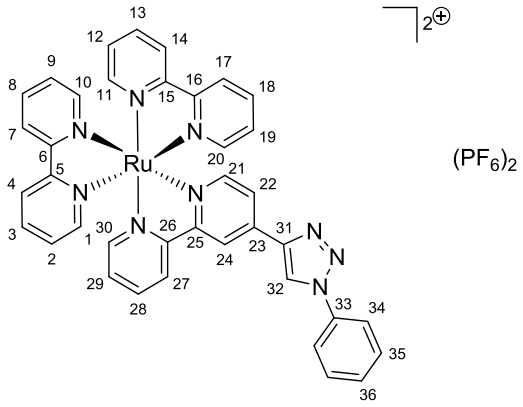

L2-Ru1

Amounts/parameters used in **R1**: **Ru1** (40.0 mg, 45.3 µmol), **L2** (13.4 mg, 99.7 µmol, 2.25 eq.), sodium ascorbate (6.00 mg, 30.3 µmol, 0.66 eq.), copper(II) sulfate (1.61 mg, 10.1 µmol, 0.22 eq.), ammonium hexafluorophosphate (73.4 mg, 453 µmol, 10.0 eq.); time 18 h. **L2-Ru1** (28.4 mg, 28.3 µmol, 63%, Lit.[335]: 79%) was isolated as orange, crystalline solid.

mp: 210-212 °C; **TLC** (CH_2Cl_2/MeOH 9:1 v/v): R_f = 0.08; **^{1}H-NMR** (400 MHz, acetone-*d*$_6$): δ = 9.39 (s, 1H, 32-H), 9.23 (d, *J* = 1.6 Hz, 1H, 24-H), 8.99 (d, *J* =8.0 Hz, 1H, 27-H), 8.83 (dd, *J* = 8.0 Hz, *J* = 1.6 Hz, 4H, 4-H/7-H/14-H/17-H), 8.25-8.19 (m, 6H, 1-H/10-H/11-H/20-H/21-H/30-H), 8.13 (t, *J* =6.0 Hz, 1H, 22-H), 8.11-8.07 (m, 5H, 3-H/8-H/13-

H/18-H/28-H), 7.96 (d, *J* = 7.6 Hz, 2H, 34-H), 7.68-7.57 (m, 8H, 2-H/9-H/12-H/19-H/26-H/35-H/36-H) ppm; **^{13}C-NMR** (101 MHz, acetone-*d*$_6$): δ = 158.8 (C_q, C-25), 158.1 (C_q, C-5/15), 158.1 (C_q, C-6/C-16), 158.0 (C_q, C-26), 153.1 (C_t, C-1/C-11), 152.8 (C_t, C-10/C-20), 152.7 (C_t, C-21), 152.7 (C_t, C-30), 144.8 (C_q, C-31), 140.6 (C_q, C-23), 139.0 (C_t,C-3/C-8/C-13/C-18), 138.9 (C_t, C-28), 137.6 (C_q, C-33), 130.9 (C_t, C-35), 130.2 (C_t, C-36), 128.9 (C_t, C-29), 128.8 (C_t, C-2/C-12/C-9/C-19), 125.5 (C_t. C-27), 125.3 (C_t, C-4/C-7/C-14/C-17), 123.9 (C_t, C-22), 123.0 (C_t, C-32), 121.3 (C_t, C-34), 120.9 (C_t, C-24) ppm; **^{19}F-NMR** (376 MHz, acetone-*d*$_6$): δ = -72.4 ppm (d, 12F, P*F*$_6$); **^{31}P-NMR** (162 MHz, acetone-*d*$_6$): δ = -144.4 ppm (septett, 1P, *P*F$_6$); **FT-IR** (ATR): $\tilde{\nu}$ = 1728 (w), 1624 (w), 1601 (w), 1504 (w, ν(C=C)$_{arom}$, ν(C=N)$_{arom}$), 1466 (w, ν(C=C)$_{arom}$, ν(C=N)$_{arom}$), 1442 (w), 1313 (w), 1242 (w), 1163 (w), 1038 (w), 825 (s, ν(P-F)), 758 (s, ν(P-F)), 733 (m), 688 (w), 656 (w), 607 (w) cm^{-1}; **Raman** (λ_{ex} = 445 nm): $\tilde{\nu}$ = 664 (w), 860 (br), 1024 (m), 1170 (m), 1273 (m), 1314 (m), 1484 (s), 1556 (s), 1600 (s), 2328 (w); **UV/Vis** (MeCN): λ_{max} (lg ε) = 455 (5.25), 288 (5.94), 245 (5.62) nm (c = 1.84·10^{-4} mol l^{-1}); **HRMS** (m/z, ESI,+): [M]$^+$ calc. for $C_{38}H_{29}N_9Ru$: 356.5794; found, 356.5792; **EA** (calc., found for $C_{38}H_{29}N_9RuP_2F_{12}$): C (45.52, 45.44), H (2.92, 2.98), N (12.57, 12.19).

6.4.3.3 CuAAC reaction between L6 and Ru1

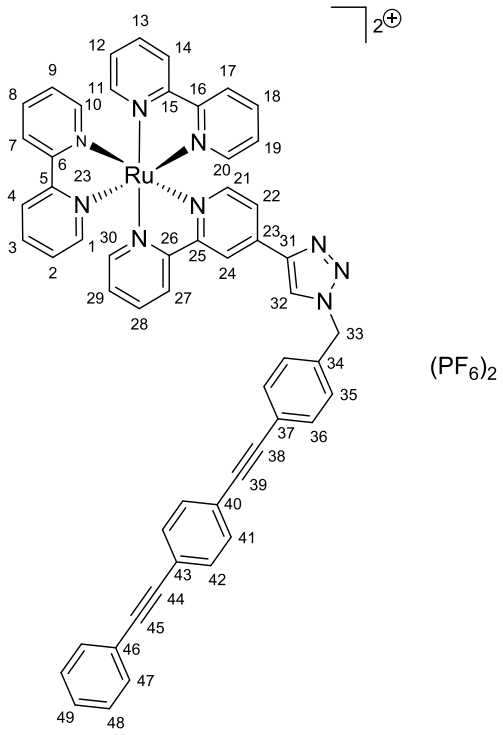

L6-Ru1

Amounts/parameters used in **R1**: **Ru1** (44.0 mg, 49.0 µmol, 1.00 eq), **L6** (25.0 mg, 73.5 µmol, 1.50 eq.), sodium ascorbate (7.80 mg, 39.2 µmol, 0.80 eq.), copper(II) sulfate (3.10 mg, 19.6 µmol, 0.40 eq.), ammonium hexafluorophosphate (79.9 mg, 490 µmol, 10.0 eq.); time 3 d. **L3-Ru1** (25.0 mg, 20.4 µmol, 42%) was isolated as orange, crystalline solid.

mp: 235-236 °C; **TLC** (CH_2Cl_2/MeOH 9:1 v/v): R_f = 0.08; **^{1}H-NMR** (400 MHz, acetone-*d*$_6$): δ = 9.16 (d, *J* = 1.4 Hz, 1H, 24-H), 8.95 (d, *J* = 8.0 Hz, 1H, 27-H), 8.87 (s, 1H, 32-H), 8.84-8.82 (m, 4H, 4-H/7-

H/14-H/17-H), 8.24-8.18 (m, 6H, 3-H/8-H/13-H/18-H/28-H/30-H), 8.09-8.06 (m, 5H, 1-H/10-H/11-H/20-H/21-H), 8.00 (dd, *J* = 6.0 Hz, *J* = 1.8 Hz, 1H, 22-H), 7.62-7.56 (m, 13H, 2-H/9-H/12-H/19-H/29-H/36-H/41-H/42-H/47-H), 7.47-7.43 (m, 5H, 35-H/48-H/49-H), 5.83 (s, 1H, 33-H) ppm; **^{13}C-NMR** (101 MHz, acetone-*d*$_6$): δ = 158.6 (C_q, C-25), 158.1 (C_q, C5/C-15), 158.1 (C_q, C-6/C-166), 158.1 (C_q, C-26), 153.0 (C_t, C-21), 152.8 (C_t, C-30), 152.7 (C_t, C-1/C-11), 152.7 (C_t, C-10/C-20), 144.4 (C_q, C-31), 141.0 (C_q, C-23), 138.9 (C_t, C-3/C-8/C-13/C-18/C-28), 137.1 (C_q, C-34), 132.9 (C_t, C-36), 132.5 (C_t, C-41/C-42), 132.4 (C_t, C-47), 129.7 (C_t, C-49), 129.5 (C_t, C-48), 129.3 (C_t, C-35), 128.9 (C_t, C-29), 128.8 (C_t, C-2/C-9/C-12/C-19), 125.5 (C. C-27), 125.3 (C_t, C-4/C-7/C-14/C-17), 125.2 (C_t, C-32), 124.3 (C_q, C-40 or C-43), 124.0 (C_q, C-37), 123.9 (C_t, C-22), 123.7 (C_q, C-40 or C-43), 123.6 (C_q, C-46), 120.9 (C_t, C-24), 92.1 (C_q, C-45), 91.3 (C_q, C-38), 90.3 (C_q, C-39 or C-44), 89.5 (C_q, C-39 or C-44), 54.4 (C_s, C-33) ppm; **^{19}F-NMR** (376 MHz, acetone-*d*$_6$): δ = -72.4 ppm (d, 12F, P*F*$_6$); **^{31}P-NMR** (162 MHz, acetone-*d*$_6$): δ = -144.4 ppm (septett, 1P, *P*F$_6$); **FT-IR** (ATR): $\tilde{\nu}$ = 2921 (w, ν_{as}(C-H)$_{arom}$), 2854 (w, ν_s(C-H)$_{arom}$), 1624 (w), 1603 (w), 1519 (w, ν(C=C)$_{arom}$), 1464 (w, ν(C=N)$_{arom}$), 1442 (w, ν(C=N)$_{arom}$), 1365 (w), 131 (w), 1234 (w), 1026 (w), 829 (vs, ν(P-F)), 760 (s, ν(P-F)), 731 (w), 690 (w), 660 (w) cm^{-1}. **Raman** (λ_{ex} = 445 nm): $\tilde{\nu}$ = 662 (w), 849 (br), 1025 (m), 1172 (m), 1275 (m), 1313 (m), 1485 (s), 1556 (s), 1599 (s), 2194 (w); **UV/Vis** (MeCN): λ_{max} (lg ε) = 455 (3.72), 339 (4.24, sh), 319 (4.41), 289 (4.53), 245 (4.15) nm (c = 4.45·10^{-5} mol l^{-1}); **HRMS** (m/z, ESI,+): $[M]^+$ calc. for $C_{55}H_{39}N_9Ru$: 463.6180; found, 463.6186; **EA** (calc., found for $C_{55}H_{39}N_9RuP_2F_{12}$): C (54.28, 54.51), H (3.23, 3.48), N (10.36, 10.26).

6.4.3.4 Synthesis of triphenylphosphinecopper(I) iodide (31)[355]

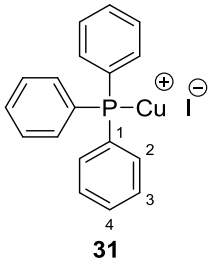

31

Under nitrogen atmosphere copper(I) iodide (286 mg, 1.50 mmol, 1.00 eq) was dissolved in 30 mL MeCN. After dropwise addition of triphenylphosphine (393 mg, 1.50 mmol, 1.00 eq.) in 10 mL MeCN, the reaction mixture was stirred for 3 h at r.t. The precipitate was filtered off, washed several times with MeCN and dried *in vacuo*. **31** (642 mg, 1.42 mmol, 95 %, lit.[355] 97%) was obtained as colorless powder.

mp: 275 °C; **TLC** (CH_2Cl_2/MeOH 9:1 v/v): R_f = 0; **^{1}H-NMR** (400 MHz, DMSO-*d*$_6$): δ = 7.49-7.40 (br. m, 15H, 2-H, 3-H, 4-H) ppm; **^{13}C-NMR** (101 MHz, DMSO-*d*$_6$): δ = 133.5

(d, C_t, C-2), 132.7 (d, C_q, C-1), 130.1 (C_t, C-4), 128.7 (C_t, C-3) ppm; **^{31}P-NMR** (162 MHz, DMSO-*d_6*): δ = -6.40 (s, 1P, *P*Ph_3); **FT-IR** (ATR): $\tilde{\nu}$ = 3052 (w, ν(C-H_{arom})), 1477 (w), 1432 (m, ν_{as}(P-C_{aryl})), 1309 (w), 1178 (w), 1155 (w), 1095 (m, ν_s(P-C_{aryl})), 1068 (w), 1027 (w), 997 (w), 919 (w), 746 (vs, δ(C-H_{arom})), 692 (vs, δ(C-H_{arom})), 620 (w) cm^{-1}.

6.4.3.5 CuAAC reactions of L1/L2 with Ru2

General procedure (R2): Under argon atmosphere **Ru2** (35.3 mg, 40.0 µmol, 1.00 eq.), the used azide (**L1** or **L2**) (100 µmol, 2.50 eq.) and sodium ascorbate (5.94 mg, 30.0 µmol, 0.75 eq.) were dissolved in 3.50 mL CH_2Cl_2 and 3.50 mL water. The mixture was degassed, **31** (4.53 mg, 10.0 µmol, 0.25 eq.) was added and the solution stirred for 4 d at r.t. The reaction mixture was diluted with water and CH_2Cl_2 and the phases were separated. The aqueous phase was extracted with CH_2Cl_2 (8x 30 mL). The combined organic phases were washed with water, dried over sodium sulfate and the solvent removed *in vacuo*. The residue was solved in acetone and a solution of ammonium hexafluorophosphate solution (73.4 mg, 453 µmol, 10.2 eq.) in water was added dropwise while stirring. After one night in the fridge the precipitate was filtered off, washed with cold MeOH (1x 5 mL), cold water (1x 5 mL) and diethylether (5x 5 mL). The crude product was purified using column chromatography on silica (CH_2Cl_2/MeOH = 92:8).

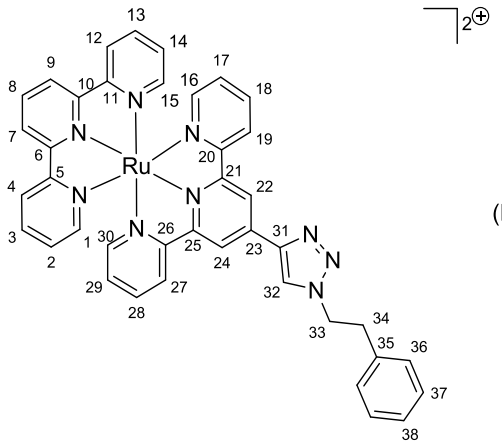

L1-Ru2

L1-Ru2 (26.0 mg, 24.3 µmol, 64%) was isolated as red, crystalline solid.

mp: >330°C; **TLC** (CH_2Cl_2/MeOH 98:.2 v/v): R_f = 0.16; **^{1}H-NMR** (400 MHz, acetone-*d_6*): δ = 9.40 (s, 2H, 22-H/24-H), 9.07 (d, *J* = 8.3 Hz, 2H, 7-H/9-H), 9.01 (s, 1H, 32-H), 8.95 (d, J = 8.3 Hz, 2H, 19-H/27-H), 8.80 (d, J = 8.1 Hz, 2H, 4-H/12-H), 8.58 (t, J = 8.2 Hz, 1H, 8-H), 8.10-8.04 (m, 4H, 3-H/13-H/18-H/28-H), 7.84-7.82 (m, 2H, 1-H/15), 7.72-7.71 (m, 2H, 16-H/30-H), 7.37-7.25 (m, 9H, 2-H/14-H/17-H/29-H/36-H/37-H/38-H), 4.94 (t, J = 7.1 Hz, 2H, 33-H), 3.47 (t, J = 7.1 Hz, 2H, 34-H) ppm; **^{13}C-NMR** (101 MHz, acetone-*d_6*): δ = 159.2 (C_q, C-5/C-11), 156.7 (C_q, C-6/C-10), 156.5 (C_q, C-

21/C-25), 153.6 (C_t, C-1/C-15), 153.5 (C_t, C-16/C-30), 144.7 (C_q, C-23/C31), 139.8 (C_q, C-21/C-25), 139.1 (C_t, C-3/C-13/C-18/C-28), 138.4 (C_t, C-35), 137.0 (C_t, C-8), 129.7 (C_t, C-36 or C-37), 129.5 (C_t, C-36 or C-37), 128.7 (C_t, C-17/C-29), 128.6 (C_t, C-2/C-14), 127.7 (C_t, C-38), 125.6 (C_t, C-19/C-27), 125.4 (C_t, C-4/C-12), 125.0 (C_t, C-32), 124.8 (C_t, C-7/C-9), 120.2 (C_t, C-22/C-24), 52.5 (C_s, C-33), 36.9 (C_s, C-34) ppm; **^{19}F-NMR** (376 MHz, acetone-*d_6*): δ = -72.5 ppm (d, 12F, P*F_6*); **^{31}P-NMR** (162 MHz, acetone-*d_6*): δ = -144.4 ppm (septett, 1P, *P*F_6); **FT-IR** (ATR): $\tilde{\nu}$ = 3643 (w), 3430 (w), 1622 (w), 1448 (w, ν(C=N)$_{arom}$), 1389 (w), 1288 (w), 1228 (w), 1032 (w), 823 (vs, ν(P-F)), 7666 (s, ν(P-F)), 701 (w) cm^{-1}; **Raman** (λ_{ex} = 445 nm):$\tilde{\nu}$ = 673 (w), 726 (w), 803 (w), 1018 (m), 1053 (w), 1164 (w), 1285 (w), 1325 (w), 1487 (s), 1547 (s), 1599 (s), 2330 (w); **UV/Vis** (MeCN): λ_{max} (lg ε) = 484 (5.26), 308 (6.14), 279 (5.82), 274 (5.85) nm (c = 4.54·10^{-4} mol l^{-1}); **HRMS** (m/z, ESI,+): [M]$^+$ calc. for $C_{40}H_{31}N_9RuPF_6$: 884.1388; found: 884.1392; **EA** (calc., found for $C_{40}H_{31}N_9RuP_2F_{12}$): C (46.70, 47.06), H (3.04, 2.77), N (12.25, 12.33).

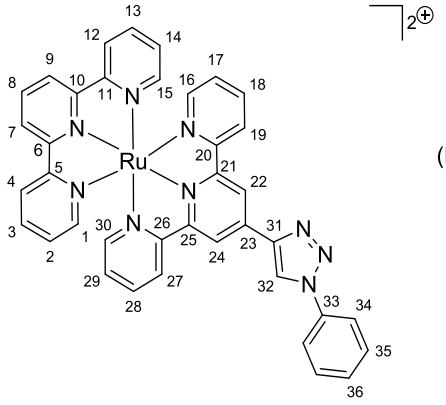

L2-Ru2

L2-Ru2 (12.0 mg, 11.5 µmol, 30%) was isolated as red, crystalline solid.

mp: >330°C; **TLC** (CH_2Cl_2/MeOH 98:.2 v/v): R_f = 0.18; **^{1}H-NMR** (400 MHz, acetone-*d_6*): δ = 9.63 (s, 1H, 32-H), 9.54 (s, 2H, 22-H/24-H), 9.08 (d, J = 8.1 Hz, 2H, 7-H/9-H), 9.00 (d, J = 8.1 Hz, 2H, 19-H/27-H), 8.81 (d, J = 8.1 Hz, 2H, 4-H/12-H), 8.59 (t, J = 8.1 Hz, 1H, 8-H), 8.16-8.06 (m, 6H, 3-H/13-H/18-H/28-H/34-H), 7.84 (d, J = 5.0 Hz, 2H, 1-H/15-H), 7.77-7.62 (m, 5H, 16-H/30-H/35-H/36-H), 7.38-7.32 (m, 4H, 2-H/14-H/17-H/29-H) ppm; **^{13}C-NMR** (101 MHz, acetone-*d_6*): δ = 159.2 (C_q, C-5/C-11), 159.2 (C_q, C-20/C-26), 156.9 (C_q, C-6/C-10), 156.4 (C_q, C-21/C-25), 153.6 (C_t, C-1/C-15/C-16/C-30), 145.9 (C_q, C-31/C-33), 139.2 (C_t, C-3/C-13/C-18/C-28), 137.8 (C_q, C-23), 137.1 (C_t, C-8), 131.0 (C_t, C-35), 130.3 (C_t, C-36), 128.8 (C_t, C-17/C-29), 128.6 (C_t, C-2/C-14), 125.6 (C_t, C-19/C-27), 125.4 (C_t, C-4/C-12), 124.8 (C_t, C-7/C-9), 122.8 (C_t, C-32), 121.3 (C_t, C-34), 120.4 (C_t, C-22/C-24) ppm; **^{19}F-NMR** (376 MHz, acetone-*d_6*): δ = -72.4 ppm (d, 12F, P*F_6*); **^{31}P-NMR** (162 MHz, acetone-*d_6*): δ = -144.5 ppm (septett, 1P, *P*F_6); **FT-IR** (ATR): $\tilde{\nu}$ = 3641 (w), 3058 (w, ν(C-H)), 1701 (w), 1624 (w), 1603 (w), 1504 (w, ν(C=C)$_{arom}$),

1448 (w, ν(C=N)$_{arom}$), 1390 (w), 1245 (w), 1038 (w), 825 (vs, ν(P-F)), 760 (s, ν(P-F)), 690 (w) cm^{-1}; **Raman** (λ_{ex} = 445 nm): $\tilde{\nu}$ = 672 (w), 726 (w), 803 (w), 1017 (m), 1164 (w), 1286 (w), 1326 (w), 1487 (s), 1547 (s), 1598 (s), 2330 (m); **UV/Vis** (MeCN): λ_{max} (lg ε) = 484 (5.18), 308 (5.86), 278 (5.74), 275 (5.73) nm (c = 2.84·10^{-4} mol l^{-1}); **HRMS** (m/z, ESI,+): [M]$^+$ calc. for $C_{38}H_{27}N_9RuPF_6$: 856.1075; found, 856.1063; **EA** (calc., found for $C_{38}H_{27}N_9RuP_2F_{12}$): C (45.61, 45.47), H (2.72, 2.62), N (12.60, 12.70).

6.5 Functionalization of ND particles and diamond materials

6.5.1 Functionalization with linker molecules

6.5.1.1 Grafting of tolane-based linker L5

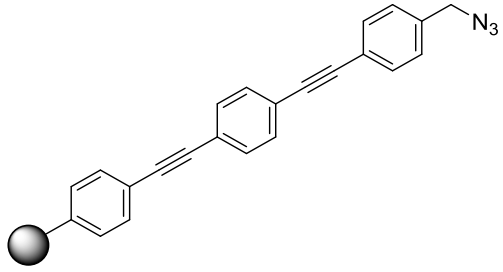

mDND-L5b/L5e/L7

Functionalization with diazonium salt L7

To a dispersion of **mDND** (100 mg) in 9.0 mL water the diazonium salt **L7** (224 mg, 0.50 mmol) was added and the mixture was treated utilizing an ultrasonic horn for 1 h with water bath cooling and 2 h without. Upon centrifugation, **mDND-L7** was washed (acetone (8x), THF (3x), water (2x), THF (3x) and acetone (3x)) and obtained as a gray-yellowish particle dispersion.

Recovery: 10 mL (9.2 mg/mL); **FT-IR** (DRIFTS): $\tilde{\nu}$ = 3443 (s), 2209 (m, ν(C≡C)), 2099 (s, ν(N=N=N)), 1914 (m), 1698 (w), 1599 (w), 1518 (m, ν(C=C)$_{arom}$), 1409 (w), 1304 (w), 1103 (w), 839 (w, δ (C-H$_{arom}$)) cm^{-1}; **Raman** (λ_{ex} = 445 nm): $\tilde{\nu}$ = 1126 (w), 1398 (w), 1446 (m), 1593 (s), 2208 cm^{-1}; **Surface loading** (TGA): 0.15 mmol g^{-1}, Δm (140 – 450 °C) = -5.0%; fragment: $C_{23}H_{14}N_3$); **EA**: C 73.25, H 2.55, N 3.98 wt.%; **DLS** (H_2O): 10% < 135 nm, 50% < 170 nm, 90% < 212 nm; ζ (H_2O): +33.5 mV (pH = 6.1).

Functionalization via *in situ* diazotation of L5

mDND (120 mg, 5.10 mL) was diluted with 20 mL water or 0.5 N hydrochloric acid and **L5** (105 mg, 0.30 mmol. 1.00 eq.) was added. At 80°C, isoamyl nitrite (87.9 mg, 0.75 mmol, 100 µl, 2.50 eq.) was added and the mixture was stirred for 18 h. After centrifugation, **mDND-L5** was washed (acetone (3x), water (1x), THF (3x), DMSO (5x),

isopropanol (3x), acetone (5x) and water (3x)) and obtained as an orange-yellowish (solvent: water) or gray-yellowish (solvent: hydrochloric acid) particle dispersion.

mDND-L5e (solvent: water): **Recovery**: 10 mL (11.7 mg/mL); **FT-IR** (DRIFTS): $\tilde{\nu}$ = 3390 (br. m), 3078 (w), 2952 (w, ν(C-H)), 2210 (m, ν(C≡C)), 2101 (vs, ν(N=N=N)), 1922 (m), 1698 (m), 1596 (m, $\nu(C=C)_{arom}$), 1519 (m, $\nu(C=C)_{arom}$), 1407 (w), 1343 (w), 1305 (w), 1246 (w), 1169 (w), 1104 (w), 1016 (w), 838 (s, $\delta(C\text{-}H_{arom})$), 759 (w), 692 (w), 558 (w) cm^{-1}; **Raman** (λ_{ex} = 445 nm): $\tilde{\nu}$ = 1127 (m), 1170 (w), 1149 (w), 1587 (s), 2208 (w) cm^{-1}; **EA**: C 85.73, H 2.21, N 4.37 wt.%; **UV/Vis** (MeCN): λ_{max} = 324 , 286 (sh), 243 (sh) nm; **Surface loading** (TGA): 0.22 mmol g^{-1}, Δm (145 – 465 °C) = -7.7%; fragment: $C_{23}H_{14}N_3$); **DLS** (H_2O): 10% ≤ 97.7 nm, 50% ≤ 178 nm, 90% ≤ 332 nm; ζ (H_2O): +41.1 mV (pH = 6.2).

mDND-L5b (solvent: hydrochloric acid): **Recovery**: 10 mL (11.6 mg/mL); **FT-IR** (DRIFTS): $\tilde{\nu}$ = 3498 (br. m), 2882 (w, ν(C-H)), 2210 (m, ν(C≡C)), 2101 (vs, ν(N=N=N)), 1922 (m), 1598 (m, $\nu(C=C)_{arom}$), 1519 (m, $\nu(C=C)_{arom}$), 1281 (w), 839 (s, $\delta(C\text{-}H_{arom})$) cm^{-1}; **Raman** (λ_{ex} = 445 nm): $\tilde{\nu}$ = 1128 (m), 1171 (w), 1149 (w), 1452 (w), 1590 (s), 2209 (m) cm^{-1}; **UV/Vis** (MeCN): λ_{max} = 325 , 286 (sh), 241 (sh) nm; **EA**: C 88.46, H 1.74, N 2.87 wt.%; **Surface loading** (TGA): 0.11 mmol g^{-1}, Δm (145 – 465 °C) = -3.5%; fragment: $C_{23}H_{14}N_3$); **DLS** (H_2O): 10% ≤ 50.5 nm, 50% ≤ 83.9 nm, 90% ≤ 205 nm; ζ (H_2O): +30.1 mV (pH = 6.0).

6.5.1.2 Grafting of phenylene-based linker molecules L1 and L2

6.5.1.2.1 DND particles

General Procedure (F1): **mDND** or **H-DND** was dispersed in water and heated up to 80 °C. After addition of amine-bearing linker (1.00 eq.) and amyl nitrite (1.25 eq.), the dispersion was stirred at 80 °C for 25 h. The ND particles were isolated via centrifugation and washed with acetone (3x), DMF (3x), $CHCl_3$ (3x), acetone (3x) and water (3x).

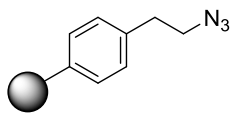

mDND-L1c

Amounts used in **F1**: **mDND** (1.00 g), 80 mL water, **L1** (1.46 g, 9.00 mmol), amyl nitrite (1.58 g, 13.5 mmol, 1.82 mL). **mDND-L1c** was obtained as gray-brown dispersion.

Recovery: 98 mL (10.0 mg/mL); **FT-IR** (DRIFTS): $\tilde{\nu}$ = 3691 (w), 3429 (br., ν(O-H)), 2952 (w, ν(C-H)), 2104 (vs, ν(N=N=N)), 1660 (br. m), 1512 (m, $\nu(C=C)_{arom}$), 1352 (w),

828 (s, δ(C-H_{arom})) cm^{-1}; **Raman** (λ_{ex} = 445 nm): $\tilde{\nu}$ = 1329 (s, ν(diamond), D band), 1601 (br, G band) cm^{-1}; **UV/Vis** (MeCN): λ_{max} = 315, 269 (sh) nm; **Surface. loading** (TGA): 0.22 mmol g^{-1}, Δm (150 – 360 °C) = -3.3%; fragment: $C_8H_8N_3$); **EA**: C 84.25, H 1.87, N 3.07 wt.%; **DLS** (H_2O): 10% ≤ 31.7 nm, 50% ≤ 54.2 nm, 90% ≤ 107 nm; ζ (H_2O): +40.8 mV (pH = 6.3).

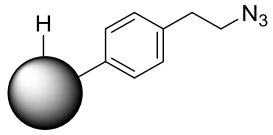

H-DND-L1

Amounts used in **F1**: **H-DND$_{IAF}$** (55 mg), 10 mL water, **L1** (81.0 mg, 0.50 mmol), amyl nitrite (87.9 mg, 0.75 mmol, 101 µL). **H-DND-L1** was obtained as gray-brown dispersion.

Recovery: 5 mL (10.0 mg/mL); **FT-IR** (DRIFTS): $\tilde{\nu}$ = 3400 (br, ν(O-H)), 2947 (w, ν_{as}(C-H)), 2875 (w, ν_s(C-H)), 2101 (vs, ν(N=N=N)), 1591 (w), 1502 (m, ν(C=C)$_{arom}$), 1298 (w), 826 (s, δ(C-H_{arom})), 666 (w) cm^{-1}; **Raman** (λ_{ex} = 445 nm): $\tilde{\nu}$ = 1332 (s, ν(diamond), D band), 1588 (br, G band) cm^{-1}; **Surface. loading** (TGA): 0.35 mmol g^{-1}, Δm (155 – 370 °C) = -5.0%; fragment: $C_8H_8N_3$); **DLS** (H_2O): 10% ≤ 68.0 nm, 50% ≤ 156 nm, 90% ≤ 706 nm; ζ (H_2O): +42.9 mV (pH = 6.2).

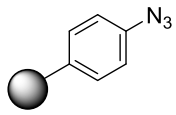

mDND-L2c

Amounts used in **F1**: **mDND** (1.00 g), 80 mL water, **L2** (1.21 g, 9.00 mmol), amyl nitrite (1.58 g, 13.5 mmol, 1.82 mL). **mDND-L2c** was obtained as brown dispersion.

Recovery: 20 mL (21.5 mg/mL); **FT-IR** (DRIFTS): $\tilde{\nu}$ = 3407 (br., ν(O-H)), 2958 (w, ν(C-H_{arom})), 2414 (m), 2255 (m), 2124 (vs, ν(N=N=N)), 1683 (w), 1600 (w), 1505 (m, ν(C=C)$_{arom}$), 1292 (w), 1184 (w), 1129 (w), 837 (s, δ(C-H_{arom})) cm^{-1}; **Raman** (λ_{ex} = 445 nm): $\tilde{\nu}$ = 322 (w, ν(diamond), D band), 1582 (br, G band) cm^{-1}; **UV/Vis** (MeCN): λ_{max} = 316, 271 (sh) nm; **Surface loading** (TGA): 0.33 mmol g^{-1}, Δm (140 -460 °C) = -4.1%; fragment: $C_6H_4N_3$); **EA**: C 74.61, H 2.60, N 13.17 wt.%; **DLS** (H_2O): 10% ≤ 49.5 nm, 50% ≤ 740 nm, 90% ≤ 1490 nm; ζ (H_2O): +41.0 mV (pH = 6.1).

6.5.1.2.2 H-terminated diamond foam (H-foam)

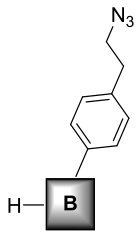

H-Foam-L1b

Amounts used in **F1**: **H-Foam** (119 mg), 5 mL water, **L1** (81.0 mg, 0.50 mmol), amyl nitrite (87.9 mg, 0.75 mmol, 101 µL). **H-Foam-L1b** was washed using a shaker, covering the foam with 3 mL of solvent for each washing step. **H-Foam-L1b** was obtained as blueish foam.

Recovery: 121 mg; **Raman** (λ_{ex} = 445 nm): $\tilde{\nu}$ = 1151 (m), 1331 (s, ν(diamond), D band), 1511 (vs) cm^{-1}.

6.5.1.2.3 BND particles

General Procedure (B1): **BND** or **H-BND** was dispersed in MeCN and heated up to 80 °C. After addition of amine-bearing linker (1.00 eq.) and amyl nitrite (1.50 eq.), the dispersion was stirred at 80 °C for 25 h. The ND particles were isolated via centrifugation and washed with acetone (3x), water (3x), MeCN (3x), acetone (3x), isopropanol (3x) and water (3x).

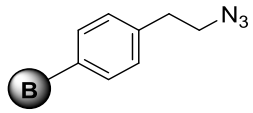

BND-L1c

Amounts used in **B1**: **BND4** (110 mg), 12 mL MeCN, **L1** (194 mg, 1.20 mmol), amyl nitrite (211 mg, 1.80 mmol, 0.24 mL). **BND-L1c** was obtained as blueish dispersion.

Recovery: 15 mL (7.1 mg/mL); **Raman** (λ_{ex} = 445 nm): $\tilde{\nu}$ = 1328 (s, ν(diamond), D band), 1532 (br, G band) cm^{-1}; **Surface. loading** (TGA): 0.13 mmol g^{-1}, Δm (160 – 380 °C) = -1.9%; fragment: $C_8H_8N_3$); **DLS** (H_2O): 10% ≤ 403 nm, 50% ≤ 999 nm, 90% ≤ 1680 nm; ζ (H_2O): -40.7 mV (pH = 5.6).

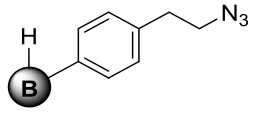

H-BND-L1

Amounts used: **H-BND3$_{CEA}$** (82 mg), 10 mL MeCN, **L1** (162 mg, 1.00 mmol), amyl nitrite (176 mg, 1.50 mmol, 0.20 µL). **H-BND-L1** was obtained as dark-blueish dispersion.

Recovery: 10 mL (8.0 mg/mL); **Raman** (λ_{ex} = 445 nm): $\tilde{\nu}$ = 1328 (s, ν(diamond), D band), 1532 (br, G band) cm^{-1}; **Surface. loading** (TGA): 0.12 mmol g^{-1}, Δm (160 – 400 °C) = -1.7%; fragment: $C_8H_8N_3$); **DLS** (H_2O): 10% ≤ 209 nm, 50% ≤ 646 nm, 90% ≤ 1450 nm; ζ (H_2O): -13.5 mV (pH = 6.1).

6.5.1.2.4 H-terminated diamond spheres (H-spheres)

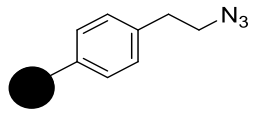

H-spheres-L1

Amounts used in **B1**: **H-spheres** (1.5 mg), 3 mL MeCN, **L1** (16.2 mg, 100 µmol), amyl nitrite (17.6 mg, 150 µmol, 20.4 µL). **H-spheres-L1** was washed applying a cautious centrifugation protocol (max. 500 rpm). The particles were obtained as dark-black dispersion and directly used in the next reaction step without characterization due to the small amount of sample available.

6.5.1.3 Attachment of phenylene-based linker molecules L8 and L9

General Procedure in (F2): In a first step, **mDND** was dispersed in water and heated up to 80 °C. After addition of amine-bearing linker (1.00 eq.) and amyl nitrite (1.50 eq.) the dispersion was stirred at 80 °C for 20 h. The ND particles were isolated via

centrifugation and washed with water (3x), acetone (5x), MeCN (3x), DMSO (3x) and water (3x). To the Boc-functionalized particles in aqueous dispersion conc. hydrochloric acid was added to form a concentration of 6 M. After stirring at r.t. for 6 h, the ND particles were isolated via centrifugation and washed with water (5x) until a neutral pH was obtained.

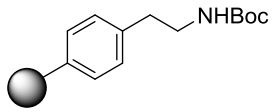

mDND-L8$_{Boc}$

Amounts used in **F2**: **mDND** (300 mg), 30 mL water, **L8** (591 mg, 2.50 mmol), amyl nitrite (439 mg, 3.75 mmol, 522 µL). **mDND-L8$_{Boc}$** was obtained as grayish dispersion.

Recovery: 30 mL (9.7 mg/mL); **FT-IR** (DRIFTS): $\tilde{\nu}$ = 3692 (w), 3393 (br, ν(O-H)), 2956 (w, ν(C-H)), 2919 (w), 1692 (m, ν(C=O)), 1646 (w), 1535 (w), 1514 (m, ν(C=C)$_{arom}$), 1460 (w), 1368 (w), 1172 (w), 828 (s, δ(C-H$_{arom}$)) cm^{-1}; **Raman** (λ_{ex} = 445 nm): $\tilde{\nu}$ = 1331 (w, ν(diamond), D band), 1591 (br, G band) cm^{-1}; **Surface. loading** (TGA): 0.29 mmol g^{-1}, Δm (150 – 450 °C) = -6.6%; fragment: $C_{13}H_{18}NO_2$); **DLS** (H_2O): 10% ≤ 46.9 nm, 50% ≤ 77.4 nm, 90% ≤ 246 nm; ζ (H_2O): +36.0 mV (pH = 6.2).

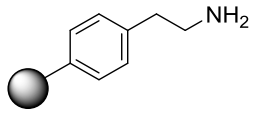

mDND-L8

Amounts used in **F2**: **mDND-L8$_{Boc}$** (270 mg), 15 mL water, 15 mL conc. hydrochloric acid. **mDND-L8** was obtained as grayish dispersion.

Recovery: 25 mL (10.4 mg/mL); **FT-IR** (DRIFTS): $\tilde{\nu}$ = 3689 (w), 3463 (br, ν(O-H)), 2955 (w, ν_{as}(C-H)), 2897 (w, ν_s(C-H)), 1710 (m), 1631 (w), 1501 (m, ν(C=C)$_{arom}$), 1326 (w), 815 (s, δ(C-H$_{arom}$)) cm^{-1}; **Raman** (λ_{ex} = 445 nm): $\tilde{\nu}$ = 1329 (w, ν(diamond), D band), 1598 (br, G band) cm^{-1}; **Surface. loading** (TGA): 0.24 mmol g^{-1}, Δm (150 – 450 °C) = -2.8%; fragment: $C_8H_{10}N$); **DLS** (H_2O): 10% ≤ 25.8 nm, 50% ≤ 44.7 nm, 90% ≤ 97.0 nm; ζ (H_2O): +43.1 mV (pH = 6.2).

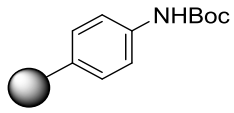

mDND-L9$_{Boc}$

Amounts used in **F2**: **mDND** (200 mg), 20 mL water, **L9** (156 mg, 0.75 mmol), amyl nitrite (132 mg, 1.13 mmol, 152 µL). **mDND-L9$_{Boc}$** was obtained as grayish dispersion.

Recovery: 20 mL (9.9 mg/mL); **FT-IR** (DRIFTS): $\tilde{\nu}$ = 3411 (br, ν(O-H)), 2958 (w, ν(C-H)), 2919 (w), 1710 (m), 1678 (m, ν(C=O)), 1607 (m), 1515 (m, ν(C=C)$_{arom}$), 1346 (m), 899 (w), 841 (m, δ(C-H$_{arom}$)), 761 (w) cm^{-1}; **Raman** (λ_{ex} = 445 nm): $\tilde{\nu}$ = 1329 (w, ν(diamond), D band), 1598 (br, G band) cm^{-1}; **UV/Vis** (MeCN): λ_{max} = 271 (sh) nm; **Surface. loading** (TGA): 0.31 mmol g^{-1}, Δm (150 – 460 °C) = -6.0%; fragment: $C_{11}H_{14}NO_2$); **DLS** (H_2O): 10% ≤ 44.6 nm, 50% ≤ 68.2 nm, 90% ≤ 127 nm; ζ (H_2O): +39.7 mV (pH = 6.8).

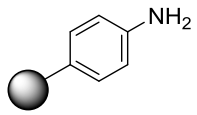

mDND-L9

Amounts used in **F2**: **mDND-L9$_{Boc}$** (170 mg), 256 mL water, 25 mL conc. hydrochloric acid. **mDND-L9** was obtained as grayish dispersion.

Recovery: 15 mL (10.9 mg/mL); **FT-IR** (DRIFTS): $\tilde{\nu}$ = 3385 (br, ν(O-H)), 2956 (w, ν(C-H)), 1710 (m), 1606 (w), 1515 (m, ν(C=C)$_{arom}$), 1270 (m), 838 (m, δ(C-H$_{arom}$)) cm^{-1}; **Raman** (λ_{ex} = 445 nm): $\tilde{\nu}$ = 1329 (w, ν(diamond), D band), 1596 (br, G band) cm^{-1}; **UV/Vis** (MeCN): λ_{max} = 271 (sh) nm; **Surface. loading** (TGA): 0.26 mmol g^{-1}, Δm (155 – 460 °C) = -2.5%; fragment: C_6H_6N); **DLS** (H_2O): 10% ≤ 56.1 nm, 50% ≤ 91.5 nm, 90% ≤ 180 nm; ζ (H_2O): +48.4 mV (pH = 6.9).

6.5.2 CuAAC reactions on ND particles and diamond materials

6.5.2.1 CuAAC reactions of linker functionalized particles and materials

General procedure (C1): Under argon atmosphere the azide-functionalized particles/materials (1.00 eq; calculated via TGA surface loading) were dispersed in a DMF/water (40 mL/10 mL) mixture. The alkyne-functionalized complex (2.00 eq or 3.00 eq.) was added and the dispersion was degassed. Reaction specific copper catalyst was added and the dispersion sonicated for 30 min. After the given reaction time at the given temperature,s the ND particles were isolated via ultracentrifugation (15 min at 52 k rpm) and washed with acetone (3x), MeOH (3x), 0.1 M EDTA-solution (3x), water (3x), acetonitrile (3x), isopropanol (3x), acetone (3x), water (3x) yielding a stable, aqueous dispersion.

6.5.2.1.1 CuAAC reaction of mDND-L1/H-DND-L1 with Ru1

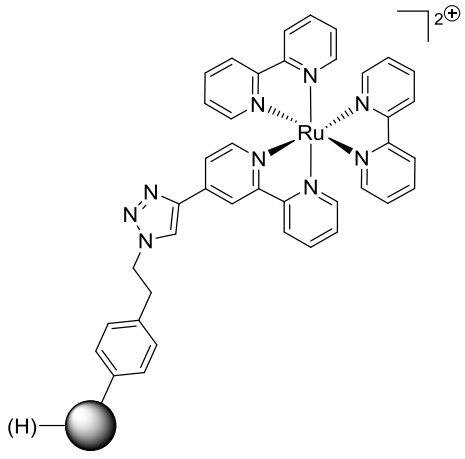

mDND-L1-Ru1c/H-DND-L1-Ru1

Amounts used for **mDND-L7-Ru1c** in **C1**: **mDND-L1c** (240 mg, 53.0 µmol), **Ru1** (93.7 mg, 106 µmol, 2.00 eq.). Copper(II) sulfate (6.74 mg, 42.2 µmol, 0.80 eq.), sodium ascorbate (16.7 mg, 84.5 µmol, 1.60 eq.); 6 d at r.t. As reaction control still showed free azide, the reaction temperature was increased to 70 °C for further 8 d. **mDND-L1-Ru1c** was obtained as yellowish dispersion.

Recovery: 20 mL (11.0 mg/mL); **FT-IR** (DRIFTS): $\tilde{\nu}$ = 3349 (br, ν(O-H)), 2956 (w, ν_{as}(C-H)), 2922 (w), 2873 (w, ν_s(C-H)), 1617 (br), 1462 (m, ν(C=C)$_{arom}$, ν(C=N)$_{arom}$), 1444 (w,

ν(C=C)$_{arom}$, ν(C=N)$_{arom}$), 1378 (w), 1244 (w), 1161 (w), 844 (w, δ(C-H$_{arom}$)), 767 (m, δ(C-H$_{arom}$)), 731 (w, δ(C-H$_{arom}$)) cm^{-1}; **Raman** (λ_{ex} = 445 nm): $\tilde{\nu}$ = 664 (w), 1029 (m), 1165 (m), 1266 (w), 1315 (m), 1324 (m), 1482 (s), 1558 (s), 1598 (s); **UV/Vis** (MeCN): λ_{max} = 455 (br.), 289, 246 (sh), 211 nm; **Surf. loading** (TGA): 0.11 mmol g^{-1}, Δm (155 – 470 °C) = -8.0%; fragment: $C_{40}H_{32}N_9Ru$); **EA**: C 82.50, H 1.47, N 3.28, Ru 0.52 wt.%; **DLS** (H_2O): 10% ≤ 44.9 nm, 50% ≤ 70.0 nm, 90% ≤ 137 nm; ζ (H_2O): +21.9 mV (pH = 6.2).

Amounts used for **H-DND-L1-Ru1** in **C1**: **H-DND-L1** (30 mg, 13.0 µmol), **Ru1** (23.3 mg, 26.4 µmol, 2.00 eq.), **31** (23.9 mg, 52.8 µmol, 4.00 eq.), sodium ascorbate (21.0 mg, 106 µmol, 8.00 eq.); 6 d at 70 °C. **H-DND-L1-Ru1** was obtained as yellowish-gray-dispersion.

Recovery: 5 mL (5.8 mg/mL); **FT-IR** (DRIFTS): $\tilde{\nu}$ = 3692 (w), 3383 (br, ν(O-H)), 3073 (w), 2957 (w, ν_{as}(C-H)), 2878 (w, ν_s(C-H)), 1619 (br. m), 1507 (w), 1463 (m, ν(C=C)$_{arom}$, ν(C=N)$_{arom}$), 1443 (w, ν(C=C)$_{arom}$, ν(C=N)$_{arom}$), 1389 (w), 768 (m, δ(C-H$_{arom}$)), 731 (w, δ(C-H$_{arom}$)), 611 (w) cm^{-1}; **Raman** (λ_{ex} = 445 nm): $\tilde{\nu}$ = 660 (w), 1022 (m), 1314 (m), 1482 (s), 1553 (s), 1597 (s); **UV/Vis** (MeCN): λ_{max} = 466 (br.), 293, 248 (sh) nm; **Surf. loading** (TGA): 0.22 mmol g^{-1}, Δm (150 – 465 °C) = -16.2%; fragment: $C_{40}H_{32}N_9Ru$); **DLS** (H_2O): 10% ≤ 37.5 nm, 50% ≤ 111 nm, 90% ≤ 279 nm; ζ (H_2O): +33.9 mV (pH = 6.1).

6.5.2.1.2 CuAAC reaction of mDND-L1 with Ru2

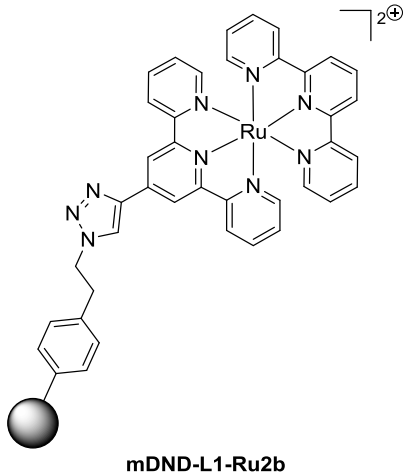

mDND-L1-Ru2b

Amounts used in **C1**: **mDND-L1c** (240 mg, 53.0 µmol), **Ru2** (93.4 mg, 106 µmol, 2.00 eq), **31** (19.1 mg, 42.2 µmol, 0.80 eq.), sodium ascorbate (16.7 mg, 84.5 µmol, 1.60 eq.); 8 d at r.t. As reaction control still showed free azide, the reaction temperature was increased to 70 °C for further 5 d. **mDND-L1-Ru2b** was obtained as red-brownish dispersion.

Recovery: 20 mL (10.9 mg/mL); **FT-IR** (DRIFTS): $\tilde{\nu}$ = 3404 (br, ν(O-H)), 2951 (w, ν_{as}(C-H)), 2100 (w), 1602 (br. w), 1445 (m, ν(C=C)$_{arom}$, ν(C=N)$_{arom}$), 1389, 1245 (w), 876 (w, δ(C-H$_{arom}$)), 770 (m, δ(C-H$_{arom}$)), 722 (w, δ(C-H$_{arom}$)) cm^{-1}; **Raman** (λ_{ex} = 445 nm): $\tilde{\nu}$ = 670 (w), 1019 (m), 1158 (m), 1250 (w), 1322 (m), 1324 (m), 1460 (s), 1551 (s), 1597 (s); **UV/Vis**

(MeCN): λ_{max} = 487 (br.), 333 (sh), 313, 274 (br) nm; **Surf. loading** (TGA): 0.16 mmol g^{-1}, Δm (150 – 530 C) = -12.1%; fragment: $C_{40}H_{30}N_9Ru$); **EA**: C 80.78, H 1.77, N 4.00, Ru 1.18 wt.%; **DLS** (H_2O): 10% ≤ 42.2 nm, 50% ≤ 72.0 nm, 90% ≤ 282 nm; ζ (H_2O): +23.8 mV (pH = 6.3).

6.5.2.1.3 CuAAC reaction of mDND-L1 with 5

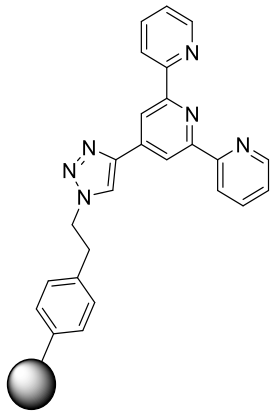

mDND-L1-typ$_c$

Amounts used in **C1**: **mDND-L1c** (250 mg, 55.0 µmol), **5** (42.4 mg, 165 µmol, 2.00 eq.), copper(I) iodide (47.2 mg, 248 µmol, 4.50 eq.), diisopropylethylamine (128 mg, 990 µmol, 9.00 eq), sodium ascorbate (98.1 mg, 495 µmol, 6.00 eq.); 9 d at r.t. As reaction control still showed free azide, the reaction temperature was increased to 60 °C for further 5 d. **mDND-L1-typ$_c$** was obtained as grayish dispersion.

Recovery: 20 mL (12.1 mg/mL); **FT-IR** (DRIFTS): $\tilde{\nu}$ = 3426 (br, ν(O-H)), 2951 (w, ν_{as}(C-H)), 2100 (w), 1609 (br. w), 1471 (m, ν(C=C)$_{arom}$, ν(C=N)$_{arom}$), 1436 (w, ν(C=C)$_{arom}$, ν(C=N)$_{arom}$), 1397 (w), 893 (w, δ(C-H$_{arom}$)), 795 (m, δ(C-H$_{arom}$)), 744 (w, δ(C-H$_{arom}$)) cm^{-1}; **Raman** (λ_{ex} = 445 nm): $\tilde{\nu}$ = 1327 (m, ν(diamond), D band), 1580 (br, G band); **UV/Vis** (MeCN): λ_{max} = 281 (br.) nm; **Surf. loading** (TGA): 0.22 mmol g^{-1}, Δm (155 – 475 C) = -8.6%; fragment: $C_{25}H_{19}N_6$); **DLS** (H_2O): 10% ≤ 64.0 nm, 50% ≤ 101 nm, 90% ≤ 191 nm; ζ (H_2O): +20.7 mV (pH = 5.9).

6.5.2.1.4 CuAAC reaction of mDND-L2 with Ru1

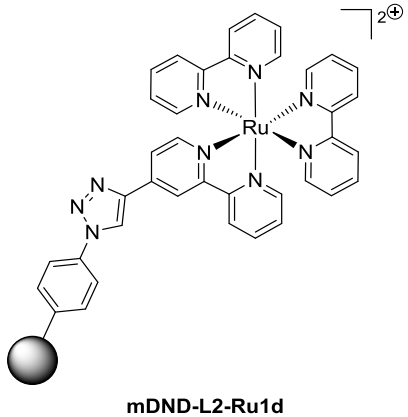

mDND-L2-Ru1d

Amounts used in **C1**: **mDND-L2c** (220 mg, 33.0 µmol), **Ru1** (87.5 mg, 99.0 µmol), **31** (59.8 mg, 132 µmol, 4.00 eq), sodium ascorbate (52.3 mg, 264 µmol, 8.00 eq.); 13 d at 70 °C. **mDND-L2-Ru1d** was obtained as brownish-orange dispersion.

Recovery: 20 mL (11.0 mg/mL); **FT-IR** (DRIFTS): $\tilde{\nu}$ = 3371 (br, ν(O-H)), 2958 (w, ν(C-H)), 2216 (w), 2122 (w), 1604 (w), 1515 (m, ν(C=C)$_{arom}$), 1463 (m, ν(C=C)$_{arom}$, ν(C=N)$_{arom}$), 1444 (w, ν(C=C)$_{arom}$, ν(C=N)$_{arom}$), 1395 (w), 1314 (w), 839 (w, δ(C-H$_{arom}$)), 767 (m, δ(C-H$_{arom}$)), 731 (w, δ(C-H$_{arom}$)) cm^{-1}; **Raman** (λ_{ex} = 445 nm): $\tilde{\nu}$ = 664 (w), 1023 (m), 1173 (m), 1232 (w), 1314 (m), 1483 (s), 1556 (s), 1596 (s); **UV/Vis** (MeCN): λ_{max} = 471 (br.), 294, 250 (sh) nm; **Surface loading** (TGA):

0.21 mmol g^{-1}, Δm (150 – 565 °C) = -15.0%; fragment: $C_{38}H_{27}N_9Ru$); **EA**: C 78.76, H 2.21, N 4.64, Ru 1.00 wt.%; **DLS** (H_2O): 10% ≤ 31.4 nm, 50% ≤ 74.6 nm, 90% ≤ 374 nm; ζ (H_2O): +19.1 mV (pH = 6.0).

6.5.2.1.5 CuAAC reaction of mDND-L2 with Ru2

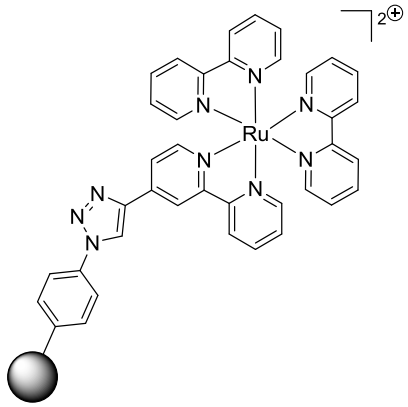

mDND-L2-Ru2b

Amounts used in **C1**: **mDND-L2c** (220 mg, 33.0 µmol), **Ru2** (87.3 mg, 99.0 µmol), **31** (59.8 mg, 132 µmol, 4.00 eq), sodium ascorbate (52.3 mg, 264 µmol, 8.00 eq.); 13 d at 70 °C. **mDND-L2-Ru2b** was obtained as brownish-red dispersion.

Recovery: 20 mL (11.1 mg/mL); **FT-IR** (DRIFTS): $\tilde{\nu}$ = 3383 (br, ν(O-H)), 2954 (w, ν(C-H_{arom})), 2215 (w), 2121 (w), 1604 (w), 1515 (m, ν(C=C)$_{arom}$), 1449 (m, ν(C=C)$_{arom}$, ν(C=N)$_{arom}$), 1389 (w), 1246 (w), 837 (w, δ(C-H_{arom})), 771 (m, δ(C-H_{arom})) cm^{-1}; **Raman** (λ_{ex} = 445 nm): $\tilde{\nu}$ = 664 (w), 1051 (m), 1323 (m), 1500 (w), 1554 (s), 1599 (s); **UV/Vis** (MeCN): λ_{max} = 490 (br.), 334 (sh), 313, 274 (br.) nm; **Surface loading** (TGA): 0.16 mmol g^{-1}, Δm (155 – 560 °C) = -11.7%; fragment: $C_{38}H_{26}N_9Ru$); **EA**: C 79.57, H 2.02, N 4.15, Ru 1.01 wt.%; **DLS** (H_2O): 10% ≤ 59.2 nm, 50% ≤ 113 nm, 90% ≤ 487 nm; ζ (H_2O): +24.1 mV (pH = 6.1).

6.5.2.1.6 CuAAC reaction of mDND-L2 with 5

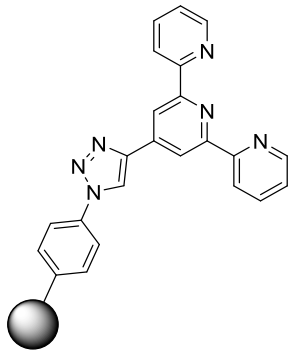

mDND-L2-tpy$_b$

Amounts used in **C1**: **mDND-L2c** (220 mg, 33.0 µmol), **5** (25.5 mg, 99.0 µmol, 3.00 eq.), **31** (59.8 mg, 132 µmol, 4.00 eq), sodium ascorbate (52.3 mg, 264 µmol, 8.00 eq.).; 13 d at r.t. **mDND-L2-tpy$_b$** was obtained as grayish dispersion.

Recovery: 20 mL (11.2 mg/mL); **FT-IR** (DRIFTS): $\tilde{\nu}$ = 3365 (br, ν(O-H)), 2956 (w, ν(C-H_{arom})), 2218 (w), 2121 (w), 1610 (w), 1515 (m, ν(C=C)$_{arom}$), 1397 (m, ν(C=C)$_{arom}$, ν(C=N)$_{arom}$), 1317 (w), 1043 (w), 839 (w, δ(C-H_{arom})), 794 (m, δ(C-H_{arom})), 745 (w, δ(C-H_{arom})) cm^{-1}; **Raman** (λ_{ex} = 445 nm): $\tilde{\nu}$ = 1333 (w, ν(diamond), D band), 1584 (br, G band); **UV/Vis** (MeCN): λ_{max} = 288 (br.) nm; **Surf. loading** (TGA): 0.30 mmol g^{-1}, Δm (150 – 495 C) = -11.1%; fragment: $C_{23}H_{15}N_6$); **DLS** (H_2O): 10% ≤ 93.9 nm, 50% ≤ 129 nm, 90% ≤ 182 nm; ζ (H_2O): +23.3 mV (pH = 6.2).

6.5.2.1.7 CuAAC reaction of mDND-L5 with Ru1

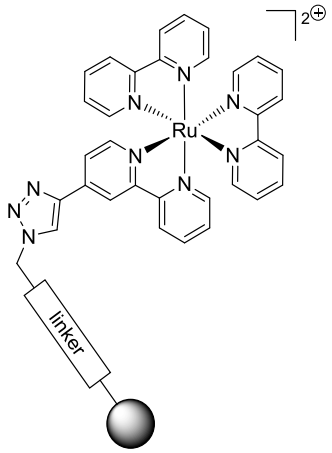

mDND-L5-Ru1b

Amounts used in **C1**: **mDND-L5j** (250 mg, 47.5 µmol), **Ru1** (83.9 mg, 95.0 µmol), **31** (86.0 mg, 190 µmol, 4.00 eq), sodium ascorbate (38.0 mg, 380 µmol, 8.00 eq.); 5 d at 70 °C and 14 d at 80 °C. **mDND-L5-Ru1b** was obtained as brownish-orange dispersion.

Recovery: 25 mL (9.5 mg/mL); **FT-IR** (DRIFTS): $\tilde{\nu}$ = 3414 (br., ν(O-H)), 3078 (w), 2952 (w, ν(C-H)), 2210 (m, ν(C≡C)), 2101 (m, ν(N=N=N)), 1922 (m), 1663 (w), 1603 (m), 1518 (m, $\nu(C=C)_{arom}$), 1465 (w, $\nu(C=C)_{arom}$, $\nu(C=N)_{arom}$), 1444 (w, $\nu(C=C)_{arom}$, $\nu(C=N)_{arom}$), 1407 (w), 1253 (w), 1169 (w), 1105 (w), 1017 (w), 839 (s, $\delta(C\text{-}H_{arom})$), 766 (m, $\delta(C\text{-}H_{arom})$), 730 (w, $\delta(C\text{-}H_{arom})$), 662 (w), 545 (w) cm^{-1}; **Raman** (λ_{ex} = 445 nm): $\tilde{\nu}$ = 664 (w), 735 (w), 1124 (m), 1173 (m), 1320 (w), 1443 (w), 1484 (w), 1585 (s), 2202 (m) cm^{-1}; **UV/Vis** (MeCN): λ_{max} = 471 (br.), 363 (sh), 334 (sh), 296, 243 (sh) nm; **Surface loading** (TGA): 0.18 mmol g^{-1}, Δm (150 – 450 °C) = -16.9%; fragment: $C_{55}H_{39}N_9Ru$); **DLS** (H_2O): 10% ≤ 58.2 nm, 50% ≤ 169 nm, 90% ≤ 303 nm; ζ (H_2O): +31.6 mV (pH = 6.1).

6.5.2.1.8 CuAAC reaction of BND-L1/H-BND-L1 with Ru1

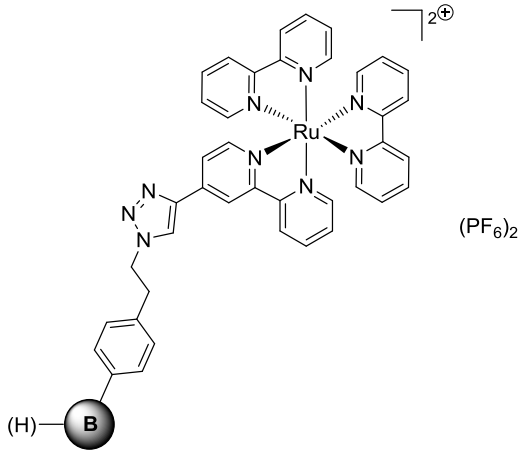

BND-L1-Ru1/H-BND-L1-Ru1

Amounts used for **BND-L1-Ru1** in **C1**: **BND-L1c** (105 mg, 16.5 µmol), **Ru1** (29.2 mg, 33.0 µmol, 2.00 eq.), **31** (30.0 mg, 66.0 µmol, 2.00 eq.), sodium ascorbate (26.2 mg, 132 µmol, 8.00 eq.); 7 d at 70 °C. **BND-L1-Ru1** was obtained as slightly yellowish, gray-blueish dispersion.

Recovery: 10 mL (10.0 mg/mL); **Raman** (λ_{ex} = 445 nm): $\tilde{\nu}$ = 1020 (w), 1328 (vs, ν(diamond), D band), 1483 (m), 1555 (m), 1600 (m); **UV/Vis** (MeCN): λ_{max} = 463 (br.), 291, 243 (sh), 212 nm; **Surf. loading** (TGA): 0.08 mmol g^{-1}, Δm (150 – 460 °C) = -5.9%; fragment: $C_{40}H_{32}N_9Ru$); **DLS** (H_2O): 10% ≤ 209 nm, 50% ≤ 527 nm, 90% ≤ 1730 nm; ζ (H_2O): -7.51 mV (pH = 6.2).

Amounts used for **H-BND-L1-Ru1** in **C1**: **H-BND-L1** (80 mg, 12.3 µmol), **Ru1** (21.7 mg, 24.6 µmol, 2.00 eq.), **31** (22.3 mg, 49.2 µmol, 4.00 eq.), sodium ascorbate (19.5 mg, 98.4 µmol, 8.00 eq.); 7 d at 70 °C. **H-DND-L1-Ru1** was obtained as dark-gray dispersion.

Recovery: 10 mL (7.8 mg/mL); **Raman** (λ_{ex} = 445 nm): $\tilde{\nu}$ = 1025 (w), 1328 (vs, ν(diamond), D band), 1484 (m), 1551 (w), 1600 (w); **UV/Vis** (MeCN): λ_{max} = 468 (br.), 300 (sh), 233 (sh) , 212 nm; **Surf. loading** (TGA): 0.12 mmol g^{-1}, Δm (150 – 465 °C) = -8.8%; fragment: $C_{40}H_{32}N_9Ru$); **DLS** (H_2O): 10% ≤ 1000 nm, 50% ≤ 1350 nm, 90% ≤ 1750 nm; ζ (H_2O): +3.79 mV (pH = 6.2).

6.5.2.1.9 CuAAC reaction of H-Foam-L1 with Ru1

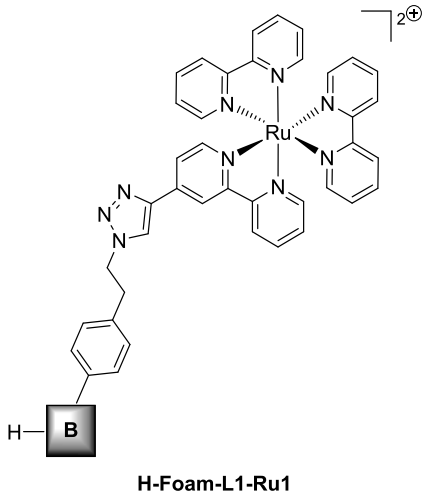

H-Foam-L1-Ru1

Amounts used in **C1**: **H-Foam-L1b** (121 mg), **Ru1** (13.3 mg, 15.0 µmol, 1.00 eq.), **31** (13.6 mg, 30.0 µmol, 2.00 eq.), sodium ascorbate (11.9 mg, 60.0 µmol, 4.00 eq.), DMF/water (8 mL/2 mL); 9 d at 70 °C, 4 d at r.t. **H-Foam-L1-Ru1** was obtained as slightly reddish, blueish foam membrane.

Recovery: 121 mg; **Raman** (λ_{ex} = 445 nm): $\tilde{\nu}$ = 1030 (w), 1151 (m), 1332 (s, ν(diamond), D band), 1489 (w), 1511 (vs), 1533 (w), 1597 (w).

6.5.2.1.10 CuAAC reaction of H-spheres-L1 with Ru1

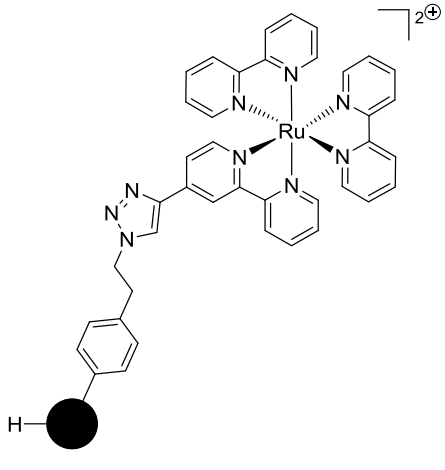

H-spheres-L1-Ru1

Amounts used in **C1**: **H-spheres-L1** (~1.5 mg), **Ru1** (3.97 mg, 4.50 µmol, 1.00 eq.), **31** (4.08 mg, 9.00 µmol, 2.00 eq.), sodium ascorbate (3.57 mg, 18.0 µmol, 4.00 eq.), DMF/water (4 mL/1 mL); 7 d at 70 °C. **H-spheres-L1-Ru1** was obtained as dark-black dispersion.

Recovery: ~1.00 mg; **Raman** (λ_{ex} = 445 nm): $\tilde{\nu}$ = 845 (br), 1027 (w), 1371 (vs, D band), 1484 (s), 1589 (vs, G band); **UV/Vis** (MeCN): λ_{max} = 472 (br.), 295 (sh), 213 nm; **DLS** (H_2O): 10% ≤ 647 nm, 50% ≤ 844 nm, 90% ≤ 1090 nm; ζ (H_2O): +12.9 mV (pH = 6.2).

6.5.2.2 CuAAC reaction of N_3-DND with Ru1/Ru2

General procedure (C2): Under nitrogen atmosphere **N_3-DNDc** (20 mg) was dispersed in a mixture of 8 mL DMF and 2 mL water. The ruthenium complex (9.00 µmol, 1.00 eq.) was added and the mixture was degassed. **31** (8.16 mg, 18.0 µmol, 2.00 eq.) and sodium ascorbate (7.14 mg, 36.0 µmol, 4.00 eq.) were added and the mixture was stirred for 7 d at r.t. The particles were isolated and washed with acetone (3x), MeOH (3x), 0.1 M EDTA-solution (3x), water (3x), MeCN (3x), isopropanol (3x) and water (3x) yielding the functionalized particles as slight reddish, grayish dispersion.

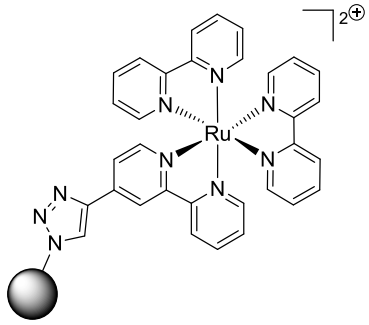

N_3-DND-Ru1

Recovery: 5 mL (3.9 mg/mL); **FT-IR** (DRIFTS): $\tilde{\nu}$ = 3431 (br, ν(O-H)), 2961 (m, ν_{as}(C-H)), 2925 (m, ν_{s}(C-H)), 1994 (w), 1787 (m, ν(C=O)), 1638 (s), 1465 (m, ν(C=C)$_{arom}$, ν(C=N)$_{arom}$), 1446 (m, ν(C=C)$_{arom}$, ν(C=N)$_{arom}$), 1270 (s), 767 (m, δ(C-H$_{arom}$)) cm^{-1}; **Raman** (λ_{ex} = 445 nm): $\tilde{\nu}$ = 665 (m), 853 (w), 1022 (w), 1169 (w), 1271 (m), 1314 (s), 1484 (s), 1556 (s), 1601 (s) cm^{-1}; **UV/Vis** (MeCN): λ_{max} = 477 (br), 291, 242 (sh) nm; **Surf. loading** (TGA): 0.08 mmol g^{-1}, Δm (160 – 450 C) = -5.3%; fragment: $C_{32}H_{22}N_9Ru$); **DLS** (H_2O): 10% ≤ 85.3 nm, 50% ≤ 175 nm, 90% ≤ 366 nm; ζ (H_2O): -33.3 mV (pH = 5.6).

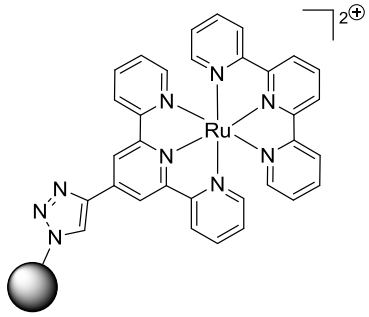

N_3-DND-Ru2

Recovery: 5 mL (4.0 mg/mL); **FT-IR** (DRIFTS): $\tilde{\nu}$ = 3419 (br, ν(O-H)), 2961 (m, ν(C-H)), 2046 (w), 2004 (w), 1789 (m, ν(C=O)), 1632 (s), 1604 (m, ν(C=C)$_{arom}$), 1451 (m, ν(C=C)$_{arom}$, ν(C=N)$_{arom}$), 1284 (s), 789 (m, δ(C-H$_{arom}$)), 771 (m, δ(C-H$_{arom}$)) cm^{-1}; **Raman** (λ_{ex} = 445 nm): $\tilde{\nu}$ = 669 (w), 839 (w), 1016 (m), 1158 (w), 1318 (s), 1478 (s), 1542 (s), 1596 (s) cm^{-1}; **UV/Vis** (MeCN): λ_{max} = 501 (br), 311, 273 (sh) nm; **Surf. loading** (TGA): 0.08 mmol g^{-1}, Δm (160 – 455 C) = -5.1%; fragment: $C_{32}H_{22}N_9Ru$); **DLS** (H_2O): 10% ≤ 77.7 nm, 50% ≤ 153 nm, 90% ≤ 365 nm; ζ (H_2O): -28.7 mV (pH = 5.6).

6.5.3 *In situ* complex formation on ND particles

General procedure: Under argon atmosphere the terpyridine functionalized particles (250 mg) were dispersed in 40 mL EtOH. Ruthenium(III) chloride hydrate (498 mg, 2.40 mmol) was added and the dispersion was sonicated for 30 min. After heating the

mixture to reflux for 72 h the ND particles were isolated via ultracentrifugation and washed with EtOH (3x), water (3x), acetone (3x), isopropanol (3x), EtOH (3x), water (3x), yielding a stable, dark-black aqueous dispersion.

6.5.3.1 Complex formation on mDND-L1-tpy$_c$

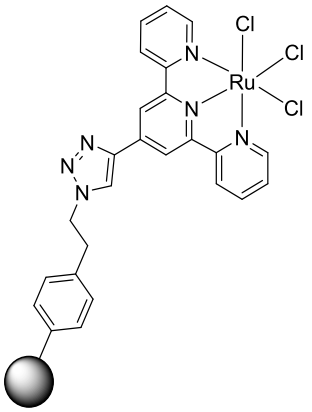

mDND-L1-Ru4b

Recovery: 25 mL (10.0 mg/mL); **FT-IR** (DRIFTS): $\tilde{\nu}$ = 3413 (br, ν(O-H)), 2953 (w, ν(C-H)), 1987 (w), 1618 (m), 1474 (m, ν(C=C)$_{arom}$, ν(C=N)$_{arom}$), 1431 (m, ν(C=C)$_{arom}$, ν(C=N)$_{arom}$), 794 (m, δ(C-H$_{arom}$)), 750 (m, δ(C-H$_{arom}$)) cm^{-1}; **Raman** (λ_{ex} = 445 nm): $\tilde{\nu}$ = 599 (m), 1327 (s, ν(diamond), D band), 1600 (br, G band) cm^{-1}; **UV/Vis** (MeCN): λ_{max} = 332, 288 nm; **Surface loading** (TGA): 0.23 mmol g^{-1}, Δm (145 – 550 °C) = -14.3%; fragment: $C_{25}H_{19}N_6RuCl_3$); **EA**: C 75.80, H 1.52, N 3.77, Cl 4.01, Ru 3.77 wt.%; **DLS** (H_2O): 10% ≤ 51.2 nm, 50% ≤ 81.5 nm, 90% ≤ 184 nm; ζ (H_2O): +39.9 mV (pH = 5.1).

6.5.3.2 Complex formation on mDND-L2-tpy$_b$

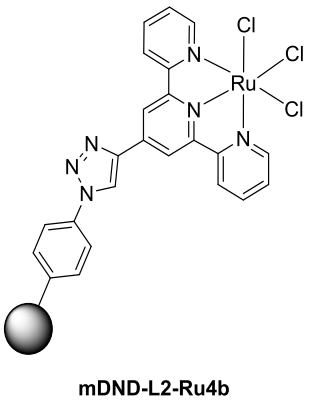

mDND-L2-Ru4b

Recovery: 25 mL (10.5 mg/mL); **FT-IR** (DRIFTS): $\tilde{\nu}$ = 3076 (br, ν(O-H)), 2954 (w, ν(C-H$_{arom}$)), 1973 (w), 1618 (m), 1515 (m, ν(C=C)$_{arom}$), 1473 (m, ν(C=C)$_{arom}$, ν(C=N)$_{arom}$), 1431 (m, ν(C=C)$_{arom}$, ν(C=N)$_{arom}$), 1240 (m), 1160 (w), 841 (m, δ(C-H$_{arom}$)), 791 (m, δ(C-H$_{arom}$)) cm^{-1}; **Raman** (λ_{ex} = 445 nm): $\tilde{\nu}$ = 674 (m), 823 (m), 1327 (s, ν(diamond), D band), 1584 (br, G band) cm^{-1}; **UV/Vis** (MeCN): λ_{max} = 295 (sh), 260 (br.) nm; **Surface loading** (TGA): 0.31 mmol g^{-1}, Δm (145 – 475 °C) = -18.4%; fragment: $C_{23}H_{15}N_6RuCl_3$); **EA**: C 55.85, H 1.69, N 4.25, Cl 11.17, Ru 7.44 wt.%; **DLS** (H_2O): 10% ≤ 170 nm, 50% ≤ 249 nm, 90% ≤ 378 nm; ζ (H_2O): +38.6 mV (pH = 5.4).

6.5.4 Carboxamide coupling of mDND-L8/L9 with Ru3

General procedure (A1): The amino-functionalized particles (1.00 eq) were dispersed in a EtOH/water mixture (2:3). After addition of **Ru3** (2.00 eq), 1-Ethyl-3-(3-dimethyl-aminopropyl)carbodiimide (10.0 eq.) and *N*-Hydroxysuccinimide (25.0 eq.) dissolved in a EtOH/water mixture (2:3) were added dropwise and the reaction was stirred at r.t. for 3 d. The ND particles were isolated via ultracentrifugation and washed with water

(4x), MeOH (3x), acetone (3x), isopropanol (3x), water (3x), yielding a stable, slightly purple aqueous dispersion.

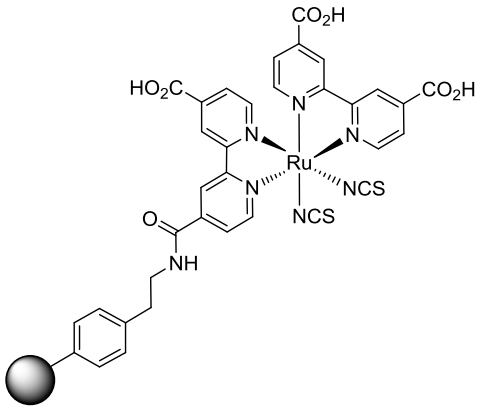

mDND-L8-Ru3

Amounts used in **A1**: **mDNDL8** (250 mg, 75.0 µmol), EtOH/water (20 mL/30 mL) **Ru3** (105 mg, 150 µmol), EDC (288 mg, 750 µmol), NHS (432 mg, 1.88 mmol), EtOH/water (20 mL/30 mL).

Recovery: 20 mL (9.8 mg/mL); **FT-IR** (DRIFTS): $\tilde{\nu}$ = 3385 (br, ν(O-H)), 2954 (m, ν(C-H)), 2104 (s, ν(SCN)), 1999 (s, ν(SCN)), 1701 (w, ν(C=O)), 1611 (m), 1544 (m, $\nu(C=C)_{arom}$, $\nu(C=N)_{arom}$), 1365 (m), 1233 (w), 911 (w), 787 (s, $\delta(C\text{-}H_{arom})$), 724 (w), 700 (m, $\delta(C\text{-}H_{arom})$) cm^{-1}; **Raman** (λ_{ex} = 532 nm): $\tilde{\nu}$ = 479 (br), 695 (w), 1034 (w), 1272 (w), 1319 (m), 1469 (s), 1535 (s), 1604 (s) cm^{-1}; **UV/Vis** (MeCN): λ_{max} = 522 (br), 387 (br), 311, 252 (sh) nm; **Surf. loading** (TGA): 0.19 mmol g^{-1}, Δm (170 – 470 C) = -15.5%; fragment: $C_{34}H_{24}N_7O_7S_2Ru$); **DLS** (H_2O): 10% ≤ 183 nm, 50% ≤ 488 nm, 90% ≤ 1360 nm; ζ (H_2O): -11.0 mV (pH = 5.6).

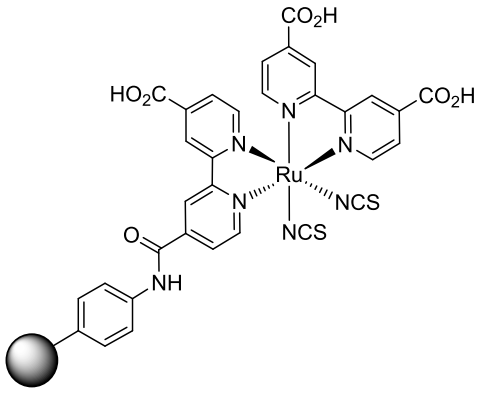

mDND-L9-Ru3

Amounts used in **A1**: **mDNDL9** (20 mg, 7.50 µmol), EtOH/water (4 mL/6 mL) **Ru3** (10.6 mg, 15.0 µmol), EDC (14.4 mg, 75.0 µmol), NHS (21.7 mg, 188 µmol), EtOH/water (4 mL/6 mL).

Recovery: 3 mL (6.5 mg/mL); **FT-IR** (DRIFTS): $\tilde{\nu}$ = 3391 (br, ν(O-H)), 2962 (m, ν(C-H)), 2107 (s, ν(SCN)), 1988 (s, ν(SCN)), 1730 (m, ν(C=O)), 1614 (w), 1504 (m, $\nu(C=C)_{arom}$, $\nu(C=N)_{arom}$), 1370 (w), 1259 (w), 914 (w), 787 (s, $\delta(C\text{-}H_{arom})$) cm^{-1}; **Raman** (λ_{ex} = 532 nm): $\tilde{\nu}$ = 479 (br), 699 (w), 1016 (w), 1274 (w), 1313 (m), 1466 (s), 1535 (s), 1598 (s) cm^{-1}; **UV/Vis** (MeCN): λ_{max} = 532 (br), 393 (br), 312, 259 (sh) nm; **Surf. loading** (TGA): 0.11 mmol g^{-1}, Δm (150 – 470 C) = -9.1%; fragment: $C_{32}H_{20}N_7O_7S_2Ru$); **DLS** (H_2O): 10% ≤ 106 nm, 50% ≤ 373 nm, 90% ≤ 1320 nm; ζ (H_2O): -10.4 mV (pH = 5.7).

6.5.5 Metal-coating of ND particles

General procedure (M1): Milled ND particles were dispersed in water to give a concentration of 0.5 mg/mL. After addition of copper(II) acetate monohydrate (1.00 eq.), the dispersion was placed on a shaker overnight. The dispersion centrifuged (5k rpm, 30 min) and the blue-colored, clear supernatant was removed. The particles were redispersed in water and a 80 wt% solution of hydrazine hydrate (1.00 eq.) was added dropwise. The dispersion turned copper-red within 30 min. The dispersion was stirred at r.t. for 20 h, then the liquid phase was removed via centrifugation and the particles were washed with water (3x) using the ultracentrifuge (52k rpm, 20 min).

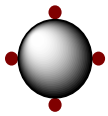

Cu-oDND

Amounts used in **M1**: Milled **oDND** (25 mg, 0.50 mL), 49.5 mL water, copper acetate monohydrate (1.99 g, 10.0 mmol), 10 mL water, 80 wt% solution of hydrazine hydrate (501 mg, 10.0 mmol). **Cu-oDND** was obtained as copper-red dispersion.

Recovery: 5 mL (5.2 mg/mL); **FT-IR** (DRIFTS): $\tilde{\nu}$ = 3371 (br, ν(O-H)), 1769 (s, ν(C=O)), 1628 (m), 1428 (w), 1324 (w), 633 (m, ν(Cu-O)), 529 (w, ν(Cu-O)) cm^{-1}; **Raman** (λ_{ex} = 445 nm): $\tilde{\nu}$ = 628 (w), 788 (br), 1320 (s, ν(diamond), D band), 1590 (br, G band) cm^{-1}; **EA**: C 75.84, H 1.20, N 2.14, Cu 10.75 wt.%; **DLS** (H_2O): 10% ≤ 552 nm, 50% ≤ 1310 nm, 90% ≤ 5260 nm; ζ (H_2O): +8.56 mV (pH = 6.1).

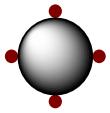

Cu-NH_2-DND

Amounts used in **M1**: Milled **NH_2-DND** (25 mg, 0.50 mL), 49.5 mL water, copper acetate monohydrate (1.99 g, 10.0 mmol), 10 mL water, 80 wt% solution of hydrazine hydrate (501 mg, 10.0 mmol, 0.61 mL). **Cu-NH_2-DND** was obtained as copper-red dispersion.

Recovery: 5 mL (5.3 mg/mL); **FT-IR** (DRIFTS): $\tilde{\nu}$ = 3693 (w), 3398 (br, ν(O-H), ν(NH_2)), 2944 (w, ν_{as}(C-H)), 2878 (w, ν_s(C-H)), 1640 (s, ν(NH_2)), 1565 (m), 1398 (w), 1333 (w), 1241 (br), 1159 (w), 837 (w, δ(C-H)), 611 (m, ν(Cu-O)), 526 (m, ν(Cu-O)) cm^{-1}; **Raman** (λ_{ex} = 445 nm): $\tilde{\nu}$ = 622 (w), 782 (br), 1316 (s, ν(diamond), D band), 1573 (br, G band) cm^{-1}; **EA**: C 67.91, H 0.64, N 3.31, Cu 15.29 wt.%; **DLS** (H_2O): 10% ≤ 39.7 nm, 50% ≤ 377 nm, 90% ≤ 1090 nm; ζ (H_2O): +38.6 mV (pH = 6.2).

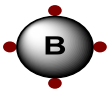

Cu-BND

Amounts used in **M1**: **BND5** (20 mg), 40 mL water, copper acetate monohydrate (1.59 g, 8.00 mmol), 8 mL water, 80 wt% solution of hydrazine hydrate (400 mg, 8.00 mmol, 0.49 mL). **Cu-BND** was obtained as slightly copper-red, blueish dispersion.

Recovery: 3 mL (7.1 mg/mL); **Raman** (λ_{ex} = 445 nm): $\tilde{\nu}$ = 1319 (vs, ν(diamond), D band), 1524 (br, G band) cm^{-1}; **DLS** (H_2O): 10% ≤ 285 nm, 50% ≤ 433 nm, 90% ≤ 709 nm; ζ (H_2O): -20.7 mV (pH = 5.7).

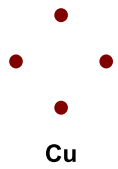

Amounts used in **M1**: 2.50 mL water, copper acetate monohydrate (99.8 g, 0.50 mmol), 80 wt% solution of hydrazine hydrate (50.1 mg, 10.0 mmol, 2.00 eq). **Cu** particles were obtained as copper-red dispersion.

Recovery: 5 mL (6.0 mg/mL); **FT-IR** (DRIFTS): $\tilde{\nu}$ = 641 (m, ν(Cu-O)) cm^{-1}; **Raman** (λ_{ex} = 445 nm): $\tilde{\nu}$ = 411 (w), 486 (w), 641 (vs), 792 (w), 1030 (br), 1271 (w) cm^{-1}; **DLS** (H_2O): 10% ≤ 640 nm, 50% ≤ 1250 nm, 90% ≤ 2550 nm; ζ (H_2O): +34.2 mV (pH = 6.8).

7. Index of abbreviations

abs.	absolute
AcOH	acetic acid
arom	aromatic
at.%	atomic percent
ATR	attenuated total reflection
arb.u.	arbitrary units
B	boron
BDD	boron-doped diamond
Boc	*tert*-Butyloxycarbonyl
bpy	2,2'-Bipyridyl
ca.	circa
calc.	calculated
CB	conduction band
CBM	conduction band maximum
CCS	carbon capture and storage
conc.	concentrated
CO	carbon monoxide
CO_2	carbon dioxide
CO_2RR	carbon dioxide reduction reaction
COSY	correlation spectroscopy
CuAAC	copper(I)-catalyzed alkyne-azide cycloaddition
CVD	chemical vapor deposition
CyH	cyclohexane
DDH	direct dehydrogenation
DEPT	distortionless enhancement by polarization transfer
DFT	density functional theory
DIPA	diisopropylamine
DIPEA	diisopropylethylamine
DLS	dynamic light scattering
DMEDA	dimethyethylenediamine
DMF	dimethylformamide
DMFC	direct methanol fuel cell
DMSO	dimethylsulfoxide
DND	detonation nanodiamond
DPP	dressed photon and phonon
DRIFTS	diffuse reflectance infrared fourier transform spectroscopy
EA	elemental analysis
EDC	1-ethyl-3-(3-dimethylamino-propyl)carbodiimide
EDTA	ethylenediaminetetraacetate
EDX	energy dispersive X-ray spectroscopy
EELS	electron energy loss spectroscopy
EPR	electron paramagnetic resonance
eq.	equivalent
ESI	electronspray ionisation
et al.	others (lat. et alii)
EtOAc	ethylacetate
EtOH	ethanol
Fig.	figure
FT-IR	Fourier-transform infrared spectroscopy
GC	gas chromatography
GGA	generalized gradient approximation
GP	general procedure
HER	hydrogen evolution reaction
HMBC	hetereonuclear multiple bond correlation

HOMO	highest occupied molecular orbital
HPHT	high pressure high temperature
HRMS	high resolution mass spectrometry
HSQC	heteronuclear single quantum coherence
IL	ionic liquid
IR	infrared
Lit.	literature
LUMO	lowest occupied molecular orbital
M	molarity
MALDI	matrix assisted laser desorption/ionization
MeCN	acetonitrile
MeOH	methanol
MLCT	metal to ligand charge transfer
mp	melting point
MS	mass spectrometry
Ms	mesyl
N	normality
NaAsc	sodium ascorbate
ND	nanodiamond
NEA	negative electron affinity
NHS	N-hydroxysuccinimide
NMR	nuclear magnetic resonance
NP	nanoparticle
NV	nitrogen vacancy
ODH	oxidative dehydrogenation
ORR	oxygen reduction reaction
P	phosphorus
PE	photoemission
PEG	polyethylenglycol
PS	polystyrene
ppm	parts per million
quant.	quantitative
r_f	retention factor
rpm	rotations per minute
rt	room temperature
SEM	scanning electron microscope
SHE	standard hydrogen electrode
TBAF	tetrabutylammonium fluoride
TEA	triehtylamine
TEM	transmission electron microscope
TFA	trifluoroacetic acid
TGA	thermogravimetric analysis
THF	tetrahydrofurane
TM	transition metal
TMSA	trimethylsilylacetylene
TNT	trinitrotoluene
TOC	total organic carbon
TOF	time of flight
tpy	2,2’:6’,2”-terpyridyl
TLC	thin layer chromatography
UDD	ultradispersed diamond
UV/Vis	ultraviolet/visible
VB	valence band
VBM	valence band maximum
wt.%	weight percent
XAS	X-ray absorption spectroscopy
XPS	X-ray photoelectron spectroscopy
XRD	X-ray diffraction
XRF	X-ray fluorescence
ζ	zeta potential

Signal description in NMR spectra:

s	singlet
d	doublet
dd	doublet of doublets
ddd	doublet of doublets of doublets
t	triplet
q	quartet
m	multiplet
br	broad signal
C_p	primary carbon
C_s	secondary carbon
C_p	tertiary carbon
C_p	quarternary carbon

Signal description in IR, UV/Vis spectra:

vs	very strong
s	strong
m	medium
w	weak
br	broad
sh	shoulder
v	stretching vibration
δ	in-plane deformation/bending vibration
γ	out-of-plane deformation/bending vibration
s	symmetric
as	antisymmetric

8. References

1. B. P. p.l.c., *BP Statistical Review of World Energy*, 2018, **67**, 1-54.
2. W. Zhong, J. D. Haigh, *Weather*, 2013, **68**, 100-105.
3. P. Nejat, F. Jomehzadeh, M. M. Taheri, M. Gohari, M. Z. Abd. Majid, *Renewable Sustainable Energy Rev.*, 2015, **43**, 843-862.
4. E. I. Koytsoumpa, C. Bergins, E. Kakaras, *J. Supercrit. Fluids*, 2018, **132**, 3-16.
5. D. Y. C. Leung, G. Caramanna, M. M. Maroto-Valer, *Renewable Sustainable Energy Rev.*, 2014, **39**, 426-443.
6. G. Zhao, X. Huang, X. Wang, X. Wang, *J. Mater. Chem. A*, 2017, **5**, 21625-21649.
7. R. Francke, B. Schille, M. Roemelt, *Chem. Rev.*, 2018, **118**, 4631-4701.
8. Q.-W. Song, Z.-H. Zhou, L.-N. He, *Green Chem.*, 2017, **19**, 3707-3728.
9. O. A. Shenderova, G. McGuire, in *Ultrananocrystalline diamond*, eds. O. A. Shenderova and D. M. Gruen, William Andrew Publishing, Norwich (NY), 2006, ch. 3, pp. 79-114.
10. F. P. Bundy, H. T. Hall, H. M. String, R. H. Wentdorf, *Nature*, 1955, **176**, 51-55.
11. P. S. DeCarli, J. C. Jamieson, *Science*, 1961, **133**, 1821-1822.
12. G. Burkhard, H. Tamura, Y. Tanabe, A. B. Sawaoka, K. Yamada, *Appl. Phys. Lett.*, 1995, **66**, 3131-3133.
13. N. R. Greiner, D. S. Phillips, J. D. Johnson, F. Volk, *Nature*, 1988, **333**, 440-442.
14. O. A. Shenderova, V. V. Zhirnov, D. W. Brenner, *Crit. Rev. Solid State Mater. Sci.*, 2002, **27**, 227-356.
15. V. N. Mochalin, O. Shenderova, D. Ho, Y. Gogotsi, *Nat. Nanotechnol.*, 2011, **7**, 11-23.
16. A. Y. Vul, A. T. Dideikin, A. E. Aleksenskii, M. V. Baidokova, in *Nanodiamond* eds. P. O´Brien and O. A. Williams, The Royal Society of Chemistry, Cambridge (UK), 2014, DOI: 10.1039/9781849737616-fp001, ch. 2, pp. 27-48.
17. O. A. Shenderova, N. Nunn, in *Nanodiamonds*, ed. J. C. Arnault, Elsevier, Amsterdam, Netherlands, 2017, ch. 2, pp. 25-36.
18. A. Krüger, in *Neue Kohlenstoffmaterialien*, Teubner Verlag, Wiesbaden, 2007, ch. 5, pp. 331-351.
19. P. W. Chen, Y. S. Ding, Q. Chen, F. L. Guang, S. R. Yun, *Diamond Relat. Mater.*, 2000, **9**, 1722-1725.
20. T. Jiang, K. Xu, *Carbon*, 1995, **33**, 1663-1671.
21. J. T. Paci, H. B. Man, B. Saha, D. Ho, G. C. Schatz, *J. Phys. Chem. C*, 2013, **117**, 17256-17267.
22. N. B. Manson, J. P. Harrison, M. J. Sellars, *Phys. Rev. B*, 2006, **74**, 104303-104313.
23. I. Vlasov, O. Shenderova, S. Turner, O. I. Lebedev, A. A. Basov, I. Sildos, M. Rahn, A. A. Shiryaev, G. Van Tendeloo, *Small*, 2010, **6**, 687-694.
24. T. Plakhotnik, H. Aman, *Diamond Relat. Mater.*, 2018, **82**, 87-95.
25. A. D. Greentree, I. Aharonovich, S. Castelletto, M. W. Doherty, L. P. McGuiness, D. A. Simpson, *Opt. Photonics News*, 2010, **21**, 20-25.
26. A. Krueger, *Chem. Eur. J.*, 2008, **14**, 1382-1390.
27. K. Turcheniuk, V. N. Mochalin, *Nanotechnol.*, 2017, **28**, 252001-252028.
28. S.-A. Martel-Estrada, *Nanosci. Nanotachnol.*, 2018, **8**, 11-24.
29. A. M. Schrand, S. A. C. Hens, O. A. Shenderova, *Crit. Rev. Solid State Mater. Sci.*, 2009, **34**, 18-74.

30. P. W. May, *Phil. Trans. R. Soc. Lond. A*, 2000, **358**, 473-495.
31. J. E. Butler, Y. A. Mankelevich, A. Cheesman, J. Ma, M. N. Ashfold, *J. Phys.: Condens. Matter.*, 2009, **21**, 364201-364220.
32. J. E. Butler, R. L. Woodin, *Phil. Trans. R. Soc. Lond. A*, 1993, **342**, 209-224.
33. S. Ferro, *J. Mater. Chem.*, 2002, **12**, 2843-2855.
34. D. G. Goodwin, *J. Appl. Phys.*, 1993, **74**, 6888-6894.
35. O. A. Williams, M. Nesládek, *Phys. Status Solidi A*, 2006, **203**, 3375-3386.
36. O. Auciello, A. V. Sumant, *Diamond Relat. Mater.*, 2010, **19**, 699-718.
37. V. Baranauskas, B. B. Li, A. Peterlevitz, M. C. Tosin, S. F. Durrant, *J. Appl. Phys.*, 1999, **85**, 7455-7458.
38. M. Z. Othman, P. W. May, N. A. Fox, P. J. Heard, *Diamond Relat. Mater.*, 2014, **44**, 1-7.
39. S. A. Kajihara, A. Antonelli, J. Bernholc, R. Car, *Phys. Rev. Lett.*, 1991, **66**, 2010-2013.
40. M. A. Pinault, J. Barjon, T. Kociniewski, F. Jomard, J. Chevallier, *Phys. B*, 2007, **401-402**, 51-56.
41. J. H. Luong, K. B. Male, J. D. Glennon, *Analyst*, 2009, **134**, 1965-1979.
42. E. Gheeraert, P. Gonon, A. Deneuville, *Diamond Relat. Mater.*, 1993, **2**, 742-745.
43. E. A. Ekimov, V. A. Sidorov, E. D. Bauer, N. N. Mel´nik, N. J. Curro, J. D. Thompson, S. M. Stishov, *Nature*, 2004, **428**, 542-545.
44. S. Heyer, W. Janssen, S. Turner, Y.-G. Lu, W. S. Yeap, J. Verbeeck, K. Haenen, A. Krueger, *ACS Nano*, 2014, **8**, 5757-5764.
45. E. A. Ekimov, O. S. Kudryavtsev, A. A. Khomich, O. I. Lebedev, T. A. Dolenko, Vlasov, II, *Adv. Mater.*, 2015, **27**, 5518-5522.
46. A. Afandi, A. Howkins, I. W. Boyd, R. B. Jackman, *Sci. Rep.*, 2018, **8**, 3270-3279.
47. S. Koizumi, M. Kamo, Y. Sato, H. Ozaki, T. Inuzuka, *Appl. Phys. Lett.*, 1997, **71**, 1065-1067.
48. T. Kociniewski, M. A. Pinault, J. Barjon, F. Jomard, J. Chevallier, C. Saguy, *Diamond Relat. Mater.*, 2007, **16**, 815-818.
49. W. Janssen, S. Turner, G. Sakr, F. Jomard, J. Barjon, G. Degutis, Y.-G. Lu, J. D'Haen, A. Hardy, M. V. Bael, J. Verbeeck, G. V. Tendeloo, K. Haenen, *Phys. Status Solidi RRL*, 2014, **8**, 705-709.
50. A. Lazea, J. Barjon, J. D'Haen, V. Mortet, M. D'Olieslaeger, K. Haenen, *J. Appl. Phys.*, 2009, **105**, 083545.
51. H. Kawashima, H. Kato, M. Ogura, D. Takeuchi, T. Makino, S. Yamasaki, *Diamond Relat. Mater.*, 2016, **64**, 208-212.
52. H. Kato, H. Watanabe, S. Yamasaki, H. Okushi, *Diamond Relat. Mater.*, 2006, **15**, 548-553.
53. H. Kato, T. Makino, S. Yamasaki, H. Okushi, *J. Phys. D: Appl. Phys.*, 2007, **40**, 6189-6200.
54. B. Butorac, A. Mainwood, *Phys. Rev. B*, 2008, **78**, 235204.
55. M. E. Zvanut, W. E. Carlos, J. A. Freitas, K. D. Jamison, R. P. Hellmer, *Appl. Phys. Lett.*, 1994, **65**, 2287-2289.
56. V. Nadolinny, A. Komarovskikh, Y. Pal'yanov, I. Kupriyanov, *Phys. Status Solidi A*, 2013, **210**, 2078-2082.
57. V. Nadolinny, A. Komarovskikh, Y. Palyanov, A. Sokol, *Phys. Status Solidi A*, 2015, **212**, 2568-2571.
58. K. Tanabe, K. Nakazawa, J. Susantyo, H. Kawarada, S. Koizumi, *Diamond Relat. Mater.*, 2001, **10**, 1652-1654.

59. R. Sauer, N. Teofilov, K. Thonke, S. Koizumi, *Diamond Relat. Mater.*, 2004, **13**, 727-731.
60. J. Barjon, P. Desfonds, M. A. Pinault, T. Kociniewski, F. Jomard, J. Chevallier, *J. Appl. Phys.*, 2007, **101**, 113701.
61. K. Haenen, M. Nesládek, L. De Schepper, R. Kravets, M. Vaněček, S. Koizumi, *Diamond Relat. Mater.*, 2004, **13**, 2041-2045.
62. H. Kato, D. Takeuchi, M. Ogura, T. Yamada, M. Kataoka, Y. Kimura, S. Sobue, C. E. Nebel, S. Yamasaki, *Diamond Relat. Mater.*, 2016, **63**, 165-168.
63. H. Kato, D. Takeuchi, N. Tokuda, H. Umezawa, S. Yamasaki, H. Okushi, *Phys. Status Solidi B*, 2008, **205**, 2195-2199.
64. M.-A. Pinault-Thaury, I. Stenger, F. Jomard, J. Chevallier, J. Barjon, A. Traore, D. Eon, J. Pernot, *Phys. Status Solidi A*, 2015, **212**, 2454-2459.
65. M. Kataoka, N. Morioka, Y. Kimura, S. Sobue, H. Kato, D. Takeuchi, S. Yamasaki, *Phys. Status Solidi A*, 2016, **213**, 2650-2653.
66. V. Y. Dolmatov, N. M. Lapchuk, T. M. Lapchuk, B. T. T. Nguyen, V. Myllymäki, A. Vehanen, R. Y. Yakovlev, *J. Superhard Mater.*, 2016, **38**, 219-229.
67. N. T. T. Binh, V. Y. Dolmatov, N. M. Lapchuk, V. I. Shymanski, *J. Appl. Spectro.*, 2017, **84**, 780-784.
68. Z. Vlčková Živcová, O. Frank, S. Drijkoningen, K. Haenen, V. Mortet, L. Kavan, *RSC Adv.*, 2016, **6**, 51387-51393.
69. P. Happel, T. Waag, M. Schimke, S. Schweeberg, A. Muzha, K. Fortak, D. Heesch, L. Klask, M. Pilscheur, F. Hoppe, T. Lenders, J. Meijer, G. Lepperdinger, A. Krueger, *Adv. Funct. Mater.*, 2018, **28**, 1802873.
70. M. I. Landstrass, K. V. Ravi, *Appl. Phys. Lett.*, 1989, **55**, 975-977.
71. V. Chakrapani, J. C. Angus, A. B. Anderson, D. W. Scott, B. R. Stoner, G. U. Sumanasekera, *Science*, 2007, **318**, 1424-1430.
72. C. E. Nebel, *Nat. Mater.*, 2013, **12**, 780-781.
73. P. A. Glans, T. Learmonth, K. E. Smith, S. Ferro, A. De Battisti, M. Mattesini, R. Ahuja, J. H. Guo, *Appl. Phys. Lett.*, 2013, **102**.
74. C.-F. Chen, S. H. Chen, *Diamond Relat. Mater.*, 1995, **4**, 451-455.
75. K. M. O'Donnell, T. L. Martin, M. T. Edmonds, A. Tadich, L. Thomsen, J. Ristein, C. I. Pakes, N. A. Fox, L. Ley, *Phys. Status Solidi A*, 2014, **211**, 2209-2222.
76. C. E. Nebel, *Science*, 2007, **318**, 1391-1392.
77. S. Kono, K. Mizuochi, G. Takyo, N. I. Plusnin, T. Aoyama, T. Goto, T. Abukawa, A. Namba, Y. Nishibayashi, T. Imai, *Surf. Sci. Nanotech.*, 2007, **5**, 33-40.
78. F. A. M. Koeck, R. J. Nemanich, A. Lazea, K. Haenen, *Diamond Relat. Mater.*, 2009, **18**, 789-791.
79. T. Masuzawa, Y. Kudo, H. Mimura, Y. Neo, K. Okano, T. Yamada, *Phys. Status Solidi A*, 2016, **213**, 2063-2068.
80. D. Zhu, L. Zhang, R. E. Ruther, R. J. Hamers, *Nat. Mater.*, 2013, **12**, 836-841.
81. J. Ristein, L. Ley, *Phys. Rev. Lett.*, 1997, **78**, 1803-1806.
82. D. Takeuchi, H. Kato, G. S. Ri, T. Yamada, P. R. Vinod, D. Hwang, C. E. Nebel, H. Okushi, S. Yamasaki, *Appl. Phys. Lett.*, 2005, **86**, 823-825.
83. D. Takeuchi, C. E. Nebel, S. Yamasaki, *Diamond Relat. Mater.*, 2007, **16**, 823-825.
84. K. R. Siefermann, Y. Liu, E. Lugovoy, O. Link, M. Faubel, U. Buck, B. Winter, B. Abel, *Nat. Chem.*, 2010, **2**, 274-279.
85. R. J. Hamers, J. A. Bandy, D. Zhu, L. Zhang, *Faraday Discuss.*, 2014, **172**, 397-411.

86. M. Kapilashrami, G. Conti, I. Zegkinoglou, S. Nemšák, C. S. Conlon, T. Törndahl, V. Fjällström, J. Lischner, S. G. Louie, R. J. Hamers, L. Zhang, J. H. Guo, C. S. Fadley, F. J. Himpsel, *J. Appl. Phys.*, 2014, **116**, 143702.
87. T. Petit, M. Pfluger, D. Tolksdorf, J. Xiao, E. F. Aziz, *Nanoscale*, 2015, **7**, 2987-2991.
88. J. L. White, M. F. Baruch, J. E. Pander, Y. Hu, I. C. Fortmeyer, J. E. Park, T. Zhang, K. Liao, J. Gu, Y. Yan, T. W. Shaw, E. Abelev, A. B. Bocarsly, *Chem. Rev.*, 2015, **115**, 12888-12935.
89. J. Qiao, Y. Liu, F. Hong, J. Zhang, *Chem. Soc. Rev.*, 2014, **43**, 631-675.
90. E. V. Kondratenko, G. Mul, J. Baltrusaitis, G. O. Larrazábal, J. Pérez-Ramírez, *Energy Environ. Sci.*, 2013, **6**, 3112-3135.
91. A. Dhakshinamoorthy, S. Navalon, A. Corma, H. Garcia, *Energy Environ. Sci.*, 2012, **5**, 9217-9233.
92. X. Chang, T. Wang, J. Gong, *Energy Environ. Sci.*, 2016, **9**, 2177-2196.
93. B. Mei, A. Pougin, J. Strunk, *J. Catal.*, 2013, **306**, 184-189.
94. X. Min, M. W. Kanan, *J. Am. Chem. Soc.*, 2015, **137**, 4701-4708.
95. D. Gao, H. Zhou, J. Wang, S. Miao, F. Yang, G. Wang, J. Wang, X. Bao, *J. Am. Chem. Soc.*, 2015, **137**, 4288-4291.
96. X. Feng, K. Jiang, S. Fan, M. W. Kanan, *J. Am. Chem. Soc.*, 2015, **137**, 4606-4609.
97. L. Chen, Z. Guo, X. G. Wei, C. Gallenkamp, J. Bonin, E. Anxolabehere-Mallart, K. C. Lau, T. C. Lau, M. Robert, *J. Am. Chem. Soc.*, 2015, **137**, 10918-10921.
98. C. Liu, B. Yang, E. Tyo, S. Seifert, J. DeBartolo, B. von Issendorff, P. Zapol, S. Vajda, L. A. Curtiss, *J. Am. Chem. Soc.*, 2015, **137**, 8676-8679.
99. J. Medina-Ramos, R. C. Pupillo, T. P. Keane, J. L. DiMeglio, J. Rosenthal, *J. Am. Chem. Soc.*, 2015, **137**, 5021-5027.
100. A. Alissandratos, C. J. Easton, *Beilstein J. Org. Chem.*, 2015, **11**, 2370-2387.
101. W.-W. Zheng, Y.-H. Hsieh, Y.-C. Chiu, S.-J. Cai, C.-L. Cheng, C. Chen, *J. Mater. Chem.*, 2009, **19**, 8432-8441.
102. B. Moosa, K. Fhayli, s. Li, K. Julfakyan, A. Ezzeddine, N. M. Lhashab, *J. Nanosci. Nanotech.*, 2014, **14**, 332-343.
103. L. Y. Bian, Y. H. Wang, J. Lu, J. B. Zang, *Diamond Relat. Mater.*, 2010, **19**, 1178-1182.
104. H. Ashassi-Sorkhabi, B. Rezaei-Moghadam, E. Asghari, *J. Taiwan Inst. Chem. Eng.*, 2017, **75**, 263-270.
105. L. La Torre Riveros, R. Guzman-Blas, A. E. Mendez-Torres, M. Prelas, D. A. Tryk, C. R. Cabrera, *ACS Appl. Mater. Interfaces*, 2012, **4**, 1134-1147.
106. L. Roldán, A. M. Benito, E. García-Bordejé, *J. Mater. Chem. A*, 2015, **3**, 24379-24388.
107. H. Ba, J. Luo, Y. Liu, C. Duong-Viet, G. Tuci, G. Giambastiani, J.-M. Nhut, L. Nguyen-Dinh, O. Ersen, D. S. Su, C. Pham-Huu, *Appl. Catal. B*, 2017, **200**, 343-350.
108. L. Zhang, R. J. Hamers, *Diamond Relat. Mater.*, 2017, **78**, 24-30.
109. X. Sun, Y. Ding, B. Zhang, R. Huang, D. Chen, D. S. Su, *ACS Catal.*, 2015, **5**, 2436-2444.
110. M. Gruttadauria, F. Giacalone, R. Noto, *Chem. Soc. Rev.*, 2008, **37**, 1666-1688.
111. K. Goldberg, A. Krueger, T. Meinhardt, W. Kroutil, B. Mautner, A. Liese, *Tetrahedron: Asymmetry*, 2008, **19**, 1171-1173.
112. B. List, *Chem. Commun.*, 2006, **8**, 819-824.
113. S. Mukherjee, J. W. Yang, S. Hoffmann, B. List, *Chem. Rev.*, 2007, **107**, 5471-5569.

114. D. W. MacMillan, *Nature*, 2008, **455**, 304-308.
115. W. Zheng, C. Lu, G. Yang, Z. Chen, J. Nie, *Catal. Commun.*, 2015, **62**, 34-38.
116. S. Itsuno, M. M. Hassan, *RSC Adv.*, 2014, **4**, 52023-52043.
117. T. Meinhardt, D. Lang, H. Dill, A. Krueger, *Adv. Funct. Mater.*, 2011, **21**, 494-500.
118. A. E. Fernandes, A. M. Jonas, O. Riant, *Tetrahedron*, 2014, **70**, 1709-1731.
119. A. Barras, S. Szunerits, L. Marcon, N. Monfilliette-Dupont, R. Boukherroub, *Langmuir*, 2010, **26**, 13168-13172.
120. H. C. Kolb, M. G. Finn, K. B. Sharpless, *Angew. Chem., Int. Ed.*, 2001, **40**, 2004-2021.
121. Q. Wang, S. Chittaboina, H. N. Barnhill, *Lett. Org. Chem.*, 2005, **2**, 293-301.
122. L. Zhang, X. Chen, P. Xue, H. Y. Sun, I. D. Williams, K. B. Sharpless, V. V. Fokin, G. Jia, *J. Am. Chem. Soc.*, 2005, **127**, 15998-15999.
123. M. Meldal, C. W. Tornoe, *Chem. Rev.*, 2008, **108**, 2952-3015.
124. D. Font, C. Jimeno, M. A. Pericás, *Org. Lett.*, 2006, **8**, 4653-4655.
125. P. Riente, J. Yadav, M. A. Pericás, *Org. Lett.*, 2012, **14**, 3668-3671.
126. K. Zeitler, I. Mager, *Org. Lett.*, 2010, **12**, 1480-1483.
127. K. Nakagawa, T. Hashida, C. Kajita, N. Ikenaga, T. Kobayashi, M. Nishitani-Gamo, T. Suzuki, T. Ando, *Catal. Lett.*, 2002, **80**, 161-163.
128. T. Tsoncheva, V. Mavrodinova, L. Ivanova, M. Dimitrov, S. Stavrev, C. Minchev, *J. Mol. Catal. A: Chem.*, 2006, **259**, 223-230.
129. K. Nakagawa, H. Nishimoto, Y. Enoki, S. Egashira, N. Ikenaga, T. Kobayashi, M. Nishitani-Gamo, T. Ando, T. Suzuki, *Chem. Lett.*, 2001, **30**, 460-461.
130. K. Nakagawa, K. Okumura, T. Shimamura, N. Ikenaga, T. Suzuki, T. Kobayashi, M. Nishitani-Gamo, T. Ando, *Chem. Lett.*, 2003, **32**, 866-867.
131. K. Nakagawa, M. Yamagishi, H. Nishimoto, N. Ikenaga, T. Suzuki, T. Kobayashi, M. Nishitani-Gamo, T. Ando, *Chem. Mater.*, 2003, **15**, 4571-4575.
132. B. Zhong, J. Zhang, B. Li, B. Zhang, C. Dai, X. Sun, R. Wang, D. S. Su, *Phys. Chem. Chem. Phys.*, 2014, **16**, 4488-4491.
133. I. I. Kulakova, *Phys. Solid State*, 2004, **46**, 636-643.
134. G. P. Bogatyreva, M. A. Marinich, E. V. Ishcnenko, V. L. Gvyazdovskaya, G. A. Bazalii, N. A. Oleinik, *Phys. Solid State*, 2004, **46**, 738-741.
135. M. Veres, E. Perevedentseva, A. V. Karmenyan, S. Tóth, M. Koós, *Phys. Status Solidi C*, 2010, **7**, 1211-1214.
136. L. Zhang, H. Liu, X. Huang, X. Sun, Z. Jiang, R. Schlögl, D. Su, *Angew. Chem., Int. Ed.*, 2015, **54**, 15823-15826.
137. V. Mavrodinova, M. Popova, I. Kolev, S. Stavrev, C. Minchev, *Appl. Surf. Sci.*, 2007, **253**, 7115-7123.
138. V. Mavrodinova, M. Popova, D. Mitev, S. Stavrev, S. Vassilev, C. Minchev, *Catal. Commun.*, 2007, **8**, 1502-1506.
139. E. A. Tveritinova, I. I. Kulakova, Y. N. Zhitnev, A. N. Kharlanov, A. V. Fionov, W. Chen, I. Buyanova, V. V. Lunin, *Russ. J. Phys. Chem. A*, 2013, **87**, 1114-1120.
140. E. V. Golubina, E. S. Lokteva, A. V. Erokhin, A. A. Veligzhanin, Y. V. Zubavichus, V. A. Likholobov, V. V. Lunin, *J. Catal.*, 2016, **344**, 90-99.
141. O. V. Turova, E. V. Starodubtseva, M. G. Vinogradov, V. I. Sokolov, N. V. Abramova, A. Y. Vul, A. E. Alexenskiy, *Catal. Commun.*, 2011, **12**, 577-579.
142. N. A. Magdalinova, M. V. Klyuev, T. G. Volkova, N. N. Vershinin, V. A. Bakaev, O. N. Efimov, I. I. Korobv, *Russ. Chem. Bull., Int. Ed.*, 2011, **60**, 1085-1089.
143. N. A. Magdalinova, P. A. Kalmykov, M. V. Klyuev, *Pet. Chem.*, 2012, **52**, 299-304.

144. N. A. Magdalinova, P. A. Kalmykov, M. V. Klyuev, *Russ. J. Gen. Chem.*, 2014, **84**, 33-39.
145. P. A. Kalmykov, N. A. Magdalinova, M. V. Klyuev, *Pet. Chem.*, 2015, **55**, 63-67.
146. P. A. Kalmykov, M. V. Klyuev, *Pet. Chem.*, 2016, **56**, 27-32.
147. D. S. Su, N. Maksimova, J. J. Delgado, N. Keller, G. Mestl, M. J. Ledoux, R. Schlögl, *Catal. Today*, 2005, **102-103**, 110-114.
148. K. Nakagawa, C. Kajita, N. Ikenaga, T. Suzuki, T. Kobayashi, M. Nishitani-Gamo, T. Ando, *J. Phys. Chem. B*, 2003, **107**, 4048-4056.
149. K. Nakagawa, C. Kajita, N. Ikenaga, M. Nishitani-Gamo, T. Ando, T. Suzuki, *Catal. Today*, 2003, **84**, 149-157.
150. S. Lee, M. Di Vece, B. Lee, S. Seifert, R. E. Winans, S. Vajda, *ChemCatChem*, 2012, **4**, 1632-1637.
151. G. Xiong, J. Sang, *J. Mol. Catal. A: Chem.*, 2014, **392**, 315-320.
152. T. Kondo, T. Morimura, T. Tsujimoto, T. Aikawa, M. Yuasa, *Sci. Rep.*, 2017, **7**, 8651.
153. Z. Zhao, W. Li, Y. Dai, G. Ge, X. Guo, G. Wang, *ACS Sustainable Chem. Eng.*, 2015, **3**, 3355-3364.
154. Z. Zhao, Y. Dai, *J. Mater. Chem. A*, 2014, **2**, 13442-13451.
155. Z. Zhao, Y. Dai, G. Ge, Q. Mao, Z. Rong, G. Wang, *ChemCatChem*, 2015, **7**, 1070-1077.
156. H. Ba, L. Truong-Phuoc, Y. Liu, C. Duong-Viet, J.-M. Nhut, L. Nguyen-Dinh, P. Granger, C. Pham-Huu, *Carbon*, 2016, **96**, 1060-1069.
157. T. T. Thanh, H. Ba, L. Truong-Phuoc, J.-M. Nhut, O. Ersen, D. Begin, I. Janowska, D. L. Nguyen, P. Granger, C. Pham-Huu, *J. Mater. Chem. A*, 2014, **2**, 11349-11357.
158. D. Su, N. I. Maksimova, G. Mestl, V. L. Kuznetsov, V. Keller, R. Schlögl, N. Keller, *Carbon*, 2007, **45**, 2145-2151.
159. J. Zhang, D. S. Su, R. Blume, R. Schlögl, R. Wang, X. Yang, A. Gajovic, *Angew. Chem., Int. Ed.*, 2010, **49**, 8640-8644.
160. X. Liu, B. Frank, W. Zhang, T. P. Cotter, R. Schlögl, D. S. Su, *Angew. Chem. , Int. Ed.*, 2011, **50**, 3318-3322.
161. X. Sun, R. Wang, B. Zhang, R. Huang, X. Huang, D. S. Su, T. Chen, C. Miao, W. Yang, *ChemCatChem*, 2014, **6**, 2270-2275.
162. R. Wang, X. Sun, B. Zhang, X. Sun, D. Su, *Chem. Eur. J.*, 2014, **20**, 6324-6331.
163. J. Diao, Z. Feng, R. Huang, H. Liu, S. B. Hamid, D. S. Su, *ChemSusChem*, 2016, **9**, 662-666.
164. B. Li, D. Su, *Chem. Asian J.*, 2013, **8**, 2605-2608.
165. S. Mao, B. Li, D. Su, *J. Mater. Chem. A*, 2014, **2**, 5287-5294.
166. T. Liu, S. Ali, B. Li, D. S. Su, *ACS Catal.*, 2017, **7**, 3779-3785.
167. J. V. Macpherson, *Phys. Chem. Chem. Phys.*, 2015, **17**, 2935-2949.
168. U. Mahtab, A. Ejaz, H. Fayyaz, M. R. Anwar, R. Rizwan, *Appl. Surf. Sci.*, 2015, **334**, 40-44.
169. I. A. Novoselova, E. N. Fedoryshena, E. V. Panov, A. A. Bochechka, L. A. Romanko, *Phys. Solid State*, 2004, **46**, 748-775.
170. A. E. S. Fischer, Greg M., *J. Electrochem. Soc.*, 2005, **152**, B369-B375.
171. V. M. Swope, I. Sasaki, A. Ay, G. M. Swain, *ECS Trans.*, 2007, **3**, 27-36.
172. A. Ay, V. M. Swope, G. M. Swain, *J. Electrochem. Soc.*, 2008, **155**, B1013-B1022.
173. L. La Torre Riveros, D. A. Tryk, C. R. Cabrera, *Rev. Adv. Mater. Sci.*, 2005, **10**, 256-560.

174. L. La Torre Riveros, K. Soto, D. A. Tryk, C. R. Cabrera, *J. Phys.: Conf. Ser.*, 2007, **61**, 1022-1026.
175. K. B. Holt, C. Ziegler, D. J. Caruana, J. Zang, E. J. Millan-Barrios, J. Hu, J. S. Foord, *Phys. Chem. Chem. Phys.*, 2008, **10**, 303-310.
176. K. B. Holt, D. J. Caruana, E. J. Millán-Barrios, *J. Am. Chem. Soc.*, 2009, **131**, 11272-11273.
177. K. B. Holt, C. Ziegler, J. Zang, J. Hu, J. S. Foord, *J. Phys. Chem. C*, 2009, **113**, 2761-2770.
178. J. Zang, Y. Wang, L. Bian, J. Zhang, F. Meng, Y. Zhao, S. Ren, X. Qu, *Electrochim. Acta*, 2012, **72**, 68-73.
179. Y. Liu, S. Chen, X. Quan, H. Yu, H. Zhao, Y. Zhang, G. Chen, *J. Phys. Chem. C*, 2013, **117**, 14992-14998.
180. Y. Liu, S. Chen, X. Quan, X. Fan, H. Zhao, Q. Zhao, H. Yu, *Appl. Catal., B*, 2014, **154-155**, 206-212.
181. K. Nakata, T. Ozaki, C. Terashima, A. Fujishima, Y. Einaga, *Angew. Chem., Int. Ed.*, 2014, **53**, 871-874.
182. A. S. Varela, N. Ranjbar Sahraie, J. Steinberg, W. Ju, H. S. Oh, P. Strasser, *Angew. Chem., Int. Ed.*, 2015, **54**, 10758-10762.
183. Y. Liu, S. Chen, X. Quan, H. Yu, *J. Am. Chem. Soc.*, 2015, **137**, 11631-11636.
184. Y. Liu, Y. Zhang, K. Cheng, X. Quan, X. Fan, Y. Su, S. Chen, H. Zhao, Y. Zhang, H. Yu, M. R. Hoffmann, *Angew. Chem., Int. Ed.*, 2017, **56**, 15607-15611.
185. L. Dong, J. Zang, Y. Wang, H. Pan, Y. Wang, Y. Zhao, J. Su, *J. Electrochem. Soc.*, 2013, **161**, F185-F191.
186. L. Dong, J. Zang, J. Su, Y. Jia, Y. Wang, J. Lu, X. Xu, *Electrochim. Acta*, 2015, **174**, 1017-1022.
187. X. Liu, Y. Wang, L. Dong, X. Chen, G. Xin, Y. Zhang, J. Zang, *Electrochim. Acta*, 2016, **194**, 161-167.
188. D.-W. Wang, D. Su, *Energy Environ. Sci.*, 2014, **7**, 576-591.
189. K.-H. Wu, Y. Liu, J. Luo, B. Wang, J. Xu, C. Pham-Huu, D. Su, *ACS Catal.*, 2017, **7**, 3295-3300.
190. Y. Wu, J. Zang, L. Dong, Y. Zhang, Y. Wang, *J. Power Sources*, 2016, **305**, 64-71.
191. G. R. Salazar-Banda, K. I. B. Eguiluz, L. A. Avaca, *Electrochem. Commun.*, 2007, **9**, 59-64.
192. N. Spatura, X. Zhang, T. Spatura, D. A. Tryk, A. Fujishima, *J. Electrochem. Soc.*, 2008, **155**, B264-B269.
193. L. La Torre Riveros, E. Abel-Tatis, A. E. Méndez-Torres, D. A. Tryk, M. Prelas, C. R. Cabrera, *J. Nanopart. Res.*, 2011, **13**, 2997-3009.
194. L. La Torre Riveros, K. Soto, M. A. Scibioh, C. R. Cabrera, *J. Electrochem. Soc.*, 2010, **157**, B831-B836.
195. L. Y. Bian, Y. H. Wang, J. B. Zang, J. K. Yu, H. Huang, *J. Electroanal. Chem.*, 2010, **644**, 85-88.
196. J. Zang, Y. Wang, L. Bian, J. Zhang, F. Meng, Y. Zhao, R. Lu, X. Qu, S. Ren, *Carbon*, 2012, **50**, 3032-3038.
197. V. Celorrio, D. Plana, J. Flórez-Montaño, M. G. Montes de Oca, A. Moore, M. J. Lázaro, E. Pastor, D. J. Fermín, *J. Phys. Chem. C*, 2013, **117**, 21735-21742.
198. J. Schneider, M. Matsuoka, M. Takeuchi, J. Zhang, Y. Horiuchi, M. Anpo, D. W. Bahnemann, *Chem. Rev.*, 2014, **114**, 9919-9986.
199. A. Fujishima, T. N. Rao, D. A. Tryk, *Electrochim. Acta*, 2000, **45**, 4683-4690.
200. K.-D. Kim, N. K. Dey, H. O. Seo, Y. D. Kim, D. C. Lim, M. Lee, *Appl. Catal., A*, 2011, **408**, 148-155.

201. L. M. Pastrana-Martínez, S. Morales-Torres, S. A. C. Carabineiro, J. G. Buijnsters, J. L. Faria, J. L. Figueiredo, A. M. T. Silva, *ChemPlusChem*, 2013, **78**, 801-807.
202. M. J. Sampaio, L. M. Pastrana-Martínez, A. M. T. Silva, J. G. Buijnsters, C. Han, C. G. Silva, S. A. C. Carabineiro, D. D. Dionysiou, J. L. Faria, *RSC Adv.*, 2015, **5**, 58363-58370.
203. H. I. Kim, H.-N. Kim, S. Weon, G.-H. Moon, J.-H. Kim, W. Choi, *ACS Catal.*, 2016, **6**, 8350-8360.
204. D. M. Jang, Y. Myung, H. S. Im, Y. S. Seo, Y. J. Cho, C. W. Lee, J. Park, A. Y. Jee, M. Lee, *Chem. Commun.*, 2012, **48**, 696-698.
205. D. M. Jang, H. S. Im, Y. Myung, Y. J. Cho, H. S. Kim, S. H. Back, J. Park, E. H. Cha, M. Lee, *Phys. Chem. Chem. Phys.*, 2013, **15**, 7155-7160.
206. Z. Lin, J. Xiao, L. Li, P. Liu, C. Wang, G. Yang, *Adv. Energy Mater.*, 2016, **6**, 1501865.
207. V. Keller-Spitzer, Q. Minetti, N. Keller, V. Pichot, D. Spitzer, *Internat. Pat.*, 2016, **WO 2016/193464 A1**.
208. Y. A. Haleem, Q. He, D. Liu, C. Wang, W. Xu, W. Gan, Y. Zhou, C. Wu, Y. Ding, L. Song, *RSC Adv.*, 2017, **7**, 15390-15396.
209. S. Navalon, M. de Miguel, R. Martin, M. Alvaro, H. Garcia, *J. Am. Chem. Soc.*, 2011, **133**, 2218-2226.
210. S. Navalon, R. Martin, M. Alvaro, H. Garcia, *ChemSusChem*, 2011, **4**, 650-657.
211. D. Sempere, S. Navalon, M. Dančíková, M. Alvaro, H. Garcia, *Appl. Catal., B*, 2013, **142-143**, 259-267.
212. S. Navalon, D. Sempere, M. Alvaro, H. Garcia, *ACS Appl. Mater. Interfaces*, 2013, **5**, 7160-7169.
213. J. C. Espinosa, S. Navalón, M. Álvaro, H. Garcia, *ChemCatChem*, 2015, **7**, 2682-2688.
214. P. Manickam-Periyaraman, S. M. Espinosa, J. C. Espinosa, S. Navalón, S. Subramanian, M. Álvaro, H. Garcia, *J. Environ. Chem. Eng.*, 2016, **4**, 4485-4493.
215. J. C. Espinosa, S. Navalón, M. Álvaro, H. García, *Catal. Sci. Technol.*, 2016, **6**, 7077-7085.
216. G. Dordelmann, T. Meinhardt, T. Sowik, A. Krueger, U. Schatzschneider, *Chem. Commun.*, 2012, **48**, 11528-11530.
217. M. Ohtani, P. V. Kamat, S. Fukuzumi, *J. Mater. Chem.*, 2010, **20**, 582-587.
218. J. R. Christianson, D. Zhu, R. J. Hamers, J. R. Schmidt, *J. Phys. Chem. B*, 2014, **118**, 195-203.
219. C. J. van der Ham, M. T. Koper, D. G. Hetterscheid, *Chem. Soc. Rev.*, 2014, **43**, 5183-5191.
220. L. Zhang, D. Zhu, G. M. Nathanson, R. J. Hamers, *Angew. Chem., Int. Ed.*, 2014, **53**, 9746-9750.
221. S. Sahu, L. Cao, M. J. Meziani, C. E. Bunker, K. A. Shiral Fernando, P. Wang, Y.-P. Sun, *Chem. Phys. Lett.*, 2015, **634**, 122-128.
222. Y. Katamune, S. Takeichi, S. Ohmagari, H. Setoyama, T. Yoshitake, *Trans. Mater. Res. Soc. Jap.*, 2015, **40**, 243-246.
223. T. Yatsui, T. Imoto, T. Mochizuki, K. Kitamura, T. Kawazoe, *Sci. Reports*, 2014, **4**, 4561-4568.
224. M. C. Benson, R. E. Ruther, J. B. Gerken, M. L. Rigsby, L. M. Bishop, Y. Tan, S. S. Stahl, R. J. Hamers, *ACS Appl. Mater. Interfaces*, 2011, **3**, 3110-3119.
225. S. Ardo, G. J. Meyer, *Chem. Soc. Rev.*, 2009, **38**, 115-164.

226. D. F. Zigler, Z. A. Morseth, L. Wang, D. L. Ashford, M. K. Brennaman, E. M. Grumstrup, E. C. Brigham, M. K. Gish, R. J. Dillon, L. Alibabaei, G. J. Meyer, T. J. Meyer, J. M. Papanikolas, *J. Am. Chem. Soc.*, 2016, **138**, 4426-4438.
227. H. B. Martin, A. Argoitia, U. Landau, A. B. Anderson, J. C. Angus, *J. Electrochem. Soc.*, 1996, **143**, L133-L136.
228. S. Nakabayashi, N. Ohta, A. Fujishima, *Phys. Chem. Chem. Phys.*, 1999, **1**, 3993-3997.
229. M. R. Das, M. Wang, S. Szunerits, L. Gengembre, R. Boukherroub, *Chem. Commun.*, 2009, **0**, 2753-2755.
230. R. E. Ruther, Q. Cui, R. J. Hamers, *J. Am. Chem. Soc.*, 2013, **135**, 5751-5761.
231. A. Krueger, D. Lang, *Adv. Funct. Mater.*, 2012, **22**, 890-906.
232. S. A. Yao, R. E. Ruther, L. Zhang, R. A. Franking, R. J. Hamers, J. F. Berry, *J. Am. Chem. Soc.*, 2012, **134**, 15632-15635.
233. C. K. Prier, D. A. Rankic, D. W. MacMillan, *Chem. Rev.*, 2013, **113**, 5322-5363.
234. K. Zeitler, *Angew. Chem., Int. Ed.*, 2009, **48**, 9785-9789.
235. J. M. Narayanam, C. R. Stephenson, *Chem. Soc. Rev.*, 2011, **40**, 102-113.
236. T. P. Yoon, M. A. Ischay, J. Du, *Nat. Chem.*, 2010, **2**, 527-532.
237. D. M. Schultz, T. P. Yoon, *Science*, 2014, **343**, 985-994.
238. C. W. Machan, M. D. Sampson, C. P. Kubiak, *J. Am. Chem. Soc.*, 2015, **137**, 8564-8571.
239. R. E. Ruther, M. L. Rigsby, J. B. Gerken, S. R. Hogendoorn, E. C. Landis, S. S. Stahl, R. J. Hamers, *J. Am. Chem. Soc.*, 2011, **133**, 5692-5694.
240. W. S. Yeap, X. Liu, D. Bevk, A. Pasquarelli, L. Lutsen, M. Fahlman, W. Maes, K. Haenen, *ACS Appl. Mater. Interfaces*, 2014, **6**, 10322-10329.
241. I. Zegkinoglou, P. L. Cook, P. S. Johnson, W. Yang, J. Guo, D. Pickup, R. González-Moreno, C. Rogero, R. E. Ruther, M. L. Rigsby, J. E. Ortega, R. J. Hamers, F. J. Himpsel, *J. Phys. Chem. C*, 2012, **116**, 13877-13883.
242. J. B. Gerken, M. L. Rigsby, R. E. Ruther, R. J. Perez-Rodriguez, I. A. Guzei, R. J. Hamers, S. S. Stahl, *Inorg. Chem.*, 2013, **52**, 2796-2798.
243. H. Krysova, L. Kavan, Z. V. Zivcova, W. S. Yeap, P. Verstappen, W. Maes, K. Haenen, F. Gao, C. E. Nebel, *RSC Adv.*, 2015, **5**, 81069-81077.
244. H. Krysova, Z. Vlckova-Zivcova, J. Barton, V. Petrak, M. Nesladek, P. Cigler, L. Kavan, *Phys. Chem. Chem. Phys.*, 2015, **17**, 1165-1172.
245. W. S. Yeap, D. Bevk, X. Liu, H. Krysova, A. Pasquarelli, D. Vanderzande, L. Lutsen, L. Kavan, M. Fahlman, W. Maes, K. Haenen, *RSC Adv.*, 2014, **4**, 42044-42053.
246. A. Krueger, M. Ozawa, G. Jarre, Y. Liang, J. Stegk, L. Lu, *Phys. Status Solidi A*, 2007, **204**, 2881-2887.
247. K. B. Holt, in *Nanodiamond* eds. P. O´Brien and O. A. Williams, The Royal Society of Chemistry, Cambridge (UK), 2014, DOI: 10.1039/9781849737616-fp001, ch. 8, pp. 131-134.
248. A. Krueger, in *Nanodiamonds*, ed. J. C. Arnault, Elsevier, Amsterdam, Netherlands, 2017, ch. 8, pp. 183-200.
249. A. Krueger, in *Nanodiamond* eds. P. O´Brien and O. A. Williams, The Royal Society of Chemistry, Cambridge (UK), 2014, DOI: 10.1039/9781849737616-fp001, ch. 3, pp. 54-67.
250. D. E. Patterson, R. H. Hauge, J. L. Margrave, *Mat. Res. Soc. Symp. Proc.*, 1988, **140**, 351-356.
251. T. Ando, J. Tanaka, M. Ishii, M. Kamo, Y. Sato, *J. Chem. Soc. Faraday Trans.*, 1993, **89**, 3105-3109.

252. T. Ando, K. Yamamoto, M. Kamo, Y. Sato, *J. Chem. Soc. Faraday Trans.*, 1995, **91**, 3209-3212.
253. C. P. Kealey, T. M. Klapötke, D. W. McComb, M. I. Robertson, J. M. Winfield, *J. Mater. Chem.*, 2001, **11**, 879-886.
254. Y. Liu, Z. Gu, J. L. Margrave, V. N. Khabashesku, *Chem. Mater.*, 2004, **16**, 3924-3930.
255. V. N. Khabashesku, J. L. Margrave, E. V. Barrera, *Diamond Relat. Mater.*, 2005, **14**, 859-866.
256. H. Touhara, F. Okino, *Carbon*, 2000, **38**, 241-267.
257. M. A. Ray, O. Shenderova, W. Hook, A. Martin, V. Grishko, T. Tyler, G. B. Cunningham, G. McGuire, *Diamond Relat. Mater.*, 2006, **15**, 1809-1812.
258. H. Huang, Y. H. Wang, J. B. Zang, L. Y. Bian, *Appl. Surf. Sci.*, 2012, **258**, 4079-4084.
259. J. Havlik, H. Raabova, M. Gulka, V. Petrakova, M. Krecmarova, V. Masek, P. Lousa, J. Stursa, H.-G. Boyen, M. Nesladek, P. Cigler, *Adv. Funct. Mater.*, 2016, **26**, 4134-4142.
260. Y. H. Wang, H. Huang, J. Zang, F. Meng, L. Dong, J. Su, *Int. J. Electrochem. Sci.*, 2012, **7**, 6807-6815.
261. B. E. Scruggs, K. K. Gleason, *J. Phys. Chem.*, 1993, **97**, 9187-9195.
262. A. M. Panich, *Crit. Rev. Solid State Mater. Sci.*, 2012, **37**, 276-303.
263. A. M. Panich, *Diamond Relat. Mater.*, 2017, **79**, 21-31.
264. A. M. Panich, H.-M. Vieht, A. I. Shames, N. Froumin, E. Osawa, A. Yao, *J. Phys. Chem. C*, 2010, **114**, 774-782.
265. M. Dubois, K. Guerin, N. Batisse, E. Petit, A. Hamwi, N. Komatsu, H. Kharbache, P. Pirotte, F. Masin, *Solid State Nucl. Magn. Reson.*, 2011, **40**, 144-154.
266. A. Krueger, in *Nanodiamonds*, ed. J. C. Arnault, Elsevier, Amsterdam, Netherlands, 2017, ch. 8, pp. 214-224.
267. J. J. Stapleton, T. A. Daniel, S. Uppili, S. O. Cabarcos, J. Naciri, R. Shashidhar, D. L. Allara, *Langmuir*, 2005, **21**, 11061-11070.
268. G. Jarre, Y. Liang, P. Betz, D. Lang, A. Krueger, *Chem. Commun.*, 2011, **47**, 544-546.
269. M. Hartmann, P. Betz, Y. Sun, S. N. Gorb, T. K. Lindhorst, A. Krueger, *Chem. Eur. J.*, 2012, **18**, 6485-6492.
270. D. Lang, A. Krueger, *Diamond Relat. Mater.*, 2011, **20**, 101-104.
271. Y. Liang, T. Meinhardt, G. Jarre, M. Ozawa, P. Vrdoljak, A. Scholl, F. Reinert, A. Krueger, *J. Colloid. Interface. Sci.*, 2011, **354**, 23-30.
272. Y. Liang, M. Ozawa, A. Krueger, *ACS Nano*, 2009, **3**, 2288-2296.
273. K. B. Holt, *Phys. Chem. Chem. Phys.*, 2010, **12**, 2048-2058.
274. A. Krüger, F. Kataoka, M. Ozawa, T. Fujino, Y. Suzuki, A. E. Aleksenskii, A. Y. Vul', E. Osawa, *Carbon*, 2005, **43**, 1722-1730.
275. M. Ozawa, M. Inaguma, M. Takahashi, F. Kataoka, A. Krüger, E. Ōsawa, *Adv. Mater.*, 2007, **19**, 1201-1206.
276. E. Osawa, *Diamond Relat. Mater.*, 2007, **16**, 2018-2022.
277. K. Sayama, H. Arakawa, *J. Phys. Chem.*, 1993, **97**, 58-60.
278. V. R. Reddy, D. W. Hwang, J. S. Lee, *Korean J. Chem. Eng.*, 2003, **20**, 1026-1029.
279. D. P. Mitev, A. T. Townsend, B. Paull, P. N. Nesterenko, *J. Mater. Sci.*, 2014, **49**, 3573-3591.
280. D. S. Volkov, M. A. Proskurnin, M. V. Korobov, *Carbon*, 2014, **74**, 1-13.

281. V. Dolmatov, V. Myllymäki, *International Patent*, 2013, **WO 2013/135305 A1**, 1-35.
282. R. A. Norwood, P. Gangopadhyay, A. Ashton Miles, J. Kato, S. Virji-Khalfan, M. Miyawaki, *US Patent*, 2015, **US 8, 940,267 B2**, 1-16.
283. V. Y. Dolmatov, A. Vehanen, V. Myllymäki, K. A. Rudometkin, A. N. Panova, K. M. Korolev, T. A. Shpadkovskaya, *Russ. J. Appl. Chem.*, 2013, **86**, 1036-1045.
284. L. Cortés-Palacios, V. I. Collins, A. D. Diaz, A. O. Lopéz, *Chem. Mater. Res.*, 2012, **2**, 31-41.
285. J. W. Blanton, *US Patent*, 1962, **3029132A**, 1-4.
286. S. S. Kouassi, J. Andji, J.-P. Bonnet, S. Rossignol, *Ceram.-Silik.*, 2010, **54**, 235-240.
287. F. Huang, Y. Tong, S. Yun, *Phys. Solid State*, 2004, **46**, 616-619.
288. A. P. Koshcheev, *Rus. J. Gen. Chem.*, 2009, **79**, 2033-2044.
289. C. Guillard, E. Puzenat, H. Lachheb, A. Houas, J.-M. Herrmann, *Int. J. Photoenergy*, 2005, **7**, 1-9.
290. S. Osswald, G. Yushin, V. Mochalin, S. O. Kucheyev, Y. Gogotsi, *J. Am. Chem. Soc.*, 2006, **128**, 11635-11642.
291. L. Gines, S. Mandal, I. A. Ashek, C. L. Cheng, M. Sow, O. A. Williams, *Nanoscale*, 2017, **9**, 12549-12555.
292. L. F. Scatena, M. G. Brown, G. L. Richmond, *Science*, 2001, **292**, 908-913.
293. T. Petit, L. Puskar, *Diamond Relat. Mater.*, 2018, **89**, 52-66.
294. T. Petit, L. Puskar, T. Dolenko, S. Choudhury, E. Ritter, S. Burikov, K. Laptinskiy, Q. Brzustowski, U. Schade, H. Yuzawa, M. Nagasaka, N. Kosugi, M. Kurzyp, A. Venerosy, H. Girard, J.-C. Arnault, E. Osawa, N. Nunn, O. Shenderova, E. F. Aziz, *J. Phys. Chem. C*, 2017, **121**, 5185-5194.
295. T. Jiang, K. Xu, S. Ji, *J. Chem. Soc., Faraday Trans.*, 1996, **92**, 3401-3406.
296. N. Gibson, O. A. Shenderova, T. J. M. Luo, S. Moseenkov, V. Bondar, A. Puzyr, K. Purtov, Z. Fitzgerald, D. W. Brenner, *Diamond Relat. Mater.*, 2009, **18**, 620-626.
297. O. Shenderova, A. M. Panich, S. Moseenkov, S. C. Hens, V. Kuznetsov, H. M. Vieth, *J. Phys. Chem. C*, 2011, **115**, 19005-19011.
298. R. Martín, P. C. Heydorn, M. Alvaro, H. Garcia, *Chem. Mater.*, 2009, **21**, 4505-4514.
299. R. Martín, M. Alvaro, J. R. Herance, H. Garcia, *ACS Nano*, 2010, **4**, 65-74.
300. M. V. Korobov, D. S. Volkov, N. V. Avramenko, L. A. Belyaeva, P. I. Semenyuk, M. A. Proskurnin, *Nanoscale*, 2013, **5**, 1529-1536.
301. J. S. Tu, E. Perevedentseva, P. H. Chung, C. L. Cheng, *J. Chem. Phys.*, 2006, **125**, 174713.
302. V. Mochalin, S. Osswald, Y. Gogotsi, *Chem. Mater.*, 2009, **21**, 273-279.
303. J. C. Arnault, H. A. Girard, *Curr. Opin. Solid State Mater. Sci.*, 2017, **21**, 10-16.
304. J. C. Arnault, S. Saada, M. Nesladek, O. A. Williams, K. Haenen, P. Bergonzo, E. Osawa, *Diamond Relat. Mater.*, 2008, **17**, 1143-1149.
305. H. A. Girard, J. C. Arnault, S. Perruchas, S. Saada, T. Gacoin, J. P. Boilot, P. Bergonzo, *Diamond Relat. Mater.*, 2010, **19**, 1117-1123.
306. O. A. Williams, J. Hees, C. Dieker, W. Jäger, L. Kirste, C. E. Nebel, *ACS Nano*, 2010, **4**, 4824-4830.
307. Y.-S. Lee, *J. Fluorine Chem.*, 2007, **128**, 392-403.
308. A. V. Grosse, C. B. Linn, *J. Org. Chem.*, 1938, **3**, 26-32.
309. M. Adamska, U. Narkiewicz, *J. Fluorine Chem.*, 2017, **200**, 179-189.
310. W. E. Jones, E. G. Skolink, *Chem. Rev.*, 1976, **76**, 562-591.

311. C. A. Leon y Leon, J. N. Solar, V. Calemm, L. R. Radovic, *Carbon*, 1992, **5**, 797-811.
312. M. A. Montes-Morán, J. A. Menéndez, E. Fuente, D. Suárez, *J. Phys. Chem. B*, 1998, **102**, 5595-5601.
313. E. M. Zagrebina, A. V. Generalov, A. Y. Klyushin, K. A. Simonov, N. A. Vinogradov, M. Dubois, L. Frezet, N. Mårtensson, A. B. Preobrajenski, A. S. Vinogradov, *J. Phys. Chem. C*, 2014, **119**, 835-844.
314. K. J. Rietwyk, S. L. Wong, L. Cao, K. M. O'Donnell, L. Ley, A. T. S. Wee, C. I. Pakes, *Appl. Phys. Lett.*, 2013, **102**, 091604.
315. I. Bravo, A. Aranda, M. D. Hurley, G. Marston, D. R. Nutt, K. P. Shine, K. Smith, T. J. Wallington, *J. Geophys. Res.* , 2010, **115**, D24317.
316. A. Freedman, *J. Appl. Phys.*, 1994, **75**, 3112-3120.
317. A. E. Aleksenskiy, E. D. Eydelman, A. Y. Vul, *Nanosci. Nanotachnol. Lett.*, 2011, **3**, 68-74.
318. K. Mikami, Y. Itoh, M. Yamanaka, *Chem. Rev.*, 2004, **104**, 1-16.
319. V. Pichot, M. Comet, E. Fousson, C. Baras, A. Senger, F. Le Normand, D. Spitzer, *Diamond Relat. Mater.*, 2008, **17**, 13-22.
320. D. Liu, L. Gou, J. Xu, K. Gao, X. Kang, *Vacuum*, 2016, **128**, 80-84.
321. P. Manimunda, A. Al-Azizi, S. H. Kim, R. R. Chromik, *ACS Appl. Mater. Interfaces*, 2017, **9**, 16704-16714.
322. P. Szirmai, T. Pichler, O. A. Williams, S. Mandal, C. Bäuerle, F. Simon, *Phys. Status Solidi B*, 2012, **249**, 2656-2659.
323. V. V. S. S. Srikanth, P. Sampath Kumar, V. B. Kumar, *Int. J. Electrochem. Sci*, 2012, **2012**, 1-7.
324. G. Zhang, S. D. Janssens, J. Vanacken, M. Timmermans, J. Vacík, G. W. Ataklti, W. Decelle, W. Gillijns, B. Goderis, K. Haenen, P. Wagner, V. V. Moshchalkov, *Phys. Rev. B*, 2011, **84**, 214517.
325. S. D. Janssens, P. Pobedinskas, J. Vacik, V. Petráková, B. Ruttens, J. D'Haen, M. Nesládek, K. Haenen, P. Wagner, *New J. Phys.*, 2011, **13**, 083008.
326. S. Choudhury, B. Kiendl, J. Ren, F. Gao, P. Knittel, C. Nebel, A. Venerosy, H. Girard, J.-C. Arnault, A. Krueger, K. Larsson, T. Petit, *J. Mater. Chem. A*, 2018, **6**, 16645-16654.
327. J. Stetefeld, S. A. McKenna, T. R. Patel, *Biophys. Rev.*, 2016, **8**, 409-427.
328. R. H. Telling, C. J. Pickard, M. C. Payne, J. E. Field, *Phys. Rev. Lett.*, 2000, **84**, 5160-5163.
329. J. Barjon, *Phys. Status Solidi A* 2017, **214**, 1700402.
330. Z. Shpilman, I. Gouzman, T. K. Minton, L. Shen, A. Stacey, J. Orwa, S. Prawer, B. C. C. Cowie, A. Hoffman, *Diamond Relat. Mater.*, 2014, **45**, 20-27.
331. D. L. Jameson, L. E. Guise, *Tetrahedron Lett.*, 1991, **32**, 1999-2002.
332. M. Zalas, B. Gierczyk, M. Cegłowski, G. Schroeder, *Chemical Papers*, 2012, **66**, 733-740.
333. V. Grosshenny, F. M. Romero, R. Ziessel, *J. Org. Chem.*, 1997, **62**, 1491-1500.
334. M. Zalas, B. Gierczyk, M. Klein, K. Siuzdak, T. Pędziński, T. Łuczak, *Polyhedron*, 2014, **67**, 381-387.
335. A. Baron, C. Herrero, A. Quaranta, M. F. Charlot, W. Leibl, B. Vauzeilles, A. Aukauloo, *Inorg. Chem.*, 2012, **51**, 5985-5987.
336. C. Herrero, A. Quaranta, R.-A. Fallahpour, W. Leibl, A. Aukauloo, *J. Phys. Chem. C*, 2013, **117**, 9605-9612.
337. I. P. Evans, G. Wilkinson, *J. Chem. Soc. Dalton Trans.*, 1973, **2**, 204-209.
338. C. E. McCusker, J. K. McCusker, *Inorg. Chem.*, 2011, **50**, 1656-1669.

339. R. Ziessel, V. Grosshenny, M. Hissler, C. Stroh, *Inorg. Chem.*, 2004, **43**, 4262-4271.
340. S. Ardo, Y. Sun, A. Staniszewski, F. N. Castellano, G. J. Meyer, *J. Am. Chem. Soc.*, 2010, **132**, 6696-6709.
341. P. B. Sullivan, J. M. Calvert, T. J. Meyer, *Inorg. Chem.*, 1980, **19**, 1404-1407.
342. S. Das, D. Pati, N. Tiwari, A. Nisal, S. Sen Gupta, *Biomacromolecules*, 2012, **13**, 3695-3702.
343. P. K. Gajula, J. Asthana, D. Panda, T. K. Chakraborty, *J. Med. Chem.*, 2013, **56**, 2235-2245.
344. A. Cwiklicki, K. Rehse, *Arch. Pharm.*, 2004, **337**, 156-163.
345. F. W. Wassmundt, W. F. Kiesman, *J. Org. Chem.*, 1995, **60**, 1713-1719.
346. N. Kornblum, G. D. Cooper, J. E. Taylor, *J. Am. Chem. Soc.*, 1950, **72**, 3013-3021.
347. M. Schonberger, M. Althaus, M. Fronius, W. Clauss, D. Trauner, *Nat. Chem.*, 2014, **6**, 712-719.
348. B. J. Barron, W.-T. Wong, P. Chiu, K. K. Hii, *ACS Catal.*, 2016, **6**, 4189-4194.
349. R. Kaur, J. M. Chitanda, D. Michel, J. Maley, F. Borondics, P. Yang, R. E. Verrall, I. Badea, *Int. J. Nanomedicine*, 2012, **7**, 3851-3866.
350. J. S. Lipkin, R. Song, E. E. Fenlon, S. H. Brewer, *J. Phys. Chem. Lett.*, 2011, **2011**, 1672-1676.
351. J. Zhang, L. Wang, J. Zhang, J. Zhu, X. Pan, Z. Chui, J. F. Wang, W. Li, Y., *J. Phys. Chem. B*, 2018, **122**, 8122-8133.
352. H. Cates, in *Encyclopedia of Analytical Chemistry*, ed. R. A. Meyers, John Wiley & Sons Ltd, Chichester, 2000, pp. 10815-10837.
353. K. O. Patten, L. Andrews, *J. Am. Chem. Soc.*, 1985, **107**, 5594-5600.
354. M. Khanal, V. Turcheniuk, A. Barras, E. Rosay, O. Bande, A. Siriwardena, V. Zaitsev, G. H. Pan, R. Boukherroub, S. Szunerits, *Langmuir*, 2015, **31**, 3926-3933.
355. A. L. Casado, P. Espinet, *Organometallics*, 2003, **22**, 1305-1309.
356. J. E. Hein, V. V. Fokin, *Chem. Soc. Rev.*, 2010, **39**, 1302-1315.
357. S. Wu, L. Chen, B. Yin, Y. Li, *Chem. Commun.*, 2015, **51**, 9884-9887.
358. J. Fujita, K. KNakamoto, M. Kobayashi, *J. Am. Chem. Soc.*, 1956, **78**, 3295-3297.
359. P. Farràs, S. Maji, J. Benet-Buchholz, A. Llobet, *Chem. Eur. J.*, 2013, **19**, 7162-7172.
360. O. A. Shenderova, I. I. Vlasov, S. Turner, G. Van Tendeloo, S. B. Orlinskii, A. A. Shiryaev, A. A. Khomich, S. N. Sulyanov, F. Jelezko, J. Wrachtrup, *J. Phys. Chem. C*, 2011, **115**, 14014-14024.
361. A. Basu, H. D. Gafney, T. C. Streaks, *Inorg. Chem.*, 1982, **21**, 2231-2235.
362. Z. C. Kennedy, C. A. Barrett, M. G. Warner, *Langmuir*, 2017, **33**, 2790-2798.
363. F. Gao, M. T. Wolfer, C. E. Nebel, *Carbon*, 2014, **80**, 833-840.
364. A. Venerosy, H. A. Girard, S. Saada, M. Sennour, I. Stenger, M. Mermoux, J. C. Arnault, *Diamond Relat. Mater.*, 2018, **89**, 122-131.
365. N. Roy, Y. Hirano, H. Kuriyama, P. Sudhagar, N. Suzuki, K. I. Katsumata, K. Nakata, T. Kondo, M. Yuasa, I. Serizawa, T. Takayama, A. Kudo, A. Fujishima, C. Terashima, *Sci. Rep.*, 2016, **6**, 1-9.
366. C. M. Welch, A. O. Simm, R. G. Compton, *Electroanalysis*, 2006, **18**, 965-970.
367. H. S. Panglipur, T. A. Ivandini, R. Wibowo, Y. Einaga, *AIP Conf. Proc.*, 2016, **1729**, 020047.
368. K. Turcheniuk, V. N. Mochalin, *Carbon*, 2016, **109**, 98-105.

369. K. Natsui, H. Iwakawa, N. Ikemiya, K. Nakata, Y. Einaga, *Angew. Chem., Int. Ed.*, 2018, **57**, 2639-2643.
370. W. B. Russel, D. A. Saville, W. R. Schowalter, in *Colloidal dispersions*, ed. W. B. Russel, Cambridge University Press, Cambridge, 1989, ch. 1, pp. 1-20.
371. Y. Hori, A. Murata, R. Takahashi, *J. Chem. Soc., Faraday Trans.*, 1989, **85**, 2309-2326.
372. T. Yoshikawa, V. Zuerbig, F. Gao, R. Hoffmann, C. E. Nebel, O. Ambacher, V. Lebedev, *Langmuir*, 2015, **31**, 5319-5325.
373. N. O. McHedlov-Petrossyan, N. N. Kamneva, A. I. Marynin, A. P. Kryshtal, E. Osawa, *Phys. Chem. Chem. Phys.*, 2015, **17**, 16186-16203.
374. L. Nicoud, M. Lattuada, S. Lazzari, M. Morbidelli, *Phys. Chem. Chem. Phys.*, 2015, **17**, 24392-23402.
375. K. Ghandi, *Green. Sustain. Chem.*, 2014, **4**, 44-53.
376. M. J. Earle, K. R. Seddon, *Pure Appl. Chem.*, 2000, **72**, 1391-1398.
377. B. Wang, L. Qin, T. Mu, Z. Xue, G. Gao, *Chem. Rev.*, 2017, **117**, 7113-7131.
378. K. L. Van Aken, M. Beidaghi, Y. Gogotsi, *Angew. Chem., Int. Ed.*, 2015, **54**, 4806-4809.
379. D. S. Silvester, R. G. Compton, *Z. Phys. Chem.*, 2006, **220**, 1247-1274.
380. Z. Xue, L. Qin, J. Jiang, T. Mu, G. Gao, *Phys. Chem. Chem. Phys.*, 2018, **20**, 8382-8402.
381. J. F. Brennecke, B. E. Gurkan, *J. Phys. Chem. Lett.*, 2010, **1**, 3459-3464.
382. S. N. V. K. Aki, B. R. Mellein, E. M. Saurer, J. F. Brennecke, *J. Phys. Chem. B*, 2004, **108**, 20355-20365.
383. M. J. Muldoon, S. N. V. K. Aki, J. L. Anderson, J. K. Dixon, J. F. Brennecke, *J. Phys. Chem. B*, 2007, **111**, 9001-9009.
384. A. Shariati, C. J. Peters, *J. Supercrit. Fluids*, 2004, **29**, 43-48.
385. K. I. Gutkowski, A. Shariati, C. J. Peters, *J. Supercrit. Fluids*, 2006, **39**, 187-191.
386. G. E. Romanos, L. F. Zubeir, V. Likodimos, P. Falaras, M. C. Kroon, B. Iliev, G. Adamova, T. J. Schubert, *J. Phys. Chem. B*, 2013, **117**, 12234-12234.
387. Max P. Bernstein, S. F. M. Ashbourn, S. A. Sandford, L. J. Allamandola, *Astrophys. J.*, 2004, **601**, 365-370.
388. A. Garza-Ortiz, P. Uma Maheswari, M. Siegler, A. L. Spek, J. Reedijk, *New J. Chem.*, 2013, **37**, 3450-3460.
389. R. Chen, Z. An, W. Wang, X. Chen, P. Chen, *Opt. Mater. Express*, 2015, **6**, 97-105.
390. J. van Houten, R. J. Watts, *J. Am. Chem. Soc.*, 1976, **98**, 4854-4859.
391. B. Durham, J. V. Caspar, J. K. Nagle, T. J. Meyer, *J. Am. Chem. Soc.*, 1982, **104**, 4803-4810.
392. K. Kalyanasundaram, *Coord. Chem. Rev.*, 1982, **46**, 159-244.
393. A. Vaidyalingam, P. K. Dutta, *Anal. Chem.*, 2000, **72**, 5219-5224.
394. L. Jarrige, G. Levitre, G. Masson, *J. Org. Chem.*, 2016, **81**, 7230-7236.
395. C. Lebee, M. Languet, C. Allain, G. Masson, *Org. Lett.*, 2016, **18**, 1478-1481.
396. A. Carboni, G. Dagousset, E. Magnier, G. Masson, *Chem. Commun.*, 2014, **50**, 14197-14200.
397. V. V. Albert, E. Badaeva, S. Kilina, M. Sykora, S. Tretiak, *J. Lumin.*, 2011, **131**, 1739-1746.
398. D. D. Perrin, in *CRC Handbook of Chemistry and Physcis*, ed. D. R. Lide, CRC Press, Boca Raton, 84th edn., 2004, ch. 8, pp. 8.46-48.47.
399. K. Kodama, A. Kobayashi, T. Hirose, *Tetrahedron Lett.*, 2013, **54**, 5514-5517.
400. C. Agnes, J. C. Arnault, F. Omnes, B. Jousselme, M. Billon, G. Bidan, P. Mailley, *Phys. Chem. Chem. Phys.*, 2009, **11**, 11647-11654.

9. Appendix

Table 53: ICP-AES and ICP-MS analysis results for untreated and treated **pDND** and **mDND**. Elements not listed have either been not detected (less than 1 ppm) or are not suitable for ICP-MS analysis. The measurement uncertainity is about ±15%.

Element [ppm]	**pDND**	**mDND**	**pDND** (Pir.+ HCl)	**mDND** (NaOH)	**pDND** (multistep)
Al	446	1160	596	531	170,8
As	2	-	-	-	-
B	26	42	314	74	31,1
Ba	3	8,1	4,4	9,1	-
Ca	30	234	818	1233	6,7
Cr	1	13	-	6	-
Cu	-	3	3	5	-
Fe	400	500	21	643	25,9
Hf	-	381	-	-	-
K	24	29	142	365	24,4
Mg	12	31	195	282	-
Mn	6	5,5	-	4,4	-
Mo	-	-	-	-	3,3
Na	69	280	1150	1580	31,6
Ni	2	2,5	12	20	-
Pb	-	-	-	-	-
S	< 20	-	-	-	95,5
Sb	-	-	-	-	-
Si	-	207	3367	4837	5,2
Sr	-	-	-	2,1	-
Ti	35	17	24	22	24,4
W	-	9	-	-	-
Zn	1	-	-	6	-
Zr	11	19300	19	15	3,9
∑	1088 ± 163	22222 ± 3333	6665 ± 1000	9665 ± 1450	423 ± 63

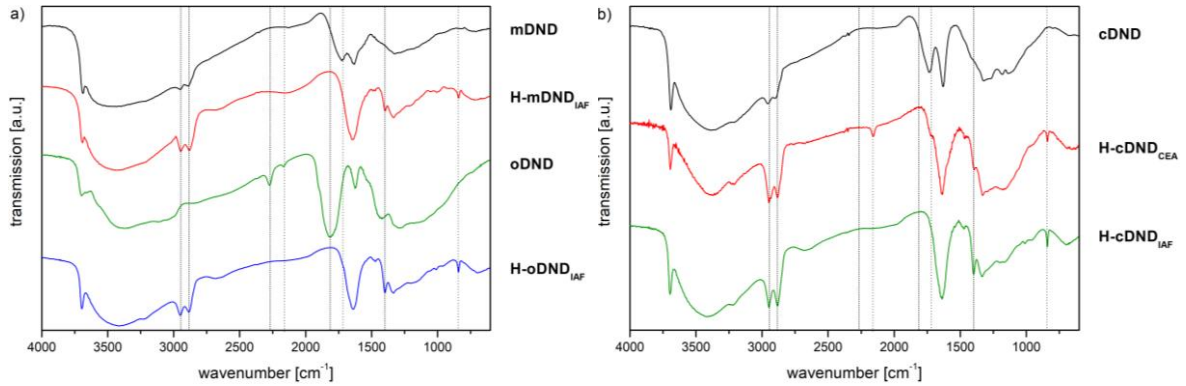

Fig. 117: DRIFT spectra of (a) **mDND**, **oDND** and the hydrogenated samples **H-mDND$_{IAF}$** and **H-oDND$_{IAF}$** and of (b) **cDND** with the respective particles **H-cDND$_{CEA}$** and **H-cDND$_{IAF}$** (right).

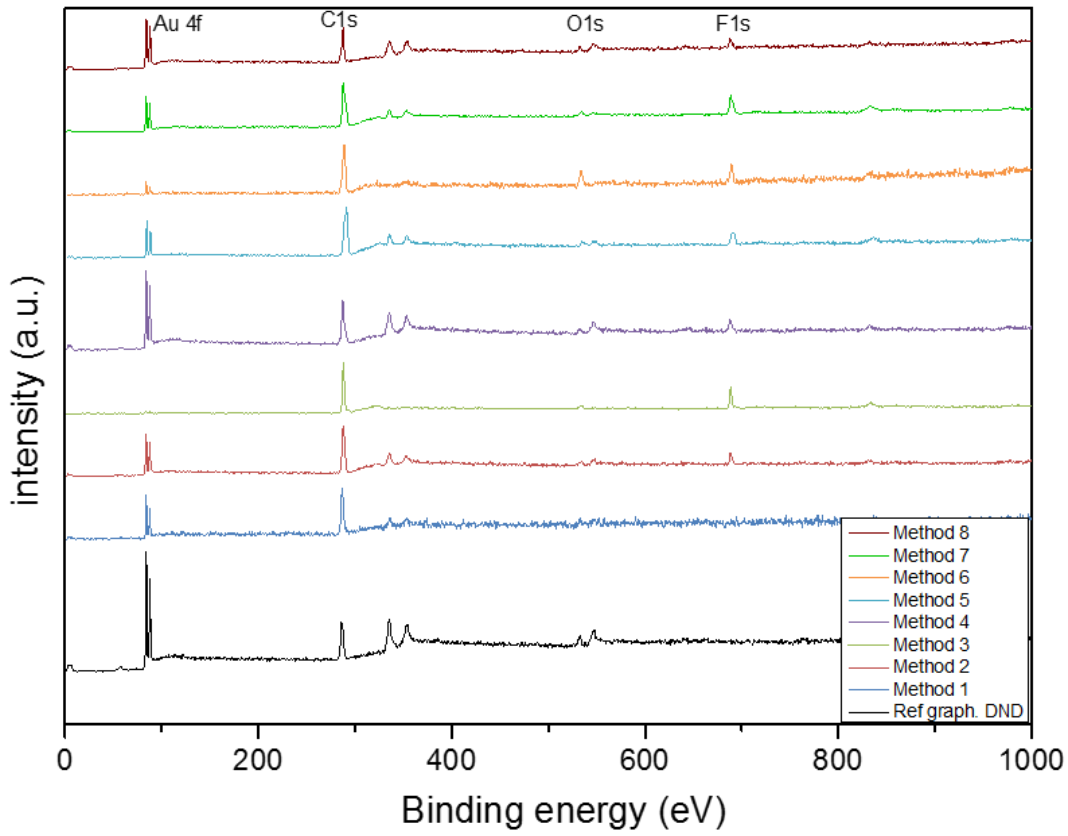

Fig. 118: XPS spectra of **F-DND1-8** (methods 1-8 respectively) and graphitized, annealed DND reference **gDND** (spectra were normalized in intensity according to C1s peak and measured by the cooperation partner CEA).

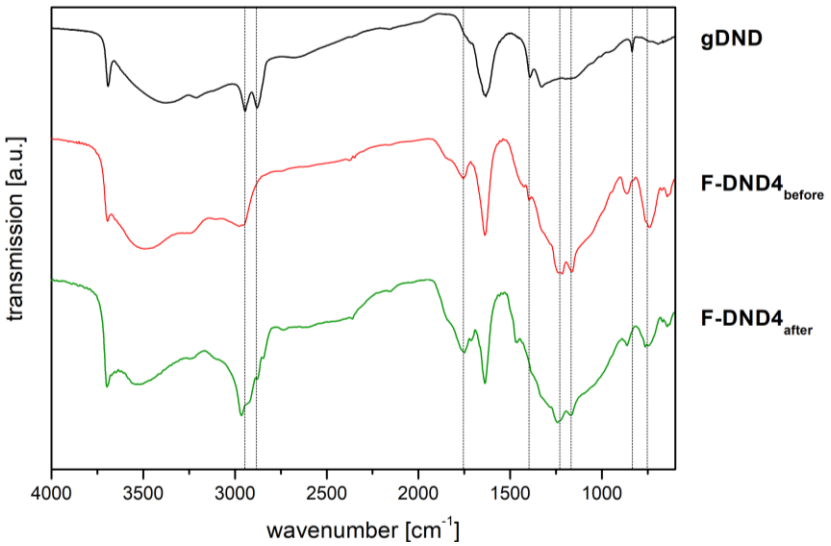

Fig. 119: DRIFT spectra of **gDND** and HF/F_2 treated **F-DND4** before and after intensive washing.

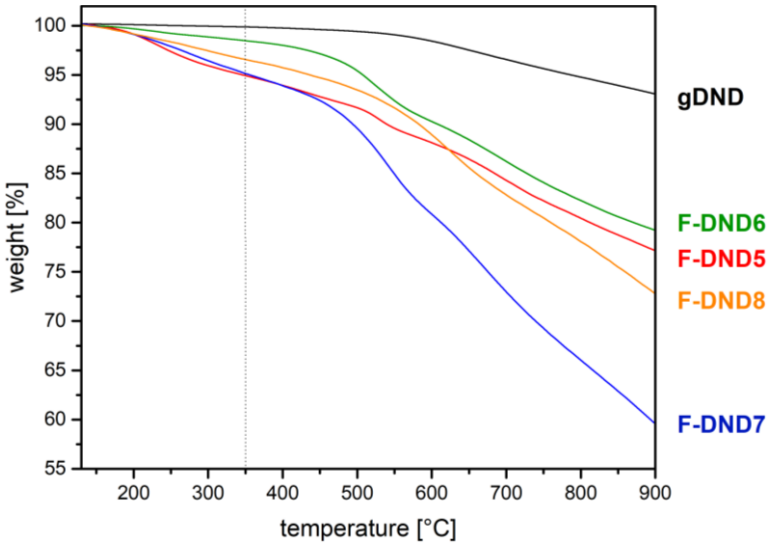

Fig. 120: Thermogravimetric analysis of **gDND** and HF/F_2 treated DNDs **F-DND5-8**.

Table 54: Particle size measurements of fractions from **BND3**.

BND3	D_V-(10) [nm]	D_V-(50) [nm]	D_V-(90) [nm]	fraction name
0.5 min at 3000 rpm	164	337	729	**BND3_330**
2.5 min at 3000 rpm	99.1	173	307	**BND3_175**
5.0 min at 3000 rpm	74.1	126	245	**BND3_125**
5.0 min at 4500 rpm	51.1	89.7	216	**BND3_90**
5.0 min at 12000 rpm	31.2	47.0	78.1	**BND3_45**

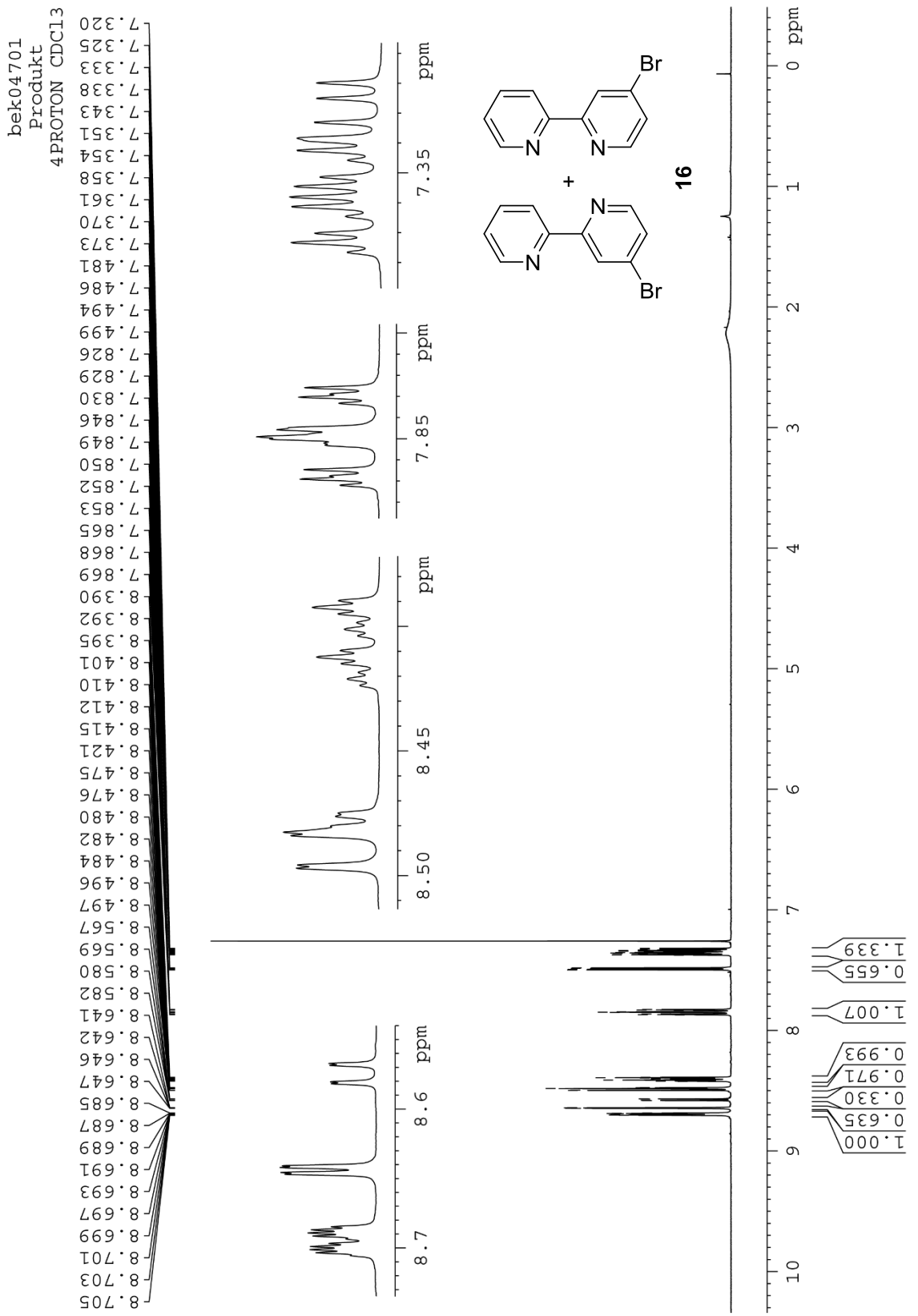

Fig. 121: ^{1}H-NMR spectrum of **16**.

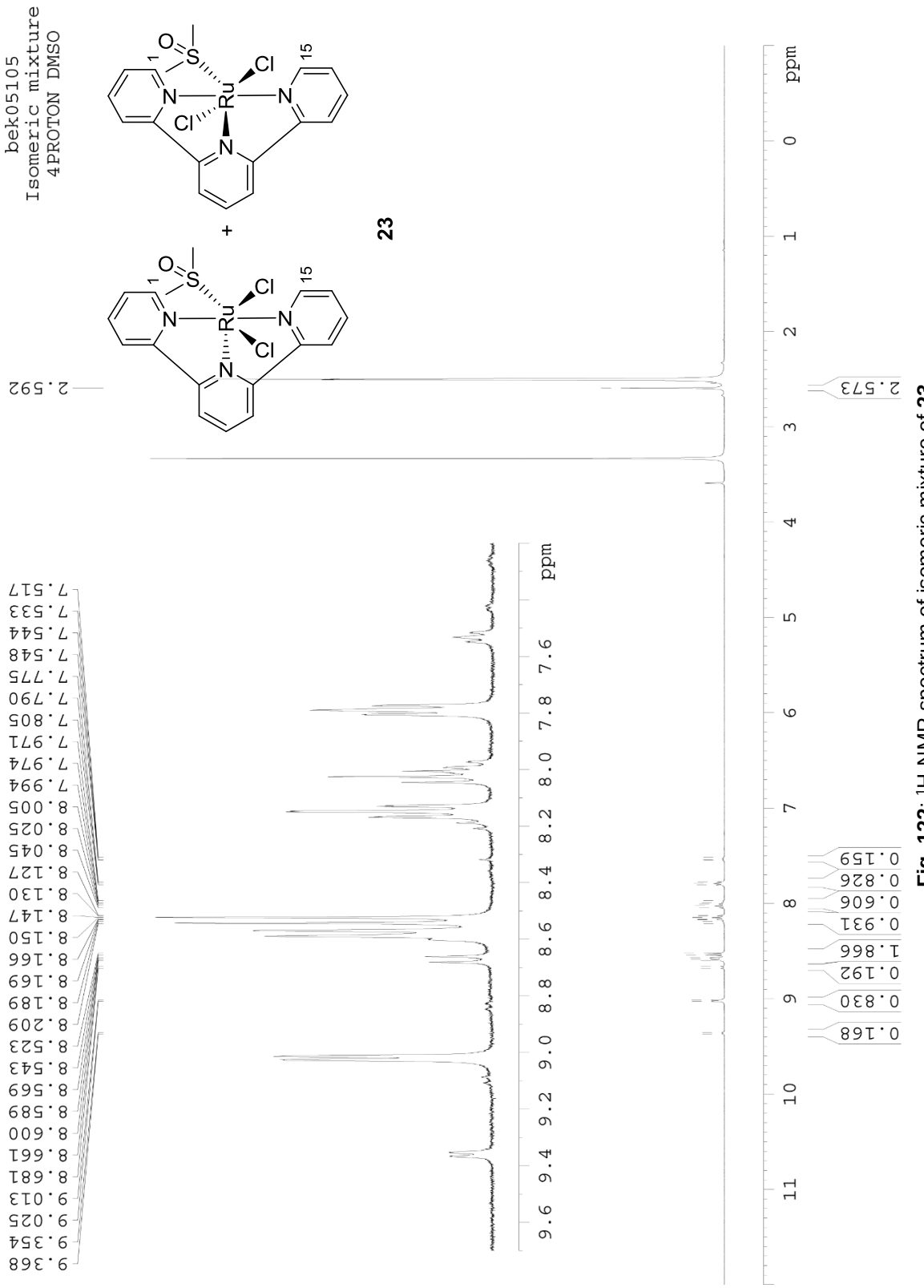

Fig. 122: ^{1}H-NMR spectrum of isomeric mixture of **23**.

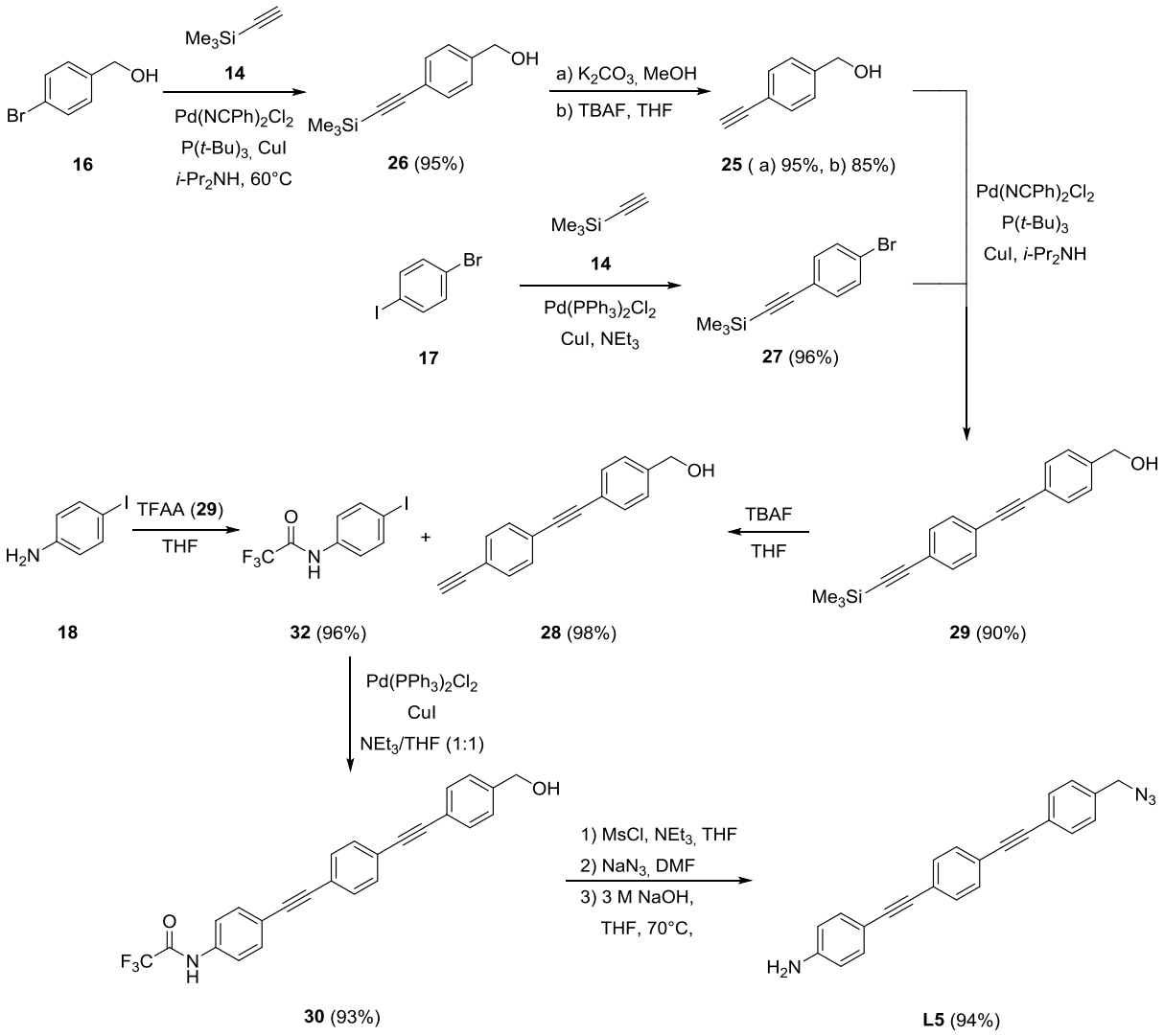

Fig. 123: Synthesis route for linker system **L5.**

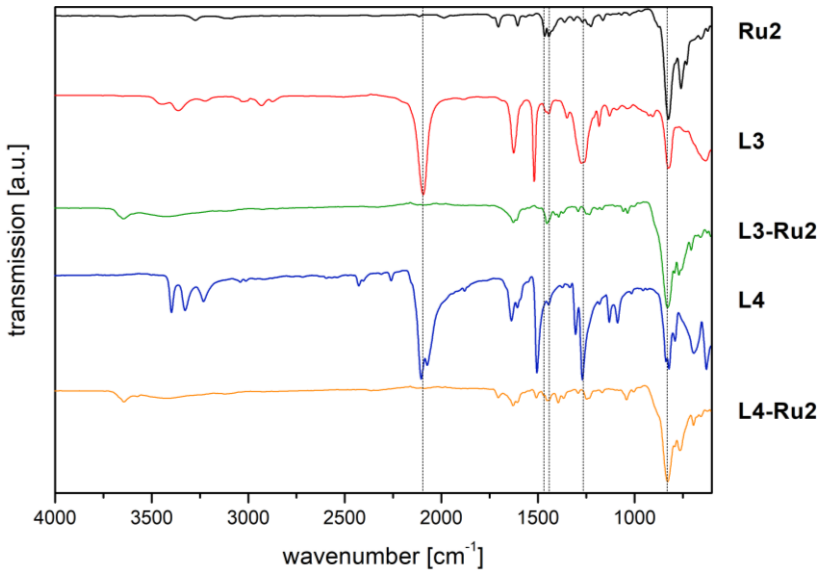

Fig. 124: ATR-FTIR spectra of **Ru2**, azide linkers **L3** and **L4** and the reference systems **L3-Ru1** and **L4-Ru1**.

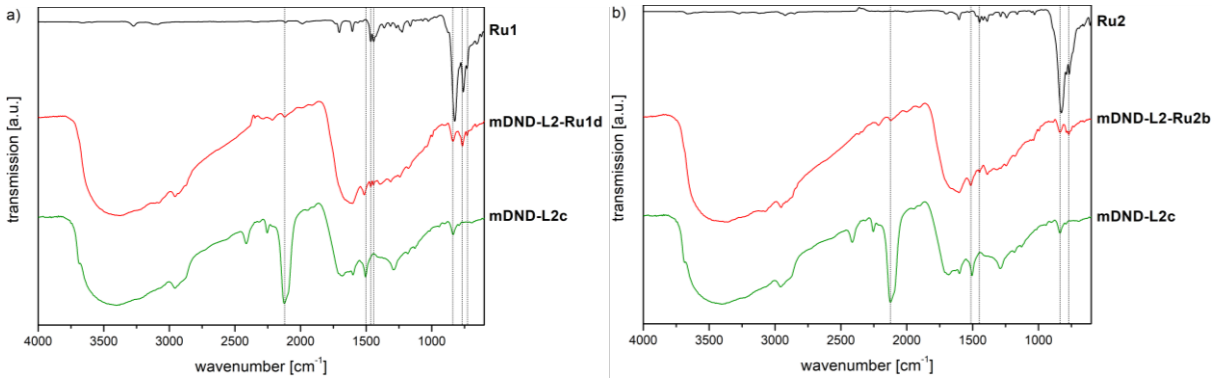

Fig. 125: IR spectra of (a) **mDND-L2c**, **mDND-L2-Ru1d** (DRIFT) and **Ru1** (ATR-FTIR) and of (b) **mDND-L2c**, **mDND-L2-Ru2b** (DRIFT) and **Ru2** (ATR-FTIR).

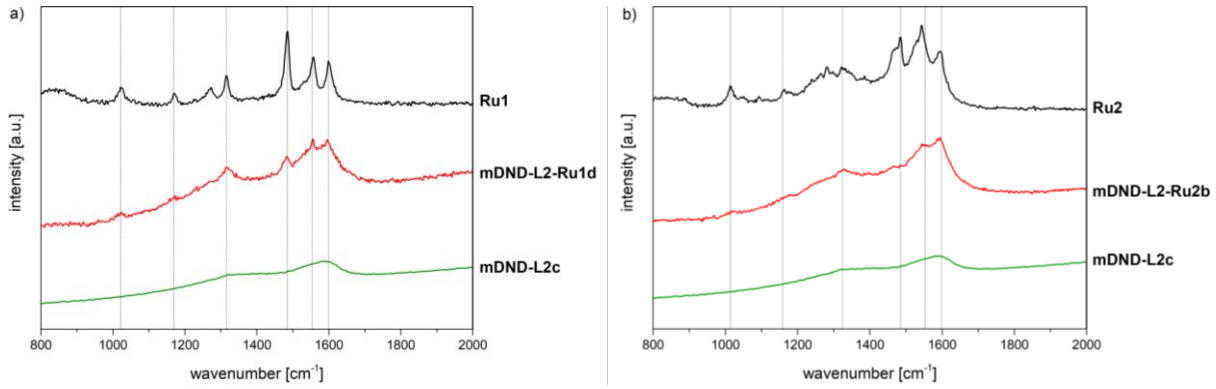

Fig. 126: Raman spectra of (a) **mDND-L2c**, **mDND-L2-Ru1d** and **Ru1** and of (b) **mDND-L2c**, **mDND-L2-Ru2b** and **Ru2** (excitation with 445 nm laser).

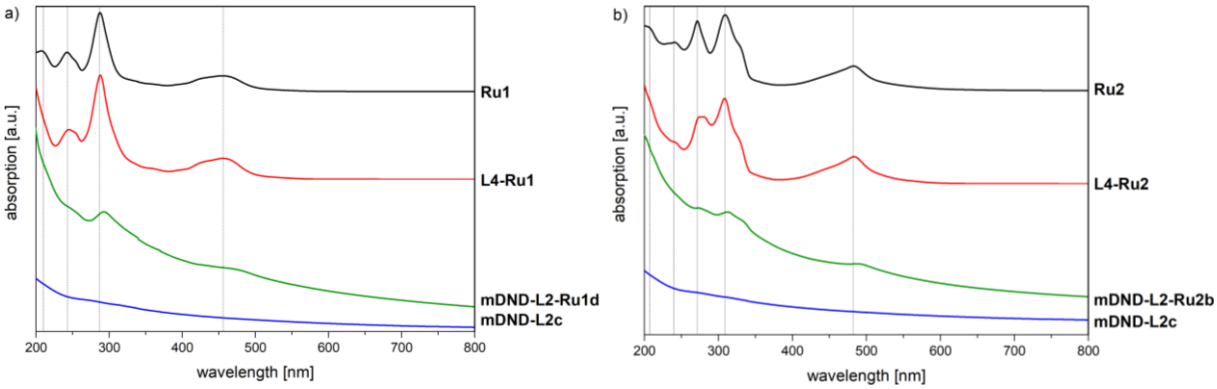

Fig. 127: UV/Vis spectra of (a) **mDND-L2c**, **mDND-L2-Ru1d**, complex **Ru1** and reference **L4-Ru1** and of (b) **mDND-L2c**, **mDND-L2-Ru2b,** complex **Ru2** and reference **L4-Ru2** (measurements in MeCN).

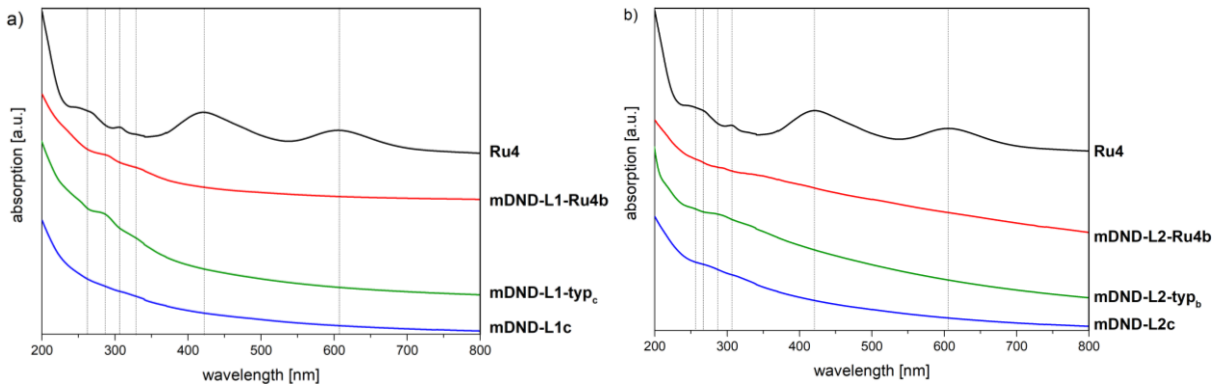

Fig. 128: UV/Vis spectra of (a) **mDND-L1c**, **mDND-L1-tpy$_c$**, **mDND-L1-Ru4b** and reference **Ru4** and of (b) **mDND-L2c**, **mDND-L2-tpy$_b$**, **mDND-L2-Ru4b** and reference **Ru4** (measurements in MeCN).

XPS analysis of Ru-functionalized mDND particles

Core level spectra of C1s, O1s, N1s, Cl2p and Ru3d$_{5/2}$ allowed to calculate the atomic concentrations of each detected element (Table 55). The oxygen atomic concentration varied from 6.6 at.% to 12.7 at.%. The presence of oxygen could be attributed to functional groups present at the nanodiamond surface. Furthermore, interactions of grafted nanodiamonds with water molecules in suspensions forming an adlayer cannot be excluded. For **mDND**, no nitrogen was detected on the surface. Thus, for all other DND samples, the detected nitrogen corresponded to nitrogen atoms contained in the attached complexes or linkers.

Table 55: Atomic concentrations of elements detected from XPS spectra for **L1**/**L2** systems

ND material	C1s [at.%]	O1s [at.%]	N1s [at.%]	Ru3d$_{5/2}$ [at.%]	Cl2p [at.%]
mDND	87.6	12.4	-	-	-
mDND-L1c	91.3	6.9	1.8	-	-
mDND-L1-Ru1c	86.8	7.3	5.6	0.3	-
mDND-L1-Ru2b	90.3	6.6	2.9	0.3	-
mDND-L1-tpyc	86.4	8.7	5.0	-	-
mDND-L1-Ru4b	84.3	12.7	2.9	0.2	-
mDND-L2c	88.6	8.2	3.2	-	-
mDND-L2-Ru1d	84.6	12.2	2.8	0.4	-
mDND-L2-Ru2b	85.9	10.5	3.6	0.1	-
mDND-L2-tpyb	86.6	9.7	3.6	-	-
mDND-L2-Ru4b	82.1	12.4	3.0	1.0	1.5

Ruthenium was detected for all Ru-functionalized DND-conjugates. The binding energy of Ru $3d_{5/2}$ was in agreement with measured values in previous studies of diamond surfaces grafted with similar Ru complexes.[400] Nevertheless, the corresponding signals for Ru $3d_{5/2}$ were weak, at 0.1-0.4 at.%, close to the detection limit of the XPS technique. For **mDND-L1-Ru4b**, no chlorine was detected. For this complex, a chlorine to Ru ratio of 1:3 was expected. For **mDND-L2-Ru4b**, nitrogen, ruthenium and chlorine were detected. Although the nitrogen chlorine ratio was as expected (2:1), the ruthenium chlorine ratio was lower (1:2 vs. 1:3). The absence/decrease of chlorine suggests modifications of the complex during or after grafting and a possible ligand exchange from chlorine to water, also explaining the higher oxygen content of **mDND-L1-Ru4b**. The higher surface loading with **L2** in comparison to **L1** can be seen by the increased nitrogen value (1.8 at.% → 3.2 at.%).

XRF analysis of Ru-functionalized mDND particles

Regarding XRF analysis, the particles **mDND-L1-Ru4b** and **mDND-L2-Ru4b** were used to illustrate the relevant signals in comparison to **mDND** (Fig. 129).

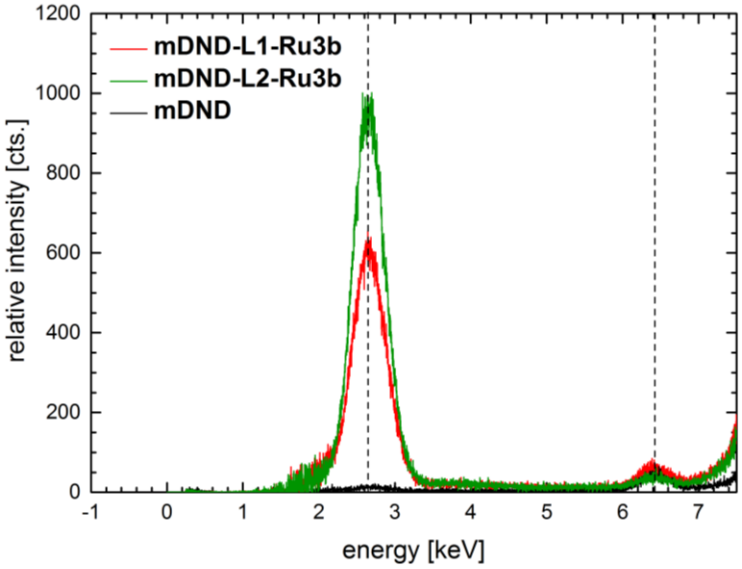

Fig. 129: XRF spectra of **mDND** and the **Ru4**-functionalized particles **mDND-L1-Ru4b** and **mDND-L2-Ru4b**.

All three samples showed a signal at around 6.4 keV, which could be related to the $K\alpha_1$ and $K\alpha_2$ emission line of iron. This contamination originated from the commercial **pDND** powder, having ~400 ppm iron impurity (chapter 3.1.1.2). The iron signals were detected for each DND powder. The most interesting signal appeared at ~2.6 keV. **mDND** showed no intensity in this region. This signal itself was a combination of the

ruthenium $L\alpha_2$, $L\alpha_1$ and $L\beta_1$ lines, as well as the chlorine $K\alpha_1$ and $K\alpha_2$ lines. It proved the attachment of **Ru4**, as well as the high intensity due to superimposed emission lines. Using dried powder, the chlorine ligand was relatively stable and not or very slowly exchanging with water. The non-conjugated systems, **mDND-L1-Ru1c/mDND-L1-Ru2b**, are shown in Fig. 130a. For **mDND-L1-Ru2b**, the signal at ~2.6 keV was increased, illustrating the presence of ruthenium. However, for **mDND-L1-Ru1c**, no clear signal was detected. This was in accordance with the XPS results, indicating that the methods were at their detection limit. The equivalent samples **mDND-L2-Ru1d/mDND-L2-Ru2b**, linked via the conjugated linker, showed both an increased ruthenium related signal (Fig. 130b).

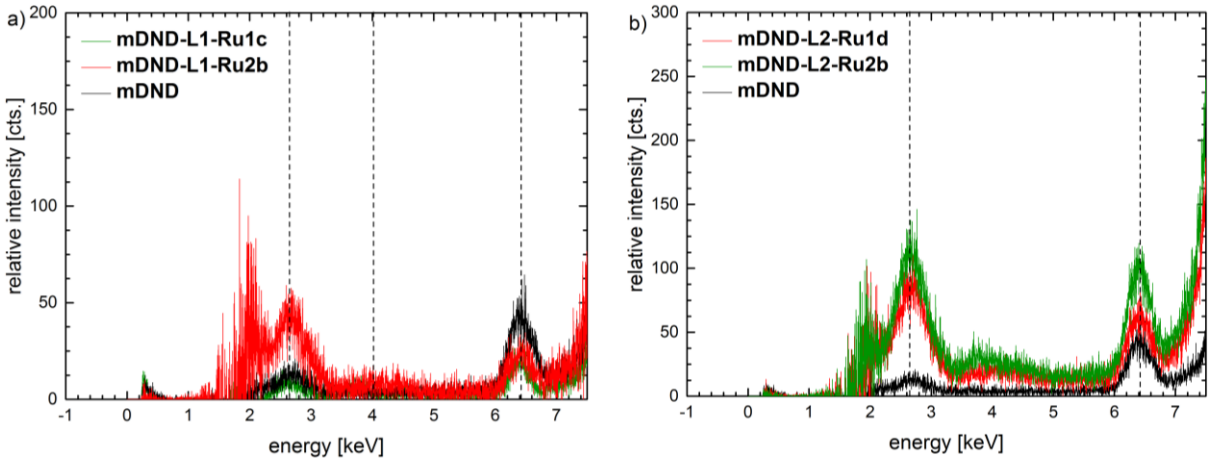

Fig. 130: XRF spectra of (a) **mDND**, **mDND-L1-Ru1c** and **mDND-L1-Ru2b** and of (b) **mDND**, **mDND-L2-Ru1d** and **mDND-L2-Ru2b**.

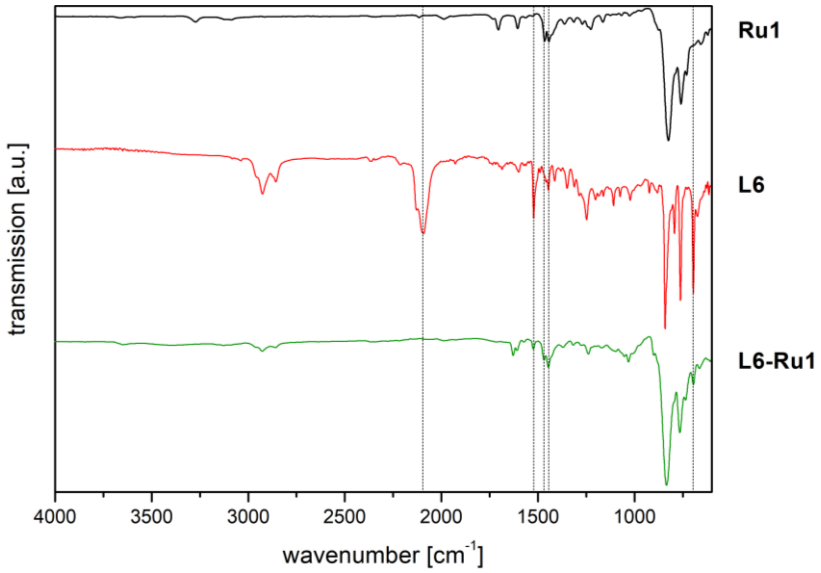

Fig. 131: Comparison of the ATR-IR spectra of reference system **L6-Ru1**, **Ru1** and linker **L6**.

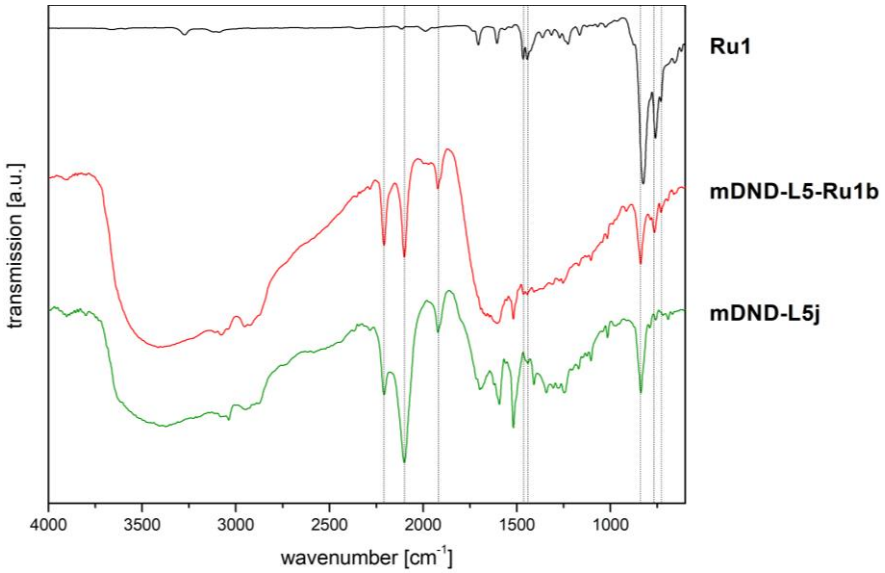

Fig. 132: IR spectra of **mDND-L5j**, **mDND-L5-Ru1b** (DRIFT) and **Ru1** (ATR-IR).

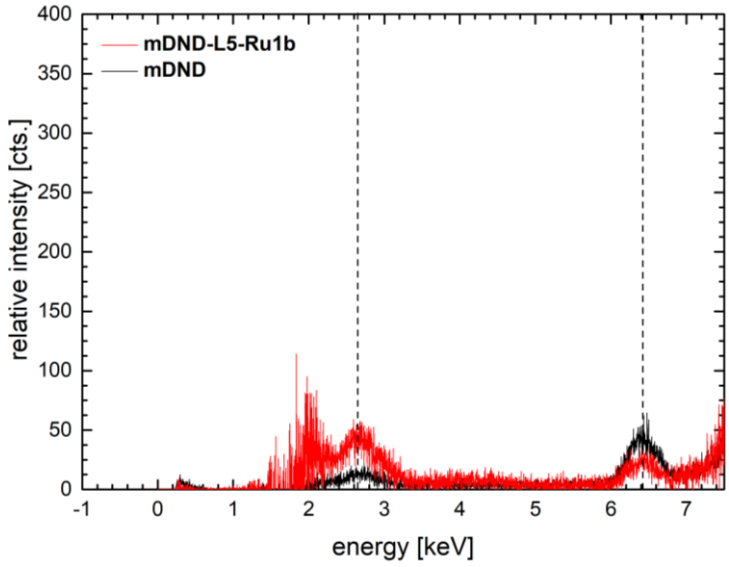

Fig. 133: XRF spectra of **mDND** and the Ru-functionalized particles **mDND-L5-Ru1b**.

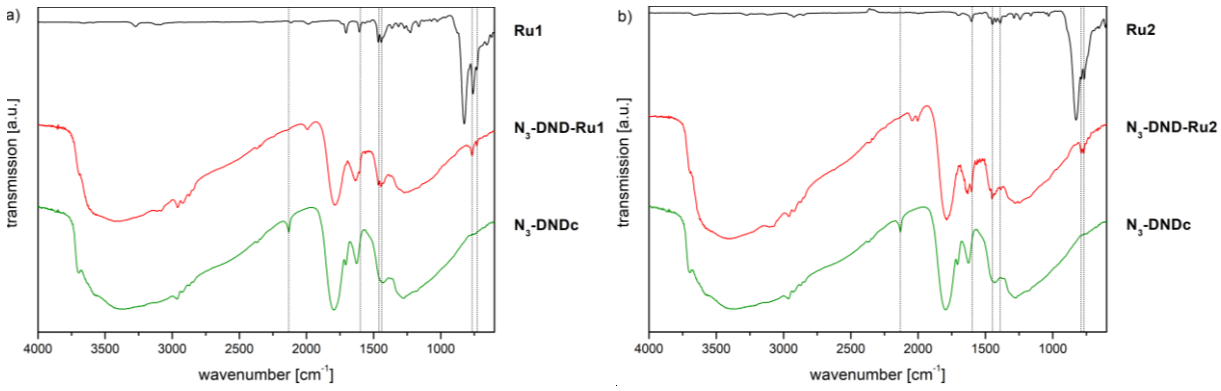

Fig. 134: IR spectra of (a) **N_3-DNDc**, **N_3-DND-Ru1** (DRIFT) and **Ru1** (ATR-FTIR) and of (b) **N_3-DNDc**, **N_3-DND-Ru2** (DRIFT) and **Ru2** (ATR-FTIR).

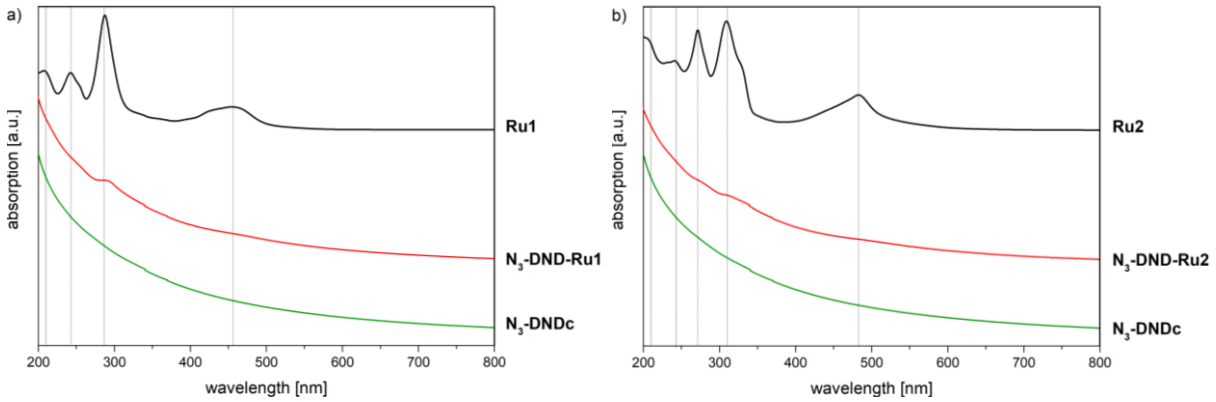

Fig. 135: UV/Vis spectra of (a) **N_3-DNDc**, **N_3-DND-Ru1** and **Ru1** and of (b) **N_3-DNDc**, **N_3-DND-Ru2** and **Ru2** (measurements in acetonitrile).

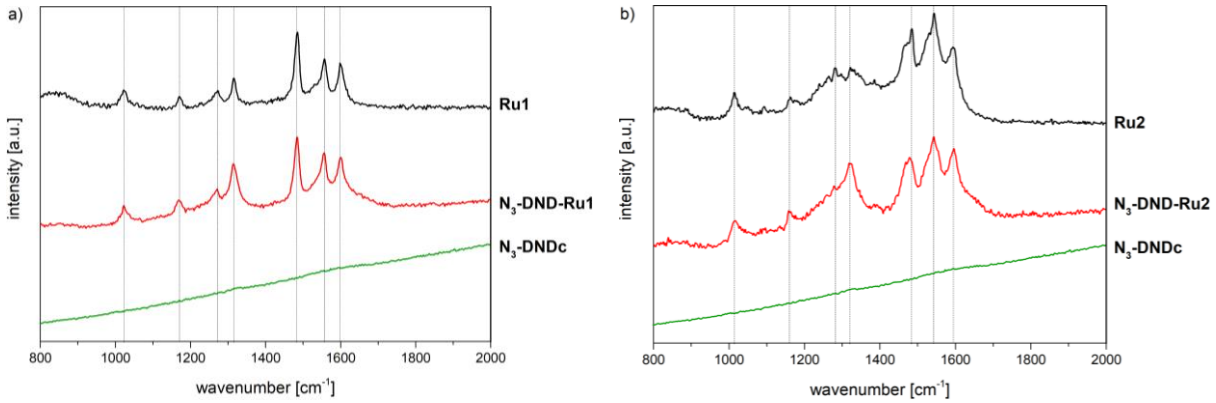

Fig. 136: Raman spectra of (a) **N_3-DNDc**, **N_3-DND-Ru1** and **Ru1** and of (b) **N_3-DNDc**, **N_3-DND-Ru2** and **Ru2** (measurements with 445 nm laser).

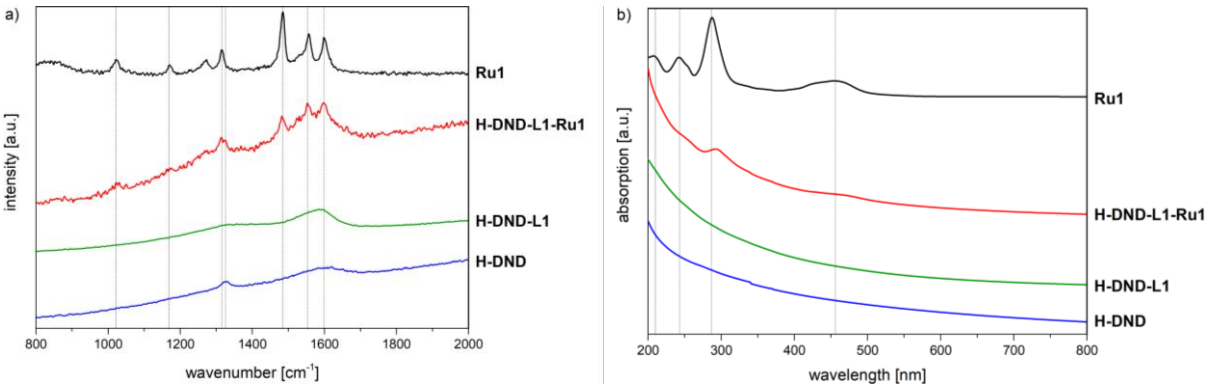

Fig. 137: a) Raman spectra of **H-DND**, **H-DND-L1**, **H-DND-L1-Ru1** and **Ru1** (measurements with 445 nm laser)and b) UV/Vis spectra of **H-DND**, **H-DND-L1**, **H-DND-L1-Ru1** and **Ru1** (measurements in acetonitrile)

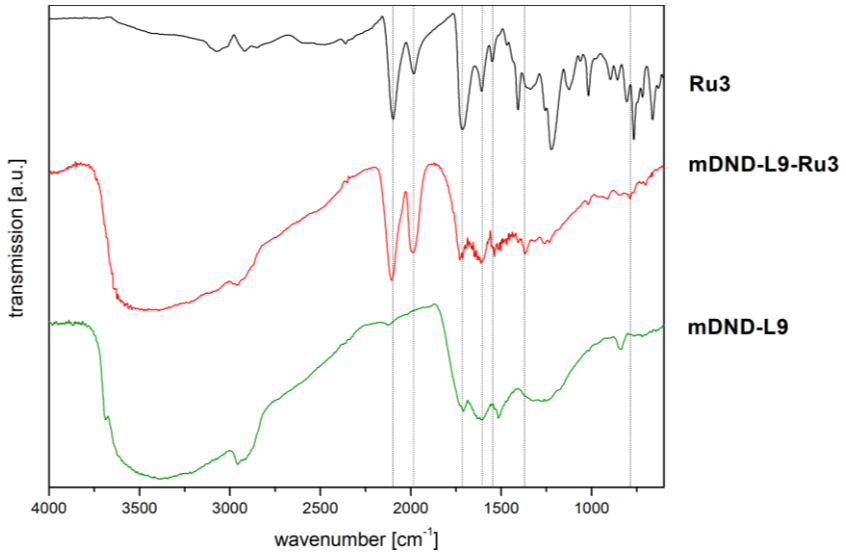

Fig. 138: IR spectra of **mDND-L9**, **mDND-L9-Ru3** (DRIFT) and **Ru3** (ATR-FTIR).

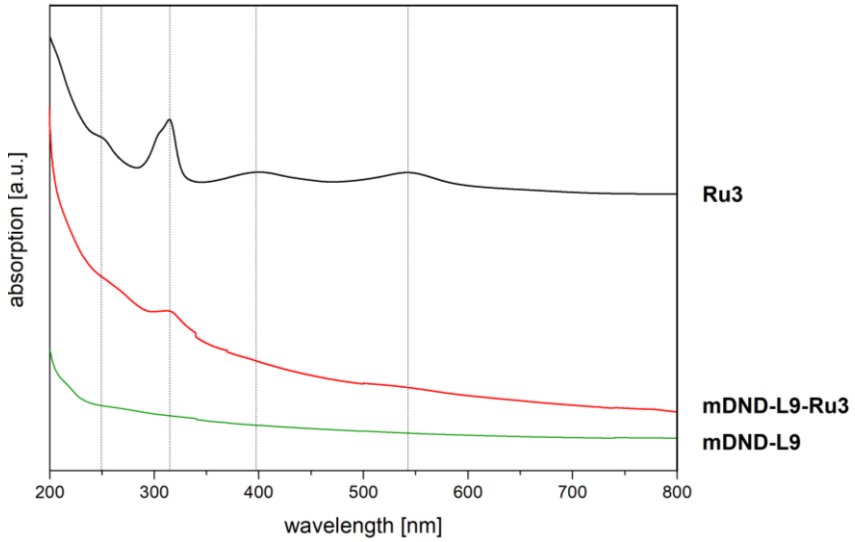

Fig. 139: UV/Vis spectra of **mDND-L9**, **mDND-L9-Ru3** and **Ru3** (measurements in MeCN).

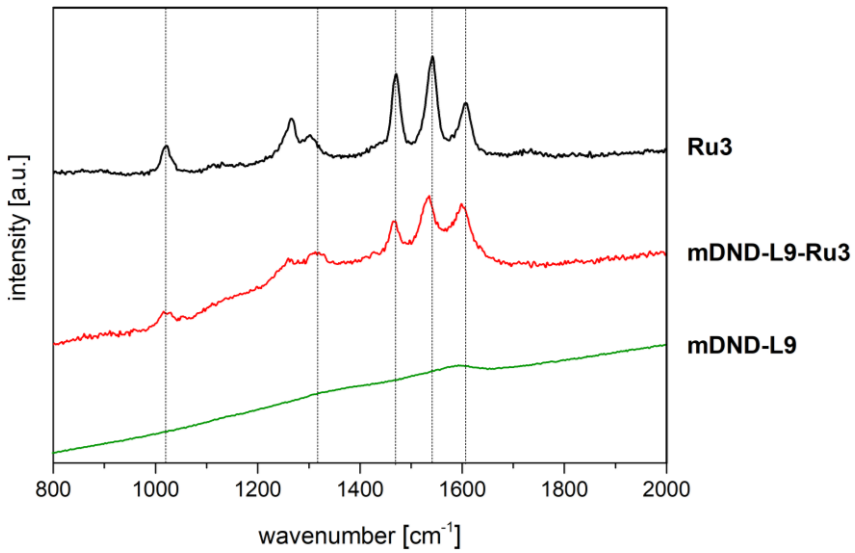

Fig. 140: Raman spectra of **mDND-L9**, **mDND-L9-Ru3** and **Ru3** (measurements with 532 nm laser).

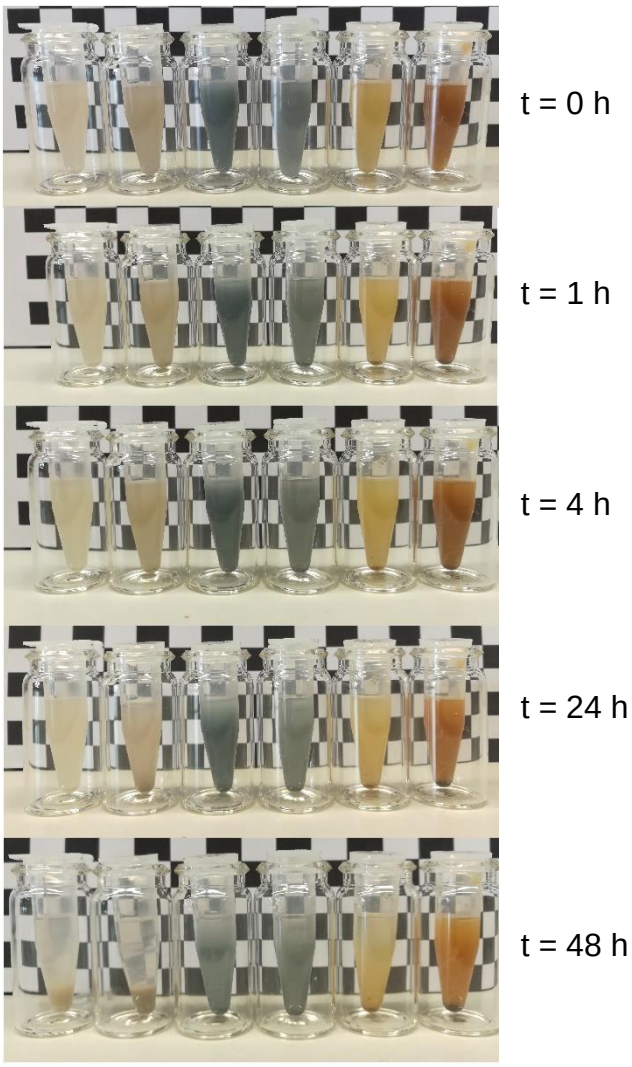

Fig. 141: Stability of **pDND**, **H-pDND$_{IAF}$**, **BND4**, **H-BND4$_{CEA}$**, **mDND-L5-Ru1b** and **mDND-L2-Ru1d** (from left to right) in N_{1123} BTA after different times.

Fig. 142: Stability of **pDND**, **H-pDND$_{IAF}$**, **BND4**, **H-BND4$_{CEA}$**, **mDND-L5-Ru1b** and **mDND-L2-Ru1d** (from left to right) in N_{1114} BTA/N_{1114} TCM (left) and N_{1123} BTA/N_{1114} TCM (right) after different times.

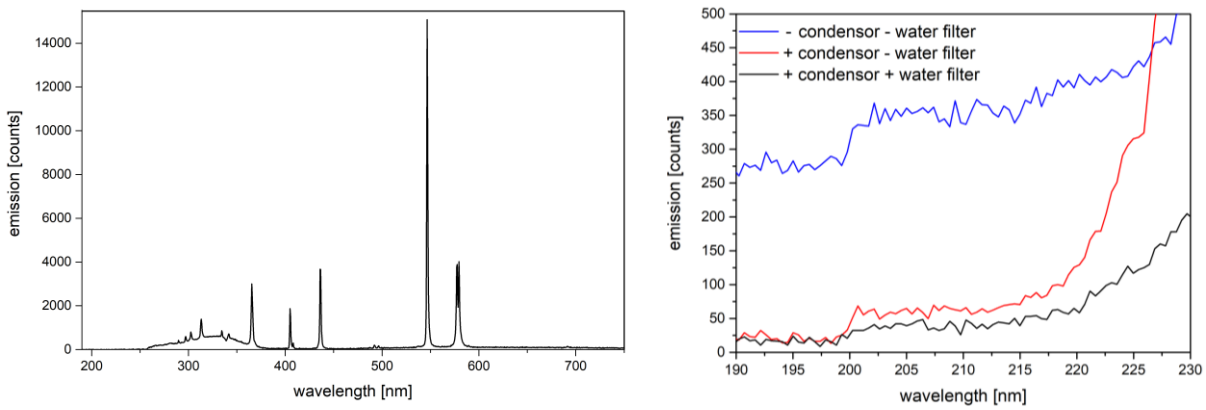

Fig. 143: Emission spectrum of 500 W Hg/Xe lamp (left) and zoom into deep UV region (190-230 nm) without optics (condenser, water filter).

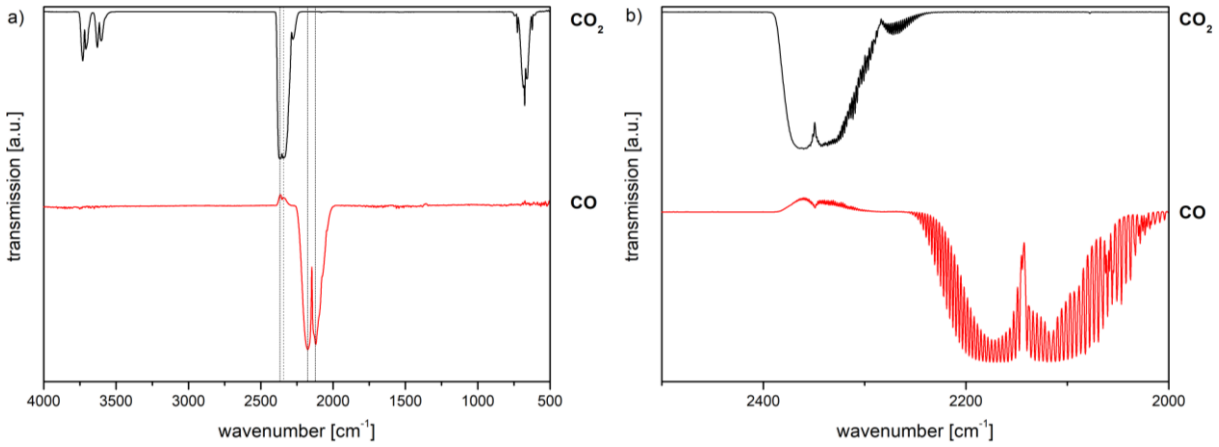

Fig. 144: FT-IR ATR spectra of (a) CO_2 and CO over the whole spectral range with a resolution of 4.0 cm^{-1} and (b) zoomed in the region of 2000-2500 cm^{-1} with a resolution of 1.0 cm^{-1}.

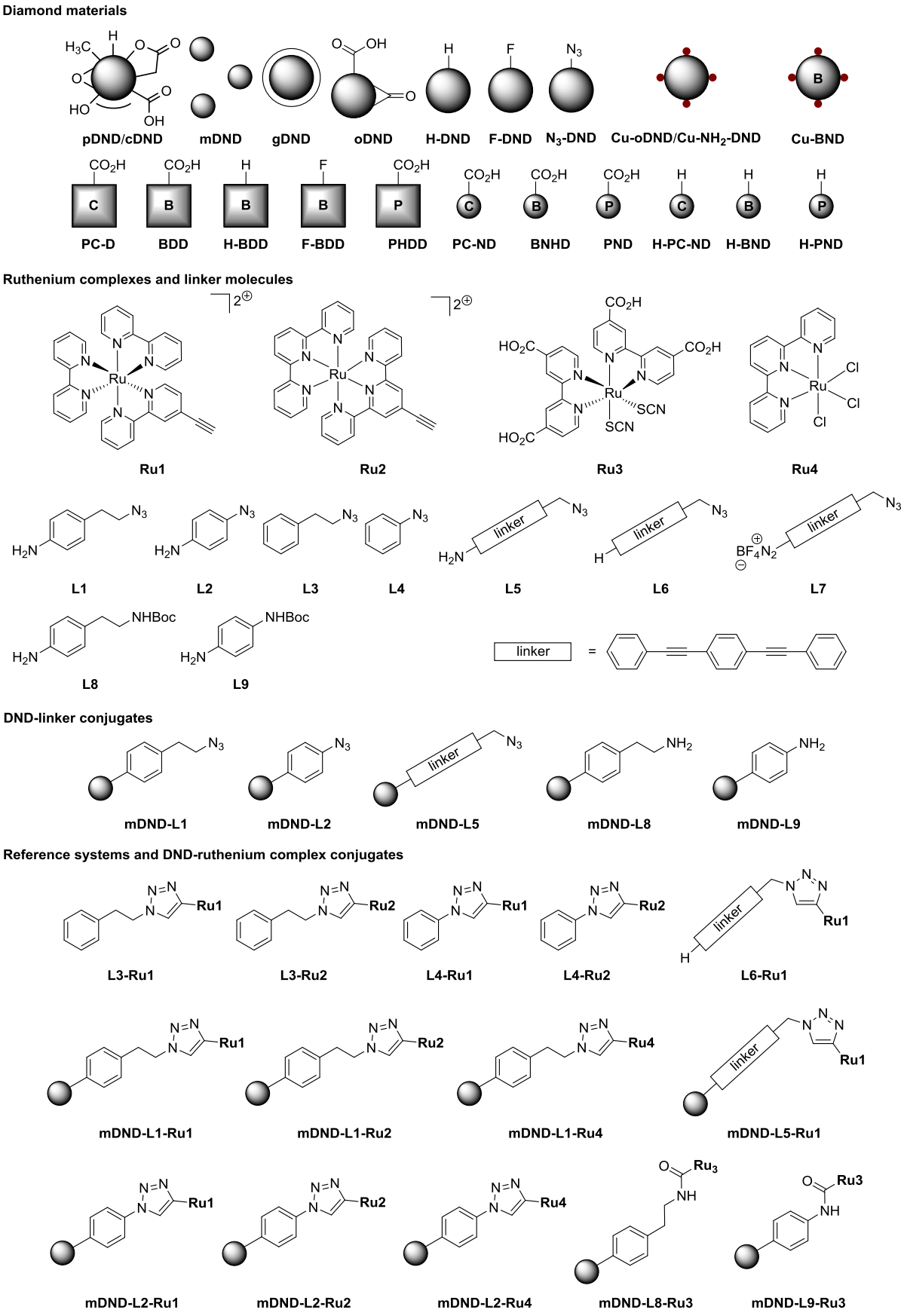

Fig. 145: Compilation of produced diamond materials, ruthenium complexes, linker and reference systems and ND-complex conjugates.